Journal of Engineering for Gas Turbines and Power

Published Quarterly by The American Society of Mechanical Engineers

VOLUME 118 • NUMBER 3 • JULY 1996

TECHNICAL PAPERS

(Contents continued)

L. Narayanaswami
Oak Ridge Universities Faculty
Research Participant;
Associate Professor,
Embry-Riddle Aeronautical University,
Daytona Beach, FL 32114

G. A. Richards
U.S. Department of Energy,
Morgantown Energy Technology Center,
Morgantown, WV 26507-0880

Pressure-Gain Combustion: Part I—Model Development

A model for aerodynamically valved pulse combustion is presented. Particular empha- sis is placed on using the model equations to identify characteristic length and time scales relevant to the design of pressure-gain combustors for gas turbine applications. The model is a control volume description of conservation laws for several regions of the pulse combustor. Combustion is modeled as a bimolecular reaction. Mixing between the fresh charge and the combustion products is modeled using a turbulent eddy time estimated from the combustor geometry and flow conditions. The model equations identify two characteristic lengths, which should be held constant during combustor scaleup, as well as certain exceptions to this approach. The effect of ambient operating pressure and inlet air temperature is also discussed.

1 Introduction

Pressure-gain combustion is an alternative to conventional (steady) combustion in gas turbines. Steady combustion is al- ways accompanied by a loss in stagnation pressure. This loss occurs during the free-expansion as air enters the combustor and also as heat is added to the flowing gases. The loss in pressure can amount to several percent of the compressor dis- charge pressure, and produces a penalty in overall cycle effi- ciency.

It is possible to produce a pressure-gain during combustion by confining the burning process. For example, the Otto cycle piston-engine draws air from ambient pressure and burns the fuel and air in a fixed volume, producing a significant pressure rise. The subsequent piston motion extracts useful work from the gas expansion. This is different from a gas turbine, where combustion occurs at nearly constant (static) pressure, without producing useful work during the gas expansion associated with heat addition. Downstream of the combustor, energy is extracted from gas expansion in the turbine rotor, but the unrestrained expansion in the combustor produces an appreciable loss in thermodynamic availability. This loss has been noted by various authors, and has been the motivation for novel compound engine cycles, typically using a piston engine as a topping cycle for a turbine. The piston engine serves to capture the expansion work from the combustion process, and the turbine extracts additional work from the exhaust stream. See the review article by Haw- thorne (1994) for an excellent discussion of these issues. A small number of compound cycle engines have been built, dem- onstrating good performance; however, the complexity of com- bined turbine and piston engines has prevented their widespread acceptance.

A different approach to capturing the benefits of confined combustion in gas turbines is to use a pulse combustor. A sche- matic of the unsteady processes occurring in a pulse combustor is shown in Fig. 1. Oscillating gas motion is used to confine the combustion process. With the correct timing of the unsteady gas flows, the fluid motion is analogous to the piston and valve assembly in a piston engine, yet without the complexity of mechanical parts. Combustion occurs (approximately) as a con- stant volume process, producing a higher stagnation pressure than the inlet air. Subsequent wave motion exhausts the combus- tion products, then recharges and compresses the combustor for the next cycle. On a time-averaged basis, the flow of gas is

from left to right in Fig. 1. In effect, the combustor pumps the air from left to right, meaning the time averaged stagnation pressure at the exhaust (P_e) must be greater than the inlet stag- nation pressure (P_i). Because of the increased stagnation pres- sure in the exhaust stream, this process has been termed *pres- sure-gain combustion.*

Early attempts to improve gas turbine efficiency using pres- sure-gain combustion are reported by Porter (1958), Thring (1961), and Muller (1971). More recently, Kentfield and co- workers produced a series of articles describing their successful development of a pressure-gain combustor suitable for a small gas turbine; see Kentfield and Yerneni (1985), Kentfield and O'Blenes (1987), Kentfield and Fernandes (1990). Based on their experiments, as much as 4 percent pressure gain is possi- ble. Lampinen et al. (1992) analyzed the potential for gas tur- bine cycle improvement using pressure gain combustion. Based on their analytic model, they concluded that pressure-gain com- bustion could improve cycle efficiency by as much as 8 percent in certain applications.

While a significant performance database has been produced by Kentfield and Fernandes (1990), the results are limited to a specific combustor design, and there is little guidance on how to scale the results for other applications and operating conditions. Aside from Kentfield's work, other recent investiga- tion of pulse combustion (e.g., Barr et al., 1993) have focused on the physics of the combustion process in mechanically valved pulse combustors. Detailed numerical models have been used to investigate complex features of the combustion process, but have provided little information about design or scaleup, especially for pressure-gain. Very few papers have addressed the valveless combustor, which is expected to form the basis of any reliable gas turbine application.

As part of the U.S. Department of Energy's Advanced Tur- bine System initiative (Geiling, 1993), investigators at the Mor- gantown Energy Technology Center are evaluating the use of pressure-gain combustion in advanced turbine systems. Techni- cal issues with unsteady flow and system control are under evaluation, with ongoing experimental work aimed at gathering data on pressure-gain performance (Gemmen et al., 1994).

This paper presents a control-volume model of a valveless pulse combustor. The essential features of the combustor geom- etry, combustion reaction rate, mixing process, and unsteady gas motion are all accounted for. The governing equations presented identify key characteristic length and time scales, while (nu- meric) solution of the equations provides a relatively efficient prediction of pulse combustor behavior. The equations identify the role of certain operating parameters of interest to gas turbine design, such as operating pressure, and inlet air temperature. A companion paper (Part II) successfully compares predictions

Copyright © 1996 by ASME

Principles of Operation
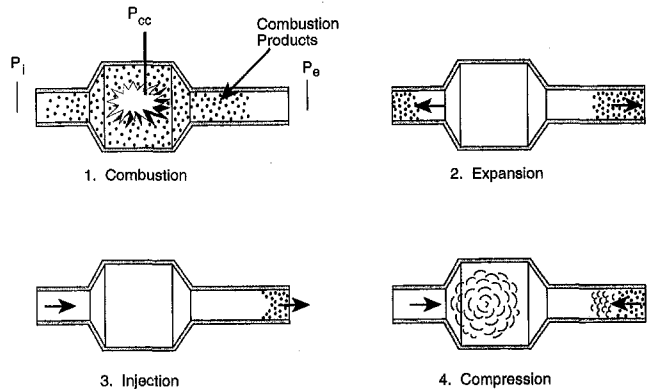
Fig. 1 Operation of an aerodynamically valved pulse combustor. The combustion event (1) raises the pressure in the combustion chamber (P_{cc}), forcing gas out of the inlet pipe and tailpipe (2), the momentum of fluid in the tailpipe draws fresh air through the inlet (3), with a subsequent compression of gases in the combustion chamber (4). On a time average, the flow is from left to right.

of the model to laboratory measurements, and confirms that the length scales identified here may be useful for scaleup.

2 Model Development

A schematic of processes occurring in a single pulse combustor cycle is shown in Fig. 2. For reference, the stations u, i, e, and d are identified with the upstream, inlet, exit, and downstream locations. Throughout this paper, the combustion zone

is defined as the region between stations i and e. It is assumed that combustion occurs only in this region, although the equations presented here can be modified to allow for combustion in the inlet and tailpipe regions as well. As shown in Fig. 2(a), air may be either drawn in or driven out through both the inlet pipe and the tailpipe. It is assumed that the fresh air is separated from the combustion gases by a contact surface, which moves through the tailpipe and inlet regions. The combustion gases are shown as shaded regions composed of fuel, air, and combustion products. Within the combustion zone, fuel and oxygen react at a rate determined by a one-step Arrhenius kinetic mechanism described below. Gaseous fuel is supplied to the shaded region in the combustion zone at a fixed rate, $\dot{m}_f$.

Figure 2(b) represents the induction of fresh air into the combustion zone. The fresh air is mixed with the combustion gases at the rate $\dot{m}_m$. This mixing rate represents the mass of fresh air that is mixed per unit time into the burning gases. The mixing rate does not necessarily equal the rate at which air enters the combustor. For example, if $\dot{m}_m$ is small compared to the rate at which gases enter through station i, a pocket of fresh air (g-region, Fig. 2(b)) will form within the combustor. This pocket is shown as a single region, but the development used here is general enough to cover multiple gas parcels within the combustor. For reference, the pocket of fresh air within the combustion zone is labeled as the g-region, and the hot gases within the combustion zone are denoted as the hot region, or h-region. The g and h-regions extend only to stations i and e; they do not include gases within the inlet or tailpipe region.

As air is mixed into the h-region, the combustion reaction accelerates, raising the temperature of the h-region and producing a pressure rise in both the g and h-regions. Both the g and h-regions are characterized by the same uniform pressure P.

——— Nomenclature ———

Note: The text uses an overbar to denote the normalized counterpart of variables listed here. The normalizing factor is listed with the variables below.

A_i = cross-sectional area of the inlet

A_s = surface area of the combustion zone

A_{sa} = surface area of the inlet pipe, ambient gas region

A_{sb} = surface area of the inlet, burned gas region

A_{tp} = cross-sectional area of the tailpipe

C_p = constant pressure specific heat = 1350 J/kg/K

C_v = constant volume specific heat = 1063 J/kg/K

e = internal energy per unit mass, subscripts a, b, u, i for ambient (a), burned (b), upstream (u), and inlet (i); normalized by $C_v T_A$

F = unit step function defined by Eq. (14)

G = unit step function, defined by Eq. (15)

h = heat transfer coefficient for the combustion zone walls = 120 W/m^2/K

K = kinetic coefficient, Eq. (19) = 1.576×10^9 s^{-1}

L_a = length of the "unburned" region of inlet; normalized with the reference length L_{ri}

L_b = length of the "burned" region of inlet; normalized with the reference length L_{ri}

L_{ed} = the eddy length, Eq. (28)

L_i = total inlet length = $L_a + L_b$; normalized with the reference length L_{ri}

L_{ri} = reference inlet length = V_c/A_i

$L_{r,tp}$ = reference tailpipe length = V_c/A_{tp}

$\dot{m}_e$ = mass flow rate through the combustion zone exit station e

$\dot{m}_f$ = mass flow rate of fuel

$\dot{m}_i$ = mass flow rate through the combustion zone inlet station i

$\dot{m}_m$ = mass mixing rate of fresh air with burning gases

$\dot{m}_u$ = mass flow rate through the upstream inlet station u

P = pressure in the combustion chamber; normalized with the ambient pressure P_A

P_A = ambient pressure, upstream of the combustor

P_i = pressure at the combustion zone inlet station i; normalized by P_a

P_{STD} = standard pressure = 101 kPa, used as a reference in the reaction rate term, Eq. (19)

P_u = pressure at the upstream end of the inlet pipe (station u); normalized by P_a

$\dot{Q}$ = heat release per unit volume

R = specific ideal gas constant = 287 J/kg/K

$S_{a,b}$ = shear stress at the inlet pipe wall calculated from Schlichting (1979) pipe formula, subscript a = ambient gas, b = burned gas; normalized by the ambient pressure P_A

S_R = stoichiometric ratio for the mass of oxygen consumed per mass of fuel burned

T_A = ambient temperature, upstream of the combustor

$\bar{T}_{act}$ = dimensionless activation temperature, Eq. (19), 50

T_{oe} = combustion zone exit stagnation temperature (station e); normalized with T_A

T_{of} = fuel supply stagnation temperature; normalized with T_A

T_{oi} = combustion zone inlet stagnation temperature (station i); normalized with T_A

T_{STD} = standard temperature, 300 K, used as a reference for reaction rate, Eq. (19)

T_w = combustion zone wall temperature = 1200 K; normalized with T_A

V_c = combustion zone volume

V_{ed} = eddy volume, Eq. (29)

V_g = g-region (cold) volume; normalized with V_c

Fig. 2(a–c) Schematic of processes occurring in an aerovalve pulse combustor

As the pressure rises, the inlet flow will reverse, as shown in Fig. 2(c). At this point, it is assumed that gases leaving through station i are drawn from the h-region, while any remaining g-region gas continues to mix with the combustion gases.

Control volume conservation laws for each of the various regions are written next. The development that follows is similar to the one proposed by Richards et al. (1993). Similar assumptions are used here, including constant specific heat, ideal gas behavior, and uniform conditions within each region. The development is based on the integral form of the conservation laws as presented in the literature (see, e.g., Moody, 1990), and also by Richards et al. (1993). Assuming uniform conditions within each region, the volume and surface integrals are reduced to

algebraic expressions, resulting in a set of first-order differential equations.

Conservation Laws Within the Combustion Zone. A conservation of energy equation is developed for the combined g and h-region by accounting for energy entering with the inlet mass flow, fuel mass flow, and exit mass flow, denoted $\dot{m}_i$, $\dot{m}_f$, and $\dot{m}_e$. These flows enter (or exit) with stagnation temperatures T_{oi}, T_{of}, and T_{oe}, respectively. The heat release per unit volume is $\dot{Q}$ in the h-region volume (V_h). Heat loss occurs by convection through a convection coefficient h to the combustion zone walls with surface area A_s, at some specified temperature T_w. Noting that ideal gas law relations imply $P = (\gamma - 1)\rho e$, and employing the assumption that the pressure is constant throughout the combustion zone volume (V_c), the energy balance for the combined g and h-region is

$$\frac{V_c}{\gamma - 1} \frac{dP}{dt} = \dot{m}_i C_p T_{oi} + \dot{m}_f C_{pf} T_{of}$$
$$- \dot{m}_e C_p T_{oe} + \dot{Q} V_h - h A_s (T_h - T_w). \quad (1)$$

The ratio of specific heats γ represents an average for the properties of air and combustion products.

Equation (1) is normalized by dividing by the ambient pressure (P_A) and combustion zone volume (V_c). Also temperatures are normalized by the ambient temperature T_A. The ambient pressure and temperature represent conditions upstream of the entire combustor (i.e., upstream of station u) and correspond to the compressor discharge conditions in a gas turbine. The h-region volume (V_h) is normalized with the combustor volume (V_c). Other variables are normalized as indicated in the nomenclature. Denoting the normalized values by an overbar, modest algebraic manipulation of Eq. (1) leads to:

$$\frac{d\bar{P}}{dt} = \gamma \left[\frac{\bar{T}_{oi}}{\tau_i} + \frac{\bar{T}_{of}}{\tau_f} \frac{C_{pf}}{C_p} - \frac{\bar{T}_{oe}}{\tau_e} \right]$$
$$+ \frac{\bar{V}_h}{\tau_c} + \frac{(\gamma - 1)}{\tau_{HT}} (\bar{T}_w - \bar{T}_h). \quad (2)$$

The various characteristic times appearing in Eq. (2) are defined in Eqs. (3)–(7) below:

Nomenclature (cont.)

V_h = h-region (hot) volume; normalized with V_c

t_Δ = large eddy time, Eq. (28)

u = velocity; normalized with u_r

u_r = reference velocity; $\sqrt{RT_A}$

U_{mean} = mean inlet velocity; see discussion below Eq. (28)

$Y_{fa\,or\,b}$ = fuel mass fraction in the ambient (a) or burned (b) inlet region

Y_{fh} = fuel mass fraction in the h-region

Y_{fi} = fuel mass fraction, combustion zone inlet, station i

$Y_{ox,a}$ = oxygen mass fraction in the ambient (a) inlet region (note $Y_{ox,a}$ = $Y_{ox,A}$)

$Y_{ox,A}$ = ambient oxygen mass fraction; upstream of the combustor

$Y_{ox,b}$ = oxygen mass fraction in the burned inlet region

$Y_{ox,g}$ = oxygen mass fraction in the g-region

$Y_{ox,h}$ = oxygen mass fraction in the h-region

$Y_{ox,i}$ = oxygen mass fraction, combustion zone inlet, station i

γ = ratio of specific heats = 1.27

ΔH_f = fuel heat of combustion per unit mass = 5×10^7 J/kg

ρ = combustion zone gas density; normalized with the ambient density ρ_A

ρ_A = the ambient air density, corresponding to conditions upstream of the combustor

ρ_a = density of the ambient gas region in the inlet; normalized with the ambient density ρ_A

ρ_b = density of the burned gas region in the inlet; normalized with the ambient density ρ_A

ρ_i = combustion zone inlet density (station i); normalized with the ambient density ρ_A

ρ_u = inlet pipe upstream density (station u); normalized with the ambient density ρ_A

τ_c = combustion time, Eqs. (6) and (19)

τ_e = exit flow time, Eq. (5)

τ_f = fuel flow time, Eq. (4)

τ_{HT} = heat transfer time, Eq. (7)

τ_i = inlet flow time, Eq. (3)

τ_m = mixing time, Eq. (8)

$\tau_{m,f}$ = fast mixing time, Eq. (29)

$\tau_{m,s}$ = slow mixing time; see the discussion following Eq. (29)

τ_{ri} = reference inlet time; $\tau_{ri} = L_{ri}/u_r = L_{ri}/\sqrt{RT_A}$

τ_u = flow time associated with station u, analogous to Eq. (3) using $\dot{m}_u$, the mass flow at station u

$$\tau_i = \frac{\rho_A V_c}{\dot{m}_i} \quad \text{(inlet flow time)} \tag{3}$$

$$\tau_f = \frac{\rho_A V_c}{\dot{m}_f} \quad \text{(fuel flow time)} \tag{4}$$

$$\tau_e = \frac{\rho_A V_c}{\dot{m}_e} \quad \text{(exit flow time)} \tag{5}$$

$$\tau_c = \frac{P_A}{\dot{Q}\,(\gamma - 1)} \quad \text{(combustion time)} \tag{6}$$

$$\tau_{HT} = \frac{\rho_A R V_c}{h A_s} \quad \text{(heat transfer time)} \tag{7}$$

For later use, we also define the mixing time:

$$\tau_m = \frac{\rho_A V_c}{\dot{m}_m} \quad \text{(mixing time)} \tag{8}$$

Notice that the reciprocal of these time scales enter into Eq. (2) and represent rates for the various processes. Also note that τ_i, τ_e, τ_c, and τ_m are not constants but are calculated from other equations presented later. The inlet and exit flow times have negative values when the flow reverses in either the inlet or tailpipe; i.e., when the flow is moving from right to left at station i or station e.

The approach to developing the remaining conservation laws for the combustion region is similar to that used for the energy Eq. (2). Full details of this control-volume analysis for energy, mass, and species conservation can be found in Richards et al. (1994). The resulting equations are a balance of a storage term versus input, exit, and generation. Unit step functions F and G are defined below to distinguish whether the combustor is expelling h-gases backward through the inlet, or ingesting fresh charge. The balance equations are:

Overall Combustor Mass Conservation:

$$\frac{d\bar{p}}{dt} = \frac{1}{\tau_i} + \frac{1}{\tau_f} - \frac{1}{\tau_e} \tag{9}$$

g-Region Mass Conservation:

$$\frac{d}{dt}(\bar{p}_g \bar{V}_g) = F\frac{1}{\tau_i} - \frac{1}{\tau_m} \tag{10}$$

g-Region Energy Conservation:

$$\frac{d}{dt}(\bar{P}\bar{V}_g) = F\frac{\bar{T}_{oi}}{\tau_i} - \frac{\bar{T}_g}{\tau_m} + \frac{\gamma - 1}{\gamma}\,\bar{V}_g\,\frac{d\bar{P}}{dt} \tag{11}$$

h-Region Species; f = fuel, o = oxygen:

$$\frac{d}{dt}(\bar{p}_h Y_{fh} \bar{V}_h)$$
$$= \frac{1}{\tau_f} + Y_{fh}\left[-\frac{1}{\tau_e} + \frac{1}{\tau_i}(1 - F)\right] - \frac{C_v T_A}{\Delta H_f}\frac{\bar{V}_h}{\tau_c} \tag{12}$$

$$\frac{d}{dt}(\bar{p}_h Y_{ox,h} \bar{V}_h)$$
$$= Y_{ox,A}\frac{G}{\tau_m} + Y_{ox,i}\frac{1 - GF}{\tau_i} - Y_{ox,h}\frac{1}{\tau_e} - \frac{C_v T_A}{\Delta H_f}\frac{\bar{V}_h}{\tau_c}S_R \tag{13}$$

Unit Step Functions F and G:

$$F = \begin{cases} 1 & \text{when the inlet flow velocity is positive (or zero)} \\ 0 & \text{when the inlet flow velocity is negative} \end{cases} \tag{14}$$

$$G = \begin{cases} 1 & \text{when the } g\text{-region is present} \\ 0 & \text{when the } g\text{-region is absent} \end{cases} \tag{15}$$

In addition to these equations, the normalized form of the ideal gas law and two relations between the volume and density of g and h-regions are needed to complete the combustion zone description:

$$\bar{P} = \bar{p}_j \bar{T}_j \ (j = g \text{ or } h) \tag{16}$$

$$\bar{V}_g + \bar{V}_h = 1 \tag{17}$$

$$\bar{p}_g \bar{V}_g + \bar{p}_h \bar{V}_h = \bar{p} \tag{18}$$

Before introducing the conservation laws for the inlet and tailpipe, it is reiterated that this set of equations depends on characteristic times that vary throughout the combustion cycle and are not constants. The inlet and exit times have instantaneous values determined from conservation laws in the inlet and tailpipe. The mixing time is described later. The combustion time is determined from an Arrhenius rate law for bimolecular reaction of fuel and oxygen in the h-region. The form of this rate law and the specific rate constants are taken from Kretschmer and Odgers (1972). After considerable algebraic manipulation of the rate law in Kretschmer and Odgers (1972), the combustion time is

$$[\tau_c]^{-1} = K(\gamma - 1)\left(\frac{P_A}{P_{STD}}\right)\left(\frac{T_{STD}^{0.5}}{T_A^{1.5}}\right)\frac{\Delta H_f}{R}$$
$$\times \bar{P}^2\,\bar{T}_h^{-1.5}\,Y_{ox}\,Y_f\exp(-\bar{T}_{act}/\bar{T}_h). \tag{19}$$

Values for the various constants are included in the nomenclature. P_{STD} and T_{STD} represent standard conditions of 101 kPa and 300 K, respectively. Again, the ambient conditions P_A and T_A represent conditions of the air supplied to the combustor; these correspond to conditions at the compressor discharge in a gas turbine.

Conservation Laws Within the Inlet and Tailpipe Regions. The tailpipe and inlet equations are essentially identical in form and will be described below for the inlet only. Analogous expressions apply to the tailpipe, except as noted.

The gases within the inlet are treated as a slug flow with velocity u. A contact surface may exist within the inlet when fresh air is drawn from the ambient surroundings (Fig. 2a) and flows to station i. For purposes of normalization, it is convenient to identify a reference inlet length L_{ri} as the ratio of the combustor volume and the inlet cross-sectional area (see the nomenclature). Also, a reference velocity u_r is defined as $\sqrt{RT_A}$. Then, letting $\bar{L}_a$ denote the normalized length between station u and the contact surface, the contact surface motion is tracked via these kinematic relations:

$$\frac{d\bar{L}_a}{dt} = \frac{\bar{u}}{\tau_{ri}}; \quad \bar{L}_b = \bar{L}_i - \bar{L}_a, \tag{20}$$

where τ_{ri} is a reference time for the inlet processes, as defined in the nomenclature. The regions on either side of the contact surface are characterized by a single value for all properties. The subscript "a" corresponds to gases drawn from the ambient, while the subscript "b" indicates properties of the burned gas region. The combustion reaction is assumed to be quenched in the burned region; the concentrations of any residual fuel and oxygen are tracked by the model. Conservation of mass in the ambient and burned region have the following forms, respectively:

$$\frac{d\bar{p}_a}{dt} = \frac{\bar{p}_u - \bar{p}_a}{\tau_{ri}}\frac{\bar{u}}{\bar{L}_a} \tag{21}$$

$$\frac{d\bar{p}_b}{dt} = \frac{\bar{p}_b - \bar{p}_i}{\tau_{ri}}\frac{\bar{u}}{\bar{L}_b}. \tag{22}$$

Next, a momentum balance equation is written for the combined ambient and burned regions. This equation balances the change of momentum for both regions with the corresponding friction and pressure forces acting on the slug of fluid. The friction forces are calculated by multiplying the wall shear stresses $\bar{S}_a$ and $\bar{S}_b$ (normalized by the ambient pressure) by the surface areas A_{sa} and A_{sb} in each region. These stresses are calculated using a conventional friction coefficient f as defined by Schlichting (1979) (i.e., $S_a = f\rho_a u^2/8$). After some algebraic manipulations using Eqs. (20)–(22), the momentum balance is

$$(\bar{\rho}_a \bar{L} + \bar{\rho}_b \bar{L}_b)\frac{d\bar{u}}{dt} = \frac{\bar{P}_u - \bar{P}_i}{\tau_{ri}} - \frac{\bar{S}_a A_{sa} + \bar{S}_b A_{sb}}{\tau_{ri}A_i}. \quad (23)$$

An individual energy balance is written next for the ambient and burned regions. The energy balance for these two regions must account for pressure forces performing work at each end of the fluid regions a and b. The pressures at stations i and e are determined from boundary conditions described later. The pressure at the contact surface is calculated from a momentum balance applied to regions a and b *individually,* in contrast to the overall momentum balance for both regions given by Eq. (23). Using the resulting expression for the contact surface pressure, and combining with Eqs. (20)–(22), the energy balance for each region is

$$\bar{\rho}_a \bar{L}_a \frac{d\bar{e}_a}{dt} = \frac{\bar{e}_u - \bar{e}_a}{\tau_u} + \frac{\bar{S}_a A_{sa}\bar{u}}{\tau_{ri}A_i} \quad (24)$$

$$\bar{\rho}_b \bar{L}_b \frac{d\bar{e}_b}{dt} = \frac{\bar{e}_b - \bar{e}_i}{\tau_i} + \frac{\bar{S}_b A_{sb}\bar{u}}{\tau_{ri}A_i} \quad (25)$$

Here, τ_u is analogous to Eq. (3), using $\dot{m}_u$ instead of $\dot{m}_i$. Finally, species conservation is written for fuel and oxygen in the burned region, assuming again that the combustion reaction is quenched in the burned region. Although the reaction is quenched, the species mass fractions can change via changing boundary conditions at station i. Combining with mass conservation Eqs. (20)–(22), the species equations are

$$\bar{\rho}_b \bar{L}_b \frac{dY_{fb}}{dt} = \frac{Y_{fb} - Y_{fi}}{\tau_i} \quad (26)$$

$$\bar{\rho}_b \bar{L}_b \frac{dY_{ox,b}}{dt} = \frac{Y_{ox,b} - Y_{ox,i}}{\tau_i} \quad (27)$$

Equations (20)–(27) describe the behavior of the inlet. A similar set of expressions applies to the tailpipe. A simple change of subscripts will produce the tailpipe equations and thus they will not be presented here.

Boundary conditions for the various regions are specified in the following manner: Given the assumption of isentropic acceleration *from* the combustor *into* either pipe, the velocity and pressure are related by a transcendental equation. It is thus necessary to root-find iteratively to produce boundary conditions that satisfy both the combustion zone and tailpipe zone equations. For flow *into* the combustor *from* either pipe, no iteration is needed because the fluid is assumed to enter the combustor at the combustor pressure; i.e., a free-jet entrance. Similar comments apply to boundary conditions at stations u and d.

In summary, conservation laws for each zone of the pulse combustor have been developed. Equations (2), (9)–(13), and (16)–(18) describe the g and h-regions in the combustion zone. Equations (20)–(27) apply to the inlet, with an analogous set for the tailpipe. To complete a solution to these equations, it is necessary to model the mixing process.

Mixing Model. The mixing process is represented in the governing equations by the mixing rate $\dot{m}_m$ as used in Eq. (8). Both comprehensive and approximate fluid mechanic models

t_a : Contact surface enters the combustor

t_b : Mixing rate increases

t_c : g-Region volume drops to zero

t_d : Inlet flow reverses
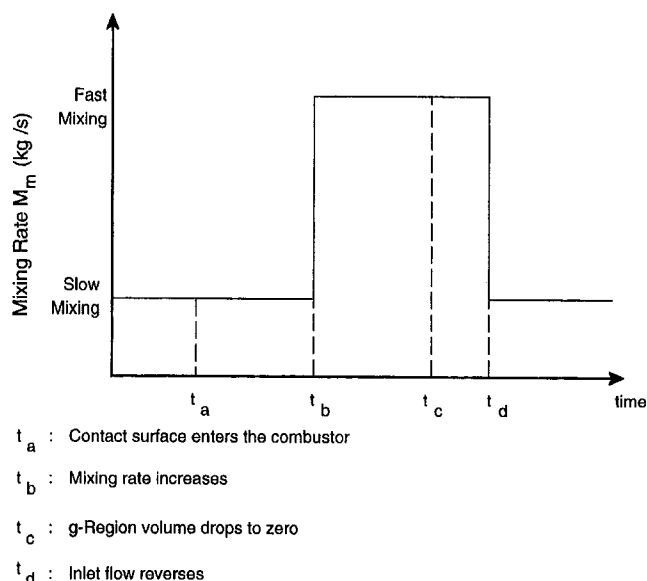
Fig. 3 The mixing process, alternating between the fast and slow mixing rates

have been used to predict $\dot{m}_m$ in specific pulse combustor simulations (Barr et al., 1993). While a similar approach could be used here, a phenomenological model is shown to be adequate for describing experimental data in Part II of this paper. The model is based on the work of Broadwell and Breidenthal (1982), who describe mixing as a two-step process. The first step reduces large fluid eddies to a small scale, with relatively slow mixing between species. The second step is a fast mixing process, where small eddies are rapidly mixed by molecular diffusion. Figure 3 represents this two-step process in a pulse combustor. At time t_a, the contact surface enters the combustor, supplying fresh air to form the g-region. This fresh air mixes slowly while the initial eddy size is reduced. Fast mixing commences at time t_b and continues until the g-region is consumed at time t_c. Depending on the mixing rate and flow rate at station i, the g-region volume may disappear before the inlet flow reverse ($t_c < t_d$ as shown). Conversely, with different flow and mixing rates, some g-volume may continue to mix after the inlet flow reverses ($t_c > t_d$). Both possibilities are included in this paper.

The mixing model equations do not refer specifically to the mixing rate, but instead to the characteristic mixing time, τ_m, defined by Eq. (8). Thus, corresponding to the mixing rates identified on Fig. 3, we define the following:

$\tau_{m,f}$: the fast mixing time, corresponding to the fast mixing rate;

$\tau_{m,s}$: the slow mixing time, corresponding to the slow mixing rate; and

t_Δ: the large eddy time, $t_b - t_a$.

Because of the phenomenological description of mixing, only approximate values can be assigned to these mixing parameters. However, for design purposes, initial estimates are easily calculated as follows: Referring to Fig. 4, the large eddy time is the eddy length divided by mean inlet velocity U_{mean}.

$$t_\Delta = \frac{L_{ed}}{U_{mean}}. \quad (28)$$

The mean inlet velocity U_{mean} is calculated by dividing the mean volume flow rate by the inlet area. The fast mixing time is estimated by recognizing that the quantity of mass in the eddy
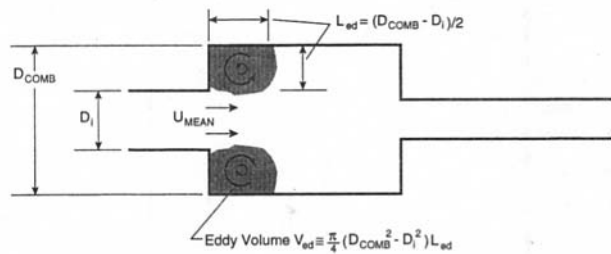
Fig. 4 Definition of parameters used in mixing time definitions

must mix during the large eddy time. Thus, using the nomenclature on Fig. 4,

$$\tau_{m,f} = \frac{V_c}{V_{ed}} t_\Delta. \qquad (29)$$

For the experimental conditions studied in Part II of this paper, Eqs. (28) and (29) produce values 0.5 ms and 5 ms respectively. These values were used to begin calculations. Comparison with actual experimental data in Part II of this investigation gave the best agreement with somewhat longer values of 2 ms and 30 ms, respectively.

Finally, we note that the slow mixing time, $\tau_{m,s}$, serves to limit the mixing process during the initial portion of eddy lifetime. In the Broadwell and Breidenthal mixing model, the mixing rate should be very slow during the initial eddy lifetime, such that $\tau_{m,s}$ can be made arbitrarily large during the initial mixing process. Comparison of numerical results showed this parameter had little effect on computed solutions as long as the slow mixing time was more than three times the value of $\tau_{m,f}$. A value of $\tau_{m,s} = 100$ ms was used in the calculations.

3 Discussion of Characteristic Lengths, Operating Parameters

Before considering the solutions of the governing equations, valuable insights can be gained from inspection of the equations themselves. Except as noted later, the normalized equations do not refer directly to the combustor volume, but to the ratio of combustor volume to inlet area L_{ri} (and associated tailpipe reference length $L_{r,tp}$). This can be shown, for example, in the definition of the flow time, Eq. (3), by expressing the mass flow, $\dot{m}_i$, as the product of density, velocity, and inlet area. The characteristic length, L_{ri}, appears in the resulting expression. Also note that the fuel time, Eq. (4), can be maintained constant for any value of the combustor volume by simply changing the fuel flow in proportion to the combustor volume. Thus, except as mentioned below, the solution of the equations represents a family of combustors of various volumes, but having constant values of L_{ri} and $L_{r,tp}$.

This result is useful for design purposes because information from an operating combustor can be scaled to a different volume combustor by simply holding L_{ri} and $L_{r,tp}$ constant. Note that the inlet (and tailpipe) lengths are also normalized with L_{ri} (and $L_{r,tp}$), such that the physical length of these components should remain constant during volume-scaling. This approach to scaling is demonstrated in Part II of this paper. It is noteworthy that Kentfield and Speirs (1991) used several scale relationships without any theoretical basis. One particular geometry follows the theoretical approach presented here.

Exceptions to this scale-relationship occur in three processes: mixing, frictional flow losses, and heat transfer. The mixing parameters do not depend directly on the combustor volume, but on the large eddy time and eddy volume, Eqs. (28) – (29). As a result, for the same combustor performance, a significant change in combustor volume must be accompanied by some method to maintain mixing time scales. This can be accom-

plished by using several inlets as in Kentfield and Speirs (1991), with the large eddy time defined on the basis of individual inlets. However, the ratio of surface area to cross-sectional area in Eqs. (23) – (25) must be altered to account for multiple inlets. This area ratio directly affects the frictional flow resistance in the inlet (and tailpipe), and is obviously larger with multiple inlets. This area ratio and the heat transfer time, τ_{HT}, do not scale directly with the combustor volume. The relative change in τ_{HT} and area ratio terms can make these differences insignificant, however, as in Part II of this paper. In other situations, it is recommended that the size of these terms be estimated before scaling. A full solution of the governing equations (below) can provide design guidance where large changes in mixing parameters, heat transfer, or area ratio terms are expected.

In gas turbine applications, the ambient pressure, P_A, and temperature, T_A, represent conditions at the compressor discharge. Because development tests at elevated pressure and temperature are costly, it is particularly useful to identify the effect of these parameters on the combustor behavior. Note that the governing equations have been normalized with T_A, P_A, and ρ_A via the ideal gas law. If these ambient parameters do not appear explicitly in the governing equations, the normalized solutions would be independent of the ambient conditions. The actual solution would then scale with the ambient conditions. For example, if P_A does not appear explicitly, then the time-averaged flow rate, the oscillating pressure amplitude, and the fuel flow, etc., would all scale in direct proportion to the operating pressure. The pulsating frequency would be unchanged.

Careful inspection of the governing equations shows that P_A appears only in the combustion time, Eq. (19).[1] Equation (19) indicates that the combustion time is inversely proportional to the ambient pressure. In practice, reductions in the combustion time are limited by the rate at which oxygen is mixed into the hot gases, and this mixing rate does not vary with pressure. As a result, the (normalized) combustor behavior is expected to be least sensitive to pressure for large P_A, where mixing controls the heat release. At low pressure, where chemical reaction controls the heat release, variation in the normalized combustor response with pressure are expected. At higher pressure, combustor behavior should be relatively insensitive to changes in pressure. Initial experimental studies at elevated pressure have confirmed this type of behavior (Gemmen et al., 1994).

The ambient air temperature T_A involves further complications. The ambient air temperature appears in the combustion time (Eq. (19)), in the definitions of the reference inlet velocity, and time u_r and τ_{ri} (see Eqs. (20) – (23) and the nomenclature). For the same mass flow, the large eddy time is smaller at higher T_A because the mean inlet velocity is higher (Eq. (28)). Because of these combined effects, it is recommended that a full solution of the governing equations be conducted to investigate the effect of T_A. No general predictions can be made by looking at the equations themselves.

4 Solution of the Governing Equations

The solution of the governing equations has been obtained by applying the Euler predictor–corrector algorithm. The solution method is straightforward and involves direct marching from one time to the next. The simulation is started by simply specifying a high initial temperature. Subsequent combustion begins the oscillation. Depending on the geometry and operating conditions, combustion will continue as a steady flame, blow out, or oscillate. The present model will predict any of these responses, depending on conditions. Periodic heat release is not imposed. In this paper, just one sample result is reported to demonstrate

---

[1] This can be verified in Eq. (3), for example, by writing the mass flow $\dot{m}_i$ as the product of inlet density, velocity, and area; the *normalized* density will then appear in Eq. (3). In Eq. (7), it should be recognized that the heat transfer coefficient is almost proportional to the ambient density.
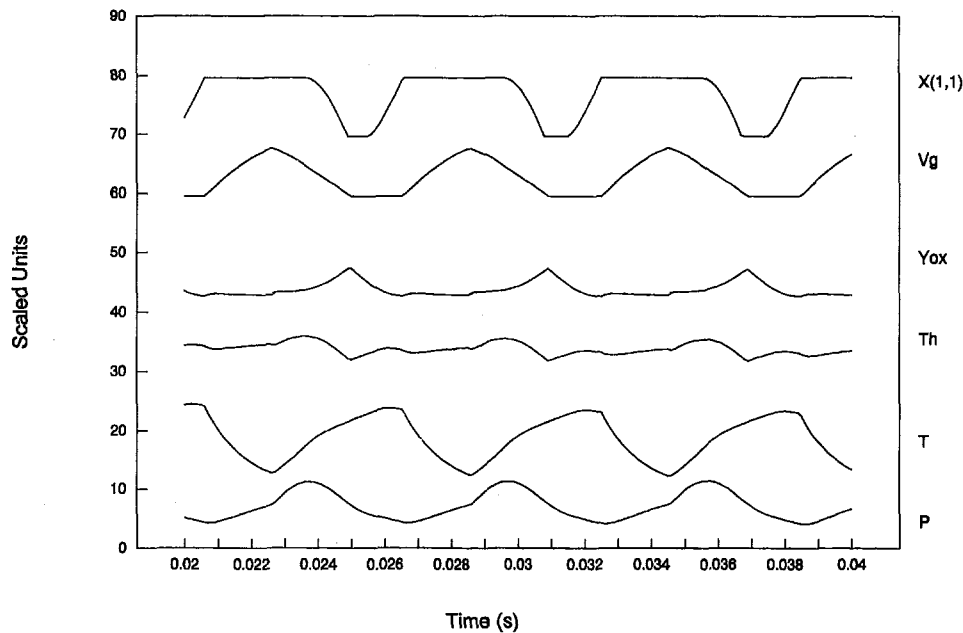
Fig. 5 Predicted time history of selected variables. The variables are scaled and offset to fit conveniently on the graph.

the type of behavior observed for oscillating combustion. Various parameters used for this simulation correspond to the combustor geometry in Part II of this paper. Figure 5 represents a portion of the time history for the variables indicated on the right margin of the graph. The magnitude of each variable was scaled and offset appropriately to fit on the figure, with "X" representing the location of the inlet contact surface. The contact surface location X is measured from the upstream end of the inlet (station u in Fig. 2), such that the maximum value of X indicates that the contact surface has moved to the combustor inlet, station i. The time axis starts at 0.02 seconds from the start of the simulation; limit cycle behavior is already evident. The combustor pressure P and mean temperature T show a nearly sinusoidal behavior with a frequency of 167 Hz. The effect of mixing and combustion can be recognized after the contact surface is swept into the combustor (the beginning of the maxima in X). The g-region volume, V_g, grows almost steadily for the duration of the eddy time (2 ms). As expected, $Y_{ox,h}$ and $\bar{T}_h$ are almost constant during this time. After the eddy time, rapid mixing occurs, and the g-volume begins to shrink. The oxygen concentration increases, while the hot region temperature (initially) rises. The implication is that the combustion reaction is consuming oxygen slower than oxygen is being mixed in from the g-region. The oxygen mass fraction continues to grow even after the contact surface has been pushed back out of the inlet. Oxygen consumption (i.e., combustion) continues almost until the contact surface again re-enters the combustor. In summary, Fig. 5 shows how combustion, mixing, and gas flow participate in the oscillation; similar plots of different operating conditions are reported by Richards et al. (1993).

5 Summary and Conclusions

A control-volume formulation for the conservation laws describing an aerovalve pulse combustor has been presented. A single-step, bimolecular reaction is used to describe combustion. The mixing process between fresh air and combustion products is described as a two-step process, with relatively little mixing occurring as large fluid eddies are reduced to small scale. The time scales that characterize the mixing process can be estimated from the geometry and flow conditions. The normalized governing equations identify two characteristic lengths that should be

held constant during volume scaling of a given combustor design. Complications to this scaling rule are possible in the heat transfer, mixing, and frictional loss terms. Initial estimates of the importance of these terms can be made by inspection of the equations themselves, followed by solution of the governing equations for cases of interest.

The model presented here is computationally very simple; the governing equations were solved on a VAX 6520 computer, run interactively. The calculation and output to the screen occurred approximately 20 times slower than the physically computed time; i.e., a simulation of a 100 Hz oscillation was computed at a 5 Hz rate. The prospect of using this model to explore geometric and operational changes to the pulse combustor rapidly requires validation that the simple control volume formulation can correctly capture the relevant physics. To address this need for validation, Part II of the present paper (Richards and Gemmen, 1996) compares the predictions of this model to laboratory measurements.

References

Barr, P. K., Bramlette, T. T., Gunn, M. E., Keller, J. O., Kezerle, J. A., and Roose, T. R., eds., 1993, "Special Issue on Pulse Combustion," *Combustion Science and Technology*, Vol. 94, No. 1–6.

Broadwell, J. E., and Breidenthal, R. E., 1982, "A Simple Model of Mixing and Chemical Reaction in a Turbulent Shear Layer," *J. Fluid Mech.*, Vol. 125, pp. 397–410.

Geiling, D. W., ed., 1993, *Proc. Joint Contractors Meeting: FE/EE Advanced Turbine Systems Conference, FE Fuel Cells and Coal-Fired Heat Engines Conference*, DOE/METC-93/6132, NTIS/DE93011308.

Gemmen, R. S., Richards, G. A., and Janus, M. C., 1994, "Development of a Pressure-Gain Combustor for Improved Cycle Efficiency," presented at the ASME Cogen-Turbo Power Meeting, Portland, Oregon, Oct. 25–27.

Hawthorne, W. R., 1994, "Reflections on United Kingdom Aircraft Gas Turbine History," ASME JOURNAL OF ENGINEERING FOR GAS TURBINES AND POWER, 116, pp. 495–510.

Kentfield, J. A. C., and Fernandes, L. C. V., 1990, "Improvements to the Performance of a Prototype Pulse, Pressure-Gain, Gas Turbine Combustor," ASME JOURNAL OF ENGINEERING FOR GAS TURBINES AND POWER, Vol. 112, pp. 67–72.

Kentfield, J. A. C., and O'Blenes, M., 1987, "Methods for Achieving a Combustion-Driven Pressure-Gain in Gas Turbines," ASME Paper No. 87-GT-126.

Kentfield, J. A. C., and Speirs, B. C., 1991, "A Multiple-Inlet Core for Gas Turbine, Pulse, Pressure-Gain Combustors," ASME Paper No. 91-GT-304.

Kentfield, J. A. C., and Yerneni, P., 1985, "Pulsating Combustion Applied to a Small Gas Turbine," ASME Paper No. 85-GT-52.

Kretschmer, D., and Odgers, J., 1972, "Modeling of Gas Turbine Combustors—A Convenient Reaction Rate Equation," ASME JOURNAL OF ENGINEERING FOR POWER, pp. 173–180.

Lampinen, M. J., Turunen, R., and Koykka, M., 1992, "Thermodynamic Analysis of a Pulse Combustion System and Its Application to Gas Turbines," *Int. J. Energy Research,* Vol. 16, pp. 259–276.

Moody, F. J., 1990, *Introduction to Unsteady Thermofluid Mechanics,* Wiley, New York.

Muller, J. L., 1971, "Theoretical and Practical Aspects of the Application of Resonant Combustion Chambers in Gas Turbines," *J. Mech. Eng. Sci.,* Vol. 13, No. 3, pp. 137–150.

Porter, C. D., 1958, "Valveless-Gas-Turbine Combustors With Pressure Gain," ASME Paper No. 58-GTP-11.

Richards, G. A., Morris, G. J., Shaw, D. W., Keeley, S. A., and Welter, M. J., 1993, "Thermal Pulse Combustion," *Combustion Science and Technology,* Vol. 94, pp. 57–85.

Richards, G. A., Gemmen, R. S., and Narayanaswami, L., 1994, *Aerovalve Pulse Combustion,* DOE/METC-94/1009, NTIS/DE94012262.

Richards, G. A., and Gemmen, R. S., 1996, "Pressure-Gain Combustion: Part II—Experimental Results," ASME JOURNAL OF ENGINEERING FOR GAS TURBINES AND POWER, Vol. 118, this issue, pp. 469–473.

Schlichting, H., 1979, *Boundary-Layer Theory,* 7th ed., McGraw-Hill Publishers, p. 597.

Thring, M. W., ed., 1961, *Pulsating Combustion—The Collected Works of F. H. Reynst,* Pergamon Press, Oxford, United Kingdom.

Pressure-Gain Combustion: Part II—Experimental and Model Results

G. A. Richards

R. S. Gemmen

U.S. Department of Energy,
Morgantown Energy Technology Center,
Morgantown, WV 26507-0880

An experimental investigation of aerovalve pulse combustion is presented. The experimental measurements compare favorably with model predictions from a control-volume analysis of the pulse combustor. Particular emphasis is placed on the mean pressure differences through the combustor as an indicator of the so-called pressure gain performance. Both the operating conditions and combustor geometry are investigated. It is shown that complex fluid/combustion interactions within the combustor make it difficult to isolate the effect of geometric changes. A scaling rule developed from the control-volume analysis is used to produce a combustor geometry capable of producing pressure gain.

1 Introduction

In Part I of this article (Narayanaswami and Richards, 1996), a simplified model for aerovalve pulse combustion is presented. The model is a control-volume formulation for the conservation laws in three distinct regions of an aerovalve pulse combustor. The model was developed specifically to allow rapid investigation of the geometric parameters typical of pulse combustor geometries. While such models are frequently used to provide first-order predictions to the behavior of complex processes, such treatments apparently have not been applied thus far to pulse combustion phenomena, with predictions being directly compared to experimental data. Hence, in this paper, predictions from the model of Narayanaswami and Richards (1996) are compared to experimental data to gain confidence that the model does indeed represent the basic features of the combustor performance. In addition, the model is used to explain several features of the laboratory data. The model and experimental results suggest a complicated (and unexpected) interaction between the aerovalve inlet and tailpipe flows. Furthermore, it is shown that certain geometric parameters appearing in the equations of the model are useful in scaling a given combustor so as to achieve pressure gain.

Particular emphasis is placed in this work on measurements associated with so-called pressure gain because of the potential benefit to gas turbine cycle-efficiency. As described in Part I of this paper, the *unsteady* processes that produce pressure gain increase the time-averaged stagnation pressure of gases moving through the combustor. This is in stark contrast to the pressure loss associated with conventional *steady* combustors. As an example of the benefits of unsteady combustion, Kentfield and Fernandes (1990) show that an aerovalve pulse combustor installed in a small gas turbine can produce a pressure gain of up to 4 percent of the compressor outlet pressure, with a resulting increase in turbine cycle efficiency of 4 percent.

2 Phenomenological Description of Pressure Gain

Figure 1 is a sketch of the basic aerovalve pulse combustor geometry used in the current work. (Other pressure gain geometries are possible as well; see e.g., Kentfield (1993) and George and Coriliss (1988).) As shown in Fig. 1, the combustor is divided into three components: the inlet, the combustion cham-

ber, and the tailpipe. Each of these components is defined by a length and diameter, as shown. An inlet plenum is also defined on the figure. Air supplied to the inlet plenum passes through the pulse combustor from left to right. The pressures P_{10}, P_{20}, and P_{30} are the *mean* stagnation pressure values for the inlet plenum, the combustion chamber, and in the jet exiting the tailpipe.

Under steady oscillation, inlet plenum air is periodically injected into the combustion chamber where it mixes with fuel and previous products of combustion and ignites. The pressure gain process occurring during combustion raises the stagnation pressure of the gases passing through the system, such that $P_{20} > P_{10}$. The stagnation pressure, P_{20}, is subsequently converted to kinetic energy in the tailpipe. If tailpipe losses are small, P_{30} will also be greater than P_{10}.

The measurements presented in this paper are frequency and rms pressure amplitude. Additionally, because the goal is to produce a combustor capable of providing a pressure gain, the overall mean pressure difference across the pulse combustor, $P_{10} - P_{30}$ (where *negative values represent gain*), is also presented. The mean pressure difference from inlet to combustion chamber is also of fundamental value, since it is the combustion process occurring in the combustion chamber that produces the pressure gain. Hence, to investigate the pressure gain capabilities of a given geometry, the pressure difference across the inlet ($P_{10} - P_{20}$) is also presented. Finally, the mean pressure difference across the tailpipe is also presented, $P_{20} - P_{30}$, for use in subsequent discussions.

3 Experimental Description

The experimental pulse combustor is shown in Fig. 2. The pulse combustor is fabricated from standard straight-walled pipe components, and is mounted inside a 20-cm-dia sheet metal duct. The duct is divided into three plenums, labeled from left to right: inlet plenum, dilution plenum, and exhaust plenum. Combustion air enters the inlet plenum, passes through the pulse combustor inlet, reacts with fuel in the combustion chamber, and passes into the exhaust plenum. (The inlet pipe is not shown in the upper figure in order to show the fuel entry point more clearly.) The dilution plenum is not directly relevant to this investigation because the dilution air is added merely to lower the exhaust temperature before exiting the laboratory. The concentric baffles at the right end of the dilution plenum provide an axisymmetric dilution mixing region downstream of the pulse combustor tailpipe, which is the subject of a separate study (Gemmen et al., 1993).
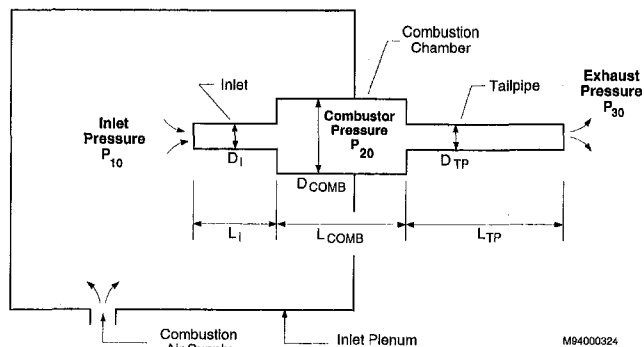
Fig. 1   Schematic of an aerovalve pulse combustor

	Lengths (m)			Diameters (m)	
Inlet	L_i	0.102	Inlet	D_i	0.0127
Tailpipe	L_{tp}	0.600	Tailpipe	D_{tp}	0.0191
Combustor	L_{comb}	0.152	Combustor	D_{comb}	0.0556

that would otherwise arrive at the water manometer. Tests are conducted without the tee-connection, and with transducer connection tubes of various lengths, to ensure that the dynamic pressure signal is not influenced by acoustics in the connecting tube. The dynamic pressure is measured with a Kistler, Inc., Model 206 piezoelectric transducer, with the amplified output digitized and stored on a personal computer for subsequent analysis.

The mean pressure of the inlet plenum was monitored with a Setra, Inc., diaphragm-type electronic differential-pressure-gage, connected through a port attached to the top of the plenum and with the reference end tied to the exhaust plenum. Initial tests using a dynamic pressure transducer in this location showed that the inlet plenum experienced a small amplitude pressure oscillation during operation. The amplitude was typically less than 1 percent of the combustion chamber oscillation, and was considered negligible.

A detailed cross section of the pulse combustor is shown in the lower portion of Fig. 2. Natural gas enters the combustor via a 3.1-mm-dia, stainless steel tube cantilevered along the axis of the pulse combustor. Fuel exits the steel tube through two directly opposed 1.5-mm-dia holes. The combustor, manufactured from standard pipe unions welded together, allows different size inlets to be readily attached. A spark plug is used for initial ignition only and is then turned off. A 6.4-mm-dia tube is attached to the combustion chamber for measuring both mean chamber pressure and dynamic chamber pressure via a tee-connection. For the flow rates studied here, the mean velocity in the combustion chamber is small enough that the combustion chamber mean static and stagnation pressure are treated as equal. The mean combustion chamber pressure is measured using a water manometer with the reference end tied to the exhaust plenum. The connection to the combustion chamber is preceded by a 7-m-long coil of tubing to dampen oscillations

4   Model and Experimental Parameters

The combustor geometry shown in Fig. 2 was treated as a baseline case. For combustion air ranging between 2 and 8 grams per second, this geometry produced oscillating combustion within a frequency range of 150 to 190 Hz. Waveforms were generally sinusoidal, with some showing higher harmonics.

Geometric dimensions used in both experiment and model are shown in Table 1, using the nomenclature of Fig. 1. The model was run interactively, with the user specifying an upstream pressure and temperature equal to the measured laboratory values. It was generally found that the simulation overpredicted the air mass flow rate at a given plenum pressure. It was also found that the simulation would seldom predict stable oscillations for fuel-lean conditions. The failure of the model to predict fuel-lean operation is similar to the results for a thermal pulse combustor model reported by Richards et al. (1993). The observed discrepancy for the fuel-lean cases may be the consequence of the simplified kinetic scheme used by Kretschmer and Odgers (1972). Because the present model would seldom predict stable oscillations for fuel-lean operation, all the numerical results are reported at a fixed equivalence ratio of 1.05. However, because of material limitations, the laboratory data were collected at a fixed equivalence ratio of 0.82.

In the model described in Part I, mixing is treated as a two-step process characterized by the large-eddy time scale, t_Δ, and time scales associated with the rate of slow and fast mixing, $\tau_{m,s}$ and $\tau_{m,f}$, respectively. These time scales can be estimated from time-averaged flow rate and inlet geometry. For an average air flow rate of 5 g/s, the model predicts $t_\Delta = 0.5$ ms, $\tau_{m,f} = 5$ ms, and $\tau_{m,s} = 100$ ms. In practice, it was found that better agreement with the lab data was obtained with mixing constants 4 to 6 times slower: $t_\Delta = 2$ ms, $\tau_{m,f} = 30$ ms, and $\tau_{m,s} = 100$ ms. These mixing parameters were fixed in the results presented later. Although Part I of this paper suggests that these parameters should be scaled to the average air flow rate (which is not known a priori, and thus requires iterative solutions), reasonable results were obtained over the range of operating conditions with fixed mixing parameters. This approach may be inadequate for wide variations in flow rate, particularly at very low flow rates, as discussed below.

Fig. 2   Experimental pulse combustor. Not shown is the exhaust plenum extending more than 6 m before exiting the laboratory building. A decoupling chamber at the end of the exhaust plenum effectively muffles the system.
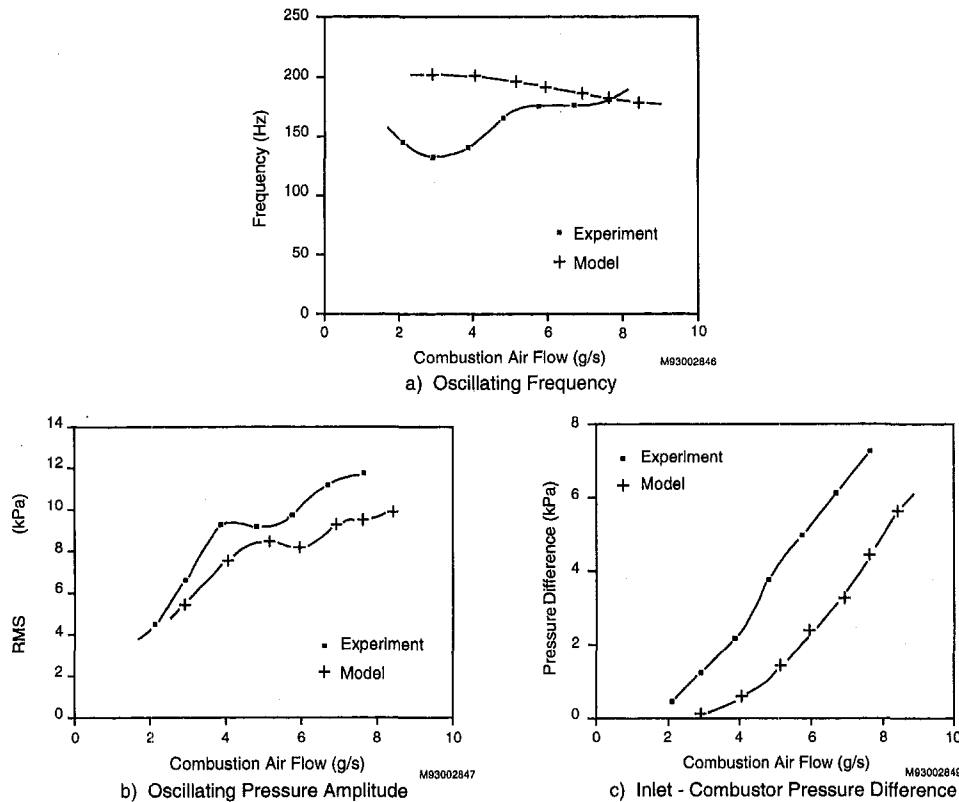
Fig. 3 Comparison of laboratory data and model predictions for frequency, oscillating pressure amplitude, and pressure differences

5 Comparison of Experimental and Numerical Results

Figure 3 shows a comparison of laboratory data and measurements from the laboratory combustor. The frequency is predicted reasonably well (Fig. 3(a)), except at the lower flow rates as discussed below. In Fig. 3(b), the measured and predicted root-mean-square pressure levels are seen to agree very well over the range of operation. In Fig. 3(c), the measured and predicted pressure differences between the inlet and the combustion chamber (i.e., the magnitude of pressure loss) agree well with respect to trend. Results presented later will demonstrate how geometric changes deduced from theory can be used to achieve pressure gain.

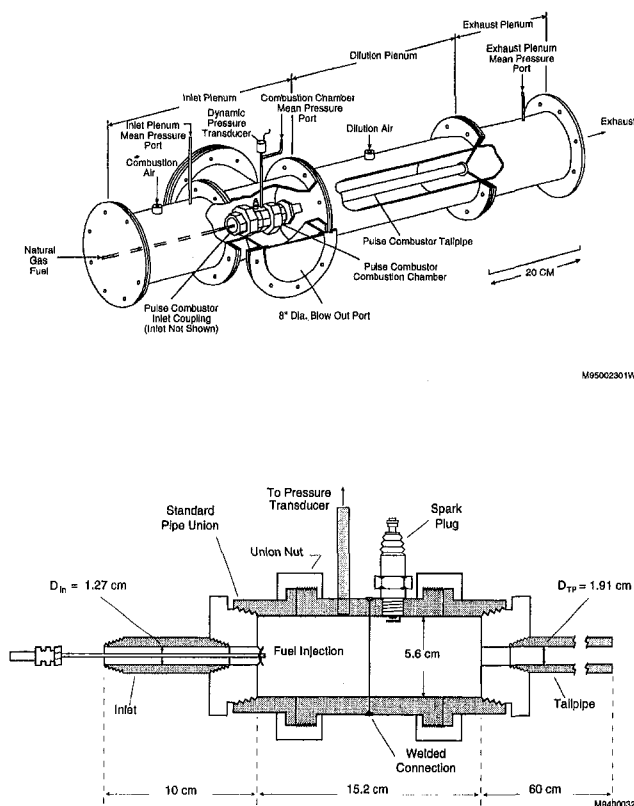The greatest discrepancy between experimental and model results occurs at low flow rates. As Broadwell and Breidenthal (1982) suggest, their two-step mixing model is applicable to large Reynolds number flows. Accordingly, at the lowest flow rates used in the present study, the simple two-step mixing model is not entirely adequate, suggesting that a more detailed model is required for the low flow rates.

6 Effects of Combustor Geometry

The present model was developed to help identify the effect of geometric changes. Figures 4 and 5 show a comparison of model and experimental results as a function of the combustor inlet length. The model was run by iteratively selecting an inlet pressure to produce the same flow rate as existed in the lab (6 g/s). As noted before, the lab data were limited to an equivalence ratio of 0.82, while the simulation was performed at an equivalence ratio of 1.05.

Comparing the figures, the laboratory data and model predictions each show a marked effect of the inlet length on the combustor performance. Understandably, the operating frequency is reduced with increased inlet length. At lower frequen-

cies, the rms pressure is expected to be larger since more fuel is burned in each cycle. This is evident in both laboratory and model results. Figures 5(a) and 5(b) compare the pressure differences for the model and experimental results. The simulation overpredicts the pressure differences in most cases. However, the qualitative behavior of the various pressure differences is similar in both the simulation and the laboratory data, with some difference for the inlet-combustor pressure difference. The laboratory data show that the inlet-combustor pressure difference is less sensitive to the inlet length as compared to the model, which indicates a modest increase with inlet length. Comparing the experimental and model results show that the *tailpipe pressure drop* is approximately doubled by increasing
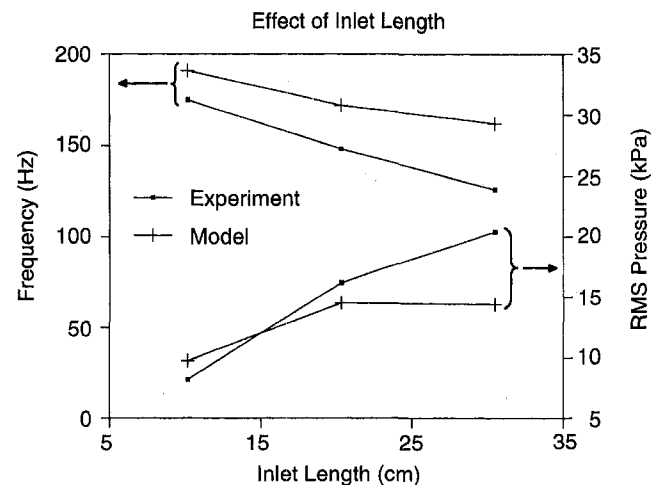
Fig. 4 Laboratory data and model predictions for frequency and rms pressure as a function of inlet length
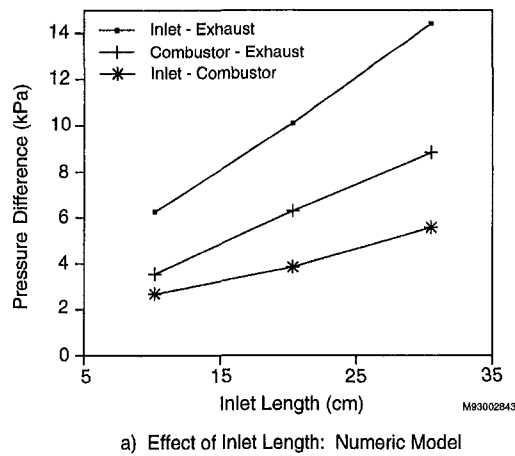
a) Effect of Inlet Length: Numeric Model
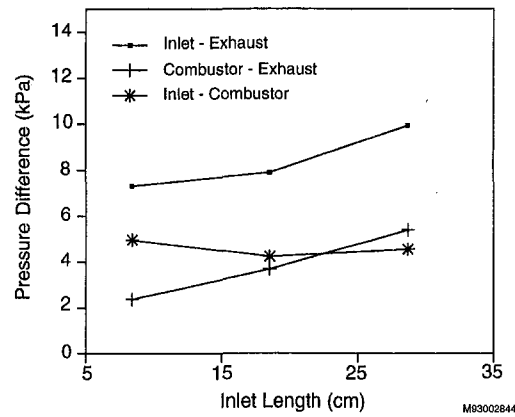
Fig. 5 Model predictions (a) and laboratory data (b) for the pressure difference as a function of the inlet length

a) Inlet Length: 10 cm

b) Inlet Length: 30 cm

Fig. 6 Model predictions of the inlet and tailpipe gas velocity for the 10-cm and 30-cm inlet lengths

the *inlet length* from 10 to 30 cm. Stated differently, the longer *inlet* case needs twice the mean pressure to drive the same mass flow through the *tailpipe*. This result is attributed to the *unsteady* nature of the flow, as indicated by inspecting the predicted tailpipe velocity shown in Fig. 6. It is seen that the higher amplitude, low-frequency oscillation associated with the longer inlet causes significant flow reversal (i.e., negative velocities) in the tailpipe. The shorter inlet, with a higher frequency and lower amplitude oscillation, shows little tailpipe flow reversal. The net effect of the flow reversal is that the tailpipe is effectively "blocked" to exiting gases for a portion of the combustor cycle. This blockage results in a higher mean pressure to drive out the same quantity of gas through the tailpipe, consistent with Fig. 5.

7 Geometric Configurations for Pressure Gain

The behavior described above emphasizes the complex interaction that exists between the various combustor components. When seeking to optimize the combustor for pressure gain, it is inadequate to consider the effect of changes to a single geometric parameter. For example, changes to the inlet may produce unexpected results because of interaction with a specific tailpipe geometry.

Since prior work has shown specific designs providing pressure gain (e.g., Kentfield and Fernandes, 1990), and since basic similarity principles should hold for the pressure gain process, it was recognized that the pressure gain shown by the Kentfield and Fernandes geometry (excluding a taper on the tailpipe) could possibly be scaled to a geometry convenient to our laboratory. It was noted that the existing combustor volume (Table 1) was smaller than the Kentfield and Fernandes geometry by
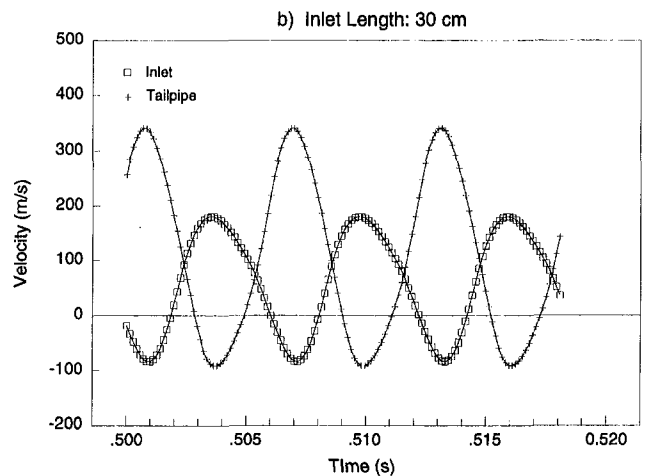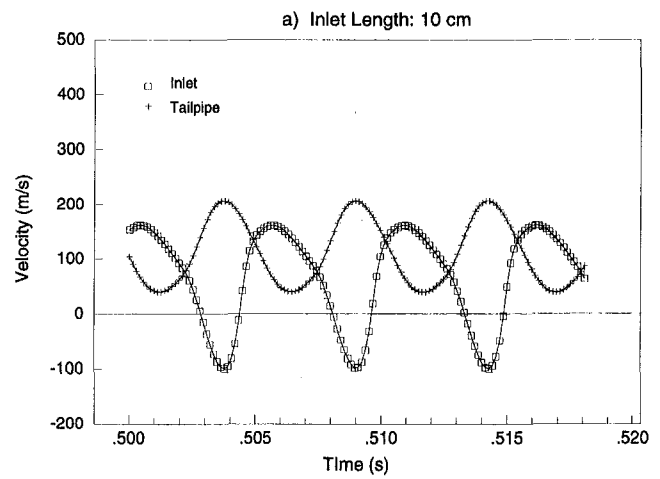
a factor of 1.7. As described in Part I of this paper, the combustor volume enters the calculations directly in the definition of two characteristic lengths: the ratios of the combustor volume to the inlet and tailpipe areas. Changes to the combustor volume must be matched by corresponding changes to the inlet and exit areas such that these characteristic lengths remain constant. The model equations also suggest that the inlet and tailpipe lengths should be held constant during scaling. Consequently, it was possible to scale the Kentfield geometry by merely holding the ratio of the combustor volume to inlet and exit areas constant. This identified a combustor geometry that should produce pressure gain, yet was different from the one reported by Kentfield. The resulting geometric parameters are shown in Table 2. Notice that the combustion chamber dimensions are the same as those shown in Table 1; this particular geometry was readily installed in the lab by exchanging the inlet and tailpipe from the base case geometry.

Figure 7 shows a comparison of the measured and predicted inlet-combustion chamber pressure difference, $P_{10} - P_{20}$, for the geometry listed in Table 2. As before, the simulation was

Table 2 Dimensions of the pressure-gain combustor

Lengths (m)			Diameters (m)		
Inlet	L_i	0.152	Inlet	D_i	0.0222
Tailpipe	L_{tp}	0.900	Tailpipe	D_{tp}	0.0191
Combustor	L_{comb}	0.152	Combustor	D_{comb}	0.0556
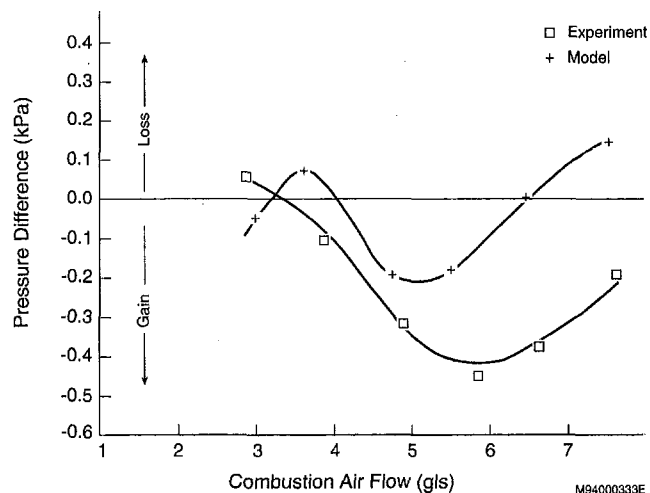
Fig. 7 Inlet-combustor pressure difference for the scaled combustor geometry listed in Table 2

performed for equivalence ratio 1.05, while lab tests were limited to 0.82. while there is a difference in the magnitude of the predicted-versus-measured pressure gain, the minima in both the laboratory data and model predictions suggest that an optimum flow rate exists for pressure gain.

8 Summary

The goal of this investigation was to confirm the model predictions presented in Part I, and provide further insight into the design of pulse combustors capable of producing pressure gain. For fixed mixing parameters, the laboratory data and model predictions are generally in good agreement, except at low combustion air flow rates. At low air flow rates, the simple mixing model used in Part I may not adequately describe the mixing process. Changes to a single geometric parameter, such as the inlet length, are shown to produce complex behavior which could be interpreted with the model results. Scaling relations presented in the model were used to scale a published combustor geometry to produce pressure gain.

Because the model presented in Part I is computationally simple, it is possible to survey a wide range of geometric and operating conditions, seeking the desired pressure-gain performance. Using this model, a survey of various combustor geometries is being conducted currently, with promising cases planned for investigation in the laboratory, both at one atmosphere, and at elevated pressure (Gemmen et al., 1994). There has been no prior work aimed at designing a pressure-gain combustor for high-pressure operation.

References

Broadwell, J. E., and Breidenthal, R. E., 1982, "A Simple Model of Mixing and Chemical Reaction in a Turbulent Shear Layer," *J. Fluid Mech.*, Vol. 125, pp. 397–410.

Gemmen, R. S., Rogers, W. A., and Richards, G. A., 1993, "Experimental and Numerical Investigation of a Confined Pulse Combustor Tailpipe Exhaust Mixing With a Steady Jet," presented at the Central and Eastern States Section Joint Meeting of the Combustion Institute, New Orleans, LA, Mar. 15–17.

Gemmen, R. S., Richards, G. A., and Janus, M. C., 1994, "Development of a Pressure-Gain Combustor for Improved Cycle Efficiency," presented at the ASME Cogen-Turbo Power Meeting, Portland, Oregon, Oct. 25–27.

George, P. E., and Coriliss, J. M., 1988, "Development of a Rotary Valve for Pulse Combustion Applications," NTIS N-8920486, GRI 88/0185.

Kentfield, J. A. C., and Fernandes, L. C. V., 1990, "Improvements to the Performance of a Prototype Pulse, Pressure-Gain, Gas Turbine Combustor," ASME JOURNAL OF ENGINEERING FOR GAS TURBINES AND POWER, Vol. 112, pp. 67–72.

Kentfield, J. A., 1993, *Nonsteady One-Dimensional, Internal, Compressible Flows, Theory and Applications,* Oxford Univ. Press, New York.

Kretschmer, D., and Odgers, J., 1972, "Modelling of Gas Turbine Combustors—A Convenient Reaction Rate Equation," ASME JOURNAL OF ENGINEERING FOR POWER, Vol. 94, pp. 173–180.

Narayanaswami, L., and Richards, G. A., 1996, "Pressure-Gain Combustion, Part I: Model Development," ASME JOURNAL OF ENGINEERING FOR GAS TURBINES AND POWER, Vol. 118, this issue, pp. 461–468.

Olorunmaiye, J. A., 1985, "Numerical Simulation and Experimental Studies of Highly Loaded Valveless Pulsed Combustors," Ph.D. Thesis, Univ. of Calgary, Calgary, Alberta, Canada.

Richards, G. A., Morris, G. J., Shaw, D. W., Keeley, S. A., and Welter, M. J., 1993, "Thermal Pulse Combustion," *Combustion Science and Technology*, Vol. 94, pp. 57–85.

Wave Cycle Design for Wave Rotor Gas Turbine Engines With Low NOx Emissions

M. R. Nalim[1]
CFD Research Corporation,
Huntsville, AL 35805

E. L. Resler, Jr.
Sibley School of Mechanical
and Aerospace Engineering,
Cornell University,
Ithaca, NY 14853

The wave rotor is a promising means of pressure-gain for gas turbine engines. This paper examines novel wave rotor topping cycles that incorporate low-NO_x combustion strategies. This approach combines two-stage "rich-quench-lean" (RQL) combustion with intermediate expansion in the wave rotor to extract energy and reduce the peak stoichiometric temperature substantially. The thermodynamic cycle is a type of reheat cycle, with the rich-zone air undergoing a high-pressure stage. Rich-stage combustion could occur external to or within the wave rotor. An approximate analytical design method and CFD/combustion codes are used to develop and simulate wave rotor flow cycles. Engine cycles designed with a bypass turbine and external combustion demonstrate a performance enhancement equivalent to a 200–400 R (110–220 K) increase in turbine inlet temperature. The stoichiometric combustion temperature is reduced by 300–450 R (170–250 K) relative to an equivalent simple cycle, implying substantially reduced NO_x formation.

Introduction

The development of more efficient, less polluting gas turbines requires the pressure ratios and temperatures of conventional components to be pushed to unproved limits, while curbing the formation of oxides of nitrogen (NO_x) at high temperatures. The wave rotor is a single component combining gas compression, expansion, and possibly combustion, with the potential for significantly increasing specific power and decreasing fuel consumption in advanced turbine engines.

A wave rotor utilizes direct fluid–fluid energy exchange in channels using pressure waves, as in a shock tube. A number of channels separated by thin walls are arrayed on the periphery of a cylindrical rotor. The wave processes are made periodic by turning the rotor to connect the channels intermittently with appropriately located inlet and outlet manifolds. The closing and opening of the ends of each channel, by the use of stator end plates between the manifolds, initiates compression or expansion waves in the channel, similar to the breaking of a shock tube diaphragm. The simplest wave rotors have straight constant-area axial channels and are turned by an external drive. Free-running wave rotors and wave turbines may have slanted or curved channels for self-rotation and shaft work output. A "wave rotor combustor" is a wave rotor in which combustion occurs on-board, within its channels.

An important feature of wave rotors is that when the channel walls are alternately exposed to hot and cold fluid, their temperature can be maintained below the peak temperature in the fluid. In a gas turbine engine this feature permits using a cycle that circumvents the usual turbine inlet temperature (TIT) limitation. Considerable historical information and reviews of progress in wave rotors can be found in the proceedings of the 1985 Naval Postgraduate School Wave Rotor Workshop (Shreeve and Mathur, editors) and the works of Sladky (1984), Azoury (1965–66), and Foa (1960). Currently, a research program at the NASA Lewis Research Center is pursuing basic studies of wave rotor performance and loss mechanisms (Wilson, 1993),

to obtain reliable models that will be useful in future aircraft propulsion designs. Recent work at Cornell University focused on analytic methods (Resler et al. 1994) and NO_x control (Nalim et al., 1993; Nalim, 1994a).

Topping Cycle With External[2] Combustion. The most straightforward application of a wave rotor in a gas turbine is to provide a topping cycle to increase the efficiency and overall cycle work. Low-pressure air is compressed in the wave rotor passages by compression waves generated by hot combustion gases from an external steady flow combustor. The hot gases expand and cool before being sent to the turbine, which therefore operates at a lower temperature than the combustor exit.

The application of a wave rotor in a topping cycle has several advantages over turbomachinery technology:

(a) Flow passages are self-cooled since they are alternately exposed to cool compressor discharge air and hot combustor exit flow. Thus, it is able to provide higher peak cycle temperatures without the need for correspondingly advanced materials.

(b) The rotational speed can be kept relatively low, resulting in greater durability and/or higher peak cycle temperatures.

(c) It can provide efficient compression at the high-pressure end of the cycle where conventional compressors suffer from severe tip leakage due to the small flow passage.

(d) It provides a rapid response to transient operating conditions.

NO_x Emissions. Improvement of gas turbine performance requires a higher peak cycle temperature, but this may increase NO_x emissions. Near-stoichiometric mixtures produce the most NO, the major component of engine NO_x. Here, NO formation estimates are presented as grams of equivalent NO_2 per kg fuel, called the NO_x emissions index ($EINO_x$).

One NO_x-reducing combustor scheme being considered for advanced aircraft and other applications is the Rich-Quench-Lean (RQL) concept. The two-stage RQL scheme employs fuel-rich combustion in the first stage, where NO_x formation is low because of low oxygen availability, despite fast kinetics.

---

[2] External to the rotor, but still internal in the thermodynamic sense of combustion in the working fluid.
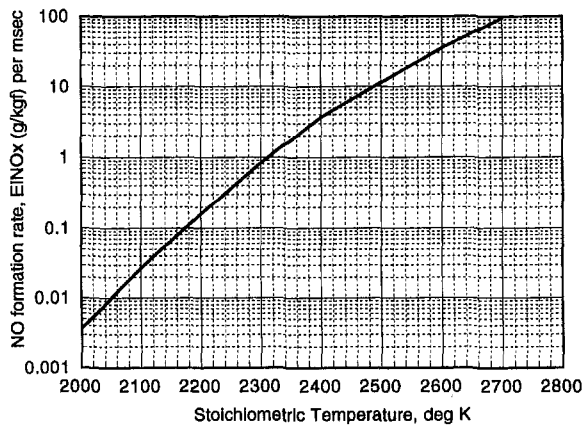
Fig. 1 NO formation at stoichiometric conditions

Additional air is then injected into the rich-burn products with very rapid mixing to a sufficiently low temperature to minimize NO_x formation, and combustion is completed in the now lean mixture.

There are two major challenges encountered with this scheme. First, the rich zone is very hot (2200–2500 K), but the combustor wall cannot be cooled by a film of air as in ordinary combustors since excessive NO_x will be formed. Second, the large volume of air that bypassed the rich-burn section must quickly mix with the rich burn products without forming excessive NO_x. The peak temperature in the mixing zone and the pressure drop available for injection of air are critical factors controlling mixing-zone NO_x formation. The use of a wave rotor allows both these critical parameters to be addressed. Most NO_x in RQL combustors is produced in the mixing zone, where a diffusion-type flame exists with near-stoichiometric conditions. The mixing rate (and NO_x) depends on the momentum flux ratio of the two streams at injection. A pressure difference of about 8–10 percent is desirable for mixing, but this results in a significant efficiency penalty for conventional engines. Figure 1 is a graph of the NO formation rate in a stoichiometric mixture, based on Zeldovich kinetics. It illustrates the strong temperature dependence of the NO formation rate, and thus the importance of limiting the stoichiometric temperature.

Wave Rotor Engine Concepts With Low NO_x Potential

Although the wave rotor permits a higher combustor exit temperature relative to the TIT, NO_x limitations may still constrain combustor temperatures. We seek to design a wave rotor flow cycle and a corresponding engine cycle to mitigate or circumvent this constraint, and even to enhance the effectiveness of the combustor strategies used to reduce NO_x.

The wave rotor allows two new concepts to control NO_x while boosting engine performance. One concept is to stage the combustion process in rich and lean sections, similar to the RQL scheme, and to use a wave rotor between the stages to extract energy from the rich product gas. The product gas cools by expansion ("wave quenching" at constant composition) in

the wave rotor and thus lowers the stoichiometric temperature in the mixing zone of the second stage where most NO_x is otherwise produced in RQL-type combustors. Also, part of the energy extracted is available via the wave rotor to boost the pressure of the bypass air injected in the second stage. The pressure differential for mixing can be increased to about 10 percent without a significant penalty, for enhanced mixing and minimal residence time at stoichiometric conditions. We refer to this concept as Rich-Wave-Quench-Lean (RWQL).

The other concept is to accomplish combustion within the wave rotor channels, followed by immediate wave expansion of the hot gas, so that the residence time at peak temperature is minimal. The near-constant-volume combustion produces a pressure gain. In general, this may be done with lean or rich combustion. For combination with the RWQL concept, the wave rotor provides the rich combustion stage. Its additional advantages are that: (a) the need for a high temperature liner for the rich combustion zone is eliminated, (b) residence time at peak temperature could be reduced to a fraction of a millisecond, and (c) mechanical complexity is reduced; the ducting is much simplified and fewer special-shape manifolds are needed. In-rotor combustion is less well understood and more challenging than steady-flow combustors, and has not been convincingly demonstrated in practice. Well-controlled intermittent combustion with sufficient rapidity and reliability would have to be achieved. With rich combustion, mixing with air at high temperature must be controlled. Therefore, the emphasis in this paper will be on the RWQL concept with external, rather than with in-rotor combustion.

The RWQL thermodynamic cycle is similar to a reheat cycle, with a part of the air participating in the high-pressure rich-burn stage. The cycle work and efficiency of the cycle is thus considerably enhanced beyond conventional Brayton cycle performance for the same TIT, while mixing-zone NO_x formation is greatly reduced. The reduction in stoichiometric temperature is equivalent to a reduction in inlet temperature for a unitary combustor. NO_x emissions are expected to be considerably less than with RQL or lean-premixed-pre-vaporized (LPP) combustion in simple cycles.

Splitter RWQL Scheme. The simplest version of the RWQL approach is the "Splitter" RWQL scheme, in which the air being compressed within the wave rotor is split in two streams: (1) a medium-pressure stream for injection into the quick-mix zone, and (2) a high-pressure stream for the rich stage. This is schematically illustrated in Fig. 2, with alternate flow paths for rich stage combustion external to the rotor or within the rotor (heavy broken line).

Wave Turbine and Bypass Turbine RWQL Schemes. The extent of expansion of the rich product gas is determined by the work transfer effected in the wave rotor. In the ordinary splitter scheme (with external or internal combustion, and axial blades), this is limited to the compression work for the medium and high-pressure streams. However, if the wave rotor is designed with slanted or curved channels so that shaft work is produced in addition to the compression work (making it a wave turbine), the "wave quench" effect can be considerably enhanced.

─────── **Nomenclature** ───────────────

a = speed of sound
a_1 = reference speed of sound
ϕ = fuel/air equivalence ratio
γ = specific heat ratio
η = cycle efficiency
K = degrees Kelvin
L = length of channel

M = Mach number
p = pressure
P = "rightward moving" characteristic quantity, speed $(u + a)$
Q = "leftward moving" characteristic quantity, speed $(u - a)$
R = gas constant
R = degrees Rankine

ρ = density
s = entropy
t = time
T = temperature
u = fluid velocity
x = position along channel
y = fraction of engine flow in a particular stream
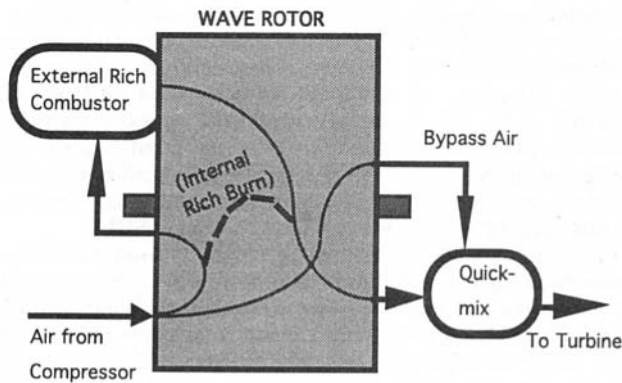
Fig. 2 Splitter RWQL scheme

The practicality of a wave turbine will depend on matching shaft power to drive requirements. An alternative scheme that allows a large wave quench without the complication of a wave turbine is the "Bypass Turbine" RWQL scheme, illustrated in Fig. 3. Bypass air is boosted to the same high pressure as the rich-burn air, thus absorbing a considerable amount of energy from the expanding rich product gas. The excess work must be extracted in a bypass turbine.

The reduction in stoichiometric temperature can be amplified by heat transfer from the rich product gas to the bypass air, via the channel walls and by cooling the rich burner (if external), as well by an optional heat exchanger following the wave rotor. In this way, the bypass air will also contribute to the upper stage of the thermodynamic cycle.

Methods of Analysis

The following methodology is used to analyze the flow and design the wave rotor:

(a) Initially an approximate nonlinear analytical method is used, which allows a parametric study and gives a design starting point. It uses the theory of characteristics, with some assumptions, and includes losses peculiar to the wave rotor. This method is described in detail by Resler et al. (1994) and Nalim (1994a).

(b) Using boundary condition information from the approximate analysis, a computer code using the method of characteristics generates a wave diagram and provides a preliminary simulation with port timings and fluxes. This code is described by Nalim (1994a).

(c) Detailed CFD calculations are then made using the CFD-FASTRAN finite-volume code. This code solves the time-accurate flow equations. Flux-difference splitting with a min-mod limiter, and explicit Runge–Kutta integration was satisfactory for stable and efficient computation.

(d) For internal combustion simulation, a version of CFD-FASTRAN with reactive flow capability is used, and preliminary results have been obtained.

Governing Equations for Analytical and Characteristics Methods. At the simplest level, the wave rotor treated as a "black box" must satisfy the conservation laws. The unsteady flow processes in the wave channels are periodic, and there is no net accumulation of mass or energy in the rotor. Therefore conservation of mass and energy is required of the steady port flows, summed together with any shaft work contribution.

For the internal flow analysis, the length-to-width ratio of the wave-rotor channels is assumed to be sufficiently large for the flow to be treated as one dimensional. Viscous forces and dissipation, heat transfer, and finite-channel-width effects are neglected; however, shock losses are incorporated in the flow

solution. Thus, the one-dimensional nonsteady Euler equations apply for the flow in a wave channel.

Using the ideal gas law and the relation $a^2 = \gamma p / \rho$ for the speed of sound, the conservation equations can be written in terms of a and the entropy, s. The hyperbolic character of the equations leads to solutions that can be described in terms of waves. For multi-isentropic flows in constant area straight channels, where individual particles of fluid each have constant (if different) entropy, the equations can be written (see, e.g., Kantrowitz, 1958) as

$$\frac{\delta^{\pm}}{\delta t}\left(\frac{2}{\gamma-1}a \pm u\right) = \frac{a}{\gamma R}\frac{\delta^{\pm} s}{\delta t}$$

where the directional derivatives are defined by

$$\frac{\delta^{\pm}}{\delta t} = \frac{\partial}{\partial t} + (u \pm a)\frac{\partial}{\partial x}.$$

A third equation is necessary to specify the entropy. For homoentropic flow, the characteristic quantities are constant along the respective characteristic directions (i.e., $P = 2a/(\gamma - 1) + u$ = constant along 'P' or '+' characteristics).

Wave Diagrams. The unsteady flow process within the wave rotor is best illustrated by a wave diagram. This may be viewed as an x-t diagram, which is a time history of the flow in any single channel. Alternatively, it may be viewed as an instantaneous "snapshot" of the flow in the entire rotor (ignoring the channel walls), with the rotor "unwrapped" or developed.

Figure 4 is a generic wave diagram for the RWQL schemes with external combustion. The numerals/letters indicate various states or regions of the flow; the ports will be referred to by the adjacent flow region with flow variables identical to those at the port in the channel frame of reference. In the case of the splitter scheme, the shaded port adjacent to state 1 will be open, whereas for the bypass-turbine scheme it will be closed by the end plate.

Figure 5 is a generic wave diagram for a class of schemes with internal combustion; alternate reaction fronts are indicated for shock ignition and spark/heat ignition.

Parametric Study Using Approximate Analytic Method

A major impediment to the successful design of useful wave rotor cycles has been the lack of complete closed-form analytic solutions for most wave rotor flows with significant work exchange. Given boundary conditions based on preliminary design, numerical codes can be applied. While such codes are necessary for the accurate analysis of a wave cycle design, they
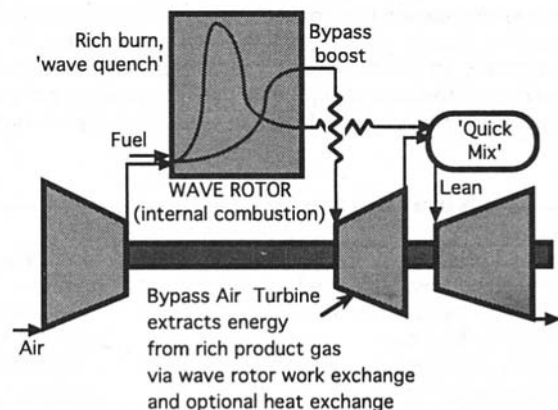
Fig. 3 Bypass turbine RWQL scheme
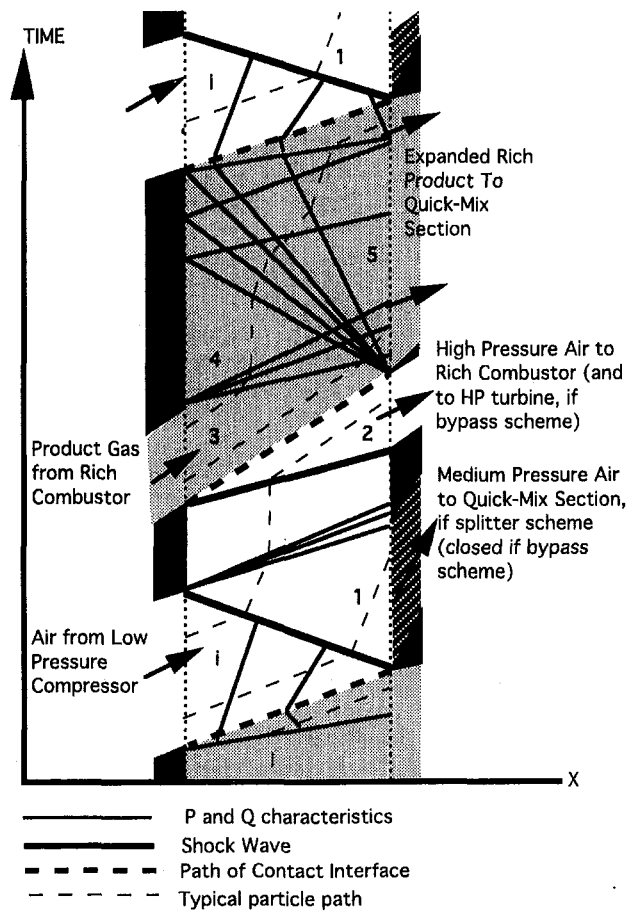
Fig. 4 Wave diagram for RWQL schemes with external combustion

TIME

Expanded Rich
Product To
Quick-Mix
Section

High Pressure Air to
Rich Combustor (and
to HP turbine, if
bypass scheme)

Medium Pressure Air
to Quick-Mix Section,
if splitter scheme
(closed if bypass
scheme)

Product Gas
from Rich
Combustor

Air from Low
Pressure
Compressor

X

——————— P and Q characteristics
▬▬▬▬▬▬▬ Shock Wave
▬ ▬ ▬ ▬ ▬ Path of Contact Interface
— — — — — Typical particle path

TIME

(Bypass
Air)

Expanded
combustion
product

Air from
compressor

Ignitor

(Blowby
air)

Add
fuel

X

▨▨▨▨▨▨▨ Reaction front induced by shock wave
▨▨▨▨▨▨▨ Reaction front initiated by spark/heat

Fig. 5   Wave diagram for internal combustion wave rotor (note Fig. 4 legend)
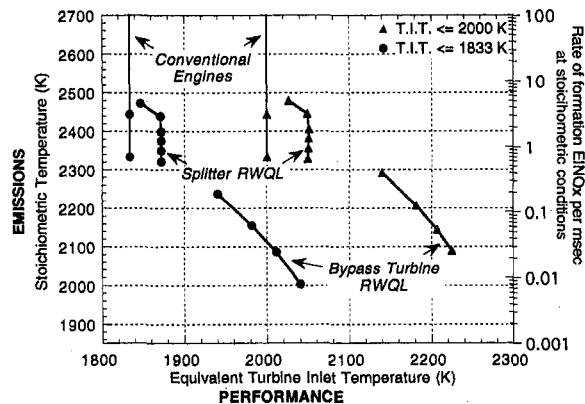
Fig. 6 Performance and emissions reduction potential of RWQL schemes

are not by themselves helpful to generate new cycles or to guide a designer quickly to a choice between various wave features.

It is therefore advantageous to develop approximate analytical relations for the nonlinear wave phenomena that occur in wave rotors, making simplifications that lead to useful expressions for preliminary design. The analyses used here are primarily applicable to wave cycles that have uniform flow in a majority of the ports; however, they do yield a complete design of such cycles in an integral sense. The details of any actual nonuniform flow in some ports can then be computed. Using this approach a wave rotor cycle is formulated to perform a desired function as an engine component. The input and output flows of the wave rotor are matched to the constraints imposed by the connecting components, such as a turbine or combustor, and the design performance of the combined system is evaluated. Detailed numerical simulation is then used to refine this model.

The parametric study provides a comparative assessment of the two versions of the RWQL scheme relative to conventional cycle engines. The performance of the RWQL cycle is computed (net cycle work and efficiency) for each combination of parameters, and is then expressed in terms of an equivalent conventional cycle with the same performance. This equivalent cycle is assumed to use perfect loss-free turbomachinery and have a 5 percent combustor pressure drop. The analytic solution is easily set up to optimize the preliminary design with respect to performance and NO_x reduction. This may not necessarily be the optimal solution if detailed flow computation is used. Nevertheless, it is a useful indication of the relative payoff possible with different approaches.

The wave cycle design for the RWQL scheme has a multiplicity of objectives, including bypass air boost pressure and reduction in stoichiometric temperature (whereas four-port topping cycle designs seek only maximum pressure gain). Also, the pressure boost sought for the injection of air in each combustion zone is narrowly specified (around 10 percent pressure drop with some allowance for unaccounted losses). The feasibility of the scheme as judged by these measures and subject to these constraints is sensitive to details of the wave cycle design.

The predicted performance varied with zone stoichiometries and maximum permitted combustion temperature. It was generally found that the performance was better with both rich and lean zone equivalence ratios closer to unity, and with higher rich zone combustion temperature. The results of the analysis are presented in terms of the following variables, which are measures of the performance improvement and NO_x emissions reduction potential:

1 Stoichiometric temperature in the RWQL cycle, which is a measure of the NO_x formation in the mixing zone.
2 Stoichiometric temperature in the equivalent performance simple cycle (a measure of the avoided NO_x).
3 TIT in the RWQL cycle.
4 TIT in the equivalent performance simple cycle, which is a measure of the performance of the RWQL cycle in conventional terms.

Plots of the stoichiometric temperature versus the equivalent TIT are shown in Fig. 6, for two fixed values of the actual TIT limit : 3300 R (1830 K) and 3600 R (2000 K). The ambient temperature is fixed at 400 R (220 K). On the right-hand side, an approximate scale is indicated for the Zeldovich NO formation rate at stoichiometric conditions corresponding to the left-
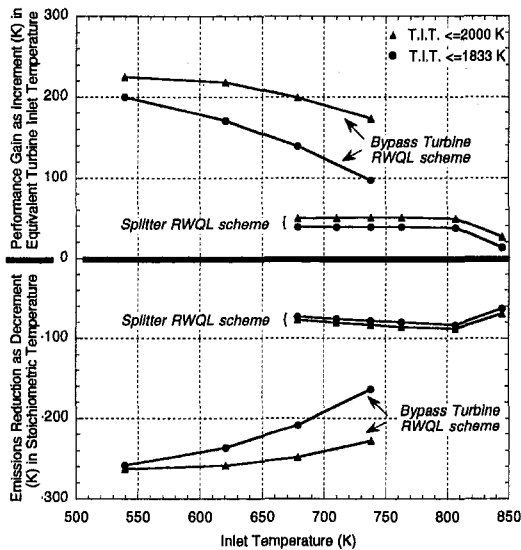
Fig. 7 Increment in equivalent TIT and decrement in stoichiometric temperature

hand side stoichiometric temperature (see Fig. 1). The rich zone equivalence ratio is fixed at 1.8 for the splitter cycle and at 1.5 for the bypass cycle, so that both meet a rich zone temperature limit of 4500 R (2500 K). The computed results are plotted for a range of inlet conditions to the wave rotor, which satisfies the constraints (as turbocompressor pressure ratio is varied).

Corresponding plots are shown in Fig. 7 of the increment in TIT (equivalent minus actual, upper plot), which is a measure of performance improvement, and the decrement in stoichiometric temperature (actual minus equivalent, lower plot) which is a measure of the reduction in mixing-zone NO formation. Clearly, the bypass turbine scheme is considerably more effective. Note that the results for the bypass turbine do not include the effect of the optional heat exchanger shown in Fig.3 (which would enhance the performance and temperature reduction further).

A sample preliminary design of the bypass turbine scheme (without heat exchange), optimized for temperature limits approximately within those mentioned above, is represented in Fig. 8. This design, involving external rich-stage combustion, was the basis for a detailed flow simulation described below.

The output and thermal efficiency of this engine cycle is calculated to be equivalent to a conventional cycle with a TIT of 3900 R(2170 K) and a stoichiometric temperature of 4130 R(2300 K), whereas the actual TIT is 3500 R(1940 K) and the mixing zone stoichiometric temperature is 3660 R(2030 K). Note that the overall equivalence ratio of 0.85 represents a heat rate about twice that of conventional and advanced low NO_x engines (without reheat or afterburn).

NO formation is estimated ($EINO_x$ units) as follows:

- Rich zone maximum NO (equilibrium) = 1.6;
- Rich product gas equilibrium NO (after expansion) = 0.001;
- NO formation rate in stoichiometric zone = 0.004 per ms.

The rich-zone NO is expected to be lower than the theoretical maximum, and the mixing zone contribution is expected to be minimal, as discussed later.

Channel Flow Simulation

Splitter RWQL Cycle Flow Simulation. The splitter RWQL wave cycle has an inherent limitation similar to that

observed in the three-port splitter cycle (e.g., Wilson, 1993), i.e., the outflow/inflow pressure gain for the "throughflow" (bypass exit flow) varies about inversely with the mass fraction exiting in this port (Region 1 in Fig. 4).

In the analytic model of the splitter cycle, there is no "dead time" between ports i and 3, i.e., 3 opens the instant i is closed. This results in excessive velocity and pressure boost in stream 2 to the rich stage burner. Figure 4 shows a finite dead time, which reduces this loss, because the air in the channel is brought to rest between states 1 and 2. The bypass port duration, and the exit pressure of the high-pressure stream, is adjustable for maximum benefit. With these features, however, the analytic solution is not applicable. This discussion does not apply to the bypass turbine cycle since port 1 is absent and the channel flow is always brought to rest in region 1 before port 3 is opened.

The bypass air pressure boost is partly determined by the back pressure in port 5, which must be sufficiently high for the lean combustion stage to be thermodynamically worthwhile. The split air mass ratio and the pressure boost were significantly influenced by the degree of evacuation of the channel when the air inlet port is opened, and by the back pressure at port 5, when other parameters were held constant.

An effort was made to optimize the air inflow velocity as determined by the timing of the inlet port opening. The analytic model sets the inlet Mach number to 1.0, since this results in a nearly uniform state 1 in the channel, and allows approximate analytic relations between the various thermodynamic states to be established. From the detailed numerical calculations, it was observed that Mach 1 inflow resulted in a more nonuniform hot gas outflow (greater losses). Advancement of the opening time such that the inflow Mach number averaged about 0.6 resulted in better performance.

The trends predicted by the analytic methods (for Mach 1 inflow) are confirmed. The simulations indicate that the stoichiometric temperature in the mixing zone can be reduced by about 100 R(60 K) compared with an equivalent performance cycle with RQL combustion. Simultaneously, the TIT is reduced by 50 R (30 K). These benefits are concomitant and cannot be traded against each other, since they both arise from the magnitude of the work transfer that the wave rotor provides from the hot gas to the air.

Bypass Turbine RWQL Cycle Flow Simulation. In the bypass-turbine RWQL scheme (Fig. 3), all the air intended for combustion is pressurized to the maximum pressure of the wave rotor. While a fraction of the air is used for rich combustion at the high pressure, the remainder, preferably after some heat addition, is expanded in a turbine, "in parallel" with the expansion of the rich gas in the wave rotor. The work produced in the turbine represents energy from combustion that is extracted
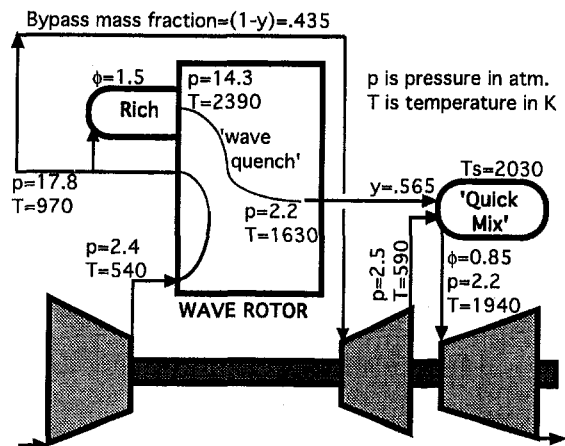
Fig. 8 Sample bypass RWQL cycle

prior to the combustion gas reaching the stoichiometric state. The two streams are mixed at the exit pressure of the rich gas from the wave rotor. This effectively allows the engine to approach the performance of the ideal stoichiometric engine, while keeping NO_x emissions and the actual turbine temperature within significantly lower limits than expected with an equivalent simple-cycle engine.

CFD simulation of the sample bypass turbine design confirmed the reductions in stoichiometric temperature and in TIT. Figure 9 is a method-of-characteristics solution of a wave cycle for the bypass-turbine RWQL scheme, based on the design of Fig. 8. A distinguishing feature is that no wave compression (which could increase NO_x formation) is allowed for the hot combustion gas. Figure 10 is a T-S diagram for the engine cycle corresponding to the simulation.

The inviscid flow equations were used in this analysis. Shock losses and losses due to nonuniform flows are accounted, but not viscous and thermal effects. If heat transfer is included or augmented, it is expected that further reduction in stoichiometric temperature will be seen.

Internal Combustion Wave Rotor Analysis

A preliminary study of combustion in the rotor was undertaken to examine the possible combustion modes and estimate
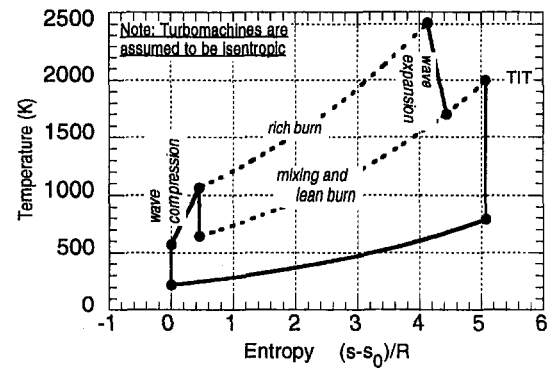
Fig. 10   T-S diagram for sample wave-rotor engine cycle

the burn duration. The numerical analysis was limited to the combustion phase of the wave cycle, ignited by shock heating. The combustion of propane and butane in air was computed, using a simplified (four-step, seven species) global reaction mechanism. Details of results are given by Nalim (1994b).

As expected, the ignitability of a mixture is a strong function of the temperature. Shock ignition was achieved for inflowing stoichiometric mixtures at a temperature above 600 K and a Mach number of about 0.8, compressed to rest in the wave rotor by the stopping shock (see Fig. 5). Reaction in the end wall gas (where the shock begins) generates pressure waves, which quickly build up into a detonation front.

For many applications, high inlet temperatures over a range of operating conditions may be unlikely, and the detonation/shock-ignition mode may be impractical or unreliable. Also, the extremely high transient peak pressure and heat load of a detonation front may be structurally unacceptable. In any case, there is considerable uncertainty about the autoignition kinetics and induction times of many fuels. For better control of the timing and rate of reaction, it may be advisable to limit the initial temperature so compression ignition is not spontaneous and to use a timed ignition source to initiate the reaction front.

Lengthwise flame propagation by laminar deflagration is very slow relative to the time scale of wave motion. Multiple ignition locations along the channel may be used. Once initiated, flame propagation will generate compression heating of the rest of the mixture and may accelerate the reaction front(s). For rapid and reliable combustion with a wide range of inlet conditions, a turbulent flame front similar to that in spark-ignited reciprocating engines is desirable. Turbulence may be generated during inflow, and by injection of a hot gas jet (or two) from a previously fired channel (suggested by early researchers as an ignition method). These design requirements will require further investigation, as part of a complete wave cycle design. A complete design would also require consideration of the methods for restarting the cycle and establishing periodic flow.

For minimum NO_x formation, the time spent at peak temperature should be kept small. This is possible if an expansion wave is set up to follow the combustion front closely, exhausting the hot gas. The timing of the exhaust port opening has to be adjusted so as not to permit the expansion to quench the combustion front.

NO_x Assessment

There is a trade-off between rich-zone and mixing-zone NO_x formation, which requires optimization of the system to minimize total NO_x. In conventional RQL systems the mixing zone is responsible for most of the NO_x. In the RWQL schemes, slightly higher rich zone NO_x may be seen, but the mixing zone NO_x will be drastically reduced.

Because of the thermodynamic advantage of maximizing the heat release at the highest pressure zone, the rich zone may

Fig. 9   Method-of-characteristics computed solution of the wave cycle for the sample bypass turbine RWQL scheme

operate at a lower equivalence ratio (less rich) than for typical RQL systems. This will also avoid soot formation. When the parameters are optimized for minimum NO_x, it is expected that any increase in rich zone NO_x will be more than offset by the reduction in mixing-zone NO_x.

Rich Zone NO. The NO formation in the rich section depends on a complex reaction kinetic mechanism, the flow pattern, and the time available. In general it has a faster time scale than in lean mixtures. Conventional RQL combustors with direct fuel injection normally provide a long residence time for homogenization and equilibration of the rich mixture before injection of bypass air. This ensures that the mixture is uniformly at rich low-NO_x conditions. In contrast, RWQL designs with external or internal rich combustion should be designed to minimize the residence time of the rich mixture at combustion temperature, provided heat release is substantially realized.

The residence time in the rich combustor can be very short because it is not required to equilibrate and mix thoroughly before expansion. Indeed, continuation of mixing and reaction of some residual fuel during and after expansion in the wave rotor will be beneficial, since this will provide radicals that can reduce NO as the temperature falls. Sufficient time can be provided downstream for homogenization (aided by wave-rotor-induced flow shear) and approach to low-NO_x equilibrium at lower temperature before injecting bypass air.

Mixing Zone NO. Mixing zone NO formation is governed primarily by the peak temperature (near-stoichiometric mixture) and the residence time at high temperatures. The residence time depends on the rate and completeness of mixing.
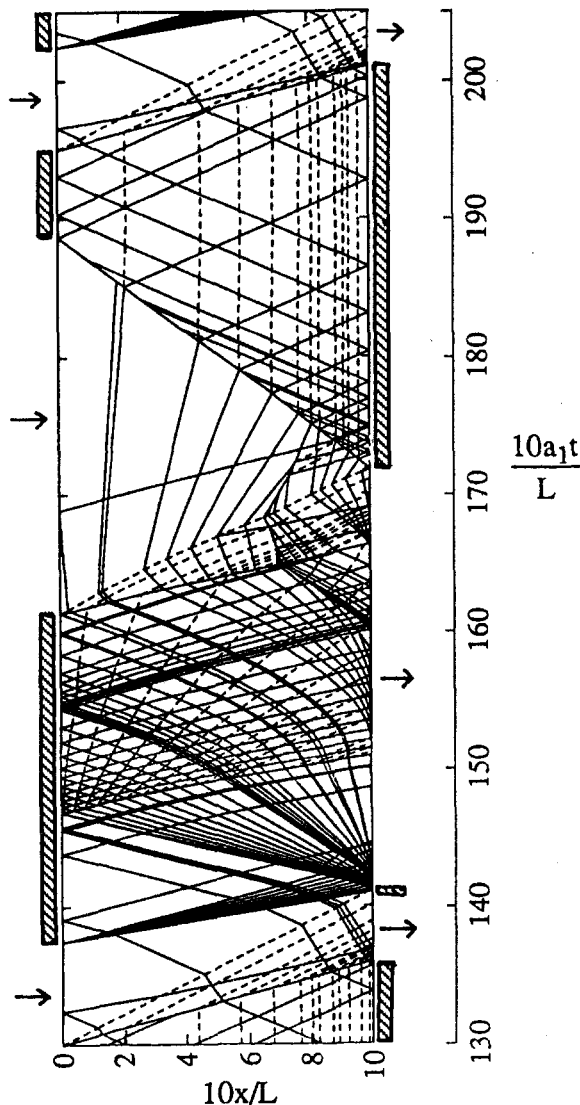
The main design variables determined from the overall cycle design are: (a) available pressure differential between the rich product gas and the bypass air; (b) bypass to mainstream mass flow ratio; (c) the temperature of each stream; and (d) the equivalence ratio of the rich zone.

Dilution zone mixing studies (Holdeman, 1991) have identified two significant design parameters that influence the mixing pattern: jet-to-mainstream momentum flux ratio (J) and orifice spacing-to-duct height ratio (S/H). It has been shown that the mixing can be considerably enhanced by increasing the pressure differential (and thus J).

For the example design presented previously the peak stoichiometric temperature is 3660 R (2030 K), and the peak NO formation rate is only 0.004 per ms. By contrast, for a conventional cycle with RQL combustion and equivalent performance, the corresponding peak NO formation rate is about 1 per ms. The increased mixing rate will also help. Therefore, the contribution to NO formation in the mixing zone of the wave rotor engine cycle can be expected to be minimal.

Conclusions

Design and simulations performed indicate a substantial benefit in performance enhancement and emissions reduction by using the RWQL concept. It provides the benefits of wave rotor enhancement of gas turbine engines, while controlling NOx emissions. Rich-Wave-Quench-Lean (RWQL) cycles have been developed and examined parametrically. CFD simulations have been performed on the unsteady wave rotor flows and periodic solutions have been obtained for cycles matched to an external combustion scheme. Preliminary reactive-flow CFD simulations have also been performed on the combustion stage of internal-combustion wave rotor cycles. The bypass turbine scheme is considerably more effective than the splitter scheme because of the large work transfer from the rich product gas to the air. Although this introduces greater complexity, especially with external combustion, the payoff is substantial, with the stoichiometric temperature in the mixing zone being reduced by 450 R (250 K), and engine performance improved equivalent to a nearly 400 R (220 K) rise in TIT. Equivalent benefits could be obtained if the wave rotor produces shaft work instead of the bypass turbine. Alternately, the bypass turbine's output and the overall performance and temperature reductions could be enhanced by augmenting heat transfer from the rich gas to the bypass air. The mechanical complexity could be simplified, and additional benefits obtained, if internal combustion is accomplished. In particular, the rich zone NO_x formation could be reduced, losses reduced, and pressure gain increased. Issues relating to combustion rate, consistency, and hardware design remain to be addressed.

References

Azoury, P.H., 1965–1966, "An Introduction to the Dynamic Pressure Exchanger," *Proc. IMechE,* Vol. 180, Part 1.

Foa, J.V., 1960, *Elements of Flight Propulsion*, Wiley, New York.

Holdeman, J.D., 1993, "Mixing of Multiple Jets With a Confined Subsonic Crossflow," *Progress in Energy and Combustion Sciences*, Vol. 19, pp. 31–70.

Kantrowitz A., 1958, "One-Dimensional Treatment of Nonsteady Gas Dynamics," in: *Fundamentals of Gas Dynamics*, H.W. Emmons, ed., Princeton University Press.

Nalim, M.R., Mocsari, J.C., and Resler, E.L., Jr., 1993, "Wave Cycle Design for NO$_x$-Limited Wave Rotor Core Engines for High Speed Propulsion," ASME Paper No. 93-GT-426.

Nalim, M.R., 1994a, "Wave Cycle Design for Wave Rotor Engines With Limited Nitrogen Oxide Emissions," Ph.D. Thesis, Cornell University, Ithaca, NY.

Nalim, M.R., 1994b, "Advanced Wave Rotor Design for Low NO$_x$ Turbine Engines," NASA SBIR Phase I Contract No. NAS3–27208 Final Report, Proj. 4355, CFD Research Corp., Huntsville, AL.

Resler, E.L, Jr., Mocsari, J.C., and Nalim, M.R., 1994, "Analytic Design Methods for Wave Rotor Cycles," *Journal of Propulsion and Power*, Vol. 10, No. 5, pp. 683–689.

Shreeve, R.P. ,and Mathur, A., eds., 1985, *Proc.1985 ONR/NAVAIR Wave Rotor Research and Technology Workshop*, Naval Postgraduate School, Monterey, CA.

Sladky, J.F., Jr., ed., 1984, "Machinery for Direct Fluid-Fluid Energy Exchange," Vol. AD-07, Aerospace Div., ASME.

Wilson, J., and Fronek, D., 1993, "Initial Results From the NASA-Lewis Wave Rotor Experiment," Paper No. AIAA-93-2521.

A Conceptual Design Methodology for Predicting Bleed and Horsepower Requirements of Military Aircraft Engines

J. D. Cyrus
Naval Aircraft Warfare Center,
Warminster, PA 18974

Conceptual design codes have been developed to provide conceptual design estimates of bleed and horsepower extraction requirements of advanced military aircraft. This paper describes the methodology for the computer codes. The validity of the models was assessed by generating bleed and horsepower estimates for four advanced aircraft configurations not included in the data base and comparing the model estimates to manufacturer's estimates.

Background

In conceptual design studies the propulsion engineer is typically tasked to provide installed engine performance data decks to the aircraft conceptual designer, who will run the decks in an aircraft synthesis model. In preparing the decks, the propulsion engineer and aircraft conceptual designer working together are typically able to develop inlet and nozzle configurations that can then be used as a basis for estimating inlet losses, and spill drags, nozzle pressure losses, and throttle dependent drags. But all too often the propulsion engineer tries to get a definition of engine bleeds and horsepower extractions from the aircraft conceptual designer and the latter in turn expects to get them from the propulsion engineer. In actuality, this communication loop is fundamentally wrong; to assess bleed and horsepower extraction requirements, the propulsion engineer or aircraft conceptual designer should have approached the bleed and horsepower users.

The first step in developing computer codes for estimating bleed and horsepower usage was to identify the overall bleed and horsepower requirements for contemporary aircraft. Then, the major bleed and horsepower using subsystems were identified. After the users were identified, a series of data bases was developed to quantify the uses for various subsystems. Analytical correlations were then developed to establish bleed and horsepower losses for existing and developmental aircraft (in the data base. Finally, stand-alone computer codes were developed to facilitate calculations.

Engine Bleed Flow Requirements for Existing Aircraft

Bleed flow data were obtained for six contemporary combat aircraft. Bleed flow rates in pounds per minute (PPM) are shown in Table 1.

The bleed flows for these engines varied over a range of 28-105 PPM. Bleed flows requirements were obtained for the F-14 and FA-18 across the flight envelope; these vehicles showed a variation in bleed flow of approximately 3:1.

The principal bleed users for military aircraft are shown below:

- On Board Inert Gas Generating System (OBIGGS) or fuel tank pressurization system
- On Board Oxygen Generating System (OBOGS) used to supply air to the crew
- Rain Removal System
- Fuel Pressurization System (when an OBIGGS is not available)
- Cabin air for the crew
- Avionics cooling
- Ice protection.

Horsepower Extraction for Various Aircraft

Horsepower extraction requirements were obtained for a number of contemporary military aircraft as well as for a number of preliminary aircraft designs. The maximum horsepower extraction requirements are shown in Table 2 for various aircraft–engine combinations.

The total horsepower demand on the engine is the sum of the horsepower for:

- Avionics power
- Environmental Control System (ECS)
- Hydraulics for flight management

Bleed and Horsepower Use Methodology

Parasitic demands upon the engine result from bleed demands (from the OBIGGS, OBOGS, rain removal, defog, ice protection, and cabin air cooling systems), from electrical power requirements (for avionics and other power users) and from power requirements for hydraulic systems. The avionics require cooling to remove waste heat; this is supplied by the Environmental Control System (ECS) via an air cycle system, a vapor cycle [refrigeration] system, or a combination system, which uses both air cycle and vapor cycle cooling. The air cycle typically uses engine bleed (and the methodology assumes that an air cycle is driven by engine bleed—but, it should be noted that occasionally for turboshaft systems such as the P-3 and V-22, the air cycle may be driven by the power output shaft). The vapor cycle ECS compressors can be driven by electrical, hydraulic, shaft, or bleed power; however, only electrically driven compressors are in use or in development. Therefore, the methodology assumes that electrical power is used to run its compressors. A schematic diagram of the methodology used to assess bleed and horsepower demands is presented in Fig. 1.

Table 1 Engine bleed flow rates for military aircraft

Aircraft	Bleed Flow PPM
F-14 D	28/87
F-15 C/D	38/84
F-15 E	48/105
FA-18 A/B	30/54
FA-18 E/F	50/87
F-22	66

Fig. 2 Cabin airflow cooling

Table 2 Maximum horsepower extraction for various aircraft

A/C	ENGINE	HPX (Per Eng)
F-14	TF30	85-125
F-14 D	F110	85
F-15 C/D	F110	120-130
F-15 E	F110	170-190
FA-18 C/D	F404	55-97
FA 18 E/F	F414	85-165
F-22	F119	250 AVE
F-22	F119	500 MAX

Bleed Calculations

A FORTRAN computer code, BLDHP.FOR, was developed to analyze bleed flow requirements for the total aircraft and per engine. The bleed requirements of the OBIGGS, OBOGS, rain removal, defog, and cabin air cooling systems depicted in Fig. 1 can be analyzed directly. In addition, the avionics may impose an indirect bleed penalty on the aircraft through the environmental control system (ECS). Since almost all the electrical power supplied to the avionics is converted into waste heat (except for a fraction of the energy supplied to the radar, which is radiated away) the cooling load for the avionics will be the same order of magnitude as the electrical load. This cooling load is typically handled by the ECS using an open-loop bleed air system (which uses bleed air) or by a closed-loop vapor cycle system (which predominantly uses electrical power). On occasion, the avionics equipment in the cockpit will be cooled by bleed air even when a closed-loop vapor cycle system is

used to cool the bulk of the avionics. Bleed air is typically available in the cockpit for crew use and for defogging.

OBIGGS System. The OBIGGS was assumed to supply inert gases to the fuel tanks to maintain pressurization. Based on FA-18 and manufacturer's preliminary design data it was assumed that the air required varies directly as a function of power setting.

$$B3IG = 5*PS/50 \ [PPM]$$

where

$$PS = \text{Power Setting}$$
$$PS = 20 @ \text{ Idle}$$
$$PS = 35 @ \text{ Cruise power}$$
$$PS = 50 @ \text{ Intermediate rating}$$
$$PS = 100 @ \text{ Maximum rating}$$

OBOGS System. Based on FA-18 18 and manufacturer's preliminary design data, the OBOGS was assumed to provide one PPM of air per crew member throughout the flight envelope.

Rain Removal System. Data for a number of aircraft showed that the rain removal system would use from 20 to 28 PPM when in operation; the model assumed a constant value of 25 PPM while in use. It was assumed that the rain removal system would be in use during operation at less than 10,000 ft; this includes the following conditions:

- Ground idle
- Takeoff
- Climb
- Descent
- Loiter
- Approach

Fig. 1 Bleed and horsepower methodology schematic
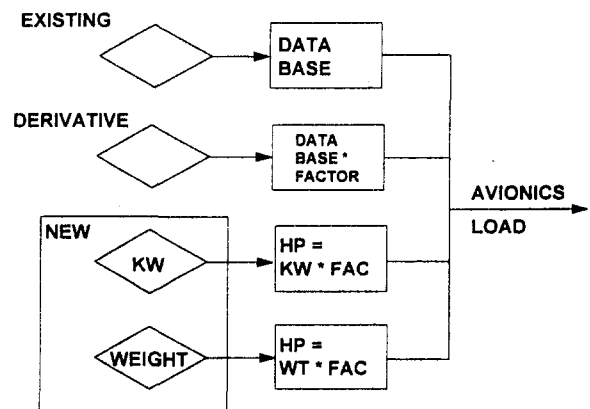
Fig. 3 Avionics bleed estimation methodology
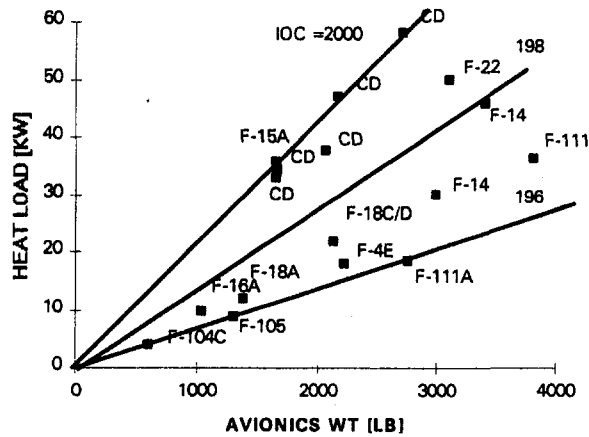
Fig. 4 Avionics weight-heat load correlation

Fig. 6 Conventional bootstrap environmental control system

Cabin Defog System. Cabin defogging is a pilot-selected option on the F-14 and FA-18. The cabin defog system uses air normally provided for cabin air cooling and heating; it does not require any additional bleed from the engine.

The FA-18 cabin airflow cooling schedules shown in Fig. 2 for single seat and two seat variants were used in the bleed model.

Horsepower Calculations

As described above, the principle horsepower users for the aircraft are the electrical load of the avionics system and the hydraulics load of the flight management system. In addition, there will be an electrical load imposed by the fans of the air cycle ECS or the compressor of a vapor cycle ECS.

Avionics System. An extensive data base was developed for avionics systems. This data base quantifies avionics power requirements (or heat loads) and weights for numerous aircraft in the inventory. A methodology, shown schematically in Fig. 3, was developed to provide estimates of avionics power requirements. To maximize accuracy, the database should be used directly when information is available. For aircraft not in the database, weight–power (see Fig. 4) and aircraft model–power (see Fig. 5) correlations were developed to estimate the power requirements. It was found that avionics weights (and therefore power requirements) for derivative aircraft were typically 30 percent higher than the previous model. It was also found that avionics power requirements (or avionics heat load) correlated with avionics weight and an aircraft initial operational capability (IOC); this can be used to estimate requirements for new aircraft or to check the power requirements for derivative aircraft.

Environmental Control System. The avionics heat load is cooled by the Environmental Control System (ECS). The three different types of ECS that are considered in the model

include a bootstrap open-loop air cycle system, shown in Fig. 6, which uses engine bleed air to provide cooling for the cockpit and avionics, an electrically driven closed-loop vapor cycle system, shown in Fig. 7, which also cools the cockpit and avionics, and a combination system, which typically uses an open-loop air cycle system to provide cooling air for the cockpit and a vapor cycle system to provide liquid cooling for avionics. The methodology was developed to analyze the case where a portion of the avionics waste heat is cooled by fuel.

An extensive data base was developed to identify system parameters for environmental control systems; these include:

- System type
  - Air cycle
  - Vapor cycle
  - Combination air cycle + vapor cycle
- Refrigerant used, if applicable
- Cooling capability (load)
- Engine bleed (PPM)
- Weight
- Temperature
  - Inlet
  - Outlet

In Fig. 8, it can be seen that data from this set show a good correlation of increasing cooling capability (cooling load) with weight. When weight data are available this relationship can be used to provide a check on the avionics power because the cooling capacity of the system should equal or exceed the waste heat generated by the avionics (and the waste heat generated is essentially all the power input into the avionics).

Fig. 5 Avionics power growth for new models
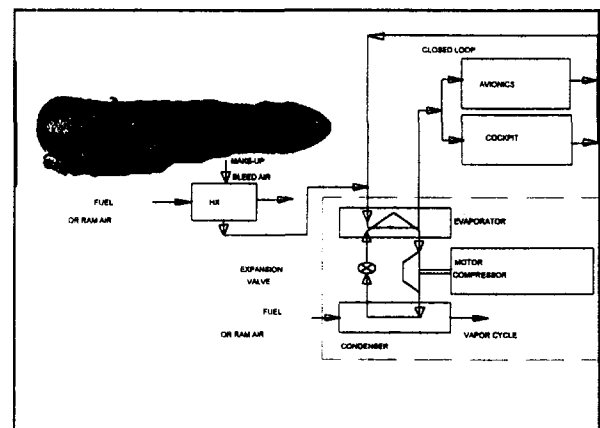
Fig. 7 Vapor cycle environmental control system
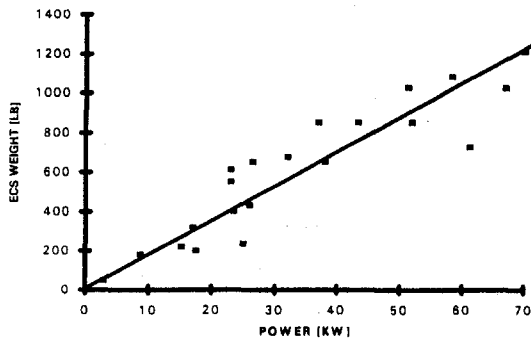
Fig. 8 Cooling capacity variation with weight for ECS

Fig. 10 F-18 throttle usage on air–ground mission

Bootstrap Open-Loop Air Cycle System. The bootstrap open-loop air cycle system uses engine bleed air. The bleed air from the engine is typically cooled by ram air taken from the inlet or a separate intake. The bleed air is then compressed (and heated) and then run through a second heat exchanger, which is cooled by either ram air or fuel. The air is then expanded through a turbine, which serves the dual functions of driving the compressor and cooling the air. The cooled air is then delivered to the avionics and cockpit where it provides cooling and is then typically dumped overboard. The cooling capacity of the air is calculated in the model by the relationship:

$$h = C_p * (T_{out} - T_{in})$$

where:

C_p = specific heat at constant pressure = 0.24 Btu/lb°F
T_{out} = cooling air discharge temperature (specify for advanced technologies default value = 160°F, historical)
T_{in} = cooling air entry temperature = 40°F at SLS and 0°F at altitude

Unlike the vapor cycle system, the air cycle system does not require a supplemental pressurization source. However, because air is typically taken from the high-pressure compressor discharge at temperatures of up to 1000°F and discharged at temperatures of approximately 160°F, the system is markedly inefficient.

Vapor Cycle System. The vapor cycle system depicted in Fig. 7 uses a closed-loop system to provide cooling to the cockpit and avionics. The coolant loop is itself cooled by a refrigeration loop driven by an electrically powered motor. For the system shown, a small quantity of bleed air is taken from the engine to make up for air use or leakage. This can realistically be

assumed to be zero for analytical purposes. Power is required to drive the vapor cycle motor compressor for the refrigeration loop. Data for two advanced vapor cycle systems is available: The F-22 compressor requires 30 kW of power and provides 50 KW of cooling [60 percent]; the Energy Efficient Environmental Control System, EEECS, flight tested on the P-3 at NAWC AD WAR, required 28.2 kW of power to provide 42.2 KW of cooling [66 percent]. The methodology assumes that the compressor load is approximately 63 percent of the cooling load.

Combination ECS. For those vehicles with a combination system, the methodology allows the user to specify the fraction to be cooled by the air cycle system. Engine bleed is then calculated for cooling the fraction in the air cycle portion of the system and power is calculated for the vapor cycle compressor in the liquid refrigeration loop as described above.

Hydraulic Power

Hydraulic power data were obtained from the NAWC AD WAR Fluid System Branch for four existing and one advanced aircraft. It was found that hydraulic power correlates roughly with TOGW (see Fig. 9). The TOGW correlation was used in the model to provide a first-order estimate of steady-state hydraulic power requirements. It was assumed that hydraulic power requirements would correlate with the usage of hydraulic powered equipment including:

- Wing leading and trailing edge devices
- Horizontal tail surfaces
- Vertical tail surfaces
- Speed brakes
- Landing gear
- Armament

For up-and-away flight, it was assumed that maneuvering loads would require the use of control surfaces which in turn would require hydraulic power. The Navy's Generalized Engine Throttle Usage Prediction program (GETUP) was used to calcu-

Fig. 9 Hydraulic system HP variation with TOGW

Table 3 Hydraulic system spread sheet

HYD CALC	IDL	TO	CLIM	CRU	COM	LOI	DES	APP
Events/Sec		0.1	0.092	0.02	0.72		.007	.227
NZ	1	1.75	1.5	1.25	4.6	1.25	1.25	2.0
NZ/NZ MAX	0.21	0.38	0.32	0.27	1.0	0.27	0.27	0.43
Hyd Fac	0.46	1.0	0.56	0.52	1.0	0.52	0.46	1.0

late maneuvering loads for the F-18 A/B on a postmaintenance check flight (PMCF) and an air-to-ground mission (depicted in Fig. 10) a variety of mission segments were "flown" including: takeoff, climb, cruise, descent, approach, landing, air–air combat, air–ground combat, landing, touch-and-go.

The frequency, duration, and magnitude of the maneuvering loads for the FA-18 A/B were established for each of the above segments. It was found that combat was far and away the most demanding of the up-and-away flight segments. The other segments performed various maneuvers with fairly uniform G loadings within the segment. It was found that variations in up-and-away maneuvering loads correlated well with the square root of the normalized hydraulic load.

The model was set up to use the maximum hydraulic loads during the takeoff and approach segments. Data from a flying quality manual for the F-14 showed that the approach segments had marked throttle excursions. In addition to using flight control hydraulics, the vehicles also retract and extend the landing gear during these segments. Speed brakes may also be employed during the approach segment. A hydraulic system spread sheet, HYDCALC.XLS, was developed to calculate hydraulic system loads for various mission segments. This spreadsheet is shown in Table 3.

Comparison of Bleed/Horsepower Model Estimate to Manufacturer's Estimates

The NAWCADWAR bleed flow model was used to calculate the bleed and horsepower that the AFX airframe contractors configurations would need based upon their subsystems. The calculated results were then compared to manufacturer's estimates. Since the manufacturer's AFX configurations were not included in the original database, this provided a first-order check on the accuracy of the model.

The NAWCADWAR model bleed flow estimates varied from 66 to 110 percent of the manufacturer's bleed flow estimates; the average bleed flow was 93 percent of the manufacturer's estimate.

As a starting point for the NAWCADWAR horsepower estimation methodology, avionics weights were obtained for the manufacturer's AFX systems. The avionics power requirements were then calculated using the avionics weights and the correlation is depicted in Fig. 4. These estimates were then compared to the manufacturer's cited values; good agreement was obtained
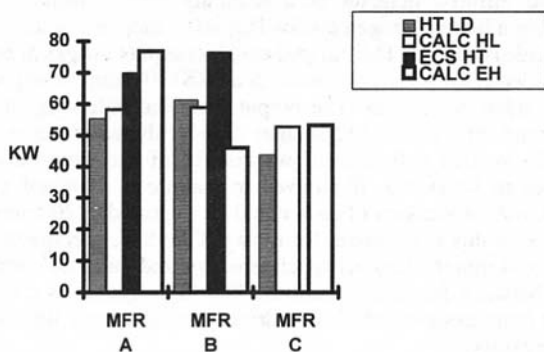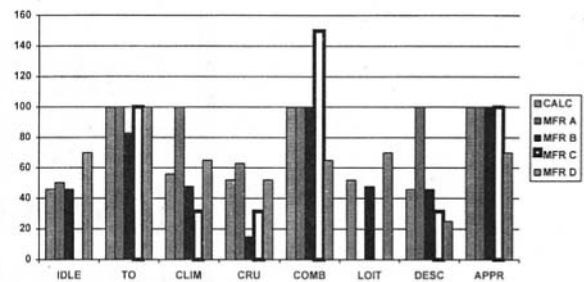
Fig. 12 Hydraulic horsepower comparison across mission

between the predicted and manufacturer's heat loads; the difference ranged from two to nine hp.

The ECS cooling loads were used as a check on the avionics power requirements using the methodology described above. The ECS weights cited by the manufacturer were used to estimate the ECS cooling load. The ECS cooling load should equal or exceed the avionics power required. As shown in Fig. 11. this was found to be the case for both the manufacturer's cited values and the calculated values except for the case of the calculated cooling load of Manufacturer B.

The NAWCADWAR estimates of the maximum hydraulic horsepower varied from 77 to 134 percent of the manufacturer's estimates; the average NAWCADWAR estimate was 99 percent of the manufactuer's estimate.

The hydraulic system calculation model was also used to assess the variation in hydraulic horsepower for a variety of mission segments. To simplify the analysis of the segment-to-segment variations, the manufacturer's maximum values were input into the model and the variation across mission segments was calculated; a representative comparison is presented in Fig. 12. In general, the correlation between the manufacturer's cited values and the calculated values is very good.

The total horsepower per engine was obtained by summing the avionics, hydraulics, and ECS horsepowers. The NAWCADWAR estimates were found to vary from 95 to 116 percent of the manufacturer's estimates. The average discrepancy between the method and the manufacturer's estimates was 4 percent.

Conclusions

The methodologies were compared to manufacturer's estimates of bleed and horsepower requirements for four AFX configurations. Good correlations were obtained between the sub-elements of the bleed and horsepower codes and the manufacturer's estimates. The average unexplained bleed error for the four cases was less than eight percent. The average calculated horsepower error for the four cases was four percent. The average discrepancies between the method prediction and the manufacturer's estimates would suggest that the methodology is conceptually sound. An examination of the maximum discrepancies between the code and the manufacturer's estimates indicates that the user should—at this stage of development—proceed with caution. But it is anticipated that the code/methodology will benefit from use and that new data from existing aircraft and new proposals will improve the accuracy and reduce the magnitude of its errors. It is anticipated that periodic updates to the code will be made to improve its accuracy.

Fig. 11 Heat load comparisons

W. A. Ellingson

S. A. Rothermel

Energy Technology Division,
Argonne National Laboratory,
Argonne, IL 60439-4838

J. F. Simpson

Solar Turbines, Inc.,
San Diego, CA 92186-5376

Nondestructive Characterization of Ceramic Composites Used as Combustor Liners in Advanced Gas Turbines

Nondestructive characterization (NDC) methods, which can provide full-field information about components prior to and during use, are critical to the reliable application of continuous fiber ceramic matrix composites in high-firing-temperature (>1350°C) gas turbines. [For combustor liners, although they are nonmechanical load-bearing components, both thermal characteristics and mechanical integrity are vitally important.] NDC methods being developed to provide necessary information include x-ray computed tomography (mainly for through-wall density and delamination detection), infrared-based thermal diffusivity imaging, and single-wall through-transmission x-ray imaging (mainly for fiber content and alignment detection). Correlation of the data obtained from NDC methods with subscale combustor liner tests have shown positive results at thermal cycling temperatures from 700°C to 1177°C.

Introduction

Continuous fiber ceramic matrix composites (CFCC's) are being evaluated for their application to natural-gas-fired industrial gas turbine engines. These material systems include $SiC_{(f)}/SiC$, $Al_2O_{3(f)}/SiC$, and $Al_2O_{3(f)}/Al_2O_3$. CFCC material systems offer many advantages including: noncatastrophic failure, high fracture toughness at elevated temperature (>1250°C), and reduction in engine emissions by virtue of allowing higher gas-firing temperatures. For reliable operation, these applications require that uniform thermal properties be assured both prior to insertion of the component and during the life-time of the component. Development of nondestructive methods that can measure uniform thermal properties, e.g., diffusivity, thus is of prime importance. A nondestructive technique based on infrared thermographic imaging is one likely candidate for characterizing the uniformity of thermal properties. Thermographic techniques offer certain advantages, including: noncontact, full-field potential, high sensitivity, and usually reasonable cost.

Usually, thermographic imaging systems are used to obtain surface temperature maps at some instant in time or to observe changes in surface temperature as a function of time. In such cases, no thermal property of the material is determined, only surface temperature. However, in 1961 Parker et al. described a method that allows determination of thermal diffusivity by monitoring a thermal transient. This technique utilizes a thermal pulse (e.g., high-energy flash lamp) on one side of a specimen and a method (e.g., infrared imaging camera) to monitor the thermal transient on the back of the specimen. Quantification of thermal diffusivity measurements can thus be accomplished provided calibration methods are available (Steckenrider et al., 1994).

In this work, $SiC_{(f)}/SiC$ CFCC materials produced by isothermal CVI and $SiC_{(f)}/SiC$ produced by polymer-derived SiC were studied by a "home-built" flash thermal diffusivity system designed to be flexible to allow study of engineering components. Specimens examined included thermally shock damaged

specimens and subscale combustor liners being developed for natural gas fired gas turbines.

Thermal Imaging System

The thermal imaging system developed for this work is shown in Fig. 1. It consists of a commercially available flash heating system in the form of a 6.4 Kj flash lamp system, a commercially available infrared imaging system with a 3–12 μ optical band-pass lens system, a PC computer with on-board digital frame grabber board and a 128 × 8-bit frame cache memory and locally written software for acquiring the data and for computation of thermal diffusivity. The test specimen is placed between the flash lamp and the infrared camera. For the specially prepared specimens (including thermally shocked specimens), insulation was provided such that nominally one-dimensional heat flow resulted. For our experiments we used diatomaceous earth as the insulator.

The infrared detector is a scanning-type radiometer employing a liquid nitrogen cooled HgCdTe (mercury–cadmium–telluride) detector. The infrared camera outputs images at nominal video rates (≈30 frames/s) in an RS170 format using standard video equipment. The output from the video signal was digitized into 512 × 512 images at 8-bit dynamic range. The locally written software allows control of the time between frames to be stored. If allowed to capture at standard video rates, only 4 seconds of data could be captured (120 frames). Although this is adequate for most $SiC_{(f)}/SiC$, specimens less than 3–4 mm thick, other specimens required more time separation between frame acquisitions. The flash system is a 6.4 kJ flash lamp system, which can drive more than one flash lamp if necessary.

In this work we have assumed that for the relatively low temperatures of the experiments, the thermal properties are independent of temperature, thus allowing the well-known Fourier–Biot equation (Touloukian et al., 1973) to take the form

$$\rho C_p \frac{\partial T}{\partial t} = K \frac{d^2 T}{dx^2} \tag{1}$$

where

ρ = material density
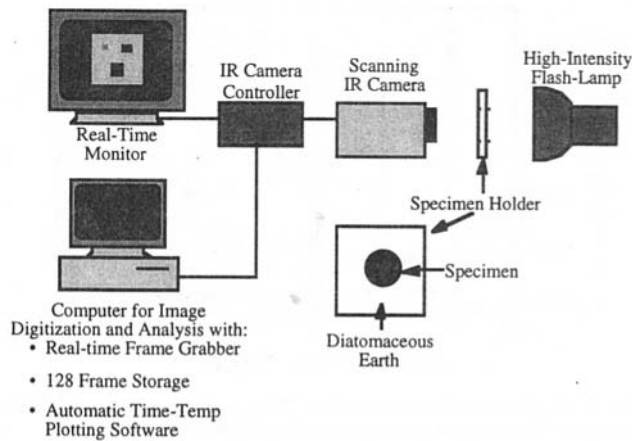
Fig. 1 Schematic diagram of thermal diffusivity system

C_p = material specific heat
κ = thermal conductivity.

However, if one defines thermal diffusivity, α, as

$$\alpha = \frac{K}{\rho C_p} \qquad (2)$$

then Eq. (1) becomes

$$\frac{\partial T}{\partial t} = \alpha \frac{d^2 T}{dx^2} \qquad (3)$$

The American Society for Testing Materials (ASTM, 1994) has shown that α can be determined as

$$\alpha = \frac{L^2 \cdot 0.13879}{t_{1/2}} \qquad (4)$$

where

L = specimen thickness
t = time required to reach $\frac{1}{2}$ the maximum surface temperature.

This is the method that was employed in all this work.

Calibration of the system is performed by using a graphite sample from the National Institute for Science and Technology (NIST). The thermal diffusivity value of this sample was provided and was stated to be 72×10^{-6} m²/s. The length of sample provided allowed us to make specimens of 4, 11, and 19 mm in thickness. Figure 2 shows typical surface temperature versus time plots obtained from the 11 and 19 mm thick samples
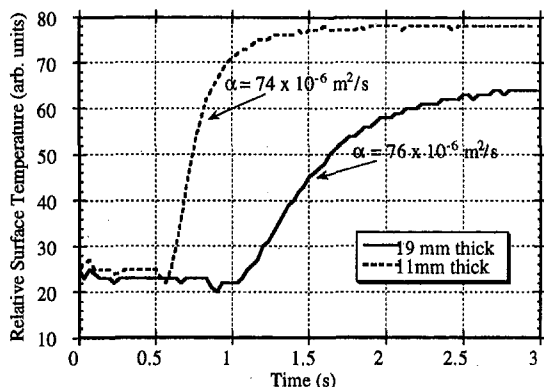
Fig. 2 Typical temperature—time plots obtained by the thermal diffusivity imaging system

Table 1 Specimen dimensions for the thermal diffusivity measurement

Material	Specimen Dimension
Nextel™ fiber CVI SiC composite	4 x 6 x 10 mm
Nicalon™ fiber/polymer-derived SiC composite	2.6 x 4.6 x 10 mm

and the resulting thermal diffusivity values obtained, i.e., 74 and 76×10^{-6} m²/s, respectively.

In order to obtain full-field thermal diffusivity image maps, locally written software had to be developed. The software developed utilized the digitized time-dependent image sequence of 512×512 images. However, the 512×512 images were partitioned into arrays of a size that could be specified for the particular application. For the combustor liner work, 0.5 mm $\times$ 0.5 mm regions on the liner resulted in 11 pixels by 11 pixels (i.e., each pixel was about 50 μm). The thermal diffusivity for each region was calculated over these regions. The resulting diffusivity values were then normalized to 16-bit integers and arranged in an image file format to allow a thermal diffusivity to be presented.

Specimen Description

We examined 2 different types of specimens; (*a*) flexure bar specimens (see Table I) and (*b*) subscale combustor liners 20 cm (8″) dia by 40 cm (16″) long and 20 cm (8″) dia by 20 cm (8″) long with wall thicknesses of 3.5 mm.

Thermal Shock. The CFCCs tested were Nextel™ 312 fiber-reinforced CVI SiC matrix composite, and Nicalon™ fiber-reinforced polymer-derived SiC composites. The Nextel™ fiber/CVI SiC composite had a carbon interlayer between fibers and the matrix, and the Nicalon™ fiber/polymer-derived SiC composite had a proprietary fiber coating and filler materials. The fibers in the two composites were 2-D plain woven.

Subscale Combustor Liner. The SiC$_{(f)}$/SiC combustor liners were produced using a Nicalon™ fiber/SiC matrix using isothermal CVI. The weave of the liners was an angle interlock weave. Figure 3 is a photograph of one of the liners showing the rough surface which was observed on these liners. The data acquisition setup for thermal diffusivity image mapping was slightly different than that shown earlier in Fig. 1. For these studies, the flash lamp was inserted inside the liner and the camera was mounted so that it would observe the outer surface. This setup is shown schematically in Fig. 4. The outer surface of each liner was marked into approximately 50 mm $\times$ 50 mm segments of the full field. A special heat shield setup was internal to the combustor to act as a special radiation reflecting system. This allowed the flash lamp energy to heat only the particular segment of interest and allowed faster data acquisition of other regions on the liners. Prior to obtaining any data on the liner, calibration was established by placing the NIST calibration specimens in the position of the liner. Adjustments to the experimental setup were made such that the calibration values were as close as possible to the desired values.

Results

Thermal Shock Studies. The results of utilizing the system to detect thermal shock damage are shown in Figs. 5–8. The thermal diffusivity of the CFCCs is plotted as a function of the quench temperature difference or number of quench cycles. In the case of Nextel™ fiber/CVI SiC it is seen from Fig. 5 that the diffusivity of the composite remains largely unchanged up to $\Delta T = 400°C$, then it decreases with increasing quench temperature difference. At $\Delta T = 1000°C$, a drop of 40 percent in

Fig. 3 Photograph of SiC$_{(f)}$/SiC combustor liner

Fig. 6 Thermal diffusivity of Nicalon™ fiber/polymer-derived SiC composite as a function of the quench temperature difference

measured thermal diffusivity was observed. It has been suggested (Singh and Wang, 1994) that the decrease in thermal diffusivity caused by thermal shock damage may be attributed to: (1) the formation of cracks in the matrix, (2) debonding of fibers from the matrix, and (3) removal of the carbon interlayer by oxidation. One specimen was heated to 1020°C and allowed

Fig. 7 Thermal diffusivity of Nextel™ fiber/CVI SiC composite as a function of the number of quench cycle
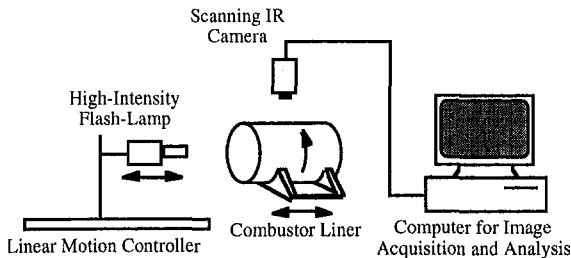
Fig. 4 Schematic diagram of experimental setup used to obtain full field thermal diffusivity image maps of the subscale combustor liners
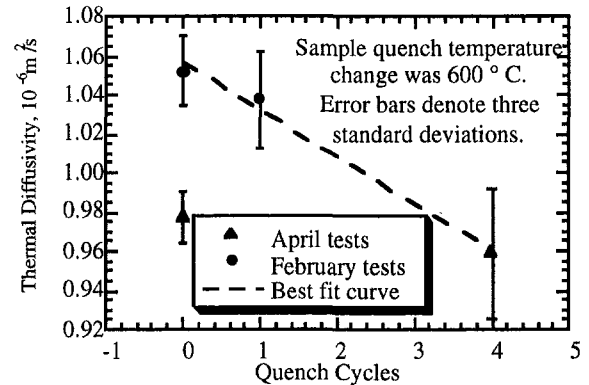
Fig. 8 Thermal diffusivity of Nicalon™ fiber/polymer-derived SiC composite as a function of the number of quench cycle

to cool down slowly in air with no water quenching. The measured thermal diffusivity of this specimen, see Fig. 5, exhibited a 25 percent decrease. It has been suggested that these data show all three factors that could contribute to the decrease in thermal diffusivity.

Figure 6 shows the measured thermal diffusivity of the Nicalon™ fiber/polymer-derived SiC composite. These data suggest that the measured thermal diffusivity decreased at a ΔT as low as 200°C, but this measured change is easily within experimental error and likely is not actual, as 200°C is not high enough to oxidize the carbon interlayer. Further, the detected decrease in thermal diffusivity continued to a $\Delta T = 800$°C. At $\Delta T = 1000$°C, the thermal diffusivity showed an unexpected increase to about its original value.

Fig. 5 Thermal diffusivity of Nextel™ fiber/CVI SiC composite as a function of the quench temperature difference

(a) Liner 1

(b) Liner 2

(c) Liner 3
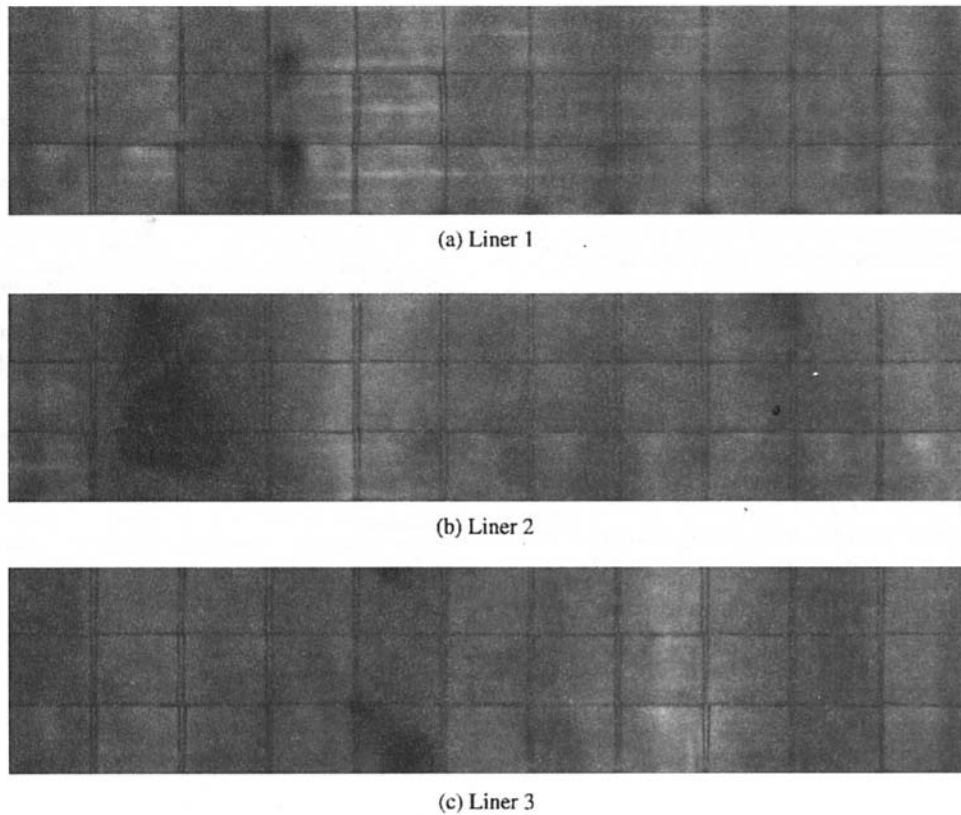
Fig. 9 Thermal diffusivity maps of solar turbines subscale combustor liners

The measured thermal diffusivity of both composite material systems quenched at $\Delta T = 600°C$ showed an expected decrease as the number of quench cycles increased. These are shown in Figs. 7 and 8. The 600°C ΔT quench was considered to be above the ΔT_c of the composites but was also sufficiently high for oxidation of carbon interlayer. Many factors could be contributing to the detected change in thermal diffusivity. The thermal shock damage intensified with increasing number of quench cycle. However, a detailed microstructural analysis is needed to determine the degree of induced microcracking.

These results suggest that the infrared camera, flash system method of determining thermal diffusivity measurement may be a viable technique for detecting material changes, including thermal shock damage, in CFCCs. It is to be noted that in these specimens, thermal shock is anticipated to be the major, though not exclusive, source of thermal diffusivity degradation.

Subscale Combustor Liners. Combustor liners being developed for applications to advanced gas turbines were also analyzed using the setup described earlier utilizing the software package that creates thermal diffusivity maps. Since the entire surface of the liner could not be viewed with the IR camera at one time, the surface of the liner was divided into 33 sectors approximately 50 mm × 50 mm. These 33 frame sequences

were then combined in order to obtain one complete image that represents the entire surface of the combustion liner. The time for complete data acquisition was approximately 4 hours with the entire system currently manually operated. Over 168,000 thermal diffusivity calculations were made to produce each of the grayscale maps.

The grayscale thermal diffusivity maps for three subscale liners are shown in Fig. 9. The thin gray grid lines are caused by emissivity variations from a tape used to mark off the sections on the liner. The dark black ''tick'' marks on the bottom of each image map indicate the visibly determined location of a seam running the length of each combustion liner.

It is apparent that not all the visibly determined seams caused thermal diffusivity variations. Seams are created by overlapping segments of the SiC fabric at time of fabrication. Other seams were made by placing segments of SiC fabric up against each other without overlap. No change in thermal diffusivity was detected. In the liner shown a part of the oxidation resistant coating was chipped. This is visible a third of the way from the bottom between the second and third seams and shows as a region of lower thermal diffusion.

There are several prominent features on the diffusivity image maps shown as large dark (low diffusivity) regions on all three liners. These areas were unexpected regions of low thermal
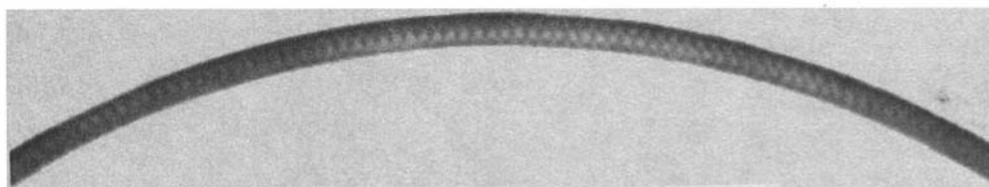
Fig. 10   2-mm-thick x-ray CT cross section of region of SiC/SiC subscale combustor liner showing region of low density

diffusivity. To establish if the regions of detected low thermal diffusivity were delaminations or regions of low mass density, possibly caused by lack of infiltration of the matrix, an x-ray computed tomographic imaging analysis was conducted. The data were obtained using Argonne's microfocus-x-ray CT system (Sivers et al., 1995). An example of the resulting data, see Fig. 10, showed that indeed, the regions of low thermal diffusivity could be correlated to regions of low density likely caused by incomplete infiltration of the matrix during processing. Thus the full field thermal diffusivity map data were verified by x-ray CT data.

Conclusions

We have found that full-field thermal diffusivity image mappings of engineering scale CFCC components for gas turbines can be accomplished using a system of commercially available components with specially developed software. Further, the flash thermal diffusivity imaging system can also be used as viable method to detect thermal shock damage as part of material development. It has been suggested that this may be a more sensitive technique than current destructive methods, which rely on measurement of retained strength.

References

American Society for Testing and Materials, 1994, "Standard Test Method for Thermal Diffusivity of Solids by the Flash Method," *Annual Book of ASTM Standards,* Vol. 14.02 (General Test Methods, Nonmetal; Laboratory Apparatus; Statistical Methods; Forensic Sciences), ASTM, Philadelphia, pp. 883–890.

Parker, W. J., Jenkins, R. J., Butler, C. P., and Abbott, G. L., 1961, "Flash Method of Determining Thermal Diffusivity, Heat Capacity and Thermal Conductivity," *J. Applied Physics,* Vol. 32, No. 9, pp. 1679–1684.

Singh, R., and Wang, H., 1994, "Fracture and Damage: Thermal Shock Behavior of CFCC's," Bimonthly Period Report, April–May 1994, Continuous Fiber Ceramic Composites Program, Oak Ridge National Laboratory, pp. 70–75.

Sivers, E. A., Ellingson, W. A., Snyder, S. A., and Holloway, D. A., 1995, "CT Multiscan: Using Small Area Detectors to Image Large Components," ASME Paper No. 95-GT-297; accepted for publication in the ASME JOURNAL OF ENGINEERING FOR GAS TURBINES AND POWER.

Steckenrider, J. S., Ellingson, W. A., and Rothermel, S. A., 1994, "Full-Field Characterization of Thermal Diffusivity in Continuous-Fiber Ceramic Composite Materials and Components," *Thermosense XVII: An International Conference on Thermal Sensing and Imaging Diagnostic Applications,* SPIE Proceedings Vol. 2473, S. Semanovich, ed., SPIE, Bellingham, WA (in press).

Touloukian, Y. S., Powell, R. W., Ho, C. Y., and Nicolaou, M. C., 1973, "Thermal Diffusivity," *Thermophysical Properties of Matter,* Vol. 10, IFI/Plenum, New York, pp. 3a–5a.

Nondestructive Evaluation of Thermally Shocked Silicon Carbide by Impact-Acoustic Resonance

R. A. Bemis
Caterpillar, Inc.,
Peoria, IL 60482

K. Shiloh
Soreq Nuclear Research Center,
Yavne, Israel

W. A. Ellingson
Argonne National Laboratory,
Argonne, IL 60439

Monolithic ceramics are under consideration as structural components for hot-stage sections of gas-fired turbine engines. In addition to manufacturing quality control, other important aspects for this application include life prediction modeling and time between engine overhauls. One nondestructive evaluation (NDE) method that provides information about material condition involves an analysis of resonant vibrations. In previous work by this general approach, changes in modal parameters have been related to bulk defect mechanisms such as microcracking due to thermal shock damage. In this work resonant vibrations from monolithic ceramic specimens were excited by an instrumented impact hammer and detected by a noncontact acoustic microphone over frequencies up to 100 kHz. Computer-based analysis of vibration signatures from test specimens allowed extraction of modal frequencies and damping constants. Downward shifts in detected resonant frequencies and increases in internal friction or (specific) damping capacity measurements were obtained from SiC cylindrical rings, and these measurements were shown to relate to thermal shock severity. This NDE method not only provides measurable parameters that could be used as accept–reject criteria for in-line process inspection, it also provides a means for tracking the mechanical integrity of in-service engine components to support life prediction modeling.

Introduction

Ceramics are increasingly important engineering materials, particularly for use in high-combustion-temperature, gas-fired turbine engines due to their exceptional mechanical and thermal properties. However, due to inherent brittleness and low fracture toughness, these materials are susceptible to damage that could lead to catastrophic failure. Therefore, the practical use of structural ceramics in engines depends on the ability to detect a defective component nondestructively during initial manufacture and throughout its service life. Since it is also desirable to do as much on-engine component testing as possible, or at least to minimize engine disassembly, noncontact detection methods with the potential for in-situ detection capability are also preferred.

This nondestructive evaluation (NDE) objective has been approached in previous materials research work by analyzing resonant vibration modes for different combinations of material type, specimen geometry, and methods of excitation and detection. Copolla and Bradt (1973) linked thermal shock severity and fracture strength to sonic (elastic) modulus and specific damping capacity measurements on SiC flexure bars using continuous excitation and contact detection. Coppack (1980) used impact excitation and contact detection to correlate sonic modulus with destructive modulus of rupture from rectangular bars of refractory brick. More recently, Chu et al. (1993) refined the correlation between thermal shock severity and sonic modulus by measuring ultrasonic stress wave velocities in rectangular plates of Al_2O_3 and reaction bonded Si_3N_4. Thus, modal parameters detected by vibration analysis provide a set of quantitative

NDE measures that have previously been related to mechanical properties and bulk defects.

In this work vibration modes of thermally shocked SiC rings were analyzed using an instrumented tap test based on impact excitation, noncontact acoustic detection and free fixturing (Bemis, 1994). Computer-based analysis of impact-acoustic response (IAR) measurements allowed extraction of modal frequencies and damping constants from detected resonant vibrations. The amount of variation in detected modal parameters between as-machined SiC ring specimens was initially determined. Downward shifts in detected resonant frequencies and increases in specific damping capacity or internal friction measurements were then determined for each specimen as a function of thermal shock severity. Both temperature effects and cyclic effects of thermal shock treatment were included in these experiments.

Experimental Procedure

Each ring-shaped SiC specimen was freely supported from its inner diameter by a rubber band stretched into tension. Vibrations were excited by a tap from an impact hammer upon each ring's outer surface and in a radial direction as illustrated in Fig. 1. A microphone was used to detect specimen vibrations acoustically up to 100 kHz. Impact excitation and acoustic response waveforms from each IAR measurement were digitized, then transferred to a personal computer for extraction of modal parameters by both time and frequency domain analyses.

The fundamental vibration mode of each test specimen was detected in this work by using to advantage the low-frequency nature of impact excitation. That is, the vibration with strongest amplitude also occurred lowest in frequency. This dominant resonance was, therefore, considered the fundamental mode for analysis purposes. Modal frequencies and damping values were computed from this fundamental mode in these experiments.
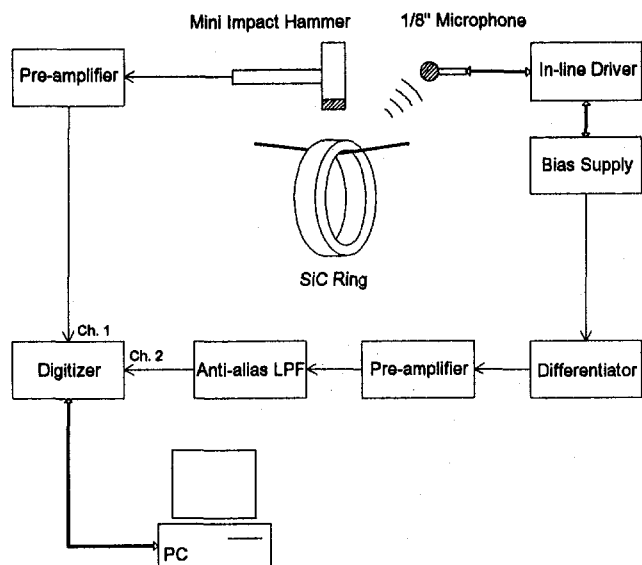
Fig. 1 Schematic diagram of IAR test system

Table 1 Thermal shock treatment of SiC rings

Ring No.	Furnace T (°C)	Initial Condition
7	250	edge chips
6	800	edge chips
5	400	edge chips; I.D. non-cleanup
4	550	edge chips
3	450	okay
9	500	edge chips; I.D. non-cleanup
2	350	edge chips; I.D. non-cleanup
1	300	edge chips; I.D. non-cleanup
8	250	edge chips; I.D. non-cleanup

The fundamental resonant frequency of each test specimen was measured in the frequency domain. A discrete frequency spectrum was computed from each microphone output signal or acoustic response waveform using the fast Fourier transform (FFT). The location of maximum magnitude in each response spectrum was taken as the fundamental frequency. The accuracy of this measured frequency was enhanced by time domain windowing prior to FFT computation (Bemis, 1994; Iwasaki, 1991). Previous work by Spinner and Tefft (1961) has established theoretically and experimentally that the square of the fundamental frequency is proportional to the bulk elastic modulus of a test specimen.

The specific damping capacity of each test specimen was measured in the time domain. The Hilbert transform was used to obtain the exponentially decaying preenvelope or analytic signal from each acquired acoustic waveform (Poularikas and Seeley, 1985). The logarithmic amplitude of this pre-envelope waveform was then fitted by a straight line, the slope of which was taken as the exponential decay rate. The decay rate, σ, of each measurement was normalized by its dominant frequency, f_o, to compute the dimensionless critical damping coefficient,

$$\zeta = \frac{-\sigma}{2\pi f_o} \tag{1}$$

Modal damping, which is sometimes called specific damping capacity, was determined by Zener (1948) to be directly proportional to bulk material damping or internal friction of a test specimen.

Sample Preparation

Test specimens were obtained for these experiments from a SiC heat exchanger pipe axially sectioned into nine rings. Each ring measured 30.5 mm outer diameter, 4 mm wall thickness, and 12.5 mm axial width. All nine rings were intentionally ground using the same machining fixture in an effort to obtain uniform dimensions between specimens. After machining, however, imperfections were noted on some inner diameters, which were attributed to incomplete surface clean-up. Some of the rings also had slightly chipped edges. Due to these observed geometric variations, the dimensional tolerance for these nine specimens was determined to be less than 1 percent in the as-machined condition.

Thermal shock treatment was achieved by holding each SiC ring specimen in a crucible inside an electric oven at a chosen temperature for at least 30 minutes. Each furnace heated ring was then dropped by way of the crucible into a full container (i.e., 80 cm deep and 30 × 30 cm square) of 20°C water. (Note: No appreciable change in water temperature was detected in these experiments.) A single quench into cold water was performed for all nine rings over a range of furnace-heated temperatures listed in Table 1, which also lists the machined surface quality of each specimen before quenching. Repeated cold water quenchings were also performed on two of the rings using the lowest furnace temperature (i.e., 250°C).

Experimental Results

Prior to thermal shock treatment, four IAR signatures were obtained from each specimen for a baseline comparison. Since multiple resonant modes generally appeared in each vibration spectrum, and since the strongest mode also had the lowest frequency, the largest amplitude vibration detected from each specimen was considered to be the fundamental frequency for analysis purposes. The baseline frequencies of all nine specimens (which are listed in Table 2) were measured with 0.001–0.2 percent repeatability (i.e., as determined by the ratio of standard deviation to mean value over four measurements per specimen). The maximum fluctuation between specimens in terms of this detected frequency was found to be 0.37 percent (i.e., as determined by one-half maximum the difference divided by the mean value).

Temperature Effect of Thermal Shock. A single-cycle cold water quench of each SiC ring was performed from the furnace temperatures listed in Table 1. Each specimen was then inspected for visible damage. Through-wall cracks were observed in the most severely quenched specimens (i.e., furnace temperatures $\geq$ 450°C). IAR signatures were then acquired for a comparison before and after quenching.

Table 2 lists the detected fundamental frequencies of each specimen both before and after quenching. Regardless of the observed through-wall cracks, these data follow a trend in which frequency essentially decreases with temperature.

The initial fundamental frequencies listed in Table 2 vary somewhat between as-machined specimens. The temperature

Table 2 Frequency measurements before and after thermal shock from different furnace heated temperatures

Furnace T(°C)	Before Quench μ (kHz)	Before Quench σ (Hz)	After Quench μ (kHz)	After Quench σ (Hz)
250	29.659	1.100	29.619	0.489
250	29.585	2.210	29.280	2.853
300	29.517	62.855	27.463	7.952
350	29.690	0.736	22.378	13.254
400	29.581	0.307	21.881	20.825
450	29.658	12.565	21.767	910.831
500	29.663	1.243	22.270	4,376.986
550	29.705	0.331	20.900	15.607
800	29.654	4.248	20.356	43.686
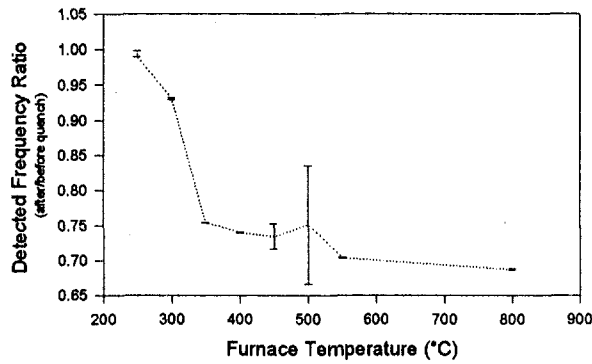
Fig. 2 Temperature effect of thermal shock on detected frequency ratio after/before quenching

Fig. 4 Temperature effect of thermal shock on detected damping ratio after/before quenching

effect is, therefore, more accurately illustrated by plotting the ratio of after-quench to before-quench detected fundamental frequencies as shown in Fig. 2, which is more indicative of thermal shock damage per specimen. Fig. 2 shows a region of sharply dropping frequency up to 350°C, then a region of gradual decrease at higher temperatures. These results resemble SiC material behavior shown by Copolla and Bradt (1983).

The error bars plotted in Fig. 2 were calculated for each specimen by adding together the standard deviations of four measurements each, before and after quenching. Since two specimens were thermally shocked using the lowest furnace temperature, two plot points appear in Fig. 2 with vertical alignment at 250°C. The vertical separation between these two points should not be confused with error bars. Both data points actually display error bars of their own that are negligible at this plot scale factor.

Figure 3 displays a plot of damping measurements obtained from each specimen before and after quenching. Error bars in Fig. 3 were simply the standard deviation of four repeated measurements per specimen.

Due to baseline fluctuations between specimens, however, a better view of increased damping with temperature was obtained by plotting the after/before quench damping ratios as shown in Fig. 4. Error bars in Fig. 4 were computed by adding together the previous standard deviations from damping measurements before and after quenching.

Cyclic Effect of Thermal Shock. Rings 7, 8 were quenched a second and third time each in 20°C water from a 250°C furnace temperature. Ring 8 showed no visible evidence of thermal shock damage, but a through-wall crack appeared in specimen 7 after the third quench.

The detected modal parameters of both rings are plotted against the number of quench cycles in Fig. 5, where error bars

are the standard deviations of four repeated measurements per specimen.

The ratios of detected modal parameters after/before quenching are plotted against the number of quench cycles in Fig. 6, which provides a common scale on which to compare the behavior of each specimen. Error bars in Fig. 6 were computed by adding together the previous standard deviations from modal parameter measurements before and after quenching.

Discussion

It should first be noted that detection of modal frequencies and damping coefficients does not necessarily measure the same phenomena of a test specimen. Whereas clearly the resonant frequency is the direct square root of elastic modulus, damping has been shown to express in many cases the material strength, which is generally an inelastic mechanical property.

Fig. 5 Cyclic effect of thermal shock on detected modal parameters before and after quenching

Fig. 3 Temperature effect of thermal shock on detected damping coefficients before and after quenching
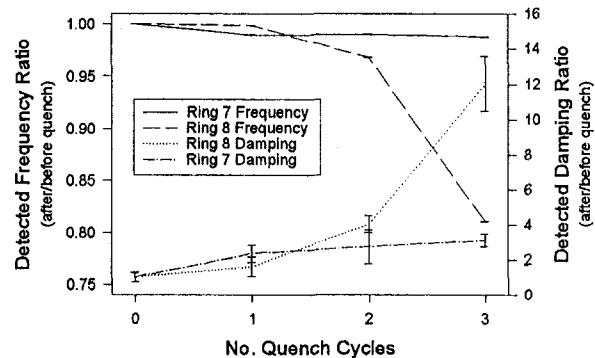
Fig. 6 Cyclic effect of thermal shock on ratio of modal parameter ratios after/before quenching
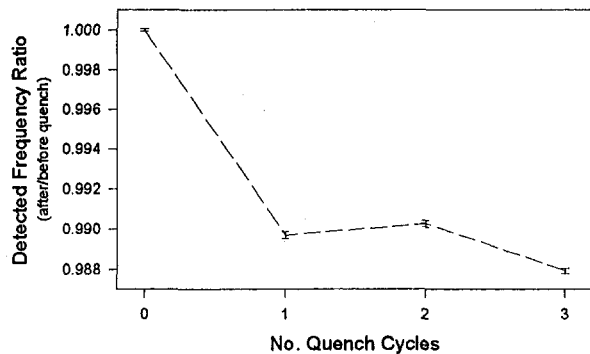
Fig. 7 Cyclic effect of thermal shock on the detected fundamental frequency of ring specimen No. 8

Fundamental frequencies detected in these experiments were shown to decrease with thermal shock severity by small amounts, such as -0.3 percent for the onset of damage from a quench at 250°C, and by as much as -50 percent for a severe quench at 800°C. The variation in damping values due to the same damage, however, was much larger. Damping was shown to increase by 100 percent at the onset of damage (i.e., 250°C quench), and by 900 percent for high damage (i.e., 400°C quench). For very severe damage (i.e., $\geq$450°C quench), no meaningful conclusions could be deduced without additional work. Fortunately, this last fact is not too disturbing. Since such high damage was detected visibly, in practice no sophisticated NDE method would be required for such an extreme case.

Frequency measurements from the IAR test system described here involve a precision of better than 0.1 percent, and provided a clear dominant resonant frequency (Bemis, 1994). Frequencies plotted in Figs. 5 and 6 had negligibly small error bars, which underscores the high repeatability of these measurements. Therefore, decreasing frequency with quench cycles was attributed mainly to reduced elastic modulus due to thermal shock damage. However, the nature of this decrease was very different between two specimens that were repeatedly quenched.

Ring 8 decreased in fundamental frequency mostly after the first quench, then remained essentially constant after the second and third quench cycles. The damping of Ring 8 also appeared to increase more from the first quench than after the second or third times. This agreement between frequency and damping behavior suggests that the first quench was more damaging to Ring 8 than were the other two quench cycles.

Ring 7, however, behaved quite differently. Ring 7 progressively decreased in frequency and increased in damping with each quench cycle. Changes in frequency and damping with quench cycles were more closely correlated to each other in Ring 7, and these changes were also larger in magnitude than modal parameter changes for Ring 8. A through-wall crack in Ring 7, which was observed after the third quench, follows this more dramatic behavior. These data suggest that Ring 7 had lower resistance to thermal shock damage than did Ring 8, but the reason for reduced damage resistance is unknown.

In these experiments damping generally increased with temperature up to 400°C. At higher temperatures the damping behavior was rather arbitrary, which was consistent with observed postquench through-wall cracks. Severe quench cracks also offer an explanation for high variance in otherwise repeatable measurements of fundamental frequency shown in Fig. 2—at least for the 450 and 500°C temperatures. In support of this explanation the through-wall crack in the 500°C specimen,

which varied most in resonant frequency, also had a jagged crack shape, whereas rather straight cracks occurred in the 450, 550, and 800°C specimens. The crack explanation is, however, somewhat weakened by low variance from the 550 and 800°C specimens.

Frequency domain extraction of modal damping was not included in these experiments due to insufficient discrete frequency resolution (Bemis, 1994). The time decay method that was instead used for damping measurements yielded useful results, but reliable calculations still remain to be worked out. Several factors influence so far the reliability of these results. The need to filter out irrelevant frequencies is obvious. Filtering out split frequencies and closely coupled modes is the most difficult challenge. Split modes cause beatnotes or fluctuations in the envelope of an acoustic waveform. This in turn affects the average slope calculation, especially when less than one fluctuating cycle is present. For high damping cases care must also be taken to define clearly the changeover between envelope decay and waveform noise.

Repeated quenching of Ring 8 actually appeared to increase the detected fundamental frequency slightly after the second quench, as shown in Fig. 7. Although this may be theoretically disturbing, the amount of change was so small that it was not taken seriously, especially since error bars nearly overlapped between sets of four repeated measurements each.

A key result of this work was to detect the onset of thermal shock damage prior to catastrophe by IAR testing, using either damping or frequency measures. Onset in SiC occurs at about 250°C according to literature (Copolla and Bradt, 1973).

Summary

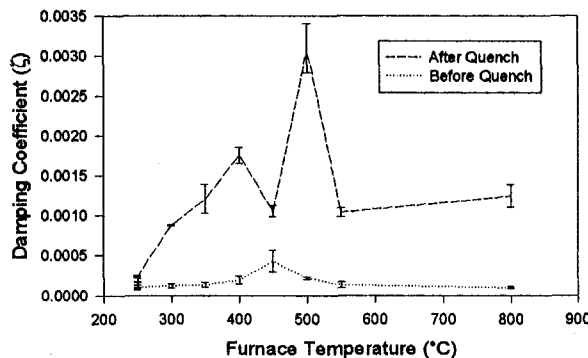Thermal shock damage was inflicted in furnace-heated, SiC ring specimens by cold water quenching in order to cause both temperature effects and cycling effects. These quench conditions were shown to relate to changes in modal parameters extracted from IAR measurements. Fundamental frequencies, which decreased only slightly with quench severity, were detected with good precision—at least for all practical situations. Damping measurements, on the other hand, increased dramatically with quench severity but were detected with only modest accuracy due to present limitations of simplified analysis methods. Altogether, this simple IAR test has shown detection sensitivity to thermal shock damage in SiC. Refinements are now needed in modal parameter extraction in order to realize the full potential of this promising NDE method.

References

Bemis, R. A., 1994, "Digital Signal Processing for Non-destructive Evaluation of Ceramics Using Impact-Acoustic Response Measurements," M.S.E.E. Thesis, Illinois Institute of Technology, Chicago, IL.

Chu, Y. C., Hefetz, M., and Rokhlin, S. I., 1993, "Ultrasonic Assessment of Microcrack Damage in Ceramics," *Review of Progress in Quantitative Nondestructive Evaluation*, Plenum Press, New York, pp. 2175–2182.

Copolla, J. A., and Bradt, R. C., 1973, "Thermal-Shock Damage in SiC," *Journal of the American Ceramic Society*, Vol. 56, No. 4, pp. 214–218.

Coppack, T. J., 1980, "A Method for Thermal Cycling Refractories and an Appraisal of Its Effect by a Nondestructive Technique," read at the Edinburgh meeting of the Refractories Section, Sept. 10.

Iwasaki, K., 1991, "Improvement of FFT Spectra by Synchronization of Input Signal at First and Last Zero-Crossing Points," *Proc. Fifth International Symposium on Nondestructive Characterization of Materials*, Karuizawa, Japan, symposium sponsored by Iketani Science and Technology Foundation, pp. 233–243.

Poularikas, A. D., and Seeley, S., 1985, *Signals and Systems*, Prindle, Weber & Schmidt, Boston, MA, pp. 216–217.

Spinner, S., and Tefft, W. E., 1961, "A Method for Determining Mechanical Resonance Frequencies and for Calculating Elastic Moduli From These Frequencies," *Proc. ASTM*, pp. 1221–1238.

Zener, C., 1948, *Elasticity and Anelasticity of Metals*, University of Chicago Press, Chicago, IL.

R. R. Judkins

D. P. Stinton

Fossil Energy Program,
Metals and Ceramics Division,
Oak Ridge National Laboratory,
Oak Ridge, TN 37831

R. G. Smith

E. M. Fischer

J. H. Eaton

B. L. Weaver

J. L. Kahnke

D. J. Pysher

3M Company,
St. Paul, MN 55144

Development of Ceramic Composite Hot-Gas Filters

A novel type of hot-gas filter based on a ceramic fiber-reinforced ceramic matrix was developed and extended to full-size, 60-mm OD by 1.5-m-long, candle filters. A commercially viable process for producing the filters was developed, and the filters are undergoing testing and demonstration throughout the world for applications in pressurized fluidized-bed combustion (PFBC) and integrated gasification combined cycle (IGCC) plants. Development activities at Oak Ridge National Laboratory (ORNL) and at the 3M Company, and testing at the Westinghouse Science and Technology Center (STC) are presented. Demonstration tests at the Tidd PFBC are in progress. Issues identified during the testing and demonstration phases of the development are discussed. Resolution of the issues identified during testing and the status of commercialization of the filters are described.

Introduction

The successful development and deployment of several advanced coal-fueled gas turbine technologies depend greatly on the ability to clean fuel or combustion gas streams of particulates prior to these gases being passed through the turbines. Of these technologies, IGCC and PFBC are nearest to commercialization. Rigid ceramic filters of a variety of designs are either commercially available or under development in programs around the world. Several filter designs are in use or are being developed. The most popular is the candle filter, which resembles a laboratory test tube in having one end closed and a flanged opening at the other.

Rigid ceramic candle filters are currently being developed to remove hot particulates from PFBC and IGCC gas streams being introduced into gas turbines. In these environments the filters will be subjected to nominal temperatures of 600 (IGCC) to 850°C (PFBC) at nominal system pressures of about 1.0–3.0 MPa. However, in several demonstration projects, lower filtration temperatures (250–500°C for IGCCs and 700–750°C for PFBCs) may be used to demonstrate filtration system concepts. In use, filtration of particulate-laden gas occurs by flow from the outside of the filter to the inside, thus trapping the particles in a cake on the outside of the filter. The filters are repeatedly cleaned by pulses of gases directed from the inside of the filter to the outside. These gas pulses impose thermal shocks on the filters, because the cleaning gas is typically at a much lower temperature than the gas being filtered. In an IGCC system, a reducing atmosphere is obtained and in a PFBC system, an oxidizing atmosphere is obtained. Environments that are corrosive to some ceramic materials can also exist in these systems.

Many different materials—oxides, nonoxides, or combinations of these types—may be used for these candle filters. The most popular oxide ceramics include alumina/mullite, cordierite, aluminosilicate foam/fibers, clay-bonded alumina, fireclay, and continuous fiber ceramic composites produced by chemical vapor infiltration (CVI). Nonoxide ceramics include clay-bonded silicon carbide, sintered silicon nitride, reaction-bonded silicon nitride, recrystallized silicon carbide, and CVI silicon carbide fiber-reinforced composite filters. Fabric filter materials include various grades of silica-alumina-boria, alumina-silica, and silicon carbide-silica. Most commercial and near-commercial ceramic filters are made of bonded ceramics. Although these bonded ceramic filters have performed well in less demanding applications, their performance in PFBC and IGCC has been erratic. Breakages have occurred as a result of thermal and mechanical shocks.

In a joint effort at ORNL and the 3M Company, a ceramic composite filter has been developed that could offer a viable alternative to monolithic filters [1, 2]. The 3M Brand Ceramic Composite Filter provides several benefits to a filtering system over conventional monolithic ceramic filters. Some of the benefits that derive from ceramic composites are lighter weight; excellent thermal shock resistance; a balance of toughness and strength; good thermomechanical properties at high temperature; thin filter walls with reduced pressure drops; and the capability to retrofit into existing filter holders. One of the concerns about conventional ceramic candle filters is their relatively poor resistance to thermal shock. In tests at 3M to compare the thermal shock tolerance of several varieties of filters, specimens were heated to 1000°C and then immersed in water, a very severe test. The best performance was by a ceramic composite filter specimen, which retained 27 percent of its initial burst strength after eight of these thermal shock cycles as compared to a clay-bonded silicon carbide monolithic filter specimen, which degraded to about 18 percent of its initial burst strength after
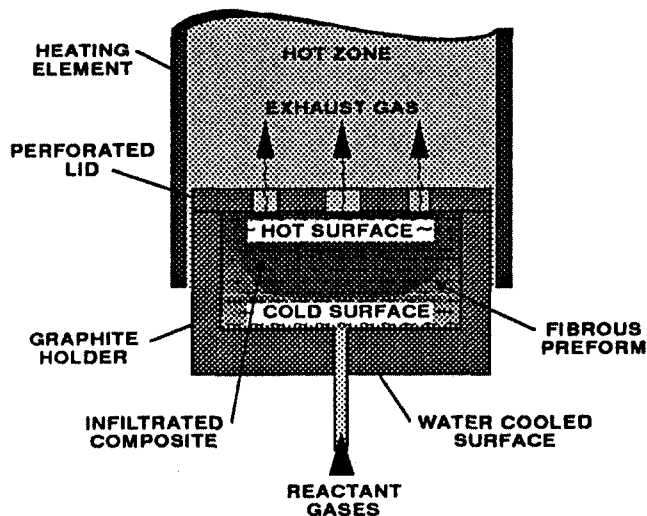
Fig. 1 Chemical vapor infiltration process schematic

Fig. 3 Examples of ORNL filter concepts

only one cycle and thereafter had burst strengths too weak to measure [3].

Process Development at ORNL

Filter development was begun at ORNL in FY 1986 as an exploratory effort derived from another ORNL project on the development of dense ceramic composites for heat exchanger applications. That project, which is funded by the U.S. DOE Office of Fossil Energy Advanced Research and Technology Development (AR&TD) Materials Program, involves the production of ceramic composites by chemical vapor infiltration (CVI) and deposition of a ceramic matrix into a structural form, hereinafter preform, of ceramic fibers. Figure 1 is a schematic of the CVI process. In the CVI process for producing a composite ceramic with a silicon carbide matrix, tricholoromethylsilane is entrained in a stream of hydrogen, transported to the filter preform, and thermally decomposed to deposit a matrix of silicon carbide. As depicted in Fig. 1, controlled heating of the preform results in uniform deposition of silicon carbide throughout the filter preform.

Much of the interest in ceramic composite filters derives from their improved strain tolerance as compared to monolithic ceramics. Figure 2 graphically illustrates the improvement in strain tolerance that results from the composite structure. If this strain tolerance can be retained in the filter structures during operation, it would provide a significant performance advantage over monolithic filters. In this figure, the curve for the monolithic ceramic indicates very little strain tolerance, i.e., a load

is applied until stresses exceed the strength of the material and then it breaks catastrophically. The curve for the ceramic composite suggests considerable strain tolerance. This strain tolerance is due to stress relief occurring by several mechanisms. As load is applied, cracking of the matrix may occur with load transfer to the fibers. Load carrying is transferred from matrix to fiber via the fiber–matrix interface. Increased loading may also result in debonding of the fiber-matrix interface. As load is applied, shear stresses exerted on the interface increase until debonding occurs. Thus, details of the appearance of stress-deflection curves for composite materials depend on several factors such as fiber loading and strength of the interfacial bond, but Fig. 2 is representative of the general appearance. Discontinuities in the curve correspond to stress and deflection conditions resulting from matrix cracking, debonding, and fiber breaking events as the specimen was loaded.

Several concepts for ceramic composite filters were examined at ORNL, and some of these are shown in Fig. 3. Based on initial results, the ORNL filter work was continued under DOE-Morgantown Energy Technology Center (METC) Surface Gasification Materials Program sponsorship in FY 1987, and the AR&TD Materials Program also continued to support CVI process development and the evaluation of the filters. Tests of filter specimens were conducted at ORNL, Acurex Corporation, and the Coal Research Establishment (United Kingdom). The ORNL work was continued from FY 1988 through 1991 under METC Advanced Research funding. In FY 1989, the 3M Company was awarded a contract on the AR&TD Materials Program through competitive bidding to produce full-size candle filters.

To aid the project in addressing relevant issues, a project was conducted by Acurex Corporation and Virginia Polytechnic Institute and State University to assess the causes of failure of ceramic filters [4]. Several common failure modes were identified. These included thermal and mechanical shock, strength degradation during use, plugging, cracking/breaking at the flange/candle body junction, and binder degradation due to chemical attack. Suspected causes of these failures were improper mounting techniques, tubesheet design, pulse cleaning, candle design, system transients, and corrosive contaminants in gas streams.

Many other tests and investigations of the suspected modes and causes of failures of ceramic candle filters as well as ceramic materials in other applications have been conducted [5–18].

Full-Size Filter Development at the 3M Company

In the first quarter of 1993, the 3M Company completed the development of its first-generation ceramic composite candle filter. This first-generation filter, shown in Fig. 4, was a filament-wound structure with three plies of Nextel™ 312, an alumina-boria-silica fiber, with a filter surface on the exterior of the candle. The filter surface is a barrier layer of random fibers. The binder for the filter is a silicon carbide matrix deposited by chemical vapor deposition (CVD).

Two of the first-generation filters were tested at the Westinghouse Science and Technology Center (STC) in March 1993. These tests were conducted in a simulated PFBC environment at 815 to 830°C for a total of 136.4 operating hours. Ten turbine

Fig. 2 Comparison of the strain tolerance of monolithic and composite ceramics
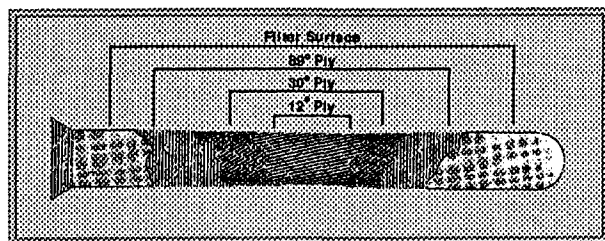
Fig. 4 First-generation 3M Company ceramic composite filter

trip simulation thermal transients were made and the filters withstood these transients without cracking or failure. Filter performance was good and consistent with that of other ceramic candle filters. Thus, the Westinghouse test demonstrated that a workable filter surface on a strong substrate had been developed. However, the test also revealed a need for improved filter construction. One candle filter experienced patchy cleaning and partial (≈ 75 percent) loss of the filter surface. A need was identified for further work on the CVI bonding of the filter surface to the intermediate layer and substrate, which was suspect during filter fabrication at 3M. Increased reinforcement of the seal flange to permit forming a tighter seal was also identified as a needed improvement. Details of this phase of the filter development are presented in a 3M Company report [19].

Improvements in filter construction and fabrication processing were made by 3M. Among the most significant changes were strengthening of the flange seal area; replacement of the filament-wound structure by a braided structure; and the incorporation of an open-braided outer layer to address the problem of sloughing off of the filter surface. The braided structure offers significant economic advantages to filament winding. The resultant structure incorporates a filter surface sandwiched between a tightly braided inner layer and the open-braided outer layer of ceramic oxide fibers. This open-braided outer layer is evident in Fig. 5, which is a photograph of the 3M Brand Ceramic Composite Filter, Type 203, and a clay-bonded silicon carbide filter.

Tests of Type 203 Filters

Testing of six of the 3M Company's second-generation filters, the Type 203 filter, was conducted at Westinghouse STC in December 1993. These filters were tested to measure filter cleanability and operating characteristics under PFBC conditions. The filters were mounted in a standard monolithic candle filter holder. Prior to mounting the filters, the pressure drop of each was measured at room temperature as a function of equivalent face velocity by flowing air into the top of the filter through a rubber stopper. After mounting the filters and closing the test system, the filter pressure drop was determined at various face velocities at both ambient temperature and at operating temperature.

The test was scheduled for 175 hours at a filter temperature of 815–830°C with a system operating pressure of 0.69 to 0.86 MPa. Tests were conducted for 172 total operating hours using two lots of ash, first using the "Old Grimethorpe Ash," which is a commonly used ash obtained from the Grimethorpe (United Kingdom) PFBC, and then a more difficult to filter ash called "Red Grimethorpe Ash." The inlet gas flow had an ash concentration of 2000 ppm. The air flow rate was 499 kg/h with a filter face velocity of 3.56 cm/s. Cleaning pulses were triggered when the differential pressure from ash cake buildup reached 7.5 to 9.5 kPa. The cleaning pulses were of 0.4 second duration from a pressure tank of 2.1 MPa. The tests were run on a 12-hours per day schedule for the first three days and then run 24 hours per day until the test was finished. Samples of effluent were taken from the clean side of the chamber through high

efficiency filter paper at various times throughout the filter test to calculate the clean side ash concentration.

During the changeover from the Old Grimethorpe Ash to the Red Grimethorpe Ash, 14 turbine trip simulations were run over a 12 hour period to subject the filters to the thermal shocks typical of a system trip or fast shutdown. These simulations involved shutting off the gas burner and decreasing the air flow to zero in steps to cause rapid cooling of the filters. The air flow and gas burner were then restarted to rapidly bring the temperature back to operating conditions [20].

The individual ceramic composite filter pressure drops were determined as a function of face velocity. Permeances, face velocity divided by pressure drop, at ambient temperatures ranged from 113 to 247 ms^{-1}/MPa (11.3 to 24.7 ms^{-1}/bar). Very similar and consistent results were obtained for all six filters. This consistency is important in operation, because it suggests that each filter will handle a proportionate amount of the total gas flow. The pressure drop measurements in the test system were 1.9 kPa at a face velocity of 3.3 cm/s at ambient temperature and 2.5 kPa at a face velocity of 3.5 cm/s at 815°C. The system measurements are higher than for the individual filters because they include the total test system of filters, holders, plenum, and pulse system.

The filters were pulse cleaned approximately every two and one-third hours while using the Old Grimethorpe Ash for a total of 49 pulses. For the Red Grimethorpe Ash, the filters were pulse cleaned every one and one-third hours for a total of 30 pulses. Thirty-four clean side ash concentration samples were taken during the 172 hours of testing. The sampling times ranged from 30 minutes to 5 hours for a total of about 100 hours of sampling. The average (mean) clean side ash concentration was 2.5 ppm. All samples save one indicated an ash concentration of less than 4 ppm (see Fig. 6). No filter seal leakage was observed during the sampling. Acceptable levels, i.e., turbine tolerance levels for erosion considerations, of ash concentration are about 10 ppm for 1 μm particle size and about 1 ppm for 10 μm particle size; the Type 203 filters appear to have met these criteria.

Relative filter permeability, the ratio of filter permeability at any time to the initial filter permeability, is a good indicator of filter performance. Figure 7 presents the results of calculations of relative filter permeability of the Type 203 filters. The figure indicates that the filters have become well conditioned after
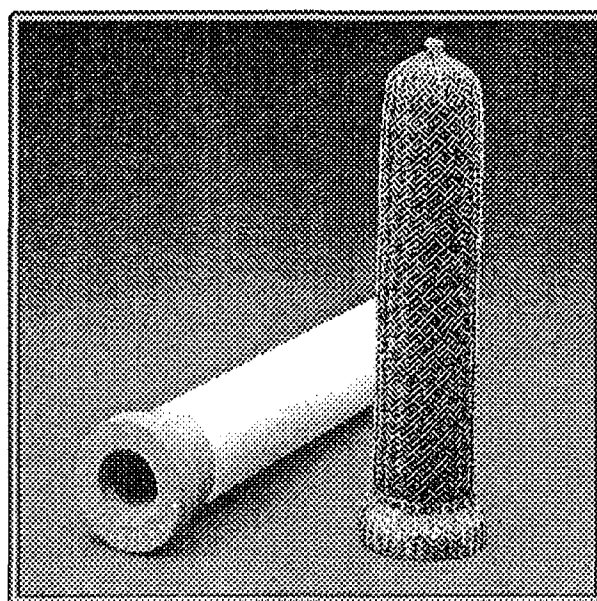
Fig. 5 Second-generation 3M ceramic composite filter and a clay-bonded silicon carbide filter
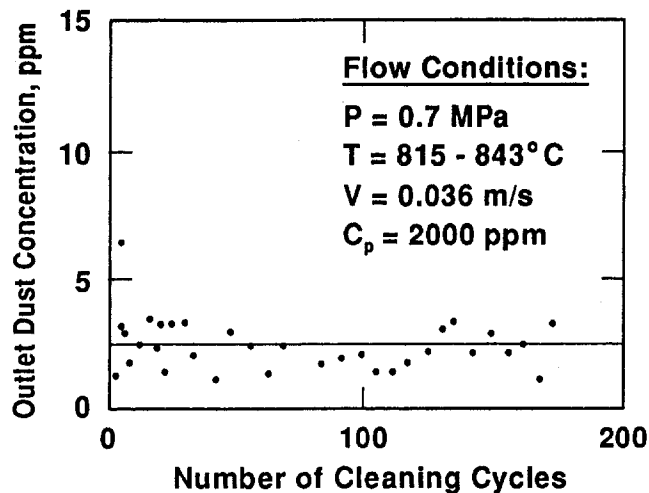
Fig. 6   Filter test outlet ash concentration

about 50 cleaning cycles and that relative filter permeability has become constant. Under this condition, ash buildup during filtering is constant and ash removal is consistent during the cleaning cycles. After testing, the filters had a uniform, about 1.5 mm thick, ash coating on the filter surfaces, which is indicative of a properly functioning set of filters. No irregularities were observed on the thin ash coating. Gaskets in the mounting system were clean and intact. A potential concern about the Type 203 filters had been that the open-braided outer surface would trap dust in sufficient quantity that the dust would begin to sinter and grow, thus forming larger, more tenacious filter cakes. However, no such problems were encountered in the Westinghouse STC tests.

The Type 203 filters met or exceeded all performance criteria for a successful test. They proved to be more durable than the previous design, and none of the filter surfaces came off during the tests. Dust removal efficiencies exceeded 99.8 percent with <4 ppm dust in the exit gas from the filters. The filters reached stable, conditioned permeability after 50 cleaning cycles. Permeance values and trends were consistent with clay-bonded filters. Acceptable cleaning of the filters was maintained using up to 2.1 MPa pulses of cleaning gas. Mounting and gasketing maintained dust seals without apparent leakage. Post-test examination indicated significant strength retention. There was no damage (breakage, cracks, distortion, etc.) apparent to the 3M filters as a result of the test.

Tests at the Tidd PFBC Demonstration Project

In August 1994, three Type 203 filters were installed in the filter vessel at the Tidd PFBC Demonstration Project (Tidd) for testing. Tidd is a 70 MWe PFBC demonstration plant in Brilliant, Ohio. The demonstration is part of the DOE's Clean Coal Technology Program. At Tidd, a small fraction (design basis is one-seventh) of the total process gas stream, i.e., a slipstream, may be diverted to the filter system, which can accommodate up to 384 candle filters. In this test at Tidd, performance of the 3M filters was good and demonstrated their ability to function in this environment for over 1600 hours. Although data analysis for this test is incomplete, and thus the conclusions we have drawn are preliminary, the following observations may be pertinent and useful.

The Tidd demonstration was extremely useful in identifying issues related to the Type 203 filters. Two of the three filters were broken at some time during the demonstration run. Although the exact time of breakage was not established, and we believe cannot be established unequivocally, they appear to have functioned for over 1000 hours (a borescope examination of

the interior of the filter vessel revealed that the filters were in place and intact). The breaks in the candle filters occurred at the top of the filters just below the holder. Since only the flange areas of the broken filters were salvaged after the demonstration, actual causes of the failures also cannot be established unequivocally. We have speculated that the filters were broken as a result of ash buildup and bridging. Ash buildup was present on the one Type 203 filter remaining in the system and this buildup extended to the area of the other two Type 203 filters that were broken. A phenomenon has occurred in the Tidd filter system resulting in filter breakage that appears to result from "bending forces from ash bridging from the inner candles to the outer candles" [21]. Although data and data analysis available at this time are insufficient to confirm that similar bending forces were operative in breakage of the Type 203 filters, that failure mechanism is a possibility. Based on this possibility and simulation tests at the 3M Company laboratories in which similar breakage has been demonstrated, certain changes in the mounting devices used for the Type 203 filters were made. Subsequent laboratory simulation tests using the modified mounting devices indicated that the modifications were effective in preventing breakage. If ash buildup and bridging were the causal factors in the breakage of the two filters in the Tidd demonstration, these modifications should prove to be beneficial.

Our conclusion from the Tidd demonstration and analysis of the filter that performed well for over 1600 hours is that the Type 203 filter concept has excellent potential for application in PFBC systems. It is an effective and efficient filter; it experiences no apparent chemical deterioration; it retains a significant percentage (75 percent) of as-manufactured strength after exposure; and no inherent problems with the filter structure have been identified.

Ten Type 203 filters were installed at the Tidd plant in December 1994. In this test, the modified mounting devices are being used. In addition to improvements in the candle filter mounting hardware, 3M is also working on design changes to the filters that will further strengthen the flange area and improve the performance of the filter at the closed end. These design modifications were not made in time to be incorporated into the filters used in this second Tidd Plant test. This test at Tidd is expected to continue until March 1995. The ceramic composite filters will be further evaluated on test completion. Tests in other operating PFBC plants are presently being pursued.

Conclusions

The 3M Company ceramic composite filters have performed well in PFBC simulation tests at Westinghouse STC. They have
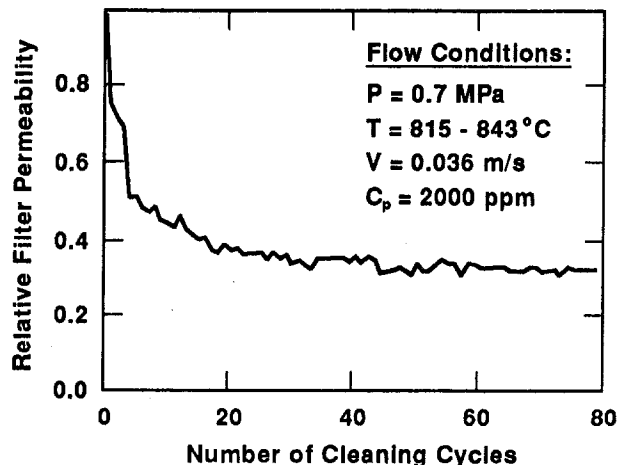
Fig. 7   Relative filter permeability of the 3M ceramic composite filters

demonstrated the ability to function well for over 1600 hours in the Tidd PFBC. Additional in-plant tests at the Tidd PFBC Demonstration Project are in progress to identify any additional issues and to demonstrate the adequacy of these filters in PFBC systems. Both the simulation tests and the plant tests are providing data for the use of these filters. These and other tests and demonstrations of the composite filters should provide further evidence of the efficacy of these filters. Each step in the development process has resulted in insights into the development of superior filters. The Type 203 filters have now been provided for testing in several facilities worldwide, including PFBC and IGCC plants.

The 3M Company is commercializing the Type 203 filter. Design modifications to the filter construction are being made based on evaluation of results of tests at Westinghouse STC and at the Tidd PFBC Demonstration Project. A commercially viable process for producing the filters has been developed and demonstrated. The success of this testing and demonstration phase is vital to this novel filter concept, which we believe will offer a viable lightweight composite filter alternative for PFBC and IGCC applications.

This project provides an excellent example of cooperation between the Department of Energy-Fossil Energy AR&TD Materials Program, Coal Technology Programs, and industry. It is a most successful example of technology transfer from a national laboratory to the industrial sector. This project also confirms the validity of the research and development (R&D) approach which involved good technical assessments of requirements and a disciplined approach to the R&D needed to satisfy those requirements.

References

1 Judkins, R. R., Stinton, D. P., Smith, R. G., and Fischer, E. M., "Ceramic Fiber Ceramic Matrix Filter Development," *Proc. Coal-Fired Power Systems 94—Advances in IGCC and PFBC Review Meeting,* DOE/METC-94/1008, Vol. 1 (DE94012252), U.S. Department of Energy, Morgantown, WV, June 1994, pp. 145–151.

2 Stinton, D. P., Lowden, R. A., and Chang, R., "Fabrication of Fiber-Reinforced Hot-Gas Filters by CVD Techniques," *Ceram. Eng. Sci. Proc.,* Vol. 9(9–10), 1988, pp. 1233–1244.

3 White, L. R., and Kafka, T. M., *Fabrication of Commercial-Scale Fiber-Reinforced Hot-Gas Filters by Chemical Vapor Deposition,* ORNL/Sub/89SB482/01, 3M Company, St. Paul, MN, Nov. 1992.

4 Sawyer, J., *Assessment of the Causes of Failure of Ceramic Filters for Hot-Gas Cleanup in Fossil Energy Systems and Determination of Materials Research and Development Needs,* ORNL/Sub/86-57964/01, Acurex Corporation, Mountain View, CA, Jan. 31, 1989.

5 Clark, R. et al., "Some Recent Experiences With the EPRI Hot-Gas Rigid Ceramic Filter at Grimethorpe PFBC Establishment," *Proc. of the 12th International Conference on Fluidized Bed Combustion,* ASME, New York, 1993, pp. 1251–1258.

6 Valentino, K. R., et al., "Durability Testing of Ceramic Candle Filters in PFBC Environments," *Proc. of the 12th International Conference on Fluidized-Bed Combustion,* ASME, New York, 1993, pp. 1375–1383.

7 Tressler, R. E., "High-Temperature Stability of Non-oxide Structural Ceramics," *MRS Bull.,* Vol. XVIII(9), 1993, pp. 58–63.

8 Alvin, M. A., Lane, J. E., and Lippert, T. E., *Thermal-Chemical Degradation of Ceramic Cross-Flow Filter Materials-Phase 1,* DOE/MC/25034-2967, Westinghouse Electric Corporation Science and Technology Center, Nov. 1989.

9 Jacobson, N. S., "Corrosion of Silicon-Based Ceramics in Combustion Environments," *J. Am. Ceram. Soc.,* Vol. 76(1), 1993, pp. 3–28.

10 Jacobson, N. S., and Smialek, J. L., "Hot Corrosion of Sintered α-SiC at 1000°C," *J. Am. Ceram. Soc.,* Vol. 68(8), 1985, pp. 432–439.

11 Smialek, J. L., and Jacobson, N. S., "Mechanism of Strength Degradation for Hot Corrosion of α-SiC," *J. Am. Ceram. Soc.,* Vol. 69(10), 1986, pp. 741–752.

12 Fox, D. S., and Smialek, J. L., "Burner Rig Hot Corrosion of Silicon Carbide and Silicon Nitride," *J. Am. Ceram. Soc.,* Vol. 73(2), 1990, pp. 303–311.

13 Fox, D. S., Jacobson, N. S., and Smialek, J. L., "Hot Corrosion of Silicon Carbide and Silicon Nitride at 1000°C," in: *Corrosion and Corrosive Degradation of Ceramics,* R. E. Tressler and M. McNallan, eds., American Ceramic Society, Westerville, Ohio, 1990 [also *Ceram. Trans.,* Vol. 10, Feb. 1990], pp. 227–249.

14 Alvin, M. A., et al., "Evaluation of Ceramic Filter Material, Selection for Application," *Proc. Coal-Fired Power Systems '93/Advances in IGCC and PFBC Contractor's Review Meeting,* DOE/METC 93/6131, Morgantown, WV, June 1993.

15 Alvin, M. A., et al., *Degradation of Cross-Flow Filter Material,* DOE/METC-90/6110, DOE Morgantown Energy Technology Center, Morgantown, WV, Mar. 1990.

16 Sawyer, J., Vass, R. J., Brown, N. R., and Brown, J. J., "Corrosion and Degradation of Ceramic Particulate Filters in Direct Coal-Fired Turbine Applications," ASME JOURNAL OF ENGINEERING FOR GAS TURBINES AND POWER, Vol. 113, 1991, pp. 602–606.

17 Carpenter, H. W., "SiC Tubes Exhibit Excellent Performance in Fluidized-Bed Heat Exchanger Tests," *Materials & Components in Fossil Energy Applications,* DOE/FE-0054/54, U.S. DOE, Washington, D. C., Feb. 1, 1985, pp. 1–4.

18 Stringer, J., "Ceramic Filter Experience at the Grimethorpe PFBC," presented at the 36th ASME International Gas Turbine and Aeroengine Congress and Exposition, Brussels, Belgium, June 12, 1990.

19 Smith, R. G., Eaton, J. H., and Leitheiser, M. A., *Fabrication of Full-Scale Fiber Reinforced Hot-Gas Filters by Chemical Vapor Deposition,* ORNL/Sub/89-SB482C/02, 3M Company, St. Paul, MN, Apr. 1994.

20 Smith, R. G., Eaton, J. H., and Leitheiser, M. A., *Full-Scale Fiber-Reinforced Hot-Gas Filter Testing Under Tasks 9 and 10,* ORNL/Sub/89-SB482C/04, 3M Company, St. Paul, MN, Sept. 1994.

21 Mudd, M. J., and Hoffman, J. D., "Tidd PFBC Hot Gas Filter Operating Experience: July 1993–April 1994," *Proc. of the Coal-Fired Power Systems 94—Advances in IGCC and PFBC Review Meeting,* DOE/METC-94/1008, Vol. 1 (DE94012252), U.S. Department of Energy, Morgantown, WV, June 1994, pp. 519–534.

A Review of the Efficacy of Silicon Carbide Hot-Gas Filters in Coal Gasification and Pressurized Fluidized Bed Combustion Environments

R. R. Judkins

D. P. Stinton

J. H. DeVan

Metals and Ceramics Division,
Oak Ridge National Laboratory,
Oak Ridge, TN 42066

Reviews of relevant literature and interviews with individuals cognizant of the state of the art in ceramic filters for hot-gas cleaning were conducted. Thermodynamic calculations of the stability of various ceramic phases were also made. Based on these calculations, reviews, and interviews, conclusions were reached regarding the use of silicon carbide-based ceramics as hot-gas filter media. Arguments are presented that provide the basis for our conclusion that high-purity silicon carbide is a viable material in the integrated coal gasification combined cycle (IGCC) and pressurized fluidized-bed combustion (PFBC) environments we examined. Clay-bonded materials are, we concluded, suspect for these applications, their extensive use notwithstanding. Operations data we reviewed focused primarily on clay-bonded filters, for which a great deal of experience exists. We used the clay-bonded filter experience as a point of reference for our review and analysis.

Summary

Based on a review of pertinent literature and interviews with several cognizant individuals who are conducting research and development on hot-gas cleaning devices, we have reached the following conclusions relative to the efficacy of silicon carbide hot-gas filters in dry ash (nonslagging) coal gasification and pressurized fluidized bed combustion environments and in slagging systems, provided molten slag does not contact the material.

The life-limiting failure mode of ceramic candle filters, including silicon carbide as well as other materials, is still conjectural, since failures in plant tests and demonstrations have generally been unusual or the result of abnormal operating conditions. For the most part these failures have been due to thermal and/or mechanical shocks resulting from upset conditions and faulty designs. Based on our discussions with several sponsors, designers, and operators of these tests and demonstration units, we consider the statement above to be the consensus.

In addressing concerns about the ability of silicon carbide to withstand coal gasification and pressurized fluidized-bed combustion environments, we have reviewed literature that presented the results of laboratory and in-plant tests of ceramic filters and ceramic filter materials. We have retrieved archival data of tests performed for other purposes that appear to be consistent with recent results directed specifically to filter performance. Most of these data related to refractory and heat exchanger tests. In addition, the thermodynamics of the relevant systems were analyzed using phase stability calculations.

We conclude that high-purity silicon carbide is a viable material in the IGCC and PFBC environments we examined. Clay-bonded materials are suspect, their extensive use notwithstanding. Under some off-design circumstances, our analysis also suggests that pure silicon carbide may be chemically degraded.

Based on the data we have reviewed, most materials being considered for ceramic filters are likely to be degraded by hot corrosion if contacted by molten slag (this is in addition to a major fouling problem should slag adhere to the filter surfaces).

In our reference PFBC in which filters would be exposed to the PFBC environment at 870°C and 1 MPa, an incredible deviation in flue gas chemistry, i.e., no SO_2, would have to occur to form even the most stable of sodium-silicon compounds ($Na_2Si_2O_5$). Any sodium introduced with the coal in the form of a silicate or NaCl will be converted to Na_2SO_4 during the combustion process. Similarly, if the binder phase of a clay-bonded SiC filter contains sodium silicate, it would be subject to this conversion with the concomitant degradation of mechanical properties. Thus, only in the absence of SO_2, which is unlikely in a PFBC system, would the stability of a clay-bonded SiC be assured. For pure SiC with or without SiO_2, silicate formation is suppressed by only a very low concentration of SO_2. This suggests that pure SiC filters should not experience alkali attack in a typical PFBC environment.

In our reference IGCC system in which filters would be exposed to the gasifier atmosphere at 650–870°C and 3.1 MPa, the stable forms of sodium are either carbonates or chlorides, depending on the HCl concentration in the product gas. At HCl concentrations above approximately 400 vppm, SiC is not affected by any of the sodium-containing species. Below this level of HCl, sodium silicates may be stable, depending on the sodium concentration in the product gas. The presence of a dolomite trap ahead of the filter would not affect the stability of SiC from the standpoint of sulfur removal; however, such a trap could potentially aid the chemical stability of SiC by interaction with and removal of Na_2CO_3.

Introduction

The successful development and deployment of several advanced coal-fueled gas turbine technologies depend greatly on the ability to clean fuel or combustion gas streams of particulates prior to these gases being passed through the turbines. These technologies include integrated gasification combined cy-

cles, pressurized fluidized bed combustors, and direct coal-fired turbines. Other systems could benefit from dependable hot gas cleaning filters that can operate at temperatures up to 1000°C. Rigid ceramic filters of a variety of designs are either commercially available or under development in programs around the world. Generally, ceramic filters can be classified into three types: (1) tubular filters, which generally have one end closed (candle filters) although some designs, most notably that of Asahi Glass, do not have a closed end; (2) crossflow filters, which are very compact, i.e., have high surface area/volume ratios, and are designed to permit inlet and outlet gases to flow perpendicularly to each other; and (3) fabric filters, which are made from ceramic fibers formed into a mat or woven into a cloth.

Rigid ceramic candle filters are currently being developed to remove particulates from gas streams being introduced into hot-gas turbines. Filter systems large enough to handle the volume of gases for typical IGCC or PFBC systems will be extremely expensive. For example, a 300 MWe oxygen-blown IGCC power plant will generate a gas flow of about 8 m³/s. In order to filter such a large volume of gas, approximately 130 m² of filter area or 1660 candle filters would be required. An air-blown gasifier would generate twice the gas flow and therefore, require approximately 3300 candle filters. Pressurized fluidized bed combustion systems generate five times the volume of gas of an air blown gasifier and would require 16,000 candle filters. Assuming candle filters could be purchased in large quantities for $300 each, the capital cost of one set of candles would range from about $0.5 million for an oxygen blown gasifier to $5-million for a PFBC [1].

Many different materials, oxides, nonoxides, and mixed, may be used for any of these filter types. The most popular oxide ceramics include alumina/mullite, cordierite, aluminosilicate foam/fibers, clay-bonded alumina, fireclay, and continuous fiber ceramic composites produced by chemical vapor infiltration (CVI). Nonoxide ceramics include clay-bonded silicon carbide, sintered silicon nitride, reaction-bonded silicon nitride, recrystallized silicon carbide, and CVI silicon carbide fiber-reinforced composite filters. Fabric filter materials include various grades of silica-alumina-boria, alumina-silica, and silicon carbide-silica. Most commercial and near-commercial ceramic filters are made of bonded ceramics. Several advanced concepts are being investigated and developed, including a composite silicon carbide filter developed at Oak Ridge National Laboratory (ORNL), which is being scaled to full-size filters by 3M Company of St. Paul, Minnesota.

The work discussed here was directed toward a determination of the ability of silicon carbide filters to perform in integrated gasification combined cycle and pressurized fluidized bed combustion environments. Several research groups (see "Laboratory Tests" section, herein) have reported data that suggest the use of silicon carbide as a ceramic filter material may be limited because of corrosive attack by alkali metal compounds and/or steam. Because of the commitment by the DOE Fossil Energy Advanced Research & Technology Development (AR&TD) Materials Program and ORNL to the development of composite ceramics made of silicon carbide, dense as well as porous, an assessment of the efficacy of silicon carbide in these environments was indicated. Although a similar assessment of other materials would be useful, our funding and time constraints, as well as the extensive work we have conducted on silicon carbide, dictated that this assessment be limited to silicon carbide ceramics.

The primary issue we desired to address was the potential for degradation of ceramic filters by corrosion or reaction of the gases and their contaminants in the respective systems with the ceramic filter materials. Other failure modes such as thermal or mechanical shock were outside the scope of this assessment although they are vitally important to the use of ceramic filters.

A ceramic filter may be classified as both a structural and a functional material. The terms "structural" and "functional" refer to, respectively, materials that have some load-carrying ability and materials that possess particular properties enabling them to perform specific functions. Ceramic filters must have the requisite properties to withstand the mechanical and thermal loading experienced in the filter application. At the same time, they must have an appropriate architecture for particulate filtration. In the filter application, chemical reactions may occur between the filter materials and the gaseous constituents that result in the degradation of both the structural and functional abilities of the filters.

A general consideration of corrosive attack and the concomitant degradation of properties will be informative. Silicon- and aluminum-based ceramics are most often used for ceramic filters. Reaction products of these ceramics and alkali metal compounds would be alkali metal silicates and alkali metal aluminates. If an alkali metal compound reacted with the ceramic material, certain phase and morphological changes would occur. The result would be the swelling or contracting of the structure, which would lead to a decrease in strength. The fundamental issue we had to deal with was whether these deleterious reactions will occur in the coal gasification and pressurized fluidized bed combustion systems of interest. If the reactions will occur, then clearly the use of ceramic filters will be limited to some extent. If the reactions will not occur or if their effects can be mitigated in some way, ceramic filters may be useful in these systems. Our approach to this assessment was to review the pertinent literature and to interview individuals working in this field. All individuals and groups we contacted were quite responsive to our requests for information [2–10].

This modestly funded (one man-month's effort) assessment was intended to provide a sufficient review of the state of the art in ceramic filters to guide us in our continuing development of silicon carbide ceramics and to aid us in the identification of any needed research. It was not intended to be an exhaustive survey of the matter of the use of ceramic filters for IGCC and PFBC systems.

Phase Stability Considerations

To be useful in IGCC or PFBC systems, ceramic filters must resist chemical attack by compounds of a relatively wide range of elements, including C, O, S, H, Cl, Na, and K. The following sections discuss the equilibrium phase relations among these elements at relevant filter service conditions and the most probable chemical reactions between these elements and SiC [11]. First to be considered is the combustion situation, where there is excess oxygen, and, secondly, the gasification situation, which is relatively reducing with respect to oxygen and where some designs show a sulfur absorber (dolomite) ahead of the filter. The initial gas compositions used in these calculations were taken from listings of nominal compositions reported by Westinghouse [12] in an analysis of the degradation mechanisms of filter materials. These compositions provide the required calculational input data for all elements except Na and K. Sodium exists primarily in two forms in coal—NaCl (from ground water) and sodium silicate (in clay)—and the calculations examine the stability of both forms and their reaction products in the presence of SiC. Potassium was not included as a reactive species in these calculations, since reactions with Na (chemically similar to K) were assumed to be potentially more detrimental. Our results appear to be consistent with results published earlier by researchers at the National Aeronautics and Space Administration—Lewis Research Center (NASA-Lewis) concerning alkali effects on SiC and Si_3N_4 heat engine components [13–17].

Pressurized Fluidized Bed Combustion (PFBC). The reference temperature and pressure for the PFBC calculations were 870°C and 1 MPa [12]. The percentages of CO_2, CO,

Table 1 Percentages of initial and equilibrated gas species

Source	Gas Composition (volume %)								
	N_2	O_2	CO_2	CO	H_2O	SO_2	H_2	H_2S	CH_4
				PFBC					
Reference Flue Gas	75.25	3.45	13.63	--	7.33	0.34	--	--	--
Equilibrium Gas Mixture at 870 C	75.22	3.41	13.62	--	7.33	0.34	--	--	--
				Texaco Gasifier					
Reference Product Gas	0.81	--	7.95	38.84	25	--	26.38	0.92	0.1
Equilibrium Gas Mixture at 870 C	0.86	--	18.01	28.52	20.56	--	27.59	0.94	3.49
Equilibrium Gas Mixture at 800 C	1.02	--	23.22	23.08	21.43	--	23.13	0.92	7.16

H_2O, H_2, and SO_2 for the nominal PFBC combustion gas composition were used to fix the concentrations of C, O, S, and H in the gas phase. As shown in Table 1, equilibrium calculations based on the amounts of these latter elements gave essentially the same percentages of gas phase species at 870°C as in the reference atmosphere. However, an SO_3 concentration of 0.082 percent (not listed in the reference atmosphere) is also required to hold the SO_2 concentration at the given level of 0.34 percent. The activity, partial pressure, of S_2 in the equilibrium atmosphere is 3.6×10^{-23} Pa. Adding sodium in the form of NaCl to this atmosphere yields two condensed phases at equilibrium, Na_2SO_4 and NaCl. However, the presence of excess NaCl in the reference atmosphere requires a chlorine pressure of 2 MPa and an HCl pressure of 0.13 MPa. Since the latter pressure is higher than that normally detected in a PFBC flue gas, it can be assumed that NaCl actually will decompose in the bed to form principally gaseous HCl and solid Na_2SO_4. Adding sodium in the form of a carbonate or silicate also will produce Na_2SO_4. Reacting SiC together with any of the known forms of sodium in coal in this PFBC atmosphere results in the presence of two equilibrium condensed phases—SiO_2 and Na_2SO_4. NaCl would also co-exist as a third phase if a high enough chlorine activity could be sustained, as discussed above. Within the listings of condensed species for which free energy data exist, these are the only silicon- or sodium-containing condensed phases that are stable in this PFBC atmosphere.

At the oxygen partial pressure, 0.035 MPa, in the reference atmosphere, the SO_2 partial pressure must be below 3.4×10^{-2} Pa (34 ppb) to allow the existence of the most stable sodium–silicon compound ($Na_2Si_2O_5$) at 870°C. Accordingly, any sodium introduced with the coal in the form of a silicate (clay) should convert to Na_2SO_4 given the nominal SO_2 activity in the PFBC atmosphere. Similarly, any alkali silicates that may be present in a clay-bonded SiC filter will be potentially subject to sulfation by SO_2 and SO_3 in the PFBC combustion atmosphere. It also follows that, in testing the compatibility of SiC (or SiO_2) with NaCl or Na_2SO_4, the level of SO_2 is a most important parameter. In the absence of SO_2, e.g., in air, silicate formation is favored, whereas maintaining only a relatively small concentration of SO_2 will suppress silicate formation.

The addition of $CaO/CaCO_3$ (or $MgO/MgCO_3$) to the PFBC system is obviously significant in controlling the SO_2 and S_2 activities. As expected, calculations showed that the sulfate phase is the most stable form of Ca (or Mg) in the PFBC atmosphere, and the presence of this phase did not change the predominance of SiO_2 as the most stable transformation product of SiC.

The most volatile of the sodium-containing species in the PFBC atmosphere is NaCl, which has an equilibrium pressure of 100 Pa over condensed NaCl. However, as noted above, NaCl will decompose in the combustor to form HCl and Na_2SO_4, and the NaCl pressure in the flue gas will depend on the steady-state HCl pressure in the gas. The NaCl pressure corresponding

to an HCl level of 1000 vppm is 0.1 Pa. The next most volatile species is Na_2SO_4, which attains a pressure of 0.003 Pa over condensed Na_2SO_4. These pressures are so low that the mass of sodium transported to the filter by solid particles should far outweigh that transported by vapor.

Integrated Coal Gasification Combined Cycle. The reference temperature for the gasifier calculations was set at 650–870°C and the gas pressure at 3.1 MPa [12]. The input levels of C, O, S, and H were defined in terms of the nominal CO_2, CO, H_2O, H_2, and CH_4 concentrations of a Texaco entrained-bed gasifier product gas [12]. Table 1 compares the input concentrations of the latter species with concentrations attained after equilibration (in a closed system) at 870°C and 800°C. Unlike the case above for the PFBC, the reference gas composition is not an equilibrium mixture at either of the designated temperatures. The shift to equilibrium increases the H_2/H_2O ratio, decreases the CO/CO_2 ratio, and significantly increases the CH_4 concentration. Some calculations were made in which the concentrations of H_2 and H_2O, CO and CO_2, and H_2 and CH_4, respectively, were fixed at the initial reference values, and, to the extent that this was examined, the results were consistent with the conclusions discussed below for the equilibrated gas mixtures. Two different starting assumptions were examined relative to the reaction of the equilibrated product gas with SiC. In the first case the phase stabilities of relevant sodium compounds in the product gas were established, and the reactivities of the predominant forms of sodium were assessed relative to SiC at 870°C. In the second case, the product gas and sodium species were equilibrated with dolomite [$(Ca,Mg)CO_3$] and combined with SiC at a slightly reduced temperature of 800°C. The latter case was intended to cover gasifier designs where a dolomite trap is included ahead of the filter [12].

NaCl will exist as a stable condensed phase in the equilibrated product gas in Table 1 providing an HCl level of 18 vppm (or greater) can be sustained in the system. Na_2CO_3 becomes the predominant sodium-containing phase below $\approx$18 vppm HCl. The most stable sulfur species with sodium is Na_2S, but this species can exist only if the carbon activity of the product gas is reduced from the equilibrium activity of 0.062 to $\leq$0.0005 (given the oxygen and sulfur activities in this gasifier atmosphere). Even at the relatively low oxygen activity ($\approx 10^{-19}$ MPa) and high carbon activity of this gasifier atmosphere, SiC is not stable and transforms to SiO_2. As in the case of the PFBC, the stability of SiO_2 will depend on the Na_2O activity. Since the SO_3 activity in the reference gasifier is infinitesimal, the Na_2O activity in this case is set by the HCl and the CO_2 activities in the system. If the HCl gas concentration is above $\approx$400 vppm, the Na_2O activity is less than that required to convert SiO_2 to the most stable sodium silicate, $Na_2Si_2O_5$; i.e., SiO_2 will co-exist with solid (or gaseous) NaCl. Reducing the exposure temperature to 650°C lowers this critical HCl concentration to above $\approx$30 vppm. Over the range 18 to 400 vppm HCl, where NaCl is still the predominant form of sodium, the Na_2O activity is sufficient to initiate silicate formation, and at lower levels of HCl, where Na_2CO_3 becomes predominant, formation of Na_2SiO_3 is predicted. Accordingly, SiC filters are subject to reaction with sodium under gasifier conditions at low HCl activities, and, if bonded with clay that contains alkali silicates, could be subject to decomposition by the reverse reaction at higher HCl activities.

The most volatile of the sodium-containing species in the gasifier atmosphere is NaCl, whose equilibrium pressure over condensed NaCl is 100 Pa. Unlike the case for the PFBC, this NaCl pressure can be sustained with as little as 18 vppm HCl in the product gas, and therefore it appears to be a realistic pressure for any gasifier operating on a medium or high chlorine coal. The next most volatile species is NaOH, with an equilibrium pressure over solid NaCl of about 1 Pa. Thus, vapor transport of sodium will occur to a greater extent in the reference

gasifier concept than in the PFBC concept; however, considering the mass of particulates normally picked up by the filter, particulate transport should still be the dominant transport process in both concepts.

Most of the gasifier concepts addressed [12] include a dolomite trap ahead of the filter. Accordingly, calculations were made to evaluate the reaction of the product gas with $(Ca,Mg)CO_3$. The temperature for these calculations was adjusted downward from the 870°C gasifier outlet to 800°C to account for heat losses. With dolomite present, the sulfur activity is defined by the two-phase $CaCO_3/CaS$ equilibrium. Equilibration of the product gas with dolomite at 800°C results in a reduction of the H_2S concentration from the initial level of 0.92 percent (Table 1) to an equilibrium level of 0.36 percent. If the H_2 and H_2O concentrations of the product gas are fixed at their reference levels of 26.38 and 25.0 percent, respectively (Table 1), then the H_2S concentration drops from 0.92 to 0.33 percent. Increasing the temperature of the dolomite to 870°C would reduce the equilibrium level of H_2S to 0.16 percent. These calculations show that the $MgCO_3$ component of the dolomite actually does not play a role in sulfur capture at the reference product gas temperature and pressure. MgS does not form at the carbon and oxygen activities set by the product gas, and MgO is the predominant phase. The reaction of H_2S with the dolomite will not affect any of the chemical equilibria discussed above for sodium and SiC, and there is no apparent interaction of the dolomite with HCl. One important chemical effect of the dolomite could be the absorption of Na_2CO_3, since the phase diagram for Na_2CO_3 and Ca_2CO_3 shows several intermediate mixed carbonate species. Unfortunately free energy data are lacking by which to assess this effect on Na_2CO_3 activity. Any reduction in Na_2CO_3 activity by such a mechanism ahead of the filter obviously would reduce the potential for reaction with SiC.

Laboratory Tests

Evaluation of candle filters during in-plant testing has indicated a degradation in mechanical strength with exposure time and thermal cycles [18]. The cause of the degradation has not been established unequivocally but could result from thermal shock or corrosive attack by alkali metals, steam, or HCl. To investigate hot corrosion of filter materials, various corrosion test facilities have been constructed. A test has been utilized at NASA-Lewis [17] and ORNL [19] that paints a Na_2SO_4 solution onto SiC specimens and anneals them in air at high temperatures. Since all sodium introduced into the PFBC would be converted to solid Na_2SO_4 and gaseous HCl (see phase stability considerations), this test was thought to simulate the temperature and alkali present in a PFBC environment. Exposure of even highly dense sintered SiC specimens or very pure chemically vapor deposited SiC under these conditions resulted in severe corrosion at temperatures above $\approx$800°C. The Na_2SO_4 appeared to react with the native SiO_2 protective layer and form a low-melting glass that flowed off the SiC specimens.

Our calculations based on phase stability considerations (see preceding section) suggest that this test may not accurately simulate PFBC conditions. These thermodynamic calculations predict that in air, Na_2SO_4 would dissociate into Na_2O and SO_2. The activity of Na_2O is therefore responsible for the reaction with SiO_2 and the formation of the low-melting glass. In an actual PFBC the partial pressure of SO_2/SO_3 would be sufficient to stabilize Na_2SO_4 and prevent dissociation into Na_2O and SO_2. Therefore, these calculations suggest that in a PFBC environment, no reaction would occur between Na_2SO_4 and SiO_2 because of the minimal activity of Na_2O. For this test to simulate a PFBC environment accurately, coated specimens would need to be annealed in air containing a representative amount of SO_2/SO_3.

A test that applies Na_2SO_4 directly onto SiC also ignores the effect of the dust cake. As discussed previously, vapor phase transport of sodium species would be minimal compared to the mass of sodium transported by solid ash particles. Research has shown that the dust cake applied during conditioning of the filters is not removed by pulse cleaning. If conditioning of the filters were performed with materials free of sodium, a barrier would be present to separate the sodium-containing ash from the SiC filters.

A second test facility was developed at Westinghouse [20] to evaluate the resistance of filter materials to sodium containing vapors. In this test, water saturated with NaCl is vaporized and incorporated into a gas stream of air that passes through a filter specimen at the test temperature. This test was thought to simulate the temperature, steam, and alkali content of a PFBC environment. Evaluation of materials using this test indicates severe corrosion of SiC at 870°C. Corrosion is thought to occur under these conditions because NaCl dissociates to Na_2O and HCl. The activity of Na_2O is again responsible for the reaction with the native SiO_2 protective layer. This test also probably does not simulate a PFBC environment because SO_2/SO_3 is not added to the air and no dust cake is present. If SO_2/SO_3 were present, NaCl would dissociate to form stable Na_2SO_4 and HCl. Therefore, in a PFBC environment, the activity of Na_2O should be minimal and SiC should not react with these sodium species.

A third test facility was developed at Virginia Polytechnic Institute and State University (VPI) [8] to simulate the effects of a PFBC environment on filter materials. In this test air, water and sodium nitrate are introduced at high temperature into a stainless steel vessel to simulate the temperature, pressure, steam, and alkali conditions present in a PFBC. Evaluation of clay-bonded candle filters has shown significant degradation at 870°C. This test, as the others, probably does not accurately simulate a PFBC environment because SO_2/SO_3 is not added to the air and no dust cake is present. If SO_2/SO_3 were present, sodium nitrate would dissociate to form stable Na_2SO_4 and a nitrogen-containing gas. Therefore, in a PFBC environment, the activity of Na_2O would be minimal and SiC should not react with these sodium species.

Sawyer, Vass, Brown, and Brown [21, 22] published an excellent review article on the corrosion and degradation of ceramic particulate filters. This review addressed many laboratory studies as well as laboratory analyses of filters exposed in plants. A detailed summary of that review is not presented here; rather, the salient conclusions will be summarized. Their conclusions based on their own analyses and their reviews of work performed by others were that "presently available ceramic filters have serious mechanical limitations" and that redesign and possibly new materials would be needed; that "chemical attack by alkali metal compounds is a serious, long-term problem for the aluminosilicates;" and that "chemical attack of SiC and Si_3N_4 by steam and alkali metal compounds appears to pose possible problems."

In fluidized-bed heat exchanger tests performed in a small FBC test unit at Rocketdyne [23] silicon carbide tubes were found to exhibit excellent performance. In those tests, three types of SiC tube materials, siliconized SiC tubes, sintered α-SiC tubes, and chemical vapor deposited (CVD) tubes, were investigated. These SiC materials did not experience any corrosive degradation nor were their strengths degraded. Specifically, no evidence of corrosion was observed by microstructural or compositional analysis; no measurable erosion occurred; differences in strength between exposed and unexposed tubes were within the normal scatter in data; and no trend in decreasing strength was observed.

In-Plant Tests

This section presents some of the results of in-plant tests that relate to silicon carbide filters. Most of the material was obtained from the *Proceedings: Second EPRI Workshop on Filtration of Dust From Coal-Derived Reducing and Combustion*

Gases at High Temperature [24] and through personal conversations with cognizant individuals [4, 6, 7]. As before, this was meant to be a representative survey but not necessarily a comprehensive one.

Integrated Coal Gasification Combined Cycle. The current generation candle filters have yet to demonstrate the necessary durability (at least one year and probably much longer) to be used in full-scale power plants. Candle filters are susceptible to failure (cracking) due to thermal and mechanical stresses particularly near the flanged ends. These stresses have been attributed to improper mounting techniques, tubesheet design, pulse cleaning, candle design, and system transients. Candle filters are sealed to the tubesheet by some clamping or hold-down devices such as venturi weights that lie on top of the flange of the candle. Very large pressures can build up inside the filter vessel, causing dust to leak through this filter-tubesheet seal. Catastrophic failure often results when the pressure builds to a sufficient level inside the vessel to lift the candle away from the tubesheet. The rapid release of pressure causes the candle to crash back onto the tubesheet causing fracture. Improper flange design was a typical cause of failure in early candles. Similarly, improperly designed equipment used for pulse cleaning can cause cracking due to thermal shocks. These types of failures have essentially been eliminated after many years of testing and experience with ceramic filters. None of the reports of filter failures in pilot plant tests has been attributed to chemical degradation.

There is evidence of chemical degradation of the candle filters that makes the candle susceptible to thermal and mechanical shock after many hours of service. Chemical degradation is very difficult to identify in filters that have failed in service. Examination of chemical degradation in a laboratory environment is equally difficult because conditions inside a filter vessel are impossible to duplicate. Although gas compositions are known and can be simulated in the laboratory, the positive or negative effects of the dust cake are difficult if not impossible to determine. Relevant experience with SiC-based ceramic candle filters based on several years of coal gasification pilot plant operation is summarized below [24]:

• Forty-four each Industrial Filter and Pump Manufacturing Co. and Schumacher candle filters performed well in a full-stream test in Shell's 250 Mg/d, 2.5 MPa unit in Deer Park, Texas. The filters were operated for approximately 5000 hours at ≈260°C using nine different coals.

• Nine Schumacher candle filters were tested in a slipstream of Rheinbraun's 700 Mg/d, 1.0 MPa oxygen-blown gasifier in Berrenrath, Germany. The candles were tested for >500 hours at a temperature of about 300°C. The filters functioned without incident while operating with brown coal.

• Ninety Schumacher candle filters were tested at 300 to 320°C in Rheinbraun's 150 Mg/d, 2.5 MPa oxygen-blown gasifier in Wesseling, Germany. After more than 5000 hours the filters continued to perform well while using brown and bituminous coals.

• Various NGK and Schumacher candle filters were tested at ≈400°C in CRIEPI's 2 Mg/d, 1.7 MPa pilot plant in Yokosuka, Japan. The candles, which were pulse cleaned with recycled gas, functioned satisfactorily for the duration of the test.

• Two ceramic filter test configurations were tested at 430 to 620°C in the Kellogg-Rust-Westinghouse (KRW) 20 Mg/d, 1.6 MPa pilot plant in Madison (Waltz Mill Site), Pennsylvania [25]. Numerous candle filter failures were experienced during about 1300 hours of testing. In the first campaign, 14 of 33 filters failed. All of the failures occurred because of thermal shock-induced stresses caused by water injection upstream of the filters. In the second campaign, seven of thirty filters were broken due (presumably) to mechanical stresses resulting from high fluid momentum. In the last pilot plant test, one filter element fractured and three had cracks in the mounting collar.

These failures were attributed to the seal arrangement and not to the filters. KRW suggested that the filter seal could be redesigned to eliminate thermally and mechanically induced stresses. Filters would be expected to perform well in the redesigned system.

• Five each Didier and Schumacher candle filters were tested at 630 to 700°C in the Technical Research Center of Finland's 2 Mg/d, 0.5 MPa fluid bed pilot plant in Otaniemi, Finland. The filters performed satisfactorily on brown coal, peat, and biomass fuels. Some difficulties did occur when attempting to filter wood-derived gases that contained tar that blinded the filters.

• Nineteen Schumacher candle filters and four Westinghouse crossflow filters were tested for >900 hours at 650 to 760°C in Texaco's 20 Mg/d, 2.5 MPa pilot plant in Montebello, CA. These candle filters failed to perform in an adequate fashion because the characteristics of the ash (very adherent) made them nearly impossible to clean. The high pulse gas consumption used in an attempt to clean the filters led to the thermal shock failures of numerous candles.

• Approximately 15 to 20 additional tests of ceramic candle filters in coal gasification systems are planned for the next 3 to 5 years. The evidence collected to date indicates that clay-bonded ceramic filters operate for long periods without difficulty at temperatures below about 650°C. Operation of filters at higher temperatures is hampered by blinding or plugging of the open porosity by tars or carbon. There is no experimental evidence of chemical degradation of candle filters at these temperatures.

In a DOE Fossil Energy AR&TD Materials Program sponsored project administered by The Materials Properties Council [26], alloys and refractories were tested in laboratories and in operating pilot plants. Although the test program for refractories was not directed to the filter application, the information is relevant for the present assessment. In both laboratory and pilot plant tests, clay-bonded and oxynitride bonded silicon carbides were significantly degraded by coal gasification atmospheres. However, high-purity sintered α-SiC was unaffected by the coal gasification exposures [26].

Pressurized Fluidized-Bed Combustion. Some of the most relevant data for this assessment are those obtained in tests at the Grimethorpe PFBC in the United Kingdom. In addition to reports of these tests, discussions were held with cognizant EPRI and British Coal Corporation personnel [6, 7]. In addition, notes from a presentation made by Stringer of EPRI at the 1990 ASME International Gas Turbine Conference in Brussels, Belgium, were also useful [27].

The first Grimethorpe test, conducted in 1987 at 850°C and 1.0 MPa for 800 hours, involved 130 Schumacher candle filters (clay-bonded SiC). Some of the candles in this test were broken due to faulty hold-down devices. There were also losses in permeance and cleaning difficulties were experienced, but these were not serious. In the second Grimethorpe test, breakage of filters was again a problem. In this second test, the cause of the breakage was again the hold-down device, a gravity hold-down unit.

Based on analyses of the Grimethorpe filters, filter strength is apparently degraded as a result of cracking due to thermal shocks. There is no evidence to suggest alkali attack in the Grimethorpe tests. Filters have been examined specifically for evidence of alkali compounds and none has been found. Steam may be a cause for concern, although there is no evidence from Grimethorpe to suggest steam is a problem. PFBCs may offer sufficient flexibility that filters can be operated over a wide range of temperatures (700°C ≤ T ≤ 1050°C). The prevailing opinion seems to be that clay-bonded SiC ceramic candle filters probably will not have utility at temperatures > 1050°C; they will be limited in use at ≈850°C; and they should be successful at ≤700°C. Based on the evidence we have examined in this

assessment, we believe this opinion is correct. However, based on the evidence and our analysis, we do not believe this conclusion and the temperature restriction apply to high-purity SiC without binder phases.

Conclusions

Based on the results of this brief study of the use of silicon carbide as a filtration medium in IGCC and PFBC systems, a few critical conclusions and recommendations are in order. These are listed below (not necessarily in order of priority):

- Of those reported failures discovered in this review that have occurred in hot gas particulate removal devices, all have been attributed to stresses imposed by abnormal or unexpected thermal and/or mechanical transients during operation. This suggests a critical need for detailed design analyses of areas susceptible to thermally or mechanically induced breakage such as the flange or collar region of ceramic candle filters.
- Based on our analysis, pure silicon carbides should not be chemically degraded in our reference PFBC environment. Bonded silicon carbides, particularly clay-bonded materials, are suspect and may be limited in applicability in this environment. The most likely chemical degradation is that due to alkali metal compounds and/or steam. Additional studies are in order to unequivocally establish or refute alkali and/or steam corrosion as a degradation mechanism.
- Reaction of SiC with oxygen and sodium to form silicates is predicted in the reference gasifier at 870°C if the HCl concentration in the product gas stream runs below ≈400 ppmv. If the filter temperature is lowered to 650°C, only ≈30 ppmv of HCl would be required to suppress silicate formation. Placement of a $CaCO_3$-containing trap ahead of the filter could limit silicate formation, assuming Na_2CO_3 carried in the gas stream will chemically combine with the $CaCO_3$.
- Contact of silicon carbide filters with molten coal ash slag containing alkali metal sulfates may result in hot corrosion as a result of dissolution of silica formed on the surface of the silicon carbide. Studies to determine the extent of this hot corrosion are needed.
- Ceramic composites offer advantages over monolithic ceramics in hot gas filtration applications because of their greater resistance to chemical degradation and to thermal and mechanical shocks. Very favorable results were obtained at the Westinghouse Science and Technology Center in 1993 on 3M ceramic composite candle filters [28]. An in-plant test of the 3M filters should be identified to confirm their advantages.
- Clay-bonded silicon carbide filters are probably acceptable for use in coal gasification and pressurized fluidized bed combustion environments at ≤700°C; they may be appropriate for use at 850°C, but caution should be exercised; and their use is highly questionable at 1000°C or greater.

In addition to these conclusions, it is instructive to consider the relevant major conclusions from the EPRI Workshop as stated in the August 25, 1992, letter from Epstein and Brown of EPRI to the Workshop participants [29]. We list those relevant conclusions and make remarks about them as appropriate vis-à-vis the goals of this study.

- "In an oxidizing atmosphere in the presence of moisture and alkali it appears that the SiC materials begin to show serious degradation in strength at temperature above 850°C."

This conclusion is probably correct for *clay-bonded* SiC materials and probably does not apply to high-purity SiC. Our results suggest this conclusion must be qualified in two respects. First, the oxidizing atmosphere must be free of SO_2 to form even the most stable of sodium–silicon compounds; this is a very unlikely situation in a coal combustion, i.e., oxidizing, atmosphere. Thus, clay-bonded SiC containing alkali silicates in the binder

are almost certain to chemically degrade. Second, pure SiC is almost certain not to degrade.

- "Most failures of the tubular filter system appear to be associated with excessive temperature gradients resulting from either localized combustion or mixing of cool and hot gas streams."
- "There have been failures in both candle and tubular filter systems that have not been fully understood. Continuing investigations on failure mechanisms are ongoing."
- "A number of new materials and concepts including alumina candles, alumina-silicate fibrous candles and tubesheets, CVD Nextel fibers with SiC, and the application of extruded honeycomb ceramic shapes are being developed. Further long term testing under real gas conditions is required on these materials and concepts."

Acknowledgments

References

1 Epstein, M., "Overview of Dust Filtration From Coal-Derived Reducing Gases at High-Temperature," in: *Proc. Second EPRI Workshop on Filtration of Dust From Coal-Derived Reducing and Combustion Gases at High Temperature,* R. C. Bedick, M. Epstein, and R. A. Brown, eds., Electric Power Research Institute, Palo Alto, CA, Mar. 11–13, 1992.

2 Wheeler, G. F., U.S. Department of Energy, Washington, DC, personal communications to R. R. Judkins, Sept. 1992.

3 Dennis, R. A., Holcombe, N. T., and Ness, H. M., personal communications to J. H. DeVan, R. R. Judkins, and D. P. Stinton, Sept. 1992.

4 Cherish, P., M. W. Kellogg Co., Houston, TX, personal communication to R. R. Judkins, Sept. 3, 1992.

5 Moore, W., DOE Fossil Energy, Washington, DC, personal communication to R. R. Judkins, Sept. 3, 1992.

6 Stringer, J., Electric Power Research Institute, Palo Alto, CA, personal communication to R. R. Judkins, Sept. 9, 1992; Clark, R., et al., "Some Recent Experiences With the EPRI Hot-Gas Rigid Ceramic Filter at Grimethorpe PFBC Establishment," *Proc. 12th Int. Conf. on Fluidized-Bed Combustion,* ASME, New York, 1993, pp. 1251–58.

7 Smith, M. A., British Coal Corporation Coal Research Establishment, Cheltenham, England, personal communication to R. R. Judkins, Sept. 16, 1992.

8 Brown, J. J., Virginia Polytechnic Institute and State University, Blacksburg, VA, personal communication to D. P. Stinton, Nov. 9, 1992; Valentino, K. R., et al., "Durability Testing of Ceramic Candle Filters in PFBC Environments," *Proc. 12th Int. Conf. on Fluidized-Bed Combustion,* ASME, New York, 1993, pp. 1375–83.

9 Alvin, M. A., Westinghouse Electric Corporation, Pittsburgh, PA, personal communications to J. H. DeVan and D. P. Stinton, Nov. 1992.

10 Tressler, R. E., Pennsylvania State University, State College, PA, personal communication to D. P. Stinton, May 17–18, 1993; Tressler, R. E., "High-Temperature Stability of Non-oxide Structural Ceramics," *MRS Bulletin,* Vol. XVIII(9), 1993, pp. 58–63.

11 Besmann, T. M., *SOLGASMIX-PV, A Computer Program to Calculate Equilibrium Relationships in Complex Chemical Systems,* ORNL/TM-5775, Oak Ridge National Laboratory, Apr. 1977.

12 Alvin, M. A., Lane, J. E., and Lippert, T. E., "Thermal-Chemical Degradation of Ceramic Cross-Flow Filter Materials-Phase 1," DOE/MC/25034-2967, Westinghouse Electric Corp. Science and Technology Center, Nov. 1989.

13 Jacobson, N. S., "Corrosion of Silicon-Based Ceramics in Combustion Environments," *J. Am. Ceram. Soc.,* Vol. 76(1), 1993, pp. 3–28.

14 Jacobson, N. S., and Smialek, J. L., "Hot Corrosion of Sintered α-SiC at 1000°C," *J. Am. Ceram. Soc.,* Vol. 68(8) 1985, pp. 432–39.

15 Smialek, J. L., and Jacobson, N. S., "Mechanism of Strength Degradation for Hot Corrosion of α-SiC," *J. Am. Ceram. Soc.,* Vol. 69(10), 1986, pp. 741–752.

16 Fox, D. S., and Smialek, J. L., "Burner Rig Hot Corrosion of Silicon Carbide and Silicon Nitride," *J. Am. Ceram. Soc.,* Vol. 73(2), 1990, pp. 303–311.

17 Fox, D. S., Jacobson, N. S., and Smialek, J. L., "Hot Corrosion of Silicon Carbide and Silicon Nitride at 1000°C," in: *Corrosion and Corrosive Degradation of Ceramics,* R. E. Tressler and M. McNallan, eds., *Ceramic Transactions,* Vol. 10, Feb. 1990, pp. 227–249.

18 Alvin, M. A., et al., "Evaluation of Ceramic Filter Material, Selection for Application," presented at the Coal-Fired Power Systems '93/Advances in IGCC and PFBC Contractor's Review Meeting, Morgantown, WV, 1993.

19   Graham, D. W., and Stinton, D. P., "Chemical Vapor Deposition of Ta₂O₅ Corrosion Resistant Coatings," *Proc. 1992 Coatings for Advanced Heat Engines Workshop,* Monterey, CA, Aug. 3–6, 1992, in press.

20   Alvin, M. A., Lippert, T. E., Bachovchin, D. M., Lane, J. E., Tressler, R. E., and Jukus, K., *Degradation of Cross-Flow Filter Material,* DOE/METC-90/6110, DOE Morgantown Energy Technology Center, Mar. 1990.

21   Sawyer, J., Vass, R. J., Brown, N. R., and Brown, J. J., "Corrosion and Degradation of Ceramic Particulate Filters in Direct Coal-Fired Turbine Applications," ASME Journal of Engineering for Gas Turbines and Power, Vol. 113, 1991, pp. 602–606.

22   Sawyer, J., *Assessment of the Causes of Failure of Ceramic Filters for Hot-Gas Cleanup in Fossil Energy Systems and Determination of Materials Research and Development Needs,* ORNL/Sub/86-57964/01, Acurex Corporation, Mountain View, CA, Jan. 31, 1989.

23   Carpenter, H. W., "SiC Tubes Exhibit Excellent Performance in Fluidized-Bed Heat Exchanger Tests," in: *Materials & Components in Fossil Energy Applications,* DOE/FE-0054/54, U.S. Department of Energy, Feb. 1, 1985, pp. 1–4.

24   Bedick, R. C., Epstein, M., and Brown, R. A., eds., *Proc. Second EPRI Workshop on Filtration of Dust From Coal-Derived Reducing and Combustion Gases at High Temperature,* Electric Power Research Institute, Palo Alto, CA, Mar. 11–13, 1992.

25   Haldipur, G. B., Schmidt, D. K., and Smith, K. J., *A 50-Month Gasifier Mechanistic Study and Downstream Unit Process Development Program for the Pressurized Ash-Agglomerating Fluidized-Bed Gasification System,* DOE/MC/21063-2740, Vol. I, DOE Morgantown Energy Technology Center, Morgantown, WV, Mar. 1989, pp. 86–106.

26   Criss, G. H., and Firestone, R. F., "Performance of Refractories in Coal Conversion Pilot Plants," in: *The Properties and Performance of Materials in the Coal Gasification Environment,* V. L. Hill and H. L. Black, eds., American Society for Metals, Metals Park, OH, 1981, pp. 97–124.

27   Stringer, J., "Ceramic Filter Experience at the Grimethorpe PFBC," presented without publication at the 36th ASME International Gas Turbine and Aeroengine Congress and Exposition, Brussels, Belgium, June 12, 1990.

28   Smith, R. G., 3M Company, St. Paul, MN, personal communication to R. R. Judkins, Jan. 31, 1994.

29   Epstein, M., and Brown, R. A., EPRI letter dated Aug. 25, 1992, to David P. Stinton.

Biomass-Gasifier/Aeroderivative Gas Turbine Combined Cycles: Part A—Technologies and Performance Modeling

S. Consonni
Dipartimento di Energetica,
Politecnico di Milano,
Milan, Italy

E. D. Larson
Center for Energy and
Environmental Studies,
School of Engineering and Applied Science,
Princeton University,
Princeton, NJ 08544

Gas turbines fueled by integrated biomass gasifiers are a promising option for base-load electricity generation from a renewable resource. Aeroderivative turbines, which are characterized by high efficiencies at smaller scales, are of special interest because transportation costs for biomass constrain biomass conversion facilities to relatively modest scales. Commercial development activities and major technological issues associated with biomass integrated-gasifier/gas turbine (BIG/GT) combined cycle power generation are reviewed in Part A of this two-part paper. Also, the computational model and the assumptions used to predict the overall performance of alternative BIG/GT cycles are outlined. The model evaluates appropriate value of key parameters (turbomachinery efficiencies, gas turbine cooling flows, steam production in the heat recovery steam generator, etc.) and then carries out energy, mass, and chemical species balances for each plant component, with iterations to insure whole-plant consistency. Part B of the paper presents detailed comparisons of the predicted performance of systems now being proposed for commercial installation in the 25–30 MW_e power output range, as well as predictions for advanced combined cycle configurations (including with intercooling) with outputs from 22 to 75 MW_e. Finally, an economic assessment is presented, based on preliminary capital cost estimates for BIG/GT combined cycles.

Introduction

Biomass is of interest as an energy source because it is potentially renewable and would have no net carbon dioxide emissions associated with its use: New biomass growth absorbs the carbon dioxide released in converting previously grown biomass to energy.

Biomass accounts for 3 to 4 percent of total primary energy use in the US, which is roughly the average for industrialized countries as a group (Hall et al, 1993). Over 9 GW of steam-turbine biomass power generating capacity are already installed in the United States today, compared to nearly 700 GW of total utility generating capacity (EIA, 1993). With relatively low operating efficiencies (below 25 percent on a lower heating value basis or 20 percent on a higher heating value basis[1]), existing biomass power facilities rely on low, zero, or negative cost biomass for fuel, primarily residues of agro- and forest product-industry operations. The use of excess agricultural land has been proposed for the United States (Solar Thermal, 1992) and Europe (Shell, 1992) to supply biomass energy feedstocks while reducing present agricultural subsidies. Total cropland idled in the U.S. in 1990, either to support crop prices or to control erosion, was some 33 million hectares, and it has been projected that some 52 million hectares will be idled by 2030 as a result of continued farm productivity gains, despite an expected doubling of maize, wheat, and soybean exports (USDA, 1989). For Western Europe, one analysis shows that

50 to 100 million hectares less land might be needed for food production in 2015 than in 1990 (Netherlands, 1992).

In developing countries, biomass provides an estimated 38 percent of primary energy needs (Hall et al., 1993). Most of this biomass is used very inefficiently for household cooking. Modernizing the use of biomass for energy through power generation could contribute to a much-needed expansion of electricity supply while helping to promote rural industrialization, stem urban migration, and provide energy inputs for agricultural modernization (Williams, 1994). Also, establishing biomass energy production on deforested or otherwise degraded lands, of which there are an estimated 800 million hectares in developing regions (Grainger, 1988), could help restore such lands to productive use while decreasing pressure to cut existing forests.

While there will be a continuing role for biomass power generation based on use of low-cost residue fuels, a more significant potential for power generation exists if technologies are developed to enable economical use of purpose-grown biomass crops, which will be more costly than most residue biomass that is used for energy today. Gas turbines fueled by biomass through integrated gasification systems are promising alternatives to steam turbine systems that may make plantation-based electric power generation a competitive option (Williams and Larson, 1993). Aeroderivative gas turbines are of special interest because of their high efficiencies at relatively modest scales (Fig. 1). Biomass conversion facility sizes are constrained by high transport costs arising from the low volumetric energy density of biomass (Larson, 1993).

Biomass Integrated Gasifier/Gas Turbine Technology

Biomass-integrated gasifier/gas turbine (BIG/GT) systems will be similar in some respects to coal integrated-gasifier/gas turbine systems, but biomass is more reactive than coal and so can attain very high gasification efficiencies with gasification temperatures lower than those required for coal (Larson, 1993).

---

[1] The HHV for wood (assuming a composition of $CH_{1.52}O_{0.68}$) is about 19.2 MJ per kg of dry matter. For this wood composition, the ratio of the LHV per unit dry mass to the HHV per unit dry mass is $[1.022 - (0.0346 \text{ mc} + 0.093)/(1 - \text{mc})]$ where mc is the moisture mass fraction in the wood. Wood delivered to a conversion facility typically has a moisture content of 50 percent. For such wood, the LHV is approximately 80 percent of the HHV.
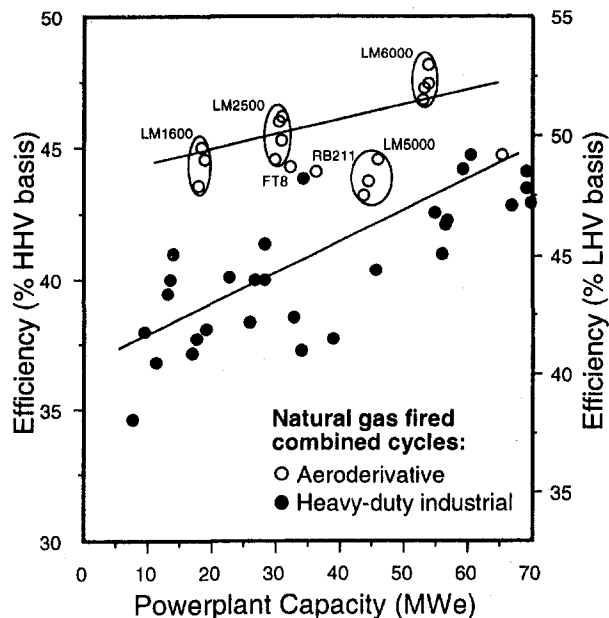
Fig. 1 Design-point efficiencies of natural gas-fired combined cycles based on aeroderivative and heavy-duty gas turbines. Each point is a combined-cycle package offered by an individual vendor (Anon, 1993). The lines highlight the trend of increasing efficiency with size within the capacity range shown, but do not represent curve fits of the points.

This permits a variety of alternative gasifier designs to be considered—all involving dry-ash removal—with the potential for reduced costs. Also, most biomass contains little or no sulfur, the removal of which at elevated temperature is a key obstacle to the commercialization of economically viable coal integrated-gasifier/gas turbine technology. Against these benefits for biomass are alkali and moisture contents that are higher than for coal, and physical characteristics that make feeding biomass into a gasifier more challenging.

The basic BIG/GT combined cycle (BIG/GTCC) concept involves sizing and drying of the feedstock, followed by gasification, gas cooling, gas cleanup, and gas combustion in a gas turbine. Steam is raised by heat recovery from several sources in the cycle for use in a steam bottoming cycle.

Biomass Gasifiers. Biomass gasifiers operate in one of two ways: with heat supplied directly (by partial oxidation of the feedstock) or indirectly (through a heat-exchange mechanism).

Direct heating is the basic principle applied in pressurized reactors for gasifying coal. Oxygen is used as the gasifying agent to achieve the high temperatures required for efficient coal gasification. The higher reactivity of biomass permits the use of air instead of oxygen. This is fortuitous because oxygen is relatively costly at the modest scales that will characterize BIG/GT systems. The most promising directly heated reactor designs for BIG/GT applications are fluidized beds (Fig. $2(a,b,c)$). A number of large ($>$ 30 MW biomass input) atmospheric-pressure, air-blown units are operating commercially today, most of which are supplying fuel gas to lime kilns at pulp mills (Larson, 1993). Pressurized designs are now the focus of pilot-scale demonstration efforts in several countries (see below).

A key feature of indirectly heated designs, which are not well suited to most coals because of low operating temperature (700–850°C), is that they can produce a gas undiluted by nitrogen, without the use of costly oxygen. To date, two reactor designs, both involving fluidized beds, have been tested at pilot scale and atmospheric pressure. To provide heat to gasify the biomass, one design utilizes an in-bed heat exchanger, while the other utilizes a circulation of hot sand (see Fig. $2(d)$ and discussion below).

Demonstration Efforts. Interest in BIG/GT technology is growing worldwide, and a number of commercially oriented development efforts are ongoing.

The first BIG/GT system ever built, a 6 MW_e plus 9 MW_{th} (20 MW biomass input) combined-cycle district-heating cogeneration facility in Varnamo, Sweden, began integrated operation in 1995. The project is a joint venture of Sydkraft, Sweden's largest privately owned and second largest electric utility, and A. Ahlstrom Corp., a Finnish boiler and gasifier manufacturer. The facility includes a pressurized circulating fluidized-bed gasifier (Fig. $2(b)$) and ceramic filters for gas cleanup at elevated temperature (Stahl et al., 1993). The joint-venture company, Bioflow, has now begun commercial marketing of the technology. Ahlstrom, with Sydkraft, is also building a 7 MW_{th} pressurized CFB gasification pilot plant to use for further development of the technology of biomass and coal gasification.

A commercial-scale demonstration of a BIG/GT combined cycle is planned for a site in Northeast Brazil, backed by a $30 million grant from the Global Environment Facility (Elliott and Booth, 1993). The project is being led by the Alternative Resources Division of the Hydroelectric Company of Sao Francisco (CHESF), the utility that serves Northeast Brazil. CHESF's interest stems in part from studies that have identified some 200 GW of potential BIG/GT capacity that could be supported from energy plantations that might be established in their service territory (Carpentieri et al., 1993). Other participants on the project team include CVRD (a large Brazilian mining and forestry company), Shell Brasil (an affiliate of the Shell International Petroleum Company), CIENTEC (a Brazil-

---

Nomenclature

$\dot{m}$ = mass flow, kg/s
mc = moisture content, kg H_2O/kg moist biomass
p = pressure, bar
P = power output, MW
T = temperature, °C
W = specific work, kJ/kg
β = gas turbine pressure ratio
Δp = pressure drop, Pa
ΔT = temperature difference, °C
η = efficiency

Subscripts

a = air
db = dried biomass

el = electric generator (or motor)
org = organic
p = polytropic
th = thermal

Acronyms

BCL = Battelle Columbus Laboratory
BIG = Biomass Integrated Gasifier
EJ = 10^{18} joules
GE = General Electric Company
GJ = 10^9 joules
GTCC = gas turbine combined cycle
HHV = higher heating value
HP = high pressure
HRSG = heat recovery steam generator

IGCC = integrated gasification combined cycle
IGT = Institute of Gas Technology
IGTCC = intercooled gas turbine combined cycle
LHV = lower heating value
LP = low pressure
Nm^3 = normal m^3 (0°C, 1 atm)
ppbw = parts per billion by weight
ppmw = parts per million by weight
TIT = turbine inlet temperature (first rotor inlet)
TOT = turbine outlet temperature
TPS = Termiska Processor Studsvik (Swedish company)

a) Pressurized, bubbling
fluidized-bed gasifier
(15-25 bar, 850-1000 C)

b) Pressurized, circulating
fluidized-bed gasifier
(20-30 bar, 900-1000 C)

c) Near-atmospheric pressure,
circulating fluidized-bed gasifier
and catalytic tar cracker (TPS design)
(1-2 bar, 900-950 C)

d) Near-atmospheric pressure,
indirectly-heated gasifer
(BCL design)
(1-2 bar, 850-900 C)
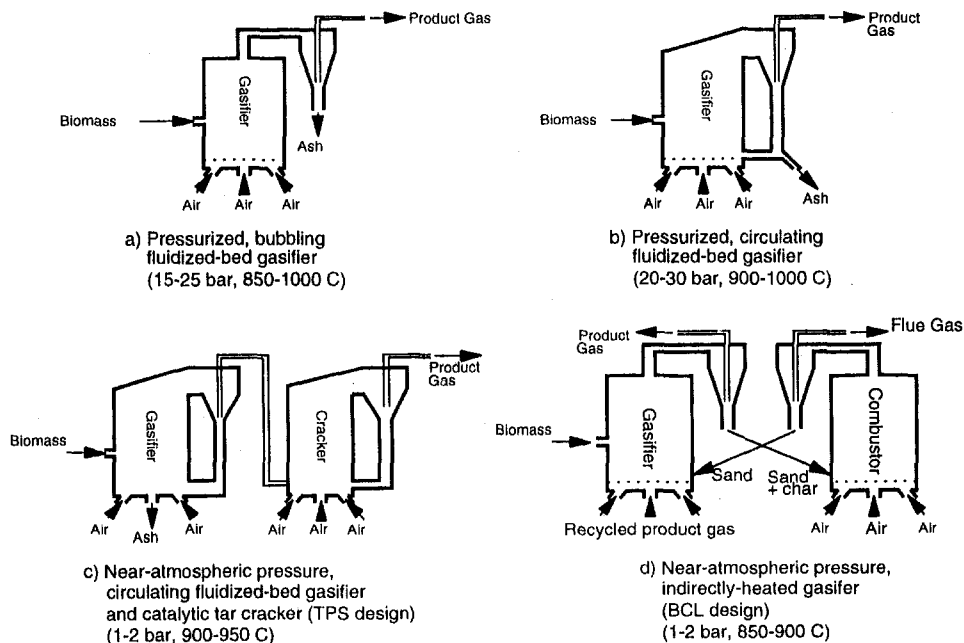
Fig. 2 Gasifier designs that are under development for BIG/GT plants, including (a) pressurized bubbling fluidized bed (IGT and Enviropower); (b) pressurized circulating fluidized bed (Bioflow); (c) atmospheric pressure, circulating fluidized bed with catalytic tar cracker (TPS); and (d) atmospheric pressure, indirectly heated gasifier (BCL)

ian gasification research and development institute), Eletrobras (the federal parent utility of CHESF), and the Brazilian Ministry of Science and Technology. Preliminary engineering and pre-erection hardware development on two competing designs will be completed in 1994, with construction slated to begin shortly thereafter. The competing designs are being developed by Bioflow—a scaled-up version of their Varnamo facility—and TPS, a Swedish gasifier development company that has proposed a design based on atmospheric-pressure circulating fluid-bed gasification, followed by a separate catalytic reactor for reforming the heavy hydrocarbon fraction of the gas leaving the gasifier (Fig. 2(c)) (Blackadder et al., 1994).

ENEL, the Italian electric utility, has been among the promoters of "Bio-Elettrica," a joint venture involving Lurgi (Germany), South Western Power (UK), and EdP (Portugal) that is planning the construction of a 12 MW$_e$ BIG/GT system based on an atmospheric, fluidized-bed, air-blown Lurgi gasifier. Some financial support is being provided from the Thermie Program of the European Community. The plant is based on two Ruston Typhoon turbines with combustors modified for low heating value fuel, and it will include cold gas cleanup and supplemental firing. Construction is scheduled for 1996/97, with startup in 1998/99 (Donatini, 1994).

In the United States, the Department of Energy and the Pacific International Center for High Technology Research are working to scale up the pressurized, bubbling fluidized-bed gasifier technology (Renugas) developed at the Institute of Gas Technology (IGT) (Fig. 2(a)). IGT has extensive pilot-scale operating experience with this technology (Lau et al., 1993). Testing recently began on a 100 tonne per day facility in Hawaii that will use bagasse, the residue of sugarcane milling, as the feedstock (Overend and Bain, 1993). The gasifier will be used to test hot gas cleanup systems developed by Westinghouse (Wiant et al., 1993). Coupling to a gas turbine of 3–5 MW$_e$ output is anticipated in 1997.

Another bubbling fluidized-bed gasifier technology, U-Gas, originally developed by IGT for coal, is under license to Enviropower Oy, a joint-venture company of Tampella,

a Finnish equipment supplier to the forest products industry, and Vattenfall, Sweden's largest electric utility. A pilot-scale U-gas system (rated capability of 10 MW coal input) has been undergoing testing at Tampella's research center in Tampere, Finland, since late 1991, and modifications were completed in late 1992 to permit operation on biomass (Bodlund et al., 1993). Nearly 1000 hours of testing with biomass were completed successfully in 1993, including tests with ceramic hot gas filters (Anon., 1994). Additional tests were done recently.

An indirectly heated gasifier being actively developed for gas turbine applications is the Battelle Columbus Laboratory (BCL) gasifier. The BCL design is an atmospheric-pressure twin, short-residence-time fluidized-bed, in which a combustor unit provides heat to a separate gasification unit via circulating sand (Fig. 2(d)). Residual char from the gasifier provides the fuel for the combustor. Product gas is recirculated as the fluidizing agent, along with some steam. The technology has been extensively evaluated at bench scale (500 kg/h capacity) (Feldman et al., 1988). A 200 kW$_e$ gas turbine was coupled to the bench scale unit for testing in early 1994 (Paisley, 1994), and construction started in 1995 in Vermont state on a demonstration 200 tonne per day BCL gasifier with eventual coupling planned to a gas turbine.

A second indirectly heated gasifier is being developed by Manufacturing and Technology Conversion International (MTCI) in the United States. The MTCI design involves an atmospheric-pressure, bubbling fluidized-bed heated by in-bed heat exchanger tubes. Pulse combustion of some of the product gas supplies heat to the heat exchanger, and steam or recirculated product gas is the fluidizing agent. A bench-scale MTCI gasifier has been tested extensively on a variety of fuels, including biomass (MTCI, 1990). The company's commercialization efforts are presently concentrated on applications at kraft pulp mills, where the feedstock would be black liquor, the lignin-rich byproduct of cellulose extraction (Larson, 1992). MTCI recently began testing a pilot-scale unit (2–3 tonnes per hour of black liquor) at a Weyerhaeuser pulp mill in North Carolina.

Finland's largest electric utility, Imatran Voima Oy (IVO) is developing a BIG/GT cycle designed specially for fuels with high moisture content, up to 70 percent (Hulkkonen et al., 1993, 1991). The innovative feature of this cycle, called IVOSDIG, is the use of direct, pressurized steam drying of the fuel, with some of the steam evolved from the biomass used for injection into the gas turbine. The use of the evolved steam increases power output and evidently contributes to a relatively high overall cycle efficiency. IVO is focusing its development effort on the dryer and associated feeding system, and plans to adopt a gasifier developed elsewhere. Based on 1000 hours of testing at pilot-scale (1 tonne per hour feed rate) at up to 27 bar pressure, the dryer concept appears to be quite promising. IVO is now seeking to carry out a larger-scale demonstration that would include a gas turbine and hot gas cleanup system.

Technological Issues. Aside from the choice of gasification technology, some of the key tradeoffs involved in designing and commercializing BIG/GT systems relate to pressurized versus atmospheric pressure gasification, hot versus cold gas cleanup, the adaptability of commercial gas turbines, and the integration between the dryer, the gas production equipment, and the turbomachinery.

Pressurized Versus Nonpressurized Gasification. Pressurized gasification is preferred to atmospheric pressure gasification because it avoids thermodynamic losses associated with compressing the fuel gas; these losses are typically higher than those associated with compressing the fluidizing agent. Offsetting this benefit would be operational challenges of feeding biomass to pressurized reactors, including losses of inert gas if lockhoppers are used (Miles and Miles, 1988). Ongoing development work promises substantial reductions in lockhopper losses with alternative feeding systems (Skog, 1993). Unlike atmospheric-pressure gasification, pressurized gasification requires successful large-scale demonstrations before the technology can be considered commercially ready. Given the success with pilot-scale pressurized gasifiers to date (Evans et al., 1988; Sinclair and Waldheim, 1985; Anon., 1994), major problems with demonstrating pressurized gasification are not anticipated.

The commercial-scale pressurized systems now being developed will operate with a pressure in the range 20 to 35 bar, which is sufficient to directly fuel existing small-to-medium power output aero-engines (with pressure ratio ranging from 18 to 22), but insufficient to feed large, latest-generation engines with pressure ratios around 30 or future advanced intercooled versions under study by all major manufacturers (Stambler, 1993; Cohn et al., 1993). Aside from mechanical integrity and energy balance considerations, a further increase of the gasification pressure requires an assessment of a number of technological issues, key among which are biomass feeding, bed fluidization characteristics and chemical kinetics, and the design impacts of higher heat release densities. To fuel advanced gas turbines with pressurized gasifiers currently being developed, an alternative approach would involve boosting the pressure of the syngas rather than (or in addition to) that of the fluidizing air.

Gas Cleaning. Gas turbine hardware considerations will impose constraints on the level of particulates, alkali metals, and condensible tars in the fuel gas delivered to the gas turbine combustor.[2] The levels that can be tolerated by a gas turbine are not well established because of a lack of operating experience.

Contaminant limits presently specified by gas turbine manufacturers, therefore, are probably conservative. Additional contaminants of concern from an emissions standpoint are nitrogen compounds, especially ammonia derived from nitrogen in the biomass feedstock.

Particulates, even in relatively small quantities, can cause turbine blade erosion. Lightweight aeroderivative turbines are especially susceptible. As a result, manufacturers specify stringent particulate limits. For example, General Electric (GE) specifications for its turbines (both heavy duty and aeroderivative varieties) require a total concentration below 1 ppmw at the turbine inlet, with 99 percent of the particles less than 10 μm diameter.[3] This corresponds to a particulate concentration in uncombusted low-heating-value gas of about 3–5 ppmw. Since particulate concentrations in raw gas from most fluidized bed gasifiers will be 5000 ppmw (Solantausta et al., 1990) to 10,000 ppmw (Brown et al., 1987) or higher, it is likely that very high efficiency filtration (ceramic or sintered-metal) and/or wet scrubbing of the raw gas will be required (Kurkela et al., 1993).

Alkali metals corrode turbine blades. Gas turbine manufacturers specify maximum allowable alkali concentrations of about 4 ppbw in the combustion products for aeroderivative gas turbines and 2 or 3 times this level for heavy duty gas turbines (Leonard, 1992). The 4 ppbw corresponds to about 20 ppbw in uncombusted low-heating-value gas. During biomass gasification, alkali metals such as sodium and potassium contained in the feedstock are vaporized and leave the gasifier with the product gas. At exit temperatures in excess of about 600°C, these metals will remain in the vapor phase and their concentrations will far exceed maximum concentrations tolerable to the gas turbines. For removal, the key step is cooling the gas in the presence of solids or liquids on which the condensed vapors can deposit and be removed from the gas stream. Cooling to 350°C to 400°C before particulate removal may be sufficient. Alternatively, wet scrubbing can be used, which would result in more significant cooling and provide essentially complete alkali removal.

Tars (condensible organic compounds) form during the gasification of biomass and account for 0.5 to 1.5 percent by mass of the product gas from a typical fluidized-bed gasifier, depending on temperature (Kurkela et al., 1993). If tars condense on cool surfaces, severe operating problems can result, including constricted piping or clogged valves and filters. Tars will often constitute an important enough energy component of the fuel gas that removing them from the gas would result in a loss of system efficiency. Two approaches are being taken for dealing with tars in BIG/GT systems. In the approach being pursued by Bioflow and Enviropower, dolomite in the fluid bed acts as both the bed material and tar-cracking catalyst. Dolomite leaving the gasifier is recycled back through a cyclone to the reactor. The product gas is then cooled to 350 to 400°C, enough to condense alkali vapors, but not enough to condense any but the heaviest tars the gas might contain. Thus, there appears to be a temperature window of 300 to 600°C within which problems with both condensed tars and vaporized alkalis might be avoided. A second approach involves the use of dolomite or some other catalyst in a separate reactor placed immediately after the gasifier (Blackadder et al., 1994; Paisley and Litt, 1993). Additional air is provided to the catalytic "cracker" to maintain an elevated temperature. The second reactor leads to the production of a gas with very low levels of tar, so that cold, wet scrubbing can be used with relatively little loss of chemical energy.

Nitrogen oxides (NO$_x$) can be produced in a gas turbine combustor from nitrogen in the combustion air (thermal NO$_x$)

---

[2] Two other potential contaminants are sulfur and chlorine. Neither of these is found in large quantities in most biomass feedstocks. Furthermore, sulfur is only problematic when it appears as an alkali sulfate. Thus, if the alkali metal content in the gas is lowered to satisfactory levels, sulfur is unlikely to cause problems. Another potential problem is the formation of acids from chlorine or sulfur, the condensation of which in the heat recovery steam generator could cause corrosion problems. If flue gases are used to dry biomass, however, the HRSG exhaust temperature will be high enough that this problem would not be encountered.

[3] The GE limits are 600 ppbw of particulates less than 10 μm diameter, 6 ppbw of particulates between 10 and 13 μm diameter, and 0.6 ppbw of particulates larger than 13 μm diameter (Leonard, 1992).

or from compounds produced during gasification from nitrogen in the feedstock (fuel-bound NO_x). Thermal NO_x is the dominant concern in the combustion of natural gas, because of the high flame temperature generated. Thermal NO_x formation with the combustion of low-heating-value gas is likely to be very low due to the lower flame temperatures (Kelsall et al., 1991). (This is especially true for gas from directly heated gasifiers.) Fuel-bound NO_x is potentially more problematic (Leppalahti, 1993), although for low-nitrogen biomass (like some tree species) fuel-bound NO_x may not be a problem except where NO_x emission standards are quite strict. Nitrogen typically leaves a fluidized-bed gasifier primarily as ammonia (NH_3), with an order of magnitude less leaving as hydrogen cyanide (HCN). Pressurization increases the NH_3 and decreases the HCN concentrations, and when dolomite is used for tar cracking, the HCN concentration is reduced significantly (Leppalahti et al., 1991). A wet scrubbing step following the gasifier can completely remove ammonia, thereby essentially eliminating fuel-bound NO_x. Alternatively, catalytic decomposition or selective oxidation of NH_3 at elevated temperature may be possible (Leppalahti, 1993). If fuel-bound NO_x is unacceptably high, an economically undesirable fall-back option is selective catalytic reduction technology applied to the stack gas.

The demonstration of gas cleanup will be a key element to the successful development of BIG/GT systems. Ceramic filter systems coupled to pressurized gasifiers have been tested at pilot scale by Enviropower, are presently being tested at the Varnamo facility in Sweden, and will be tested with the IGT pilot-plant gasifier in Hawaii. Wet scrubbing would entail some thermodynamic penalty and would require additional waste water treatment, but there is less uncertainty at present as to the cleaning effectiveness of such systems.

Suitability of Commercial Gas Turbines for Biomass-Derived Fuel. Three issues to consider in assessing the suitability of biomass-derived fuel gas for aeroderivative gas turbines are combustion stability, magnitude of pressure loss through the fuel injection system, and mass flow limits through the turbine.

Biomass-derived gases will have much lower energy contents per unit volume (5–6 MJ/Nm^3 for directly heated gasification and about 10 MJ/Nm^3 for indirectly heated gasification) than the natural gas or distillate fuel (35–40 MJ/Nm^3) for which most gas turbine combustors have been designed. With gasified biomass, combustors must accommodate larger volumetric flows of gas to achieve an equivalent energy release. The can-type combustors used in many industrial turbines generally provide adequate cross section and volume for complete and stable combustion with acceptable pressure drops. A number of different industrial gas turbines have operated successfully on the low-energy off-gas from blast furnaces for the last two to three decades. Between 1950 and 1980, Brown Boveri turbines logged in excess of 2.3 million hours operating on gas with a heating value of about 3 MJ/Nm^3 (Basler and Korosi, 1981). Since 1958, Mitsubishi has installed and operated a dozen or more gas turbines running on blast furnace gas with heating values ranging from 2.9 to 9.9 MJ/Nm^3 (Anon., 1991). Other successes with blast furnace gas have also been reported (Knapf and Stephens, 1958; Muyama et al., 1984; Kelsall et al., 1991; Becker and Schetter, 1993).

There has been no comparable commercial operating experience with low heating-value fuels in aeroderivative gas turbines, which utilize more compact combustors. However, pilot-scale experimental work suggests that combustion stability of such fuels would not be a problem with existing aeroderivative turbine combustors. Specifically, GE carried out successful combustion studies of low heating value gases using their LM500 and LM2500 gas turbine combustor designs (Bahr et al., 1985). The GE work indicated that a gas that might be derived from air-blown coal gasification—having a heating value as low as 3.7 MJ/Nm^3—could be burned successfully in these combustors,[4] providing there was some hydrogen in the gas.[5]

Air-blown biomass gasifiers are expected to produce gas with a heating value of 5 to 6 MJ/Nm^3 and a hydrogen content in the range of 10 to 20 percent by volume. Indirectly heated gasifiers would produce gas with about double this heating value. Thus, there may be little problem with combustibility of biomass-derived gas in aeroderivative turbine combustors. Recent testing at GE with simulated biomass-derived gas combustion in an LM2500 combustor further supports this conclusion (Neilson, 1994). Testing with other gas turbines would be important to confirm combustibility in each case.

A second issue with use of commercial gas turbines is the impact on overall cycle efficiency of the pressure loss associated with injecting the large fuel volume into the combustor through a nozzle originally designed for a fuel with much higher energy density. Pressure loss would be compounded when hot gas cleanup is used, due to the higher fuel gas temperature at the combustor inlet. With some existing turbines, no nozzle modifications may be required. In other cases, minor modifications would probably be sufficient. In the longer term, new turbines optimized for low heating value gas might include a complete nozzle/combustor re-design.

The third issue relates to the increase in mass flow through the turbine expander (relative to natural gas firing) caused by the larger fuel flow rate. Since essentially all turbines operate under choked flow conditions at the expander inlet, larger mass flows can be accommodated only by increasing the turbine inlet pressure or decreasing the temperature.[6] The latter would reduce efficiency. Higher turbine inlet pressure forces an increase in the compressor pressure ratio and moves the compressor toward its stall limit. For pressurized BIG/GT systems, the compressor outlet can be bled to provide fluidization air. Since the mass flow of air needed for the gasifier is approximately equal to the fuel flow, the mass flows through the turbine and through the compressor will differ by only a small amount, resulting in only a marginal increase in the pressure ratio, with little or minor compressor stall concerns. In atmospheric fluidized beds, where there is no need for high-pressure air, the issue is more critical. In most cases, the use of low-heating-value fuels will require some modification to the turbine. The issues here are equivalent to those posed by steam injection, and similar hardware modifications would be appropriate.[7]

As a final consideration, a brief comparison of some characteristics of aeroderivative and heavy-duty turbines may be useful. The former are preferable for their high efficiency at small scale (see Fig. 1) and typically wider stall margin. On the other hand, due to their more rugged construction, the latter can tolerate more significant deviations from design operation

---

[4] In the tests done by General Electric, gas heating values below 3.7 MJ/Nm^3 could not be tested due to limitations in the experimental arrangement.

[5] Hydrogen is desirable because it has a much higher flame propagation speed than CO or CH_4, the main other combustible components in biomass-derived gas. In the GE tests, stable combustion was achieved with a gas heating value of 3.7 MJ/Nm^3 and hydrogen content ranging from 8 to 26 percent by volume. Hydrogen contents lower than 8 percent were not investigated, except for one case with CO as the only combustible constituent in the gas. In this case, a gas heating value above 6.1 MJ/Nm^3 was required for stable combustion. As these results suggest, the higher the hydrogen content, the lower the minimum heating value required for successful combustion.

[6] Under choked conditions, the "reduced mass flow," $\dot{m}(RT_o)^{0.5}/p_o$, is essentially constant. T_o and p_o refer to total temperature and pressure at the turbine inlet, R is the gas constant, and $\dot{m}$ is the actual mass flow.

[7] Two modifications for avoiding compressor stall are modifying the geometry of the HP turbine (increasing blade height or nozzle discharge angle) and decreasing the compressor air flow by adjusting the inlet guide vanes. The former approach has been adopted by GE for the steam-injected version of the LM2500: An enlargement of the HP turbine nozzle area of the base LM2500 by approximately 3 percent allows the compressor of the modified engine with full steam injection to run at approximately the same operating point as the base engine without steam injection (Palmer and Erbes, 1993). However, for this LM2500, the amount of steam injected is only a fraction of that produced in the HRSG; full steam injection would require further enlargements of the HP turbine nozzle area.

(albeit with attendant efficiency reductions): larger mechanical and thermal stresses, higher particulate contents, slightly more corrosive combustion gases, etc.

Integration Between Gasifier and Power Plant. Several important opportunities arise for integrating the gasification and power islands in BIG/GT systems. (*i*) Syngas produced by the gasifier must be cooled to at least 300 to 400°C for particulate and alkali removal (see earlier discussion). This allows the production of a significant amount of HP steam for use in a bottoming steam cycle. (*ii*) Directly heated pressurized gasification requires a substantial amount of high-pressure air for bed fluidization. Besides efficiency considerations (gas turbine compressors are clearly more efficient than other industrial compressors), compressor stall can be avoided by bleeding fluidization air from the gas turbine (see discussion above). (*iii*) Medium-to-low temperature heat made available by the coolers placed along the path of the fluidization air or of the syngas can be utilized to preheat the water of the steam bottoming cycle. The recovery of such medium-low-temperature heat is particularly effective when the flue gases are used to dry the biomass, because the relatively high gas temperature at the HRSG exit (about 200°C) creates a need for low temperature heat to preheat liquid water. (*iv*) Biomass drying can be accomplished by using flue gases exiting the HRSG.

In summary, although integration with BIG/GT systems is somewhat different from that of coal-fired IGCCs (the gasifier requires no steam, there is no desulfurization or oxygen production system, and there is extensive fuel drying), proper dryer/gasifier/gas-turbine/steam-cycle integration is key to achieving top overall efficiencies.

Performance Modeling and Assumptions

The performance of BIG/GT combined cycles is modeled here based on three different gasifier designs that have been proposed for commercial-scale BIG/GT power plants: pressurized circulating fluidized bed, near-atmospheric pressure circulating fluidized bed with separate tar cracker, and near-atmospheric pressure indirectly heated twin fluidized bed (Fig. 2(*b*, *c*, *d*).

Table 1 Characteristics of biomass fuel assumed for the calculations presented in the paper. Moisture and composition are expressed as percent mass fractions. The right column reports the mass fractions of the corresponding "equivalent fuel" with the same heating value, same ash and moisture content, and same ultimate composition.

Feed wood		Equivalent fuel	
Moisture	50.0	CH₄	6.950
LHV, MJ/kg	8.11	CO	10.78
HHV, MJ/kg	10.0	CO₂	19.72
		C₂H₂	0.016
Dried wood		C₂H₄	3.157
Moisture	15.0	C₂H₆	2.229
LHV, MJ/kg	15.50	C₃H₈	0.042
HHV, MJ/kg	17.00	H₂	0.344
		H₂S	0.006
Bone dry wood		NH₃	0.317
C	49.98	N₂	0.016
H	6.12	O₂	0.721
O	42.49	SO₂	0.048
N	0.55	C (solid)	5.250
S	0.06	ash	0.800
Ash	0.80	liquid water	50.00
LHV, MJ/kg	18.66	LHV, MJ/kg	8.11
HHV, MJ/kg	20.00	HHV, MJ/kg	10.0

Table 2 Syngas composition assumed for the systems based on directly heated gasifiers and ranges indicated by gasifier developers (percent by volume). For the pressurized gasifier, the gas composition specified by the gasifier developer (Bioflow) is that found after the hot gas filter. For the atmospheric gasifier, the difference between raw gas and clean gas compositions is due to moisture elimination in the scrubber.

Com-ponent	Pressurized gasifier		Atmospheric gasifier		
	This paper	Bioflow	This paper		TPS
	raw gas (=clean gas)	clean gas	raw gas	clean gas	clean gas
Ar	0.48	–	0.5	0.5	–
CO	16.1	14-18	19.8	21.7	21
CO₂	11.8	10-14	10.4	11.4	11
CH₄	5.3	4-6	2.6	2.9	3
C₂Hₓ	0.12	0.06-0.3	0.9	1.0	1
H₂	10.2	8-12	14.8	16.3	17
H₂O	12.2	9-15	11.6	3.2	3
N₂	43.4	43-47	39.1	43	44
LHV, MJ/Nm³	5.13	4.8-5.2		6.15	6.0

Computation Model. The results of performance modeling that are presented in Part B of this paper were obtained using an enhanced version of a calculation model originally developed to predict the performance of complex gas–steam cycles (Consonni, 1992). The system of interest is defined as an ensemble of components, which can be of twelve basic types: pump, compressor, combustor, gas turbine expander, heat exchanger, mixer, splitter, steam cycle (includes HRSG, steam turbine, pump, and all auxiliaries), oxygen separation plant, shaft (accounts for turbomachine spool interconnections and electric losses), saturator, and "chemical converter." By specifying chemical equilibrium at the outlet of the mixer and heat exchanger elements, these can be used to simulate chemical reactors. Operating characteristics and mass and energy balances of each component are calculated sequentially and iteratively until the conditions (pressure, temperature, mass flow, etc.) at all interconnections converge to a stable value. The basic model is extensively described elsewhere (Consonni et al., 1991; Lozza, 1990; Lozza et al., 1993; Chiesa et al., 1993, 1994). Only two enhancements that were introduced to facilitate modeling of BIG/GT systems are discussed here.

One enhancement relates to the flow splitter, which splits a flow of given composition into two streams. This component was used to simulate the separation of (*i*) condensate from vapor, (*ii*) ash from unconverted carbon leaving the gasifier and in the filter, and (*iii*) for the BCL gasifier, char from product gas at the gasifier outlet (see Fig. 2(*d*)).

The chemical converter was used in mass and energy balance calculations of the gasifier. The chemical converter element permits the thermal balance of a reactor to be calculated for a specified inlet composition and for which enough information is provided to calculate the outlet composition (which need not be at equilibrium). The outlet composition can be defined either explicitly, by assigning molar concentrations of the outlet flow, or implicitly, by identifying which chemical species are present at the outlet and specifying the molar ratios between some of them. In the former case, the calculation simply verifies by atom balances that the inlet and outlet flows are consistent; in the latter case, the program solves a set of linear equations arising from imposing the condition that each atomic species is con-

Table 3 Comparison between reported gas compositions for the system based on the BCL gasifier (Breault and Morgan, 1992) and those assumed (raw gas) and calculated (clean gas and combustor effluent) for the configuration reported in Fig. 3 of Part B. Since the composition of the combustor effluent is determined by imposing the same air fuel ratio assumed by Breault and Morgan, the discrepancy in the oxygen content has no apparent justification. In any case, its influence on overall plant performance is negligible.

Compo-nent	Raw syngas		Clean syngas		Combustor effluent	
	B.& M. (1992)	this paper	B.& M. (1992)	this paper	B.& M. (1992)	this paper
Ar	–	–	–	–	–	0.9
CO	36.2	35.5	45.3	45.0	–	–
CO_2	8.7	8.5	10.9	10.8	14.1	12.9
CH_4	12.3	12.0	15.3	15.3	–	–
C_2H_4	4.1	4.0	5.1	5.1	–	–
C_2H_6	0.54	0.9	0.67	1.1	–	–
H_2	16.0	15.9	20.4	20.2	-	-
H_2O	21.6	21.2	1.84	1.6	8.2	7.6
N_2	0.41	0.7	0.52	0.9	75.9	74.5
O_2	–	–	–	–	1.81	4.1
Tar g/kg_{gas}	4.12	–	–	–	–	–

served from inlet to outlet. Once the outlet composition has been calculated (or verified), the thermal balance around the reactor is calculated by imposing either the heat losses or the outlet temperature.

One other model enhancement relates to the thermodynamic properties assumed for biomass. The properties of gaseous species, which are all chemically well defined, are based on JANAF data (Stull and Prophet, 1971; Gardiner, 1984), while for water the SI tables are used (Schmidt, 1982). Biomass has no pure chemical characterization. However, the thermal balance calculations of interest here require only a correct estimate of the biomass heating value, the ash and moisture content, and the atomic ratios H/C, O/C, N/C, and S/C. Thus, biomass can be effectively simulated as a mixture of pure chemical species—hereafter called the "equivalent fuel"—exhibiting the same heating value, the same ash and moisture content, and the same atomic ratios (Consonni, 1987). The equivalent fuel for biomass is determined by means of a numerical optimization procedure. Table 1 reports the results of this optimization for a dry biomass composition of $CH_{1.46}O_{0.64}$, a composition representative of dry wood chips. The results in Table 1 are adopted for all model calculations here.

Assumptions. Since the aim of the analysis here is to assess the performance potential of BIG/GT plants, the modeling has been done rather accurately for the components that are crucial to the energy and mass balances (the gasifier, the gas turbine, the steam cycle, the heat exchanger network), but rather simplistically for the components that, despite their technological relevance, have little impact on the plant mass and energy flows (e.g., the hot gas filter).

Syngas Composition at Gasifier Exit. The gasifier energy, mass, and atomic species balances are performed using the chemical converter described above, thus avoiding the need to model the complex chemical kinetic and transport phenomena occurring in the gasifier. Chemical equilibrium can be assumed

at the gasifier exit with entrained-bed coal gasification, but because biomass gasification temperatures are substantially lower than with coal, significant departures from equilibrium are found in the product gas composition. Since gasifier modeling is far beyond the scope of this paper, biomass syngas compositions (Tables 2 and 3) are assumed here based on empirical data provided by the gasifiers' developers.

Gas Turbines. Three "reference" gas turbines are considered in the modeling here: (i) an existing GE LM2500, with only minor modifications needed to operate with low-energy

Table 4 Assumptions adopted for calculations in this paper

Auxiliary power consumption
Fuel handling and drying: 20 kJ/kg_b
Lockhoppers: 10 kJ/kg_{db} for nearly-atmospheric gasification, 80 kJ/kg_{db} for gasification at 30 bar, 110 kJ/kg_{db} for gasification at 48 bar
Inert gas production: 300 kJ per kg of inert gas

Dryer
Biomass dried from 50% to 15% mc and exits at 70°C

Gasifier
Heat loss, as a fraction of biomass HHV: 0.6% (pressurized), 1% (nearly-atmospheric, directly-heated), 2% (nearly-atmospheric, indirectly heated)
Δp: 6% (pressurized), 0.2 bar (nearly-atmospheric)

Gas turbine compressor
Maximum η_p 90%, η_{org}=0.997, inlet Δp (filter)=1 kPa, leakage (at HP exit)=0.8% of inlet $\dot{m}$

Other compressors
η_p=0.80, $\eta_{org}\eta_{el}$=0.90, no leakage

Gas turbine combustor
Δp/p 3%, heat losses 0.4% of fuel LHV input. Syngas pressure at fuel valve 40% higher than air pressure

Gas turbine expander
Maximum η_p 89% (cooled stages) and 92.5% (uncooled stages). Blade temperature 830°C (nozzle) and 800°C (turbine). Film and convection cooling parameters (for definitions see Consonni et al. [1991]): r_{fc}=0.20, Z=36 for LM2500; r_{fc}=0.25, Z=100 for other engines. All other parameters as in Macchi et al. [1994]

Heat exchangers
Δp/p 2%, minimum ΔT 15°C (gas-liquid) or 30°C (gas-gas). If T>300°C, heat losses 2% of heat transferred

HRSG and steam cycle
Approach ΔT=25°C, pinch point ΔT=10°C. Heat losses 0.7% of heat released by gas. Steam turbine expansion calculated according to Lozza (1990). Pressure drops: gas-side 3 kPa, superheaters 10%, economizers 25%. Steam pressures and temperatures (unless otherwise indicated): evaporator 67 bar (283°C), deaerator 1.43 bar (110°C), condenser 0.056 bar (35°C), superheater outlet 450°C

Others
Ambient air: T=15°C, P=101325 Pa, humidity 60%
Ambient water: T=15°C, P=101325 Pa
Minimum stack temperature=93°C
Filters and scrubbers Δp/p=3% (at scrubber exit gas is always saturated)
Pumps η=65% (includes electric and organic losses)
η_{el} varies with power as in Consonni and Macchi [1988]

Table 5 Performances predicted for the "reference" simple cycle engines (ISO conditions, no inlet/outlet pressure losses) used as a basis for the calculation of BIG/GT systems.

Engine	GE LM2500	25 MW class	GE LM1600
TIT, C	1232	1200	1210
β	18.8	20	22
$\dot{m}_a$, kg/s	68.8	77.9	45.0
η, %	35.9	37.0	36.5
W, kJ/kg$_a$	321.0	321.0	305.4
P, MW$_e$	22.04	25.0	13.74
TOT, C	519	496	483

content fuel; (ii) a generic "25-MW$_e$ class" engine, optimized for biomass gas, representing medium power output, multispool aeroderivative turbines like those offered by all three major manufacturers (TurboPower, Cooper/Rolls, and General Electric); the cooling technology and the turbomachinery of these engines are assumed to be state of the art, i.e., somewhat better than those of presently operating LM2500 machines; (iii) the GE LM1600 (also optimized for biomass-derived gas), representing smaller power output, high-performance aeroengines with the same technological sophistication as the 25 MW$_e$ class engines.[8]

Assuming natural gas fuel and the parameters listed in Table 4, the calculation model produces the simple cycle gas turbine design-point performances reported in Table 5. The performances of the LM2500 and LM1600 agree quite well with published values (Anon., 1993). For the LM2500 there is also excellent agreement with a recent study by Palmer and Erbes (1993).

Other Assumptions. Table 4 provides all key assumptions adopted for all major components of the BIG/GT cycles for the mass and energy balance calculations presented here. Additional key assumptions are:

(i) The biomass dryer is modeled as a noncontact heat exchanger: Flue gases from the HRSG provide the heat required to heat the biomass and evaporate its moisture. The water vapor produced in this process is later mixed with the flue gases before the stack. The assumed raw feedstock moisture content is 50 percent.[9] Measures would need to be taken in practice to minimize the risk of spontaneous combustion in such a dryer.

(ii) Electricity required for fuel handling and lockhopper compression are specified as inputs that are proportional to the amount of biomass handled.

(iii) The gasifier is modeled as a "chemical converter" of biomass (equivalent fuel) and air, which are transformed into syngas with specified molar ratios (CO/CO_2, H_2/H_2O, CH_4/H_2, etc.) based on empirical data. The presence of dolomite in gasifiers is neglected for the purpose of thermal balance calculations.

(iv) The alkali content of the syngas exiting the gasifier is neglected, and tar content is implicitly accounted for by assuming that all carbon (except for unconverted carbon discharged

with the ash) and hydrogen in the biomass feedstock appears in the syngas.

(v) The filter for particulate removal is represented by a flow splitter whereby all solids contained in the stream exiting the syngas cooler (ash and unconverted carbon) are separated from the gas phase and discharged to ambient.

(vi) Besides the data reported in Table 4, all other inputs required by the gas and steam turbine models have been set to values representative of state-of-the-art technology; the actual correspondence between the predictions produced with such input data and the performances of modern combined cycle systems has been successfully verified in a number of previous works: Lozza (1990), Consonni et al. (1991), Consonni (1992), Macchi et al. (1994).

Summary

Part A of this two-part paper has discussed the technology of biomass-gasifier/gas turbine power generation, reviewed ongoing efforts to develop, demonstrate, and commercialize the technology, highlighted key technological issues impacting the performance and cost of BIG/GT systems, and outlined a computational model used to predict the performance of alternative BIG/GT cycle configurations. Part B of this paper gives results of the performance calculations and preliminary economic assessments.

Acknowledgments

References

Anon., 1991, "Technical Information of Mitsubishi Low BTU Gas Firing Gas Turbines," informational literature, Mitsubishi Heavy Industries, Ltd., Tokyo, Sept.

Anon., 1993, "Performance Specs," *Gas Turbine World,* Vol. 13, July, pp. 24–30.

Anon., 1994, "Biomass Looks Good for Gasification Process," *Modern Power Systems,* Apr., pp. 61–65.

Bahr, D. W., Sabla, P. E., and Vinson, J. W., 1985, "Small Industrial Gas Turbine Combustor Performance With Low BTU Gas Fuel," ASME Paper No. 85-IGT-125.

Basler, B., and Korosi, A., 1981, "Combustion of Fuels With Low Hydrogen Content in BBC Gas Turbines," publication No. CH-T 113 423 E, Brown Boveri Company, Baden, Switzerland.

Becker, B., and Schetter, B., 1993, "Use of LHV Gas in a Gas Turbine," *Bioresource Tech.,* Vol. 46, pp. 55–64.

Blackadder, W. H., Lundberg, H., Rensfelt, E., and Waldheim, L., 1994, "Heat and Power Production Via Gasification in the Range 5–50 MW$_e$," *Advances in Thermochemical Biomass Conversion,* by A. V. Bridgwater, ed., Blackie Academic & Professional, London, pp. 449–75.

Bodlund, B., Bergman, J., and Lindman, N., 1993, "Power From Biomass in Sweden," *Proceedings: Strategic Benefits of Biomass and Waste Fuels,* Electric Power Research Institute, Palo Alto, CA.

Breault, R., and Morgan, D., 1992, "Design and Economics of Electricity Production From an Indirectly-Heated Biomass Gasifier," for Battelle Memorial Institute (Columbus, OH) by Tecogen, Inc., Waltham, MA, Oct. 22.

Brown, M. G., Baker, E. G., and Mudge, L. K., 1987, "Evaluation of Processes for Removal of Particulates, Tars, and Oils From Biomass Gasifier Product Gases," *Energy From Biomass and Wastes X,* Institute of Gas Technology, Chicago, pp. 655–77.

Carpentieri, A. E., Larson, E. D., and Woods, J., 1993, "Future Biomass-Based Power Generation in Northeast Brazil," *Biomass and Bioenergy,* Vol. 4(3), pp. 149–73.

Chiesa, P., Consonni, S., Lozza, G., and Macchi, E., 1993, "Predicting the Ultimate Performance of Advanced Power Cycles Based on Very High Temperature Gas Turbine Engines," ASME Paper No. 93-GT-223.

Chiesa, P., Lozza, G., Consonni, S., and Macchi, E., 1994, "An Assessment of the Thermodynamic Performance of Mixed Gas-Steam Cycles. Part B: Water-Injected and HAT Cycles," ASME Paper No. 94-GT-424; ASME JOURNAL OF ENGINEERING FOR GAS TURBINES AND POWER, Vol. 117, 1995, pp. 499–508.

---

[8] The LM1600 has been selected because it is the only aeroderivative now commercially available for electric power generation in this size class.

[9] A moisture content of 50 percent is typical for freshly cut wood. In many tropical and subtropical regions of the world, it may be feasible to field-dry logs to 35 percent before transporting them to the power plant for chipping, drying to 15 percent mc, and gasification. Overall plant efficiency might increase substantially. Using 35 percent mc feedstock instead of 50 percent mc would reduce the amount water to be evaporated in the dryer from 0.824 tonnes per tonne of dry biomass to 0.362 tonnes, or a 56 percent reduction in drying duty.

Cohn, A., Hay, G. A., and Hollenbacher, R. H., 1993, "The Collaborative Advanced Gas Turbine Program—a Phase I Project Status Report," *Proc. 12th EPRI Gasification Conference,* San Francisco, Oct. 27–29.

Consonni, S., 1987, "A Computer Program to Calculate Working Fluid Thermodynamic Properties of Steam-Injected Gas Turbine Cycles," CEES/Princeton Univ. working paper 87.

Consonni, S., 1992, "Performance Prediction of Gas/Steam Cycles for Power Generation," Ph.D. Thesis No. 1893-T, Mechanical and Aerospace Engineering Dept., Princeton Univ., Princeton, NJ.

Consonni, S., and Macchi, E., 1988, "Gas Turbine Cycles Performance Evaluation," *Proc. 2nd ASME Cogen-Turbo,* Montreaux, Switzerland, pp. 67–77.

Consonni, S., Lozza, G., Macchi, E., Chiesa, P., and Bombarda, P., 1991, "Gas-Turbine-Based Advanced Cycles for Power Generation. Part A: Calculation Model." *Proc. 1991 Yokohama International Gas Turbine Congress,* Gas Turbine Society of Japan, Tokyo, pp. III-201-210.

Donatini, F., 1994, ENEL CRTN, Pisa, Italy, personal communication.

EIA (Energy Information Admin.), 1993, *Annual Energy Review 1992,* DOE/EIA-0384(92), US Dept. of Energy, Washington, DC, June.

Elliott, T. P., and Booth, R., 1993, *Brazilian Biomass Power Demonstration Project,* Special Project Brief, Shell International Petroleum Company, London, Sept.

Evans, R. J., Knight, R. A., Onischak, M., and Babu, S. P., 1988, *Development of Biomass Gasification to Produce Substitute Fuels,* PNL-6518, Battelle Pacific Northwest Lab, Richland, WA.

Feldmann, H. F., Paisley, M. A., Appelbaum, H. R., and Taylor, D. R., 1988, *Conversion of Forest Residues to a Methane-Rich Gas in a High-Throughput Gasifier,* PNL-6570, Pacific Northwest Laboratory, Richland, WA.

Gardiner, W. C., ed., 1984, *Combustion Chemistry,* Springer-Verlag, New York.

Grainger, A., 1988, "Estimating Areas of Degraded Tropical Lands Requiring Replenishment of Forest Cover," *International Tree Crops Journal,* Vol. 5, pp. 31–61.

Hall, D. O., Rosillo-Calle, F., Williams, R. H., and Woods, J., 1993, "Biomass for Energy: Supply Prospects," in: *Renewable Energy: Sources for Fuels and Electricity,* T. B. Johansson, H. Kelly, A. K. N. Reddy, and R. H. Williams, eds., Island Press, Washington, DC, pp. 593–651.

Hulkkonen, S., Raiko, M., and Aijala, M., 1991, "New Power Plant Concept for Moist Fuels, IVOSDIG," ASME Paper No. 91-GT-293.

Hulkkonen, S., Aijala, M., and Raiko, M., 1993, "Development of an Advanced Gasification Process for Moist Fuels," *Proceedings of the 12th Coal Gasification Conference,* Electric Power Res. Inst., Palo Alto, CA.

Kelsall, G. J., Smith, M. A., Todd, H., and Burrows, M. J., 1991, "Combustion of LCV Coal Derived Fuel Gas for High Temperature, Low Emissions Gas Turbines in the British Coal Topping Cycle," ASME Paper No. 91-GT-384.

Knapf, G. H., and Stephens, J. O., 1958, "Gas Turbines for Blast Furnace Blowing," ASME Paper No. 58-GTP-14.

Kurkela, E., Stahlberg, P., Laatikainen, J., and Simell, P., 1993, "Development of Simplified IGCC Processes for Biofuels: Supporting Gasification Research at VTT," *Bioresource Technology,* Vol. 46, pp. 37–47.

Larson, E. D., 1992, "Biomass-Gasifier/Gas Turbine Cogeneration in the Pulp and Paper Industry," ASME JOURNAL OF ENGINEERING FOR GAS TURBINES AND POWER, Vol. 114, pp. 665–75.

Larson, E. D., 1993, "Technology for Electricity and Fuels From Biomass," *Annual Review of Energy and the Environment,* Vol. 18, pp. 567–630.

Lau, F. S., Carty, R. H., Onischak, M., and Bain, R. L., 1993, "Development of the IGT Renugas Process," *Proceedings: Strategic Benefits of Biomass and Waste Fuels,* Electric Power Research Institute, Palo Alto, CA.

Leonard, G., 1992, General Electric Company, Marine and Industrial Engines Division, Evendale, OH, personal communication.

Leppalahti, J., 1993, "Formation and Behavior of Nitrogen Compounds in an IGCC Process," *Bioresources Technol.,* Vol. 46, pp. 65–70.

Leppalahti, J., Simell, P., and Kurkela, E., 1991, "Catalytic Conversion of Nitrogen Compounds in Gasification Gas," *Fuel Processing Technology,* Vol. 29, pp. 43–56.

Lozza, G., Chiesa, P., and Consonni, S., 1993, "Modelization of Integrated Coal Gasification Combined Cycles" [in Italian]. *Proc. VII Meeting on Combined Cycles: Technical and Economic Outlook* (Milan, Oct. 1993), pp. 287–312, Pitagora publisher, Bologna, Italy.

Lozza, G., 1990, "Bottoming Steam Cycles for Combined Gas-Steam Power Plants: a Theoretical Estimation of Steam Turbine Performance and Cycle Analysis," *Proc. 1990 ASME Cogen-Turbo,* New Orleans, LA, pp. 83–92.

Macchi, E., Consonni, S., Lozza, G., and Chiesa, P., 1994, "An Assessment of the Thermodynamic Performance of Mixed Gas-Steam Cycles, Part A: Intercooled and Steam-Injected Cycles," ASME Paper No. 94-GT-423; ASME JOURNAL OF ENGINEERING FOR GAS TURBINES AND POWER, Vol. 117, 1995, pp. 489–498.

Miles, T. R., and Miles, T. R., Jr., 1988, "Reliable Feed Systems for Thermochemical Conversion," *Research in Thermochemical Biomass Conversion,* Elsevier Applied Science, London, pp. 1156–69.

MTCI (Manufacturing and Technology Conversion International, Inc.), 1990, *Testing of an Advanced Thermochemical Conversion Reactor System,* Battelle Pacific Northwest Lab., Richland, WA.

Muyama, A., Hiura, H., and Morimoto, K., 1984, "Repowering in Steel Works by Introducing a Blast-Furnace Gas-Firing Gas Turbine," ASME JOURNAL OF ENGINEERING FOR GAS TURBINES AND POWER, Vol. 106, pp. 806–811.

Netherlands Scientific Council for Government Policy, 1992, *Grounds for Choice: Four Perspectives for the Rural Areas in the European Community,* The Hague, The Netherlands.

Neilsen, C., 1994, Marine and Industrial Engines Division, General Electric, Cincinnati, Ohio, personal communication, May.

Overend, R. P., and Bain, R. L., 1993, "The DOE/NREL National Biomass Power Program Gasification Project Updates," *Proceedings of the 12th Coal Gasification Conference,* Electric Power Res. Inst., Palo Alto, CA.

Paisley, M. A., and Litt, R. D., 1993, "Hot-Gas Conditioning of Biomass Derived Synthesis Gas," *Proceedings, First Biomass Conference of the Americas,* NREL/CP-200-5768, National Renewable Energy Laboratory, Golden, CO, pp. 1133–47.

Paisley, M., 1994, Battelle Columbus Laboratory, personal communication, Columbus, Ohio, Jan.

Palmer, C. A., and Erbes, M. R., 1993, "LM2500 Fired on Low Btu Fuels," Final report prepared by Enter Software for the Technical Research Center of Finland (Epsoo, Finland), Jan. 28th.

Schmidt, E., 1982, *Properties of Water and Steam in SI Units,* Springer-Verlag, Berlin.

Shell International Petroleum Company, 1992, "Biofuels in the European Community," Management Brief, Shell Center, London, May.

Sinclair, A., and Waldheim, L., 1985, "MINO Feasibility Study, Concluding Report," Studsvik Energiteknik AB, Nykoping, Sweden.

Skog, E., Project Mgr., 1993, Varnamo Demonstration Program, Sydkraft Konsult, personal communication, Malmo, Sweden, Dec.

Solantausta, Y., Kurkela, E., Leppalahti, J., and Sipila, K., 1990, "Combined-Cycle Power Production From Biomass," presented at the CEC Workshop on Large Scale Electricity Production From Biomass, Florence, Italy, Nov. 22.

Solar Thermal and Biomass Power Division, 1992, "Electricity From Biomass: A Development Strategy," Office of Solar Energy Conversion, US Department of Energy, DOE/CH10093-152, Washington, DC, Apr.

Stahl, K., Skog, E., and Lundqvist, R., 1993, "The Biomass IGCC Demonstration Power Plant, Varnamo, Sweden," *Proceedings of the 12th Coal Gasification Conference,* Electric Power Res. Inst., Palo Alto, CA.

Stambler, I., 1993, "Next Generation 'Superfans' Could Plug Electric Utility Capacity Gaps," *Gas Turbine World,* May–June, pp. 46–54.

Stull, D. R., and Prophet, H., Project Directors, 1971, *JANAF Thermochemical Tables,* 2nd ed., U.S. National Bureau of Standards, Washington D.C.

USDA (US Dept. Agriculture, Soil Conservation Service), 1989, "The 2nd RCA Appraisal: Soil, Water, and Related Resources on Non-Federal Land in the United States—Analysis of Condition and Trends, Washington DC.

Wiant, B. C., Bachovchin, D. M., Carty, R. M., Horazak, D. A., and Ruel, R. H., 1993, "Biomass Gasification Hot Gas Cleanup for Power Generation," *Proceedings of the First Biomass Conference of the Americas,* NREL/CP-200-5768, National Renewable Energy Laboratory, Golden, CO, pp. 571–82.

Williams, R. H., 1994, "Roles for Biomass Energy in Sustainable Development," *Industrial Ecology and Global Change,* R. H. Socolow et al., eds., Cambridge University Press, Cambridge, United Kingdom.

Williams, R. H., and Larson, E. D., 1993, "Advanced Gasification-Based Biomass Power Generation," in: *Renewable Energy: Sources for Fuels and Electricity,* T. B. Johansson, H. Kelly, A. K. N. Reddy, and R. H. Williams, eds., Island Press, Washington, DC, pp. 729–85.

Biomass-Gasifier/Aeroderivative Gas Turbine Combined Cycles: Part B—Performance Calculations and Economic Assessment

S. Consonni

Dipartimento di Energetica,
Politecnico di Milano,
Milan, Italy

E. D. Larson

Center for Energy and
Environmental Studies,
School of Engineering and Applied Science,
Princeton University,
Princeton, NJ 08544

Gas turbines fueled by integrated biomass gasifiers are a promising option for base-load electricity generation from a renewable resource. Aeroderivative turbines, which are characterized by high efficiencies in small units, are of special interest because transportation costs for biomass constrain conversion facilities to relatively modest scales. Part A of this two-part paper reviewed commercial development activities and major technological issues associated with biomass integrated-gasifier/gas turbine (BIG/GT) combined cycle power generation. Based on the computational model also described in Part A, this paper (Part B) presents results of detailed design-point performance calculations for several BIG/GT combined cycle configurations. Emphasis is given to systems now being proposed for commercial installation in the 25–30 MW$_e$ power output range. Three different gasifier designs are considered: air-blown, pressurized fluidized-bed gasification; air-blown, near-atmospheric pressure fluidized-bed gasification; and near-atmospheric pressure, indirectly heated fluidized-bed gasification. Advanced combined cycle configurations (including with intercooling) with outputs from 22 to 75 MW are also explored. An economic assessment is also presented, based on preliminary capital cost estimates for BIG/GT combined cycles and expected biomass costs in several regions of the world.

First Generation BIG/GTCC Technology

Two cycle configurations that might be considered first-generation aeroderivative-based biomass integrated-gasifier/gas turbine (BIG/GT) technology have been proposed for commercial demonstration in Brazil and a third is under consideration for demonstration in the US. The three different gasifiers associated with these configurations are incorporated into performance models here. The gas turbine assumed in each case is General Electric's LM2500, which is currently under testing (with only minor modifications) by General Electric for eventual use in the Brazilian demonstration project (see Part A of this paper), and for which others' performance estimates are available for comparison.

One configuration utilizes a pressurized, air-blown gasifier, with gasification air being extracted from the gas turbine compressor and passed through a boost compressor before being used in the gasifier. The hot gasifier product gas is used to raise steam before passing through ceramic filters at elevated temperature and on to the gas turbine combined cycle. This configuration is similar in many respects to configurations of simplified (air-blown) integrated gasifier/gas turbine combined cycles using coal (Corman, 1986). The configuration for biomass assumed here resembles the one proposed by Bioflow for the Brazilian demonstration project (Elliott and Booth, 1993). Input assumptions are based on the characteristics of the proposed Bioflow system.

A second BIG/GT configuration utilizes near-atmospheric pressure air-blown gasification[1] using ambient air for gasification. The hot gasifier product gas is used to raise steam and is then cooled to near ambient temperature in a wet scrubber before being compressed for delivery to the gas turbine. This configuration resembles the one proposed by TPS for the Brazilian demonstration project (Elliott and Booth, 1993). Input assumptions are based on characteristics of the proposed TPS system.

The third BIG/GT configuration is similar to the second, except that the gasifier is a near-atmospheric, indirectly heated unit. Input assumptions used to model this configuration are based on characteristics of proposed BIG/GT systems that would use the Battelle Columbus Laboratory gasifier (Paisley, 1994).

General Considerations. Each gasifier has been modeled as a "chemical converter," imposing the raw syngas composition that produces the clean gas compositions indicated by developers (see Tables 2 and 3 in Part A); given these outlet compositions and the inlet conditions, outlet temperatures are calculated from energy balances, after accounting for heat losses that are assumed to be a fraction of the higher heating value of the input biomass: 0.6 percent with pressurized gasification, 1 percent for the atmospheric-pres-

---

[1] Low-pressure gasification has not received much attention for coal-IGCC systems, because at the large scale anticipated for commercial coal systems (400 to 800 MW$_e$ units), the physical size of the gasifier would probably make for unfavorable economics. Also, coal can be fed more easily into a pressurized reactor than can biomass, so there has been little need to consider low-pressure systems, which tend to be less efficient than systems using pressurized gasifiers.

sure, directly heated gasifier, and 2 percent for the indirectly-heated gasifier.[2]

Since the calculation model cannot reliably predict variations of syngas composition and temperature ensuing from different operating conditions (e.g., different fluidization flow rates and temperatures), the gasifier input and output conditions have been kept within the narrow ranges that give good agreement with the syngas compositions estimated by the gasifier developers. Thus, the cycles described below represent what could be realized with gasifiers with given (not necessarily optimal) operating conditions.

The low heating value of biomass-derived gas imposes two important changes in the operation of an existing LM2500 machine. To achieve a TIT of 1232°C (as with natural gas) would require a fuel volume flow that may send the compressor into stall and produce unacceptable combustion conditions (instability and large pressure drop—see Part A). Thus, the TIT is derated to 1100°C, and the pressure ratio is slightly increased (to 19.3), whereby the higher turbine mass flow can be handled through the same HP turbine nozzle of the natural gas version (Palmer and Erbes, 1993) for both the pressurized and the indirectly heated gasifiers. For the latter, the higher energy content of the product gas also permits a TIT of 1232°C. For the near-atmospheric pressure, directly heated gasifier, the volumetric flow at the turbine inlet is too high to achieve even the derated TIT. Either an increase of the HP turbine cross section or a further increase in the pressure ratio is needed to reach 1100°C.

The assumed steam cycle features a single evaporation pressure of 67 bar (60 bar at the steam turbine inlet), a maximum super-heater exit temperature of 450°C, a deaerator operating at 110°C (1.43 bar) and condensation at 35°C. Because the HRSG exhaust must be at a high temperature (around 200°C) for biomass drying, advantages from multiple evaporation pressures are marginal.

Pressurized, Directly Heated Gasifier. In this configuration (Fig. 1), biomass chips are first dried using the gas leaving the HRSG, reducing their moisture content from 50 to 15 percent. The dried biomass is then introduced into the pressurized circulating fluidized-bed gasifier (Fig. 2(b) in Part A) to produce raw syngas at 28.6 bar, 953°C. (The gasifier pressure is set such that the fuel gas arrives at the gas turbine combustor

fuel valve at a pressure 1.4 times the combustor pressure.[3]) The raw syngas is cooled to 350°C in an evaporator feeding the HRSG drum, filtered, and eventually injected into the gas turbine combustor. Fluidization air bled from the gas turbine compressor is first cooled to 60°C and then further compressed to about 30.5 bar; cooling ahead of the booster compressor reduces compression work and allows use of commercially available intercooled industrial compressors. Low temperature heat is recovered in the air cooler and in the compressor intercooler to heat part of the condensate that is sent to the deaerator.[4] The relatively high HRSG exit temperature needed for biomass drying (210°C) also requires preheating of the economizer feedwater using steam bled from the steam turbine.

The calculation is carried out by imposing three conditions that essentially reproduce conditions indicated by Bioflow for a similar cycle configuration: (i) a ratio of gasifier-air flow to raw biomass (50 percent mc) input of 0.92, which yields a syngas composition close to that indicated by Bioflow; (ii) inert gas (N₂ only) addition through lockhoppers and for pulse-cleaning of candle filters of 0.05 kg per kg of raw biomass[5]; and (iii) a syngas temperature of 350°C at the inlet of the filter.

As shown in Fig. 1, this cycle has calculated net and gross power outputs of 28.8 MW$_e$ and 30.6 MW, respectively, and net and gross efficiencies of 45 and 48 percent (LHV basis). The gross values agree reasonably well with Bioflow estimates of 31 MW and 46.7 percent, respectively, for a similar cycle configuration (Brascep et al., 1992). The calculated gasifier outlet temperature of 953°C appears consistent with the range 950 to 1000°C indicated by Bioflow for their pilot facility at Varnamo, Sweden (Bioflow, 1994a). The calculated value depends sensitively on the assumed heat losses (0.6 percent of the biomass HHV in our case, or 468 kW$_{th}$).

Nearly Atmospheric, Directly Heated Gasifier. In this configuration (Fig. 2), the gasifier operates at 2 bar and is followed by a second reactor designed to crack the tars to lighter permanent gases (Fig. 2(c) in Part A), thereby allowing gas cleaning by low-temperature scrubbing without concerns for tar condensation. The raw syngas from the cracker passes through

---

[2] The 0.6 percent assumed for the pressurized case is based on verifications by Schombacker (1993) of data for pressurized fluidized bed coal gasifiers reported by Dawkins et al. (1985); the higher loss assumed for the atmospheric, directly heated gasifier accounts for two reaction vessels and a much lower syngas density (translating into higher reactor surface area per unit heat in); the 2 percent loss assumed for indirectly-heated gasifiers is based on Paisley (1994).

[3] The overpressure that will be required to inject the fuel into the gas turbine combustor is not known with certainty. The required pressure would be higher, the higher the fuel gas temperature and the lower the heating value of the fuel. For a lack of information on the required overpressure with different gas temperatures and heating values, an overpressure of 40 percent is adopted for all calculations in this paper.

[4] Some improvement could come from preheating the fluidization air just ahead of the gasifier using the heat from the air cooler. This would allow recovery of the heat in a higher quality form (e.g., high-pressure steam from the raw syngas cooler, instead of low-temperature feedwater). This option has not been considered here because doing so would require more extensive data than were available on the gasifier operating conditions.

[5] This estimate is based on inert gas consumption for double lockhopper systems indicated by Miles and Miles (1988) and candle filters indicated by Skog (1993).

——— **Nomenclature** ———

mc = moisture content, kg H₂O/kg moist biomass
β = gas turbine pressure ratio
ΔT = temperature difference, °C
η = efficiency

Subscripts

a = air
db = dried biomass
el = electric generator (or motor)
org = organic
p = polytropic
th = thermal

Acronyms

BCL = Battelle Columbus Laboratory
BIG = Biomass Integrated Gasifier
EJ = 10^{18} joules
GE = General Electric Company
GEF = Global Environment Facility
GJ = 10^9 joules
GTCC = gas turbine combined cycle
HHV = higher heating value
HP = high pressure
HRSG = heat recovery steam generator

IGCC = integrated gasification combined cycle
IGT = Institute of Gas Technology
LHV = lower heating value
LP = low pressure
Nm^3 = normal m^3 (0°C, 1 atm)
ppbw = parts per billion by weight
ppmw = parts per million by weight
TIT = turbine inlet temperature (first rotor inlet)
TPS = Termiska Processor Studsvik (Swedish company)

point #	T °C	P bar	ṁ kg/s
1	15	1.013	68.0
2	457	19.4	50.7
3	1147	18.8	62.9
4	472	1.07	72.4
5	210	1.04	72.4
6	93	1.013	75.6
7	15	1.013	7.86
8	70	1.013	4.62
9	953	28.6	12.2
10	350	28.0	12.2
11	457	19.4	7.24
12	60	19.0	7.24
13	99	30.4	7.24
14	35	0.056	11.0
15	120	4.50	8.87
16	283	67.0	6.96
17	443	60.3	12.0
18	110	1.43	0.10

$P_{net} = 28.8$ MW$_e$
$\eta_{net, HHV} = 36.6\%$
$\eta_{net, LHV} = 45.2\%$

Auxiliares [kW$_e$]
Dryer + Lock hop. 527
Air booster 503
Inert gas 124
Steam cycle 643

Fig. 1 Schematic, with temperature, pressure, and flow predictions for a BIG/GT combined cycle based on pressurized, directly heated gasification and the LM2500 gas turbine using 50 percent mc biomass. The predicted performance is for TIT = 1100°C, which is lower than the rated capability of existing LM2500 machines, because existing machines may be unable to reach the rated TIT with the indicated low calorific value gas (due to mass flow limitations of the expander).

point #	T °C	P bar	ṁ kg/s
1	15	1.013	68.0
2	457	19.4	57.6
3	1147	18.8	67.8
4	468	1.07	77.7
5	205	1.04	77.7
6	99	1.013	80.9
7	15	1.013	7.61
8	70	1.013	4.48
9	900	2.0	11.0
10	602	1.96	11.0
11	480	1.92	11.0
12	212	1.88	11.0
13	90	1.76	11.0
14	35	1.73	10.3
15	158	27.7	10.3
16	450	27.1	10.3
17	15	1.013	6.57
18	391	2.20	6.57
19	35	0.056	9.57
20	120	4.80	7.64
21	283	67.0	3.18
22	439	60.3	9.57

$P_{net} = 25.9$ MW$_e$
$\eta_{net, HHV} = 34.0\%$
$\eta_{net, LHV} = 41.9\%$

Auxiliares [kW$_e$]
Dryer + Lock hop. 197
Air compr. 697
Syngas compr. 4990
Steam cycle 551

Fig. 2 Schematic, with temperature, pressure, and flow predictions for a BIG/GT combined cycle based on near-atmospheric pressure, directly heated gasification and the LM2500 gas turbine with TIT = 1100°C and using 50 percent mc biomass

P_{net} [MW$_e$] = 24.5 (29.5) $\eta_{net,\,HHV}$ [%] = 33.3 (34.4) $\eta_{net,\,LHV}$ [%] = 41.1 (42.5)

point #	T °C	P bar	ṁ kg/s
1	15	1.013	68.0
2	457	19.4	58.5
3	1147	18.8	61.6
4	466	1.07	70.6
5	195	1.04	79.0
6	94	1.013	82.1
7	15	1.013	7.35
8	70	1.013	4.32
9	874	1.30	4.50
10	329	1.27	4.50
11	17	1.21	3.72
12	38	1.50	0.61
13	150	27.1	3.11
14	15	1.013	7.97
15	615	1.50	7.97
16	17	1.50	0.05
17	1027	1.30	8.48
18	500	1.27	8.48
19	35	0.056	9.25
20	120	4.50	1.60
21	151	3.0	0.05
22	283	67.0	3.40
23	440	60.3	9.91
24	110	1.43	0.62

Auxiliares [kW$_e$] : Dryer + Lock hopper 190
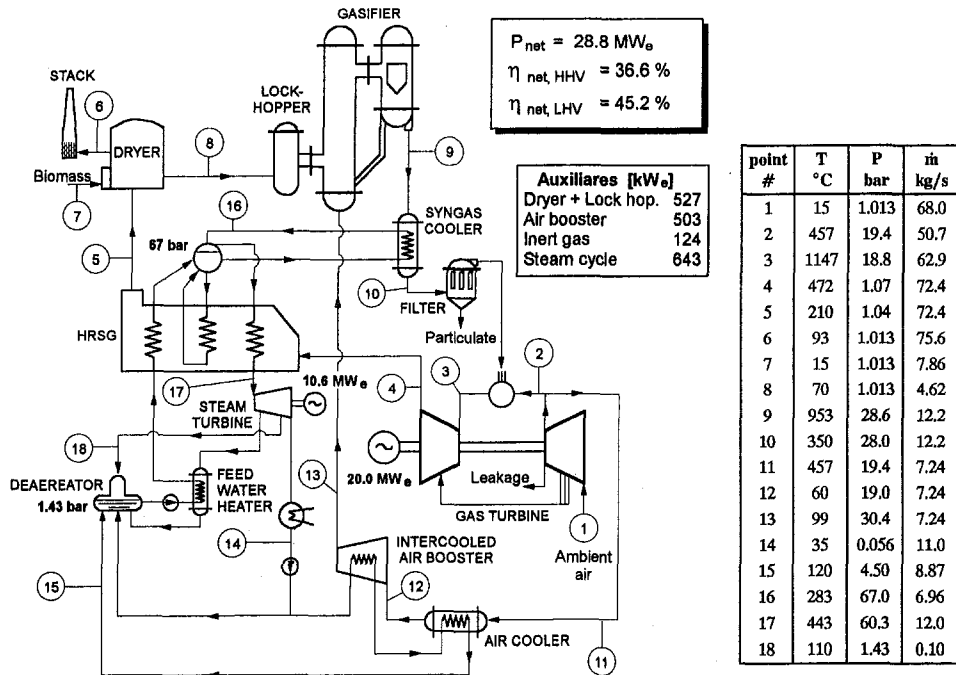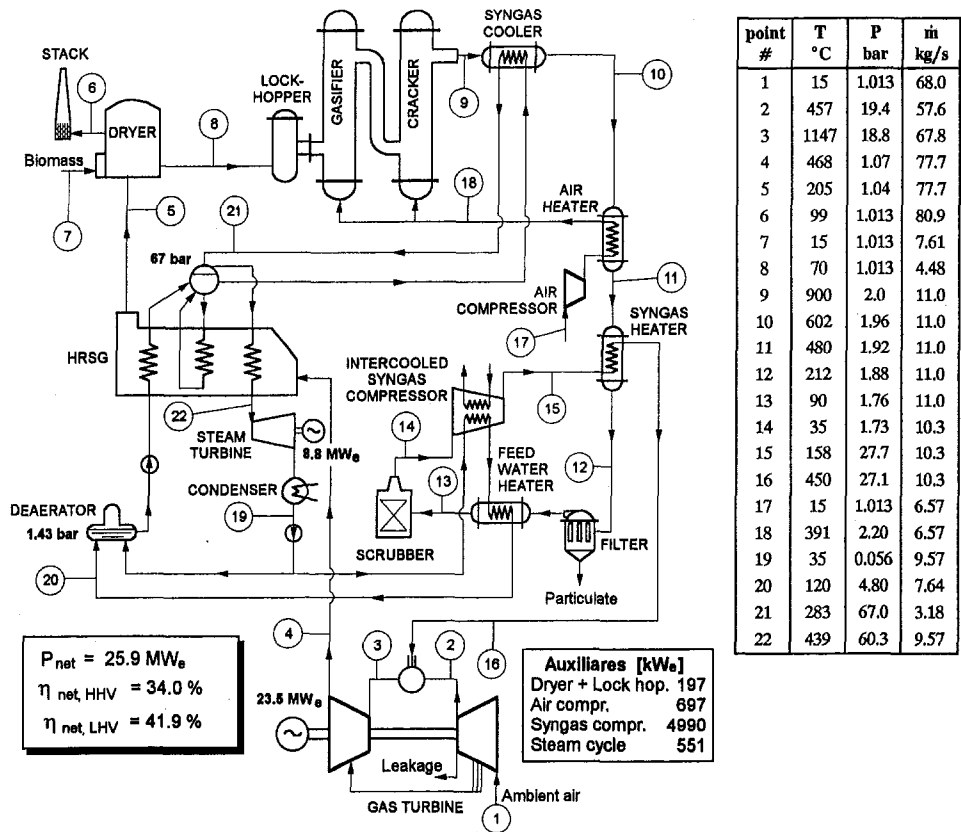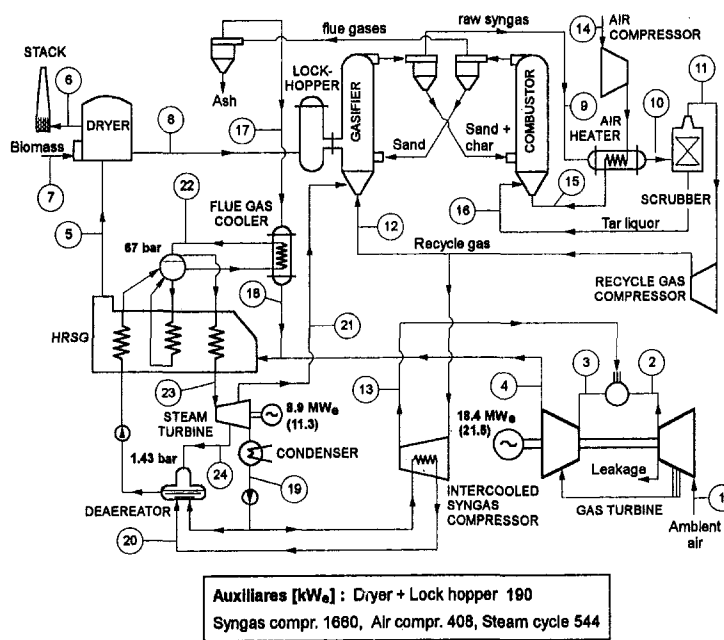Syngas compr. 1660, Air compr. 408, Steam cycle 544

Fig. 3 Schematic, with temperature, pressure, and flow predictions for a BIG/GT combined cycle based on near-atmospheric pressure, indirectly heated gasification, and the LM2500 gas turbine with TIT = 1100°C, the same TIT as Figs. 1 and 2. Values shown in parentheses are for TIT = 1232°C, the rated capability of the LM2500 with natural gas. The higher TIT can be achieved with syngas from an indirectly heated gasifier, because the gas has a much higher heating value than that from directly heated gasifiers.

an evaporator feeding the HRSG drum, an air preheater, and a preheater for the clean pressurized syngas. The raw syngas then passes a fabric filter,[6] is further cooled to 90°C in a feedwater heater, and eventually scrubbed to 35°C to remove all contaminants of concern and to reduce the moisture content to about 3 percent by volume. Finally the syngas enters an intercooled fuel compressor, which brings it to a pressure 1.4 times that of the gas turbine combustor. Low-temperature heat from syngas cooling and boost compressor intercooling is used to preheat condensate sent to the deaerator. The rather complex flow path followed by the syngas is designed to achieve two basic goals: minimize work to pressurize the syngas by compressing it at the lowest possible temperature (and thereby also avoid the use of expensive, high-temperature compressor materials)[7] and recover as much of the sensible heat in the syngas as possible.[8]

The calculation is carried out by imposing (i) a cracker exit temperature and syngas composition indicated by TPS (Lundberg, 1992; Brascep et al., 1992) (achieved in the calculation by adjusting the temperature and flow rate of gasification air); (ii) a syngas temperature at the combustor fuel valve of 450°C

(set by fuel valve materials constraints); and (iii) a syngas temperature at the scrubber inlet of 90°C. Total gasifier and cracker heat losses amount to 763 kW$_{th}$ (1 percent of the biomass HHV). Results are shown in Fig. 2.

The net power output for this cycle is estimated to be 26.1 MW, with a net efficiency of 42 percent (LHV basis). The latter is close to an estimate of 43 percent by TPS for a similar configuration (Brascep et al., 1992). Our efficiency estimate would improve after considering that the large (5 MW) fuel compressor could have a polytropic efficiency higher than the 80 percent assumed here; in any case, for this configuration auxiliary power consumption plays a major role in determining overall net performance.

Table 1 Summary of performances calculated for BIG/GT combined cycles assuming existing LM2500 gas turbine technology and alternative gasifier designs. Except for the right-most column, all estimates are based on TIT = 1100°C.

	Gasifier Design			
	Directly-heated, pressurized (Bioflow)	Directly-heated, atm. pres. (TPS)	Indirect-heated, atm. pres. (BCL), TIT (°C) = 1100	1232
Gross Power (MW$_e$)	30.6	32.3	27.3	32.8
Gas turbine	20.0	23.5	18.4	21.5
Steam turbine	10.6	8.8	8.9	11.3
Net power (MW$_e$)	28.8	25.9	24.5	29.5
Net HHV efficiency, %	36.6	34.0	33.3	34.4
Net LHV efficiency, %	45.2	41.9	41.1	42.5

---

[6] The constraints imposed on the heat exchangers (gasifier air preheated to achieve 900°C at the cracker exit and minimum temperature difference between hot and cold gas of 30°C) produce a raw syngas temperature at the fuel heater exit of 212°C (see Fig. 2). At this temperature, Nomex or Teflon fabric bag filters exhibit both adequate temperature capability and very good chemical resistance to alkali (Theodore and Buonicore, 1988). (Glass fibers also have suitable temperature capability, but lower resistance to alkali.) Lower-cost fabrics like cotton operate at around 80°C. This could be achieved by placing the feedwater heater ahead of the filter, but there would be a risk of condensation and moist particle deposition.

[7] Even at a relatively low syngas temperature (see below), syngas compression will still require in excess of 15 percent of the generated gross power. Compression at higher temperature would further increase this power consumption, thus reducing overall cycle efficiency.

[8] The only heat released to ambient is in the scrubber, from 90°C to 35°C, and at the intercooler. The latter heat loss is due to insufficient HRSG gas flow to vaporize all the water heated in the intercoolers.

Table 2 Summary of performances achievable with a fully fired 25-MW class engine (TIT = 1200°C) and with the LM1600 (TIT = 1232°C) coupled with pressurized fluidized bed gasification

	Gas Turbine	
	25-MW$_e$ class	LM1600
Gross power output (MW$_e$)	42.0	23.0
Gas turbine	27.0	15.1
Steam turbine	15.0	7.9
Net power output (MW$_e$)	39.6	21.6
Net HHV efficiency, %	38.4	37.1
Net LHV efficiency, %	47.3	45.8

Our estimate for this case is based on the assumption of a gas turbine pressure ratio of 19.3 (as assumed for the case with the pressurized gasifier) and a TIT of 1100°C. This assumes that the nozzle discharge area of the HP turbine is increased by about 7 percent. If no modification is made to the nozzle area, the pressure ratio would increase to about 20.7 (assuming stall is not reached), net output would drop by approximately 1 MW, and net efficiency would decrease by half a percentage point.

Nearly Atmospheric, Indirectly Heated Gasifier. This configuration (Fig. 3) is conceptually similar to the previous one. Also in this case raw syngas is produced at a pressure slightly above atmospheric (1.3 bar), cooled, scrubbed, and eventually compressed for injection into the gas turbine combustor. However, the gasifier design is based on that of the Battelle Columbus Laboratory (Battelle, 1993) (Fig. 2(d) in Part A), as described by Breault and Morgan (1992). The heat needed to sustain the gasification reactions and produce the outlet temperature of 874°C is provided by sand from the combustor.[9] Fuel for the combustor consists of char separated from the syngas by a cyclone and tar recycled from the syngas scrubber.[10] The combustor flue gases are cooled in an evaporator feeding the HRSG drum and then mixed with the gas turbine exhaust. The raw syngas is first used to preheat combustion air, scrubbed to 17°C[11] and, after separating the fraction used to fluidize the gasifier, compressed in an intercooled compressor. Low-temperature heat made available in the intercoolers is used to heat condensate sent to the deaerator.

Most of the parameters we have imposed to carry out the calculation are based on Breault and Morgan (1992): (i) steam and recycle gas flows to the gasifier; (ii) combustor outlet temperature of 1027°C; (iii) combustion air flow; and (iv) char recycle flow. We have additionally imposed a 1 percent sand make-up flow and, based upon suggestions from Paisley (1994), an inert gas (N$_2$) addition to the gasifier of 0.2 percent of the wet biomass flow and an overall gasifier heat loss of 2 percent of the biomass HHV. This heat loss (1480 kW$_{th}$) is much higher than for the other gasifiers, and might be explained by the large volumes of the gasifier and combustor vessels, the cyclones and the ducts for sand recycle. Whether the heat losses for this configuration are really much higher than those of the

other two systems requires verification. Results are shown in Fig. 3.

For this system the calculation has been performed for both the derated TIT of 1100°C and the standard LM2500 TIT of 1232°C, because with the medium heating value syngas produced by this gasifier the problems due to excessive syngas volume flow are much less critical. For the same TIT of 1100°C, the net efficiency of this system (33.3 percent HHV, 41.1 percent LHV) is lower than for the other two cases (Table 1). This difference is due mainly to larger heat losses and to the partial combustion of the biomass, which is thermodynamically equivalent to supplementary firing downstream of the gas turbine. The power required by the fuel compressor is much lower than in the case with the directly heated, near-atmospheric pressure gasifier due to the much lower flow rate (corresponding to the superior heating value of the gas). Increasing the TIT to 1232°C raises the net efficiency to 34.4 percent HHV basis), or approximately that for the directly heated near-atmospheric system, but gives 13 percent more power output.[12]

Beyond First-Generation BIG/GTCC

In light of expected advances in gas turbine technology (Williams and Larson, 1989; Macchi et al., 1994), we explore here BIG/GTCC systems based on advanced gas turbines that may be available by the turn of the century. A complete and systematic analysis of cycle options and gasification technologies is beyond the scope of this work. As a preliminary illustration of some possibilities, however, we present performance estimates for two advanced combined cycle configurations, both integrated with pressurized, directly heated gasification.

A second generation of BIG/GTCC technology might involve existing gas turbines fired at the TIT rated with natural gas, rather than the derated TIT considered in the previous section. Operating at rated TIT assumes that the combustor and turbomachinery are modified to handle the large mass flow ensuing from the low heating value of the fuel.[13] To represent this second generation of BIG/GTCC, we consider two gas turbine technologies: a generic 25-MW class engine and the GE LM1600 (see Table 5 in Part A). These engines have been selected to illustrate the effect of scale on overall efficiency and to appraise the power output achievable with two of the most widely used classes of aeroderivative engines. The smaller LM1600 may be an especially attractive option for many future biomass-fired facilities, because its modest size would help limit the transportation costs associated with fueling the facility.

An advanced generation of BIG/GTCC systems might utilize an intercooled combined cycle (BIG/GTICC). Intercooled aeroderivative turbines for natural gas firing are the focus of a major ongoing development effort by a multinational consortium involving 17 electric and gas industry, government, and international organizations (Cohn et al., 1993; de Biasi, 1993).[14] Also, a prototype intercooled-regenerative aeroderivative gas turbine developed by Rolls Royce with Westinghouse for the U.S. Navy began test operation in 1994. With intercooling, higher TITs are achievable due to the lower temperature of the compressor bleed air used to cool the turbine. Like simple cycle engines, intercooled engines could be fired with low heating value fuels, with appropriate combustor modifications and, if needed, increases in the turbine cross sections; the former would

---

[9] This gasifier exit temperature is slightly higher than indicated by Breault and Morgan (1992) and Paisley (1994) (860–865°C).

[10] For simplicity tars are assumed to consist of solid carbon, liquid water, and some ash.

[11] The temperature at the scrubber outlet is lower than assumed for the case with the directly heated gasifier in order to reproduce the same recycle gas composition and thus the same gasifier operating conditions as reported by Breault and Morgan (1992). In practice, the scrubber outlet temperature is likely to be higher (30 to 35°C), but this would have very marginal consequences on efficiency and power output.

[12] For comparison, Breault and Morgan (1992) estimated an efficiency of 31.4 percent (HHV basis) for a configuration like the one here, but utilizing a heavy-duty gas turbine—the GE MS6001(B). The net output for the MS6001(B) combined cycle was estimated to be 54.2 MW$_e$.

[13] Increasing the pressure ratio without modifying the turbine has not been considered because the compressor would probably not tolerate it. Also, higher pressure ratios would decrease efficiency and power output.

[14] Unlike the case for natural gas combined cycles based on intercooled aeroderivative turbines, efficiency enhancement by intercooling low pressure ratio heavy-duty gas turbines in combined cycles is negligible (Macchi et al., 1994).

GASIFIER

STACK
LOCK-HOPPER

Auxiliares [kWe]
Dryer + Lock hop. 1602
Syngas compr. 4219
Inert gas 298
Steam cycle 1530

DRYER

Biomass

67 bar

HRSG

SYNGAS COOLER

FILTER

Particulate

STEAM TURBINE — 24.9 MWe

INTERCOOLED SYNGAS COMPRESSOR

FEED WATER HEATER

CON-DENSER

10 bar

DEAEREATOR

AIR COOLER

P_{net} = 75.6 MWe

$\eta_{net, HHV}$ = 40.0 %

$\eta_{net, LHV}$ = 49.3 %

58.4 MWe

INTERCOOLER

Leakage

INTERCOOLED GAS TURBINE   Ambient air

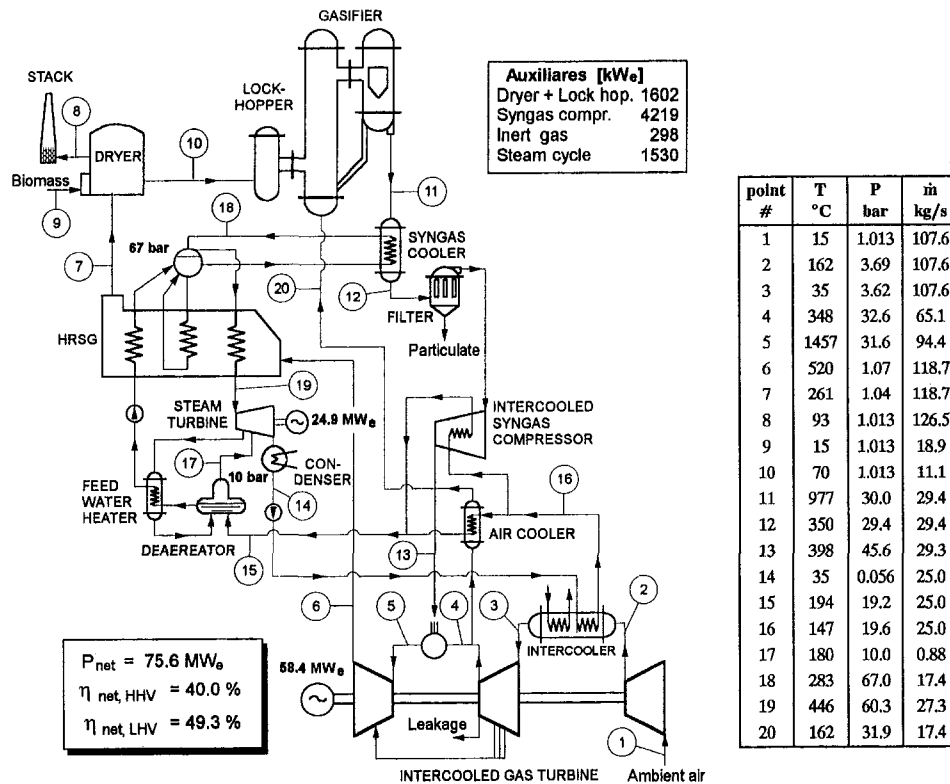| point #	T °C	P bar	ṁ kg/s
1	15	1.013	107.6
2	162	3.69	107.6
3	35	3.62	107.6
4	348	32.6	65.1
5	1457	31.6	94.4
6	520	1.07	118.7
7	261	1.04	118.7
8	93	1.013	126.5
9	15	1.013	18.9
10	70	1.013	11.1
11	977	30.0	29.4
12	350	29.4	29.4
13	398	45.6	29.3
14	35	0.056	25.0
15	194	19.2	25.0
16	147	19.6	25.0
17	180	10.0	0.88
18	283	67.0	17.4
19	446	60.3	27.3
20	162	31.9	17.4

Fig. 4 Schematic, with temperature, pressure, and flow predictions for a BIG/GT combined cycle based on pressurized, directly heated gasification and a 25-MWₑ class gas turbine in an intercooled configuration. This configuration has also been used in predicting the performance of an intercooled LM1600 gas turbine combined cycle (Table 3).

presumably be a more demanding modification because lower combustor inlet air temperatures and higher TITs both contribute to low oxygen contents (5 or 6 percent) in the exhaust gas. In our performance modeling of the BIG/GTCC, we again consider the 25-MW class engine and the LM1600.

Second-Generation BIG/GTCC—No Derating of TIT. For these calculations, the system configuration and assumptions are as for Fig. 1, with four modifications. First, the TIT and pressure ratio are assumed to be as in existing engines (Table 5 of Part A). Second, the gasification pressure is increased slightly to provide the assumed 40 percent margin for the pressure of the fuel to be injected into the combustor: 29.6 and 32.5 bar for the 25 MW and the LM1600 turbine, respectively. Third, the HRSG outlet temperature is increased to 223–226°C to maintain a stack temperature of 93°C. (Compared with the systems discussed earlier, a higher biomass-to-air flow ratio is needed to achieve the higher TIT.) Fourth, for the 25-MW class engine, steam turbine inlet conditions are increased to 80 bar and 495°C to take advantage of the higher gas turbine outlet temperature.

Our calculations indicate that by running existing gas turbines at full firing temperatures it would be possible to reach HHV efficiencies in the 37 to 38 percent range (Table 2), or approximately 1.5 percentage points higher than with the derated TIT. Differences between the performances of the 25-MW class and LM1600 turbines are due solely to the effects of scale on gas turbine and steam turbine performance. Most probably, there will also be scale effects on auxiliary power consumption (not considered here), so that the difference in power output and efficiency is likely to be somewhat larger than indicated in Table 2.

Advanced BIG/GTCC—Intercooled Combined Cycles. Intercooled gas turbine cycles appear particularly attractive for integrating with biomass gasification because—besides the ad-

vantages shared with natural gas-fired applications (Macchi et al., 1994)—most of the low-temperature heat extracted from the intercooler can be effectively used to preheat the feedwater of the steam cycle, thus compensating for the high HRSG gas exit temperature imposed by the energy requirements of the biomass dryer. This allows the deaerator to export steam to the steam turbine (Fig. 4), thus effectively behaving as a LP drum.

Aside from differences in the steam cycle configuration, a major difference between the intercooled and nonintercooled configurations is the replacement of the air booster compressor with an intercooled fuel booster compressing the syngas from 28.5 to 45.6 bar (compare Figs. 4 and 1). Such a fuel compressor is not commercial today. It would be required to handle fuel

Table 3 Summary of predicted performance of intercooled turbines coupled with pressurized fluidized bed gasification. "Fuel booster" refers to the configuration of Fig. 4. "Air booster" refers to an alternative configuration that is similar to the one depicted in Fig. 1, but with gasification at 48 bar.

	Gas Turbine			
	25-MW class		LM1600	
	Fuel booster	Air booster	Fuel booster	Air booster
Gross power (MWₑ)	83.3	83.6	45.0	45.3
Gas turbine	58.4	58.5	31.7	31.8
Steam turbine	24.9	25.1	13.3	13.5
Net power (MWₑ)	75.6	78.6	40.7	42.4
Net HHV efficiency, %	40.0	40.9	39.0	40.1
Net LHV efficiency, %	49.3	50.5	48.1	49.4

gas at 350 to 400°C, since cooling the gas below this range may lead to problems with tar condensation. Also, we have assumed that fluidization air bled from the gas turbine compressor is cooled to limit the gasifier exit temperature to 980°C. In practice, this could probably be avoided either by increasing the gasifier outlet temperature or by reducing the air flow (thus changing the syngas composition), with beneficial effects on efficiency and capital cost in both cases.

An alternative to using a high-temperature fuel booster compressor would be to maintain the cycle configuration of Fig. 1 by increasing the gasifier pressure to 48 bar. At this pressure, biomass feeding may be problematic, and further development of gasification technology would be required. In the absence of better estimates for product gas composition at 48 bar, we have carried out a cycle calculation assuming the same gas composition as for the 30-bar gasifier (see Table 2 in Part A). Additionally, lockhopper power consumption is assumed to increase from 80 to 110 kJ/kg_{db}.

For the turbine, we have selected an overall pressure ratio of 32.5. For the case using the 30-bar gasifier, fluidization air can be bled directly from the gas turbine compressor. The TIT is increased to 1380°C to take advantage of the lower turbine coolant temperature produced by intercooling, while maintaining the same metal

Table 4   Projected yields (dry tonnes/ha/year) and costs (in 1991$/GJ) of biomass from energy plantations on agricultural land in the US[a]

	1995		2010	
	Yield	Cost ($/GJ)	Yield	Cost ($/GJ)
Woody crops[b]				
Northeast	9.2	2.64	13.3	2.11
South/S.E.	10.2	2.38	14.7	1.92
Midwest	10.2	3.02	14.7	2.37
Lake States	10.2	2.59	14.7	2.07
Northwest	15.3	2.02	22.1	1.67
Grasses[c]				
Northeast	10.2	2.96	17.2	2.09
South/S.E.	14.3	2.29	24.1	1.58
Midwest	12.3	3.14	20.7	2.14
Lake States	12.3	2.72	20.7	1.89

(a) Estimates by Perlack and Wright [1993] include 24 km transport. Productivities are net of losses. A 6% discount rate is assumed for the cost estimates. Assumed land rents ($/hectare/year) are actual rents for cropland in 1993: $155 for the Northeast, $97 for the South/Southeast, $213 for the Midwest (combelt), $134 for the Lake States, and $134 for the Northwest. Costs presented by Perlack and Wright in 1993$ were converted to 1991$ by multiplying by 0.946, the US GDP deflator.

(b) The woody crops are assumed to be short-rotation varieties (higher heating value 19.75 GJ/dry tonne) having a growth period of 18 years, with harvests every 6 years. Losses amount to 5% in harvest and 1% per month during 4 months of storage (8.8% total losses). The wood is delivered as wood chips with 50% moisture content.

(c) The perennial grasses (higher heating value of 17.43 GJ/dry tonne) are assumed to be planted for a growth period of 10 years, with harvests once or twice a year (depending on the region). Losses are assumed to be 7% in harvest and 1% per month during 6 months storage (12.6% total losses). The grass is delivered as large round bales with a moisture content of 20%.

Table 5   State-by-state projections for Northeast Brazil of potential plantation area, average plantation yields (dry tonnes per hectare per year), and average biomass production costs (in 1991$/GJ) for eucalyptus wood chips delivered to a conversion facility with 33 percent moisture content[a]

State	Land area (10³ ha)	Characteristics of Potential Plantations in Northeast Brazil			
		Area (10³ ha)	Bio-mass yield[b]	Energy yield (GJ/yr)	Cost[b] ($/GJ)
Alagoas	2911	498	14.9	148	1.98
Bahia	56698	16228	12.1	3920	2.14
Ceara	14569	944	10.6	201	2.24
Maranhao	32956	16203	15.1	4905	1.97
Paraiba	5396	506	11.8	120	2.15
Pernambuco	10102	1120	9.4	211	2.37
Piaui	25466	14112	10.3	2917	2.27
R.G.d.Norte	5317	461	8.4	78	2.48
Sergipe	2186	387	13.1	102	2.07
Total	*155600*	*50459*	*12.5*	*12600*	*2.11*

(a) From Carpentieri et al. [1993].

(b) These are weighted averages estimated for growing eucalyptus wood in five bioclimatic regions within each state. The costs include 85 km transport and chipping. The moisture content of the delivered chips is 33% due to some natural drying that occurs between harvest and delivery.

temperature and the same cooling technology. This TIT corresponds to the maximum cooling flow which can be handled by the coolant circuit; criteria for determining such critical conditions are discussed by Macchi et al. (1994). The compressor inlet air flow (which determines power output) has been selected to maintain the same turbine nozzle cross sections of the reference engines (see Table 5 in Part A), implying that the intercooled engine will have approximately the same HP turbine of the simple cycle engine.[15] Finally, the temperature at the HRSG exit is increased to 261°C to provide proper biomass drying and a final stack temperature of 93°C.

Results summarized in Table 3 indicate substantial enhancements in efficiency with intercooling for both the 25-MW class engine and the LM1600. (Details for the former are shown in Fig. 4). The LM1600 BIG/GT-ICC shows an impressively high efficiency (39–40 percent HHV basis) for a total power plant capacity of only about 40 MW.

Preliminary Economic Evaluation

The BIG/GT is not yet a commercial technology. Given the performance levels estimated above, the economic viability of commercial BIG/GT power production will depend primarily on the cost for biomass fuel delivered to the facility and on the level of capital investment required.

Delivered Biomass Fuel Costs. Biomass-fired power plants operating today rely on low-cost residues for feedstocks, of which there are at present substantial underutilized supplies

---

[15] Alternatively, the same HP compressor might be used and the turbine modified (Day, 1992), which would produce larger power outputs and approximately the same efficiency.

Table 6 Estimates of long-run, commercial installed capital costs for BIG/GT combined cycle systems

Source	Capacity (MW$_e$)	Capital cost (1991$/kW)	Efficiency (percent)	Comments
Elliott & Booth (1990)	37	1250-1350	42[a]	RB211 gas turbine, Ahlstrom pressurized gasifier, ceramic filter gas cleanup; European conditions.
Elliott & Booth (1993)	25-30	1230-1420	45[a]	LM2500 gas turbine, atmospheric-pressure directly-heated gasifier.
Puhakka (1994)	30-35	1800-2370	40-50[a,b]	Commercial plant, Bioflow technology, European conditions.
Puhakka (1994)	60-70	1425-1900	40-50[a,b]	Commercial plant, Bioflow technology, European conditions.
Huotari, et al. (1993)	70	1424	43[a]	Frame 6 gas turbine (TIT=1100°C, β=17) with pressurized, directly-heated gasifier. (Excluding allowance for funds during construction.)
Breault & Morgan (1992)	54.2	1490	31.4[c]	MS6001(B) gas turbine, atm. pres., BCL gasifier; US conditions.
Solar Thermal (1992)	150	1170	34.1[c]	Pressurized gasifier, hot gas cleanup; 10th unit; U.S. conditions.

(a) Lower heating value basis.

(b) 40-45% electricity production efficiency for cogeneration operation; 45-50% efficiency for power generation only.

(c) Higher heating value basis.

that might be used to fuel BIG/GT systems.[16] Nevertheless, if electricity production from BIG/GT power plants is to make a substantial contribution to global electric power production in the long term, fuel supply from dedicated biomass energy plantations will be required. In the US and Europe, R&D efforts are focused on the production on excess agricultural land of short-rotation woody crops (SRWC), such as hybrid poplar, and on perennial grasses, such as switch-grass. With present technology for growing these fuels in the US, delivered fuel costs are estimated to be $2.0–3.0/GJ for wood chips and $2.3–3.1/GJ for bales of perennial grasses.[17] Further development and the commercialization of technology for growing biomass is projected to reduce these costs to $1.7–2.4/GJ for chips and $1.6–2.1/GJ for grasses by the year 2010 (Table 4).

In many developing countries, the climate is better suited to biomass energy crop production than the US, and thus biomass production costs can be expected to be lower. For example, in a recent assessment for the Northeast region of Brazil (a suboptimal location for biomass production due to its semi-arid climate), some 50 million hectares of land (one-third of the area of the region) were identified as potentially capable of supporting biomass plantations (Carpentieri et al., 1993). If fully planted, this area might support some 188 GW of BIG/GTCC capacity. The assessment included a review of production costs for existing large-scale industrial Eucalyptus plantations and of cost projections based on small-scale plots in the Northeast region to estimate the likely costs for widespread biomass production in the Northeast region assuming present production practices. The average costs for delivered chips range from $2.0/GJ to $2.5/GJ, with a weighted average over 50 million hectares of $2.1/GJ (Table 5).

BIG/GT Capital Costs. Because BIG/GT technology is not yet commercial, capital costs are uncertain. For BIG/aero-derivative gas turbine combined cycles in the 25–30 MW$_e$ range, target capital costs (based on prefeasibility studies) for fully commercialized plants are $1230 to $1420/kW (Table 6). Elliott and Booth (1993) suggest this range for a plant based

on an LM2500 gas turbine and atmospheric-pressure, directly heated gasification. They expect that this relatively low capital cost range can be achieved by emphasizing careful engineering design, "cookie-cutter" production of a standard design, and maximizing factory assembly so as to minimize construction times and field labor costs.

With pressurized gasification, Elliott and Booth (1993) indicate that the $1200–1400/kW cost range would be achieved at a larger scale.[18] Bioflow has estimated a cost of $1800–2400/kW for units using pressurized gasification and producing 30–35 MW$_e$ (Puhakka, 1994), the minimum-sized commercial plant being marketed by Bioflow (Bioflow, 1994b). The U.S. Department of Energy has estimated a capital cost of $1170/kW for a 150 MW$_e$ pressurized-gasifier BIG/GT combined cycle (Table 6).

Electricity Production Costs. To put capital cost estimates in perspective, it is useful to compare calculated total electricity generating costs for BIG/GT systems with costs for alternative electricity generating technologies against which BIG/GT systems must compete. The time frame of interest in this comparison is the first decade of the next century, by which time BIG/GT technology will have been commercially demonstrated, and by which time it is conceivable that biomass plantations will be established for fuel supply. BIG/GT technology would likely need to compete with power-plants burning natural gas or coal in many countries. Advances in these fossil fuel technologies can be expected. The integrated coal gasifier combined cycle (IGCC) may become the state-of-the-art for coal-fired power generation. With natural gas, advanced gas turbine cycles such as intercooled combined cycles will be developed. For many developing countries, BIG/GT technologies may need to compete against new hydroelectric facilities.

Levelized electricity production costs for BIG/GT combined cycles for investment costs of $1500 to $2000 per kW would be 4.9 to 5.7 cents per kWh, assuming O&M costs of $0.005/kWh (Elliott and Booth, 1993), a biomass fuel price of $2/GJ, a heat rate of 10.3 MJ/kWh (35% HHV basis), a 75 percent capacity factor, and utility financing under US conditions.[19] As

---

[16] The worldwide production of biomass residues from forest-product industries and production of major agricultural crops has been estimated to be about 56 EJ per year (Williams and Larson, 1993), which could support some 830 GW of BIG/GT capacity, assuming a 35 percent efficiency (HHV) and a 75 percent capacity factor.

[17] All costs in this paper are given in constant 1991$. The U.S. GDP deflator has been used to convert from other years' dollars where needed.

[18] Blackadder et al. (1994) suggest there would not be major cost benefits with pressurized systems unless the fuel input rate is above 100 MW.

[19] The recommended annual capital charge rate for utility renewable-resource power plants is 0.103, which assumes a real weighted cost of capital (discount rate) of 6.2 percent per year, a 38 percent income tax rate, an insurance and property tax rate of 2 percent of the investment capital per year, a 30-year plant

shown in Fig. 5, these costs for BIG/GTCC power compare well against electricity costs from large-scale coal-fired technologies common today (500 MW$_e$ steam plant—5.1 c/kWh) and under commercialization (800 MW$_e$ IGCC—5.3 c/kWh), assuming a coal price of $1.77/GJ, as projected for the year 2010 by the US Dept. of Energy (EIA, 1994). Figure 5 also shows the long-run marginal cost estimated for new hydroelectricity from plants that are planned for commissioning after the year 2000 in the Northeast region of Brazil (Carpentieri et al., 1993).[20] Because regional hydroelectric sources will be exhausted by about 2005, the utility serving the Northeast region is seriously evaluating the prospects for BIG/GT power plants fueled by dedicated biomass plantations. Based on Fig. 5, BIG/GTCC facilities would be competitive at the busbar with new hydroelectric power in Northeast Brazil and would also be about half as capital intensive. (The utility, CHESF, is playing a lead role in the GEF-supported demonstration of BIG/GT technology described in Part A of this paper.)

There could be reductions in electricity production costs with the development of advanced BIG/GTCC such as the intercooled combined cycle, because for the same basic engine, net power output of the ICCC is nearly double that for the conventional combined cycle. This might very well translate into a reduction in the per-kW capital cost of the system.[21] This, together with an increase of about two percentage points in efficiency, could make the intercooled BIG/GTCC competitive even with advanced natural gas fired systems, if gas prices rise as projected by the US Department of Energy. Advanced conventional combined cycles (EPRI, 1989) would produce power at a cost of about 4.3 c/kWh,[22] assuming a gas price of $3.76/GJ, as projected by the USDOE for the year 2010. Preliminary cost estimates for a 127 MW$_e$ intercooled combined cycle under development in the Collaborative Advanced Gas Turbine Project indicate a total electricity production cost of 4 c/kWh (with gas at $3.76/GJ).[23] The capital cost for an intercooled 25-MW class BIG/GTCC would need to be about $1100/kW to achieve a production cost of 4 c/kWh, assuming a biomass price of $2/GJ.

Other cycles that involve low unit capital cost efficiency enhancements may be of special interest for BIG/GT applications, especially alternatives to the steam bottoming cycle. The steam cycle is a relatively capital intensive efficiency enhancement at the modest scales needed for most BIG/GT facilities; for a 30 MW$_e$ capacity power plant with a 10 MW$_e$ bottoming steam cycle, the latter alone might cost some $1600/kW.[24] Other enhancements might be less costly. For example, one estimate of the incremental cost of capacity addition by steam injection is $660 per added kW.[25] Among the cycle enhancements that may be of interest for BIG/GT applications are various configurations involving steam injection, humid air tur-
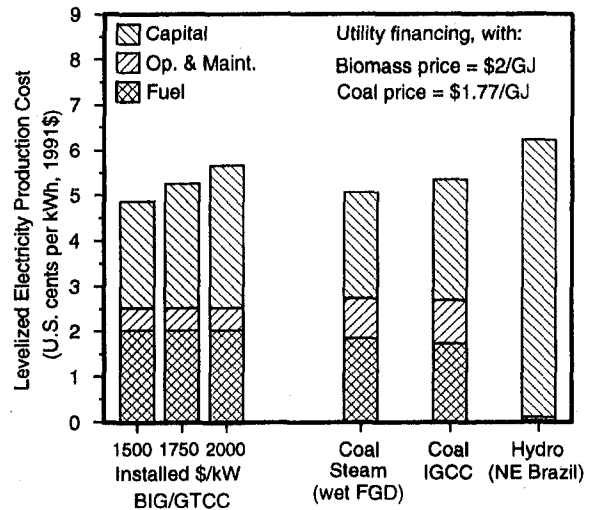

Fig. 5 Calculated electricity production costs for 25–30 MW$_e$ BIG/GT combined cycles, assuming alternative installed capital costs. The calculations assume a heat rate of 10.3 MJ/kWh (35 percent HHV efficiency), O&M costs of $0.005/kWh (Elliott and Booth, 1993), a biomass cost of $2/GJ (see Tables 4 and 5), and utility financing (see footnote 19). For comparison, the costs of power from alternative, utility financed, coal and hydroelectric plants are shown. The coal-fired facilities refer to a 500 MW$_e$ steam plant with wet flue gas desulfurization and to an 800 MW$_e$ Integrated Gasification Combined Cycle facility (EPRI, 1989). The coal price of $1.77/GJ is that projected for the year 2010 by the US Department of Energy (EIA, 1994). The cost of hydroelectricity (see footnote 20) is the average for 2255 MW of capacity that are planned to come on line in the first decade of the 21st century at various locations in the service territory of CHESF, the utility serving the Northeast region of Brazil (Carpentieri et al., 1993).

bines (Fluor Daniel et al., 1993b), and air bottoming cycles (Anon., 1991).

Conclusions

Several technological issues must be addressed in the ongoing development and demonstration of biomass-gasifier/aaoderivative gas turbine combined cycle technology, as discussed in Part A of this paper, but the technology is promising as an efficient and economical means for producing electricity from biomass. A variety of gasifier designs are potentially suitable for BIG/GTCC applications. Pressurized gasification provides a thermodynamic advantage, as illustrated in Part B of this paper, but presents greater technological development challenges. With directly heated (air-blown) gasification, some minor modifications are required to use existing aeroderivative turbines, including derating the firing temperature. Indirectly heated gasification produces a fuel gas with higher energy content so that natural-gas firing temperatures can be readily achieved with existing machines.

Expected advances in aeroderivative gas turbines (for natural gas) would further improve the performance of BIG/GTCC plants. In particular, intercooled gas turbines appear to be especially attractive for use with biomass because most of the low-temperature heat available in the intercooler can be used more effectively due to the low-temperature heat demands of biomass drying.

Preliminary cost estimates for BIG/GTCC power plants suggest electricity from modest-scale plants (20–70 MW$_e$) will compete with electricity from large-scale coal-fired power plants and, in some regions of the world, with new hydroelectric facilities.

life, and 5 year tax recovery period (EPRI, 1989). The annual capital charge rate for fossil technologies is 0.106, which derives from a 20 year tax recovery period.

[20] Assuming utility financing under Brazilian conditions: 10 percent real discount rate and 50-year hydroelectric plant lifetime.

[21] One estimate of the incremental cost for adding intercooling is $440 per kW added (50 MW$_e$ total increment) to an advanced 60 MW$_e$ aeroderivative simple cycle gas turbine (Fluor Daniel, 1993a). This is considerably lower than cost estimates for commercial BIG/GTCC units (Table 6).

[22] From EPRI (1989) for a 210 MW$_e$ system with an installed capital cost of $562/kW, a heat rate of 7.930 MJ/kWh (HHV basis), and an O&M cost of $0.0046/kWh. The cost of 4.3 c/kWh assumes a 75 percent capacity factor and a capital charge rate of 0.106.

[23] From Tittle et al. (1993) for a 127 MW$_e$ "GEX" intercooled combined cycle (based on the LM6000) with an installed capital cost of $500/kW, a heat rate of 7.236 MJ/kWh (HHV basis), and an O&M cost of $0.0045/kWh. A 75 percent capacity factor and a 0.106 capital charge rate are assumed.

[24] The installed capital cost (in 1991$/kW) for the bottoming portion of a gas turbine/steam turbine combined cycle has been estimated to be 3785 × (MW$_e$)$^{-0.374}$ for steam cycles in the capacity range from 20 to 40 MW$_e$ (Tittle et al., 1993). Extrapolating to 10 MW$_e$ gives $1600/kW.

[25] This is based on estimated installed costs for an advanced aeroderivative gas turbine of $716/kW for a 62.6 MW$_e$ simple cycle and $696/kW for the same machine with steam injection (103.9 MW$_e$ total output) (Fluor Daniel, 1993a).

References

Anon., 1991, "Low Cost 'Air Bottoming Cycle' for Gas Turbines," *Gas Turbine World,* May–June, p. 61.

Battelle, 1993, "Operation and Evaluation of an Indirectly Heated Biomass Gasifier," report to National Renewable Energy Laboratory from Battelle Columbus Laboratory, Columbus, OH.

Bioflow, 1994a, "Pressurized Gasifier," informational literature, Varkaus, Finland, received Feb.

Bioflow, 1994b, "The New Generation of Biomass Power Plants," informational literature, Varkaus, Finland, received Feb.

Blackadder, W. H., Lundberg, H., Rensfelt, E., and Waldheim, L., 1994, "Heat and Power Production Via Gasification in the Range 5–50 MW$_e$," *Advances in Thermochemical Biomass Conversion,* by A. V. Bridgwater, ed., Blackie Academic & Professional, London, pp. 449–75.

Brascep Engenharia, 1992, CHESF, Cientec, CVRD, Eletrobras, Shell Brazil, Shell International Petroleum Company, "Brazilian Biomass Power Generation: Phase I Final Report to the Global Environment Facility," Mar.

Breault, R., and Morgan, D., 1992, "Design and Economics of Electricity Production From an Indirectly-Heated Biomass Gasifier," for Battelle Memorial Institute (Columbus, OH) by Tecogen, Inc., Waltham, MA, Oct. 22.

Carpentieri, A. E., Larson, E. D., and Woods, J., 1993, "Future Biomass-Based Electricity Supply in Northeast Brazil," *Biomass and Bioenergy,* Vol. 4(3), pp. 149–73.

Cohn, A., Hay, G. A., and Hollenbacher, R. H., 1993, "The Collaborative Advanced Gas Turbine Program—a Phase I Project Status Report," *Proc. 12th EPRI Gasification Conference,* San Francisco, Oct. 27–29.

Corman, J. C., 1986, "System Analysis of Simplified IGCC Plants," prepared for the US Dept. of Energy by General Electric Company, Corporate Research and Development, Schenectady, NY.

Dawkins, R. P., et al., 1985, "Cost Growth and Performance of Kellog-Rust-Westinghouse-Gasification Combined Cycle Plants," AP-4018, Electric Power Research Institute, Palo Alto, CA.

Day, W. H., 1992, Turbo Power & Marine Systems, Connecticut, personal communication.

de Biasi, V., 1993, "Next Generation Gas Turbine Designs Taking Shape in ATS, CAGT Programs," *Gas Turbine World,* Nov.–Dec., pp. 14–20.

EIA (Energy Information Administration), 1994, "Annual Energy Outlook 1994," DOE/EIA-0383(94), US Dept. of Energy, Washington, DC, Jan.

EPRI (Electric Power Research Institute), 1989, "TAG, Technical Assessment Guide: Electricity Supply 1989," EPRI P-6587-L, Palo Alto, CA, Sept.

Elliott, T. P., and Booth, R., 1990, "Sustainable Biomass Energy," Selected Paper, Shell International Petroleum Company, London, Dec.

Elliott, T. P., and Booth, R., 1993, "Brazilian Biomass Power Demonstration Project," Special Project Brief, Shell International Petroleum Company, London, Sept.

Fluor Daniel, Inc., 1993a, "Evaluation of Advanced Gas Turbine Cycles," Gas Research Institute, Chicago.

Fluor Daniel, Inc., United Technologies, and Texaco, Inc., 1993b, "A Feasibility and Assessment Study for FT4000 Humid Air Turbine (HAT)," TR-102156, Electric Power Research Institute, Palo Alto, CA.

Huotari, J., Helynen, S., and Flyktman, M., 1993, "Indirect Biofixation of CO$_2$," CRE/CON 1424, Combustion and Thermal Engineering Laboratory, Tech. Research Center (VTT) of Finland, Jyvaskyla, Finland, Sept.

Lundberg, H., 1992, TPS, Stockholm, Sweden, personal communication, Sept.

Macchi, E., Consonni, S., Lozza, G., and Chiesa, P., 1994, "An Assessment of the Thermodynamic Performance of Mixed Gas-Steam Cycles, Part A: Intercooled and Steam-Injected Cycles," ASME Paper No. 94-GT-XXX.

Miles, T. R., and Miles, T. R., Jr., 1988, "Reliable Feed Systems for Thermochemical Conversion," *Research in Thermochemical Biomass Conversion,* Elsevier Applied Science, London, pp. 1156–1169.

Paisley, M., 1994, Battelle Columbus Laboratory, personal communication, Columbus, OH, Jan.

Palmer, C. A., and Erbes, M. R., 1993, "LM2500 Fired on Low Btu Fuels," Final report prepared by Enter Software for the Technical Research Center of Finland (Epsoo, Finland), Jan. 28th.

Perlack, R. D., and Wright, L. L., 1993, "Economics of Feedstock Supply," draft, Oak Ridge National Laboratory, Oak Ridge, TN, Nov. 18.

Puhakka, M., 1994, General Manager, Bioflow Ltd., Varkhaus, Finland, personal communication, Feb.

Schombacker, H., 1993, "Modelization of Coal Gasification Processes for Integrated Coal Gasification Combined Cycle (IGCC) Performance Prediction," Diplomthesis; Braunschweigh Technical University (Germany)/Politecnico di Milano (Italy).

Skog, E., 1993, Project Mgr., Varnamo Demonstration Program, Sydkraft Konsult, personal communication, Malmo, Sweden, Dec.

Solar Thermal and Biomass Power Division, 1992, "Electricity From Biomass: a Development Strategy," Office of Solar Energy Conversion, US Department of Energy, DOE/CH10093-152, Washington, DC, Apr.

Theodore, L., and Buonicore, A., 1988, *Air Pollution Control Equipment: Vol. I, Particulates,* CRC Press, Boca Raton, FL.

Tittle, L. B., Van Laar, J. A., and Cohn, A., 1993, "Advanced Aeroderivative Gas Turbines: A Preliminary Study," *Proc. 12th EPRI Gasification Conference,* ibid.

Williams, R. H., and Larson, E. D., 1989, "Expanding Roles for Gas Turbines in Power Generation," in: *Electricity: Efficient End Use and New Generation Technologies and Their Planning Implications,* by T. B. Johansson, B. Bodlund, and R. H. Williams, eds., Lund University Press, Lund, Sweden, pp. 503–553.

Williams, R. H., and Larson, E. D., 1993, "Advanced Gasification-Based Biomass Power Generation," in: *Renewable Energy: Sources for Fuels and Electricity,* T. B. Johansson, H. Kelly, A. K. N. Reddy, and R. H. Williams, eds., Island Press, Washington, DC, pp. 729–85.

Fluid Mechanics of Membrane-Coated Ceramic Filters

R. K. Ahluwalia

H. K. Geyer

Technology Development Division,
Argonne National Laboratory,
Argonne, IL 60439

Analytical models are formulated for evaluating the fluid mechanics of membrane-coated, dead-end ceramic filters. The models are applicable to forward flow as in the filtration mode and reverse flow as in the back-pulse cleaning mode. General criteria are derived to size the filter passages from considerations of Darcy pressure drop, friction pressure drop, and the dynamic head. These criteria together with Reynolds numbers are shown to provide measures of nonuniformities in face velocity and pressure that develop in the filter passages for atmospheric and high-pressure applications. A methodology is presented for optimizing the venturi geometry from the standpoint of minimizing pulse gas usage and controlling the thermal load imposed on the filter assembly.

Introduction

Membrane-coated ceramic filters are being developed by Cera-Mem Corporation for removal of particulate matter from flue gas and hot gas streams [1]. The filter is fabricated by coating a thin ceramic membrane (<50 μm) on a commercially available honeycomb cordierite monolith with multiplicity of passage-ways. The membrane filter operates as a dead-end filter. This flow configuration is achieved by plugging every other cell at the upstream face with a high-temperature inorganic cement (see Fig. 1). Cells that are open at the upstream face are plugged at the downstream face. The particle-laden gas is thus constrained to flow through the membrane-coated porous cell walls. The thin membrane coating has pore size approximately 100-fold finer than that of the monolith support, which has pore size ranging from 4–50 μm. Thus, the retention efficiency of the filter for entrained particles is determined by the membrane pore size. After the particulate matter has accumulated for a defined interval of time or to a defined pressure drop, the filter is back-pulsed to discharge the collected particulates. The back-pulse gas is supplied from a high-pressure reservoir through a blow hole into a converging–diverging venturi fitted to the outlet of the filter assembly.

The CeraMem filters have many advantages over conventional devices. It has filtration face velocity comparable to that for pulse jet bags at the same pressure drop but with up to 40-fold larger filtration area per volume providing a significant saving in filter vessel size/cost, structural steel requirement, and plant space. It provides complete regeneration with a simple back-pulse technique by virtue of membrane pore size smaller than the size of entrained particles so that no plugging of mono-lith/membrane pores can occur. For the same reason, membrane pore size <40 Å, it achieves complete particulate removal (>99.99 percent) even for submicron particles without depending on cake buildup. Finally, all-ceramic construction makes it a candidate for high-temperature applications.

The purpose of this study is to present analytical models for characterizing the fluid mechanics behavior of the membrane ceramic filters. The intent is to develop a model capable of evaluating the performance of these filters during forward flow (filtration mode) so that it can be used to size the filter passages for specified pressure drops. Another objective is to present a fluid mechanics model of reverse flow (backpulse cleaning) and to demonstrate its use in designing venturi geometries. The

final objective is to formulate general criteria for assessing the relative magnitudes of pressure drops due to different mechanisms and the resulting flow nonuniformities along the filter passages. At present, there are no models in literature directly applicable to dead-end membrane filters, although considerable work has been done on candle filters [2, 3].

Analytical Models

In order to analyze the forward and reverse flows, models were developed for jet entrainment and mixing, fluid flow in filter passages, and venturi nozzle and diffuser. Referring to Fig. 1, it is clear that these models can be combined appropriately to represent fluid mechanics of gas filtration and back-pulse cleaning operations.

Jet Entrainment. Entrainment of the suction/plenum gas (subscript 2) by the motive/pulse gas (subscript 1) issuing from the blow hole is modeled as a constant area mixing process. The flow is considered as steady and adiabatic. Disregarding friction at the venturi walls in the mixing zone and assuming the mixing to be complete at the end of the mixing zone, the following are the mass, momentum, and energy conservation equations [2, 4]:

$$\dot{m}_1 + \dot{m}_2 = \dot{m} \tag{1}$$

$$\dot{m}_1 u_1 + \dot{m}_2 u_2 + P_1 A_1 + P_2 A_2 = \dot{m} u + P A \tag{2}$$

$$\dot{m}_1(h_1 + u_1^2/2) + \dot{m}_2(h_2 + u_2^2/2) = \dot{m}(h + u^2/2) \tag{3}$$

It is convenient to discuss the entrainment process as a function of pressure P_2 and the critical pressure at blow hole P_c. Given P_2 and the area A_2, one can determine the temperature T_2, velocity u_2, enthalpy h_2, and the suction gas mass flow rate $\dot{m}_2$ by considering isentropic expansion of the plenum gas from the stagnation/plenum pressure P_{20} (and temperature T_{20}) to pressure P_2. If P_2 is smaller than P_c, the flow is choked at the blow hole so that $P_1 = P_c$, $M_1 = 1$, and the temperature T_1 and the pulse/motive mass flow rate $\dot{m}_1$ can be calculated accordingly. It is then a simple matter to solve Eqs. (2) and (3) for pressure (P) and temperature (T) at the end of the mixing zone. If P_2 is larger than P_c, the flow is not choked at the blow hole so that $P_1 = P_2$ and $M_1 < 1$. It is convenient and useful to perform a separate analysis of the pulse gas distribution system and obtain a relationship between $\dot{m}_1/T_1/u_1$ and P_1 from the knowledge of pulse gas reservoir pressure and temperature and the piping network (diameter, length, valves, turns, surface roughness, blow hole diameter).

Under some conditions, the entrainment ratio ($\dot{m}_2/\dot{m}_1$) can be negative. This situation is modeled by assuming that $P_2 =$
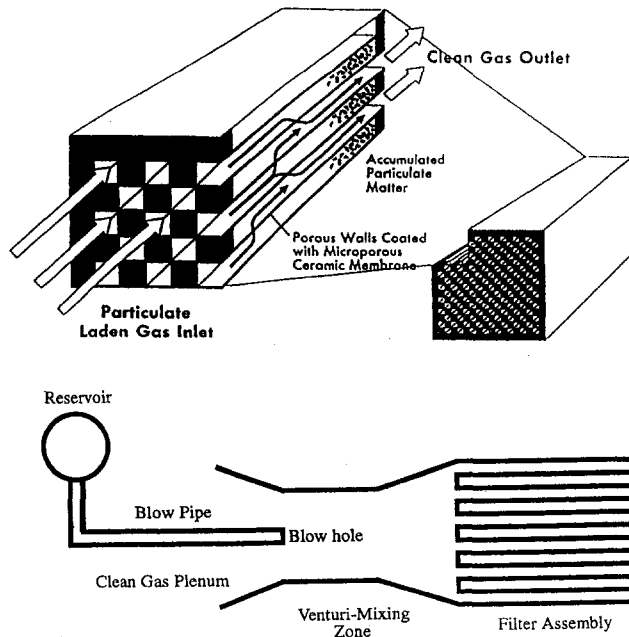

CeraMem® Ceramic Gas Filter

Fig. 1   Flow passage configuration (reproduced with permission from CeraMem Corp.)

P_{20} and $h_2 = h$. Given $\dot{m}_2$, P_2, and T_2, a procedure similar to that above is followed to determine the mass flow rate and the state points of the mixed flow. The foregoing procedure is perfectly general and equally applicable for entrainment of a dissimilar gas provided equations of state are available. The model has been generalized to handle supersonic flow as can be obtained by replacing the blow hole with a converging–diverging nozzle. In this case, special procedures are implemented to locate a shock in the diverging portion of the nozzle or in the mixing zone. This aspect of the model is not emphasized in this paper since existing designs of the filter assemblies are based purely on subsonic/sonic flow.

Filter Passages.   Consider a one-dimensional compressible flow in square channels with porous walls. Accounting for mass/momentum/energy transfer across the porous walls and the skin friction, the following set of conservation equations can be formulated for the inlet and exit channels.

Inlet Channels

$$\frac{d\dot{m}}{dx} = -4\rho W v_c \qquad (4)$$

$$\frac{d(\dot{m}u)}{dx} = -\frac{dP}{dx}A - 4\tau W \qquad (5)$$

$$\frac{d[\dot{m}(h + u^2/2)]}{dx} = -4\rho W v_c h \qquad (6)$$

$$v_c = \frac{K_{\text{eff}}}{\mu}\Delta P \qquad (7)$$

Exit Channels

$$\frac{d\dot{m}}{dx} = 4\rho W v_c \qquad (8)$$

$$\frac{d(\dot{m}u)}{dx} = -\frac{dP}{dx}A - 4\tau W \qquad (9)$$

$$\frac{d[\dot{m}(h + u^2/2)]}{dx} = 4\rho W v_c h_i \qquad (10)$$

Solution of the foregoing equations can be expedited by considering $\dot{m}$, P, and T as independent variables and manipulating the momentum and energy equations such that the derivatives of P and T are calculated sequentially rather than iteratively. For the inlet channels, the rearranged equations are

$$\frac{d\dot{m}}{dx} = -4\rho W v_c \qquad (11)$$

$$\frac{1}{P}\left(\frac{P}{\rho u^2} - \frac{c_p T/u^2}{1 + c_p T/u^2}\right)\frac{dP}{dx}$$
$$= -\frac{1}{2\dot{m}}\left(\frac{1 + 4c_p T/u^2}{1 + c_p T/u^2}\right)\frac{d\dot{m}}{dx} - 2\frac{c_f}{W} \qquad (12)$$

$$\frac{1}{T}\left(1 + \frac{c_p T}{u^2}\right)\frac{dT}{dx} = -\frac{3}{2\dot{m}}\frac{d\dot{m}}{dx} + \frac{1}{P}\frac{dP}{dx} \qquad (13)$$

Similarly, the rearranged equations for the exit channels are

$$\frac{d\dot{m}}{dx} = 4\rho W v_c \qquad (14)$$

$$\frac{1}{P}\left(\frac{P}{\rho u^2} - \frac{c_p T/u^2}{1 + c_p T/u^2}\right)\frac{dP}{dx} = -\frac{1}{2\dot{m}}\left(\frac{1 + 4c_p T/u^2}{1 + c_p T/u^2}\right)\frac{d\dot{m}}{dx}$$
$$- 2\frac{c_f}{W} + \frac{4}{W}\frac{(h_i - h)/u^2}{(1 + c_p T/u^2)}\left(\frac{v_c}{u}\right) \qquad (15)$$

$$\frac{1}{T}\left(1 + \frac{c_p T}{u^2}\right)\frac{dT}{dx}$$
$$= -\frac{3}{2\dot{m}}\frac{d\dot{m}}{dx} + \frac{1}{P}\frac{dP}{dx} + \frac{4}{W}\frac{c_p(T_i - T)}{u^2}\left(\frac{v_c}{u}\right) \qquad (16)$$

This set of ordinary differential equations is solved by a fourth-order Runge–Kutta method. In order to satisfy the outlet boundary condition in the inlet channel, $\dot{m} = 0$ at $x = L$, pressure at

---

Nomenclature

A = flow area
A_f = filtration area
c_f = skin friction coefficient
c_p = specific heat
h = enthalpy
K = permeability, m
k = permeability, m^2
L = passage length

M = Mach number
$\dot{m}$ = mass flow rate
P = pressure
T = temperature
u = flow velocity
v_c = face velocity
W = passage width

x = axial distance
ϵ = surface roughness
μ = viscosity
ρ = density
τ = shear stress

Subscripts

i = inlet channel

---

entrance to the exit channel, P at $x = 0$, is guessed and varied. Depending on the initial guess, 3 to 40 iterations are required to satisfy the outlet boundary condition.

Venturi Diffuser/Nozzle. Flow in the expanding section (area ratio > 1) of the venturi is analyzed strictly on the basis of specified diffuser pressure recovery coefficient (C_p):

$$C_p = \frac{P_2 - P_1}{P_0 - P_1} \qquad (17)$$

where P_0 and P_1 are, respectively, the stagnation and static pressures at inlet, and P_2 is the exit pressure. Flow in a converging nozzle is analyzed similarly on the basis of a specified nozzle efficiency (η):

$$\eta = \frac{h_1 - h_2}{h_1 - h_s} \qquad (18)$$

where h_1 and h_2 are, respectively, the enthalpies at nozzle inlet and exit, and h_s is the enthalpy corresponding to an isentropic expansion to the nozzle exit pressure.

Overall Solution. In the filtration mode, dirty flow enters the filter and exits through the converging–diverging venturi. For specified $\dot{m}$, this flow is analyzed by executing the filter model, the nozzle model, and the diffuser model. Within the filter model, P at $x = 0$ in the exit channel is determined iteratively such that $\dot{m}$ at $x = L$ in the inlet channel is reduced to zero.

To analyze the pulse cleaning mode, ejector model, diffuser model, and channel model are executed sequentially. An iterative procedure is required since the suction gas pressure P_2 in the ejector model is unknown. The Newton–Raphson iteration scheme is employed to determine P_2 such that the exit pressure from the filter model matches the specified pressure in the dirty gas plenum. Alternatively the suction gas flow rate $\dot{m}_2$ can be regarded as unknown and determined iteratively to satisfy the exit pressure constraint. An advantage of $\dot{m}_2$ iterations is that the possibility of negative entrainment can also be factored in. Note that separate iterations are still required within the channel model as in the analysis of the filtration mode.

Results

Filtration Pressure Drop. Figure 2 shows the pressure drop characteristics of 30.5-cm-long membrane filters as a function of channel width (W), face velocity (v_c), gas pressure/temperature, effective permeability (K_{eff}), and the equivalent sand grain roughness (ϵ). The medium is air for atmospheric system calculations and a reducing gas of molecular weight 21.9 g/gmole for the pressurized system. For either medium, the gas viscosity is represented as

$$\mu = \mu_r (T/T_r)^n$$

where $\mu_r = 2.67 \times 10^{-5}$ Pa·s, $T_r = 500$ K, and $n = 0.64$. The effective permeability may be regarded as combination of in-series resistances offered by the monolith (subscript 1), membrane (2), adherent ash deposit layer (3), and the removable ash deposit (4):

$$\frac{1}{K_{eff}} = \sum_{i=1}^{4} \frac{\Delta x_i}{k_i} \qquad (19)$$

where Δx is the thickness and k is the permeability (m²). Finally, Churchill's equation is used to determine the skin friction coefficient as a function of Reynolds number and the roughness parameter for both laminar and turbulent flows.

2-mm Channels. At 2 cm/s face velocity and $P = 1$ atm, the flow in the channels is laminar so that the pressure drop (ΔP) is independent of wall roughness. The observed experi-
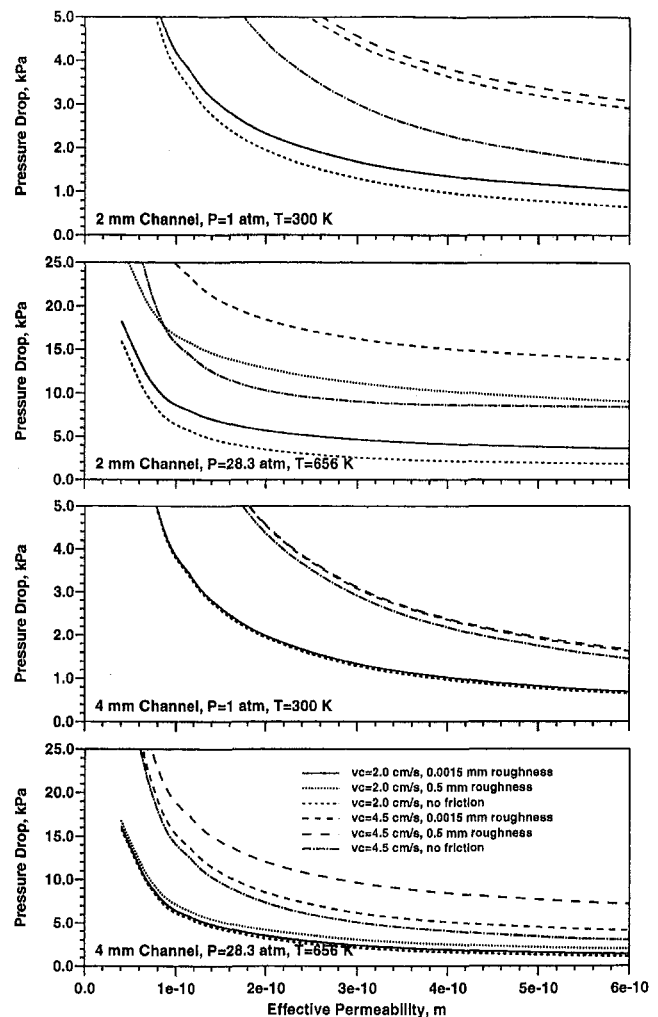

Fig. 2 Filtration pressure drop behavior as a function of channel width, face velocity, wall roughness, and gas pressure; channel length 30.5 cm

mental ΔP for clean channels is 1.3 kPa (5.2 in. H_2O) from which a K_{eff} of 4×10^{-10} m may be inferred according to Fig. 2(a). The model calculations indicate that a ΔP of 1 kPa may be attributed to Darcy flow and 0.3 kPa to friction effects. In many applications, this filter would be pulsed at ΔP of about 1.7 kPa (6.8 in. H_2O), which corresponds to a K_{eff} of 3×10^{-10} m. This implies that if ash had a specific permeability of 4.5×10^{-14} m², pulse cleaning is initiated when the cake thickness builds up to 0.038 mm.

At $v_c = 4.5$ cm/s and $P = 1$ atm, the channel flow is mostly laminar and ΔP is almost independent of the wall roughness. The observed experimental ΔP for clean channels is 3.36 kPa (13.5 in. H_2O), which compares well with a calculated value of 3.63 kPa at the above-inferred K_{eff} of 4×10^{-10} m. The calculations indicate that 2.3 kPa of ΔP may be attributed to Darcy flow and 1.3 kPa to the friction effects.

At $P = 28.3$ atm and $T = 656$ K, the channel flow becomes turbulent. At 2 cm/s face velocity and $K_{eff} = 4 \times 10^{-10}$ m, the calculated pressure drop for smooth channels is 4.3 kPa (16.6 in. H_2O) of which 2 kPa is due to friction effects. If the walls are treated as rough, the pressure drop increases to 10 kPa at 0.5 mm equivalent sand grain roughness. At this operating point, ΔP (friction) $\gg \Delta P$ (Darcy) and the flow may be regarded as friction dominated. As reference, note that ϵ for smooth cement is 0.3 mm.

At $v_c = 4.5$ cm/s and $P = 28.3$ atm, calculated ΔP for smooth channels is 15.1 kPa (60.6 in. H_2O) of which 6.4 kPa can

be attributed to friction effects. The pressure drop becomes unacceptable, >50 kPa, if the channel walls were treated as 0.5 mm rough. Given the uncertainty over ϵ, one would not select 2-mm channels for service at 4.5 cm/s face velocity in most high-pressure applications.

4-mm Channels. At $P = 1$ atm, the channel flow is laminar. The computed pressure drop is 1 kPa (4.1 in. H_2O) at $v_c = 2$ cm/s and $K_{eff} = 4 \times 10^{-10}$ m, and 2.4 kPa (9.5 in. H_2O) at $v_c = 4.5$ cm/s and same K_{eff}. More than 95 percent of computed ΔP occurs across the porous walls at $v_c = 2$ cm/s and more than 90 percent at the higher face velocity. Thus, the friction effects are not important in 4-mm channels for service at atmospheric pressures.

At $P = 28.3$ atm, the channel flow is turbulent. The computed pressure drop for smooth walls is 1.9 kPa (7.7 in. H_2O) at $v_c = 2$ cm/s and $K_{eff} = 4 \times 10^{-10}$ m, 85 percent of which is due to the porous media. The pressure drop increases to 2.5 kPa (10.2 in. H_2O) if the walls are treated as 0.5 mm rough. At the higher face velocity, 4.5 cm/s, computed ΔP is 5.1 kPa (20.5 in. H_2O) for smooth walls, 8.4 kPa (33.9 in. H_2O) for 0.5-mm rough walls, and 4 kPa (16.1 in. H_2O) for flow without friction. Thus, friction and Darcy pressure drops become equally important at 4.5 cm/s face velocity and $P = 28.3$ atm.

Pulse Cleaning of Atmospheric System. A number of parametric calculations have been performed to explore the fluid mechanics of the pulse cleaning operation. A 15.2 cm $\times$ 15.2 cm square filter assembly is selected as reference. The assembly contains 900 4 mm $\times$ 4 mm channels, each 30.5 cm long, and blocked at alternate ends. The total filtration area is 2.2 m². For pulse cleaning, compressed air at 334 K issues from a 1.9-cm-dia blow hole into a converging–diverging venturi with 10.2 cm $\times$ 10.2 cm throat cross section. The venturi and the blow pipe are located in a plenum containing air at 422 K and atmospheric pressure. Flow in the diverging portion of the venturi is modeled as a diffuser with 0.5 pressure recovery coefficient. When choked, the total flow rate through the blow hole is 0.37 kg/s at stagnation pressure (P_0) of 5.9 atm, 0.50 kg/s at $P_0 = 7.9$ atm, and 0.63 kg/s at 9.9 atm. At zero entrainment, these represent average face velocities of 15.4 cm/s, 20.7 cm/s, and 25.9 cm/s.

Role of Effective Permeability. Figure 3 displays the computed jet entrainment ratio, average face velocity, and the pressure generated inside the clean channel as a function of effective permeability ($\epsilon = 0.5$ mm). Using the filtration pressure drop data presented in Fig. 2, the results in Fig. 3 can be reinterpreted in terms of the trigger pressure drop, i.e., ΔP at which pulse cleaning is initiated. A pressure of 15.5 kPa gage (2.25 psig) is calculated at inlet to clean channel for $P_0 = 5.9$ atm and $K_{eff} = 4 \times 10^{-10}$ m, which compares favorably with 13.8 kPa gage measured in some laboratory experiments. The gage pressure is seen to increase mainly with P_0 and secondarily with decrease in K_{eff}. A higher gage pressure of 29.6 kPa can be established at 4×10^{-10} m effective permeability by raising P_0 to 9.9 atm.

A nearly uniform pressure field is established inside the clean-gas channels at low effective permeability. The pressure variation along the channel increases with K_{eff} and P_0. The face velocity field exhibits the same trends.

The amount of plenum gas entrained by the pulse jet is very sensitive to effective permeability. As K_{eff} decreases (e.g., due to deposit buildup, sintering, or low specific permeability), so does the entrainment ratio. There is a critical K_{eff} at which the net entrainment is zero and below which a part of the motive gas is reflected back into the plenum. This condition must be avoided (e.g., by more frequent pulsing) because it represents underutilization of pulse gas compression energy with concomitant reduction in face velocity. Both v_c and channel gage pressure are deemed important in determining the efficacy of the pulse cleaning operation.
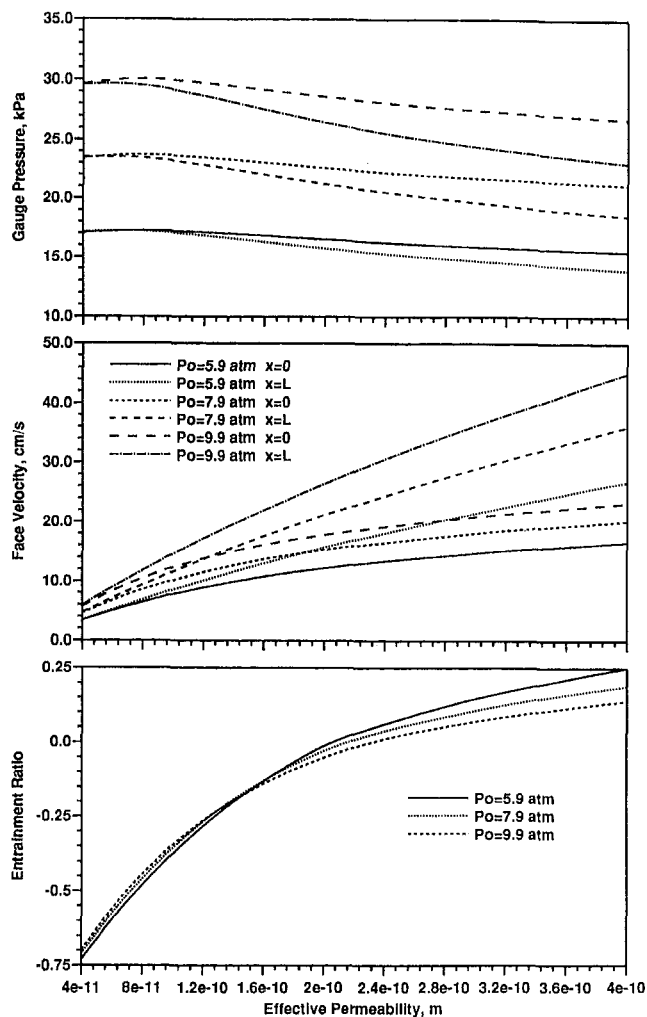
Fig. 3 Fluid mechanics of pulse cleaning operation on a 15.2 $\times$ 15.2 $\times$ 30.4 cm filter assembly attached to a 10.2 $\times$ 10.2 cm throat venturi. Compressed gas at 334 K is supplied through a 1.9-cm-dia blow hole. Exit pressure from the filter is 1 atm.

Venturi Geometry. For optimum pulse cleaning, the venturi should be designed to maximize jet entrainment. Figure 4 quantifies the improvement in pulse cleaning with narrowing of venturi throat. For $K_{eff} = 2.4 \times 10^{-10}$ m and $P_0 = 5.9$ atm, the entrainment ratio can be increased from 0.08 at $A_{th} = 100$ cm² to 1.02 at $A_{th} = 22.5$ cm² with corresponding increase in channel pressure from 16.7 kPa gage to 35.5 kPa gage.

In general, as the venturi throat is made narrower, jet entrainment increases, as does the pressure generated in the channel. There is a critical throat area, 26.5 cm² for $P_0 = 5.9$ atm, below which further increase in flow kinetic energy obtained by reduction in A_{th} and improvement in entrainment is not usefully converted to the pressure head. At this point, the excess pressure generated in the channel begins to level off or to even diminish slightly. For a given filter (L, W, and K_{eff}) and pulse system (P_0, blow hole diameter), the critical A_{th} corresponding to the maximum channel pressure, is a function of the pressure recovery coefficient. As A_{th} is further reduced, a mismatch develops between the venturi flow and the filter flow in that the pressure generated at the venturi is insufficient to drive the combined motive gas and the suction gas through and across the filter assembly. Thus, a part of the combined flow has to be reflected back into the plenum. The model has not been extended into this flow regime because it clearly represents a suboptimal operating condition.

Journal of Engineering for Gas Turbines and Power

Fig. 4 Improvement in pulse cleaning with narrowing of venturi throat; effective permeability is 2.4e-10 m
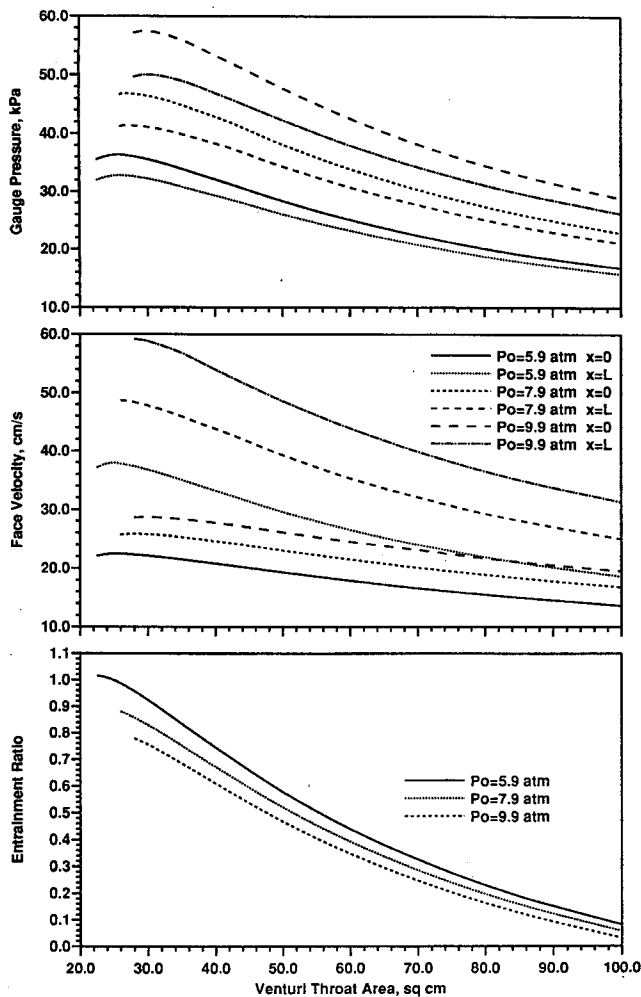
Filter Geometry. Figure 5 displays the sensitivity of pulse cleaning operation to passage geometry corresponding to the reference venturi throat area (103.2 cm^2). The pulse system variables, P_0 and blow hole diameter, are held constant as is the cross-sectional area of the filter assembly (232.2 cm^2), which implies that there are four times as many channels for 2-mm passages (100/in.^{2}) as for 4-mm channels (25/in.^{2}). Plotted in Fig. 5 is the axial variation of the pressure difference (ΔP) between the clean and dirty channels. From the Darcy equation, v_c is linearly related to ΔP through the multiplier K_{eff}/μ. It is instructive to rearrange the Darcy equation as

$$-\Delta P = \frac{\dot{m}(1 + E)}{\rho A_f K_{\text{eff}}/\mu}$$

where $\dot{m}$ is the flow rate of pulse gas and E is the entrainment ratio. The reduction in ΔP as the passages are made longer or narrower (at constant $\dot{m}$) is a direct consequence of ΔP being inversely proportional to the filtration area A_f and can be overcome (within limits of mismatch) by increasing $\dot{m}$. Of greater concern is the nonuniformity of ΔP in narrow passages, which is accentuated at large pulse gas flow rate, entrainment or dynamic head. Thus, in applications requiring large ΔP for dislodging ash deposits without nonuniformity in ΔP, short 4-mm channels should be preferred over long 2-mm channels.

Pulse Cleaning of Pressurized System. CeraMem filters are being considered for use in integrated gasification combined cycle plants (IGCC). Typically, particulate-laden reducing gas,

molecular weight ~ 21.9, is to be cleaned at high pressure (~ 28.3 atm) and temperature (656 K). Figure 6 depicts the fluid mechanics behavior of a filter assembly, 30.5 cm in diameter, pulsed with compressed gas of same composition at 50 atm stagnation pressure and 422 K temperature. For purpose of this parametric study, the blow hole diameter is held constant at 3.81 cm giving a choked flow rate ($\dot{m}$) of 9.8 kg/s. The filter assembly can contain 9400 2-mm channels ($A_f = 11.5$ m^2 at $L = 30.5$ cm) or 2350 4-mm channels ($A_f = 5.7$ m^2 at $L = 30.5$ cm). At zero entrainment the average face velocity is 5 cm/s for 2-mm channels or 10 cm/s for 4-mm channels ($L = 30.5$ cm).

Venturi Geometry. Figure 6 confirms the existence of a critical venturi throat size that maximizes jet entrainment and leads to the smallest thermal load (difference between mixed gas and plenum gas temperatures) imposed on the filter assembly by the mixed pulse gas. For reasons of structural integrity, large gage pressures shown in Fig. 6 may not be desirable. However, these results can be interpreted to mean that for specified channel geometry, reservoir pressure, and gage pressure, one can size the blow hole and the venturi throat for maximum entrainment and minimum pulse gas usage. Although the results are shown for one value of effective permeability (1.5 × 10^{-10} m) and wall roughness (0.5 mm), similar trends are obtained at all values of K_{eff} and ϵ.

Pressure Profiles. Figure 7 depicts the axial profiles of pressure difference (ΔP) between the clean and dirty channels as a function of passage width, passage length, and the friction effects. As mentioned earlier, face velocity is linearly related to ΔP through the multiplier K_{eff}/μ: $v_c \simeq 6 \times 10^{-10} \Delta P$ for
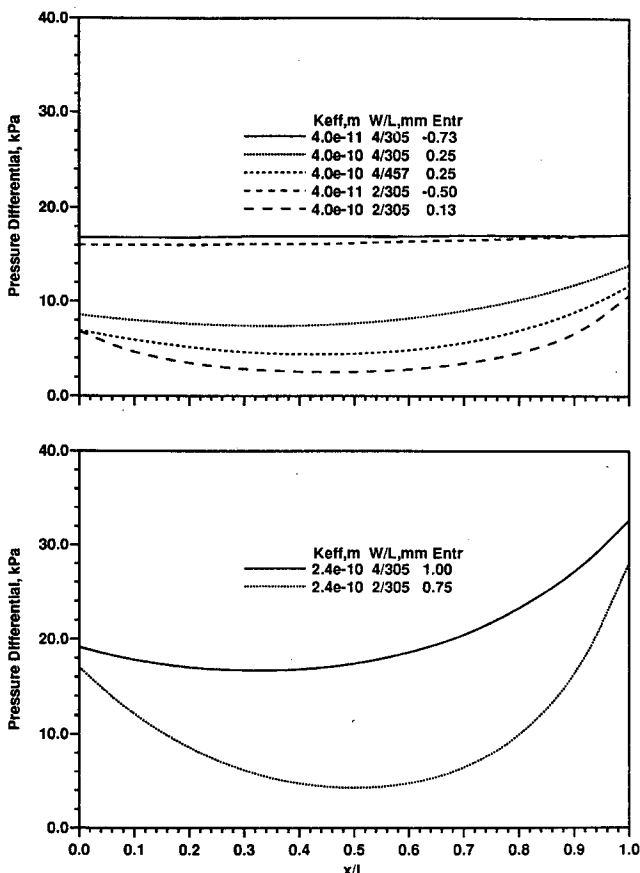

Fig. 5 Sensitivity of pulse cleaning operation to passage geometry. Venturi throat area is 103.2 cm^2 in Fig. 5(a) and 24.5 cm^2 in Fig. 5(b). The stagnation pressure is held constant at 5.9 atm.
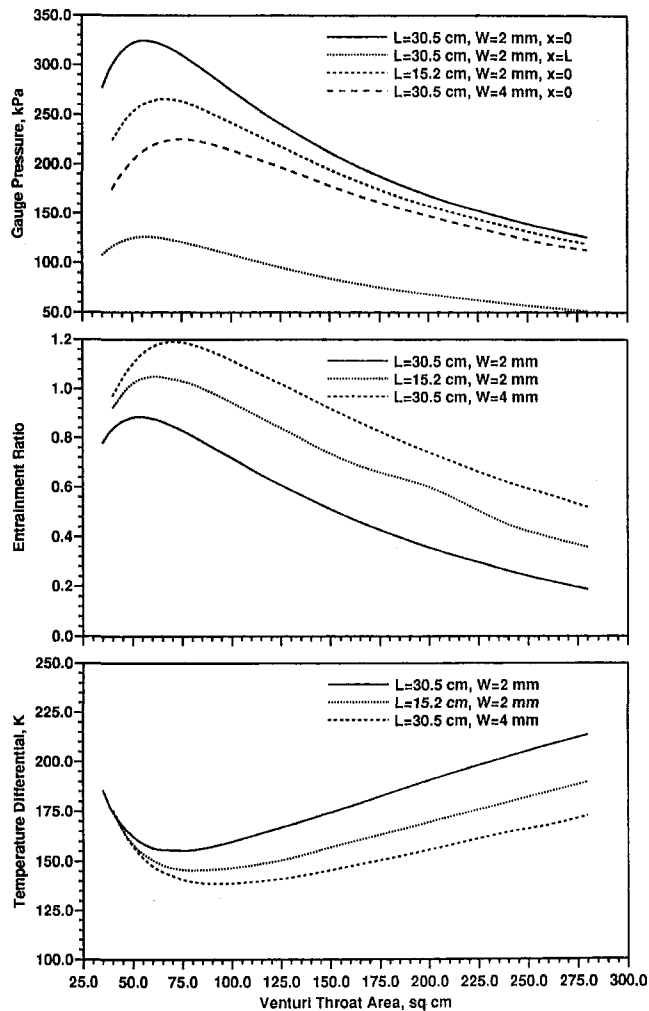
Fig. 6 Fluid mechanics of pulse cleaning operation on a 30.5-cm-dia filter assemblies: 0.5 mm wall roughness and 1.5e-10 m effective permeability. Compressed gas at 50 atm and 422 K is supplied through a 3.81-m-dia blow hole into a plenum at 28.4 atm and 656 K.

conditions of Fig. 7. The ΔP profiles are grossly nonuniform. Nonuniformity in ΔP is magnified by system pressure (compare with Fig. 5), increase in channel length or narrowing of passages. Because of pressure rise due to loss in momentum, ΔP and face velocity are significantly large in the back portion of the clean channel. Friction effects can be beneficial in maintaining finite ΔP in the front portion of the clean channel, although enhanced friction due to wall roughness produces a characteristic dip in ΔP in the middle portion of the channel.

Discussion

Pressure Drops. The filtration and pulse cleaning behavior of membrane-coated ceramic filters can be characterized on the basis of three kinds of pressures/pressure drops: Darcy pressure drop (ΔP_d), friction pressure drop (ΔP_f), and the dynamic head (ΔP_h). In selecting or designing filters and filter systems, the variables of interest are filter length (L), passage width (W), face velocity (v_c), pressure, temperature, density (ρ), venturi geometry, pulse gas reservoir pressure (P_0) and the blow hole diameter. The Darcy pressure drop ΔP_d is, of course, related to v_c and K_{eff} as

$$\Delta P_d = \frac{\mu v_c}{K_{eff}} \tag{21}$$

The friction pressure drop ΔP_f can be expressed in terms of the face velocity v_c as

$$\Delta P_f = 8c_f\rho v_c^2\left(\frac{L}{W}\right)^3 \tag{22}$$

where the friction coefficient c_f is a function of the roughness parameter (ϵ/W) and the Reynolds number (Re). In terms of v_c, Re can be written as

$$Re = 4\frac{\rho v_c L}{\mu} \tag{23}$$

Finally, the dynamic pressure head can be represented in terms of the variables of interest as

$$\Delta P_h = 16\rho v_c^2\left(\frac{L}{W}\right)^2 \tag{24}$$

It is interesting to note that whereas ΔP_d is independent of channel geometry and system pressure, ΔP_f and ΔP_h are strong functions of ρ, L, and W. For specified v_c, Reynolds number is only a function of channel length but not channel width. Consistent with the previous discussion related to Fig. 2, flow is laminar (Re < 500) for $L = 30.5$ cm, $v_c = 4.5$ cm/s at $P = 1$, and turbulent (Re $\simeq 4400$) at $P = 28.34$ atm.

Normally, the filter assembly should be designed such that the parasitic friction losses are small in comparison to the Darcy pressure drop. This criterion is satisfied if

$$\frac{W}{L} > \left(8c_f\,Re\,\frac{K_{eff}}{L}\right)^{1/3} \tag{25}$$

According to this criterion, short and wide passages are preferred over long and narrow passages. For laminar flow, as at $P = 1$ atm and $v_c < 18$ cm/s, $K_{eff} = 4 \times 10^{-10}$ m and $L = 30.5$ cm, ΔP_f is smaller than ΔP_d provided $W > 2.7$ mm. At $P = 25.3$ atm, $v_c = 4.5$ cm/s, and same K_{eff} and L, this criterion dictates that $W > 3.7$ mm.

As the gas flows down the channel (dirty channel in filtration mode and clean channel during pulse cleaning) and across the porous walls, it loses momentum and gains static pressure (ΔP_h). This pressure recovery counteracts the pressure drop due to friction effects (ΔP_f). On the other hand, the flow along the exit channel loses static pressure due to a gain in momentum, in concert with the friction pressure drop. Clearly, nonunifor-
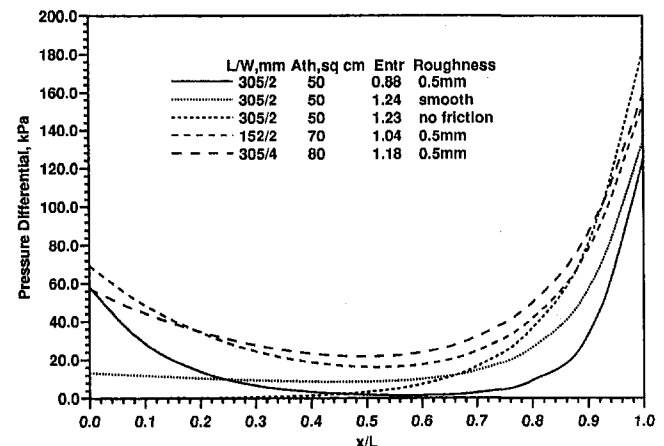

Fig. 7 Profiles of differential pressure in the clean channel during pulse cleaning operation; effective permeability 1.5e-10 m

mity in pressure and flow distributions will result if $\Delta P_h >$ ΔP_d (see Fig. 7). This criterion is satisfied if

$$\frac{W}{L} > \left(16 \text{ Re } \frac{K_{\text{eff}}}{L} \right)^{1/2}$$

According to this criterion, $W > 1.0$ mm for atmospheric operation and $L = 30.5$ cm, $K_{\text{eff}} = 4 \times 10^{-10}$ m, and $v_c = 4.5$ cm/s (Re $\simeq$ 500). Under the same conditions, but at $P = 28.3$ atm (Re $= 4400$), the criterion requires that $W > 3.0$ mm. If v_c is also raised to 30 cm/s, as during pulse cleaning, nonuniform pressure distribution may be observed (as in Fig. 7) if $W <$ 7.8 mm.

Pulse Cleaning. In general a reverse flow cleaning system must be designed to generate a pressure pulse of predetermined magnitude (ΔP) in the clean channel. Effective permeability at which cleaning is to be initiated can be inferred from the trigger pressure. Together K_{eff} and ΔP specify the required face velocity. The task is then to determine the reservoir pressure, blow hole size, and venturi geometry capable of achieving the target ΔP. For reasons stated earlier, it is desirable to minimize compressed gas usage and maximize plenum gas entrainment. A methodology to accomplish this objective is best enumerated through a sample problem. The dimensions of the filter assembly are the same as for calculations presented in Fig. 4: 15.2 cm $\times$ 15.2 cm cross section, $L = 30.5$ cm, $W = 4$ mm, 25 channels/in.^{2}, plenum pressure = 1 atm, plenum gas temperature = 422 K, and $K_{\text{eff}} = 2.4 \times 10^{-10}$ m. Figure 8 shows that for given stagnation pressure (P_0) and temperature (322 K) at the blow hole, there are many combinations of blow hole diameter and venturi throat area that can achieve the target ΔP (14 kPa/2 psig). The optimum combination is the one that leads to the maximum flow entrainment, i.e., the smallest blow hole diameter. Note that at $P_0 = 5.9$ atm the optimum nozzle/blow hole area is one-fourth of the original design (2.8 cm^2 in Fig. 3), and the venturi throat area is one-sixth of the original design (104 cm^2). The optimum combination achieves an entrainment ratio of 2.2 compared to only 0.1 in the original design.

The combination of P_0, blow hole diameter and venturi throat area that minimizes compression power can also be determined from the results presented in Fig. 8. The results favor the lowest P_0 capable of achieving the target ΔP, but other considerations such as the reservoir volume may dictate that somewhat larger P_0 be selected.

Model Assessment. Since this is a steady-state model, the transient effects/accumulation terms have been ignored. The transient effects are introduced by ash buildup during the filtration mode, time for flow reversal as the mode changes from filtration to back-pulse cleaning, mechanics of ash dislodging, and the response time of the pulse gas distribution system. Flow adjustment time (τ) for the filter system is always small and can be estimated as $L/\sqrt{\gamma RT}$. For air at 500 K and $L = 1$ m (filter and venturi length), τ is estimated as 2 ms, implying that the unsteady accumulation terms in the fluid mass, momentum, and energy equations can be neglected in all design analyses in which the period of interest is longer than 2 ms. The response time of the pulse gas distribution system is generally determined by the time constant of the solenoid pulse valve, which is generally greater than 10 ms even for fast-acting valves. As a first approximation, the steady-state model presented in this work can be applied to back-pulse cleaning during the time of valve opening and closing by employing time-varying boundary conditions for blow hole. Following a similar argument, the effect of ash buildup on porous walls can be modeled as a quasi-steady process with time-varying effective permeability given by Eq. (20) and ash deposition velocity equal to local face velocity. This feature, along with constriction in flow area due to deposit buildup, has been incorporated in
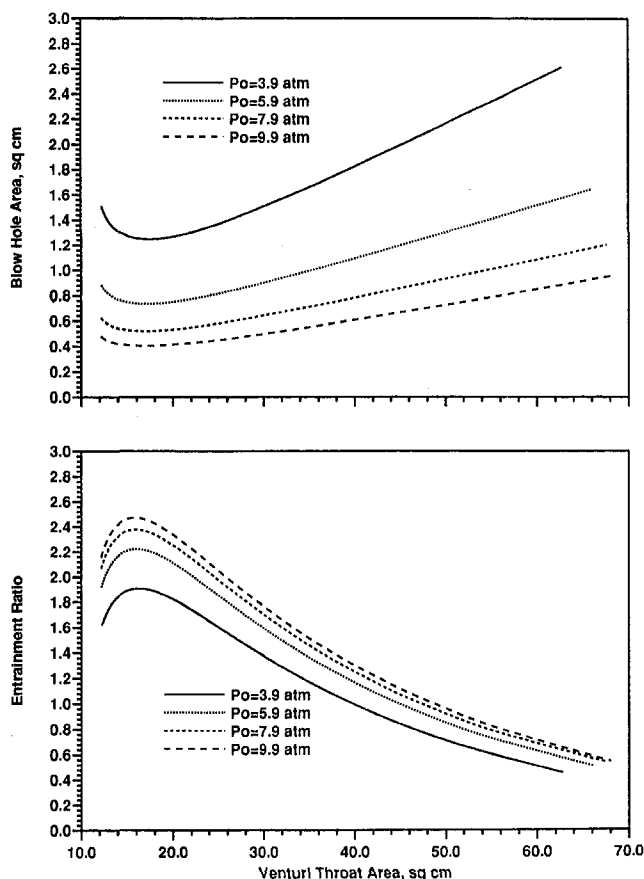
Fig. 8 Optimization of pulse cleaning system: 900 passages, $L = 30.5$ cm, $W = 4$ mm, plenum gas pressure = 1 atm, blow gas at 334 K, and 2.4e-10 m effective permeability

the model and will be presented in a future publication. Note that a transient heat conduction model is still required if one is interested in determining the temperature profiles in the monolith and the thermomechanical stresses generated as a result.

In a parallel effort, three-dimensional simulations of fluid mechanics of backpulse cleaning are being conducted. These confirm the existence of flow reflection (negative entrainment in Fig. 3) and of the optimum venturi geometry at which the entrainment ratio is maximum (as in Figs. 6 and 8). A laboratory apparatus is also being assembled to obtain experimental data and verify the fluid mechanics model [5].

Conclusions

1 In designing dead end, membrane-coated ceramic filters, attention must be paid to the Darcy pressure drop across the porous structure (ΔP_d), friction pressure drop along the passages (ΔP_f), and the dynamic head (ΔP_h). It is a prudent practice to ensure that the parasitic pressure drop (ΔP_f) is always smaller than the working pressure drop (ΔP_d). This condition will be challenged more drastically during the reverse flow (pulse cleaning) rather than the forward flow. The friction pressure drop is proportional to the gas density, square of face velocity, and cube of L/W. Thus, in applications where ΔP_f becomes comparable to ΔP_d (e.g., at high pressure), short/wide channels should be preferred over long/narrow channels.

2 Nonuniformities in face velocity and channel pressure distribution can develop at large dynamic heads. Although ΔP_h and ΔP_f have similar functional relationships with gas pressure, v_c, and L/W, the nonuniformities they introduce tend to counteract each other. In situations where ΔP_h is significant in relation to ΔP_d, peaks in face velocity and ΔP are observed near the

dead end of the inlet channel. If ΔP_f is also comparable to ΔP_d, a minimum in v_c or ΔP appears near the middle of the channel. In applications where these nonuniformities are of concern, one should investigate the possibility of decreasing L, increasing W, or reducing v_c.

3   The analytical models developed in this work constitute the requisite tools for optimizing the pulse cleaning. A methodology has been presented to size the blow hole and the venturi throat to obtain predetermined pressurization of the inlet channel while maximizing the entrainment of plenum/suction gas by the pulse/motive gas. This design point is considered optimal because it incurs minimal usage of the compressed gas and leads to the smallest thermal load on the filter assembly. Furthermore, if the reservoir pressure is regarded as variable, then a combination of P_0 and pulse gas flow rate can be determined to minimize the compression energy.

4   As future work, multidimensional flow modeling needs to be performed to guide in the selection of axial dimensions of the venturi section and ensure complete mixing of the motive gas with the suction gas.

References

1   Goldsmith, R. L., and Abrams, R. F., "Ceramic Filter for Fine Particle Control," *Ninth Annual Coal Preparation, Utilization, and Environmental Control Contractors Conference Proc.,* Pittsburgh, PA, July 1993, pp. 539–546.

2   Pitt, R. U., and Leitch, A. J., "A Simple Method to Predict the Operation of Flue Gas Filter Pulse Cleaning Systems," *Proc. 1991 International Conference (ASME) on Fluidized Bed Combustion,* Vol. 3, Apr. 1991, pp. 1267–1281.

3   Laux, S., Giernoth, B., Bulk, H., and Renz, U., "Aspects of Pulse Jet Cleaning of Ceramic Filter Elements," *Gas Cleaning at High Temperatures,* Blackie Academic & Professional, Glasgow, UK, 1993, pp. 203–224.

4   DeFarte, L. A., and Hoerl, A. E., "Optimum Design of Ejectors Using Digital Computers," *Chemical Engineering Progress Symposium Series,* No. 21, Vol. 55, 1959, pp. 43–51.

5   Ahluwalia, R. K., Geyer, H. K., Im, K. H., Zhu, C., Shelleman, D., and Tressler, R., "Assessment of Ceramic Membrane Systems," *Proc. Advanced Coal-Fired Power Systems Review Meeting,* Morgantown, WV, Mar. 1995.

A Study on Low NO$_x$ Combustion in LBG-Fueled 1500°C-Class Gas Turbine

T. Nakata

Department of Aeronautics and Space Engineering,
Tohoku University,
Sendai, Miyagi, Japan

M. Sato

T. Ninomiya

T. Hasegawa

Central Research Institute of Electric Power Industry,
Yokosuka, Kanagawa, Japan

Developing integrated coal gasification combined-cycle systems ensures cost-effective and environmentally sound options for supplying future power generation needs. The reduction of NO$_x$ emissions and increasing the inlet temperature of gas turbines are the most significant issues in gas turbine development in Integrated Coal Gasification Combined Cycle (IGCC) power generation systems. The coal gasified fuel, which is produced in a coal gasifier of an air-blown entrained-flow type has a calorific value as low as $\frac{1}{10}$ of natural gas. Furthermore, the fuel gas contains ammonia when a gas cleaning system is a hot type, and ammonia will be converted to nitrogen oxides in the combustion process of a gas turbine. This study is performed in a 1500°C-class gas turbine combustor firing low-Btu coal-gasified fuel in IGCC systems. An advanced rich-lean combustor of 150-MW class gas turbine was designed to hold stable combustion burning low-Btu gas and to reduce fuel NO$_x$ emissions from the ammonia in the fuel. The main fuel and the combustion air are supplied into a fuel-rich combustion chamber with strong swirl flow and make fuel-rich flame to decompose ammonia into intermediate reactants such as NHi and HCN. The secondary air is mixed with primary combustion gas dilatorily to suppress the oxidization of ammonia reactants in fuel-lean combustion chamber and to promote a reducing process to nitrogen. By testing under atmospheric pressure conditions, the authors have obtained a very significant result through investigating the effect of combustor exit gas temperature on combustion characteristics. Since we have ascertained the excellent performance of the tested combustor through our extensive investigation, we wish to report on the results.

Introduction

Fueled by recent energy consumption trends in Japan, the demand for electric power generation has been further increasing. There are already plans to build more thermoelectric power plants as well as nuclear power plants. The technological development of Coal-Gasification Combined-Cycle Systems has been promoted by Japan and other countries as a power generation system that can utilize coal reserves.

The combined-cycle power-generation system is a system to combine a topping cycle (gas turbine) and a Rankine cycle (steam turbine) as a bottoming cycle. In the case of the coal-gasification combined-cycle system, which uses coal as fuel, the facilities consists of the following components: coal gasifier to gasify coal and to remove ash, clean-up mechanism to desulfurize produced coal gas and to remove dust, high-temperature gas turbine, steam turbine, and exhaust heat recovery boiler. The thermal efficiency of the system differs depending on the specification of each component used. The system developed in Japan combines an air-blown entrained-bed coal-gasifier, a hot gas clean-up system, and a 1300°C-class gas turbine. The thermal efficiency of the overall IGCC system at the end of the electric transfer is 43.5 percent (on a higher heating value base). This is much improved compared to 38 to 39 percent thermal efficiency of the existing power-generation system using pulverized coal. Furthermore, by increasing the gas temperature at the gas-turbine inlet to 1500°C, it is possible to improve the thermal efficiency of the overall IGCC system up to 45 percent.

The authors are engaged in the research and development of the 1500°C-class gas-turbine combustor for the purpose of producing more cost-effective and environmentally sound options for the coal-gasification combined-cycle power-generation system. When the temperature of the gas turbine rises, the shortage of combustor wall-cooling air and the increased NO$_x$ emission become a primary concern. In order to develop the 1500°C-class gas turbine combustor, therefore, characteristics of the combustor wall-cooling efficiency and the improvement of NO$_x$ emission are considered critically important issues.

In this study, based on the knowledge obtained from the research and development of the 1300°C-class combustor, a 1500°C-class combustor is designed, assembled, and tested. The performance of the combustor is evaluated under atmospheric-pressure conditions. This report will provide useful engineering guidelines for the research and development of the gas turbine combustor.

1500°C-Class Gas Turbine Combustor for IGCC Systems Using Low-Calorie Fuel

Design Concept of the Combustor. As indicated by the fuel composition in Table 1, the coal-gasified fuel produced in an air-blown entrained-bed coal gasifier has calorific value as low as one tenth of such high-calorie gas as methane. Another characteristic of the coal-gasified fuel is that it normally contains about 1000 ppm NH$_3$, which is the source of fuel NO$_x$.

Figure 1 indicates relationship between the combustor outlet-gas temperature and the air distribution in the gas-turbine combustor using low-calorie coal-gasified fuel. To calculate air distribution, the overall amount of air is assumed to be 100 percent. The amount of air for combustion is first calculated at a theoretical mixing ratio. Then, 30 percent of the total air is considered as the cooling air for the combustor wall liner, and the remaining

Table 1 Standard composition of the coal gasified fuel

Composition			
	CO	22.9	%
	H_2	8.6	%
	CH_4	0.5	%
	CO_2	12.9	%
	H_2O	2.0	%
	N_2	53.1	%
	NH_3	1000	ppm
HHV	4190		kJ/m^3N
	(1000		$kcal/m^3N$)
LHV	3960		kJ/m^3N
	(950		$kcal/m^3N$)

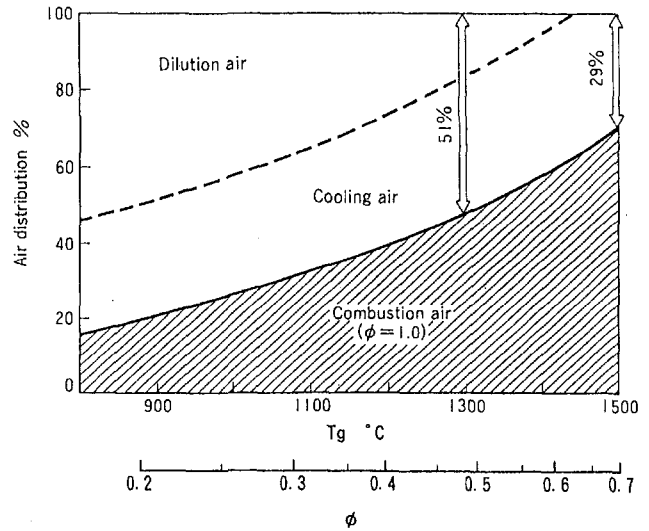Fig. 1 Air distribution design of a gas turbine combustor that burns low-Btu fuel

air is considered diluting air. According to the figure, the ratio of combustion air increases as the gas turbine temperature rises. As a result, the ratio of cooling air and diluting air decreases significantly, and thus, the flexibility of the combustor design is minimized.

To summarize these characteristics, it can be said that the design concept of the gas turbine combustor utilizing low-calorie fuel should consider the following issues when the gas-turbine temperature rises:

1 Combustion stability; it is necessary to stabilize the flame of low-calorie fuel.
2 Low NO_x-emission technology to restrain the production of fuel NO_x from NH_3 in the fuel.
3 Cooling structure to cool the combustor wall efficiently with a lower amount of air.

In this study, a 1500°C-class combustor was designed and assembled on a trial basis, building upon the model coal-gasification gas turbine combustor for low-calorie fuel [1].

Figure 2 presents characteristics of the designed and tested 1500°C-class combustor. Figure 3 illustrates the external view of the combustor. This combustor is one of the multi-can combustors that are to be used for the 150 MW-class power-generation gas turbine. The overall length of the combustor is 1320 mm and the internal diameter is 356 mm.

Assurance of Flame Stabilization. In order to assure flame stability of low-calorie fuel, an auxiliary combustion chamber is installed at the entrance of the combustor. The ratio of the fuel allocated to the auxiliary combustion chamber is 15 percent of the overall amount of fuel. The fuel and the combustion air are injected into the chamber through the subswirler with swirling angle at 30 deg. By setting the equivalence ratio in this chamber at 1.0, which is the stoichiometric ratio, under rated-load conditions, a stable flame can be maintained. As indicated in the following section, this flame is especially effective to maintain flames in the rich-combustion zone.

Fuel-NO_x Reduction. To restrict the production of fuel NO_x attributable to the NH_3 contained in the fuel, a two-stage combustion method (rich-lean combustion method) was introduced. The tested combustor has a two-chamber structure, which separates the primary combustion zone from the secondary combustion zone. In addition, the combustor has three main design characteristics as indicated below:

Design of the Air-to-Fuel Ratio in the Primary Combustor. The equivalence ratio of the primary combustor is determined based on the combustion tests previously conducted using a

Nomenclature

CH_4 = methane concentration in the fuel, Vol%
CO = CO emission concentration, ppm by volume
C.R. = conversion ratio from the ammonia in the fuel to NO_x
$F/A(W)$ = fuel-to-air ratio by weight
$F/A(V)$ = fuel-to-air ratio by volume
HHV = higher heating value of the fuel, kJ/m^3
LHV = lower heating value of the fuel, kJ/m^3
L = axial distance of the combustor, mm
NH_3 = ammonia concentration in the fuel, ppm
NO_x = NO_x emission concentration, ppm

$NO_x(16\% O_2)$ = NO_x emission concentration corrected at 16 percent oxygen, ppm
P = pressure inside the combustor, MPa
$P.F.$ = pattern factor, percent
Q_a = air flow rate, m^3/h
Q_f = fuel flow rate, m^3/h
t = time, s
T = temperature, °C
T_a = preheated air temperature, °C
T_{adia} = adiabatic flame temperature, °C
T_f = fuel inlet temperature, °C
T_g = combustor exit gas temperature, °C
T_w = liner wall temperature, °C

TFN = total fixed nitrogen = NO + HCN + HN_3
u = mean flow velocity, m/s
η = combustion efficiency, percent
λ = air ratio
CGT5001 = 1300°C-class gas turbine combustor
CGT6001 = 1300°C-class gas turbine combustor (half size for high pressurized tests)
CGT7001 = 1500°C-class gas turbine combustor for this study
ϕ = equivalent ratio
ϕ_1 = equivalence ratio in the primary combustion region
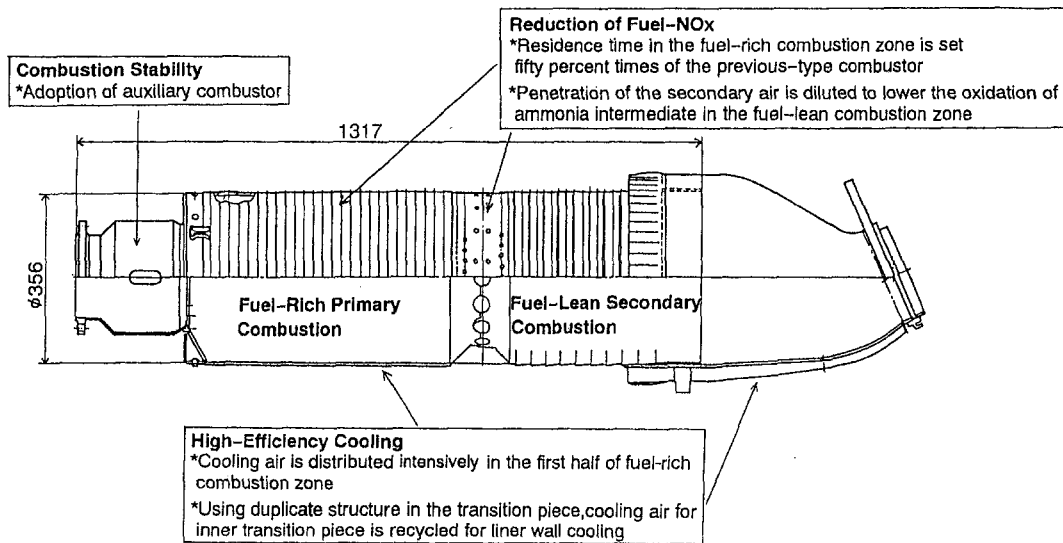ϕ_{ex} = equivalence ratio at the combustor exit

Fig. 2 Design concept of a 1500°C-class gas turbine combustor (CGT7001)

small diffusion burner [2]. Figure 4 presents an example of the test results, which indicates the influence of the air-to-fuel ratio of the primary combustor to the NO_x-conversion ratio from NH_3 at second-stage combustion; it also indicates the influence of the CH_4 concentration in the fuel. It is known from the test results that the increased fuel concentration in the primary-combustion zone will reduce the NO_x-conversion rate. However, when the fuel contains CH_4, HCN produced in the primary-combustion zone is easily converted to NO_x in the secondary-combustion area along with the decomposition of NH_3. Therefore, there is an adequate equivalence ratio, which minimizes the NO_x-conversion ratio. Based on the fact that low-calorie fuel provided for the test contained approximately 0.5 percent CH_4, the equivalence ratio in the primary-combustion area was set at 1.6. The fuel and the combustion air are injected into the chamber through the main swirler, which has 30 deg swirl angle and 15 deg introvert angle, to make these combustible gases premixed.

Residence Time in the Primary Combustor. Residence time in the primary-combustion chamber was increased 1.5 times. It has been observed in the 1300°C-class combustor tests that the part of the air that flowed through the secondary air inlet flowed backward to the primary combustion zone and as a result the fuel in the primary-combustion zone was more diluted than designed, and the planned rich-lean combustion could not be realized [3]. Based on this experience, the overall length of the primary-combustion zone was extended by about 200 mm compared to the 1300°C-class combustor. By doing so, the residence time in the primary combustor was extended from about 9 ms to 13 ms.

Introduction Method of Secondary Air. An innovative idea was applied for secondary-air introduction. With the decomposition of fuel N, a large portion of the total fixed nitrogen (TFN) produced in the primary combustion area, including NO, HCN,

and NHi, is converted to NO_x in the secondary-combustion area. The influence of secondary air-mixing conditions on the NO_x production was examined from the viewpoint of reaction kinetics. As a result, it was found that the slower mixing of the secondary air made the NO_x-conversion rate decline further (Fig. 5 [4]). Based on this result, an exterior wall was installed at the secondary air-inlet section in the tested combustor to make an intermediate-pressure zone of the dual structure. By providing this dual structure, the flow speed of the secondary air introduced to the secondary combustor decreased to 70 m/s, compared to 120 m/s without an exterior wall, thus the secondary air mixing was weakened.

Cooling of the Combustor Liner Wall. In order to compensate for the declined cooling-air ratio associated with the higher temperature of the gas turbine, the tested combustor is equipped with a dual-structure transition piece so that the cooling air in the transition piece can be recycled to cool down the combustor liner wall. The cooling air that flowed into the combustor from the exterior wall cools the interior wall with an impingement method, and moves to the combustor wall liner at the upper stream side. This method makes it possible for about 6 percent of the cooling air that is traditionally used only for cooling the transition piece to be reused for cooling the combustor liner wall.

For the auxiliary combustor and the primary-combustion zone, where temperatures are expected to be especially high,
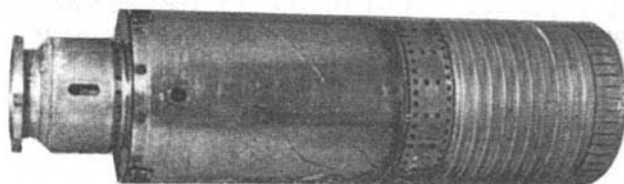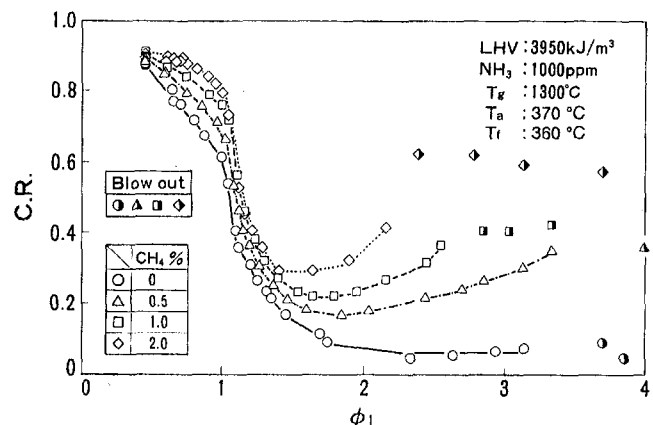

Fig. 3 Combustion liner

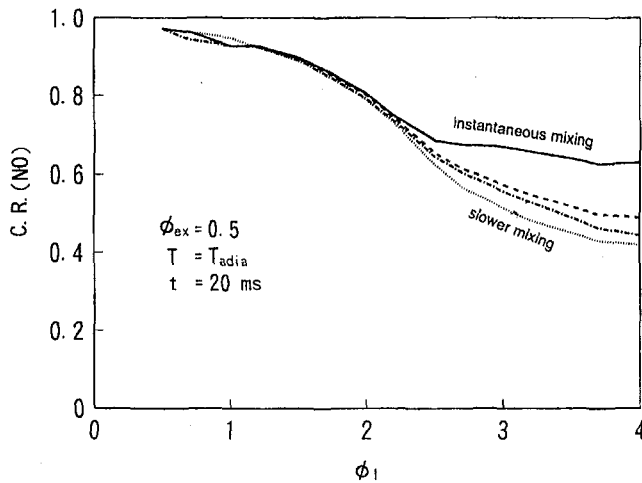
Fig. 4 Effect of methane concentration on NO_x formation

Fig. 5 Relation between primary equivalence ratio and ammonia conversion to NO$_x$ [4]

1. Outer casing
2. Liner
3. Transition piece
4. Measurement duct
5. Nozzle
6. Swirler
7. Igniter
8. Inlet air measurement
9. Liner temperature measurement
10. Combustion gas measurement

Fig. 7 Atmospheric combustion test rig

the layer-built cooling structure that combined impingement cooling and film cooling was employed. For the secondary-combustion area, the film-cooling method was used.

In addition to these design characteristics, the primary-air inlet hole is removed in order to maintain the given fuel-rich conditions in the primary-combustion zone. Also, the overall length of the tested combustor should be kept equal to that of the 1300°C-class combustor. The length of the dilution zone was reduced to compensate for the extension of the primary-combustion zone.

Test Facilities and Test Method

Test Facilities. Figure 6 shows the schematic diagram of the test facilities of the gas turbine combustor. Fuel gas is made and adjusted to have equal component characteristics of the gas produced in the air-blown, entrained-bed coal gasifier. First, the raw material LPG is separated into CO and H$_2$ by using steam. After that, it is filtered through an H$_2$ separation film to adjust the CO/H$_2$ molar rate. Then, N$_2$ is added to decrease the fuel-calorific value to the given value, and at the same time NH$_3$ is injected. The air provided to the combustor is pressurized to

2.0 MPa by using a four-stage centrifugal compressor, which has a 2810-kW motor-power output. Both fuel and air are heated separately to the given temperature with a preheater.

Figure 7 shows a cross-sectional view of the combustion-test bench of the combustor under atmospheric-pressure conditions. On the external liner wall of the combustor, about 100 sheathed type-K thermocouples with a diameter of 1 mm are welded to measure the liner-metal temperature of the combustor. The high-temperature exhaust gas was introduced into a measuring duct where gas components and temperature are to be measured after passing through the transition piece. The components of the combustion gas were analyzed by an automatic gas analyzer and each component such as NO, NO$_2$, CO, CO$_2$, O$_2$, and THC is continuously recorded and analyzed. The temperatures of the combustion gas were measured by vertically moving five R-type thermocouples inserted into the measuring duct.

Testing Method. The standard conditions in the combustion tests are summarized in Table 2. From the examination of the thermal efficiency and the compared power output, it was concluded that the pressure ratio of 1.8 MPa was the most adequate condition. Due to restrictions imposed on the test facilities, the combustion test should be done under atmospheric-pressure conditions. Therefore, the mass balance of the 1500°C-class gas turbine was examined to find the overall amount of air flow, which is converted to an amount for a single combustor. To calculate pressure conditions, each air flow condition

Fig. 6 Schematic diagram of experimental facility

Table 2 Standard test conditions

T_a	427	°C
T_f	360	°C
T_g	1500	°C
F/A(w)	0.73	
F/A(v)	0.77	
ϕ	0.62	
O_2	5.0	%
Q_a	2570	m³/h
Q_f	1950	m³/h
u	28.4	m/s
P	0.1	MPa

Fig. 8 Liner wall temperature distribution (1)
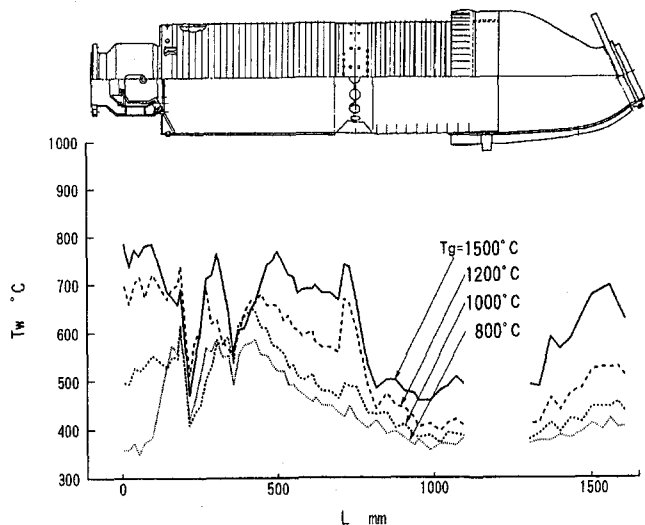
Fig. 10 Exit gas temperature distribution

was obtained and set so as to keep the cross-sectional velocity of the air flow constant.

As for fuel conditions, HHV was set at 4190 kJ/m^3, the NH$_3$ concentration was fixed at 1000 ppm, and the standard molar ratio of (CO + CH$_4$)/H$_2$ was set at 2.7.

In the combustion tests, the combustor was ignited under partial-load conditions with a lower amount of fuel flux, and then gradually changed to the rated-load conditions while gas temperatures at the combustor outlet and the liner metal were monitored.

Test Results and Discussion

Thermal Characteristics of the Combustor-Liner Metal.
Figure 8 shows the temperature distribution of the combustion-liner metal when the combustor outlet-gas temperature changes. Based on the overall temperature distribution, it was discovered that temperature increased to an adequate level and a stable flame was maintained in both the auxiliary combustion chamber and the primary chamber. Even when the combustor-outlet temperature rose to 1500°C, the liner-wall temperature remained

Fig. 9 Liner wall temperature distribution (2)

under 800°C. This indicates that the liner wall has adequate cooling efficiency.

Figure 9 shows the changes in the liner-metal temperature distribution when fuel-calorific value changes between 3430 kJ/m^3(800 kcal/m^3) and 5860 kJ/m^3(1400 kcal/m^3). At any of the calorific values, a stable flame was maintained. Even when the calorific value was lowered to 2900 kJ/m^3, the combustor maintained a stable flame.

Pattern Factor Characteristics. Figure 10 indicates the pattern factor (uneven distribution rate of the outlet-gas temperature) calculated from the gas-temperature distribution at the combustor outlet. The pattern factor was 8.3 percent under conditions such as when the combustor outlet-gas temperature was about 1500°C. This result is highly satisfactory since the design of the gas turbine requires a pattern factor of 17 percent or below. It is thought that one of the reasons for the small pattern factor is that the difference between the maximum-flame temperature and the outlet-gas temperature (Tg) narrowed as Tg rose because the maximum theoretical-flame temperature of the tested fuel is about 1660°C.

NO$_x$ Formation Characteristics. The emission concentration of thermal NO$_x$ was a minimal 3 ppm (16 percent O$_2$) under rated-load conditions where the combustor outlet-gas temperature was 1500°C. Figure 11 shows the relationship between the equivalence ratio and the conversion rate to NO$_x$ from NH$_3$. The conversion rate was a minimum of 36 percent when the combustor outlet-gas temperature was 1500°C, which was the given design condition of the tested combustor. Even under lower-load conditions, the conversion rate was as good as below 40 percent. Compared to the test results using a 1300°C-class combustor (CGT5001 [5]), the NO$_x$-conversion rate declined
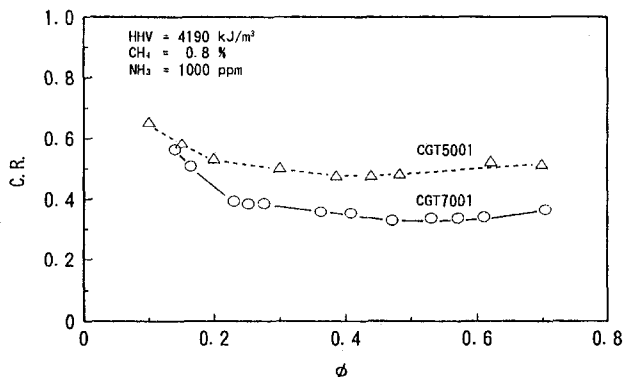
Fig. 11 Ammonia conversion ratio of the tested combustor
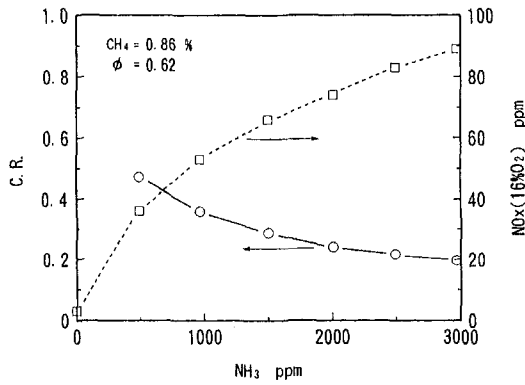
Fig. 12 Effect of ammonia concentration on C.R.
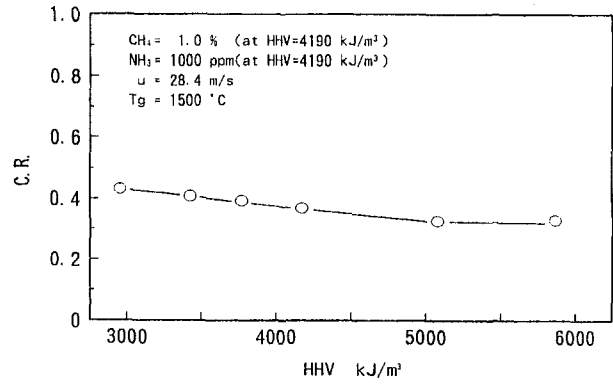
Fig. 14 Effect of heating value of the fuel on C.R.

relatively by 30 percent. It is believed that the prolongation of the residence time in the primary combustor and the slow-down of the speed of secondary-air mixing, which are the major design characteristics of the tested combustor, could further reduce fuel NO_x.

Figure 12 indicates the effect of the NH_3 concentration in the fuel under conditions such as when the combustor outlet temperature is 1500°C. The NO_x-emission concentration tends to increase and the rate of conversion to NO_x tends to decrease with an increase in the fuel NH_3 concentration. This is the same result obtained from the tests using a combustor with an outlet-gas temperature of 1300°C. When the NH_3 concentration in the fuel is 1000 ppm, which is a standard condition, the NO_x-emission concentration is 54 ppm (16 percent O_2 concentration).

Figure 13 indicates the effect of the CH_4 concentration in the fuel. Even under the same equivalence ratio conditions, the NO_x-conversion rate will decline if the CH_4 concentration decreases.

Figure 14 indicates the effect of the fuel-calorific value under rated-load conditions. With the increase in the fuel-calorific value, the NO_x-conversion rate tends to decline slightly. It is considered that the burning velocity increases as the heating value rises, and the ammonia decomposition reaction causes under fuel-rich condition in diffusion flame zone.

CO Emission Characteristics. The relation between CO-emission concentration and the combustion efficiency is shown in Fig. 15. When the combustor-outlet temperature rises, CO-emission concentration tends to increase and combustion efficiency declines. When the outlet temperature was 1500°C, the CO-emission concentration was about 3000 ppm and the combustion efficiency was 98 percent.

Figure 16 shows the combustion efficiency when the fuel-calorific value is lowered. When the fuel-calorific value is higher than 4000 kJ/m³, the combustion efficiency is higher

than 99 percent. However, the combustion efficiency declines to 95 percent when the fuel-calorific value decreases to 3000 kJ/m³.

Figure 17 compares the results of this test with the test results of the 1300°C-class combustor under atmospheric-pressure conditions (CGT5001) and with those of the high-pressure combustion tests (CGT6001). The figure also includes the results of the reaction-kinetics calculation (marked with slanted lines) in the reaction time that corresponds to the residence time (10–
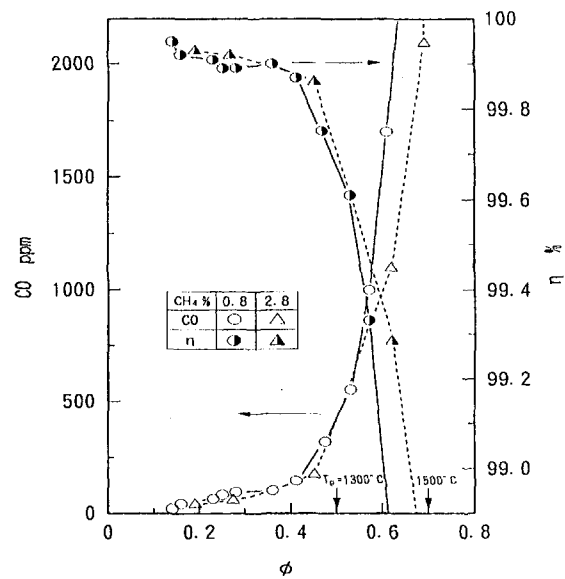
Fig. 15 CO emission characteristics
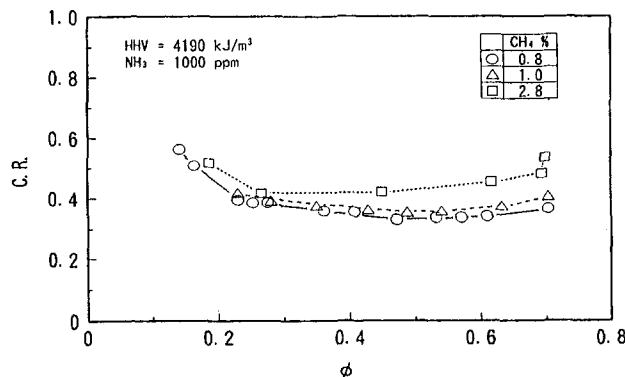
Fig. 13 Effect of methane concentration on C.R.
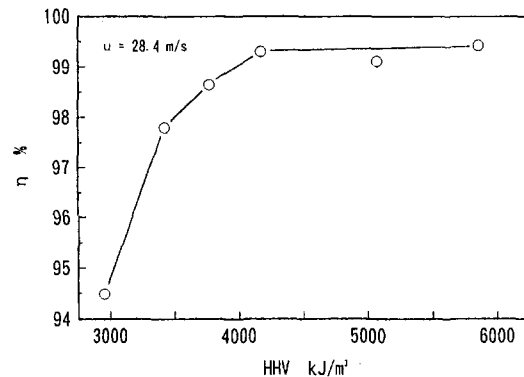
Fig. 16 Effect of heating value of the fuel on CO emission

Journal of Engineering for Gas Turbines and Power
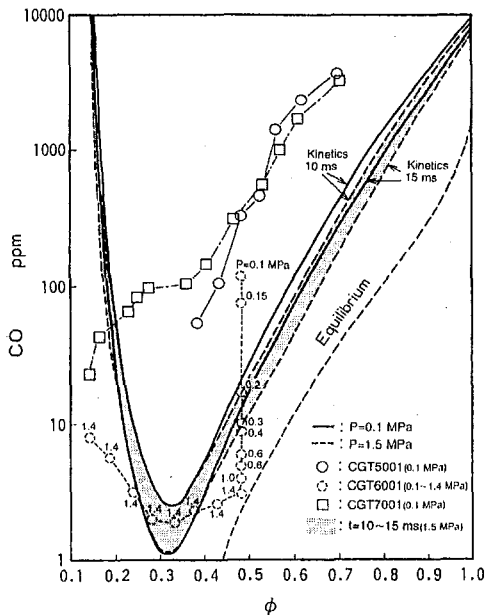
Fig. 17 Experimental and calculated CO emission

15 ms) in the gas turbine combustor, as well as the equilibrium concentration. It is understood from this figure that the CO-emission concentration tends to increase at an exponential rate with an increase in the combustor outlet-gas temperature, that is, the increase in the equivalence ratio in the combustor. This tendency sufficiently accords with the calculation results. The actual measurement indicated a value 10 times greater than the results of the reaction-kinetics calculation, and the concentration was about 100 times greater than the equilibrium concentration.

Furthermore, it is known from the high-pressure combustion tests (CGT6001), the CO-emission concentration tends to decline significantly and nearly reaches the equilibrium concentration when the pressure in the combustor increases.

Taking these characteristics into consideration, the increase in the CO-emission concentration is attributable to the delayed decomposition of CO due to the excessive-fuel concentration in the combustor. However, under high-pressure conditions, combustion efficiency will improve with the increase in pressure. Thus, under the real application conditions of the 1500°C-class gas turbine, it can be expected that the CO-emission concentration will be reduced to less than 100 ppm by the pressure effect.

Conclusion

To reiterate the results of atmospheric combustion tests written in it, they are as follows:

1　The tested combustor shows excellent combustion stability under the rated load condition. It is considered that the auxiliary combustion chamber has the desired effect on flame holding for fuel-rich combustion.
2　The liner wall temperature of the combustion chamber is lower than the allowance limit temperature of 850°C under the rated load condition. Sufficient cooling efficiency for liner wall is confirmed.
3　Thermal NO_x emission hardly increases to 3 ppm (16 percent O_2) and is still negligible even when the combustor exit gas temperature rises to 1500°C.
4　The conversion ratio from the ammonia in the fuel to NO_x shows about 36 percent, which makes a 30 percent reduction in NO_x emission. It can be considered that the effect of secondary-air mixing condition appeared sensitively in the reaction of fuel NO_x formation.

Acknowledgments

References

1　Sato, M., Ninomiya, T., Nakata, T., Ishikawa, H., Yoshine, T., and Yamada, M., "Development of a 1300°C-Class Gas Turbine Combustor Burning Coal Derived Low BTU Gaseous Fuels, Third Report," *Transactions of the Japan Society of Mechanical Engineers*, Vol. 57, No. 535, 1991, pp. 803–810.

2　Sato, M., Nakata, T., and Yamauchi, K., "NOx Emission Characteristics of Coal-Derived Low BTU Gas Fuel," *Journal of the Fuel Society of Japan*, Vol. 69, No. 10, 1990, pp. 952–959.

3　Ninomiya, T., Sato, M., Nakata, T., Yamauchi, K., Fukazawa, M., Abe, T., Ishikawa, H., Yoshine, T., Yamada, M., Hisa, S., and Hasegawa, H., "Development of a Gas Turbine Combustor for Coal Gasification, Fifth Report," *CRIEPI REPORT*, EW89010, Central Research Institute of Electric Power Industry, Yokosuka, Japan, 1990.

4　Nakata, T., Sato, M., and Hasegawa, T., "Formation Characteristics of Fuel NOx in the Combustion of Coal Gaseous-Fueled Gas Turbine," *Transactions of the Japan Society of Mechanical Engineers*, Vol. 59, No. 564, 1993, pp. 2568–2575.

5　Nakata, T., Hasegawa, T., Ninomiya, T., and Sato, M., "Development of a 1500°C-Class Gas Turbine Combustor for IGCC, First Report," *CRIEPI REPORT*, EW92001, Central Research Institute of Electric Power Industry, Yokosuka, Japan, 1992.

Applications of Accurate Isentropic Exponent Determination for Fuel Gas Measurement

D. J. Pack[1]

AlintaGas,
Perth Western Australia,
Australia

T. J. Edwards

D. Fawcett

Murdoch University,
Murdoch Western Australia,
Australia

This paper discusses the determination and application of the isentropic exponent to the various thermodynamic processes found in a high-pressure natural gas transmission system. Increasing demands for more precise measurement of natural gas, coupled with the need for greater efficiency and accountability of transportation and processing operations, had led to our research and development efforts into the more precise measurement of gas flow, and the determination of gas thermodynamic properties including isentropic exponent. The isentropic exponent has many applications, some of which include:

- *the determination of the expansion factor ϵ, for calculation of flow using an orifice or venturi-type meter;*
- *the volumetric efficiency in a reciprocating compressor;*
- *the determination of the compression head for a centrifugal compressor;*
- *the engine power required for the given conditions for a gas compressor;*
- *the calculation of discharge temperatures for compressors; and*
- *the direct measurement of gas density.*

As can be appreciated, the application of an incorrect value for the isentropic exponent represents an error in the parameter determined. For large volume gas flows, this can translate into a significant cost penalty.

The Pipeline System

AlintaGas, in conjunction with Murdoch University, both in Perth, Western Australia, have, through a number of cooperative research programs, been active in pursuing a better appreciation of the properties of the natural gases transported in the Dampier to Bunbury high-pressure transmission pipeline. This pipeline currently delivers over 90 percent of the market requirements for natural gas in Western Australia.

The Dampier to Bunbury pipeline has a total length of approximately 1540 km. Several laterals add a further 334 km of pipeline. Natural gas is sourced from four independent supplies providing an average daily throughput of about 460TJ or 11.5 million sm³. Custody transfer metering occurs along the length of the pipeline through some 36 meter stations. Metering pressures can range from 6 bar to 84 bar, gas temperatures from near 0°C to over 40°C, and gas densities from 6 kg/m³ to 76 kg/m³. Mass and energy are the metering parameters used. Turbine meters are exclusively used for volume flow within the pipeline system; however, the major gas seller uses a dual run, orifice plate equipped, metering system. Vibrating spool densitometers are utilized for the measurement of gas density at major custody transfer stations. Gas quality information is derived from on-line gas chromatograph systems.

A recent enhancement program has added a further six compressor units, bringing the total number of compressors on the pipeline to eleven. These compressors are situated approximately 130 km apart, over eight sites. The first compressor

station, which has a single unit, is situated some 130 km south of Dampier.

Description of Facilities. As the majority of the population, and hence industry, is situated in the southwest of the state, the majority of meter stations are on the southern section of the pipeline, that is, from approximately the 1340 km point southward.

The meter stations vary in size according to throughput, including turndown requirements. The stations generally have at least two meter runs, one of which is dedicated as a master or standby run. Turbine meters range in size from 50 mm to 300 mm diameter, all being ANSI class 600. Dedicated flow computers are used on each meter station run, with gas quality, pressure, temperature, density, and flow information downloaded to derive mass and energy flow rates.

To have good representational measurement of density, continuous measurement at actual pipeline conditions is essential. This is why densitometers are used at all major custody transfer meter stations. The densitometer measuring principle is based on the change in the natural frequency of an oscillating element. The natural frequency of the oscillating body diminishes as the density increases. Densitometers are measuring instruments of the second order, that is, if a meaningful reading is to be obtained, then some type of calibration scale must be assigned to the instrument. Therefore, the accuracy of reading is very dependent on the quality of calibration.

Ideally, the densitometer should be calibrated at conditions identical to normal operations and using the same gas as the test medium. Therefore, the isentropic exponent at the operating conditions needs to be known with high accuracy. With the major gas supplier metering gas into the pipeline system, via orifice plates, AlintaGas is directly interested in the performance of this metering system, as it presents the largest single flow

and hence the potential to be a significant contributor to the very complex issue of gas unaccounted for in the system.

The pipeline gas turbine driven compressor sets are sourced of two separate manufacturers. The first installed units, which were commissioned during the mid-1980s, use the LM500 gas turbine, which is a compact, high-performance unit derived from the General Electric TF34 turbofan. This gas turbine, of which five are in service on the pipeline, is in the 3000 to 6000 shaft horsepower class. The recent enhancement of the pipeline has seen the commissioning of six larger units, which consist of a Solar C505U centrifugal gas compressor and a Mars gas turbine.

Like the LM500, the Mars turbine engine is a two-shaft, variable speed, axial flow design. For the Solar Mars units, all performance curves are based on a ratio of specific heats of 1.279.

Pipeline Applications for Isentropic Exponent (k). Within the referenced pipeline system, the isentropic exponent applies to a number of processes. As already discussed, it applies to:

(a) The densitometer density determination. The meter run flow computer calculates the live density from the following relationship:

$$\rho = \frac{2d_o^1}{t_o^1}(t - t_o^1)\left[1 + \frac{K}{2t_o^1}(t - t_o^1)\right]$$

where

$$t_o^1 = t_o + N(T - T_{cal})$$

$$d_o^1 = d_o\left(1 - \frac{(rR^1)^2}{(ct)^2}\right)$$

$$c^2 = \frac{kPL}{\rho}$$

(b) Calculation of flow using an orifice plate

(i) for volume flow rate

$$Qv = \alpha\epsilon\tfrac{1}{4}\pi d^2\sqrt{\frac{2\Delta P}{\rho}}$$

(ii) alternatively for mass flow rate

$$Qm = \alpha\epsilon\tfrac{1}{4}\pi d^2\sqrt{2\Delta\rho P}$$

The expansion factor ϵ for a gas is given by:

$$\epsilon = 1 - [0.41 + 0.35\beta^4]\frac{\Delta P}{kP}$$

where

$$\beta = \frac{d}{D}\ (D = \text{i.d. of pipe})$$

(c) Calculation of expansion factor ϵ for venturi or nozzle

$$\epsilon = \frac{(1 - \beta^4)\left[\dfrac{k}{(k-1)}\right]\left(\dfrac{P_2}{P_1}\right)^{2/k}\left[1 - \left(\dfrac{P_2}{P_1}\right)^{(k-1)/k}\right]}{\left[1 - \beta^4\left(\dfrac{P_2}{P_1}\right)^{2/k}\right]\left(1 - \dfrac{P_2}{P_1}\right)}$$

(d) Calculation of compressor head, H, compression power, and discharge temperature for adiabatic process. When reasonable accuracy is required, the following equation can be used [1]:

$$H = ZRT\frac{k}{(k-1)}\left[\left(\frac{P_2}{P_1}\right)^{(k-1)/k} - 1\right]$$

From this value of H, the compression power can be calculated. The discharge temperature can be calculated from:

$$\Delta T_{actual} = T_1\left[\left(\frac{P_2}{P_1}\right)^{(k-1)/k} - 1\right]/\eta$$

As can be seen from this set of equations, which is by no means exhaustive, the isentropic exponent can be found in a variety of applications for a gas pipeline system.

The Thermodynamic Process

This section of the paper defines a number of thermodynamic processes and discusses the definition and application of the commonly applied classification of gases.

While it is true that there is not a gas that strictly obeys the well-known Boyle's and Charles' gas laws, some gases at low pressure, and generally of simple or single composition, will obey these gas laws with good approximation. However, in the transportation and metering processes of natural gas at transmission pipeline conditions, the gas deviates from the gas law conditions because of gas compressibility. This is due to the elevated pressures and the presence of heavier hydrocarbons in the gas.

These conditions have led to the concepts of an ideal gas and a real gas. Some authors [2] add a third category, that of a perfect gas. However, our discussion will be limited to the concept of an ideal and real gas.

During the compression, pressure regulation, and metering processes in a high-pressure pipeline system, the gas is changing its condition or state. Understanding these changes, which are known as thermodynamic conditions, is very important for the

--- **Nomenclature** ---

K = calibration constant of spool
L = speed of sound factor
N = temperature constant of spool
P = measured pressure
R = gas constant
T = absolute temperature
Z = compressibility factor
c = speed of sound
d = diameter of the orifice
k = isentropic exponent
r = characteristic dimensions of vibration spool

t = measured period of time
α = flow coefficient
ϵ = expansion coefficient
η = efficiency
ρ = density

Subscripts

c_p = isobaric heat capacity
c_v = isochoric heat capacity
d_o = calibration constant of spool
P_1 = upstream absolute pressure
P_2 = downstream absolute pressure

T_1 = inlet absolute temperature
T_2 = discharge absolute temperature
T_{cal} = calibration temperature
t_o = periodic time of spool in vacuum at calibrated temperature
Δ_p = pressure differential

Superscripts

d_o^1 = corrected value of d_o
t_o^1 = corrected value of t_o
R^1 = speed of sound correction to density

most efficient and economic design, operation, and precise measurement of required parameters. Three of these thermodynamic states will be discussed. They are:

- the adiabatic process,
- the isentropic process, and
- the polytropic process.

For an adiabatic process, there is no heat transfer to or from the system. An isentropic process is one of constant entropy. It is an adiabatic process that is internally reversible. Therefore, an isentropic process is adiabatic, but an adiabatic process is not necessarily isentropic. The third process, the polytropic, is one in which work is done on or by the gas and therefore there is some heat flow.

This now leads to the question of why we are so interested in the isentropic state. This is because, from the given definition, this type of process leads to the maximum output, or minimum input, for pipeline systems such as gas turbines and compressors, and also presents the optimum performance for the referenced measurement devices. It is stated that the "internally reversible process can be used as a standard to which all real processes may be compared, whether applied to a closed or open system" [3]. Therefore, we use the isentropic process as the performance indicator standard for the defined real processes.

Calculating the Thermodynamic Quantities. The equation of state for an ideal gas can be written as

$$PV = RT \qquad (i)$$

If a deviation factor is applied, such as compressibility, then Eq. (i) can be expressed as:

$$Z = \frac{PV}{RT} \qquad (ia)$$

Now for the ideal gas, Z will equal unity. If Z is not equal to unity, then the expression will represent the deviation of the gas from the ideal condition.

To account for this deviation, a number of equations have been formulated. One such well-known equation is that of van der Waal, which states:

$$P = \frac{RT}{v - b} - \frac{a}{V^2} \qquad (ib)$$

Although this equation takes account of two important theoretical postulations with regard to the molecular behavior of gases and liquids, namely the volume available to a molecule for its motion and the intermolecular attraction (which account for the $1/(v - b)$ and $1/v^2$ terms, respectively), the equation in practice is not in good agreement with observed results.

This then led to a number of other equations of state (EOS), such as the Redlich–Kwong (which adapted the van der Waal equation to experimental results), being developed. Today, a considerable number of EOS are available that take into account this gas characteristic of compressibility. The more commonly used EOS are:

1. The American Gas Association NX-19. Although introduced in 1963, this EOS is still probably the most commonly used, although the AGA-8 EOS and its adaptions are replacing it.
2. Benedict–Webb–Rubin.
3. GERG (Groupe Europeen des Recherches Gazieres). This EOS has been developed by Amsterdam University's van der Waal Laboratory.
4. Edmister.
5. The American Gas Association AGA-8.

For our research activities, we have been using an interactive program called SUPERTRAPP [4] together with DDMIX, which are based on yet another EOS, the Peng–Robinson. This program was developed by NIST (National Institute of Standards and Technology). Although high-accuracy results can be obtained from these EOS, in actual field applications the more complex sets of equations, such as AGA-8 (in its full form) and the Benedict–Webb–Rubin, cannot be economically applied. This is because of their complexity (computing power requirement) and/or the number of inputs required to the local flow computer for gas quality data if the EOS full-accuracy potential is to be realized.

However, the alternative of having overly simplified equations together with the recommended practice [5] of having a single set value for the isentropic exponent of 1.3 (or a value close to this), is just not acceptable for a transmission pipeline system. It can be seen from the results, as given later in this paper, that the isentropic exponent can be expected to have a reasonable variation in value for the gas processes and flow conditions experienced along a natural gas pipeline.

Because the modified differential Burnett apparatus, as discussed in the apparatus section, will give readings of the isentropic exponent for given gas compositions, pressures, and temperatures, these values can be applied directly to the equations as defined in the next section. From our research program, it is proposed to generate simple "look-up" tables for given sets of conditions at all flow measurement locations and gas compression/expansion processes.

The ability to apply direct experimental measurements gives a higher degree of accuracy than by calculation methods. As AlintaGas enjoys relatively stable gas compositions within the pipeline system, together with small variations in measurement parameters at most custody transfer locations, a fixed value for isentropic exponent can be used at most sites. This also ensures simplicity of operation is maintained with respect to computational equipment at the more remote locations.

The Isentropic Exponents. For an ideal gas, the ratio of specific heats is given by $\gamma = C_p/C_v$ where $C_p =$ isobaric heat capacity, and $C_v =$ isochoric heat capacity.

This ratio is of little use outside the dynamics of an ideal gas.

It is worth noting that although the ratio of specific heats and the isentropic exponent are widely used and important thermodynamic properties, these parameters are unfortunately not represented by universal scientific symbols.

For the discussion in this paper, the ratio of specific heat C_p/C_v is represented by the symbol γ and is generally limited to a perfect gas scenario, whereas the isentropic exponent is represented by the symbol k.

It is important to appreciate that for a real gas the ratio of specific heat and the isentropic exponent are not one and the same thing.

As already discussed, natural gas in a pipeline system can be subject to a number of processes. Some of the basic processes will now be discussed in order to obtain an appreciation of the relationship of the more common gas parameters to the isentropic exponent:

(a) For the constant volume heating of an ideal gas, let a mass of gas m be heated at constant volume, resulting in a temperature rise from T_1 to T_2, and pressure change from P_1 to P_2, then the heat received by the gas = mass × specific heat at constant volume × change in temperature:

$$\text{i.e. } Q = mC_v(T_2 - T_1)$$

Now if the nonflow energy equation is applied to the constant-volume heating process, then $Q = \Delta U$. Therefore,
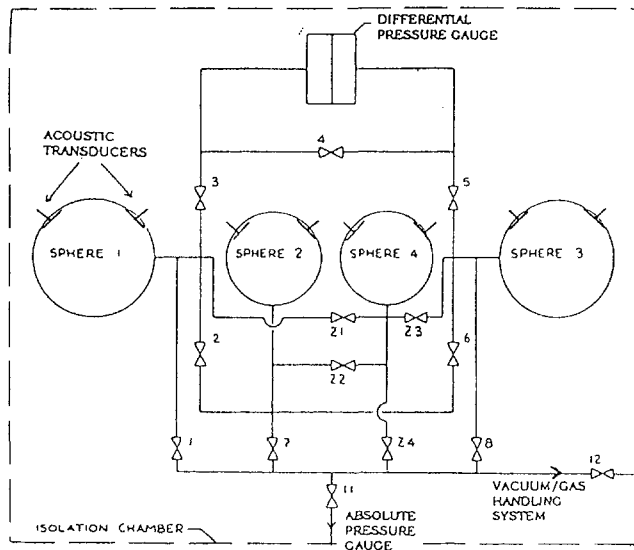
Fig. 1 Schematic of apparatus for measurement of speed of sound and compressibility factor

$$Q = \Delta U = mC_v(T_2 - T_1) \quad U_2 - U_1 = mC_v(T_2 - T_1) \quad (ii)$$

(*b*) Likewise, for the constant-pressure heating of a gas

$$Q = mC_p(T_2 - T_1)$$

with the application of the nonflow energy equation $Q = \Delta U + W$. For this case external work is done, i.e., $W = P(V_2 - V_1)$. Therefore,

$$mC_p(T_2 - T_1) = \Delta U + W$$
$$= (U_2 - U_1) + P(V_2 - V_1) \quad (iii)$$

This can be expressed as:

$$(U_2 - U_1) = mC_p(T_2 - T_1) - P(V_2 - V_1) \quad (iiia)$$

Now, since $PV = mRT$, and substituting in ($iiia$),

$$(U_2 - U_1) = mC_p(T_2 - T_1) - mR(T_2 - T_1) \quad (iv)$$

By making the assumption that the change in temperature for Eq. (ii) is the same as Eq. (iii), then

$$mC_v(T_2 - T_1) = mC_p(T_2 - T_1) - mR(T_2 - T_1)$$

from which

$$C_v = C_p - R \quad (v)$$

for the adiabatic process

$$du = -dw \quad (vi)$$

also

$$dw = PAdL \quad \text{and} \quad V = A \times L$$

$$dw = PdV \quad (vii)$$

Now from Eq. (ii)

$$du = mC_v dT$$

Substituting in (vi)

$$mC_v dT = -PdV$$

$$\frac{dT}{dV} = -\frac{P}{mC_v} \quad (viii)$$

By differentiating the characteristic equation for an ideal gas, $PV = mRT$, with respect to V,

$$P + V\frac{dP}{dV} = mR\frac{dT}{dV}$$

Substituting in ($viii$)

$$= mR\left(\frac{-P}{mC_v}\right)$$

Now from (v) $R = C_p - C_v$

$$= \frac{-(C_p - C_v)P}{C_v}$$

For an ideal gas, $C_p/C_v = \gamma$

$$\frac{dP}{P} = -\gamma\frac{dV}{V}$$

That is

$$\log_e P + \gamma \log_e V = C$$

Therefore

$$PV^\gamma = C \text{ for an adiabatic process}$$

Now for an adiabatic change of state for a real gas, we have

$$PV^k = C$$

and likewise for a polytropic process

$$PV^n = C$$

If the process can be broken down into very small time intervals, then n will approximate k.

The isentropic exponent is defined for real gases via $P\rho^{-k} = $ const, which preserves the symbolic form of the corresponding ideal gas expression $P\rho^{-\gamma} = $ const.

As has been emphasised [6], the isentropic exponent cannot be equated to the specific heat ratio in real gases, although the identification is frequently made. In an ideal gas the exponent γ is related to the speed of sound c through the relation

$$C_{\text{ideal gas}} = \left(\frac{\gamma RT}{M}\right)^{1/2}$$

Analogously, in a real gas, the isentropic exponent is related to the speed of sound by the relation:

$$C_{\text{real gas}}(P, T) = \left(k(P, T)Z(P, T)\frac{RT}{M}\right)^{1/2}$$

Hence, if c and Z are both measured, k can be calculated, with

Table 1 Nitrogen at 298.15 K

Exp N°	Pressure (Bar)	Experimental k_z	DDMIX k_D	Deviation %	STRAPP k_s	Deviation %
0	101.6314	1.60895	1.56858	-4.037	1.5923	-1.665
1	76.8822	1.55276	1.53110	-2.166	1.5521	-0.066
2	58.3567	1.51239	1.50090	-1.149	1.5184	+0.601
3	44.3499	1.48331	1.47717	-0.614	1.4913	+0.799
4	33.7464	1.46237	1.45884	-0.353	1.4701	+0.773
5	25.6801	1.44670	1.44476	-0.194	1.4536	+0.690
6	19.5501	1.43498	1.43401	-0.097	1.4409	+0.592
7	14.8893	1.42641	1.42583	-0.058	1.4313	+0.489
8	11.3221	1.41999	1.41957	-0.042	1.4238	+0.381
9	8.6222	1.41496	1.41483	-0.013	1.4182	+0.324
10	6.5593	1.41128	1.41121	-0.007	1.4138	+0.252
11	4.9926	1.40843	1.40847	+0.004	1.4105	+0.207
12	3.7948	1.40638	1.40637	-0.001	1.4080	+0.162
13	2.8831	1.40475	1.40477	+0.002	1.4060	+0.125

Table 2 Natural gas at 293.15 K

Exp N°	Pressure (Bar)	Experimental k_s	DDMIX k_D	Deviation %	STRAPP k_s	Deviation %
0	99.8865	1.90969	1.79271	-11.698	1.7645	-14.519
1	80.0255	1.71470	1.66365	-5.105	1.6379	-7.680
2	63.5188	1.58528	1.56293	-2.235	1.5411	-4.418
3	49.9892	1.49852	1.48844	-1.008	1.4687	-2.982
4	39.0999	1.43927	1.43450	-0.477	1.4156	-2.367
5	30.3854	1.39760	1.39526	-0.234	1.3768	-2.080
6	23.5202	1.36830	1.36675	-0.155	1.3486	-1.970
7	18.1303	1.34788	1.34578	-0.210	1.3281	-1.978
8	13.9374	1.33121	1.33037	-0.084	1.3131	-1.811
9	10.6899	1.31940	1.31890	-0.050	1.3021	-1.730
10	8.1868	1.31033	1.31033	0	1.2940	-1.633
11	6.2594	1.30355	1.30390	+0.035	1.2881	-1.545
12	4.7752	1.29839	1.29904	+0.065	1.2836	-1.479
13	3.6458	1.29474	1.29539	+0.065	1.2803	-1.444

Graph 1 Isentropic exponents of nitrogen at 298.15 K

the molecular weight obtained from gas chromatography measurement of the gas composition.

Apparatus

The apparatus consists of four spheres, and is shown in Fig. 1. The larger spheres V_1 and V_3 are of 10.0 cm diameter, giving a volume of 523.60 cm³ for each sphere, while the smaller spheres are of diameter 6.3 cm, with respective volumes 130.92 cm³, i.e., one quarter the volume of the large spheres. The spheres are constructed from stainless steel, with 1.5 cm wall thickness, which allows operation at pressures in excess of 200 bar.

The spheres are equatorially mounted on a plane of thick aluminum. Also mounted on this sheet is a differential pressure gage (MKS Baratron).

Each sphere is equipped with a heater, a PRT thermometer, a number of thermistors, and two miniature capacitance microphones, one of which acts as a generator of acoustic waves.

The valves shown are all-metal valves of minimum dead volume. (The total dead volume is some 4 percent of $V_1 + V_2$.) All seals between valves and ports, manifolds and spheres, and between the hemispheres, are silver O-ring seals.

The entire assembly is hung from the lid of an aluminum isolation chamber (evacuated), which in turn sits inside a large fluid bath.

The all-metal system (save for the diaphragms in the capacitance microphones) ensures that the spheres can be evacuated to 10^{-6} torr and maintain gas purity over an extended time. It also allows operation over a wide temperature range.

Each pair of spheres $\{V_1, V_2\}$, $\{V_3, V_4\}$ together with the absolute pressure gage forms a "Z meter." The first pair of spheres contains sample gas, while the second pair $\{V_3, V_4\}$ contains a reference gas (Ar, He, or N_2) with well-known volumetric properties, enabling compressibilities Z_1 to be measured either absolutely ($\{V_1, V_2\}$ alone) or relatively (with the expansions of sample gas in $\{V_1, V_2\}$ being compared to similar expansions of the reference gas in $\{V_3, V_4\}$).

The unique feature of our apparatus is that as each sphere is equipped with acoustic transducers, we can simultaneously measure acoustic and volumetric properties at each pressure expansion step. This provides a number of significant advantages:

- The spherical geometry offers minimum surface area/volume ratio and therefore enhanced accuracy for the expansion measurements, together with maximum precision in the speed of sound.
- The speed of sound is a sensitive thermometer: The ratio of the speed of sound in V_1 to that in V_2 will depend only on the temperature difference between V_1 and V_2. Thus, monitoring the speed of sound ensures that pressure measurements are made under isothermal conditions at equilibrium.
- Monitoring the resonance widths ensures that expansions are conducted in regimes free of adsorption errors.
- Acoustically derived quantities are tied to the volumetrically derived quantities determined in the same apparatus, on the same sample, leading to high internal consistency.

Table 3 Natural gas analysis

Constituent	Mole Fraction %
Nitrogen	1.210
Carbon Dioxide	2.870
Methane	87.645
Ethane	5.430
Propane	2.050
i-Butane	0.297
n-Butane	0.484
i-Pentane	0.011
n-Pentane	0.003
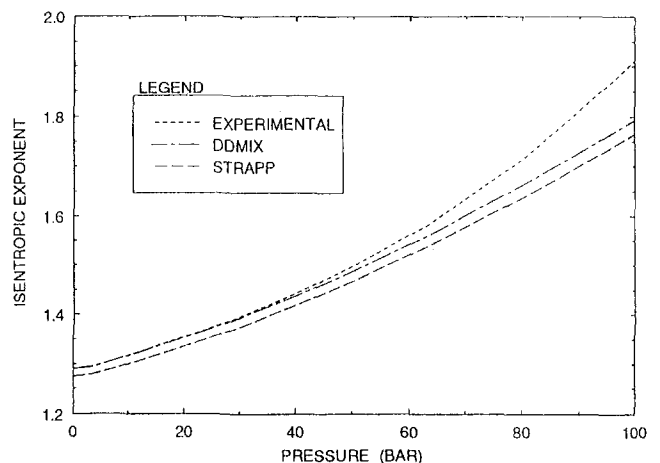
Graph 2 Isentropic exponents of natural gas at 293.15 K
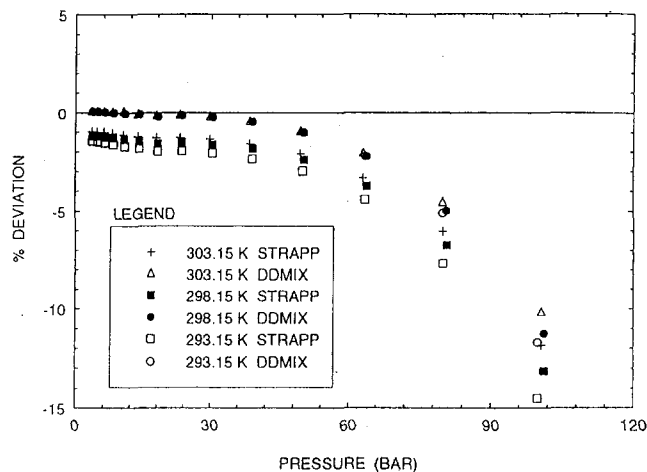
Graph 3 Isentropic exponent deviations of natural gas

The accompanying figures present typical results obtained for isentropic exponents with the apparatus and procedures described above.

Conclusions

The isentropic exponent applies to a number of processes associated with the processing, pipeline transportation, and measurement of natural gas. It is of particular importance where a gas is undergoing an expansion or compression process. The research project has demonstrated good agreement with contemporary EOS used in the calculation of isentropic exponent. Some deviation does occur between the experimentally determined and EOS calculated values for gas pressures above 60 bar. Of course the type of gas and variation in gas composition can also have an influence on the results.

If a variation in the isentropic exponent of say a few percentage points is applied to an applicable flow measurement calculation, then the resulting change in the flow calculation would be extremely small. However, for large flow systems, there is a measurable cost. For example, if a 20 percent variation in the value of isentropic exponent, which is a very realistic scenario, would be applied to the 1994 Australian national gas purchases, then this would represent a variation of around A$1,200,000 in total purchase price. Therefore, in certain applications, the isentropic exponent value applied does warrant careful consideration.

References

1   Gas Processors Suppliers Association, "Centrifugal Compressors and Expanders," *SI Engineering Data Book,* 1980, pp. 5–6.

2   Miller, R. W., *Flow Measurement Engineering Handbook,* 2nd ed., McGraw-Hill, New York, 1983.

3   Wark, K., *Thermodynamics,* McGraw-Hill, New York, 1977, p. 292.

4   NIST, "Thermophysical Properties of Hydrocarbon Mixtures SUPERTRAPP," NIST Standard Reference Database 4, National Institute of Standards and Technology, Gaithersburg, MD, 1992.

5   International Organisation for Standardisation, "Measurement of Fluid Flow by Means of Orifice Plates, Nozzles, and Venturi Tubes Inserted in Circular Cross Section Conduits Running Full," ISO 5167, Geneva, 1980.

6   Pack, D. J., and Edwards, T. J., "Improvements in Flow Measurement Uncertainty for a Natural Gas Transmission System," *Proc. Flomeko '93,* Park and Kinghorn, eds., Seoul, Korea, 1993.

Specification, Development, and Testing of the FT8-2 Dry Low NO$_x$ Control System

R. C. Bell

T. W. Prete

Turbo Power & Marine Systems, Inc.,
Middletown, CT 06457

J. T. Stewart

Woodward Governor Company,
Turbomachinery Controls,
Loveland, CO 80539

This paper describes the specification, development, and testing of the FT8-2 Dry Low NO$_x$ control system, and how the lean burn process requires an integration of the control system and combustion hardware. The FT8-2 digital fuel control system was developed to achieve the precise multizone fuel metering of both gas and liquid fuels, the calculation of combustor air flow necessary to achieve Dry Low NO$_x$ and the traditional governing/limiting control loops necessary for safe, stable engine operation. The system design goals were accomplished by the concurrent development of software-based fuel metering algorithms and fuel metering hardware. The fuel metering hardware utilizes an all-electronic valve positioner, employing a combination of feedback and software to achieve closed-loop control of actual fuel flow. Extensive testing under actual gas flow conditions and closed-loop bench testing using a real time engine model and fuel system model was conducted to prove system operation and develop system transient response prior to installation on the test engine. The setup and results of the flow testing and closed-loop testing are described. The paper describes the control scheme used to apportion the gas fuel between combustion zones and how external conditions such as ambient temperature and fuel gas composition affect the apportionment. The paper concludes with a description of the control system installation in the engine test cell and a review of engine test results.

Introduction

Emission regulations limiting the pollutants produced by land-based gas turbines have continued to become more stringent. Traditionally, gas turbine manufacturers relied on water or steam injection to lower the nitric oxide emission to the allowable limits. The use of injection, however, requires costly water treatment systems, and, in the case of water injection, results in an efficiency penalty. In 1991, Turbo Power and Marine Systems, Inc. and Pratt & Whitney embarked on the FT8 Dry Low NO$_x$ program with the goal of developing a lean burn combustion system for the FT8 with the capability of reducing emissions of NO$_x$ to less than 25 ppm, and emissions of other pollutants, such as CO and unburned hydrocarbons, to equally low levels. Another ground rule of the program was to maintain the world class performance level of the existing FT8-1 at higher ambient temperatures, while improving power output and efficiency at low engine operating ambient temperatures.

The background needed to develop this new combustion system spans 25 years, beginning with the FT4 lean burn combustion design (Lewis, 1980) and more recently a lean-premixed gas injection system for aeroderivative gas turbines (McVey, 1993). The FT8-2 combustor is based on the staged, tangential entry, premix lean burn design described by Snyder (1996).

As the development program continued, it became apparent that if the design goals were to be met there would have to be an amalgam of the engine fuel control system and the combustor hardware. In fact, the inherent complexity of the lean burn combustion system leads to an increase in fuel delivery hardware and computational requirements, straining the capability of current digital controls. It is important from both the functional and cost perspectives that the total system design be

directed toward simplicity and that the control strategy be well planned, combining emissions control, engine protection, and control loop stability, while making efficient use of the control capability. The paper describes the control approach beginning with the hardware specification and continuing through closed-loop testing and installation of the system into the engine test cell.

Although the complete FT8-2 fuel system is designed for dual fuel operation, the liquid fuel portion of the engine test program had not been completed at the time this paper was prepared. Therefore, this paper limits the discussion of the control/fuel system development to the gas fuel system.

FT8-2 DLN Combustion System

The pollutants emitted from gas turbine combustion are a function of the burner temperature at which the fuel and air are combusted. Oxides of nitrogen (NO$_x$) are formed in the hot reaction zones of combustion and grow exponentially with increasing temperature. Unburned hydrocarbons (UHC) and carbon monoxide (CO) are primarily the result of incomplete combustion. Therefore, the only practical way of controlling the production of NO$_x$ and CO is to control the temperature at which combustion takes place. The lean-premix method of NO$_x$ control works on the premise that a lean, well-mixed, homogeneous fuel–air mixture will avoid the high temperature generated by combustion near the stoichiometric ratio.

One of the challenges of operation of a practical lean-premix system is to assure sufficient flame stability margin. Since normal combustor operation takes place in close proximity to combustor "blow out," the control system must have a means to identify combustor stability margin degradation and take corrective action prior to flame extinction.

Staged Combustion

The optimum premix system would have the ability to control both the inlet air flow and the fuel flow to a precise fuel–
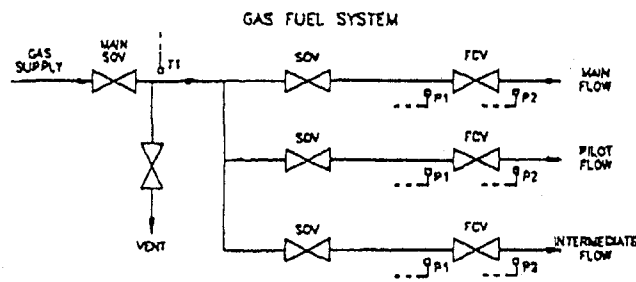
GAS FUEL SYSTEM

Fig. 1

air ratio regardless of ambient operating conditions and engine power. Presently there is no practical means for modulating combustor inlet air flow in the engine. By "staging" the combustion system the optimum system is approached, allowing for low emissions over most of the power output range. The FT8-2 Dry Low NO$_x$ system has three distinct combustion zones, each geometrically optimized for different engine power ranges and fuel–air ratios. The Main combustion zone is optimized for high power (80–100 percent), the Intermediate zone for the midpower range, and the Pilot zone, where lean burn is not possible, typically at low power and starting regions.

The FT8-2 staged system consists of 16 circumferentially spaced, tangential entry, premix nozzles. Each nozzle has three independent combustion zones, as previously discussed.

Each zone is independently fueled via three gas manifolds and three gas metering fuel valves. The control task is the precise apportionment of fuel to the three zones, based on engine operating conditions necessary to achieve the exact fuel–air ratio and resultant minimum NO$_x$ and CO emissions. The gas fuel system is shown in Fig. 1.

Control System/Fuel System Design Criteria and Specification

The requirement for three zone gas fuel apportionment and the flow control accuracy of each zone was defined by the United Technologies Research Center burner development project (Snyder et al., 1996) prior to the inception of the fuel control system design. The FT8-2 control system is a modification of the Woodward Governor NetCon 5000 based control system developed by Turbo Power & Marine for use on the FT8-1 gas turbine. It was desired to make the minimum number of modifications to this existing system for the DLN application. The FT8-1 fuel system modulating valves (one gas and one liquid for a dual fuel application) are actuated by conventional electrohydraulic servo actuators. The hydraulic source for this system is a gearbox driven hydraulic pump, which also provides hydraulic muscle for the engine Inlet Guide Vanes and Variable Stator vane actuators. When the FT8-2 DLN application was specified, it was determined that there was insufficient hydraulic pump capacity for the increased number of fuel modulating valves. The alternatives of increasing the pump capacity, use of external hydraulic source, and the use of all electric fuel modulating valves were considered. Three Woodward Governor electromechanical actuators were chosen for their accuracy of flow control, the lack of hydraulic requirements, and the improvement in reliability as compared with the contamination sensitivity of electrohydraulic actuators. Guide vane and stator vane modulation is still accomplished via conventional electrohydraulic actuators.

A flow accuracy requirement was established at the start of the DLN fuel control system development. This value was the result of previous testing of the gas fuel apportionments in the test rigs at United Technologies Research Center. The design approach by Woodward Governor during the proposal phase of the project was one of closed-loop flow control. This technique utilizes a real time solution of the compressible flow equation to compute the gas flow from valve position, gas temperature and pressure measurements, gas compressibility, and specific gravity parameters.

In summary, the fuel system design criteria and specification were primarily driven by the combustion zone flow ranges, the desired flow accuracy, the minimization of gas pressure drops, and the decision to utilize the electrically actuated modulating fuel valves.

Control System Hardware Configuration

Figure 2 defines the major components of the FT8-2 control hardware. The principal modification to the existing FT8-1 system was the requirement for the distribution of the fuel demand signal into the three zones of the Dry Low NO$_x$ fuel combustion system. The control hardware for this valve system required the addition of electronic valve control modules and one for each of the three gas valves. Three individual fuel zone shutoff values for the gas system were also incorporated. A total flow shutoff value for each inlet fuel manifold was also provided. Additional high-accuracy pressure sensors were required to determine the delta pressure across each of the three gas fuel modulating valves. A Honeywell solid-state transducer was chosen based on its extremely high accuracy, a digital serial interface to the control system hardware, and its high reliability.

In order to minimize the time requirements of the control system closed-loop testing at Woodward Governor and the installation and checkout at the engine test cell at Pratt & Whitney's Willgoos sea level test facility, the use of remote I/O was chosen. This design allowed the control system to be prewired at the Turbo Power & Marine facility in West Palm Beach, Florida, and then the major component assemblies shipped to Woodward Governor in Loveland, Colorado, where the closed-loop flow testing and closed-loop system testing, utilizing a real time electronic engine model interfaced to the control system, was performed. The use of the Remote I/O and 100 percent of the actual control hardware during testing resulted in an installation and hardware checkout time in the engine test cell of approximately one week.

A central control console was designed by Turbo Power & Marine and fabricated at its West Palm Beach, Florida, facility. This console contains the Main Chassis of the NetCon 5000 controller, a Woodward Governor OpTrend Plus CRT data monitoring system, a lighted push-button operator's control panel, a two out of three voting electronic overspeed detection system, a vibration monitoring system, three DC power supplies for control and actuator power, and a second NetCon 5000 programmed as an engine simulator for control logic validation testing. The Main Chassis of the NetCon 5000 control communicates with the Remote I/O in the engine test cell over a redundant fiber optic data link.

Engine fuel system shutdown protection is achieved by use of a Protective relay, mounted in the Remote I/O enclosure.

The relay is a multipole device, with each pole providing interruption capability of both the fuel inlet shutoff valves and the individual zone shutoff valves. The relay coil is series controlled by contacts from the NetCon 5000 controller, the Emergency Stop Push-button on the Control Console, the Overspeed Detector, the Vibration Monitor, the engine test stand gas detector system, and the engine test stand operator's Emergency Stop Push-button.

Description of Gas Valves

The high flow control bandwidth and slew rate requirements forced the valves to be both highly accurate and fast. To accomplish this using all-electric actuation, a high-speed brushless DC motor with a motor clutch and gearhead assembly were used closed-loop to the resolver feedback on the valve. The motor
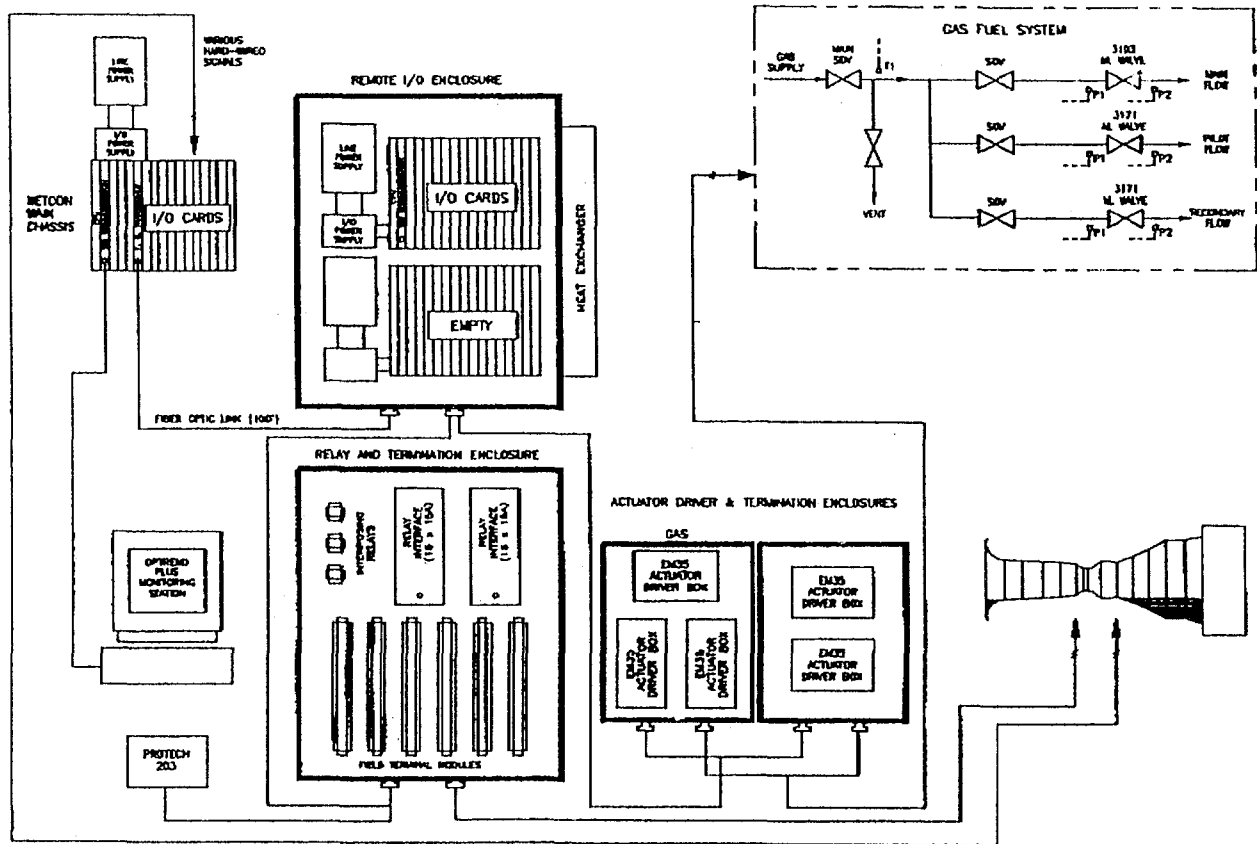
Fig. 2

uses Samarium Cobalt permanent magnets bonded and sleeved to the rotor element. All stator windings are completely sealed. Rotor position sensing is performed through the use of a brushless field director and motor velocity feedback is accomplished by means of a brushless tachometer. The output shaft from the motor gearbox is directly coupled to the valve shaft through the use of a torsional coupling. The Woodward gas fuel metering valves for each of the three flow legs are stainless steel valves with a rotary metering sleeve an a shoe-type throttling valve. The valve shoe is spring and pressure loaded against the metering port to minimize leakage and to self clean the metering port. This metering concept minimizes the valve's sensitivity to gas-borne debris, particulate contamination, and gas condensates that could change the valve's discharge characteristics. The profiled metering port is sized, for the given range of flow conditions, to take full advantage of the valve's maximum stroke. The metering port area is determined by input shaft positioning from the electric actuator. The valve has an internal return spring to return the valve to the minimum fuel flow position in the event of a power loss to the actuator.

The gas fuel system utilizes four bubble tight gas shutoff valves: one for skid inlet and one for each gas flow leg. The Woodward high-speed gas shutoff valve is a normally closed, three-stage device. Valve closure is due to a compression spring assisted by supply pressure. Redundant, vented seals in the primary stage of the valve ensure positive fuel shutoff. The unique valve design allows seal condition to be monitored continuously when the valve is in the closed state. The valve will positively seal in the reverse pressure condition. A cross section of the valve is shown in Fig. 3.

Gas Flow Algorithm

A closed-loop flow calculation utilizing the compressible flow equation is used to provide a temperature and pressure corrected mass flow solution. This calculated flow is compared to the fuel control demand flow and used to generate the setpoint for an inner position loop. This loop, with a higher bandwidth, uses a high-accuracy resolver feedback to drive the valve positioner. The total error in fuel flow control includes all contributions from the sensing elements, the positioning electronics, and the variations in the fuel properties.

Control Strategy

The design of the FT8-2 Dry Low NO$_x$ Combustor control is a modification of the standard Turbo Power & Marine FT8-1 fuel control system. This design, as shown in Fig. 4, utilizes the standard least select fuel demand signal for each of the governor control loops; NH (high rotor speed), NL (low rotor

Fig. 3

Fig. 4

speed), EGT (exhaust gas temperature), Acceleration limiting, and NP (power turbine). Each of the six standard control loops utilizes an individual PID (proportional integral derivative) algorithm to compute an output as a function of the error between the reference value and the measured value. The test engine is a gas generator only and therefore the NP control loop was not a part of the initial control testing.

The output of the least select of the five control loops is gated in a high select with the Deceleration control loop. This loop provides for stable engine operation during rapid gas generator power decreases. The additional task of the FT8-2 control system is to meter the three zones of gas fuel independently while maintaining both stable engine power/speed operation and stable combustion.

Fuel Apportionment Technique

The output signal from the least and high signal selectors of the six governing control loops is a 0 to 100 percent value from the selected PID control loop. This signal is converted into a fuel demand in pph by a linear function where zero demand represents zero fuel flow and 100 percent demand represents the maximum fuel flow as determined from the engine operating characteristics. The apportionment of this total fuel demand signal to the Pilot, Intermediate, and Main Gas Zones is scheduled as both a function of engine power operating point and a determination of either steady state or transient engine operation. The Pilot Zone percentage is first determined and the remaining available fuel percentage (simply $1 -$ Pilot Flow Demand) available for the Intermediate Zone. The remainder of $1 -$ (Pilot Zone + Intermediate Zone) is the percentage of Main Zone fuel demand. Each of the three zone fuel percentages is then multiplied by the total fuel demand in pph to provide the flow control setpoint to each of the three modulating valves. Care must be taken when the engine operating point is close to the ''turn-on'' point of a zone; i.e., the cycling of a zone shutoff valve is possible if the fuel demand signal for that zone is very small. A combination of logic designed to avoid engine operation at this point and fuel shutoff valve command signal hysteresis was used to prevent this condition.

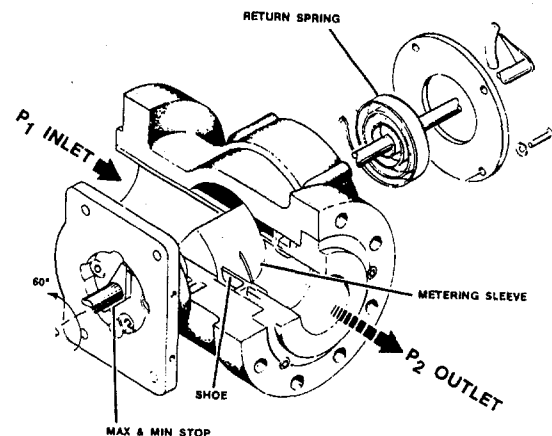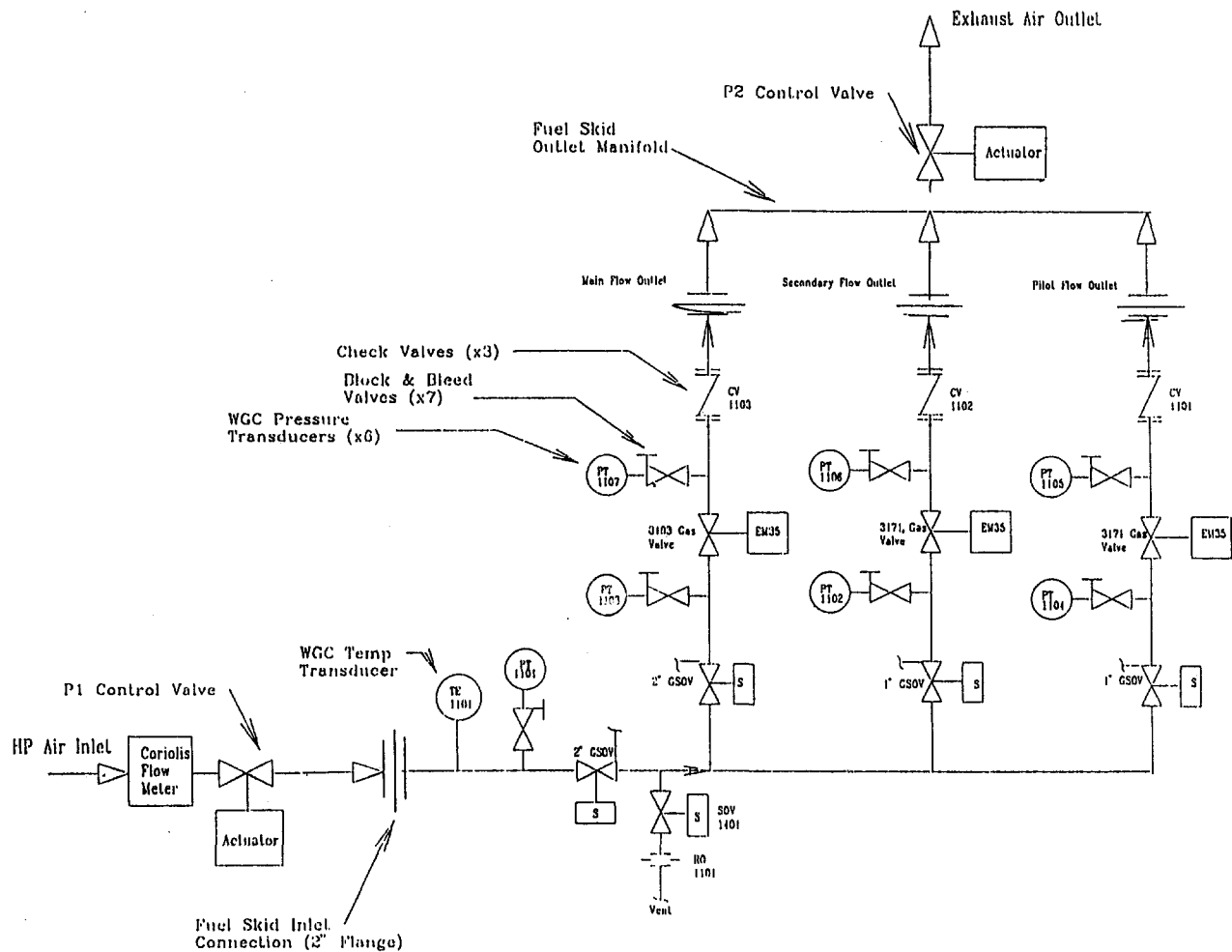The stability of the lean burn combustor is directly related to the percentage of Pilot Zone fuel. During initial engine testing it was required that the percentage of Pilot Zone fuel be an easily adjustable value. This was facilitated by use of a three-dimensional curve function, where the x axis is the engine power measurement, the z axis the desired value in pph of constant Pilot Zone fuel demand, and the y axis (the output of the schedule) the percentage of total fuel demand; i.e., the fuel demand control signal sent to the Pilot Control Value actuator output.

The utilization of a ramp function to drive the z axis and Boolean control signals from the OpTrend Monitoring system provided the ability to adjust the Pilot Zone fuel flow to any constant value during engine operation. This technique, as shown in Fig. 5, was used to establish the steady-state Pilot Zone fuel requirements necessary to minimize the engine emissions and the engine transient Pilot Zone fuel requirements necessary to maintain stable combustor operation during rapid engine accelerations and decelerations.

Engine Protection

Engine protection consists of control software limits on operating temperatures and rotor speeds. Independent high rotor overspeed protection is provided by use of the Woodward Governor Protec-203 two out of three voting solid state overspeed detector.

Combustor flameout protection is provided by use of two control software schemes: detection of an excessive fuel/air ratio and excessive negative rate of change of high compressor discharge pressure.

The excessive fuel/air ratio detector is a patented algorithm that utilizes the engine low rotor speed to derive the engine airflow and the total fuel demand from the control software to establish demanded fuel flow. The ratio of these values is compared to a limit that is based on the stoichiometric limit of the mixture. The key aspect of this technique is the use of control software fuel demand. This ensures a minimum latency time in the detection of a condition (not only actual combustor flameout) that causes the control software to increase the demanded fuel.

Fuel Metering Skid Testing

The gas and liquid fuel systems were each tested for steady-state accuracy verification and transient response. All testing was performed using the actual Engine Control, the Remote I/O, the Electric Actuator Drivers, Fuel Metering Valves, and interconnecting cables. This test method allowed for all communication, wiring, and performance problems to be identified and corrected early in the engine program. All flow testing was performed at Woodward Governor's gas and liquid flow calibration facility in Loveland, CO.

The steady-state flow accuracy testing consisted of verifying that all metering valves were able to perform closed-loop mass flow control accurately. Flow error was measured by comparing mass flow demand to the mass flow as measured by the test stand Coriolis flow meter. The accuracy of the reference meter is 0.25 percent of point over a 30 second average. For all steady-state flow tests, both the average and instantaneous flow was measured. The instantaneous flow data were graphed to determine whether any limit cycles were present that would not show up in the average flow data. Flow tests were run at varying inlet and discharge pressures to verify the closed-loop flow control's ability to correct for any variations in the system conditions. Excellent flow accuracy was obtained from the fuel metering system and no evidence of limit cycles was observed.

Fig. 5

Fig. 6

Transient Response Verification

Once the steady-state accuracy calculation was verified, the fuel and control system's dynamic responses were evaluated through testing. For all dynamic testing the results were evaluated from mass flow demand to measured mass flow. The verification of the steady-state flow accuracy allowed the flow calculation to be used as a dynamic flow meter. The use of the fuel metering valve effective area, inlet pressure and temperature, and discharge pressure was established as an accurate representation of flow during the steady-state portion of the fuel system testing.

During the dynamic testing of the fuel metering system, the system's response to ramp changes in flow, step changes in flow, and flow frequency response were evaluated. The ramp tests were performed with increasing and decreasing flows on multiple flow legs at once to determine the system's ability to respond to changes in flow in one flow path without affecting the system's ability to also change or maintain a different flow on another path. During the ramp testing no dynamic interaction between the valves was observed. All valves were able to follow the ramping demand with only a small offset error during the actual ramp.

The step tests were performed to verify the slew rate requirement of the metering valves. The amount of overshoot and the settling time were also evaluated. During the ramp and step tests the fuel system downstream pressure (engine combustor pressure) was dynamically adjusted to match the engine's characteristics and to verify the fuel system's ability to accurately control mass flow under dynamic conditions.

Frequency response testing was performed on each leg at various flow conditions. Frequency response was evaluated from mass flow demand to calculated flow from system feedback.

The actual flow test results for the dynamic testing were compared to those predicted through simulation and were found to match those generated from the fuel system model. This validated the fuel system model and enabled its use during the closed-loop simulation of the entire system, including the engine, fuel system, and actual control hardware and software.

Engine Model

A key aspect of system development testing involved the use of a real time engine simulator, interfaced to the actual control hardware. This configuration provided the ability to verify the control software under dynamic conditions that were representative of engine operation. The model software included a transfer function of the engine rotor speeds, combustor temperatures, and combustor pressures. A model of the fuel delivery system was also developed that provided the correct fuel delivery dynamics and pressure drops to the engine model. The real time model was programmed into a NetCon 5000 controller and interfaced with the engine control NetCon 5000 by use of 4–20 ma signals. The engine model NetCon was mounted into the control console, and the ability to switch from engine operation to simulator operation established by a software switch controlled from the OpTrend Monitor.

Closed-Loop Simulation

At the conclusion of the fuel system testing the engine/fuel system simulator was used to develop and validate the engine control software. The initial step in this process was the validation of the engine model with the results of the engine model produced by Pratt & Whitney. This was done by setting the fuel demand from the fuel control into a manual adjustment mode and setting fixed fuel flows. The engine model programmed into the NetCon 5000 was verified for correct rotor speeds, exhaust gas temperatures, and exhaust pressure at several steady-state fuel values. The closed-loop test setup is shown in Fig. 6.

System Transient Response

The verification of the engine model transient response was accomplished by step changes in the open-loop fuel demand values from the engine fuel control. Each small signal engine response was compared with the transient response of the Pratt & Whitney model and produced very close correlation.

The primary purpose of the closed-loop testing was the verification of the fuel control engine protection and fuel metering logic. A complete engine operating range was available in the simulation environment. This allowed for the validation of the engine starting sequence, the transient engine accelerations and decelerations, and the validation of all engine protectives. The alternative to accomplishing this testing under simulation conditions would have been costly testing in the engine test cell.

Engine Test

At the completion of system fuel flow and closed-loop testing, the control hardware was installed into the engine test facility.

The Remote I/O enclosure was mounted in the engine test cell and the fuel metering skid positioned under the test engine. Cables with quick disconnect connectors contributed to a complete installation in approximately two days. The validation of the installed system was limited to those functions unique to the test cell environment; i.e., the protective inputs from the cell gas detectors.

Engine testing to date has included the starting and acceleration to idle, steady-state operation at multiple power points from idle to 100 percent, and rapid accelerations and decelerations of varying amounts.

The validation of engine operation was completely uneventful. The fuel control system has provided the engine operation and fuel apportionment function exactly as the design required. During the initial testing phase of the engine, the majority of the effort was directed to the validation of the fuel schedules in each of the three gas fuel zones. Although close correlation with the burner development testing has been attained, adjustments were necessary in the values of control schedules. A minimum amount of time was expended in control program modification and validation due to the ability to reprogram the control system and validate the changes on the engine simulator prior to actual engine operation.

References

Lewis, G. D., 1980, "Design of a Successful Low Emissions Burner," ASME Paper No. 80-GT-12.

McVey, J. B., 1993, "Evaluation of Low-NO$_x$ Combustor Concepts for Aeroderivative Gas Turbine Engines," ASME JOURNAL OF ENGINEERING FOR GAS TURBINES AND POWER, Vol. 115, pp. 581–587.

Snyder, T. S., Rosfjord, T. J., McVey, J. B., Hu, A. S., and Schlein, B. C., 1996, "Emission and Performance of a Lean-Premixed Gas Fuel Injection System for Aeroderivative Gas Turbine Engines," ASME JOURNAL OF ENGINEERING FOR GAS TURBINES AND POWER, Vol. 118, pp. 38–45.

Parametric Modeling of Exhaust Gas Emission From Natural Gas Fired Gas Turbines

L. E. Bakken
Principal Research Advisor.

L. Skogly
Senior Engineer.

Statoil, Norway

Increased focus on air pollution from gas turbines in the Norwegian sector of the North Sea has resulted in taxes on CO_2. Statements made by the Norwegian authorities imply regulations and/or taxes on NO_x emissions in the near future. The existing CO_2 tax of NOK 0.82/Sm^3 (US Dollars 0.12/Sm^3) and possible future tax on NO_x are analyzed mainly with respect to operating and maintenance costs for the gas turbine. Depending on actual tax levels, the machine should be operated on full load/ optimum thermal efficiency or part load to reduce specific exhaust emissions. Based on field measurements, exhaust emissions (CO_2, CO, NO_x, N_2O, UHC, etc.) are established with respect to load and gas turbine performance, including performance degradation. Different NO_x emission correlations are analyzed based on test results, and a proposed prediction model presented. The impact of machinery performance degradation on emission levels is particularly analyzed. Good agreement is achieved between measured and predicted NO_x emissions from the proposed correlation. To achieve continuous exhaust emission control, the proposed NO_x model is implemented to the on-line condition monitoring system on the Sleipner A platform, rather than introducing sensitive emission sensors in the exhaust gas stack. The on-line condition monitoring system forms an important tool in detecting machinery condition/degradation and air pollution, and achieving optimum energy conservation.

Introduction

Proposed national and international guidelines normally include language that is biased toward continuous in-stack emission monitoring. The capital cost of an in-stack system is high, and in addition frequent calibration and maintenance are required. Especially for offshore installations, this places a financial burden on the operators.

Effective in 1991, Norway has introduced a CO_2 tax on natural gas and distillates used in petroleum production facilities and transport. On average, the CO_2 tax per platform is NOK 120 million/year. In total this represents approximately NOK 2.2 billion/year for Statoil as a North Sea operator. The introduction of CO_2 tax on natural gas and distillates has, however, led to a continuous effort to optimize energy conservation on offshore turbomachinery.

Further environmental restrictions are expected, especially in terms of emissions to air. The Norwegian Petroleum Directorate is at present preparing a national act for offshore emissions, which specifically includes guidelines for NO_x reduction. The conflict introducing both CO_2 and NO_x taxes is highlighted.

Introducing emission control on NO_x, whether in the form of a maximum absolute emission level or tax, requires that NO_x pollutants to the atmosphere have to be detected. Continuous detection is at present normally performed by in-stack emission monitoring. Alternatively, NO_x emissions might be established by parametric monitoring alternatives. The challenge of the latter approach lies in testing and modeling emissions to a given level of confidence.

This paper describes the field measurement results, emission scaling, and model implementation to perform on-line NO_x emission control. The major challenges include:

- field measurements of emissions and machinery condition (degradation)
- evaluation of important scaling parameters and parametric models
- development of a proposed parametric emission model to reflect machinery degradation
- implementation of the proposed NO_x model to the on-line condition monitoring system to perform continuous emission control.

In addition, gas turbine operating and maintenance costs, including emission taxes, are evaluated with respect to optimum energy conservation.

Gas Turbine Operating and Maintenance Costs

Pollutant emissions from combustion have become of great concern due to their impact on human health and nature. Restrictions in specific pollution components are introduced in several countries. Emission taxes are also introduced to curb air pollution.

At present, offshore gas turbines are operated, encouraging high thermal efficiency and low power consumption. High thermal efficiency normally demands operation close to full load, which may increase the emission of specific components. However, due to the introduction of taxes on certain emitted components, this philosophy might have to be revised.

The present emission tax on CO_2 has a substantial impact on gas turbine operating costs. Efficient operation of offshore gas turbines is most important, as optimum energy conservation on oil and gas facilities is highly influenced by gas turbine load and operating conditions. Increased tax level on CO_2, combined with a new tax or upper limit on NO_x, may change the existing operating philosophy.

Statoil has at present more than 60 gas turbines in operation. Approximately two-thirds of these are of the General Electric LM2500 type. Emission data, operation, and maintenance costs are in most cases related to operational experience from the LM2500.

Table 1 Engine operating costs due to component degradation ($P = 20$ MW)

Costs (NOK/hr)	New engine	Increased air filter loss	Reduction in η_C	Reduction in η_{HPT}	Combined degradation
CO_2-tax	4 046	4 074	4 179	4 214	4 375
Fuel costs	2 527	2 548	2 611	2 632	2 737
Maint. costs	270	270	270	270	270
Total costs	6 843	6 892	7 060	7 116	7 382

Operating and Maintenance Costs. The introduction of a CO_2 tax on fuel gas increases the operating costs of a gas turbine system dramatically. At present it is of great importance to include the influence of CO_2 taxation by focusing on optimum energy operation and maintenance.

The influence of machinery degradation on operating costs is high. Performance deterioration over 20,000 running hours represents a drop in power of up to 10 percent, at constant firing temperature. This is mainly due to inlet filter, compressor, and high-pressure turbine degradation. In-service experience shows that the main problem has become compressor fouling and erosion due to a combination of dry salt, hydrocarbons, drilling cement, and shotblast residues. However, during a hot section life cycle there will be a nonrecoverable degradation of the gas turbine due to thermal effects and mechanical wear.

To maintain high component efficiency, compressor cleaning is usually done every 750 hours, using an off-line crank washing procedure. Recently, several turbine units have been retrofitted with an on-line washing system to reduce compressor fouling effects. In addition, inlet filters are retrofitted when the pressure drop across the filter system increases by more than 100 mm H_2O. However, both filter and compressor fouling are very dependent on other platform activities.

Gas turbine *operating costs* are mainly affected by fuel costs, CO_2 tax, and maintenance costs. Almost all gas turbines are run on gaseous fuel. Fuel costs are dependent on natural gas quality at the specific installation, and in most cases in the range of NOK 0.50–0.70/Sm^3. At present the CO_2 tax is NOK 0.82/Sm^3 fuel gas. Operational experience indicates total average maintenance costs of NOK 270 per running hour.

The effect of gas turbine component degradation on performance, emissions, and operating costs is analyzed by using gas turbine simulation models (V-deck [1] and Tusipro [2]). The Tusipro model has been tuned to vendor reference performance and field test data at actual site operating conditions. The model is an important tool in investigating and establishing deterioration effects.

To highlight the influence of component deterioration on gas turbine operating costs, a case study has been performed, based on operational experience and field test performance data. The following conditions have been analyzed:

- new engine with clean air filter system
- air inlet filter loss of 150 mm H_2O
- a reduction in compressor efficiency (η_C) of 5 percent
- a reduction in high-pressure turbine efficiency (η_{HPT}) of 5 percent
- a combined degradation of the three cases defined above.

Maintenance costs are included at a constant value, based on mean time between major overhauls. The hot section repair interval (HSRI) is typically 25,000–30,000 running hours.

The results are summarized in Table 1.

Gas turbine component degradation has a great impact on total operating costs. The extra operating costs due to deterioration represent approximately NOK 4.3 million a year. In addition, deterioration causes higher firing temperature, influencing maintenance costs and intervals. The present CO_2 tax is an investment in running at high thermal efficiency and reducing power consumption by process optimization and limiting the gas turbine deterioration.

Future regulations from Norwegian authorities may include taxation on NO_x pollutants to air. To highlight the impact of an NO_x tax, an analysis has been performed based on the Swedish tax level of approximately NOK 40 per kg NO_x. In this case, gas turbine component deterioration will have an even greater impact on operating costs and maintenance intervals. Based on the same degradation cases given above, Table 2 summarizes the *increase* in operating costs under an NO_x tax regime. The increase in operational costs is related to new engine total cost (6843 NOK/h).

It can be concluded from the analysis that the introduction of an NO_x tax will influence the optimum gas turbine maintenance intervals. Depending on actual tax level, the operating philosophy is affected. For some specific operating conditions it might pay to run two gas turbine drivers at part load, compared with one at full load. Extra maintenance costs due to increased replacement of hot section components must be taken into consideration.

Nomenclature

A_{NO_x} = reference coefficient
f = fuel/air ratio
h = enthalpy
H_N = lower heating value
m = mass flow
p = pressure
P = power
t = time
T = temperature
α = constant
η = efficiency
κ = adiabatic exponent
ζ = hot section cooling air factor
Φ = relative humidity

Indices

A = air
C = compressor
FG = fuel gas
HPT = high-pressure turbine
PT = power turbine
0 = ambient (atmospheric) conditions
2 = compressor suction
3 = compressor discharge
4 = high-pressure turbine inlet
5 = high-pressure turbine discharge
6 = power turbine inlet
7 = power turbine discharge

Abbreviations

CO = carbon monoxide
CO_2 = carbon dioxide
GFA = Gullfaks A platform
HPT = high-pressure turbine
HSRI = hot section repair interval
NO = nitric oxide
NO_2 = nitric dioxide
N_2O = nitrous oxide
NO_x = nitrogen oxides
NOK = Norwegian kroner
O_2 = oxygen
SFB = Statfjord B platform
UHC = unburned hydrocarbons

Table 2 Increased operating costs due to NO$_x$ tax

Degradation costs (NOK/hr)	NO$_x$ tax not included	NO$_x$ tax included
Increased filter loss	49	147
Reduction in η_c	217	653
Reduction in η_{HT}	273	828
Combined degradation	539	1709

Table 3 NO$_x$ emissions as a function of load and degradation

Load (MW)	Anti-icing valve position (% open)	High pressure turbine disch. temperature T_{54},(°C)	NO$_x$ emission, ppmv, 15% O$_2$, dry.
14	0	737	136
14	50	760	134*
14	75	816	150
18	0	787	155
18	50	816	163

*feedback from anti-icing valve position missing

The introduction of taxes on emissions to air calls for increased focus on optimum energy conservation. The analysis underlines the importance of keeping the gas turbine performance drop within a certain limit. To control and reduce the effect of component deterioration, on-line condition monitoring systems are used. However, both periodic and condition-based maintenance are performed offshore.

Optimum Energy Conservation. An important challenge in the future development of North Sea reserves will be the exploration of new and possibly marginal fields using existing process equipment. This will necessitate process systems coping with feedstock and conditions well away from their original design base.

For some specific installations, machinery modifications have resulted in reduced operating and maintenance costs. Improvements of natural gas compressor and gas turbine operations extend both process equipment, compressor and turbine life, and major overhaul intervals. It is interesting to observe from the analysis that net savings are mainly made from low gas turbine speed and power consumption. Achieving optimum gas turbine operating conditions is an important challenge, which is given high priority in present research and development projects. Operating cost savings are for some specific installations estimated at NOK 10 million/year [3].

Optimum energy conservation for a gas turbine compression train is a complex function of operating conditions, process flexibility, and machinery condition. Existing development and analyses are based on:

- on-line condition monitoring, to detect machinery condition and component degradation
- prediction routines, to forecast degradation development as a function of time
- optimization routines, to predict optimum intervention time based on operating and maintenance costs (see Williams [4])
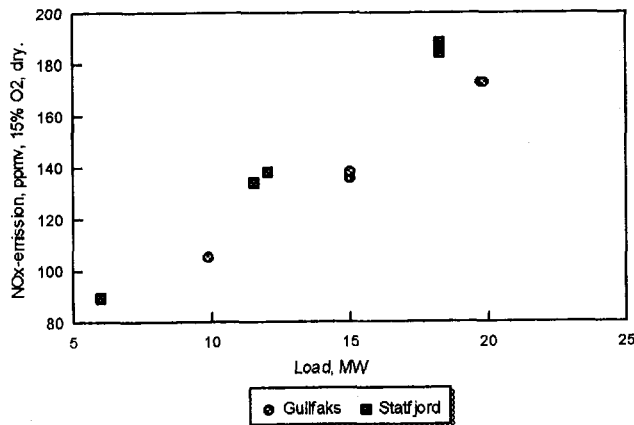
- relevant process control parameters, including interaction, product quality, and detection of operating cost savings.

The procedure given is a useful tool to evaluate the potential of new technology and systems. Attempts to perform on-line water wash on aero-derivative gas turbines have for some installations shown fewer improvements in component efficiency than expected. This is mainly due to the type of deposits, and available cleaning fluids in offshore applications.

This analysis underlines the importance of keeping the gas turbine performance drop within a certain limit. Consequently, it is important to detect machinery condition and component degradation in a reliable manner.

In future, the offshore oil and gas industry expects even harder taxes on pollution to the atmosphere. Increased tax level on CO$_2$, combined with a new tax or maximum upper limit on NO$_x$, calls for an even better optimization of energy conservation on existing offshore oil and gas production platforms. Optimum operation of offshore gas turbines is therefore an important challenge. For new installations, the air pollution taxes will affect the conceptual design either by utilizing multiphase technology to move the process from the offshore production platform to land, or by using hydropower from the onshore power grid to supply the installation.

Field Measurements and Simulated Data

The work is centered around a field test program, which allows the development of an empirical equation required for calculating emissions at different operating and ambient conditions, including typical machinery component degradation.
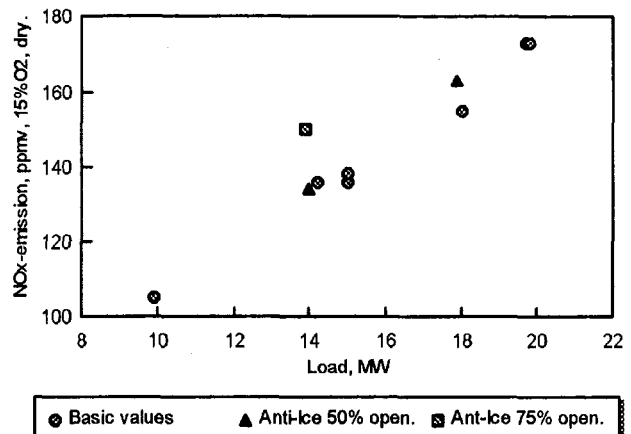

Fig. 1 Emissions of nitrogen oxides versus load from LM2500 PC and PE turbines

Fig. 2 Emissions at actual anti-icing valve position

Fig. 3 Emissions of carbon monoxides versus load from LM2500 PC and PE turbines
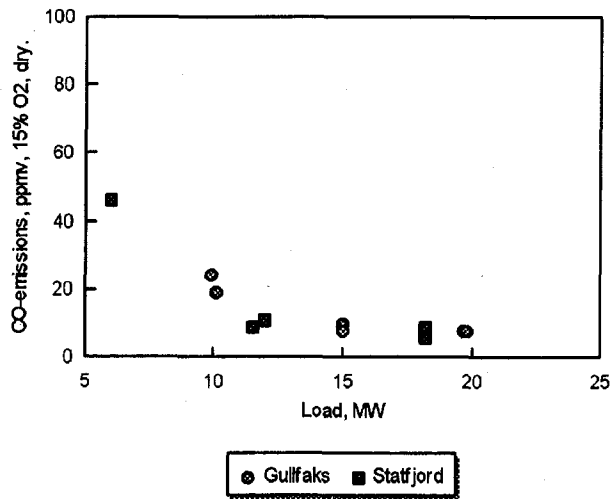

Fig. 5 Emissions of dinitrogen oxides versus load from LM2500 PC and PE turbines

In addition to field tests, measured data from the gas turbine supplier have been used. Two simulation programs have also been used in enhancing the data material. V-deck is a program developed by General Electric/Dresser Rand, which simulates an LM 2500 PE version (22 MW) gas turbine. The other model used is TUSIPRO, an in-house simulation model based on the work of M. White [3]. In this model, several NO_x correlations have been implemented to perform the present work.

The measurements were made by a third-party company, and were performed to ISO TC 192/WG 2, 1989 standard (Draft).

Instrumentation was calibrated at site according to ISO-DIS 11042/1, 1992. Experimental apparatus setup and errors are given in [6]. In addition to emission measurements, gas turbine performance, i.e., pressure and temperatures, fuel gas rate, and composition, was logged to be used in the parameter evaluation. Predicted values have been corrected according to international standards: 15 percent O_2, dry.

Field Measurements and Results. NO_x emissions were measured as a function of load and component degradation. On the Statfjord field, generator turbines of the PC version (20 MW) were measured, whereas PE type turbines (22 MW) were analyzed on the Gullfaks field. Figure 1 shows the measured values.
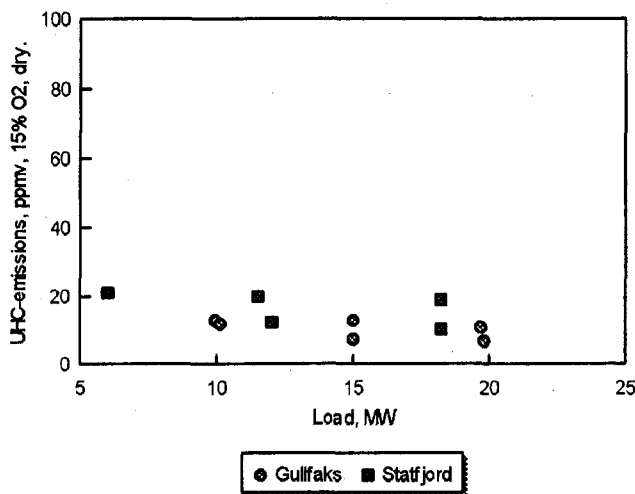

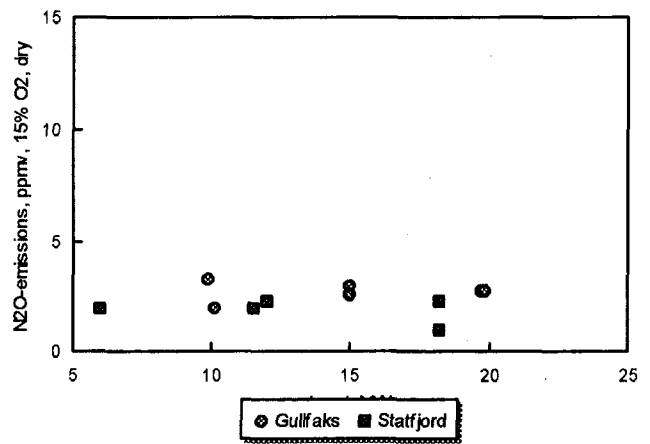Fig. 4 Emissions of unburned hydrocarbons versus load from LM2500 PC and PE turbines

Emission trends show that PC turbines give higher NO_x emissions than the PE variety, which is in accordance with manufacturer's data.

NO_x emissions were also studied as a function of load while varying the anti-ice valve position. This was done in order to establish NO_x emission levels at changed pressure, temperature and flow pattern through the gas turbine at a constant load. Current data for these emissions are given in Table 3, and a comparison with basic emissions is given in Fig. 2.

The gas turbine temperature control restricts the variation in load and anti-icing valve position. Emission data are consequently limited to an output of 18 MW. The impact of component deterioration is higher as the output increases up to full load.

Emissions of carbon monoxides (CO), unburned hydrocarbons (UHC), and dinitrogen oxide (N_2O) have also been measured as a function of load. Except from UHC, emission components are measured by a nondispersive infrared sample conditioner train with electronic interference compensation for CO and CO_2. UHC were measured as proane-equivalence on wet basis with preheated equipment. The results, which are presented in Figs. 3–5, are in accordance with data previously published. Note that the scale varies on these figures to illustrate the curve trends better.

Performance Evaluation. In the evaluation of component deterioration effects on emission levels, the turbine performance is to be established. By using the existing condition monitoring system, all relevant parameters are detected. The accuracy of the emission measurements is directly related to the uncertainties of each analyzer. The uncertainties are shown in Table 4. In addition, some inaccuracy in measuring fuel gas consumption and

Table 4 Given uncertainties in analyzers used

Analyser	Uncertainty
NO	± 0.5 % of measured value *
UHC	± 1.0 % of measured area (0-10 ppm)
N_2O	≤ ± 2.0 % of measured area (0-100 ppm)
CO	≤ ± 2.0 % of measured value *
CO_2	≤ ± 2.0 % of measured value *
O_2	≤ ± 0.1 % of measured value *

* Actual measured value given in figure 1 - 5

Table 5 Measured and logged parameters during field tests

Parameters	Symbol	Unit
Operating hours		hr
Time, measurement starts	t1	hr, min
Time, measurement ends	t2	hr, min
Fuel gas analysis	(Compositional)	mole %
Fuel gas flow	m_F	kg/s
Lower heat value	H_n	MJ/kg
Emission data		
Oxygen	O_2	ppmv
Carbon monoxide	CO	ppmv
Carbon dioxide	CO_2	ppmv
Nitrogen oxides	NO	ppmv
Nitrogen dioxides	NO_2	ppmv
Dinitrogen oxides	N_2O	ppmv
Unburned hydrocarbons	UHC	ppmv
Turbine data		
Atmospheric pressure	P_0	mbar
Atmospheric temperature	T_0	°C
Relative humidity	Φ	%
Plenum air pressure	P_2	bar
Plenum air temperature	T_2	°C
Compressor disch. pressure	P_3	bar
Compressor disch. temperature	T_3	°C

PT turbine inlet pressure	P_6	bar
PT turbine inlet temperature	T_6	°C
PT turbine outlet pressure	P_7	barg
PT turbine outlet temperature	T_7	°C
PT turbine speed	TNL	rpm
HPT turbine speed	TNH	rpm
Anti-ice valve position		% open
Generator load	DW	MW

generator power (1–2 percent of measured value and ≤ ±0.2 MW, respectively) must be considered.

Measured values and logged parameters are listed in Table 5. All values have been logged in three series, giving mean values representing the measurement period.

Emission Scaling

An interesting alternative to in-stack emission monitoring is to establish NO_x emissions by parametric monitoring. The challenge of this approach lies in testing and modeling emissions with respect to actual operating conditions and machinery degradation.

Several empirical and analytical emission models have been proposed in the literature to provide estimates of the exhaust emission of NO_x, CO, and unburned hydrocarbons. However, very few of the proposed emission models are used to perform continuous emission control at site conditions. Tuning the emission model to actual site and machinery conditions is therefore of great importance.

The objective of introducing parametric monitoring for emission control is to provide the offshore industry with a cost-effective methodology. Using the existing on-line condition monitoring system, all relevant parameters are made available, including machinery component degradation.

Emission Kinetics

Formation Mechanisms. NO_x is a term common for all nitrogen oxides, and is often represented as the sum of NO and NO_2, on weight basis. The formation of NO_x is mainly related to the thermal effects, which were first considered more than 20 years ago [5].

The concentration of important pollutants in exhaust is governed by the mean residence time in the combustion zone, the chemical reaction rates, and the mixing rates. Oxides of nitrogen are produced in the central hot region of the combustor by oxidation of atmospheric nitrogen, and most of the NO_x emitted in the exhaust is nitric oxide, NO. If fuel contains organically bound nitrogen, some of this nitrogen might form fuel NO. Particularly with fuel-rich flames, the oxidation of atmospheric nitrogen has been observed to produce prompt NO. The first three mechanisms describe the NO formation, while the last one describes the formation of NO_2.

Thermal NO. Referred to as the extended Zel'dovich mechanism, NO is formed by an oxidation of atmospheric nitrogen (N_2). The formation is very temperature dependent, i.e., a higher combustion temperature increases the NO_x formation. This mechanism is the main contributor to gas turbine NO_x formation:

$$O + N_2 = N + NO \tag{1}$$

$$N + O_2 = NO + O \tag{2}$$

$$N + OH \rightarrow NO + H \tag{3}$$
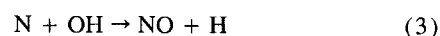
Due to its temperature sensitivity, the thermal NO is formed in the narrow region of the reaction zone. Several expressions for the rate of change of NO have been published. A representative one is given by [6]:

$$\delta[NO]/\delta t = 2AT^\alpha e^{-38440/T}[N_2][O_2] \ (mole/cm^3 \ s) \tag{4}$$

The prompt mechanism. NO is formed as a reaction of hydrocarbon fragments and atmospheric nitrogen, which are subsequently oxidized to form NO. The prompt mechanism is less understood, but is formed in the reaction zone at the fuel side. The formation is much less temperature sensitive than thermal NO:

$$CH + N_2 \rightarrow HCN + N \tag{5}$$

$$N_2 + O_2 \rightarrow 2NO \tag{6}$$
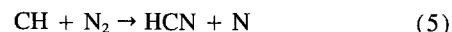
Fuel nitric oxides. Organically bound nitrogen in the fuel oxidizes to NO. This mechanism is of less importance for combustion of natural gas, due to small amounts of nitrogen compounds in the fuel. The gross characteristics of the reaction mechanism can be represented as:
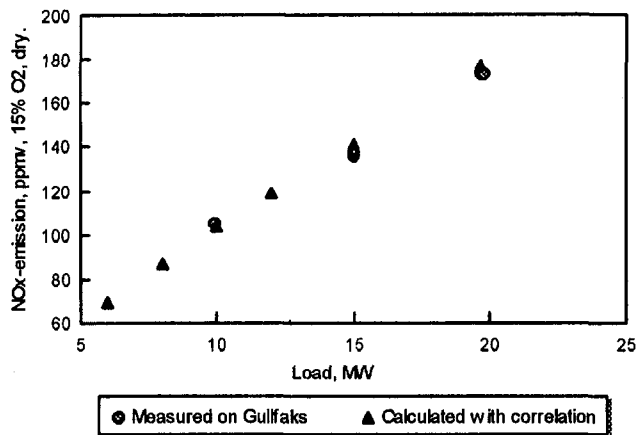
$$Fuel \ N >- HCN >- NH_i \begin{cases} + \ oxidants \rightarrow NO \\ + \ NO \rightarrow N_2 \end{cases} \tag{7}$$
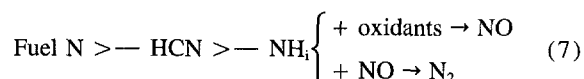
Fig. 6 NO$_x$ emissions on Gullfaks

Oxidation of NO. NO$_2$ is formed by oxidation of NO, mainly by low temperatures:

$$NO + O \rightarrow NO_2 \qquad (8)$$

NO$_x$ Emission Parameters. The objective of this project has been to establish the formation of NO$_x$ emission from the GE-LM 2500 gas turbines, without utilizing, for instance, three-dimensional combustor performance codes, with mathematical expressions based on detailed chemical kinetics schemes. This approach necessitates detailed information regarding combustor geometry, for instance.

A correlation has been developed, based on the overall NO$_x$ producing mechanism as described above. Proposed parameters should:

- describe the most important factors affecting NO$_x$ formation, combustion temperature, and residence time
- include parameters that are sensitive to gas turbine site conditions, e.g., component degradation
- be available in the existing condition monitoring or process control system

In the evaluation of important scaling parameters, emphasis is put on describing the physical and chemical processes governing the pollutant formation on an overall scale. Component deterioration entails deviation in the normal pressure/temperature path through the gas turbine, which should be included in the parametric emission model. A numerical study was conducted to determine the separate effects of such parameters as system temperature and pressure, residence time, and fuel/air ratio. The following emission parameters are most important:

- compressor discharge pressure (p_3)
- fuel-to-air ratio (f)
- combustor discharge temperature (T_4)

Compressor Discharge Pressure, p_3. Combustor inlet condition is an important factor in the formation of NO$_x$. Increased combustor inlet temperature and pressure affects the adiabatic flame temperature, and thus the NO$_x$ formation.

Through the 1970s and up to the present, several analyses have been performed on the effect of the combustor pressure. Increased combustor pressure affects the preheating of air to the combustor. The numerical study performed, and analyses made by others, conclude that pressure has a significant effect on the diffusion flame temperature. The emission measurements performed are all on gas turbines with diffusion flames. Related to component degradation, deviation in pressure and temperature profile along the gas turbine is important and the combustor pressure is therefore one major parameter in the formation of NO$_x$. Increased pressure also affects the mean residence time.

Compressor discharge pressure is measured in the condition monitoring system.

Fuel-to-Air Ratio, f. The fuel/air ratio is defined as the fuel flow rate divided by the compressor discharge air flow rate ($f = m_{FG}/m_A$). The highest combustion temperature is achieved by stoichiometric combustion, that is, equal molar amounts of fuel and oxygen. An excess or shortage of oxygen lowers the combustion temperature, and the NO$_x$ formation. This makes the fuel/air ratio an important factor in determining the NO$_x$ formation and concentrations. In addition to influencing the temperature, the air flow rate also affects the mean residence time. An increase in air flow rate decreases the mean residence time, and thus the NO$_x$ formation. The thermal NO residence time is a function of combustor diameter, air jet velocity, and stoichiometry in the primary zone.

The fuel flow rate, m_{FG}, is continuously measured in the condition monitoring system. The air flow rate is calculated by the relationship:

$$P_{PT} = [(m_A(1 - \zeta) + m_{FG})(h_6 - h_7)]/\eta_{PT} \qquad (9)$$

The enthalpies are calculated from power turbine pressures and temperatures. All the parameters are included in the condition monitoring system.

Combustor Discharge Temperature, T_4. The adiabatic flame temperature is an important parameter in the formation of NO$_x$. Combustor discharge temperature and pressure allow the discrimination between pressure effects and temperature effects. To reflect the combustion temperature, and include high-pressure turbine deterioration, the combustor discharge temperature is important. Combustor discharge temperature, T_4, is calculated from the thermodynamic relation:

$$T_4 = T_5(p_4/p_5)^{(\kappa-1)/\kappa\eta_{HPT}} \qquad (10)$$

This relationship includes the high-pressure turbine efficiency, η_{HPT}, which reflects the turbine degradation. T_4 represents the combustion temperature and thereby NO$_x$ formation better than compressor discharge temperature. The procedure includes, however, several measured parameters, which may to some extent affect the accuracy.

NO$_x$ Correlation. Several empirical and analytical emission models have been proposed in the literature to provide estimates of the exhaust emission of NO$_x$, CO, and unburned hydrocarbons. The calculation procedure for most models is based on the concept that the concentration of various species is governed by reaction rate, mean residence time, and the mixing process.
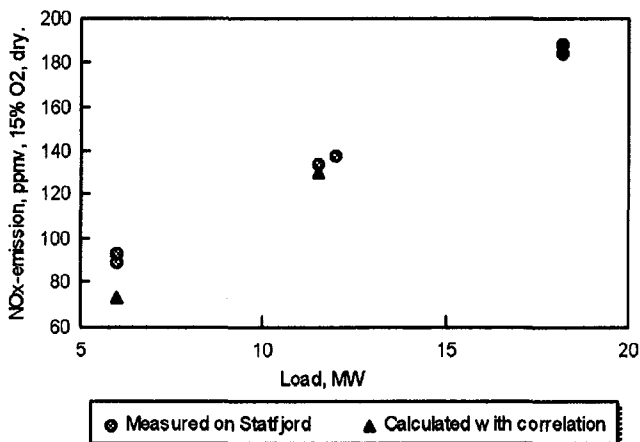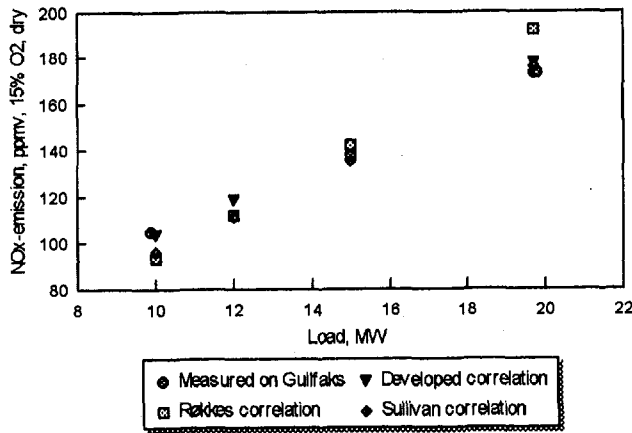

Fig. 7 NO$_x$ emissions on Statfjord

Fig. 8 NOₓ emission calculated from different correlations

Dependent on purpose, the emission models are of different levels of fidelity. Improvement in prediction accuracy is made by emission models that combine analytical capabilities of three-dimensional combustor performance codes with mathematical expressions based on detailed chemical kinetics schemes. This approach necessitates detailed information regarding combustor geometry, for instance, giving a powerful tool in optimization of the combustor design to minimize pollutant formation and maintain satisfactory stability and performance.

For the purpose of on-line prediction of NO_x emission, the empirical approach has been used. In these models the effects of system pressure, temperature, and residence time account for the lack of rules in controlling the reactions (reaction term). The proposed correlation is given in Eq. (11):

$$NO_x = 62*p_3^{0.5}*f^{1.4}*\exp(-635/T_4) \qquad (11)$$

Pressure is given in Pa, massflow in kg/s, and temperature in °C. The correlation has been developed from field measurements and simulated data at standard ambient conditions ($T_0 = 15°C$, $p_0 = 1$ bar, and $\phi_0 = 60$ percent). Correlation factors and exponents are developed by a numerical parameter analysis.

NO_x emission predictions have been compared with field measurements on Gullfaks and Statfjord. The results are presented in Figs. 6 and 7.

The calculated NO_x emissions from the developed correlation give good agreement with the measured values. The deviation between calculated and measured values in the normally operated load area is approximately 2 percent. Two previously developed correlations have given good approximation to measured values. These are Sullivan [6] and Røkke et al. [7], which correlations are given in Eqs. (12) and (13), respectively. The proposed correlation by Sullivan:

$$NO_x = A_{NO_x}*p_3^{0.5}*f^{1.4}*m_A^{-0.22}*\exp(T_3/250) \qquad (12)$$

A_{NO_x} is a reference coefficient, p_3 is given in Pa, m_A in kg/s, and T_3 in Kelvin. Sullivan's correlation has been developed based on laboratory tests of heavy-duty gas turbines, and the result is given in ppmv, wet basis. In comparison with the other correlations, the calculated value from Sullivan's correlation has been recalculated into dry basis and 15 percent O_2. The proposed correlation by Røkke et al.:

$$NO_x = 18.1*(p_3/p_2)^{1.42}*m_A^{0.3}*f^{0.72} \qquad (13)$$

Mass flow of air is given in kg/s and the result is given in ppmv, 15 percent O_2, dry. The correlation has been developed for smaller gas turbines, and has proven to correspond to measurements from some LM2500 PC machines.

A comparison between presented correlations and measured data from Gullfaks is given in Fig. 8. The figure shows that all correlations give fairly good representation of the data, whereas Røkke's correlation is more sensitive to load. The proposed correlation is specifically developed to include deterioration effects. To confirm this effect, different degradation scenarios have been analyzed. The proposed correlation is compared with Røkke's correlation in five scenarios:

1. No degradation
2. 60 mm H_2O filter loss
3. 5 percent reduction in compressor efficiency
4. 5 percent reduction in high-pressure turbine efficiency
5. Combined degradation.

The result is given in Table 6, and the difference between best and worst case (scenarios 1 and 5) is illustrated in Fig. 9. The correlation given by Sullivan is not presented.

The analysis proves the developed correlation to be sensitive to degradation, a feature that will be useful for implementation and continuous calculation of NO_x emissions. Among the degradation types analyzed the correlation is more sensitive to reduction in high-pressure turbine efficiency. Figure 9 shows the relation between load and sensitivity to degradation on the NO_x formation.

Table 6 Effect of degradation on NOₓ emissions

Correlation Load, MW	No degradation	Filter loss	5 % red. in η_C	5 % red. in η_{HP} turbine	Combined degr.
Developed	NOₓ-emissions		(ppmv, 15 % O₂, dry)		
6 MW	61.4	62.5	76.3	77.7	103.9
11 MW	100.3	101.6	120.8	123.7	160.3
16 MW	136.5	138.3	159.4	163.5	209.1
22 MW	183.3	185.6	205.4	209.9	265
Røkke	NOₓ-emissions		(ppmv, 15 % O₂, dry)		
6 MW	55.1	56	55.9	55.9	59.9
11 MW	99.9	101.4	101	100.8	107.5
16 MW	149.1	151.2	150.1	149.8	159.3
22 MW	215.7	218.8	215.3	214.8	228.1

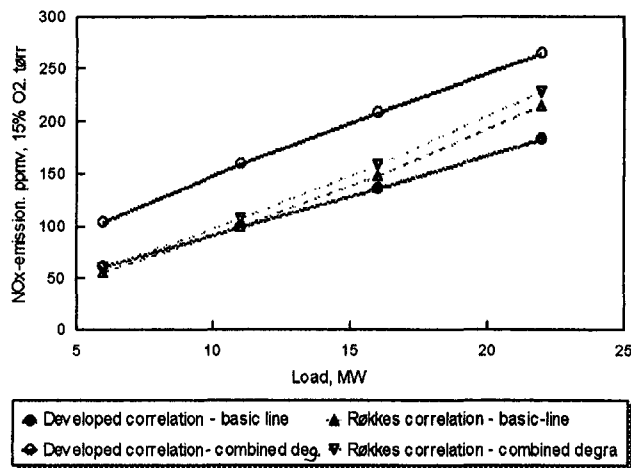| Developed correlation - basic line | Røkkes correlation - basic-line |
| Developed correlation- combined deg. | Røkkes correlation - combined degra |

Fig. 9 Illustration of sensitivity to degradation for two NO_x correlations

Implementation. Several empirical and analytical emission models have been proposed in the literature to provide estimates of the exhaust emission of NO_x, CO, and unburned hydrocarbons. However, very few of the proposed emission models are used to perform continuous emission control at site conditions. Tuning the emission model to actual site and machinery conditions is therefore of great importance.

The objective of introducing parametric monitoring for emission control is to provide the offshore industry with a cost-effective methodology. Using the existing on-line condition monitoring system, all relevant parameters are made available, including machinery component degradation.

The proposed correlation is implemented in the condition monitoring system on Sleipner A. The "principle" of parametric emission monitoring will be extensively verified by control measurements on the Sleipner A installation. A total of 150 MW is installed, representing several gas turbines to be evaluated.

The method should be verified by extensively testing a number of gas turbine prime mover types. It is important to evaluate field instrumentation requirements and test procedures, including base line emission maps for the individual machine.

The development has required working closely with the Norwegian authorities to ensure possible acceptance of the method. A final approval is intended to be included in the National Act for Emissions to Air. In this respect, factors like component deterioration effects on NO_x emissions are to be verified.

Summary and Conclusions

Environmental regulations represent an important consideration in energy production. At present, offshore gas turbines are operated, encouraging high thermal efficiency and low power consumption. High thermal efficiency normally demands operation close to full load, which may increase the emission of specific components. However, due to the introduction of taxes on certain emitted components, this philosophy might have to be revised.

Gas turbine component degradation has a great impact on total operating costs. The extra operating costs due to deterioration represent approximately NOK 4.3 million a year. In addition, deterioration causes higher firing temperature, which influences maintenance costs and intervals. The present CO_2 tax is an investment in running on high thermal efficiency and

reducing power consumption by process optimization and limiting gas turbine deterioration.

In the future, the offshore oil and gas industry expects even higher taxes on pollution to the atmosphere. Increased tax levels on CO_2, combined with a new tax or maximum upper limit on NO_x, call for an even better optimization of energy conservation on existing offshore oil and gas production platforms. It can be concluded from the analysis that the introduction of an NO_x tax will influence the optimum gas turbine maintenance intervals. Operating philosophy will be affected by the actual tax level. For some specific operating conditions it might pay to run two gas turbine drivers at part load, compared with one at full load. Extra maintenance costs due to increased replacement of hot section components should be taken into consideration.

The analysis underlines the importance of keeping the gas turbine performance drop within a certain limit. Consequently, it is important to detect machinery condition, component degradation, and emission levels in a reliable manner.

NO_x emissions have been measured as a function of load and component degradation, and a correlation has been developed, based on the overall NO_x producing mechanism. In the evaluation of important scaling parameters, emphasis is put on describing the physical and chemical processes governing the pollutant formation on an overall scale. Component deterioration entails deviation in the normal pressure/temperature path through the gas turbine, which should be included in the parametric emission model. A numerical study was conducted to determine the separate effects of such parameters as system temperature and pressure, residence time, and fuel/air ratio. The following emission parameters are most important:

- compressor discharge pressure (p_3)
- fuel-to-air ratio (f)
- combustor discharge temperature (T_4)

Based on these parameters, a NO_x prediction model is proposed:

$$NO_x = 62 * p_3^{0.5} * f^{1.4} * \exp(-635/T_4) \qquad (11)$$

The calculated NO_x emissions from the developed correlation give good agreement with the measured values. The deviation between calculated and measured values in the normally operated load area is approximately 2 percent.

The NO_x correlation is implemented in the condition monitoring system on the Sleipner A installation. This represents an interesting alternative to continuous in-stack emission monitoring, and provides the offshore industry with a cost-effective methodology for emission control. However, more rigorous testing of the proposed model will be required before it can become an alternative to in-stack emissions monitoring.

References

1 General Electric/Dresser Rand, LM2500 simulation program "V-Deck," Kongsberg, Norway, 1993.

2 White, M. F., Gas turbine simulation program "Tusipro," Norwegian Institute of Technology, 1993.

3 Bakken, L. E., "A Method to Improve Energy Conservation on Offshore Gas Compression Systems," Gas Processors Association, 1992.

4 Williams, L. J., "Optimisation of Time Between Overhauls for Gas Turbine Compressor Systems." Toronto, 1987.

5 Lipfert, F. W., "Correlation of Gas Turbine Emission Data." ASME Paper No. 72-GT-60.

6 Sullivan, D. A., "A Simple Gas Turbine Combustor NO_x Correlation Including the Effect of Vitiated Air," ASME JOURNAL OF ENGINEERING FOR POWER, Vol. 99, 1977.

7 Røkke et al., "Pollutant Emissions From Gas Fired Turbine Engine in Offshore," ASME Paper No. 93-GT-170.

B. Seyedan

P. L. Dhar

R. R. Gaur

Department of Mechanical Engineering,
Indian Institute of Technology,
New Delhi—110016, India

G. S. Bindra
Bharat Heavy Electrical Ltd.,
New Delhi 110049, India

Optimization of Waste Heat Recovery Boiler of a Combined Cycle Power Plant

In the present work a procedure for optimum design of waste heat recovery boiler of a combined cycle power plant has been developed. This method enables the optimization of waste heat recovery boiler independent of the rest of the system and the design thus obtained can directly be employed in an existing plant.

Introduction

Recently, the concept of a combined cycle power plant (CCPP) has been gaining widespread acceptance, because of its higher efficiency and reduced pollution levels. The design of such combined cycle power plants is, however, much more involved because of coupling between the two power-producing cycles, the primary gas turbine cycle and the bottoming steam cycle, brought about by the waste heat recovery boiler.

In a combined cycle power plant the air compressor, the gas and steam turbines, various pumps, valves, etc. are standard equipment, which are available in various standard sizes. A waste heat recovery boiler (WHRB) is the only key component that is usually specifically designed and built for every power plant. As the heat exchanger areas needed in a WHRB are very large, its cost is a significant fraction of the total cost of power plant. There is thus considerable scope for cost reduction of a CCPP by optimal design of its WHRB.

Since the WHRB is the equipment that couples the two power-producing cycles of a combined cycle power plant, any change in its design influences the power output of both the steam cycle and gas turbine cycle. While carrying out the search for optimal design of a WHRB, it is therefore essential to estimate the power output of a CCPP for every potential design and choose only those designs that give the total output equal to (or greater than) the rated output of power station. A procedure for simulation of combined cycle power plant is therefore a prerequisite for developing a procedure for optimum design of a WHRB.

This paper describes the details of a procedure developed for optimization of a WHRB of a CCPP using the program for performance prediction of a typical CCPP, details of which have been presented elsewhere (Seyedan et al., 1994). In order to illustrate the procedure, the optimum design of a WHRB for a typical CCPP (employing dual-pressure bottoming cycle) built by a prominent Indian company, has been carried out (Fig. 1). The present design of a WHRB is taken as the base design and the newer designs generated by this procedure are compared with it to assess the extent of cost reduction possible.

Computer Simulation Strategy

Figure 1 shows the schematic diagram of the combined cycle power plant taken up for detailed optimization of the WHRB, and Fig. 2 shows the information flow diagram indicating the strategy finally adopted for determining its performance. The

---

complete genesis of this strategy is presented elsewhere (Seyedan et al., 1994). It is obvious from the multinested nature of Fig. 2 that an iterative solution strategy would be imperative. This necessitates assumption of suitable initial values to start the simulation. The best strategy, as identified from the information flow diagram, is to assume appropriate values of the following variables:

1 Air flow rate through air compressor (M_{air})
2 Gas side pressure drop across boiler (DPB)
3 HP-pump exit pressure (P_{HPEI1})
4 LP-pump exit pressure (P_{LPEI})
5 HP-drum pressure (P_{D1})
6 HP-economizer II inlet temperature (T_{HPEI2})
7 LP-drum pressure (P_{D2})
8 Condenser pressure (P_{COND})
9 Condensate control valve pressure drop (ΔP_{v1})

This enables sequential simulation of various components and then checks are made to ensure that the assumed values of the variables satisfy the following compatibility conditions:

1 Mass balance across compressor and turbine
2 Energy balance of HP-drum
3 Mass balance across HP-pump and HP-turbine
4 Energy balance of LP-drum
5 Temperature matching at HP-Econ 2 inlet with HP-Econ 1 outlet
6 Mass balance of various streams at exit of HP-turbine and inlet to LP-turbine
7 Energy balance across condenser
8 Mass balance of deaerator tank
9 Pressure drop balance across boiler

Consequently, using a suitable algorithm, the values of the nine variables that satisfy the nine compatibility equations are found. The complete operating conditions of the systems are thus determined and the performance level achieved (i.e., its net power output) can then be easily calculated.

Strategy of Optimization

The first step in optimization is to transform the physical situation into a mathematical model, by identifying the number and type of variables, objective function, and the constraints imposed on the system.

The Objective Function

For the present case, the capital cost of the boiler (WHRB) has been taken as the objective function to be minimized.
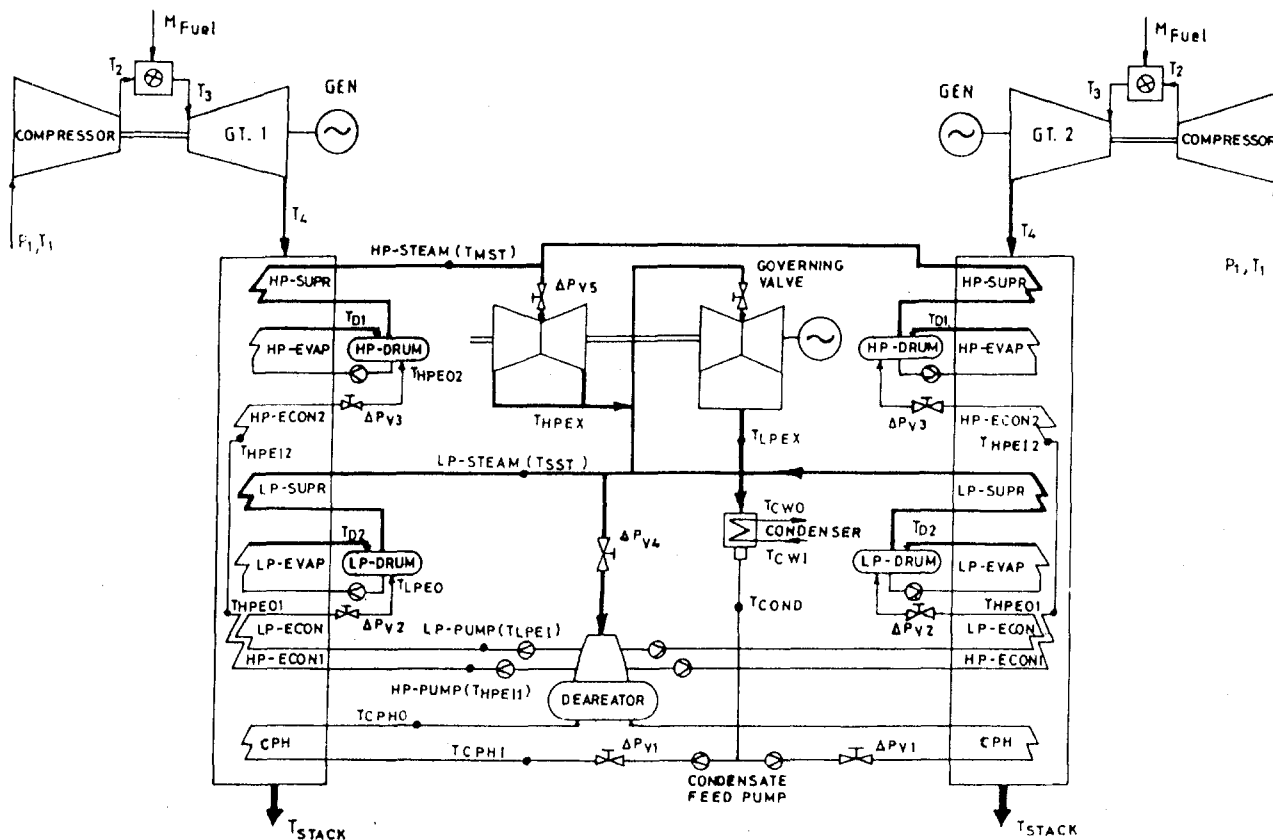
Copyright © 1996 by ASME

Fig. 1 Schematic diagram of a dual-pressure combined cycle power plant

The main components of a WHRB are the economizers, evaporators, superheaters, and the condensate preheater. The total cost of the boiler is thus the sum of the costs of these components and other related costs, such as those of interconnected piping etc.

The cost of any heat exchanger is a complex function of a number of factors like number, length, diameter, and thickness of the tubes and fins (if employed). However, practicing engineers recommend that it can be safely taken as a direct function of its total weight. Accordingly the objective function for optimization has been taken as:

$$F = \sum_{j=1}^{N} \left(\sum_{i=1}^{N_P} N_P N_T V \rho \right) \tag{1}$$

where:

N_P = number of passes
N_T = number of tubes in a row

V = volume of steel in each tub
ρ = density of tube material, kg/m^3
N = total number of heat exchangers in the WHR

Variables

The WHRB of CCPP under consideration (Fig. 1) consists of seven independent heat exchangers. Though theoretically it is possible to have different dimensions (like tube diameter length, thickness, etc.) of each of these heat exchangers, keeping in the view the current design practice, manufacturing consideration, and the need for standardization, the values of the following variables have been taken the same for each of these heat exchangers:

1 Length of tubes
2 Number of tubes in a row
3 Transverse pitch between tubes
4 Longitudinal pitch between tubes

Nomenclature

d_o = tube outer diameter, m
DPB = boiler gas side pressure drop, bar
h_f = height of fin, m
N = total number of heat exchangers in the WHRB
N_p = number of passes
N_T = number of tubes in a row
P = pressure, bar
Pcc = combined cycle power output, MW
Pcc_r = combined cycle rated power output, MW

Q = heat transfer rate, W
S_L, S_T = longitudinal and transverse pitch of a tube bank, m
T = absolute temperature, K
V = variable assumed in the simulation procedure
Vg_{max} = maximum gas velocity, m/s
Vg_r = gas velocity rated, m/s
W = work, J; width of boiler, m
ρ = mass density, kg/m^3

Subscripts and Superscripts

e, i = exit, inlet
o = outside, across
p = pump
t = turbine
V = valve
1 = compressor inlet
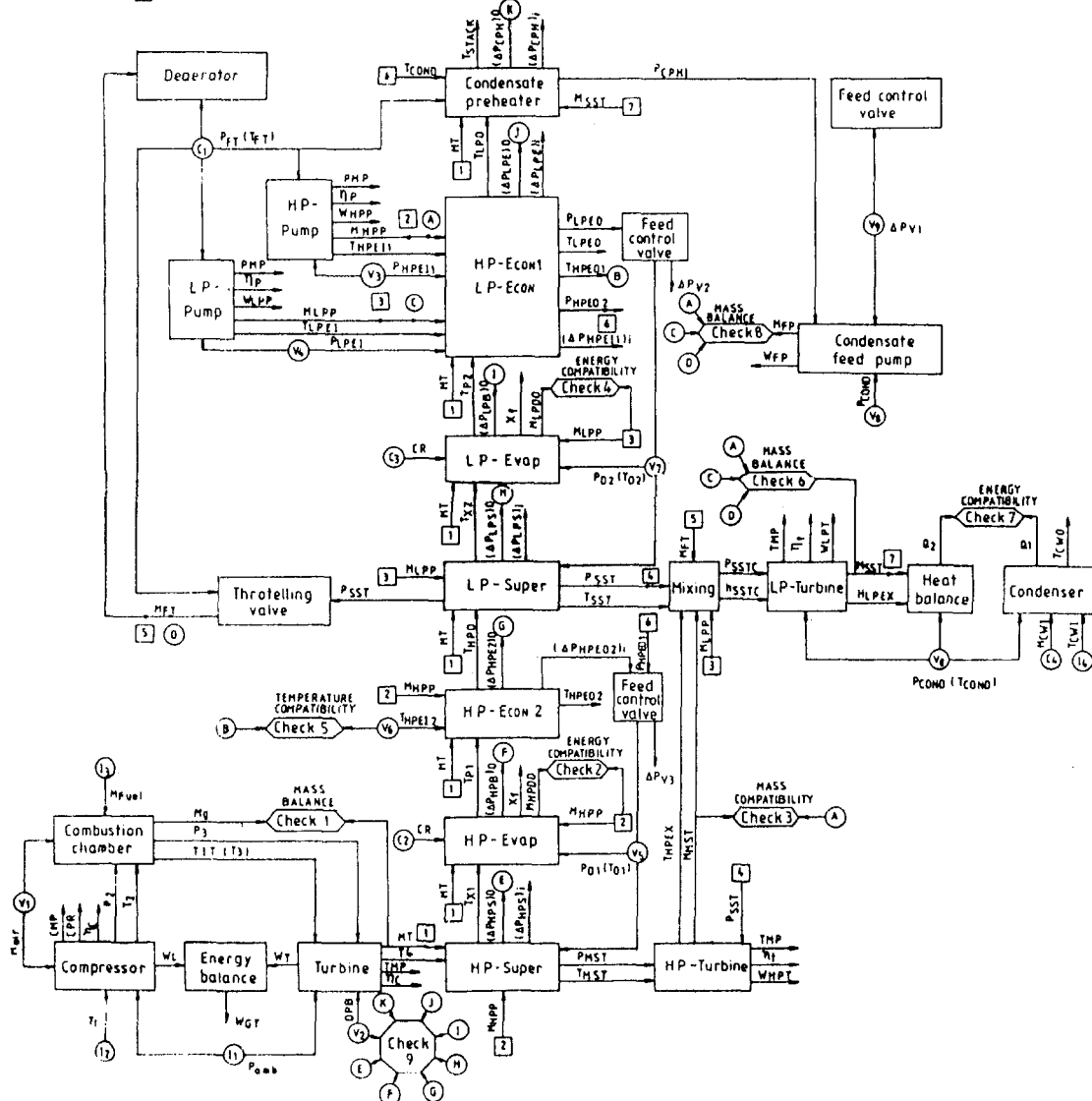2 = compressor delivery
3 = turbine inlet
4 = turbine exit

Fig. 2 Information flow diagram for a dual-pressure combined cycle

5 Number of fins per unit length
6 Height of fins
7 Thickness of fins

It is also necessary not to vary some of these dimensions (like tube length, number of tubes in a row, etc.) at various sections of the WHRB to prevent bypass of hot gases across the heat exchangers and to have proper gas approach at various sections. Again for the sake of conformity with existing configuration, the number of passes in various sections has been maintained at the same value as in the existing design. Out of these variables the number of tubes can take only integer values, while the rest can take any value greater than zero.

Constraints

To make the system optimization meaningful, it is obviously necessary to ensure that changes in the design of the WHRB are carried out subject to the constraint that the net power output does not fall below the rated value, i.e.,

$$Pcc \geq Pcc_r \qquad (2)$$

As the tube diameter, fin height, and tube spacing are independent variables to be optimized, geometric compatibility demands imposition of the following constraints:

$$S_T \geq d_o + 2h_f; \qquad (3)$$

$$S_L \geq d_o + 2h_f; \qquad (4)$$

Table 1 Existing design of various heat exchangers of a WHRB

S.No.	Heat Exchangers	No. of paths	No. of passes	No. of tubes in a row
1	HP-Superheater	4	8	98
2	HP-Evaporator	5	20	98
3	HP-Economizer II	1	18	98
4	HP-Economizer I	2	20	80
5	LP-Superheater	4	4	98
6	LP-Evaporator	4	16	98
7	LP-Economizer	2	20	18
8	Condensate Preheater	2	14	98

Table 2 Various design values of variables of a WHRB and the range of variation during optimization

S.No.	Variables	Unit	Design Value	Range of Variation
1	Length of tubes	m	18.5	10 - 25
2	Number of tubes in a row	--	98.0	60 - 130
3	Transverse pitch	mm	80.0	60 - 120
4	Longitudinal pitch	mm	70.0	60 - 100
5	Number of fins/meter	--	150.0	120 - 180
6	Height of fin	mm	15.0	5 - 20
7	Thickness of fin	mm	1.3	0.5 - 2.0

Table 4 Optimum design of a WHRB with four possible tube diameters

S. No.	Variables	Units	OD=31.8 TH=2.6	OD=25.5 TH=2.6	OD=38.1 TH=3.406	OD=51 TH=3.403
1	Length of tube	m	13.4	13.9	18.1	10.8
2	Number of tubes in arrow	--	112.0	101.0	81.0	108.0
3	Transverse pitch	mm	34.4	93.8	89.3	119.7
4	Longitudinal pitch	mm	60.0	65.9	64.9	88.6
5	Number of fins/meter	--	168.2	169.6	169.9	152.2
6	Height of fin	mm	14.9	18.5	14.3	17.9
7	Thickness of fin	mm	1.0	1.0	1.0	1.0
	Total weight	Tons	692.8	677.8	876.2	977.3

where d_o is tube outer diameter, h_f is fin height, and S_T and S_L are the transverse and longitudinal tube pitches.

Another constraint arises from the necessity of limiting the velocity of exhaust gas to restrain vibration and noise across the WHRB:

$$Vg_{max} \leq Vg_r \qquad (5)$$

For the present case the maximum gas velocity has been taken as 14.0 m/s as per current design practice in industry. Since the optimization is essentially a search procedure, in order to prevent unnecessary exploration of new designs in obviously infeasible variable space, appropriate upper and lower bounds are provided for the values of all the variables. Thus, for the system under consideration, the tube length is constrained to lie between 5 and 25 m, the transverse and longitudinal pitches are constrained to lie between 60 and 85 mm, and so on.

Optimization Procedure

Once the system variables, the objective function, and the constraints are defined, a suitable method has to be adopted to determine the values of variables that minimize the objective function while satisfying the given constraints. The design variables and constraints show that the system optimization is a mixed integer nonlinear programming problem. For such problems, a Modified Box Complex Method developed by Dhar (1974) and Dhar et al. (1987) has been found to be quite efficient (Saraf, 1979; Jain, 1994). Accordingly, this algorithm has also been employed in the present study.

Optimum Design of a Typical WHRB

This complete optimization procedure has been written into a fortran program. To test its efficiency, the optimum design of a WHRB of a typical 800 MW combined cycle power plant, manufactured by a prominent Indian company, has been carried out. For the present study the configuration of various heat exchangers of the WHRB (Fig. 1) given in Table 1 is retained. Also, to have uniform flow across the tube bundles, a constant tube diameter of 31.8 mm with 2.6 mm thickness is considered. The width of boiler is calculated as:

Table 3 Comparison of optimum design of a WHRB with an existing design

S.No.	Variables	Units	Design Value	Optimum Value	Optimum design with six variables
1	Length of tubes	m	18.5	13.4	16.8
2	Number of tubes in a row	--	98.0	112.0	85.0
3	Transverse pitch	mm	80.0	34.4	85.0
4	Longitudinal pitch	mm	70.0	60.0	62.4
5	Number of fins/meter	--	150.0	168.2	170.0
6	Height of fin	mm	15.0	14.91	15.3
7	Thickness of fin	mm	1.3	1.0	1.3
	Total weight	Tons	922.3	692.8	801.3

$$W = (N_T + 2)S_T \qquad (6)$$

where W is width of boiler and NT number of tubes in a row.

The existing design of WHRB is provided as the base design (Table 2) and starting from this the algorithm automatically generates newer designs, tests them for feasibility (i.e., whether these satisfy the various constraints) and continually changes the values of design variables (within the specified range) in such a manner that the objective function is minimized.

Results and Discussion

Table 3 shows at a glance the distinctive features of the optimum design thus obtained vis-à-vis the existing design. It is observed that the optimum design uses more of tubes of shorter length. The fin thickness is reduced to the limiting value of 1 mm, but the number of fins per meter length is increased. The optimum design results in reduction of total weight by 229.5 tons (i.e., 25 percent). In the actual design there are two modules of combined cycle power plant, each module consisting of two gas turbines with two WHRBs feeding a single steam turbine. Thus for four WHRBs, there is possibility of reduction of total weight by 918 tons, which means reduction of capital cost about 30 million rupees (US $1 million).

In order to study how much of the weight reduction was contributed primarily by reduction in fin thickness (which may be more governed by other considerations such as strength), an optimization run was also taken with fin thickness kept constant at the existing design value and the remaining six design parameters kept as free variables. The results shown in the last column of Table 3 show that even after retaining the same fin thickness as in the existing design, it is possible to achieve a weight reduction of 13.12 percent by appropriate changes in the values of other variables like the number of tubes, number of fins, and the length of the tube.

Similarly, the effect of tube diameter on optimum design has also been studied. Table 4 shows the optimum designs with four possible tube diameters, which are usually employed in boiler design. It is seen that a further reduction of about 2 percent is possible if smaller diameter tubes are employed.

Proceeding in a similar manner, it is also possible to study the influence of heat exchanger configuration on the design and thus identify the configuration that gives the lowest cost design.

References

Dhar, P. L., 1974, "Optimization in Refrigeration Systems," Ph.D Thesis, Mech. Engg. Department, IIT Delhi, India.

Dhar, P. L., and Saraf, G. S., 1987, *Computer Simulation and Design of Refrigeration Systems*, Khanna Publishers, Delhi.

Jain, S., 1994, "Studies of Desiccant Augmented Evaporative Cooling Systems," Ph.D Thesis, IIT Delhi, India.

Saraf, G. S., 1979, "Computer Simulation and Optimization of a Refrigeration System," Ph.D Thesis, IIT Delhi, India.

Seyedan, B., Dhar, P. L., Gaur, R. R., and Bindra, G. S., 1994, "Computer Simulation of a Combined Cycle Power Plant," accepted for publication in *Heat Recovery Systems & CHP*.

M. Nakhamkin

E. C. Swensen

Energy Storage and
Power Consultants, Inc.,
200 Central Avenue,
Mountainside, NJ 07092

J. M. Wilson

G. Gaul

Westinghouse Electric Corporation,
4400 Alafaya Trail,
Orlando, FL 32826

M. Polsky

Polsky Energy Corporation,
650 Dundee Road, Suite 150,
Northbrook, IL 60062

The Cascaded Humidified Advanced Turbine (CHAT)

This paper introduces the Cascaded Humidified Advanced Turbine (CHAT) plant, a gas turbine based power generation plant utilizing intercooling, reheat, and humidification. It is based upon the integration of an existing heavy duty gas turbine with an additional shaft comprising industrial compressors and high pressure expander. CHAT capitalizes on the latest proven gas turbine technology, which, combined with a sophisticated thermal cycle configuration, results in substantial improvement in gas turbine efficiency, compared to a simple cycle, while still maintaining typical advantages and merits of a combustion turbine plant. Built with a commercial combustion turbine and available industrial compressors and expanders, the CHAT plant does not require extensive product development and testing. As a result, the CHAT power plant can be offered with specific capital costs up to 20 percent lower than the combined cycle plant, and with competing efficiency. Compared to a combined cycle plant, the CHAT plant offers lower emissions (due to air humidification) and other significant operating advantages with regard to start-up time and costs, better efficiency at part load, lower power degradation at higher ambient temperatures, and simpler operations and maintenance due to elimination of the complexities and costs associated with steam production. The CHAT plant also integrates very effectively with coal gasification and particularly well with the water quench design. This feature has been discussed in previous publications.

Introduction

Engineering and development efforts to improve the efficiency and cost effectiveness of gas turbine based power plants can take several different approaches. They are:

1   Increase in turbine firing temperatures and or improvement in component efficiencies.
2   Use of sophisticated thermal cycles with compressor intercooling, recuperation, reheat, and humidification.

The first approach has primarily been adopted by the combustion turbine industry and we are witnessing current combustion turbine inlet temperatures for ''G'' type gas turbines exceeding 2600°F. This approach is supported by advances in materials and cooling techniques.

The second approach employs various combinations of reheat, intercooled, recuperated, and humidified thermal cycles, which have been theoretically proposed for many years. Still, the attempts by some manufacturers to develop these cycles resulted in the realization that very significant funds, personnel, and time are required and could not be justified, particularly considering availability of efficient and economical combined cycle (CC) plants.

The Cascaded Advanced Turbine (CAT) plant and its related CHAT technology offer an achievable and practical way of developing an advanced gas turbine plant with attractive thermal cycle features, by capitalizing on current developments in combustion turbine and industrial compressors/expanders technologies, without the need for prohibitively huge development funds.

This paper presents the CHAT plant performance, operating and cost data developed jointly by Energy Storage and Power Consultants, (ESPC), Westinghouse Electric Corporation (WEC) with support of Dresser-Rand, a consulting engineering company and a variety of equipment suppliers.

Cascaded Humidified Advanced Turbine.   As shown in the isometric presentation on Fig. 1, the basic CHAT cycle components are as follows:

*   A Westinghouse W501F derivative power generation shaft consisting of the low-pressure (LP) turbine—the W501F turbine with combustors; the LP compressor— the W501D class compressor; an upgraded generator; the shaft auxiliaries, and controls.
*   Power-balanced second shaft comprised of an intermediate pressure (IP) compressor, a high-pressure (HP) compressor, and the HP combustors/turbine assembly, the shaft auxiliaries and controls. All of the power generated by the HP turbine/expander is utilized in driving the IP and HP compressors. This shaft utilizes standard turboexpander and compressor components supplied by Dresser-Rand (D-R).
*   Various heat exchangers including compressor intercoolers, recuperator, water heaters/economizers, and fuel heaters.
*   Air saturators or humidifiers—a packed column for direct heat and mass transfer from the hot water to the motive air stream.

A brief description of the air flow path is as follows with reference made to Fig. 1.

Ambient air is drawn through air filters into the LP compressor on the power generation shaft. The LP compressor discharge air stream is directed to a water-cooled intercooler and then delivered to the IP compressor inlet on the second shaft. The discharge of the IP compressor is directed to a second intercooler and then delivered to the inlet of the HP compressor. The air is compressed in the HP barrel compressor to the maximum system pressure before it is delivered to the saturator, where the air stream, via heat and mass exchange, is humidified and preheated (utilizing hot water generated in the intercoolers and exhaust gas heat recovery water heaters). From the saturator, the air stream is directed to the recuperator for further preheating (using W501F turbine exhaust heat) and then directed to the HP combustors/turbine assembly. Fuel is added in the high-pressure combustors and the hot gas is expanded in
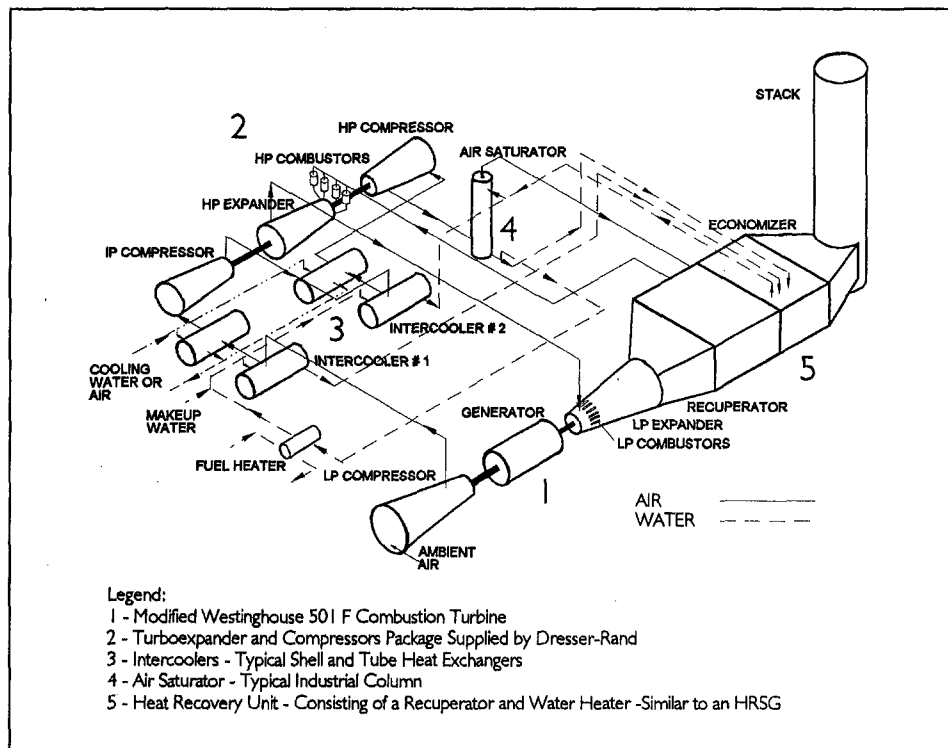
Fig. 1 CHAT plant major components

the HP turbine before being sent to the LP combustors/turbine (W501F turbine). The LP combustors increase the temperature of the flow to its design value and the gas is expanded through the W501F turbine. The exhaust gas from the turbine is routed through the recuperator and water heating sections and is then exhausted through the stack.

The guiding principles employed in the CHAT plant design are:

- Utilization of the proven W501F turbine.
- Use of industrial components with proven experience: compressors, expanders, intercoolers, water heaters, air-to-air heat exchangers, and saturators.

The following major features of the CHAT power plant contribute to its exceptional performance characteristics:

- The addition of the power-balanced second shaft significantly reduces the LP compressor discharge pressure compared to that of the W501F combustion turbine. The combination of the fired HP turbine and the use of intercoolers to reduce the IP and HP compressor power consumption results in a combined IP-HP compressor pressure ratio much higher than the HP expander. As a result, for the same overall thermal cycle pressure ratio, the required pressure ratio of the LP compressor (located on the power generation shaft) is significantly reduced with a consequent reduction in its power consumption. For the same total power produced by the W501F turbine, significantly lower power consumed by the LP compressor significantly increases the net electrical power generated.
- The addition of the motive air humidification (for the same volumetric flow expanding through the HP and LP expanders) reduces the CHAT plant required air flow to only 80 percent of the flow in the W501F simple cycle combustion turbine, contributing to a further reduction in the required LP compressor power. The moisture also provides effective utilization of cycle heat (for the aforementioned air preheating) from the intercoolers (which

would otherwise be wasted) and from the W501F turbine exhaust gas.

- This combination of reduced pressure and reduced flow in the CHAT LP compressor compared to the W501F compressor reduces the LP compressor power consumption from approximately 200 MW (air flow for maximum expander power) to approximately 60 MW. The net result is an increase in the net plant power output from 160 MW at ISO conditions in simple cycle to 300 MW in CHAT.
- The cycle configuration allows the effective utilization of the maximum design thermal power of the W501F expander at all ambient conditions, which in CT application is only fully utilized at low temperatures.
- The fuel consumption by the HP combustors is significantly reduced due to motive air sequential temperature increase in the saturator and the recuperator.
- The resulting CHAT cycle with recuperation, reheat, intercooling, and humidification features, although not theoretically optimal (due to all restrictions associated with the requirement to use only proven components), has a superior combination of performance, economics, and operating characteristics.

CHAT Key Component Descriptions

Power Generation Shaft. The power generation shaft is comprised of Westinghouse LP compressor, electrical power generator, and LP expander with auxiliaries and controls and is illustrated in the upper portion of Fig. 2. The combustors/turbine assembly of the CHAT ECONOPAC would consist of an inlet volute, combustion system, and a four-stage power turbine from the Westinghouse 501F CT. The assembly is shipped complete with rotor in place, facilitating a high-quality, low-cost erection in the field. Incorporated into the design are such features as a horizontally split case, two bearing support, turbine nozzles and blades air cooling system, compensating alignment system, sectionalized casing, and axial flow exhaust.
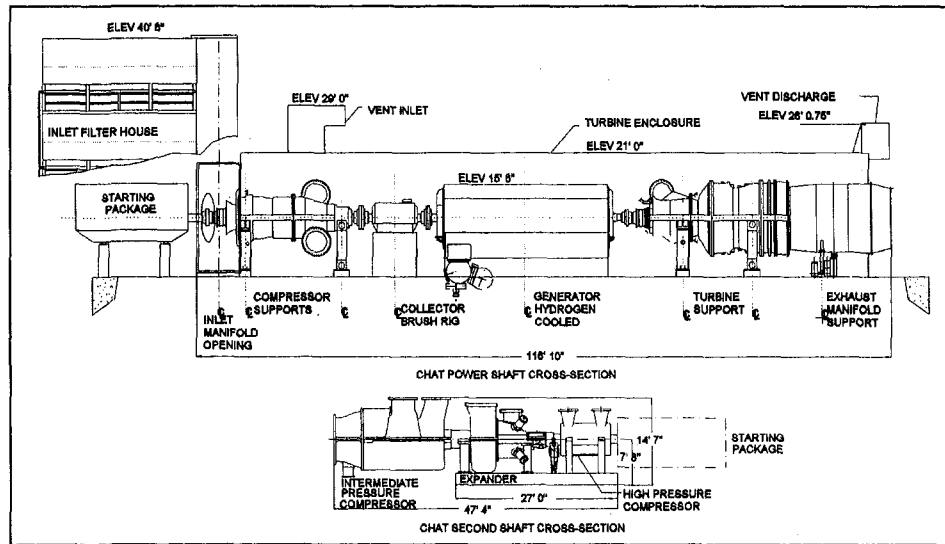
Fig. 2 CHAT shaft cross sections

The compressor of the CHAT ECONOPAC is derived from the highly reliable line of W501D class CTs utilizing the first six stages of the compressor. Due to the reduced air flow handled by the compressor, the smaller W501D class compressor can be economically utilized. The compressor assembly consists of an inlet volute, inlet guide vanes for optimum part load performance, axial compressor section, and exit volute. The compressor assembly is also shipped complete with rotor in place. Incorporated into the design are such features as a horizontally split case, two-bearing support, compensating alignment system, and sectionalized casing.

The hydrogen-cooled generator is equipped with integral lube oil and cooler piping, and necessary instrumentation. The design uses shaft-mounted axial blowers for circulating cooled hydrogen through the generator. Solid couplings connect the generator directly to the compressor and to the expander.

High-Pressure Turbomachinery Train. The high-pressure turbomachinery train, supplied by D-R, is comprised of an IP compressor, an HP compressor, and an HP combustors/turbine assembly (all operating at the same rotating speed, i.e., without gear) with auxiliaries and controls. The HP combustors/turbine assembly is located in the middle of the train and is configured to drive the IP compressor through a flexible coupling at the exhaust end of the expander and the HP compressor through a similar flexible coupling interface at the inlet end of the expander. A combination starting motor/turning gear package is connected to the outboard shaft extension of the high-pressure compressor through a clutch. The overall train is detailed in the lower portion of Fig. 2.

The IP compressor in the HP turbomachinery train is a combined axial/centrifugal compressor designed for high-volume flow and low to moderate discharge pressure. This D-R/GHH product is manufactured under the current agreement between Dresser-Rand and GHH/MAN to build axial compressors jointly for sale worldwide. This compressor design incorporates several notable features. The casing inlet is an axial design configuration to minimize inlet losses. The axial blades in the first section provide high stage efficiencies. They are followed by a volute-shape diffuser for minimization of discharge losses. The second compression section with radial impellers discharges the motive air with the pressure determined based on the overall thermal cycle optimization. The axial stages in the first section incorporate variable position stator vanes, which offer the operational flexibility of controlled flow turndown.

The HP compressor in the HP turbomachinery train is a radial split (barrel type) centrifugal compressor designed for lower volume flow and high discharge pressure. This compressor type is designed and built completely by D-R. This machine contains radial impellers only and can utilize up to ten stages of compression to produce the required discharge pressure to achieve the optimum overall pressure ratio.

The D-R EA-614 HP turbine is designed explicitly to meet the optimized CHAT power plant thermal cycle parameters and duties. It is a six-stage design, which reflects a mix of steam turbine and gas turbine technologies. These technologies are blended to address the somewhat unique operating conditions — a moderately high temperature/pressure combination, high power density, and cyclic or load following operation.

Saturator. The saturator used to humidify and preheat the compressed air in the CHAT cycle is a packed column, well known as an efficient device for transferring mass and heat in a gas–liquid contacting operation. In this application it is used to transfer the hot water mass and heat to the dry and cooler compressed air.

The saturator is a pressure vessel with internal structured or random packing as provided by several well-known process industry suppliers such as Glitsch, Norton, or Koch. The purpose of the packing is to provide an even and efficient breaking down into small droplets and distribution of the downward flowing water and the counterflowing air. Also included as part of the saturator tower internals are orificed liquid distributors, packing support grids, filter, and mist eliminator.

To protect against any liquid entrainment, a CWMS (crinkled wire mesh screen) and/or chevron style mist eliminators will be installed above the packed beds. These are used in many installations in service with rotating equipment downstream.

The packed bed height in the tower will be approximately 50 feet. Allowance for water storage at the bottom of the vessel and water entry and mist eliminators at the top of the tower will result in an overall tower height of approximately 100 feet. The vessel diameter will be approximately 16 feet with a wall thickness of approximately 5 inches. Vessel material will be carbon steel with stainless steel internal cladding. All other internals are stainless steel. Over 70 percent of the cost of the saturator is for the fabrication, transport, and installation of the vessel. The remainder is for the internals, platforms, instrumentation, engineering, etc.
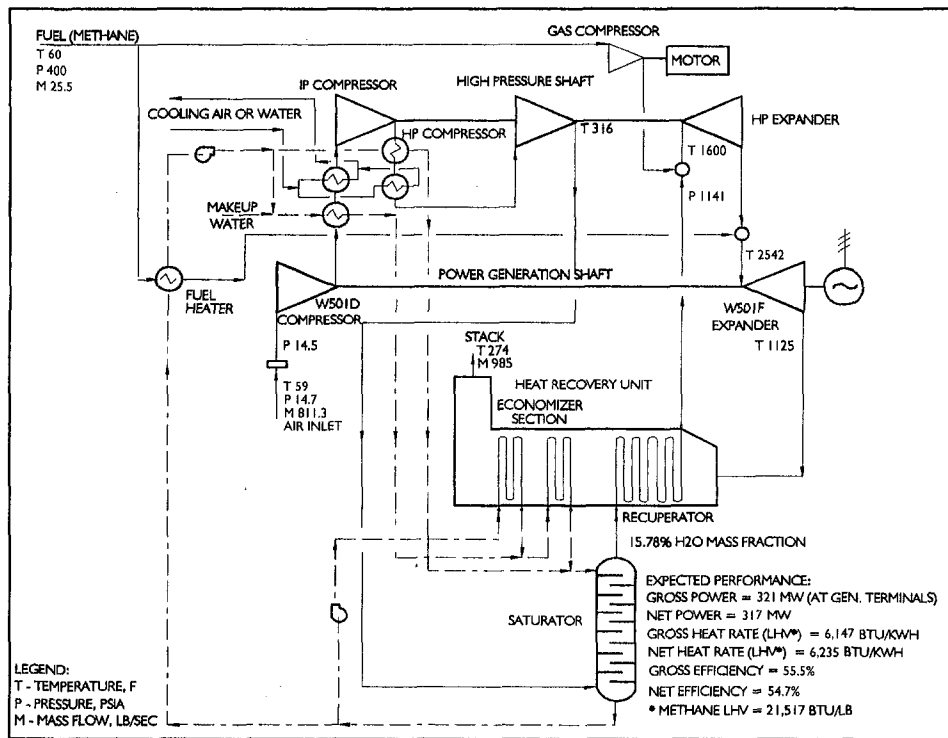
FUEL (METHANE)
T 60
P 400
M 25.5

GAS COMPRESSOR
MOTOR

IP COMPRESSOR   HIGH PRESSURE SHAFT

COOLING AIR OR WATER

HP COMPRESSOR   T 316   HP EXPANDER

T 1600

P 1141

MAKEUP
WATER

T 2542

FUEL
HEATER

W501D
COMPRESSOR

POWER GENERATION SHAFT

W501F
EXPANDER
T 1125

P 14.5

STACK
T 274
M 985

T 59
P 14.7
M 811.3
AIR INLET

HEAT RECOVERY UNIT
ECONOMIZER
SECTION

RECUPERATOR
15.78% H2O MASS FRACTION

SATURATOR

EXPECTED PERFORMANCE:
GROSS POWER = 321 MW (AT GEN. TERMINALS)
NET POWER = 317 MW
GROSS HEAT RATE (LHV*) = 6,147 BTU/KWH
NET HEAT RATE (LHV*) = 6,235 BTU/KWH
GROSS EFFICIENCY = 55.5%
NET EFFICIENCY = 54.7%
* METHANE LHV = 21,517 BTU/LB

LEGEND:
T - TEMPERATURE, F
P - PRESSURE, PSIA
M - MASS FLOW, LB/SEC

Fig. 3 CHAT cycle heat and mass balance

The saturator can operate with any clean and filtered water source as long as the dissolved substances at the water outlet remain below their precipitation concentration at the operating conditions. The water quality is maintained via a combination of the water treatment system and the saturator blowdown to purge impurities, optimized based on the plant economics.

Recuperator/Economizer. The heat recovery unit is of a horizontal finned tube design consisting of an air preheater or recuperator section and two economizer sections. Tube materials are selected for both temperature and water quality considerations.

Intercoolers. The two intercoolers are designed to transfer heat from the motive air leaving the LP compressor and the IP axial compressor to the cycle water. Each intercooler design consists of multiple shells in series. Each of the shells are crossflow, with the cycle water on the tube side and motive air on the shell side. The mechanical design corresponds with a type-AXP unit, as defined by TEMA. The shell side, tube side, and tubesheets are constructed of carbon steel and the tubing is copper nickel. The water boxes are clad in $\frac{1}{4}$ in. thick 304 stainless steel and the water box baffles are stainless steel.

CHAT Plant Performance

Figure 3 shows a simplified heat balance of the natural gas fired CHAT power plant at ISO conditions. Total net power is 317 MW at a LHV net heat rate of 6235 Btu/kWh. Turbine inlet temperatures have been chosen conservatively for the first generation plant. Consideration has been given to effects of moisture on expander cooling flows and flow path efficiencies. Potential near-term developments leading to an increase in HP turbine inlet temperatures will have a significant impact on improving both power output and heat rate.

Part-load performance, expressed as heat rate, is shown in Fig. 4 and is compared to CC and simple cycle power plants. Fig. 4 shows the CHAT power plant with power reduced to approximately 75 percent of the rated power output has still

negligible efficiency degradation. At this point, CC efficiency is reduced by nearly 4 percent, and simple cycle by nearly 10 percent. As load is reduced further, the CHAT power plant efficiency advantage increases even further: at 50 percent of the rated power output, the CHAT plant efficiency has reduced by only 7 percent in comparison to CC by 15 percent and CT by nearly 25 percent. The excellent part-load performance of the CHAT plant is explained by the additional part-load control flexibility offered by varying firing temperature of both HP and LP combustors, by varying speed on the HP turbomachinery train, by varying moisture content and by varying compressor inlet flow.

The 317 MW rated output can be increased to 325 MW by an increase in the motive air moisture level (with corresponding reduction of air flow) at the sacrifice of a small increase in heat rate.

Figure 5 represents the CHAT plant power and heat rate versus the compressor inlet temperature along with similar curves for CC and CT plants. Relative to ISO conditions, the graphs show that the CHAT plant power curve is nearly flat with only less than 2 percent power reduction at 90°F, compared to 8 percent for CC and 12 percent for CT plants. This is again attributed to the additional flexibility offered by the CHAT design, primarily the ability to increase the moisture level at higher ambient temperatures and maintain the net power.

Figure 6 compares the startup characteristics of CHAT plant versus those of a CC plant. It is predicted that CHAT will synchronize to the grid in approximately 8 minutes from a cold start, and will achieve full power in an additional 22 minutes. In comparison, the combined cycle plants typically require nearly 18 minutes for synchronization. By this time the CHAT plant is already generating approximately 140 MW. The CHAT plant is at full 300 MW output at approximately the same time as the CT of a CC plant has reached full load and the steam turbine is beginning to generate additional power. Full CC output is not reached until nearly 2 hours after the initiation to start under cold start conditions.

CHAT is expected to have a lower performance degradation at higher elevation compared to simple cycle. At an altitude of
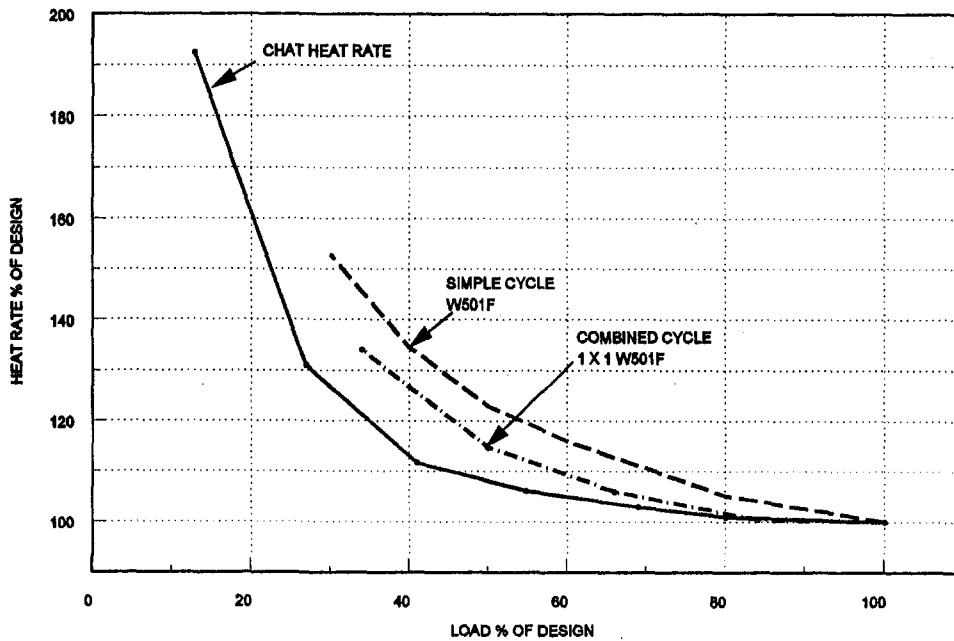
Fig. 4 CHAT cycle heat rate versus load

5000 feet, the CHAT cycle will have a 2 percent degradation in power while simple cycle power will decrease by 16 percent. This is due to the ability to increase moisture in the motive air stream, offsetting decreased motive air flow.

Emissions. Due to the addition of moisture in the CHAT plant upstream of the combustors, uncontrolled NO_x emissions are expected to be very low, in the single digit range. The approximately 16 percent moisture in the air reduces the NO_x emissions (lb pollutant/lb fuel) to approximately 2 percent of its dry levels.

CO, unburned HC, VOC's, and SO_x are expected to be at or below current gas turbine combustor technology.

Application to Future CT Improvements. Applicable improvements in component efficiencies, increases in firing temperature, etc., developed for combustion turbines will be implemented on CHAT power plants. As a result, CHAT should maintain its advantages over the CT and CC plants.

CHAT Plant Cost

CHAT plant capital cost estimates have been independently prepared by ESPC and its AE subcontractor, and by WEC. Over 90 percent of the equipment costs are based upon quoted prices. The estimated specific cost for full turn-key supply of the CHAT plant including all equipment and services within the power
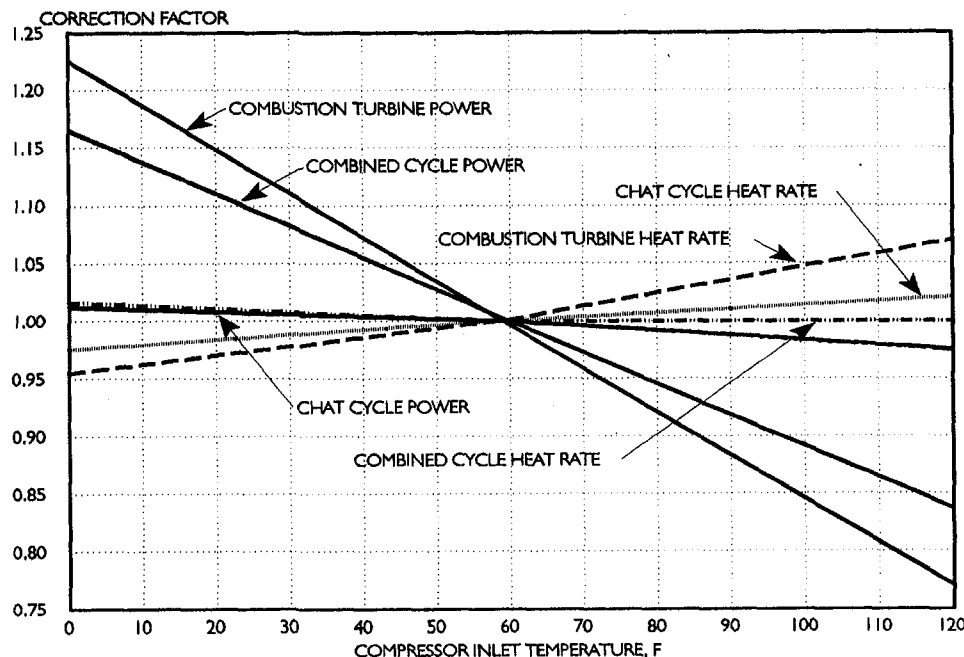
Fig. 5 CHAT ambient temperature performance correction
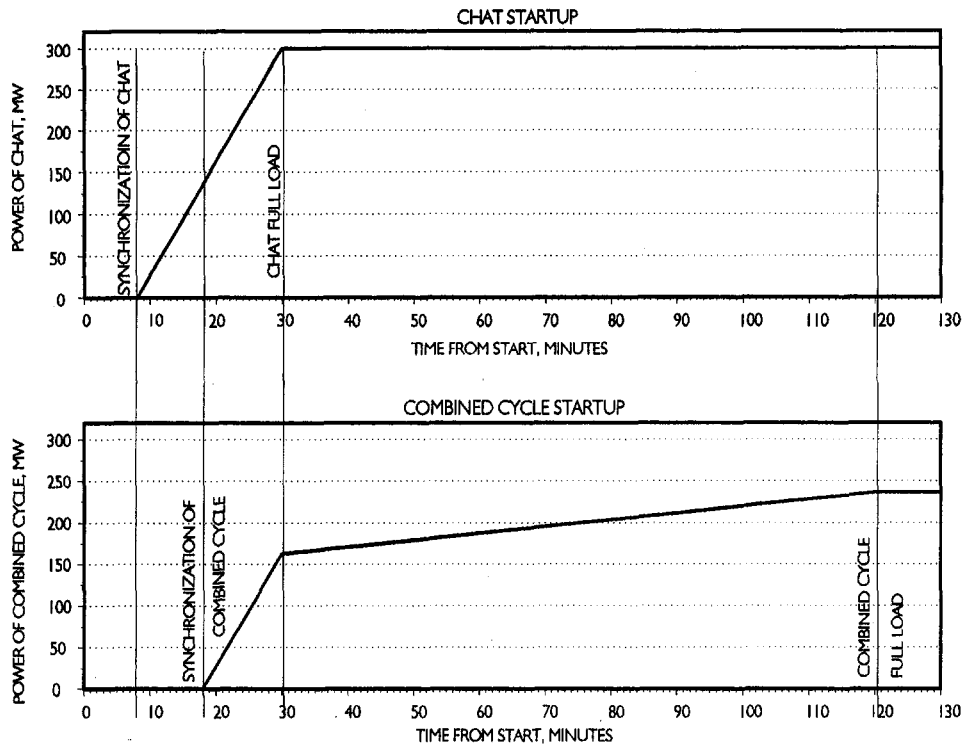
Fig. 6 Comparison of CHAT versus combined cycle start-up characteristics

plant fence line was found to be essentially the same as a W501F based combined cycle plant. The CHAT plant with the same W501F expander produces a net 317 MW versus 250 MW for the W501F combined cycle plant. The specific capital cost of the plant, $/kW, is therefore reduced in proportion to the increase in power output. The actual cost of the CHAT plant, similar to the combined cycle, is subject to the prevailing market competitiveness.

The estimated CHAT plant specific capital cost, $/kW, is therefore approximately 15–20 percent less than currently quoted representative combined cycles. In addition, if the plant is to be rated at a typical 90°F, the CHAT plant specific cost advantage increases to almost 25 percent due to the reduced power degradation, as mentioned above, compared to a CC plant.

Independent System Analyses Incorporating CHAT

An independent analysis of overall Tennessee Valley Authority (TVA) power system economics with the addition of a 300 MW CHAT plant versus a 300 MW CC versus a 300 MW CT plant was conducted by Operation Simulation Associates, Inc. (OSA). The results indicated that the CHAT plant can provide major production cost savings to the potential future TVA system. For the study period of 1998 through 2007, the CHAT option would lower TVA's system production cost by 17 million dollars over a CC plant and 80 million dollars over a CT plant. Costs are present value, 1998 dollars, using a 9 percent discount rate. Trending annual results to the year 2028, a CHAT plant would lower TVA's system production cost by 42 and 169 million dollars versus a CC and a CT plant, respectively.

Table 1 Comparison of CHAT versus combined cycle and simple cycle performance and cost

Plant Type	CHAT	Combined Cycle	Simple Cycle
Net Power, MW @ ISO Conditions	288	250	167
Net Efficiency, % / Net Heat Rate, Btu/kWh (LHV)			
Full Load	54.7/6,235	54.8/6,224	35.5/9,600
75% Load	53.6/6,370	52.9/6,450	32.9/10,362
50% Load	51.5/6,630	47.8/7,143	28.8/11,810
Ambient Temperature Effect, 59F to 90F			
% Loss of Power Output	1.5 %	10.0 %	11.0 %
% Increase in Heat Rate	1.0 %	3.0 %	4.0 %
Emissions	Lower	Base	Base
Start-Up Times	8 min to syn. plus 22 min. to full load	18 min. to syn. plus 102 min. to full load	18 min. to syn. plus 12 min. to full load
Start-Up Cost, $	$1,400	$6,500	$1,140
Load Following Capability	Excellent	Good	Good
Remote Control Capability	Yes	No	Yes

Additionally, present value calculations, which include both the 30 year production cost values and capital costs, show a savings from the CHAT plant of 97 million dollars versus the CC and 140 million dollars versus the CT plants for the 30 year period starting in 1998 and ending in 2028. The CHAT plant initial capital cost, lower O&M and start-up costs, and its ability to operate efficiently over a wide range of loads were key factors in this result.

Summary of CHAT Features

A performance comparison of the CHAT plant versus CT and CC plants is presented in Table 1. The CHAT plant combines the best features of CT and CC power plants with the following advantages:

- Capital cost 15 to 20 percent lower than CC
- O&M cost approximately 6 percent lower per year than CC
- Startup and operating response comparable to simple cycle
- Lower startup fuel consumption than CC
- Thermal efficiency competitive to CC
- Superior part load efficiency
- Lower performance degradation at higher ambient and higher elevations
- NO_x emissions low due to humidified air
- Small demineralized water requirement

Summary and Conclusions

The CHAT plant combines the best features of a combined cycle plant and a simple cycle combustion turbine. Compared to the combined cycle plant, the CHAT plant has:

- High design point net plant efficiency in the range of 54–55 percent, with significant potential for improvement
- Very efficient operation at part loads (at 50 percent load the efficiency is reduced by only 7–8 percent)

Similar to the simple cycle combustion turbine the CHAT plant has:

- Excellent start-up and load following characteristics
- Potential fully automated remote control operations
- Low installed capital costs (less than $350/kW) and short manufacturing and construction periods

These characteristics make CHAT the plant of choice for a wide range of operations from peaking through intermediate up to base load. This versatility adds another important dimension allowing an ultimate user to have the plant for all types of service (peaking, intermediate, base load) without committing himself to a long-term particular operation in times of uncertainties.

References

Nakhamkin, M., 1994, "Cascaded Advanced High Efficiency Multi-Shaft Reheat Turbine With Intercooling and Recuperation," U.S. Patent Number 5,347,806.

Nakhamkin, M., 1995, "Method of Generating Power With High Efficiency Multi-Shaft Reheat Turbine With Intercooling and Recuperation," U.S. Patent Number 5,386,688.

New 200 MW Class 501G Combustion Turbine

L. Southall

G. McQuiggan

Westinghouse Electric Corporation,
Power Generation Business Unit,
Orlando, FL 32826-2399

The 501G 60-Hz combustion turbine has been developed jointly by Westinghouse Electric Corporation, Mitsubishi Heavy Industries, Ltd., and FiatAvio. It continues a long line of large heavy-duty single-shaft combustion turbines by combining the proven efficient and reliable concepts of the 501F with the latest advances in aero technology via the Westinghouse Alliance with Rolls-Royce. The output of the 501G is over 230 MW with a combined cycle net efficiency of 58 percent. This makes the 501G the largest 60-Hz combustion turbine in the world and also the most efficient.

Introduction

The 501G is a 3600 rpm heavy-duty combustion turbine designed to serve the 60-Hz power generation needs for utility and industrial service. The 501G combines the efficient, reliable design concepts of the 501F with the latest low NO_x combustion technology and the state-of-the-art cooling utilized in advanced, high-temperature aero engines (Scalzo et al., 1989). The result is an advanced design, high-temperature, efficient, low NO_x, more powerful combustion turbine based on time-proven reliable design concepts that will satisfy the large combustion turbine power generation needs for the next decade (see Table 1). Designed for both simple and combined cycle applications, it will operate on all conventional combustion turbine fuels as well as with coal-derived low-Btu gas produced in an integrated gasification combined cycle power plant. Two units are being manufactured with both to begin operation in 1997. It will have an initial ISO rating of 230 MW at a turbine inlet temperature of 1500°C on natural gas fuel. In combined cycle applications, the net thermal efficiency of the plant is 58 percent (LHV) in power blocks of 340 MW nominal power rating.

This paper describes the features of this latest in a long line of heavy-duty combustion turbines of the 501 model series. Aerodynamic, cooling, and mechanical design improvements are discussed, along with the evolutionary changes based on time-proven design concepts. Technological advances as well as planned verification test programs are discussed including cascade, model turbine aerodynamic tests, combustor tests, rotating blade vibration tests, and shop test at load.

General Description

Figure 1 illustrates the general configuration of the 501G. Several basic design concepts are evident, such as the two-bearing single-shaft construction, cold end drive, and axial exhaust. These fundamental time-proven concepts used by Westinghouse for over 25 years have now become industry standards.

As in all past 501/701 designs, the single rotor is made up of the compressor and turbine components supported by two tilting pad bearings. For comparison with 501F, see Table 2. The 501G rotor is of bolted construction supported by two 18-in.-dia, two-element tilting-pad bearings and an upper half fixed bearing. The thrust bearing is a double-acting bearing.

The compressor rotor comprises a number of elements, spigotted and bolted together by 12 through bolts. Alignment and torque transmission are assured by the use of radial pins between

the disks. The turbine rotor section is made up of disks bolted together by 12 through bolts and using CURVIC clutches, which consist of toothed connection arms that extend from adjacent disks and interlock providing precise alignment and torque carrying features. This turbine rotor design has amassed over 10 million hours of reliable service in all sizes of combustion turbines.

The air inlet system, which contains a silencer, delivers air to the compressor via a plenum-bell mouth and houses the inlet, main journal, and thrust bearings. The compressor is a 17-stage axial flow design of 19.2:1 pressure ratio that is based on the highly successful 501F. A four-stage turbine was selected to maintain moderate aerodynamic loadings even at the increased firing temperature.

The combustion system consists of 16 can-annular combustors. This low NO_x hybrid design is an improvement on the current highly successful design that has been in commercial operation for over three years in the 701F and 501D5. The presence or absence of flame and the uniformity of distribution of fuel flow between combustors are monitored by thermocouples located downstream of the last-stage turbine blades. These can also detect combustor malfunctions when at load while U/V detectors are used to sense ignition during the early starting phase.

All engine casings are split horizontally to facilitate maintenance with the rotor in place. Inlet and compressor casings are of nodular cast iron and cast steel, respectively, while combustor, turbine, and exhaust casings are alloy steel. The inlet bearing housing is supported by eight radial struts, and the aft end bearing housing is supported by tangential struts. Airfoil-shaped covers protect the tangential struts from the blade path gases and support the inner and outer diffuser walls.

Tangential struts respond slowly during transients and maintain alignment of the bearing housing by rotating it as required to accommodate thermal expansion. Individual inner casings (blade rings) are used for each turbine stationary stage and can be readily removed and replaced or serviced with the rotor in place. Similar blade rings are used in the compressor. Another feature of these blade rings is that they have a relatively higher thermal response independent of the outer casing and can be aligned concentric to the rotor to prevent blade rubs, minimize clearance, and maximize performance.

Cooling circuits for the turbine section displayed in Fig. 2 are similar to those used on the 501F. They consist of a rotor cooling circuit and four stationary cooling circuits. Rotor cooling air is provided by compressor discharge air extracted from the combustor shell. This air is externally cooled and filtered before returning to the torque tube casing for seal air supply and for cooling of the turbine disks as well as the first, second, and third-stage turbine rotor blades. This filtered air eliminates excessive contaminants that could block critical intricate cooling passages of the rotor blades.
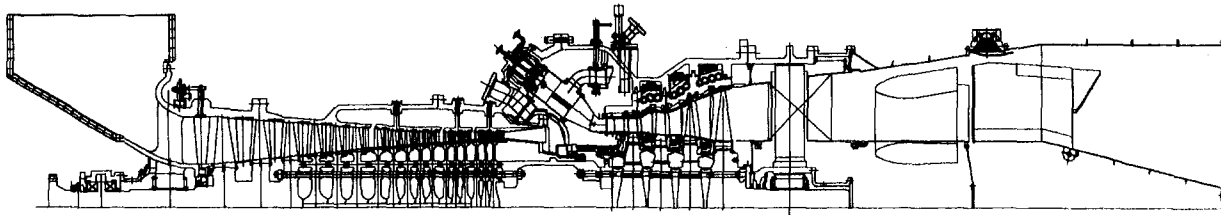
Fig. 1 501G

Table 1 501 evolution

Engine	501A	501B	501D	501D5	501DA	501FA	501G
Commercial Operation	1968	1973	1976	1982	1994	1992	1997
Power, MW	45	80	95	107	120	160	230
Rotor Inlet Temp.,' F	1615	1819	2005	2070	2150	2330	2583
Air Flow, Lb/Sec	548	746	781	790	832	961	1170
Pressure Ratio	7.5:1	11.2:1	12.6:1	14:1	15:1	15:1	19.2:1
No. Comp. Stages	17	17	19	19	19	16	17
No. Turbine Stages	4	4	4	4 ·	4	4	4
No. Cooled Rows	1	3	4	4	4	6	6
Exhaust Temp.,' F	885	907	956	981	1004	1083	1100
Heat Rate (Btu/kWh) LHV - ISO Gas							
Simple	12,600	11,600	10,925	10,040	9,900	9,610	8,860
Combined	9,000	7,350	7,280	7,055	7,024	6,429	5,883
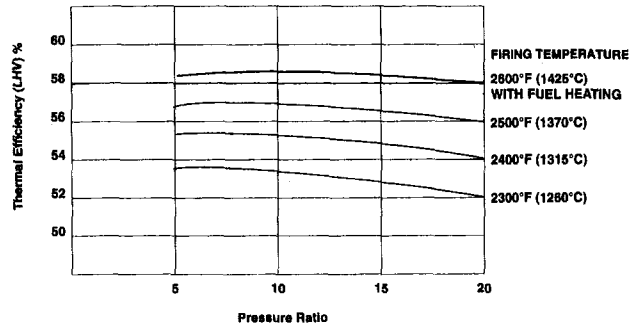
Fig. 3 Combined cycle efficiency

Direct compressor discharge air is used to cool the row 1 vane while compressor bleed air is used to provide cooling air to turbine blade ring cavities at stages 2, 3, and 4, respectively. The compressor bleed air also cools the stage 2 and 3 vane segments and provides cooling and purging air for the turbine interstage disk cavities preventing the ingestion of hot blade path gases.

The stationary vanes and rotating blades for the first two turbine stages are coated with thermal barrier coatings. Compressor diaphragms are coated to improve aerodynamic perfor-

mance and corrosion protection. For some environments, compressor rotor blades may be coated for corrosion protection.

Cycle Parameter Selections

The 501G engine, like all recently designed combustion turbines of the authors' company, is designed for both simple and combined cycle service. The operating firing temperature level is selected to be commensurate with state-of-the-art materials and the latest aero-type cooling schemes. The value selected is 1425°C at rotor inlet temperature.

After the turbine inlet temperature has been selected, the cycle pressure ratio can be chosen to maximize simple cycle power output and combined cycle efficiency. Figures 3 and 4, which are plots of simple and combined cycle efficiencies, are used to select a pressure ratio of 19.2:1. This results in a cycle that has near maximum simple cycle output with a potential combined cycle efficiency of 58 percent.

The cycle air flow was set by the turbine exit annular flow area. It can be shown that the last-stage blade stress level is

Table 2 501G versus 501F rotor design

	501F	501G
Rotor Span	294.0"	311.6"
Journal Bearings	17.0"	18.0"
		2 Tilting Pads
Thrust Bearings	22.5"	25.0"
Rotor Weights (Tons)		
Compressor	25.5	37.9
Turbine	21.0	26.9
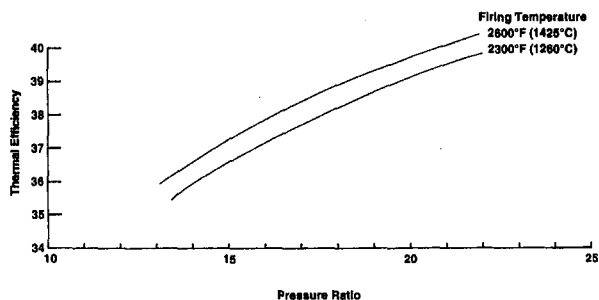
Fig. 2 Simple cycle: thermal efficiency versus pressure ratio

Fig. 4

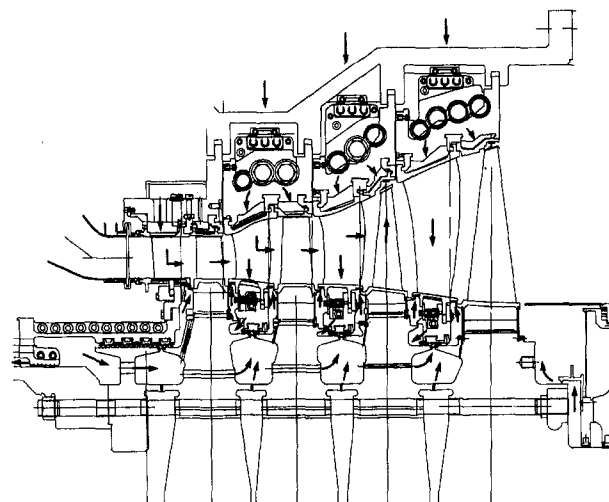**Journal of Engineering for Gas Turbines and Power**

JULY 1996, Vol. 118 / 573

directly proportional to the exit annular area. Since the long highly twisted last-stage blade is uncooled, the blade material capability and last-stage gas temperature then determine the flow capacity of the engine. A flow of 1200 lb/sec was selected, which results in a conservatively stressed blade and high power output.

Compressor Design

The compressor is a highly efficient, 17-stage axial flow compressor patterned after the proven compressor of the W501F. Flow and pressure coefficients of the 501G compressor have been kept similar to the F compressor by increasing the mean diameter of the stages to accommodate the 25 percent increase in flow. In addition, the rear stages of the new compressor have larger diameters to help balance spindle thrust. Interstage bleeds for starting and cooling flows are in the sixth and eleventh stages, with the fourteenth stage used only for supplying cooling air to the second-stage turbine stationary blading and interstage cooling system. The compressor is also equipped with variable inlet guide vanes, which improve the compressor low-speed surge characteristic and are used in combined cycle applications for improved part-load performance.

Rotor blades are multiple circular arc designs and controlled diffusion airfoils.

Stationary blading is fabricated into two 180 deg diaphragms per stage for easy removal and will maintain the highly efficient inner shroud sealing system currently used on the 501F. These seals will be supported by machined lips on the inner shroud and can be removed to facilitate inspection and maintenance of shrouds and seals. Stationary blading and shrouds are standard strength AISI 403 throughout. Abradable seals will be used to improve sealing.

Turbine Design

The design of the 501G has maintained moderate aerodynamic loadings by using a four-stage turbine with higher peripheral speed compared to the 501F. Furthermore, improvements in aerodynamic airfoil shapes have been made possible by utilization of a fully three-dimensional viscous analysis code. This sophisticated airfoil design approach was employed to assure that the turbine has the highest practical aerodynamic efficiency and the lowest cooling flow usage. The number of airfoils have been reduced relative to the 501F by approximately 15 percent. The first two turbine blades are unshrouded. The second and third blades are shrouded as on the 501F.

The first turbine stationary row consists of 32 precision-cast, single-vane segments of IN939 alloy. As in past designs, the row 1 vanes are removable, without any cover lift, through access manways. Inner shrouds are supported from the torque
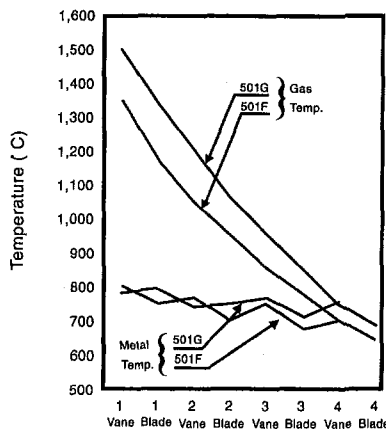

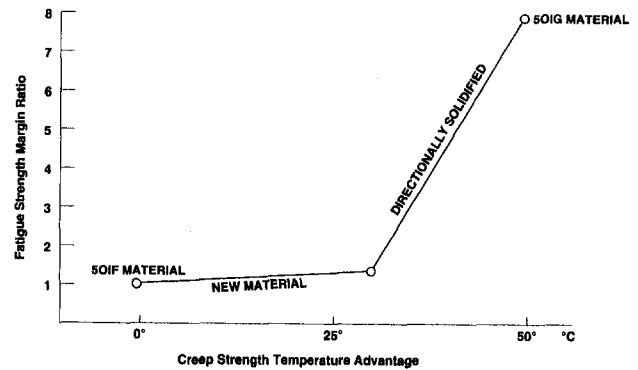Fig. 6 Directionally solidied advanced materials creep and fatigue strength improvement

tube casing to limit flexural stresses and distortion, thus maintaining control of critical row 1 vane angles. This is the same method that was used successfully on the 501F. There are 36 precision-cast, single-vane segments of IN939 material in the second turbine stationary row. The third and fourth turbine stationary rows are precision-cast vane segments with 14 three-vane and 14 four-vane segments, respectively.

Each row of vane segments is supported in a separate inner casing (blade ring) that is keyed and supported to permit radial and axial thermal response independent of possible external cylinder distortions. Blade ring distortion in the 501G turbine is further minimized by use of segmented isolation rings that support the vane segments and also ring segments over the rotor blades to form a thermal barrier between the flow path and the blade ring. As in all past designs, the interstage seal housings are uniquely supported from the inner shrouds of rows 2, 3, and 4 vane segments by radial keys that permit the thermal response of the seal housings to be independent of the more rapid thermal response of the vane segments.

Cooling of Vanes, Blades, and Disks

The cooling system shown in Fig. 4 maintains the NiCrMoV turbine disks below 400°C (752°F), which keeps the disk below the creep range and assures long life. Fleet leaders with this disk design are the W501A turbines with up to 150,000 operating hours.

Blade and vane cooling flows have been kept to a minimum while maintaining similar metal surface temperatures as used in the 501F (Fig. 5). By using thermal barrier coatings and proven aero-engine cooling schemes such as serpentine cooling passages, shower head film cooling, and shroud film cooling along with improved materials, the creep and thermal fatigue margins have been maintained or improved over the 501F (see Fig. 6).

The row 1 vane cooling is provided by impingement convection and film cooling. The film cooling holes are fan shaped and the airfoil and shrouds will be coated with a ceramic thermal barrier coating.

The row 1 vane cooling design is shown in Fig. 7. This highly effective configuration utilizes state-of-the-art concepts with three impingements inserts in combination with an array of film cooling holes and a trailing edge pin fin system. Film cooling is used at the leading edge as well as at selected pressure and suction side locations. This limits vane wall thermal gradients and external surface temperatures, while providing an efficient re-entry for spent cooling air. Pin fins are employed to increase turbulence and surface area, thereby optimizing the overall edge pin fin exit system.

Particular attention is paid to the inner and outer shrouds because of the flat temperature profile from the dry low NO_x combustor. Cooling of the shrouds will be provided by impinge-

Fig. 5 501F and 501G metal temperature comparison

Outer Shroud Impingement and Film Holes
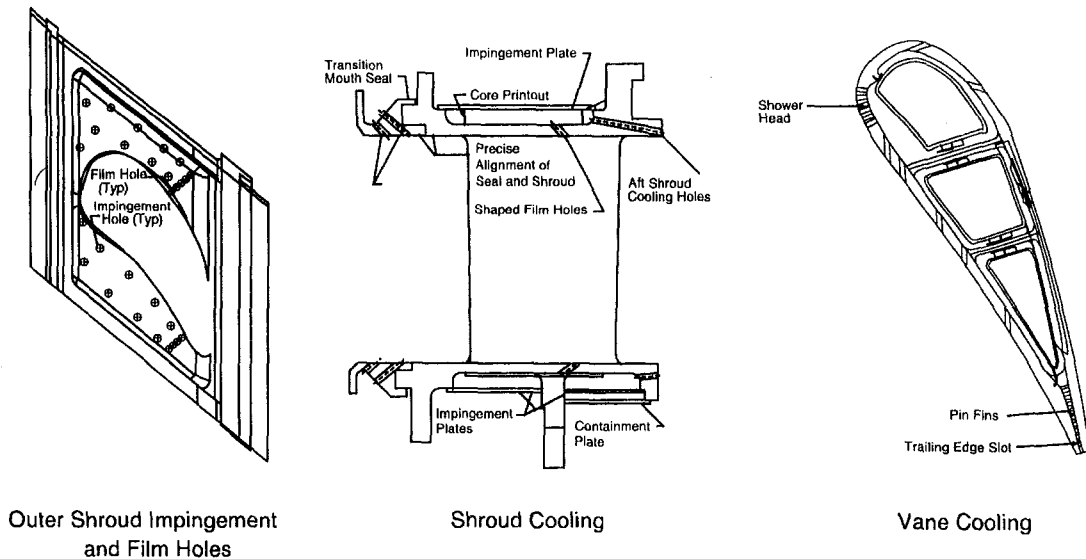
Shroud Cooling

Vane Cooling

Fig. 7   501G row 1 vane cooling

ment plates and film cooling as well as convection cooling via drilled holes.

The row 1 blade cooling consists of convectional serpentine cooling with angled turbulators. The film cooling utilizes fan-shaped cooling holes for more effective cooling. The blade also features extensive film cooling at the tip to reduce the metal temperature of the squealer tip and platform cooling holes to positively cool the inner platforms. The airfoil will be coated with a vapor deposition thermal barrier coating (Fig. 8).

The row 2 vane is cooled by a combination of impingement cooling via the inserts and film cooling using fan shaped cooling holes. The vane will be manufactured as a single vane to reduce thermal stress and to allow the vane to be coated with thermal barrier ceramic coating. As with the row 1 vane, intensive cooling schemes are applied to the inner and outer shrouds using impingement and convection cooling (Fig. 9).

The row 2 blade is cooled by convection with no film cooling. The airfoil will be coated with a vapor deposition T.B.C. (Fig. 10).

The row 3 blade cooling is unique in that it positively cools the blade tip shroud. Because of the flat profile from the combustor and because of tip leakage from the rows 1 and 2 turbine blades, it was decided to allow for positive cooling of the tip shroud. Analysis has shown that this scheme will have ample margin for cooling the shroud (Fig. 11).

Compressor bleed air from the 11th stage is used to supply cooling air to the third-stage blade ring cavity. Cooling air is

Fanned Film Holes
Thermal Barrier Coating
Optimized Wall Thickness
Full Impingement Inserts
11 Row Pin Array
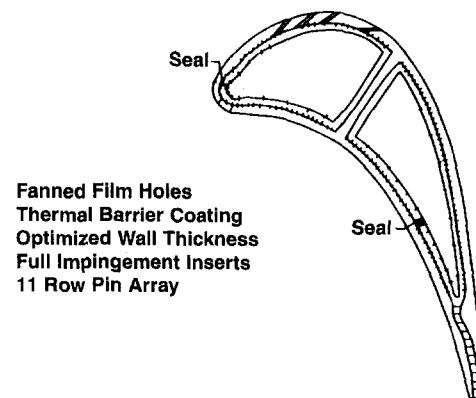
Fig. 9   501G row 2 vane cooling midheight

directed to the inlet cavity of a five-cavity multipass convective cooled vane airfoil. Leading edge cavity flow also supplies the interstage seal and cooling system while the fifth pass cavity exits at pressure side "holes" on the vane surface near the trailing edge. The fourth-stage vane is uncooled but does transport sixth-stage compressor bleed air for the fourth-row interstage seal and cooling system.

The rotating blades are precision cast of CM247 for all four rows. All rows utilize long blade root extensions or transitions
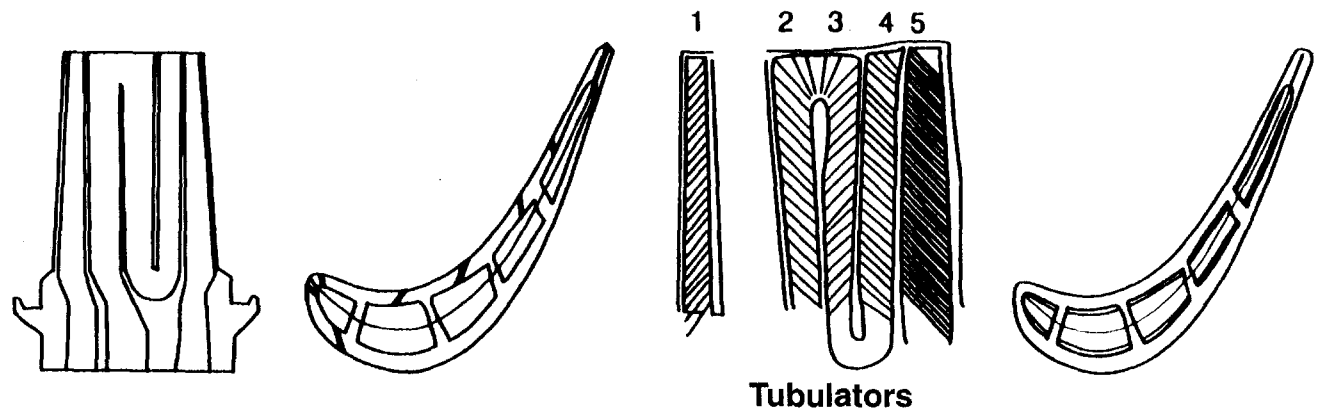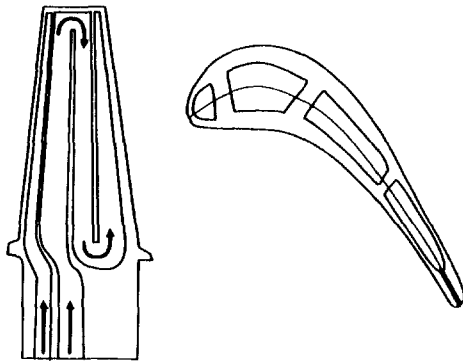

Tubulators

Fig. 8   501G row 1 blade cooling

Two circuit cooling scheme

- **Leading edge**
  Single-pass

- **Trailing edge**
  Three-pass, aft flowing serpentine
  trailing edge egection holes

Thermal barrier coating

Fig. 10   501G row 2 blade cooling

Fig. 12   501F combustion system
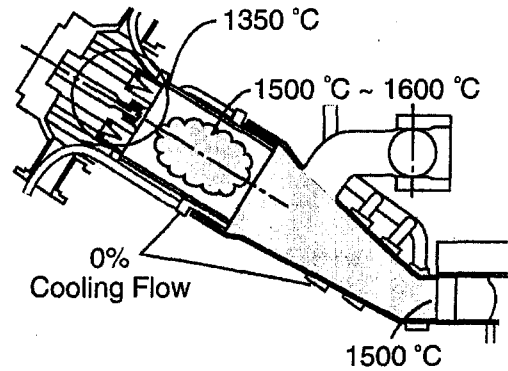
Fig. 13   501G combustion system

in order to minimize the three-dimensional stress concentration factor that results when load is transferred between cross sections of different size and shape. The blade roots are the same geometric multiple serration type used on past designs with four serrations used on the first three rows and five serrations used on the rear stage.

501G Combustor

The combustor is based on the successful dry low NO_x combustor developed for the 501F. This combustor is presently operating at a 25 ppm NO_x level at 1260°C (2300°F) R.I.T. temperature. The 501G combustor will make use of steam cooling to allow for the same NO_x reduction at the higher firing temperature. By eliminating the transition cooling air, virtually all the combustion air is introduced into the primary zone of the combustor, maintaining the flame temperature at nearly the same level as that of the 501F turbine. Therefore, NO_x levels are similar to the 501F level (see Figs. 12 and 13). Fuel heating will be used to improve the efficiency of the cycle with the heat coming from the rotor cooling air heat exchanger. The same combustor is designed to burn liquid fuel using water or steam injection to control NO_x levels. Initial emission targets are given in Table 2.

Fig. 11   501G row 3 blade cooling

Verification Testing

All new advanced technology parts applied in the 501G engine are qualified for engine use by verification tests, including: (a) rotating blade vibration, (b) turbine aerodynamic, (c) combustion tests, and (d) hot turbine cascade testing. Overall engine performance and durability will be verified by engine shop tests.

Aerodynamics

The total compressor was tested as a scaled model in a small combustion turbine in 1994. This followed extensive single and dual stage rig testing in 1993.

The turbine design tools have been verified in extensive model and rig tests, and in particular a scale model of the 501G turbine row one vane and blade was tested in 1994 and fully verified the expected aerodynamic performance.

Combustion

The development of the low NO_x combustor is being carried out using full-scale pressure and temperature rigs. The initial specification is for a 25 ppm NO_x combustor, with gradual movements to lower levels (see Table 3). The combustor is a

Table 3   501G initial emissions targets

	Natural Gas	Oil
• NOx	< 25 ppm	< 42 ppm
• CO	< 10 ppm	< 25 ppm
• UHC	< 10 ppm	< 15 ppm

dual-fuel combustor and will use water or steam to control NO_x when burning liquid fuel.

Cooling

Because of the elevated firing temperatures, it is planned to carry out a cascade test of the row one blade and vane in a full firing temperature rig facility in 1995. This test will verify operating temperatures, especially for the difficult endwall regions, before the engine is introduced into commercial operation.

In addition, cascade testing of model vanes and model tests of blades will be conducted to verify pressure loss in turbine passages and film cooling of shrouds.

Shop and Field Testing

Two prototype units will be tested, these will be fully instrumentated engines, which will be tested to full power conditions before entering commercial service in 1997 (see Fig. 14).

The prototype test is the important final stage for the confirmation of the following:

1 Compressor inlet airflow over entire IGV range
2 Compressor surge margin
3 Engine starting and acceleration characteristics
4 Mechanical integrity of the engine from starting to overspeed including rotor vibration characteristics
5 Mechanical and thermal performance of the engine over its entire operating range
6 Reliability of the engine by measurement of gas and metal temperatures, pressure, vibratory stresses, etc.
7 Emission characteristics of the engine and the effects of injection upon emissions and thermal performance

To provide these data, the engine will be extensively instrumented to measure thermodynamic values, metal temperatures, static and vibratory strains, vibration characteristics, displacements, and other parameters. Dynamic strain gauges will be installed on the turbine blades to verify dynamic responses. The signals from the rotating sensors will be transmitted by a telemetry system. Clearance measurement systems using proximity probes allow stator-to-rotor radial displacement measurements during transients. Data acquisition equipment will be installed to record the special engineering test data. This equipment includes tape recorders, spectrum analyzers, plotters, and chart recorders.
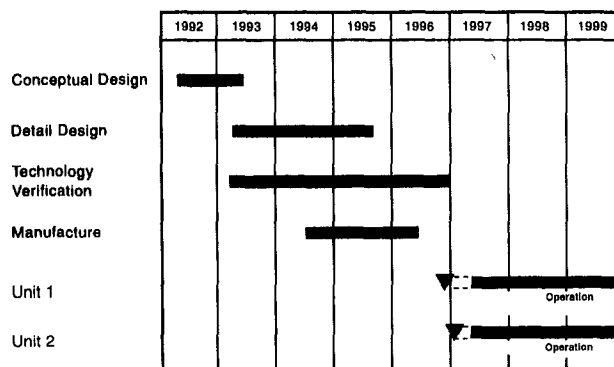

Fig. 14   501G development schedule

Table 4   501G inspection intervals

Inspection Type	Hours	Starts
Combustor	8,000	400
Turbine	24,000	1,200
Major	48,000	2,400

Gas Fuel

Life Cycle Costs

Combustion turbines are designed for long life. However, the hot parts, especially the cooled turbine components and the combustion equipment, have a finite life because of thermal fatigue cracks, corrosion, oxidation, creep, and other phenomena. In order to reduce the cost of these parts to the customer, the 501G has been designed with the objective of reducing the number of hot parts. The most expensive and most often replaced aerofoils are the row one and row two vanes and blades. Compared to the 501F, these numbers have been reduced by 20 percent.

Maintenance intervals, despite the higher firing temperatures, have been maintained at the current generation level (see Table 4). This is possible by keeping the same surface metal temperatures as exists in the 501F, and by improving the creep and thermal fatigue resistance by utilizing directionally solidified superalloys.

Conclusion

The major market drivers for combustion turbines are capital cost, operating cost, emissions, and fuel availability. To make a step change in the technology of the combined cycle projects, a new advanced design combustion turbine is introduced that is more efficient and cost effective than competitive machines currently available or projected. The 501G engine utilizing advanced aero-engine design and tools, elevated firing temperatures, and proven technology, results in a design that maximizes the output for minimum cost per kW at maximum operating efficiency. By the novel use of steam cooling, the flame temperature is kept at the same level as the 501F; thereby, the new engine will have low levels of NO_x despite the elevated rotor inlet temperature.

The resulting power plant efficiency will improve from today's best of 54 to 58 percent, an improvement of 7.4 percent. At the same time the size of the engine, compared to the 501F, will be only slightly increased. The 501G engine will produce approximately twice the output of a 501D machine and is 70 MW larger than any other currently available 60 Hz combustion turbine on the market. The high power output will further enhance the maintenance and balance of plant cost advantage of the 501G engine when compared to a plant of similar output but requiring more combustion turbines.

References

Scalzo, A. J., McLaurin, L. D., Howard, G. S., Mori, Y., Hiura, H., and Sato, T., 1989, "A New 150-MW High-Efficiency Heavy-Duty Combustion Turbine," ASME JOURNAL OF ENGINEERING FOR GAS TURBINES AND POWER, Vol. 111, pp. 211–217.

Two-Phase Air/Oil Flow in Aero Engine Bearing Chambers: Characterization of Oil Film Flows

A. Glahn

S. Wittig

Lehrstuhl und Institut für Thermische
Strömungsmaschinen,
Universität Karlsruhe (T.H.),
76128 Karlsruhe, Federal Republic
of Germany

For the design of secondary air and lubrication oil systems, a sufficient knowledge of two-phase flow and heat transfer phenomena under bearing chamber flow conditions is required. The characterization of oil film flows at the bearing chamber walls is one of the major tasks for a better understanding of these processes and, therefore, a necessity for improvements of the efficiency of aero engines. The present paper gives a contribution to this subject. Utilizing a fiber-optic LDV setup, measurements of oil film velocity profiles have been performed in our high-speed bearing chamber rig simulating real engine conditions. All data have been compared with different theoretical approaches, which have been derived from a force balance at a liquid film element, including geometric conditions and temperature dependent fluid properties, and by approaches for the eddy viscosity available in the literature.

Introduction

Performance characteristics and capabilities of modern jet engines are highly influenced by an efficient design of the secondary air system. Therefore, air has to be taken as early as possible from the compressor and has to be expelled back into the mainstream at the highest possible pressure. To meet this requirement, sufficient knowledge on discharge characteristics and heat transfer phenomena of all secondary air system components, i.e., rotating orifices, labyrinth seals, and annular gaps, are necessities within the design process. As a result, these subjects are currently investigated in comprehensive studies and worldwide research activities (Wittig and Schulz, 1992). As far as single-phase air flows are concerned, satisfying results have been elaborated for many of these components. Examples are given by the work of Waschka et al. (1990–1992), Wittig et al. (1996), and Jakoby et al. (1994), who have investigated influences of high rotational speeds on the performance of various labyrinth seal geometries and orifices, respectively. Contrary to this, little knowledge is available on the flow phenomena at the interface between the secondary air and the lubrication oil system, namely the bearing chamber.

Based on the fact that rolling element bearings cannot be substituted in aero engines within the near future, special effort has to be directed to the problem of heat generation due to bearing friction. Therefore, these bearings have to be lubricated by oil. As a consequence, chambers have to be built separating the lubricant from the hot zones of the engine in order to prevent oil fires. Bearing chamber seals (e.g., labyrinth or brush seals) have to be pressurized by air, which is supplied by the secondary air system described above. Entering the chambers, the air mixes with the lubrication oil, generating extremely complex two phase flow conditions. Finally, the air is discharged through vent lines, carrying a certain amount of oil with it.

Due to contradictory tasks in designing the flow elements upstream and downstream of the bearing chambers, a proper matching of the appropriate sealing air flows is a highly iterative

process. On one hand, the amount of sealing air flow has to be kept as small as possible, because it represents an engine power loss. On the other hand, small air flows discharged by vent pipes result in small pressure differences across the seals which can cause oil leakage and in consequence oil fire (Suter and Boyman, 1978). The amount of lubrication oil supplied to the bearing affects the pressure loss downstream of the bearing chamber and, therefore, it is an indirect design parameter for the sealing air flow. The oil flow necessary for a reliable engine operation is also influenced by the problem of heat generation to the oil, which becomes greater with increasing amounts of hot air flow into the chamber. Other problems arise due to the fact that the oil scavenged back from the bearing chamber into the reservoir has to be cooled. High oil flows require larger pumps, filters, and cooling units with the consequence of higher energy requirements for accessory drives and additional weight. Besides that, improvements in aero engine efficiency have reduced the fuel consumption considerably, thus reducing the cooling capacity for the oil heat exchangers. Therefore, to design lubrication oil flows a sufficient knowledge of all heat transfer phenomena involved in bearing chamber flow conditions is required. Additional heat sources are the bearing friction and the heat transfer from the bearing chamber walls to the oil, which is bounded to a substantial part in a rotating film at the inner side of the housing.

The characterization of oil film flows and the associated heat transfer processes is one of the major tasks for a better understanding of bearing chamber flow and, therefore, a necessity for improvements of the efficiency of secondary air systems.

The present paper gives a contribution to this subject. Based on a literature survey on film flows and an experimental determination of oil film velocity profiles, an analytical approach is given for the characterization of shear-driven oil film flows under gravity.

Two-Phase Air/Oil Flow in Bearing Chambers

Phenomenological Description—Modeling of Film Flows.
A two-phase air/oil flow pattern inside aero engine bearing chambers can be expressed simplistically, as shown in Fig. 1. The complex geometry of a real engine application has been abstracted by an annular gap between two concentric cylinders, the inner one rotating. It has been shown in comprehensive
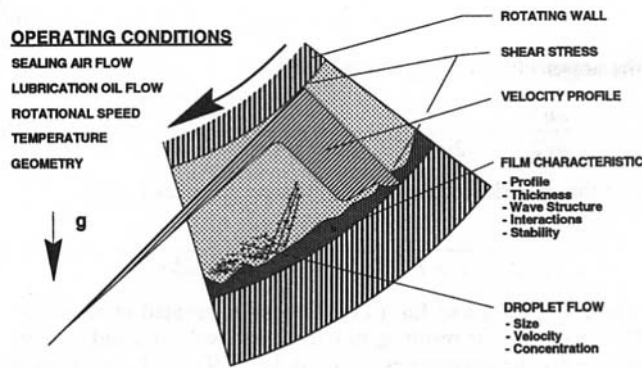
Fig. 1 Tasks in bearing chamber flow analysis

preliminary flow visualization studies that the flow field within the annular gap is characterized by a rotating oil film interspersed with small air bubbles, and by oil droplets dispersed in the turbulent air flow over the wall film.

Obviously, the interaction between air flow and wall film affects both the velocity profile of the gas phase and the properties of the oil film. The oil film acts upon the air like a rough wall, thus increasing the shear stress at the wall and the interface, respectively. The latter results in an increase of the surface velocity and can cause supercritical film flow conditions characterized by the onset of droplet removal from the film. As shown, for instance, by Himmelsbach (1992) and Wittig et al. (1992), the incorporation of a detailed analysis of all interaction processes at the gas/film interface including unsteady wave characteristics and supercritical conditions into practical applications is not possible yet. However, due to the importance of film flows for many technical applications, a considerable amount of work on the relevant topics exists. Based on these investigations, models have been developed that predict the main features of the specific film flows fairly well. On the assumption that characteristic time-averaged parameters can be used for the description of both the film flow and the interaction processes, the wavy film is treated as a film of constant height exposed to an averaged shear force resulting from the air flow at its surface. Applications of such an approach require the knowledge of the time-averaged local film thickness and the averaged film velocity profile or the mass flow rate, respectively. Furthermore, a relationship for the coupling between film and gas phase is necessary and, therefore, the research activities have been focused on these topics.

Literature Survey. Surveys on efforts on the above-mentioned research topics have been presented by Wurz (1971), Hewitt (1978), Sattelmayer and Wittig (1989), and Himmelsbach (1992).

The fundamental problem within the calculation procedure of film flows is the question of whether the flow regime is laminar or turbulent. The investigations documented in the literature do not show a uniform strategy on this topic. One reason may be given by the fact that most of the investigators could not measure velocity profiles directly. Therefore, a comparison of measured data with the appropriate values calculated from the individual theory has been performed on the basis of data that can be determined much more easily (e.g., Dukler and Bergelin, 1952; Dukler, 1960; Lee, 1965; Wurz, 1971; Sattelmayer and Wittig, 1989). Most of the investigators mentioned above have taken the time-averaged film thickness for this comparison. Other researchers (Ueda and Tanaka, 1975) have generated thick ($\bar{h}_F \simeq 4$–5 mm) viscous film flows, in order to measure velocity profiles utilizing conventional probe techniques. However, it is questionable whether their results showing laminar flow conditions can be transferred to bearing chamber flows, because their investigation covers only falling liquid films without shear forces at the interface or droplet interaction.

In recent years the development and improvement of optoelectronical measuring devices has given a much better insight into film flow behavior. Wittig et al. (1992) have reported on the assessment of different approaches for the calculation of shear driven thin ($\bar{h}_F \le 200$ μm) water films based on measurements utilizing a newly developed optical measuring device for the simultaneous determination of film thickness and velocity. In a parameter range typical for the conditions in prefilming airblast atomizers, the best fit between predicted and measured film surface velocities has been found for the assumption of a laminar film velocity profile. Besides that, they have noticed a turbulent structure of the film for a decrease in the interface shear stress and an increase in the liquid flow rate, both leading to a larger film thickness. This statement has been confirmed by the investigation of Plimon (1991) who used a modified LDV setup for the analysis of shear-driven liquid films. For water films of $\bar{h}_F \simeq 500$ μm thickness and comparatively low interface shear forces he has observed a turbulent structure.

However, a generalized statement for the liquid film flow behavior cannot be found in the literature, because experiments transferable to bearing chamber flow conditions have not been performed so far. Therefore, our own investigations on this subject have to be done. For the measurements described in this paper our compact high-speed bearing chamber test rig (Wittig et al., 1994) has been adapted to this task. The discussion of oil film velocity profiles measured under real engine conditions at our test facility has to be based on a theoretical outline on film flows and the question of whether the measured data can be expressed in terms of an analytical approach. Some of the theoretical approaches available in the literature have been used in this paper as a reference to the measurements. These theories are presented next.

Theoretical Outline on Film Flow. Neglecting pressure forces and any acceleration of the fluid, a force balance for a liquid film flowing on an inclined plane (inclination angle φ^*) results in

---

Nomenclature

b = width, m
d = diameter, m
g = acceleration of gravity, m/s^2
h = height, m
l_t = turbulent length scale, m
$\dot{m}$ = mass flow, kg/s
n_W = rotational speed, min^{-1}
n = const
r, ϕ, z = cylindrical coordinates, m, deg, m
T = temperature, K

u = velocity, m/s
u_τ = shear velocity, m/s
u^+ = nondimensional velocity
$\dot{V}$ = volume flow, m^3/s
y = distance from the wall, m
y^+ = nondimensional distance
φ^* = inclination angle, deg
κ = Von Kármán constant
ν = kinematic viscosity, m^2/s
ν_t = eddy viscosity, m^2/s
ρ = density, kg/m^3

σ = nondimensional parameter for the film velocity profile
τ = shear stress, N/m^2

Subscripts

F = film/liquid
L = air
l = laminar
t = turbulent
W = wall
I, II = chambers I, II

$$\tau = \tau_W - \rho_F g \sin \varphi^* y \qquad (1)$$

with the shear velocity

$$u_{\tau,F} = \sqrt{\tau_W/\rho_F}. \qquad (2)$$

This can be rewritten in a dimensionless form

$$\frac{\tau}{\tau_W} = 1 - \sigma y_F^+ . \qquad (3)$$

The parameter σ is given by

$$\sigma = \frac{\nu_F g \sin \varphi^*}{(\tau_W/\rho_F)^{3/2}}$$

and the dimensionless distance from the wall has been derived utilizing Eq. (2):

$$y_F^+ = y \frac{u_{\tau,F}}{\nu_F} .$$

The total shear stress in the film results from a superimposition of the molecular and the turbulent shear stress, respectively. The latter can be expressed following the Boussinesq approach. Thus,

$$\frac{\tau}{\tau_W} = \left(1 + \frac{\nu_t}{\nu_F}\right) \frac{du_F^+}{dy_F^+} , \qquad (4)$$

where ν_t is the eddy viscosity and u_F^+ is the film velocity parallel to the wall based on the shear velocity given by Eq. (2). Substituting Eq. (3) into Eq. (4) results in

$$1 - \sigma y_F^+ = \left(1 + \frac{\nu_t}{\nu_F}\right) \frac{du_F^+}{dy_F^+} \qquad (5)$$

as a universal velocity profile for shear-driven liquid films under gravity. This equation can be solved for a given relationship for the eddy viscosity. In the present study three approaches for ν_t are compared. The first one represents laminar flow conditions

$$\frac{\nu_t}{\nu_F} = 0. \qquad (6)$$

Next we have adapted an approach discussed by Wurz (1971) for horizontal flow to inclined film flows resulting in additional gravity forces. Here, the eddy viscosity is expressed in terms of the turbulent length scale:

$$\frac{\nu_t}{\nu_F} = \frac{1}{\nu_F} l_t^2 \frac{du_F}{dy_F} = \frac{1}{\nu_F} \kappa^2 y_F^2 \frac{du_F}{dy_F} . \qquad (7)$$

Finally, we have followed Dukler (1960) who proposed an empirical correlation given first by Deissler (1954):

$$\frac{\nu_t}{\nu_F} = n^2 u_F y_F \frac{1}{\nu_F} \left\{ 1 - \exp\left(-n^2 u_F y_F \frac{1}{\nu_F} \right) \right\} . \qquad (8)$$

The von Kármán constant has been set to $\kappa = 0.4$ and the empirical constant in Eq. (8) to $n = 0.109$, respectively. It should be noted that the model proposed by Dukler (1960) utilizes two approaches for the eddy viscosity, namely the correlation given in Eq. (8) for film heights in the range of $0 \leq y_M^+ \leq 20$, and another correlation in the range $y_M^+ > 20$. Based on the fact that Deissler (1954) has set $y_M^+ = 26$ as the matching point between the two approaches and our investigation covers the range of $0 \leq y_M^+ \leq 27$, for the sake of simplicity we have solely taken Eq. (8) into account.

By use of Eq. (5) the following equations can be written for the laminar profile:

$$u_F^+ = y_F^+ - \tfrac{1}{2}\sigma y_F^{+2}, \qquad (9)$$

the approach following Wurz (1971)

$$\frac{du_F^+}{dy_F^+} = -\frac{1}{2\kappa^2 y_F^{+2}} + \frac{1}{\kappa y_F^{+2}} \sqrt{\frac{1}{4\kappa^2} + y_F^{+2} - \sigma y_F^{+3}} , \qquad (10)$$

and the empirical correlation following Deissler (1954)

$$\frac{du_F^+}{dy_F^+} = \frac{1 - \sigma y_F^+}{1 + n^2 u_F^+ y_F^+ \{1 - \exp(-n^2 u_F^+ y_F^+)\}} , \qquad (11)$$

where Eq. (10) and Eq. (11) must be integrated numerically. Differences in the resulting film thickness, velocity, and velocity profile for the approaches given by Eqs. (9)–(11) are demonstrated by Fig. 2.

The equation of continuity

$$\int_0^{\overline{h}_F^+} u_F^+ dy_F^+ = \frac{\dot{V}_F/b}{\nu_F} \qquad (12)$$

has been used for the calculation of film thickness and surface velocity at a given film flow rate and temperature, representing typical bearing chamber flow conditions. In addition, the parameter σ has been varied, showing the significance of gravity forces. It can be easily seen from this example that the uncertainty in the calculation of the film thickness is about 60 percent, whereas differences in the film surface velocity are in the range of 55 percent. A more detailed discussion is given together with the presentation of measured data.

Experimental Setup

Compact High-Speed Bearing Chamber Rig. As mentioned above, the test rig developed at our institute for the investigation of air/oil flow and heat transfer phenomena in bearing chambers has been adapted to film velocity profile measurements under real engine conditions characterized, e.g., by high rotational speeds up to $n_W = 16,000$ rpm. Design considerations and a description of all test facility components are given elsewhere (Wittig et al., 1994). However, for a better understanding of air and oil flows inside the bearing chamber rig, a short description of the general arrangement is presented next. A co-axial sectional view of the test rig is shown in Fig. 3.

At each side of the squeeze film-damped roller bearing (1), separate chambers (I, II) are formed. The axial location of the rotor (2) is realized by use of a conventional groove-ball bearing (3). The chambers are bounded by a thick-walled housing (4), the roller bearing support (5), the rotor, a flange (6) realizing the sealing air supply of chamber I and the support of the housing, and a transparent cover (7) for chamber II representing the optical access for the film velocity measurements. It can be
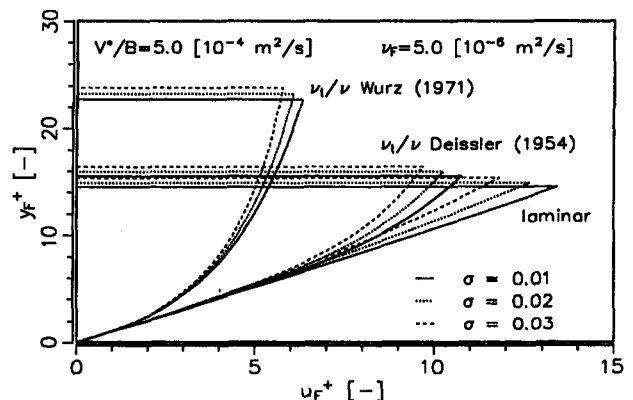

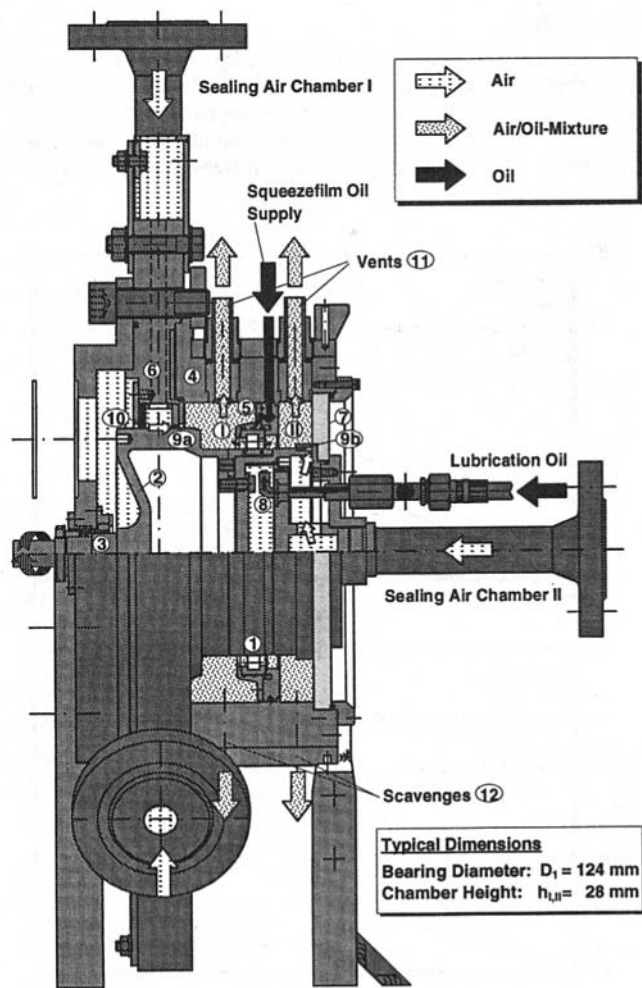Fig. 2 Comparison of film velocity profiles at bearing chamber flow conditions

Fig. 3 High-speed bearing chamber test rig

readily concluded from Fig. 3 that the bearing chamber geometries of our test rig have been abstracted from the very complex arrangements given by a real engine to a more or less rectangular shape. Thus, two different aspect ratios of $(b/h)_I = 1.62$ and $(b/h)_{II} = 0.71$ are realized, both expected to give transferable results.

However, air and oil flows have been arranged in the same way as in the real engine. An under-race lubrication (8) supplies the roller bearing with preheated oil. To prevent oil leakage the chambers are sealed using three-fin labyrinth seals (9a, b). Both labyrinth seals are pressurized by air which is preheated to the same temperature level as the lubrication oil. Air/oil mixtures are discharged through the vent lines (11) at the top of each chamber, while the oil sump at the bottom is dropped out via radial scavenges utilizing the pressure difference from the bearing chamber atmosphere to the environment. Thus, another simplification is given to a real engine application, where scavenge pumps are used. This circumstance has been considered by selecting the location of film velocity measurements and, therefore, the results gained with the setup described above will not be limited to the present investigation.

Fiber-Optic LDV Setup. The determination of all relevant operating parameters and the control of the test facility are done by use of the computer-based data acquisition described by Wittig et al. (1994). Film velocity measurements have been performed using the setup shown schematically in Fig. 4. The system presented in detail by Jakoby et al. (1994) has been used in the present investigation for the determination of oil

film velocities parallel to the housing wall. It comprises a 4 W argon-ion laser, a standard optic with 40 MHz Bragg cell, color and beam separators, and a two-dimensional fiber probe. The availability of a fiber-probe LDV system guarantees a high degree of flexibility, which is necessary for applications under real engine conditions, as given in this bearing chamber flow investigation. The signals are detected in a backscatter mode by a fiber link and photomultiplier setup in combination with filters and the counterprocessors. Working as a data link between the counterprocessors and the microcomputer (PC 80386), the interface card writes all data into the computer memory.

Due to the thin oil films in the range of 1 mm $\leq \bar{h}_F \leq 2$ mm, measurements have to be performed close to the wall and, therefore, only one component of the LDV could be used. Additional seeding of the flow is not necessary here, because small gas bubbles interspersed in the oil film as mentioned above can be used as tracer particles. All velocity profiles and measured data presented in the next section have been determined at an axial distance from the transparent cover (7, Fig. 3) large enough to avoid any effects of wall friction. Preliminary studies have shown that an axial distance of $\Delta z = 2$ mm from the cover has been sufficient for this assumption. The circumferential position of all measurements has been chosen to be φ^* = 30 deg upstream of the scavenge port (Fig. 4). Temperature measurements necessary for the calculation of oil properties have been performed 5 deg downstream from this position by use of NiCr–Ni thermocouples mounted at a radial distance of $\Delta r = 1$ mm.

Experimental Results and Discussion

This investigation has been focused on the question of whether the oil film flow in bearing chambers can be characterized by a theoretical approach for the velocity profile, which is the main presupposition for any further modeling of bearing chamber flow conditions. The analysis is based on measured data as given in Fig. 5. The operating conditions are given by a lubrication oil flow of $V_{II} = 150$ l/h and a sealing air flow of $\dot{m}_{II} = 10$ g/s to chamber II, and by rotational speeds of $n_W = 3000$ rpm to 12,000 rpm. As expected, an increase of the rotational speed results in an increase of the gas/liquid interface shear force and, as a consequence, in enhanced film velocities and decreasing film thickness.

According to the outline on film flow theories given before, transferable results can be derived by referring the data shown in Fig. 5 to the shear velocity u_τ and the kinematic viscosity ν_F, respectively. The wall shear stress, necessary for a dimensionless treatment of the oil film flow behavior, can be deter-
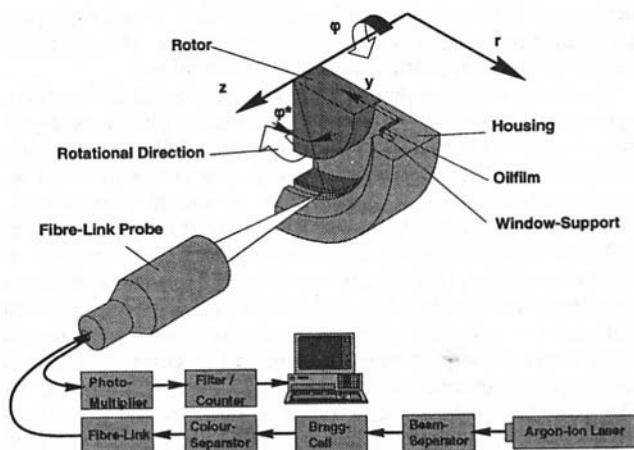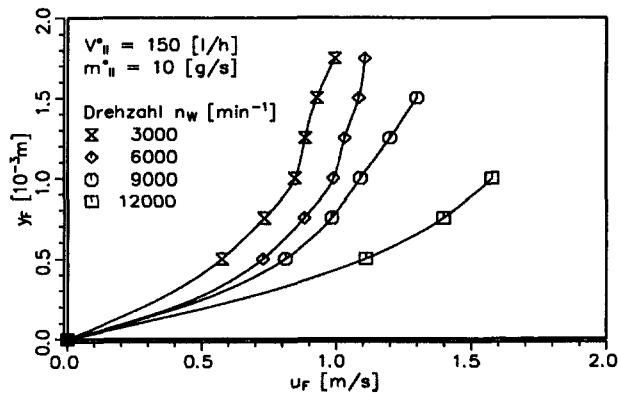

Fig. 4 LDV Setup (schematic)

Fig. 5 Film velocity profiles in bearing chamber II: $\varphi^* = 30$ deg, $\dot{V}_{II} = 150$ l/h, $\dot{m}_{II} = 10$ g/s

mined from one measured data point $u_F = f(y_F)$ by use of Eq. (5) and a given approach for the eddy viscosity (Eqs. (9)–(11)). It must be pointed out that each model for the eddy viscosity results in a different wall shear stress. Thus, different quantities have to be considered for the definition of the dimensionless parameters σ, u_F^+, and y_F^+.

A comparison between measurement and theory for each of the models given by Eqs. (9) to (11) is presented in Fig. 6. Each single frame shows one operating condition characterized by air and oil flows and rotational speed.

Assuming laminar flow conditions, wall shear stresses have been calculated iteratively from the measured values $u_F = f(y_F)$ next to the wall ($y_F = 0.5$ mm) and by use of Eq. (9). With the wall shear stress and the circumferential location of the measurements ($\varphi^* = 30$ deg) the parameter $\sigma = f(\tau_l)$ and the shear velocity $u_\tau = f(\tau_l)$ can be evaluated. Therefore, theoretical velocity profiles as a function of σ (τ_l) can be compared with measured data referred to u_τ (τ_l).

In an analogous manner, but using data points $u_F = f(y_F)$ in the middle of the film, the values $\sigma(\tau_{l, \text{Wurz}})$, $u_\tau(\tau_{l, \text{Wurz}})$, $\sigma(\tau_{l, \text{Deissler}})$, and $u_\tau(\tau_{l, \text{Deissler}})$ have been determined. Consequently, measurements and theory can be compared as well for the approaches given in Eqs. (10) and (11).

It can be readily seen from Fig. 6 that the oil film flow in bearing chambers is of turbulent character. All operating conditions considered here show poor agreement between measurement and theory when laminar flow is assumed. The discrepancies are larger for the low-speed conditions reflecting a higher influence of gravity forces as expressed in the parameter σ (see also Fig. 2).

Assuming turbulent flow conditions and following the approach for the eddy viscosity proposed by Wurz (1971), the deviations between measured and calculated velocity profiles are in the range of $\Delta u_F^+(y_F^+) = 17$ to 30 percent. This approach results in an overpredicted total wall shear stress.

However, it is also demonstrated by Fig. 6 that an excellent agreement between measurement and theory for all rotational speeds can be obtained when the approach following Deissler (1954) is used for the eddy viscosity. The comparison shows maximum deviations of $\Delta u_F^+(y_F^+) = 5$ percent next to wall. Data points in the middle of the film and next to the surface are reflected with an excellent agreement by Eq. (11). Therefore, it can be concluded that oil films under the operating conditions described here can be characterized by an analytical approach utilizing the universal velocity profile for shear-driven liquid films under gravity as given by Eq. (5) in combination with the empirical correlation for the eddy viscosity proposed by Deissler (1954). In addition, proof is given for the simplification of Dukler's (1960) proposal resulting in Eq. (11), which has been derived without consideration of a second empirical correlation for the eddy viscosity.

Conclusion

Based on LDV measurements of oil film velocity profiles, an assessment of three different approaches for the characterization of oil film velocities in bearing chambers has been performed. Turbulent flow conditions have been found for all operating conditions. An analytical approach considering temperature de-
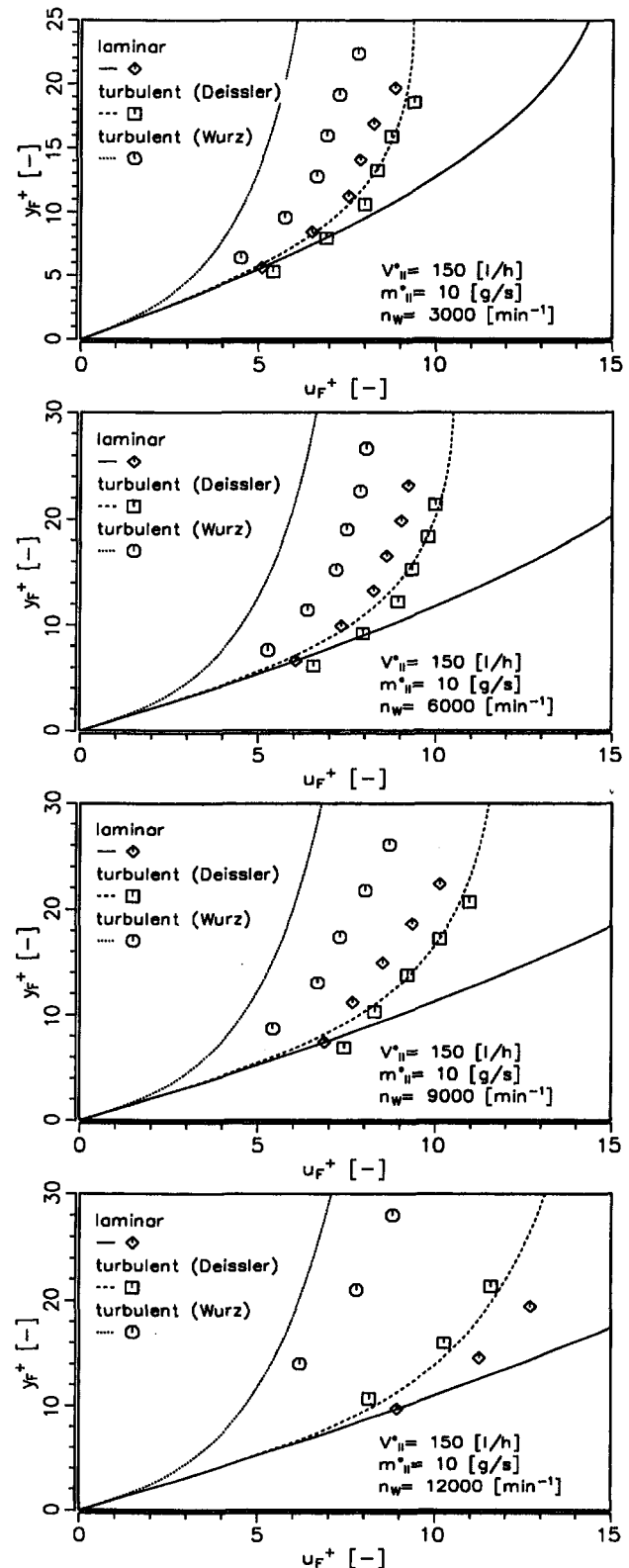

Fig. 6 Nondimensional film velocity profiles: comparison with theory

pendent liquid properties, geometric conditions, and a correlation for the eddy viscosity has been found to reflect the measured data excellently. This leads to several benefits with respect to an analysis of bearing chamber oil film flows. Due to the knowledge of the velocity profile a further modeling of the oil film behavior is possible by reducing dimensional values for film height and velocity to nondimensional flow parameters as represented by the Reynolds number. Therefore, results can be expressed in data transferable to other applications. In addition, any numerical analysis of two-phase flow phenomena in bearing chambers requires a relation for the coupling between the phases. Based on the film velocity profile presented in this paper, existing coupling approaches are expected to be adaptable to the computation of bearing chamber flows.

Acknowledgments

References

Deissler, R., 1954, "Heat Transfer and Fluid Friction for Fully Developed Turbulent Flow of Air and Supercritical Water With Variable Fluid Properties," *Transactions of the ASME*, Vol. 76, pp. 73–85.

Dukler, A. E., and Bergelin, O., 1952, "Characteristics of Flow in Falling Liquid Films," *Chemical Engineering Progress*, Vol. 48, pp. 557–563.

Dukler, A., 1960, "Fluid Mechanics and Heat Transfer in Vertical Falling-Film Systems," *Chemical Engineering Progress Symposium Series*, Vol. 56, pp. 1–10.

Hewitt, G., 1978, *Measurements of Two-Phase Flow Parameters*, Academic Press, London.

Himmelsbach, J., 1992, "Zweiphasenströmungen mit schubspannungsgetriebenen welligen Flüssigkeitsfilmen in turbulenter Heißluftströmung—Meßtechnische Erfassung und numerische Beschreibung," Dissertation, Institut für Thermische Strömungsmaschinen, Universität Karlsruhe, Germany.

Jakoby, R., Benz, E., Willmann, M., and Wittig, S., 1994, "Phase Resolved LDV-Measurements in High-Speed Rotating Disk Systems With Orifices," *Fifth International Symposium on Transport Phenomena and Dynamics of Rotating Machinery*, Vol. A, pp. 573–591.

Lee, J., 1965, "Turbulent Velocity Profile of a Vertical Film Flow," *Chemical Engineering Science*, Vol. 20, pp. 553–536.

Plimon, A., 1991, "Velocity Profiles in Shear Driven Wall Films," *Experiments in Fluids*, Vol. 11, pp. 339–340.

Sattelmayer, Th., and Wittig, S., 1989, "Performance Characteristics of Prefilming Airblast Atomizers in Comparison With Other Airblast Nozzles," *Encyclopedia of Fluid Mechanics*, Vol. 8, Golf Publishing Company.

Suter, P., and Boyman, T., 1978, "Transport Phenomena in Labyrinth-Seals of Turbomachines," AGARD *Conference Proceedings*, No. 237, pp. 8.1–8.10.

Ueda, T., and Tanaka, H., 1975, "Measurements of Velocity, Temperature, and Velocity Fluctuation Distributions in Falling Liquid Films," *International Journal of Multiphase Flow*, Vol. 2, pp. 261–272.

Waschka, W., Wittig, S., and Kim, S., 1990, "Influence of High Rotational Speeds on the Heat Transfer and Discharge Coefficients in Labyrinth Seals," ASME Paper No. 90-GT-330.

Waschka, W., Wittig, S., Scherer, Th., and Kim, S., 1991, "Leakage Loss and Heat Transfer in High-Speed Rotating Labyrinth Seals: An Experimental Verification of Numerical Codes," *Proc. 1991 Yokohama International Gas Turbine Congress*, Vol. II, pp. 239–247.

Waschka, W., Scherer, Th., Kim, S., and Wittig, S., 1992, "Study of Heat Transfer and Leakage in High-Rotating Stepped Labyrinth Seals," presented at the 4th International Symposium on Transport Phenomena and Dynamics of Rotating Machinery, Honolulu, HI.

Wittig, S., Himmelsbach, J., Noll, B., Feld, H. J., and Samenfink, W., 1992, "Motion and Evaporation of Shear-Driven Liquid Films in Turbulent Gases," ASME JOURNAL OF ENGINEERING FOR GAS TURBINES AND POWER, Vol. 114, pp. 395–400.

Wittig, S., and Schulz, A., 1992, "A Survey on Efforts in Heat and Mass Transfer Analysis in Aero Engine Secondary Air/Oil Systems," presented at the International Symposium on Heat Transfer in Turbomachinery, Athens, Greece.

Wittig, S., Glahn, A., and Himmelsbach, J., 1994, "Influence of High Rotational Speeds on Heat Transfer and Oil Film Thickness in Aero Engine Bearing Chambers," ASME JOURNAL OF ENGINEERING FOR GAS TURBINES AND POWER, Vol. 116, pp. 395–401.

Wittig, S., Kim, S., Jakoby, R., Weißert, I., 1996, "Experimental and Numerical Study of Orifice Discharge Coefficients in High-Speed Rotating Disks," ASME *Journal of Turbomachinery*, Vol. 118, pp. 400–407.

Wurz, D., 1971, "Experimentelle Untersuchung des Strömungsverhaltens dünner Wasserfilme und deren Rückwirkung auf einen gleichgerichteten Luftstrom mäßiger bis hoher Unterschallgeschwindigkeit," Dissertation, Institut für Thermische Strömungsmaschinen, Universität Karlsruhe, Germany.

The Effect of Twisted-Tape Width on Heat Transfer and Pressure Drop for Fully Developed Laminar Flow

W. M. Chakroun

S. F. Al-Fahed

Center of Research for Experimental
Thermal Sciences,
Mechanical Engineering Department,
Kuwait University,
Kuwait

A series of experiments was conducted to study the effect of twisted-tape width on the heat transfer and pressure drop with laminar flow in tubes. Data for three twisted-tape wavelengths, each with five different widths, have been collected with constant wall temperature boundary condition. Correlations for the friction factor and Nusselt number are also available. The correlations predict the experimental data to within 10 to 15 percent for the heat transfer and friction factor, respectively. The presence of the twisted tape has caused the friction factor to increase by a factor of 3 to 7 depending on Reynolds number and the twisted-tape geometry. Heat transfer results have shown an increase of 1.5 to 3 times that of plain tubes depending on the flow conditions and the twisted-tape geometry. The width shows no effect on friction factor and heat transfer in the low range of Reynolds number but has a more pronounced effect on heat transfer at the higher range of Reynolds number. It is recommended to use loose-fit tapes for low Reynolds number flows instead of tight-fit in the design of heat exchangers because they are easier to install and remove for cleaning purposes.

Introduction

Heat transfer can be greatly enhanced by the introduction of twisted-tape inserts. However, the increase in pressure drop affects the pumping power necessary to maintain the mass flow rate. Twisted-tape insert is a well-established method for enhancing heat transfer characteristic of heat exchangers that can be used in oil coolers for gas turbines. Substantial cost savings can be achieved by employing twisted tapes to improve heat transfer in industrial heat exchangers. For a given thermal duty, a smaller heat exchanger can be obtained by inserting a twisted tape. Along with the heat transfer enhancement, however, there is an increase in the frictional resistance to flow. This paper examines and demonstrates the effectiveness of using a twisted tape as a heat transfer enhancement technique for laminar flow with a constant-wall-temperature boundary condition. The gap between the twisted tape and the internal diameter of the tube will also be investigated. The motivation of the work is the desire to use a loose-fit twisted tape that is easier to install and clean when compared to one with a tight fit. The influence of the gap between the twisted tape and the tube wall on pressure drop and heat transfer will be analyzed.

Several numerical and experimental studies have been reported on twisted tape inserts. However, very few addressed the effect of the gap between the twisted tape and the internal diameter of the tube. Most of the early work was concerned with the effect of twisted tape in turbulent flow (Royds, 1921; Koch, 1958; Lopina and Bergles, 1969). Du Plessis (1982) and Monheit (1987) conducted a numerical and experimental heat transfer study, respectively, for laminar isothermal boundary condition. Bandyopadhyay et al. (1991) also reported heat transfer data for laminar flow. Their experiments were performed for a constant-heat-flux condition. Manglik and Bergles (1987, 1988, 1992a, b) reported experimental data and correlations for heat transfer and pressure drop for twisted tape. Their experiments, however, were limited to twisted tapes that have the same width as the internal diameter of the tube. In their extensive work on twisted tapes, they did not address the effect of gap width between the twisted tape and the internal diameter of the tube. Ayub and Al-Fahed (1993) reported pressure drop measurements for different twisted-tape inserts with different gap widths. Their results were limited, however, to turbulent water flow.

The presence of the twisted tape affects the flow field inside the tube. The blockage of the tube flow by the tape increases the flow velocity. In addition, the twisted tape induces a secondary flow resulting in a swirl mixing. For a tight-fit twisted tape, the tape acts as a fin. This will not be the case for loose-fit twisted tape with a smaller width. The gap between the twisted tape and the wall of the tube will be investigated in the present work. The present study includes heat transfer and friction factor measurements. The data were collected for fully developed laminar flow and constant wall temperature where the working fluid is oil. Different twisted tapes with different Y and W were investigated ($Y = H/D_i$, where H is the wavelength of the twisted tape, D_i is the internal diameter of the tube, and W is the width of the twisted tape). Fifteen different arrangements were used in this study: three twist ratios, each with five different tape widths. The schematic drawing of the twisted tape insert is shown in Fig. 1. The physical dimensions of the tapes are given below:

	Twisted tape width				
	13.2 mm	12.6 mm	12.0 mm	11.4 mm	10.8 mm
$Y = H/D_i$					
7.1	A	B	C	D	E
5.4	F	G	H	I	J
3.6	K	L	M	N	O

Experimental Procedure

The friction factor for the twisted-tape experiments was calculated by measuring the pressure drop along the tube. The

Fig. 1 Schematic drawing of twisted-tape insert
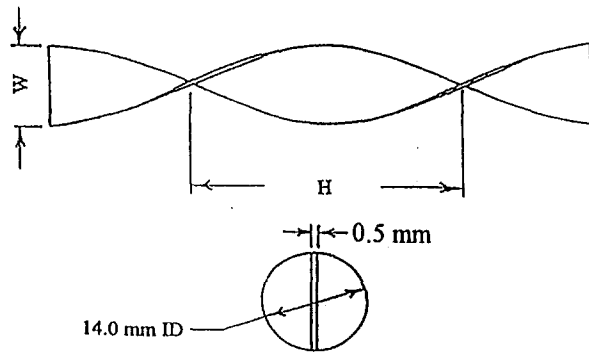

Fig. 2 Schematic diagram of the pressure drop facility

experimental setup to measure the pressure drop is shown in Fig. 2. The apparatus is designed to permit a comprehensive study of flow in tubes. It consists of a circuit through which the fluid is circulated continuously by means of a gear pump. A high-viscosity fluid was selected (Shell Tellus R5) in order to give values of the Reynolds number well in the laminar region. The oil is drawn from the reservoir and delivered by way of a Rotameter flow meter to the perspex settling chamber. The oil passes from the chamber through a parabolic bell mouth into the upper horizontal pipe in which the measurements are taken. The tube is made of copper, of 15.9 mm outside diameter and 14.0 mm inside diameter. The total length of the tube is 4.4 m; however, the test section in which the twisted tape is inserted is 2 m long. The tube is adjusted on its supports to be straight and horizontal. The arrangement of smoothing screens in the settling chamber ensures that the oil enters the tube in an undisturbed condition. Pressures are measured with a digital transducer with a range from 0 to 3 bars. The friction factor is calculated by

$$f = \frac{\Delta p}{\rho V^2/2} (D_i/L) \qquad (1)$$

A schematic diagram of the heat transfer facility is shown in Fig. 3. The rig includes two test sections of a single tube-in-tube heat exchanger. One test section carries a smooth copper tube of 14.0 mm inside diameter and a wall thickness of 1.05 mm and the second contains the same tube with a twisted-tape insert. The twisted tape was fixed at both ends inside the tube by using strings to prevent it from sliding when the flow is passing through. In both sections, saturated steam is introduced into the annulus and is used as an isothermal heat source. Shell Tellus R5 oil is used as the test fluid. The other components include a flow meter, thermocouples, and a data acquisition system. Each test section has a nominal length of 1 m, and both were preceded by a calming length of 3 m to eliminate any
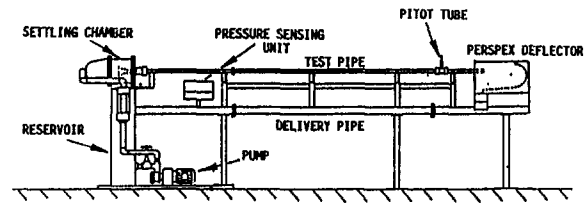
entrance effects. The system was insulated by wrapping insulation tape around the exposed portions of the tubes and the shells. The oil inlet temperature was controlled by means of a heat exchanger where chilled water is used for cooling. Annulus, wall, and test fluid temperatures were measured using gage copper-constantan thermocouples with a 273 K reference junction. Inlet and outlet fluid bulk temperatures were determined by using a mixing cup technique. The wall temperature is obtained by taking the average of 15 thermocouples installed in five axial locations along the wall of the tube. At each location three thermocouples are installed around the circumference of the tube. Each thermocouple is soldered in a groove (thermowell) inside the wall. The variation in the wall temperature axially and circonferentially was always less than 3 percent. The inside heat transfer coefficient and Nusselt number are calculated as follows:

$$Q = \dot{m}Cp(T_o - T_i) \qquad (2)$$

$$Q = h_i A_i (T_w - T_b) \qquad (3)$$

where

$$T_b = \frac{T_o + T_i}{2} \qquad (4)$$

Hence h_i and Nusselt number are calculated by

$$h_i = \frac{\dot{m}Cp(T_o - T_i)}{A_i(T_w - T_b)} \qquad (5)$$

$$\mathrm{Nu}_m = \frac{h_i D_i}{k} \qquad (6)$$

All fluid properties are evaluated at the mean bulk temperature, T_b.

The uncertainty in the experimentally determined friction factor and Nusselt numbers were estimated based on the ANSI/ASME Standard on Measurement Uncertainty (1986) following the procedure of Coleman and Steele (1989). The bias limits for all variables involved in the calculations of friction factor and Nusselt numbers were estimated. Because all thermocouples used in the Nusselt number determination were calibrated against the same standard, some elemental contributions

——— Nomenclature ———

A_c = axial cross-sectional area
A_i = circumferential area based on the inside diameter
C_p = specific heat
D_i = inside diameter
f = friction factor, Eq. (1)
f_{Sw} = swirl flow friction factor
Gz = Graetz number
H = twist wave length
h_i = inside heat transfer coefficient
k = thermal conductivity of the fluid
L = length of the test section

L_s = maximum helical flow length
$\dot{m}$ = mass flow rate
Nu_m = mean Nusselt number
Pr = Prandtl number
Q = heat gained by the oil
Re = Reynolds number
Re_{Sw} = Reynolds number based on swirl velocity
Sw = dimensionless swirl parameter
T_o = outlet oil temperature
T_i = inlet oil temperature
T_w = average wall temperature

V = average velocity
V_s = actual swirl velocity
V_a = mean axial velocity
W = width of twisted tape
Y = twist ratio = H/D_i
δ = thickness of twisted tape
Δp = pressure drop
μ = dynamic viscosity
ρ = fluid density

Subscripts

b = at bulk fluid temperature
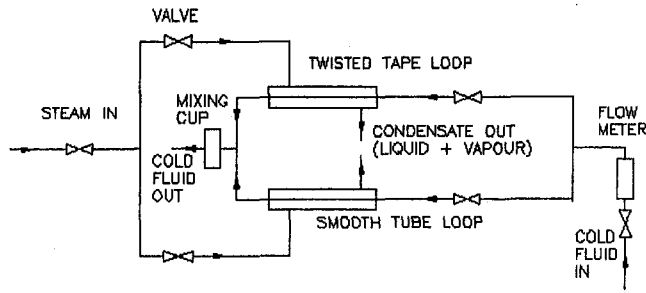w = at tube wall temperature

Fig. 3 Schematic diagram of the heat transfer facility

Fig. 5 Heat transfer data and Sieder–Tate correlation for the plain tube

to the bias limits were correlated. The effects of correlated biases were to reduce the overall uncertainty in the Nusselt number. The correlated biases were also accounted for in the uncertainty analysis. For the friction factor and Nusselt number data in this paper, the overall uncertainty ranges from 8 to 13 percent for the friction factor and from 5 to 10 percent for the Nusselt number depending on flow conditions.

Plain Tube Qualification

Pressure drop and heat transfer data were collected first for the plain tube. The plain-tube data will serve as a validation of the facility and procedure over the range of Reynolds number anticipated in the twisted-tape testing. Figures 4 and 5 show the friction-factor and heat transfer results plotted against known plain-tube correlations. Figure 4 presents the friction factor results that are calculated from the measured pressure drop using Eq. (1). The friction-factor data are in excellent agreement with the $64/\text{Re}$ equation that is the analytical solution for laminar flow in plain tube. Figure 5 presents the heat transfer data plotted as Graetz number versus $\text{Nu}_m(\mu_b/\mu_w)^{-0.14}$. The plain-tube data are found to be in good agreement with the Seider–Tate correlation:

$$\text{Nu}_m = 2.02\ \text{Gz}^{1/3}(\mu_b/\mu_w)^{0.14} \qquad (7)$$

where

$$\text{Gz} = \frac{\text{Re}_D\ \text{Pr}}{L/D} \qquad (8)$$

This equation is valid over the range of parameters $4 \leq \text{Gz} \leq$
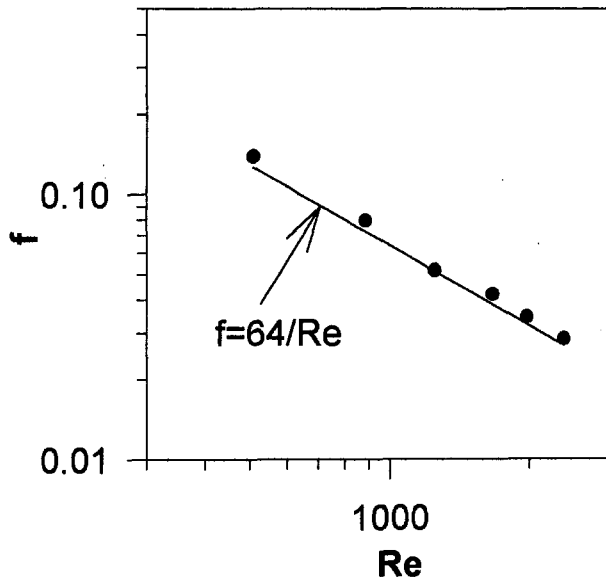
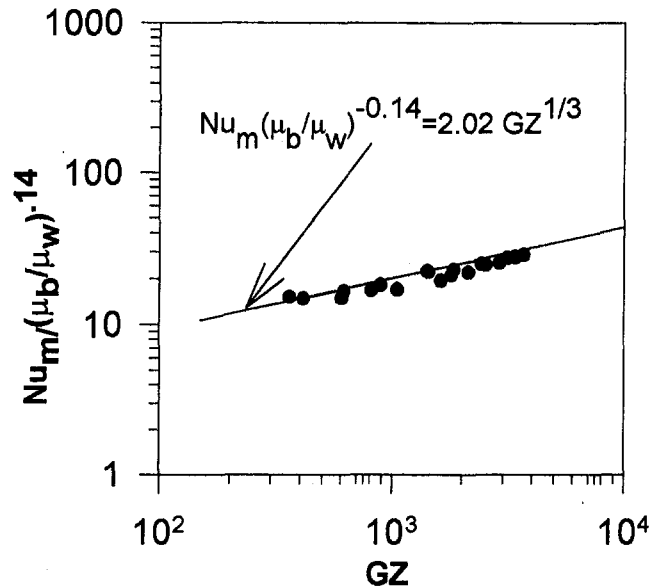Fig. 4 Friction factor data and correlation for the plain tube

10,000 and $0.0044 \leq (\mu_b/\mu_w) \leq 9.75$ and is based on the mean bulk temperature. The ranges of Reynolds number and Graetz number for the twisted-tape testing were from 230 to 2300 and from 300 to 4500, respectively.

Pressure Drop and Heat Transfer Results

The experimental study provided pressure drop and heat transfer data for 15 different twisted-tape arrangements. Three different wavelengths of H equal to 10, 7.5, and 5 cm were investigated. Data for five tape widths for every wavelength were collected.
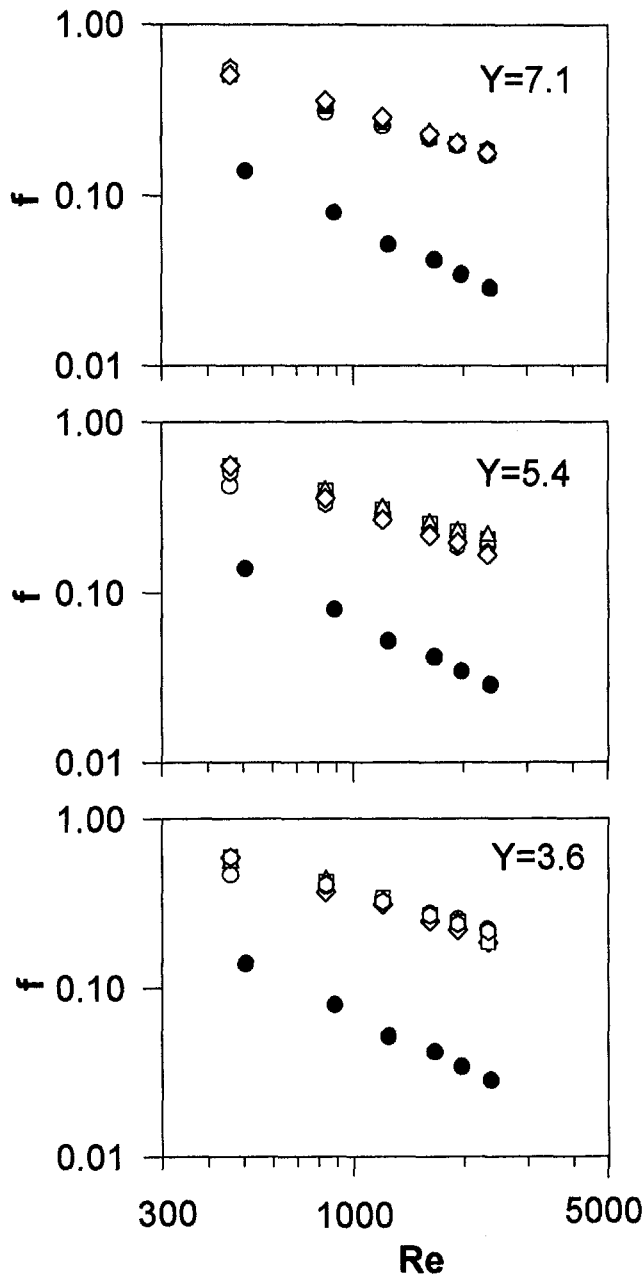
When a twisted tape is inserted inside a plain tube, it creates a swirl flow as a result, often referred to as swirling device. New flow characteristics will be created by introducing the twisted tape. Due to the helical rotating fluid flow, a centrifugal force is superimposed over the longitudinal flow, producing a secondary motion. The net effect of this change is the increase of pressure drop and heat transfer when a twisted tape is inserted into a plain tube. Figure 6 shows results for the friction factor versus Reynolds number. The friction factor for the twisted tape was three times larger at low range of Reynolds number and seven times larger for the high range of Reynolds number than that of the plain tube. No substantial effect of the tape width was noticed on the friction factor for the cases investigated in this work. In general, when the width of the twisted tape is decreased, the secondary motion will also decrease, resulting in a friction-factor values closer to the plain-tube data. For the cases investigated here, the decrease in the twisted-tape width was not enough to show a substantial decrease in pressure drop. Figure 6 shows a small decrease in friction factor for smaller tape width; however, no definite conclusion can be made since the change is within the uncertainty of the measurements.

Manglik and Bergles (1992a, b) have correlated friction factor and heat transfer data obtained with a swirl parameter that is similar to the Dean number for flow in curved tubes. The swirl parameter (Sw) describes the intensity of the secondary motion induced by the twisted tape, and is defined as

$$Sw = \frac{(\text{centrifugal force})(\text{convective inertia force})}{(\text{viscous force})^2} \qquad (9)$$

$$Sw = \frac{(\rho V^2/H)(\rho V^2/D_i)}{(\mu V/D_i^2)^2} = \frac{\text{Re}^2}{Y} \qquad (10)$$

Fig. 6 Comparison of friction factor data for twisted-tape and plain tube laminar flow

Legend for Fig. 6:
- ○ W=13.2
- ◻ W=12.6
- △ W=12.0
- ⬠ W=11.4
- ◇ W=10.8
- ● Smooth

Because the square of Reynolds number becomes very large in magnitude, the swirl parameter was redefined as

$$Sw = \frac{\mathrm{Re}_{Sw}}{\sqrt{Y}} = \frac{\mathrm{Re}}{\sqrt{Y}} \left[\pi/(\pi - 4\delta/D_i)\right]\left[1 + (\pi/2Y)^2\right]^{1/2} \quad (11)$$

where Re_{Sw} is based on the swirl velocity V_s and internal diameter of the tube D_i. The swirl parameter accounts for the tape thickness, its twist ratio, and the twisting velocity. The swirl velocity is defined as

$$V_s = V_a[1 + (\pi/2Y)^2]^{1/2} \quad (12)$$

where V_a is the axial velocity. It is defined as

$$V_a = \dot{m}/\rho A_c$$

A_c is the axial cross-sectional area:

$$A_c = [(\pi D_i^2/4) - \delta W]$$

The friction factor can be expressed in terms of swirl parameters as

$$f_{Sw} = \frac{\Delta p}{\rho V_s^2/2} (D_i/L_s) \quad (13)$$

where L_s is the maximum helical flow length and defined as

$$L_s = L[1 + (\pi/2Y)^2]^{1/2} \quad (14)$$

From these definitions

$$(f\,\mathrm{Re})_{Sw} = (f\,\mathrm{Re})[(\pi - 4\delta/D_i)/\pi][1 + (\pi/2Y)^2]^{-1} \quad (15)$$

Figure 7 shows that Eq. (15) predicts the data obtained for all 15 cases. The small fluctuation is due to the change in twisted-tape width because Eq. (15) is derived for tight-fit twisted tape where the width is essentially equal to the inside diameter.

The correlation proposed by Manglik and Bergles (1992a, b) predicts the experimental data within ±15 percent. The correlation, proposed for the friction factors for laminar swirl flow, is given by

$$(f\,\mathrm{Re})_{Sw} = 15.767[(\pi + 2 - 2\delta/D_i)/$$

$$(\pi - 4\delta/D_i)]^2[1 + 10^{-6}Sw^{2.55}]^{1/6} \quad (16)$$

Figure 8 presents the experimental data and the correlation given in Eq. (16).

For the cases investigated in this paper, the width of the tape has no definite effect on the friction factor. The result is favorable because the aim was to justify the use of loose-fit twisted-tape insert because of the ease in installing and cleaning.

As mentioned before, the heat transfer increases with a twisted tape for a variety of reasons. The blockage of the flow due to the presence of the twisted tape increases the flow velocity. The hydraulic diameter is reduced and tends to increase the heat transfer coefficient. The helical motion
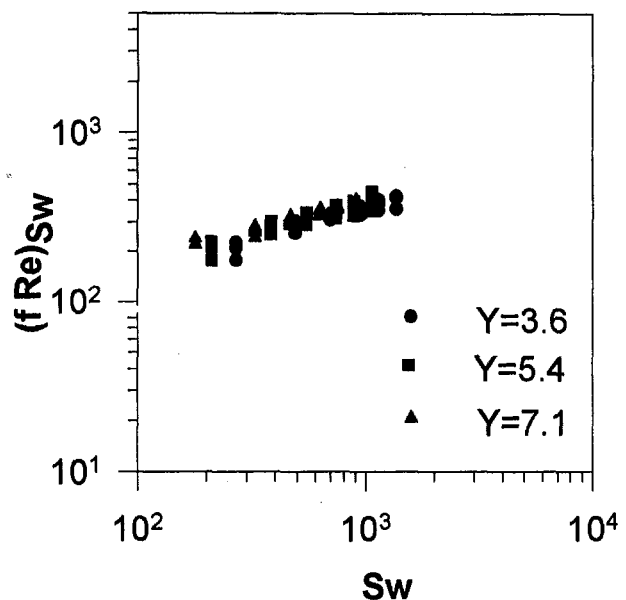

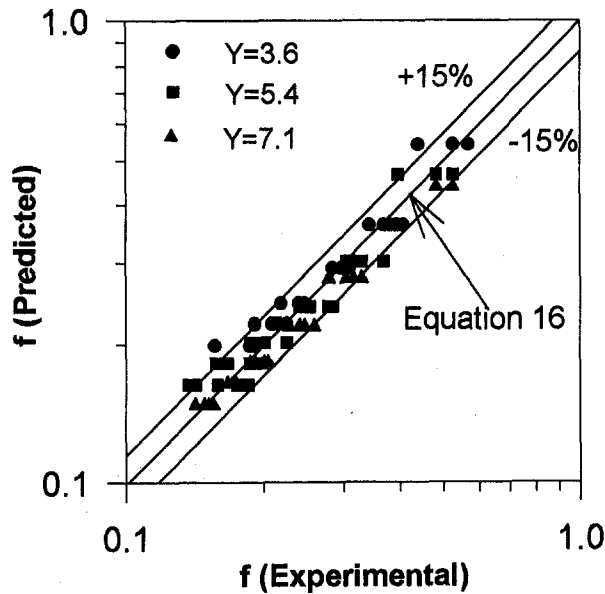**Fig. 7 Variation of friction factor with swirl parameter, Sw**

Fig. 8 Comparison of the experimental data and prediction for the friction factor
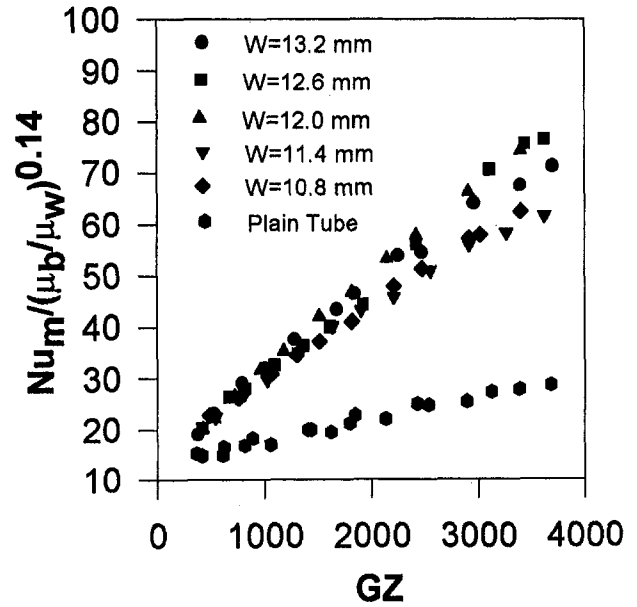

Fig. 10 Heat transfer data for different widths of the twisted tape for twist ratio of 5.4

of the fluid and the secondary flow induced by the presence of the twisted tape improves the mixing. If the width of the twisted tape is close to the inside diameter, the twisted tape will act as a fin and therefore aids in transfering heat. The Grashof number for the data collected here is smaller compared to the square of the swirl parameter. The effect of free convection is not important in this experiment and the dominant effect is the secondary motion caused by the swirl flow.

Figures 9, 10, and 11 present the heat transfer data for the twisted-tape inserts and with the plain tube. The same scale was used on all figures for ease in comparison. The heat transfer data were plotted as Graetz number versus $Nu_m(\mu_b/\mu_w)^{-0.14}$. The maximum heat transfer enhancement values for the twisted tapes are 3, 2.5, and 1.5 times for twist ratio of 3.6, 5.4, and 7.1, respectively.

Figure 9 presents the data for twist ratio of 3.6. The results were for five twist widths of W equal to 13.2 mm, 12.6 mm, 12.0 mm, 11.6 mm, and 10.8 mm. Also the plain tube results were plotted on the same figure for comparison. The figure shows that the heat transfer performance gradually decreases with decreasing tape width until W equals about 11.6 mm. The data for W equal to 10.8 mm are higher than those of 11.6 mm.

Figure 10 presents the data for twist ratio of 5.4. At the highest Graetz number, the heat transfer decreases for this case by almost 15 percent more than that obtained with Y = 3.6. For this case, the heat transfer data for W = 12.6 mm are higher than those of 13.2 mm; however, the data decrease up to W equal 11.6 mm. Again for this case, the
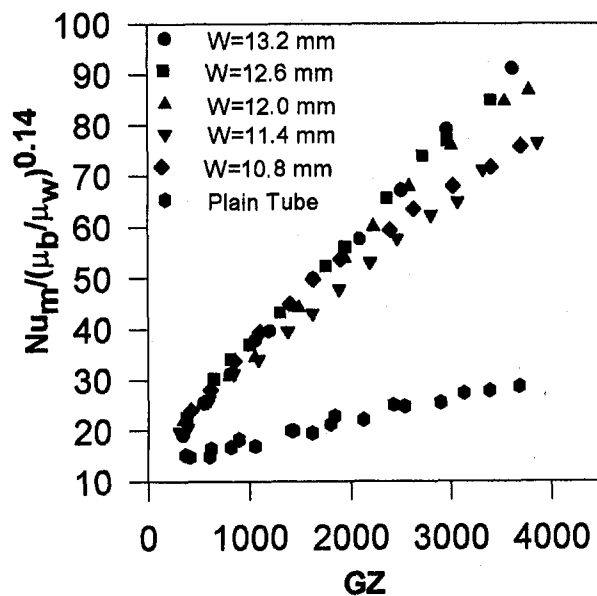

Fig. 9 Heat transfer data for different widths of the twisted tape for twist ratio of 3.6
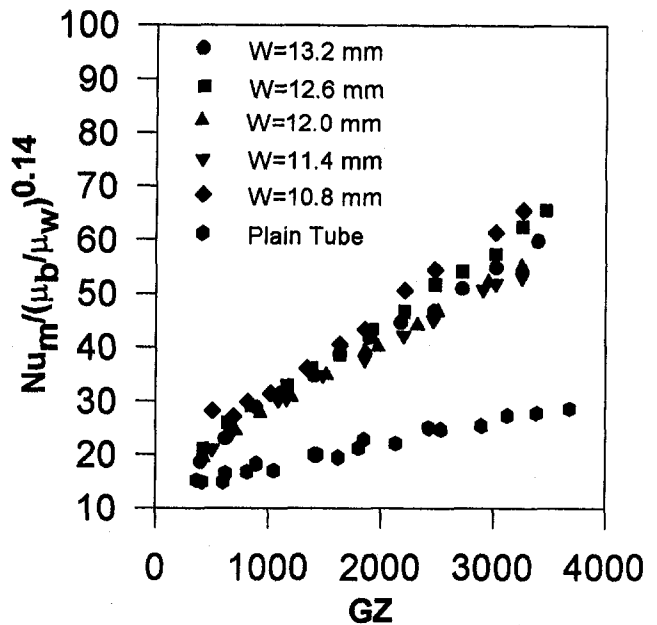

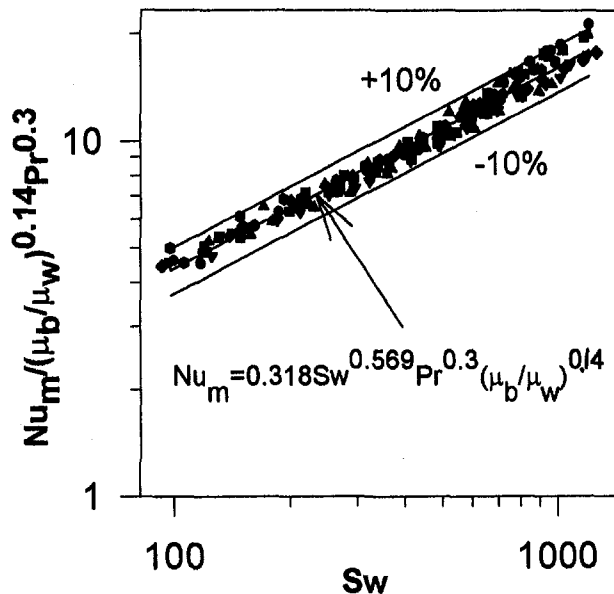**Fig. 11** Heat transfer data for different widths of the twisted tape for twist ratio of 7.1

Fig. 12 Correlation for laminar flow heat transfer in tubes with twisted-tape inserts

data for W equal to 10.8 mm are higher than those for 11.6 mm.

Figure 11 contains the data for a twist ratio of 7.1. This tape processes the smallest swirl component in the flow field. As expected, the heat transfer decreases by 28 percent from that obtained with Y equal to 3.6 at the highest value of Graetz number. For this case, the behavior of heat transfer with the width of the tape is similar to that obtained with Y equal to 5.4. The data for the case of 10.8 mm width are higher than all the others.

Two competing physical effects cause the heat transfer data to behave as shown in Figs. 9, 10, and 11. The swirl flow and helical motion inside the tube tend to increase the heat transfer. Also, when the width of the twisted tape decreases, some of the fluid is forced to flow between the tape and the tube that increases the velocity and also increases the heat transfer. For Y equal to 3.6, the swirl effect is dominant and heat transfer decreases with a decreasing the width of the tape. For the other two cases, however, the swirl effect is not as strong and the squeezed flow or the leakage effect becomes relatively important. The leakage effect for a width of 10.8 mm is more pronounced than that obtained with $W = 11.6$ mm. These results indicate that more experimental and numerical work are needed where both the twist ratio and the width of the twisted tape are design parameters in achieving an optimum heat-exchanger performance.

Since most of the uncertainties in the experiment are bias or systematic errors, the data can be compared with each other with a high degree of confidence.

The heat transfer data for all cases were correlated as suggested by Manglik and Bergles (1992a, b) to the swirl parameter Sw. The swirl parameter (Sw) describes the intensity of the tape-twist-induced secondary motion. The width of the tape is accounted for in the calculation of the swirl parameter. Figure 12 presents the experimental data and the correlation. The data are correlated by

$$Nu_m = 0.318 Sw^{0.569} Pr^{0.3} (\mu_b/\mu_w)^{0.14} \qquad (17)$$

within ± 10 percent, and the regression fit through the experimental data has a correlation coefficient of 0.99. The swirl parameter used here is defined in Eq. (11). Equation (17) gives

the correlation for laminar flow heat transfer in circular tube with twisted-tape insert of different tape widths.

Conclusion

The effect of the twisted-tape width on the heat transfer and friction-factor performance with laminar flow in circular tubes has been studied. Heat transfer and pressure drop measurements for twisted-tape ratios of 3.6, 5.4, and 7.1 were performed. Five different tape widths of W equal to 13.2 mm, 12.6 mm, 12.0 mm, 11.6 mm, and 10.8 mm for each twist ratio were investigated. The range of Reynolds number and Graetz number for the twisted-tape testing are from 230 to 2300 and from 300 to 4500, respectively.

A twisted tape causes the friction factor and heat transfer to increase by factors of 3 to 7 times and 1.5 to 3 times, respectively, compared to the plain-tube data. The magnitude depends upon the flow conditions and the twisted tape geometry. The data show that the width of the twisted tape has little effect on friction factor but more pronounced effect on heat transfer. For heat transfer, the effect of width is seen more in the high range of Reynolds number where the variation in the heat transfer to the change of width for the cases investigated in this work is about 20 percent. When the twisted-tape width decreases, the swirl effect becomes smaller but the leakage of high velocity flow between the tape and the wall of the tube becomes more intense, resulting in increase in heat transfer. Therefore, the idea that heat transfer always decreases with the decrease of the twisted-tape width is not always true. Because the effect of the width of the twisted tape is not seen for low Reynolds number flows, it is recommend to use loose-fit twisted tapes instead of tight-fit ones for low Reynolds number flows since it is easier to clean and install them.

Correlations for both friction factor and heat transfer data are available. Such correlations are based on the work of Manglik and Bergles (1992a, b). These correlations constitute good tools in the design of twisted tape insert heat exchangers.

References

ASME, 1986, *Measurement Uncertainty*, ANSI/ASME PTC 19.1-1985, Part 1.

Ayub, Z. H., and Al-Fahed, S. F., 1993, "The Effect of Gap Width Between Horizontal Tube and Twisted Tape on the Pressure Drop in Turbulent Water Flow," *Int. J. Heat Fluid Flow*, Vol. 14, pp. 64–67.

Bandyopadhyay, P. S., 1991, "Influence of Free Convection on Heat Transfer During Laminar Flow in Tubes With Twisted Tapes," *Experimental Thermal and Fluid Science*, Vol. 4, pp. 577–586.

Coleman, H. W., and Steele, W. G., 1989, *Experimental and Uncertainty Analysis for Engineers*, Wiley, New York.

Du Plessis, J. P., 1982, "Laminar Flow and Heat Transfer in a Smooth Tube With a Twisted Tape Insert," Ph.D Thesis, Dept. of Mechanical Engineering, University of Stellnbosch, South Africa.

Koch, R., 1958, "Druckverlust und Warmeubergang bei verwirbelter Stromung," *VDI-Forschungsheft 469*, Series B, Vol. 24, pp. 1–44.

Lopina, R. F., and Bergles, A. E., 1969, "Heat Transfer and Pressure Drop in Tape Generated Swirl Flow of Single-Phase Water," ASME JOURNAL OF HEAT TRANSFER, Vol. 91, pp. 434–442.

Manglik, R. M., and Bergles, A. E., 1987, "A Correlation for Laminar Flow Enhanced Heat Transfer in Uniform Wall Temperature Circular Tubes With Twisted-Tape Inserts," *Advances in Heat Transfer—1987*, ASME HTD-Vol. 68, pp. 19–25.

Manglik, R. M., Bergles, A. E., and Joshi, S. D., 1988, "Augmentation of Heat Transfer to Laminar Flow of Non-Newtonian Fluids in Uniformly Heated Tubes With Twisted-Tape Inserts," *Experimental Heat Transfer, Fluid Mechanics and Thermodynamics 1988*, R. K. Shaha et al., eds., Elsevier Science Publishing, New York, pp. 676–684.

Manglik, R. M., and Bergles, A. E., 1992a, "Heat Transfer Enhancement and Pressure Drop in Viscous Liquid Flows in Isothermal Tubes With Twisted-Tape Inserts," *Wärme- und Stoffübertragung*, Vol. 27, No. 3.

Manglik, R. M., and Bergles, A. E., 1992b, "Heat Transfer and Pressure Drop Correlation for Twisted-Tape Inserts in Isothermal Tubes: Part I—Laminar Flows," *Enhanced Heat Transfer*, ASME HTD-Vol. 68, pp. 89–98.

Monheit, M., 1987, "Experimental Evaluation of the Convection Characteristics of Tubes With Twisted Tape Inserts," *Advances in Enhanced Heat Transfer*, ASME HTD Vol. 68, 11–18.

Royds, R., 1921, *Heat Transmission by Radiation Conduction and Convection*, 1st ed., Constable and Co., London, UK, pp. 191–201.

G. L. Morrison

R. B. Winslow

H. D. Thames III

Turbomachinery Laboratory,
Texas A&M University,
College Station, TX 77843

Phase-Averaged Wall Shear Stress, Wall Pressure, and Near-Wall Velocity Field Measurements in a Whirling Annular Seal

The flow field inside a 50 percent eccentric whirling annular seal operating at a Reynolds number of 24,000 and a Taylor number of 6600 has been measured using a three-dimensional laser-Doppler anemometer system. Flush mount pressure and wall shear stress probes have been used to measure the stresses (normal and shear) along the length of the stator. The rotor was mounted eccentrically on the shaft so that the rotor orbit was circular and rotated at the same speed as the shaft (a whirl ratio of 1.0). This paper presents mean pressure, mean wall shear stress magnitude, and mean wall shear stress direction distributions along the length of the seal. Phase-averaged wall pressure and wall shear stress are presented along with phase-averaged mean velocity and turbulence kinetic energy distributions located 0.16c from the stator wall, where c is the seal clearance. The relationships between the velocity, turbulence, wall pressure, and wall shear stress are very complex and do not follow simple bulk flow predictions.

Introduction

Noncontacting seals for rotating components in turbomachines can only minimize leakage from high to low pressure regions; they cannot prevent it. This is inherently so due to the seal clearances between the rotating and stationary components that comprise them. Two such seals commonly used in turbomachines today are the labyrinth and annular seals.

Labyrinth seals can produce less leakage than annular seals for a given clearance and length, thereby providing higher efficiencies. However, the higher leakage rates in annular seals can be desirable, for they result in more damping and hence increased rotordynamic stability (Allaire et al., 1978). Annular seals are geometrically similar to plain journal bearings but present a different flow structure dominated by turbulence, fluid inertia effects, and large axial flows. In fact, there is great potential for them to be used as support elements in high-speed cryogenic turbopumps (Van Pragenau, 1990). Consequently, it is of great interest to learn more about these seals.

A simple annular seal consists of a smooth shaft rotating concentrically inside a stationary, smooth cylinder. Typically, however, annular seal applications are much more complex. For example, seal surface finishes may be hydraulically smooth but have high relative roughnesses compared to the small clearances present. Built-in misalignments and/or misalignments resulting from dynamic or static loading during operation can cause a shaft to rotate eccentrically inside its housing (Chen and Jackson, 1987). The destabilizing forces that cause the eccentricity can lead to a phenomenon called whirl in which the rotor center precesses around the center of the stator.

Due to these flow field complexities, the importance of having a solid understanding of both the fluid mechanics and rotordynamics of annular seals becomes apparent, especially since they

affect seal performance and, therefore, the efficiency and reliability of the turbomachinery in which they are installed. Much of the previous work on these seals has focused primarily on rotordynamic effects. In recent years Morrison et al. (1994) have performed measurements on the velocity field and turbulence characteristics in the clearance of a whirling annular seal. They completed an extensive three-dimensional laser-Doppler anemometer investigation of the flow field inside an annular seal with a whirl ratio of 1.00 and an eccentricity ratio of 0.50. They ran two Reynolds number conditions (12,000 and 24,000) with a Taylor number of 6600. Prominent features found include: a peak axial velocity that begins in the suction side of the seal at the inlet and rotates around to the pressure side of the seal at the exit; a vena contracta on the suction side of the rotor; a highly three-dimensional flow with large radial velocities near the inlet of the seal (made evident by recirculation zones at the inlet); and no significant increase in tangential velocity with whirling motion when compared to statically eccentric seals. In order to characterize these clearance flows further it is necessary to investigate the hydrodynamic wall pressures and shear stresses on the stator wall that surrounds the seal.

The purpose of this study is to determine mean and phase-averaged characteristics of both the pressure and shear stress along the stator wall of an annular seal experimentally using piezoresistive pressure transducers and hot-film anemometers respectively. These data will complement the existing flow field data of Thames (1992) and Morrison et al. (1994) while providing the boundary conditions necessary to develop more accurate Computational Fluid Dynamics (CFD) models and bulk flow models used for predicting annular seal flow fields. The further development of these models is necessary so they can be used to design new turbomachines with improved leakage characteristics based upon better understanding of rotordynamic stability.

Facilities

The experimental facility used for this investigation is comprised of a water storage and supply system, the seal rig test

Fig. 1 Seal test facility

Fig. 2 Pressure transducer mounting block

Fig. 3 Phase-averaged wall pressure measurement grid
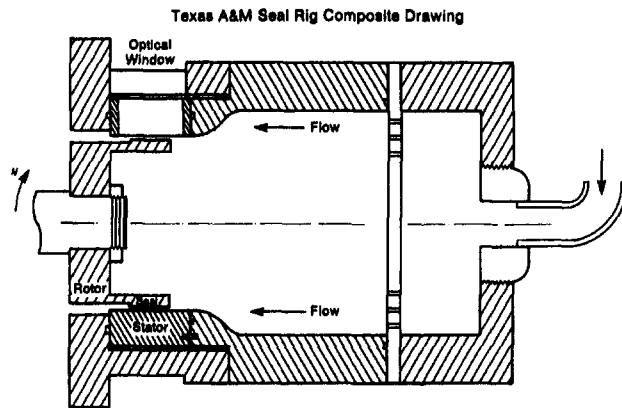
section for modeling the annular seal environment, and the piezoresistive pressure and hot-film anemometry instrumentation. These flow facilities have been previously described by Morrison et al. (1994).

Water is pumped to the test rig from a 10 m³ tank at a flow rate of 4.86 L/s and at a constant inlet pressure of 138 kPa resulting in an axial Reynolds number of 24,000. The flow rate and pressure are controlled by ball and gate valves both upstream and downstream of the rig. Flow rates are monitored by a turbine flow meter. A 70 kW rated heat exchanger connected to the supply pump bypass line provides cooling of the working fluid to maintain the operating temperature window of 30 ± 4°C. All water supplied to the test rig is filtered by a 10 μm filter bank near the discharge of the supply pump.

Figure 1 is a schematic of the seal rig that simulates the seal environment and where the pressure and shear stress measurements are made. The test section is a stainless steel design, which comprises two main parts. The first is the inlet where a stainless steel plate with 3.2 mm holes, and a fine nylon mesh are held. These pieces straighten and further filter the flow before it reaches the plenum in front of the seal. The second main part of the test section is where the stator and rotor are mounted. The rotor ($D = 0.163$ m) is mounted on an overhung shaft that is driven by an electric motor controlled by a variable frequency drive operated at 3600 rpm for this test case, resulting in a Taylor number of 6600. The clearance between the rotor and stator has a nominal value of 1.27 mm (0.050 in.) and the rotor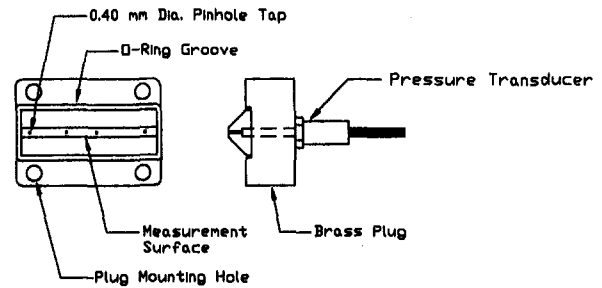 has a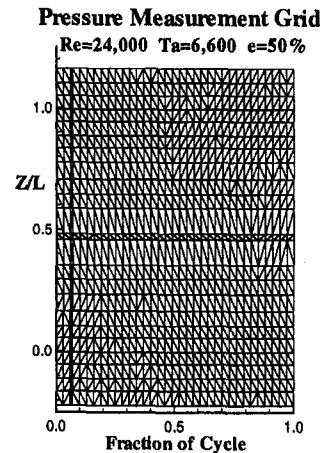 length of 35.6 mm. The seal is mounted on a brass bushing that has been machined to provide an eccentricity ratio of 50 percent. This results in the rotor whirling in a circular orbit at the same speed as the shaft rotation.

Brass instrument supports have been machined to fit into the optical window opening of the rig, which is normally used for laser-Doppler anemometer measurements. Four blocks were drilled and tapped to house the pressure transducers (Fig. 2), and four similar blocks were fabricated to hold the shear stress probes. These blocks provide several axial measurement locations from approximately six clearances upstream to five clearances downstream of the seal, resulting in axial distributions of the wall pressures and shear stresses. Figures 3–5 illustrate

Nomenclature

c = nominal clearance between rotor and stator = 1.27 mm
D = rotor diameter = 163 mm
e = rotor eccentricity ratio
L = rotor length = 35.6 mm
P = pressure
P^* = nondimensional pressure = $PL/c\Delta P$
P_{mean} = time-averaged pressure
P^*_{mean} = nondimensional mean pressure = $(P_{mean} - P_{Z/L=1.00})/\Delta P$
r = distance above centered rotor surface
Re = Reynolds number = $2\rho U_{mean} c/\mu$
T = wall shear stress

T^* = nondimensional stress = $Tc/\mu W_{sh}$
T^*_{mean} = time-averaged nondimensionalized shear stress = $T_{mean} c/\mu W_{sh}$
Ta = Taylor number = $(\rho W_{sh} c/\mu)(2c/D)^{1/2}$
U = mean axial velocity
U^* = nondimensional mean axial velocity = U/U_m
U_m = average mean axial velocity = $Q/\pi Dc$ = 7.4 m/s
uu = axial velocity variance
V = mean radial velocity
V^* = nondimensional mean radial velocity = V/U_m
vv = radial velocity variance
W = mean azimuthal velocity

W^* = nondimensional mean azimuthal velocity = W/W_{sh}
W_{sh} = rotor surface velocity = 30.9 m/s
ww = azimuthal velocity variance
Z = axial distance downstream of the seal entrance
ΔP = pressure drop from seal entrance to exit = 72.4 kPa
θ = shear stress direction, 0 deg = downstream direction, 90 deg = direction of rotor rotation
κ = turbulence kinetic energy = $(uu + vv + ww)/2$
κ^* = nondimensional turbulence kinetic energy = κ/U_m^2
μ = absolute viscosity = 7.84×10^{-4} kg/m-s
ρ = density = 999 kg/m³
$\langle\ \rangle$ = phase-averaged quantity

Shear Stress Measurement Grid
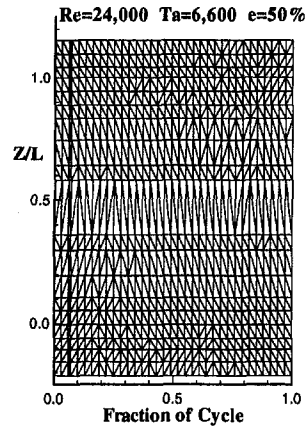
Re=24,000 Ta=6,600 e=50%

Fig. 4 Phase-averaged wall shear stress measurement grid

the measurement grids used for the pressure, shear stress, and velocity measurements. The block measurement surfaces were machined to fit flush with the stator wall so as not to disturb the flow.

Olivero-Bally et al. (1993) measured wall pressure fluctuations in turbulent boundary layers. They studied noise cancellation techniques and used pinhole-mounted transducers to improve the spatial resolution of the wall pressure data in the low and high-frequency range respectively. Pressure measurements were made in both air and water with piezoresistive transducers. In order to minimize spatial averaging effects, the transducers were mounted in plexiglass housings with 0.3-mm-dia flush-mounted pinholes. Their study indicated that by placing flush mount pressure transducers behind a small pinhole, the spatial resolution can be increased without degrading the frequency response characteristics over certain frequency ranges. This technique was used in the present study using mounting blocks as shown in Fig. 2. Kulite flush mount piezoresistive transducers were mounted in the blocks. The large cavity ended 1 mm from the block surface and a 0.40-mm-dia hole was drilled through. The assembly was mounted in the test section and the pressure transducers loosened in their mounts in order to purge any air from the cavity. This assured adequate frequency response (1 kHz) for the present study.

The mean pressures were measured with both a ScaniValve system and by recording the DC voltages from the Kulite transducers mounted in the brass blocks. Both gave the same results. The pressure transducers were calibrated each day in situ by connecting a pneumatic dead weight tester to the test section and pressurizing the test section with known pressures. The calibrations obtained were repeatable from day to day. Uncertainties on the pressure measurements are 1.5 kPa.

Hanratty and Campbell (1983) completed an extensive review of wall shear stress measurement techniques including the hot-film probe. According to the authors, the positioning of the probe relative to the wall is one of the greatest sources of error in using heated films. Pessoni (1974) found that the displacement of a commercial probe from the test section surface by 0.1 mm in a 2.5 cm air tunnel resulted in 30 to 40 percent deviations in the calibrations. Pessoni suggests either calibrating the probe in situ or in a plug of larger area and transferring the entire plug to the test section as was done in this study.

The hot-film probes used in this study (TSI 1237W) consist of a 3-mm-dia rod with the end cut off square. On this end the sensing element (a small rectangular film) is mounted. This rod is mounted in the brass blocks so that the end of the rod is flush with the block surface. The probes were calibrated in a facility consisting of two parallel smooth plates, which allows calibration of the probes while seated in the brass blocks. Pressure

taps on the back side of the calibrator are used to measure the axial pressure distribution, which verifies that dP/dX was constant indicating that the flow between the plates is fully developed. The mean shear stress on the wall is calculated in a channel of height h for a pressure drop ΔP along length L as follows (Haritonidis, 1989):

$$\overline{\tau_w} = \frac{\Delta P}{L}\frac{h}{2}$$

A Rapid Systems A/D converter possessing four channels, each with 8-bit resolution, was used to measure the AC component of the hot-film or pressure transducer signal at a sampling rate of 2000 samples/second with a low-pass filter of 1000 Hz. The external trigger was connected to an electronic proximitor probe situated at the keyway of the main seal/rotor shaft between the electric motor and the overhung shaft on which the seal is mounted. Thirty-two averages were necessary for the current study to obtain repeatable phase-averaged results. The DC value of the signal was measured using an analog voltmeter.

Determination of the shear stress was complex since the shear stress calibration was highly nonlinear. The fluctuating voltages could not be multiplied by a constant to obtain τ_w as they were for the pressure conversions. Rather, the instantaneous voltages were added to the mean voltages and then converted to the total instantaneous shear stress using the calibration curve. The mean shear stress was then calculated and subtracted from the total instantaneous shear stress to give the fluctuating shear stress component. Root-mean-squared (rms) values were calculated using these fluctuating values and an averaging scheme was also implemented to determine the phase-averaged shear stresses and phase-averaged rms values.

The flush mount hot-film probes used in this study had a rectangular sensing area, which made them sensitive to the direction of the shear stress much in the same way a single hot wire is sensitive to the velocity direction. To record the shear stress direction the probes were rotated, within specially designed probe mounts which kept them flush, to find a minimum in voltage. When the long side of the hot film is aligned with the mean shear stress vector, a minimum in heat transfer from the film occurs (Ludwieg, 1950). Hence, by slowly rotating the film in the flow, a minimum in voltage is noticeable. To isolate this direction with reasonable accuracy, the probe was rotated to an identical larger voltage on each side of the minimum voltage. The angles for these two voltages were then bisected to determine the minimum voltage angle. The probe was turned to this angle before the data acquisition was initiated. Uncertainties on the shear stress measurements are 10 percent on the magnitude and 5 deg on the direction.
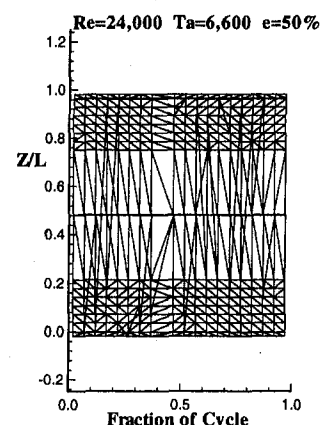
Flow Measurement Grid

Re=24,000 Ta=6,600 e=50%

Fig. 5 Phase-averaged velocity field measurement grid

Mean Pressure Profile
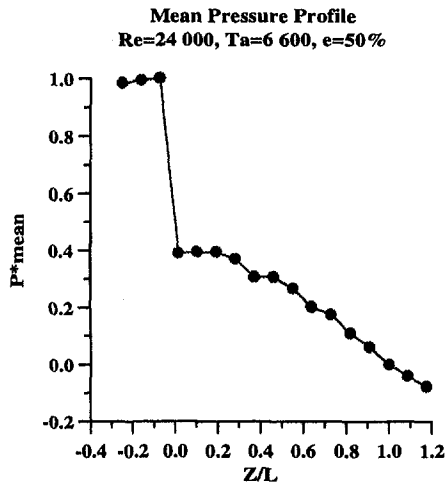**Re=24 000, Ta=6 600, e=50%**

Fig. 6 Mean pressure axial distribution

The flow field measurements presented in this paper were extracted from the data measured by Thames (1992) of which part was presented by Morrison et al. (1994). Descriptions of the laser anemometer system are included in those publications along with uncertainty estimates. Those uncertainties are ± 0.001 for $\langle \kappa^* \rangle$ and 0.015, 0.058, and 0.013 for $\langle U^* \rangle$, $\langle V^* \rangle$, and $\langle W^* \rangle$, respectively.

All of the data presented have been nondimensionalized. The mean pressures were nondimensionalized by the pressure drop from just at the seal entrance to the exit plane of the seal (72.4 kPa). This was selected based upon various seal performance data available, which nondimensionalize well using this parameter. The fluctuating pressures were nondimensionalized by $c \Delta P / L$. The shear stresses were nondimensionalized by $\mu W_{sh} / c$ (19 Pa) based upon the Stokes law of friction:

$$\tau = \mu \left[\frac{\partial U}{\partial y} + \frac{\partial V}{\partial x} \right]$$

where the velocity gradients are represented by W_{sh}/c. These nondimensionalization values also produce nondimensional fluctuating pressures and shear stresses with comparable amplitudes. The mean velocities and κ were nondimensionalized by using the bulk flow velocity, U_m (7.4 m/s) except for the azimuthal velocity, which was nondimensionalized by W_{sh} (30.9 m/s). Further information about the test facility, measurement procedure, and data availability on MS-DOS disks and hardcopy format are available from Thames (1992), Winslow (1994), and from G. L. Morrison.

Results

Figures 6 and 7 show the axial variation of the stator wall nondimensionalized mean pressure, shear stress magnitude, and shear stress direction. As the flow approaches the rotor, the wall pressure shows a slight rise in value (0.97 to 1.00) followed by a rapid decrease (0.35) at the seal inlet. This is followed by a slight increase (0.40) in pressure to $Z/L = 0.2$. This is due to a *vena contracta* effect, which produces a small recirculation zone on the rotor surface (Morrison et al., 1994). As the flow passes the vena contracta there is a pressure recovery, which is larger than the head loss associated with the wall friction resulting in a net pressure rise. Farther downstream the pressure decreases almost linearly to the seal exit due to frictional losses.

The mean wall shear stress is very small (8) just upstream of the seal and increases dramatically (28) as the flow enters the seal. The direction of the mean shear stress changes rapidly from around 115 deg (mostly tangential in the direction of rotor

rotation with a slight axial backflow) to 15 deg (predominantly downstream with a slight component in the direction of the rotor rotation) upon entering the seal. The increase in shear stress magnitude is due to the sudden tangential acceleration of the fluid caused by the rotor's presence and the even larger axial acceleration of the fluid as it enters the seal. The axial velocity increases substantially more than the tangential on the stator surface. This results in the shear stress direction becoming more axial just inside the seal. Fluid flow measurements have not been made more than $0.5c$ upstream of the seal inlet; not where θ was greater than 90 deg, hence, the exact reason for the backflow is not known. Morrison et al. (1994) showed that the axial velocity around the rotor was not uniform, having a very large value on the suction side of the seal and an almost stagnant region on the pressure side (Fig. 13). This stagnant region could actually set up a backward-flowing recirculation zone upstream of the seal where the fluid accelerating radially into the seal is blocked from entering the seal and is deflected by the stator in the upstream direction.

As the flow progresses through the seal, the axial and azimuthal velocities become relatively uniform around the seal perimeter through the central portion with a high concentration of flow on the pressure side of the seal near the exit. The magnitude of the mean shear stress decreases to around 25 through the central portion of the seal while the direction increases from 15 to 27 deg. The decrease in shear stress magnitude is due to the axial velocity slowing down after passing through the vena contracta and the flow becoming more evenly distributed around the seal. This reduces the mean velocity gradients at the wall resulting in decreased wall shear stress. The direction of the shear stress increases as the tangential velocity increases inside the seal (Fig. 14). Past $Z/L = 0.7$, the shear stress begins to increase due to further increases in the azimuthal velocity and the large axial velocities occurring on the pressure side of the seal.

The overall root mean square value of the pressure and shear stress fluctuations were measured along with the root mean square value of the phase-averaged pressure and shear stress fluctuations (Fig. 8). The value of both fluctuating pressures increased by a factor of 8 (from 2 to 16) upon entering the seal, decreased rapidly while passing through the vena contracta (16 to 10), decreased almost linearly from $Z/L = 0.2$ to 0.7 (10 to 3) to values approximately twice the value before entering the seal. They increased from 3 to 7 over the last portion of the seal. The ratio of the phase-averaged fluctuation magnitude divided by the overall fluctuation magnitude (coherence ratio) for both the pressure and shear stress is presented in Fig. 9. The pressure fluctuations increased from 65 percent coherent

Mean Shear Stress Profile
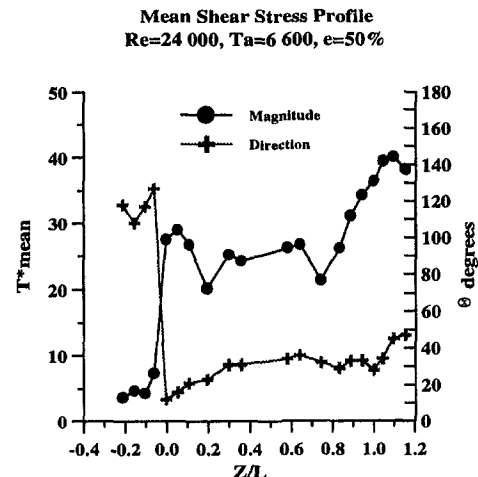**Re=24 000, Ta=6 600, e=50%**

Fig. 7 Mean shear stress magnitude and direction axial distributions
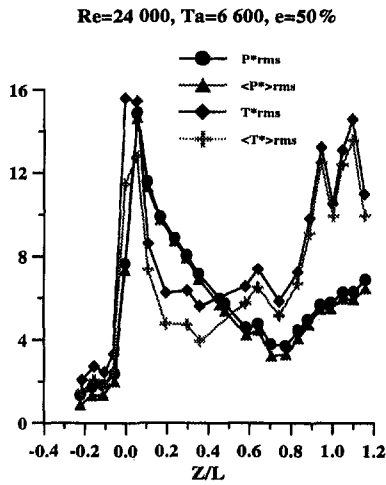
Fig. 8 Wall pressure and shear stress total and phase-averaged rms fluctuation level distributions

Fig. 10 Phase-averaged wall pressure distributions at seal inlet and exit

to over 90 percent coherent upon entering the seal and remained around 90 percent throughout the seal.

The shear stress fluctuations exhibited the same behavior as the pressure over the first 20 percent of the seal showing a dramatic increase through the entrance and into the vena contracta, decreasing rapidly to the minimum values inside the seal by $Z/L = 0.2$, increasing by 50 percent through the central portion of the seal, and increasing 100 percent as the flow approached the seal exit. At the seal exit there was a sudden decrease in the shear stress followed by a sudden increase once past the seal exit. The coherence began around 75 percent, increasing to 85 percent at the vena contracta, decreasing to 70 percent at $Z/L = 0.3$, then increasing to 90 percent at the seal exit.

The sudden increase in pressure and shear stress fluctuations at the seal inlet are due to the flow accelerating rapidly into the seal, negotiating through the vena contracta and reattaching to the wall. Also present here are the large azimuthal variations in the mean velocity components as discussed by Morrison et al. (1994). These flow phenomena result in the production of turbulence and associated pressure and shear stress fluctuations. Once inside the seal, the mean flow begins to distribute itself uniformly around the circumference of the seal, hence reducing the levels of pressure and shear stress fluctuations. Near the seal exit, the axial flow begins to increase on the pressure side of the seal (decrease on the suction side) resulting in a larger
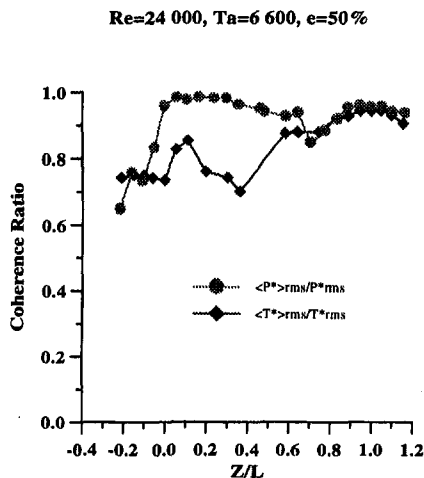
azimuthal variation of the mean flow. This results in increased pressure and shear stress fluctuations. Upon exiting the seal, the abrupt end to the seal causes the shear stresses to increase as the axial velocity decreases and the flow angle (and shear stress direction) increase. The pressure fluctuations also exhibit an increase at the exit but not as much as the shear stresses. The coherence is very large for both the pressure and shear stresses due to the large eccentricity of the seal. The entire flow field is dominated by the action of the rotor.

The phase-averaged pressure waveform present at $Z/L = -0.163, -0.004, 0.994,$ and 1.161 are presented in Fig. 10. These specific locations were extracted from Fig. 11 where the phase-averaged pressure azimuthal distribution is presented for the entire length of the seal for the purpose of providing more details of the inlet and exit areas of the seal. Fraction of a cycle represents one rotation of the rotor beginning at the maximum clearance location (0), followed by the "pressure side" of the seal (0–50 percent) where the clearance is decreasing, the minimum clearance (50 percent), and then the "suction side" of the seal (50–100 percent) where the clearance is increasing. Upstream of the seal, the pressure begins to show a cyclic behavior but with low amplitude (± 2). At the seal inlet, the pressure fluctuation amplitude ranges from -15 to 9. The highest pressure is located at 45 percent of the cycle, which is just before the minimum clearance on the pressure side of the seal. The phase-averaged pressure decreases rapidly across the minimum clearance to a low of -15 at 82 percent of the cycle. The whirling seal is building up a positive pressure on the converg-

Fig. 9 Wall pressure and shear stress coherence ratio axial distributions
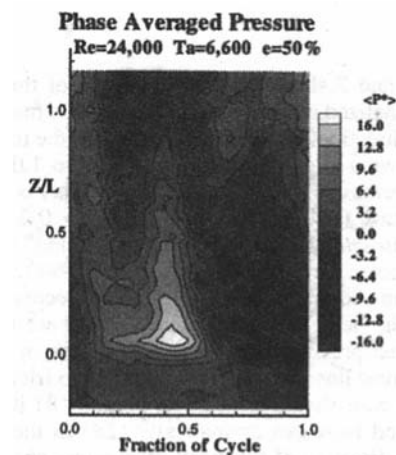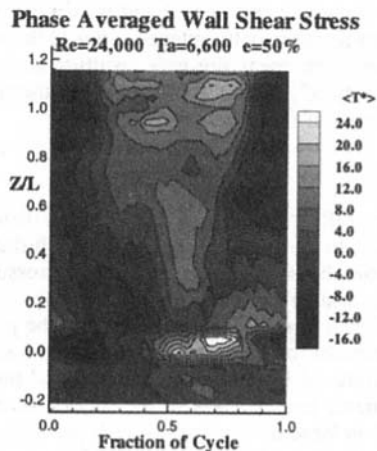

Fig. 11 Phase-averaged stator wall pressure

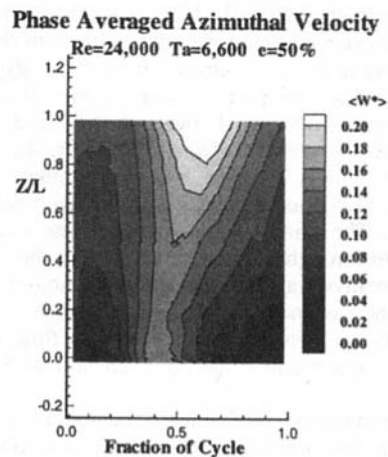Fig. 12 Phase-averaged stator wall shear stress

Fig. 14 Phase-averaged mean azimuthal (tangential) velocity distribution located 0.16c above the stator

ing side (pressure side) of the seal very rapidly as the flow enters the seal. Figure 11 shows that the phase-averaged pressure becomes more uniform in the $Z/L = 0.7$ region of the seal. However, the two pressure traces at the exit of the seal (which are very similar) show that the phase-averaged pressures have increased in value near the seal exit. The low pressure has shifted to the "pressure side" (0–50 percent of a cycle) of the seal with a double peak for the minimum pressure. The lowest (-12) occurs at 25 percent of the cycle and the other (-9) occurs at 50 percent. Another double peak occurs on the "suction side" of the seal where the pressure reaches an intermediate maximum of 6 at 73 percent of the cycle and the largest value (11) at 100 percent.

Figures 11–16 show contour plots of the phase-averaged wall pressure, wall shear stress, axial velocity, azimuthal velocity, radial velocity, and turbulence kinetic energy (κ) over one cycle (rotation) of the seal along its entire length. The measurement grids for these data have been presented in Figs. 3–5. The velocity components and κ were measured $0.16c$ above the stator by Thames (1992) using a three-dimensional laser-Doppler anemometer system described by Morrison et al. (1994) and Thames (1992). The phase-averaged wall pressure has relatively low amplitudes upstream of the seal. Upon entering the seal, the phase-averaged wall pressure increases in amplitude dramatically as shown previously in Fig. 10. The highest value (16) occurs from 30 to 50 percent of the cycle on the pressure side of the seal and decreases to the minimum value (-16) from 70 to 100 percent of a cycle on the suction side. The locations of the maximum and minimum pressures remain the
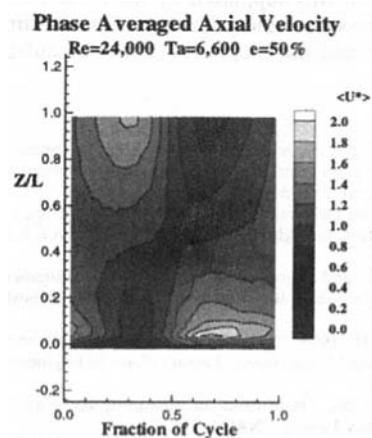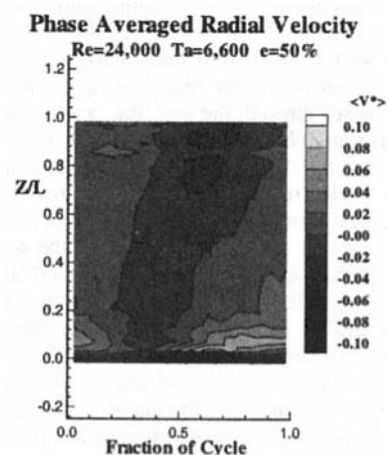

Fig. 15 Phase-averaged mean radial velocity distribution located 0.16c above the stator
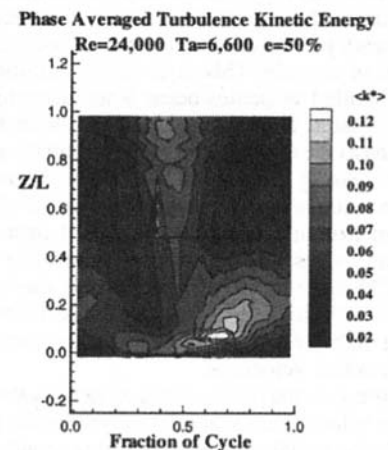
Fig. 16 Phase-averaged turbulence kinetic energy distribution measured 0.16c above the stator

Fig. 13 Phase-averaged mean axial velocity located 0.16c above the stator

same over the first half of the seal length with the magnitudes decreasing from 16 to 6 by $Z/L = 0.5$. As the flow continues through the seal, the amplitude of the phase-averaged wall pressure decreases, becoming more uniform around the seal with the pressure and suction regions switching near the seal exit.

The phase-averaged wall shear stress is shifted approximately $\frac{1}{4}$ of a cycle from the wall pressures with the maximum (24) occurring at the seal entrance from 50 to 80 percent of a cycle and the minimum (-12) occurring from 0 to 30 percent. The positive value is located between the high and low-pressure locations with the pressure decreasing in the direction of the rotor motion. This is a region of low azimuthal velocity with large azimuthal and axial gradients in the axial velocity (Figs. 13 and 14). The phase-averaged wall shear stress becomes more uniform through the central portion of the seal with the maximum positive value of 10 and a minimum of -6. The amplitudes increase near the seal exit to values as large as at the inlet with the minimum shear stress shifting to 0 percent cycle and the maximum centering itself around 50 percent of the cycle.

The phase-averaged axial velocity contours are presented in Fig. 13. Bulk flow models predict maximum axial velocity at the location of maximum clearance (0 percent of a cycle). However, for this flow field, the axial velocity has a magnitude of twice the bulk flow velocity and is located at 60–70 percent of a cycle in a region where the phase-averaged pressures are transitioning from maximum to minimum and have a value near zero. The minimum axial velocity in the inlet is on the "pressure side" of the seal from 30–40 percent of a cycle in a high-pressure region but not at the maximum pressure location. As the flow progresses through the seal, the axial velocity becomes almost uniform at $Z/L = 0.5$. However, the axial flow begins to maximize on the "pressure side" of the seal around 30 percent of a cycle, reaching a maximum for this azimuthal region at the seal exit. Likewise, a region of minimum axial velocity is located on the "suction side" of the seal. An explanation for this behavior is the flow will preferentially accelerate toward the largest clearance as happens both for a statically eccentric seal and for the minimum pressure. However, for this whirling case, the large minimum pressure is located on the suction side near the minimum clearance. This low pressure causes the flow to deviate from the maximum clearance location but not entirely into the low pressure region. This is due to the small clearance present at the minimum pressure location not being able to accept all of the fluid. Thus the bulk of the leakage occurs between the two locations.

Phase-averaged azimuthal velocities (Fig. 14) exhibit different behavior from the axial velocities. The minimum at the seal entrance occurs at the maximum clearance (0 percent) and the maximum occurs just before the minimum clearance passes by at 40 percent of a cycle. This does follow intuition since the minimum azimuthal velocities occur when the rotor is farthest away from the stator. There is a slight migration of the minimum value locations as the flow progresses downstream accompanied by an ever increasing average value in $\langle W^* \rangle$. At the exit plane, the minimum value is located around 15 percent of a cycle and the maximum azimuthal velocity is located near 60 percent. The maximum values of $\langle W^* \rangle$ tend to follow the locations of minimum $\langle U^* \rangle$ throughout the seal. This is due to the lower values of $\langle U^* \rangle$ resulting in longer residence times within the seal allowing the rotor-induced tangential shear stresses to cause increased azimuthal velocities.

Figure 15 presents the phase-averaged radial velocities. Other than the large values at the seal inlet caused by the flow rushing into the seal, the radial velocities are very small. The phase-averaged turbulence kinetic energy, $\langle \kappa^* \rangle$, in Fig. 16 is maximized at the seal inlet where the axial velocity is maximum, the azimuthal pressure variation is largest, and the vena contracta is present. This is due to the large velocity gradients resulting in lots of shearing effects generating vorticity and turbulence. The levels drop rapidly once the flow passes over the vena contracta and both the axial and azimuthal velocity gradients begin to decrease. $\langle \kappa^* \rangle$ becomes relatively uniform at the center of the seal. By the exit of the seal $\langle \kappa^* \rangle$ has reached a minimum cen-

tered around 0 percent and has a local maximum at 40 percent of a cycle. This increase in turbulence is due to the axial velocity re-establishing peaks near the exit resulting in local velocity gradients. In fact $\langle \kappa^* \rangle$ is maximized between the minimum and maximum values of $\langle U^* \rangle$ at the exit plane.

Conclusions

The stator wall pressure and shear stress distributions are directly linked to the mean flow field and turbulence levels observed $0.16c$ above the stator. The mean pressure decreases rapidly at the seal inlet as the flow accelerates into the small channel. The rush of fluid into the seal from the plenum causes a vena contracta to form immediately inside the seal inlet. The turbulence produced by the vena contracta and the large mean velocity gradients associated with the sudden acceleration into the seal result in large levels of stator wall pressure, shear stress, and flow fluctuations. The coherence levels are very large (80–90 percent) for the pressure and shear stress fluctuations due to the rotor's whirl dominating the development of the flow field. Contour plots of the phase-averaged flow field show that at the seal inlet the pressure is high on the pressure side of the seal and low on the suction side with the shear stress being approximately 90 deg out of phase. As the flow progresses through the seal, the levels of pressure and shear stress fluctuations decrease due to the turbulence levels in the seal decreasing, and the axial and tangential mean velocities becoming more uniform around the seal circumference resulting in smaller velocity gradients. The direction of the mean shear stress steadily increases from 15 deg at the seal inlet to 35 deg at the seal exit with a sudden increase to 45 deg once outside the seal. These steady increases are due to the azimuthal velocity continually increasing as the flow progresses through the seal and the sudden decrease in axial velocity as the flow exits the seal into a larger clearance area. At the seal exit the axial velocity has become largest on the pressure side of the seal as compared to the suction side at the seal inlet. This results in the phase-averaged pressure actually becoming negative on the pressure side and positive on the suction side at the seal exit. It is the axial locations of maximum azimuthal variation in $\langle U^* \rangle$, which corresponds to the areas of maximum $\langle P^* \rangle$ and $\langle T^* \rangle$ variation. Overall, the flow field is very complex with significant interplay between the mean velocity, turbulence, wall pressure, and wall shear stress. A simple assumption of no azimuthal variance of pressure or shear stress is shown to be invalid as is the assumption that the axial velocity will be maximum at the maximum clearance location. This makes the modeling of the flow field inside whirling annular seals a very difficult task.

Acknowledgments

References

Allaire, P. E., Lee, C. C., and Gunter, E. J., 1978, "Dynamics of Short Eccentric Plain Seals With High Axial Reynolds Numbers," *Journal of Spacecraft and Rockets*, Vol. 15, pp. 341–347.

Chen, W. C., and Jackson, E. D., 1987, "A General Theory for Eccentric and Misalignment Effects in High-Pressure Annular Seals," *ASLE Transactions*, Vol. 30, pp. 293–301.

Hanratty, T. J., and Campbell, J. A., 1983, "Measurement of Wall Shear Stress," *Fluid Mechanics Measurements*, Hemisphere Publishing Corporation, pp. 559–611.

Haritonidis, J. H., 1989, "The Measurement of Wall Shear Stress," *Advances in Fluid Mechanics Measurements*, Lecture Notes in Engineering, Springer-Verlag, pp. 229–261.

Ludwieg, H., 1950, "Instrument for Measuring the Wall Shearing Stress of Turbulent Boundary Layers," NACA TM 1284.

Morrison, G. L., DeOtte, R. E., and Thames, H. D., 1994, "Experimental Study of the Flow Field Inside a Whirling Annular Seal," *STLE Tribology Transactions*, Vol. 37, pp. 425–429.

Olivero-Bally, P., Forestier, B. E., Focquenoy, E., and Olivero, P., 1993, "Wall-Pressure Fluctuations in Natural and Manipulated Turbulent Boundary Layers in Air and Water," *Flow Noise Modeling, Measurement, and Control,* ASME NCA Vol. 15/FED Vol. 168, pp. 63–74.

Pessoni, D. H., 1974, "An Experimental Investigation Into the Effects of Wall Heat Flux on the Turbulence Structure of Developing Boundary Layers at Moderately High Reynolds Numbers," Ph.D. Dissertation, Mechanical and Industrial Engineering Department, University of Illinois, Urbana.

Thames, H. D., 1992, "Mean Flow and Turbulence Characteristics in Whirling Annular Seals," Master's Thesis, Texas A&M University, College Station, TX, 77843.

Van Pragenau, G. L., 1990, "Damping Bearings for Turbomachinery," NASA TP 3092, Vol. II, *Advanced Earth-to-Orbit Propulsion Technology Conference,* Huntsville, AL, pp. 155–162.

Winslow, R. W., 1994, "Dynamic Pressure and Shear Stress Measurements on the Stator Wall of Whirling Annular Seals," Master of Science Thesis, Texas A&M University, College Station, TX 77843.

Benefits of Compressor Inlet Air Cooling for Gas Turbine Cogeneration Plants

M. De Lucia

C. Lanfranchi

Dipartimento di Energetica,
Università di Firenze,
Firenze, Italy

V. Boggio
CRIT S.r.l.,
Prato, Italy

Compressor inlet air cooling is an effective method for enhancing the performance of gas turbine plants. This paper presents a comparative analysis of different solutions for cooling the compressor inlet air for the LM6000 gas turbine in a cogeneration plant operated in base load. Absorption and evaporative cooling systems are considered and their performance and economic benefits compared for the dry low-NO$_x$ LM6000 version. Reference is made to two sites in Northern and Southern Italy, whose climatic data series for modeling the variations in ambient temperature during the single day were used to account for the effects of climate in the simulation. The results confirmed the advantages of inlet air cooling systems. In particular, evaporative cooling proved to be cost effective, though capable of supplying only moderate cooling, while absorption systems have a higher cost but are also more versatile and powerful in base-load operation. An integration of the two systems proved to be able to give both maximum performance enhancement and net economic benefit.

Introduction

Gas turbine performance is strongly dependent on environmental conditions, especially air temperature. For example, for heavy frame gas turbines, at a temperature of 35°C (95°F), power output decreases as much as 20 percent with respect to ISO conditions (15°C, or 59°F, and 60 percent relative humidity), while heat rate increases by approximately 5 percent, and all these figures are almost independent of machine rating (De Lucia et al., 1994). The same is also true for aeroderivative gas turbines like the GE LM6000, whose performance charts show great sensitivity to ambient conditions, with maximum power output for an inlet air temperature of about 10°C (50°F) (Casper, 1993). The dry low-NO$_x$ version shows similar but smoother behavior, with a nearly constant power output for inlet air temperatures less than 8°C (46°F), decreasing above this value (Fig. 1).

In summer months, when ambient temperature in temperate climates can differ widely from nominal condition values, adding an air cooling system at the compressor inlet can restore nominal air conditions. In this way power generation is increased and specific consumption reduced. Cooling system design must take into account actual environmental conditions for the plant site, mainly air temperature and relative humidity. Then, data series over a period of some years should be collected, in order to use models for climate condition simulation reliably (DeLucia et al., 1994). However, differences in gas turbine plant types and applications, e.g., simple or combined cycle, base or peak-load operation, and electric or thermal load following mode, can impose different air cooling solutions. Moreover, in evaluating and comparing different air cooling plant solutions and their pros and cons, one has to take into account the strong influence of the tariff system, which often prevents energy efficiency and economies from coinciding (Hill, 1992).

The choice of the most suitable cooling system, or combination of systems, will then be based on economic and technical considerations concerning the three main means of air cooling:

(1) evaporative cooling, (2) compression refrigeration systems with or without thermal energy storage (TES), and (3) absorption chillers.

Evaporative cooling is the least complicated and least expensive solution for cooling inlet air. However, its cooling power is limited by the wet bulb temperature, so that its performance can be severely reduced for high-humidity sites and periods. Therefore, for high temperatures, which are common in summer months, it cannot cool the inlet air back to nominal conditions, but can only provide moderate cooling, variable with ambient conditions. Kolp et al. (1995) discuss the performance of such a system, in both simple and combined cycles, including supercharging.

Compression refrigeration systems, with or without TES, are much less dependent on ambient conditions. They can cool inlet air to low temperatures (down to 4°C, or 39°F, if necessary), but are more expensive and, without TES, have the disadvantage that their efficiency decreases considerably with decreasing load. Moreover, they use electricity as a primary energy source, and this can be a drawback during peak hours, when electricity demand reaches its maximum. By using an ice-based TES system, the latter disadvantage can be partly overcome. The compression refrigeration unit will produce ice during low-cost off-peak electricity periods, while during the day, ice-cooled water will be used to reduce inlet air temperature (Ebeling et al., 1994, 1992). System complexity and equipment size appear to be a major drawback, especially if the plant has to be operated in base load.

Absorption chillers (DeLucia et al., 1994) have the advantage of using thermal energy instead of electricity. They are more expensive than compression cooling without TES, but they can adapt to variable load, virtually without efficiency decrease, and appear to be suitable for base load service. Their lowest temperature limit is 6–7°C (44–45°F), and therefore they cannot be used with an ice-based TES system. The two-stage absorber version is more efficient and requires less energy and cooling water than its single-stage counterpart.

Description of the Plant

The plant considered in this paper produces both electricity and steam in cogeneration for an industrial user, in base-load operation. This plant is an interesting example of integrated energy production. The realization of several such plants is
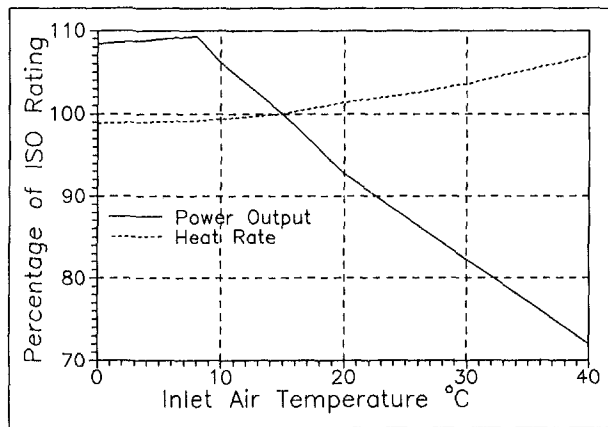
Fig. 1 Performance chart for GE LM6000 dry low-NO_x

scheduled in the next few years in Italy on various industrial sites, where there are industrial users capable of using the thermal energy produced. In the case of gas turbine combined plants, cogeneration operation for both electricity and heat production adds further constraints on heat production and enhances the gas turbine section with respect to the lower steam plant. These constraints can make the use of an inlet air cooling section for a cogeneration plant even more economical than for a normal combined cycle plant.

The plant layout is shown in Fig. 2. The topper is a GE LM6000 dry low-NO_x in combined cycle, which is equipped with a two-pressure level unfired HRSG, which produces steam at 40 bar (580 psia) and 8 bar (116 psia). The low-pressure steam is purchased by an industrial user, who needs it on a three eight-hour shift basis, i.e., round-the-clock operation (e.g., paper and pulp, food processing, or building materials sectors). Steam delivery to the industrial user is a priority and must be constantly guaranteed, i.e., the plant is operated in a thermal load following mode. The high-pressure steam expands in a turbine where two steam bleedings take place at 8 and 2.5 bar (36.3 psia), to integrate the low-pressure steam flow rate, in case the steam demand of the industrial user exceeds low-pressure boiler production. The condenser, at a pressure of 0.05 bar (0.73 psia) with cooling towers, is capable of condensing the whole steam production of the HRSG. For cogeneration plant simulation, the performance chart for inlet air temperature variation for the dry low-NO_x LM6000 gas turbine was used (Fig. 1).

Cooling Section Design

The installation of an inlet air cooling section was planned to enhance plant performance during summer months. The compression refrigeration option turned out to be hardly viable in the present application. Since the plant is designed for base-load operation, a compression refrigeration system, without TES, would consume electricity during the day, when it is most expensive, and its efficiency is strongly affected by part-load operating conditions. On the other hand, an ice-based TES for cooling inlet air back to 10°C, during the whole day in summer's hottest months, would require large equipment size, increasing plant complexity, and investment costs.

As for the absorption system, we considered both single- and two-stage configurations. Two-stage absorbers have a COP (coefficient of performance) of 1.2, almost double that of single-stage ones, typically 0.7 (ASHRAE, 1989). On the other hand, two-stage units use steam at 8 bar, whereas their single-stage equivalents need a larger steam flow rate, but at a lower pressure (2.5 bar). Since in both cases the steam is bled from the steam turbine, the cost of the electricity not produced must

be taken into account for a correct comparison. Considering condenser pressure level and an average steam turbine efficiency of 0.85, the electricity not produced is 58.3 kWh per GJ of cooling thermal load in the case of the two-stage absorber (61.5 kWh/MBtu), and 77.8 kWh per GJ of cooling thermal load in the single-stage one (82.0 kWh/MBtu). The latter's incremental electricity loss amounts to 32 percent. A further element of comparison is the cooling water required by the unit: The single-stage absorber utilizes a cooling water flow rate equal to one and a half times that of two-stage units of equal power.

As a result, the following solutions were considered:

- Case A—Two-stage absorption chiller.
- Case B—Single-stage absorption chiller.
- Case C—Evaporative cooling.

Subsequently, a further case (Case D) was also considered as an integrated solution with evaporative cooling and a two-stage absorption unit.

The single- and two-stage absorption units considered had a cooling power of 3300 kW (939 tons): enough to reduce the temperature of air flow rate at LM6000 compressor inlet from 25°C (77°F) (at 60 percent relative humidity) to 10°C. For higher air temperatures and similar humidity conditions, air cooling diminishes, because the amount of water condensing during cooling increases. So as to maintain plant load at a level not lower than 20 percent of design conditions, the absorber should work only when ambient air temperature is higher than 15°C. Total inlet pressure loss in all cases can be calculated, at a conservative estimate, as not exceeding a 25 mm (1 in.) waterhead.

Climate Effect Modeling

A crucial factor in the size and performance of an air cooling section is the climate of the chosen site. Climatic variations were simulated, using the model described by De Lucia et al. (1994), for the purpose of making a comparison between the three solutions. This model assumes that the temperature depends on solar radiation and imposes maximum temperature when solar radiation is at its highest, and vice versa. Thus the ambient temperature follows a sinusoidal curve between maximum and minimum measured temperature values. The amplitude of this curve depends also on the length of the period of light, the latitude of the site, and the meteorological day considered. The model was modified in order to take into account variations in nighttime temperature, which was assumed to be constant by De Lucia et al. (1994). A further modification was introduced with the aim of a more accurate simulation of
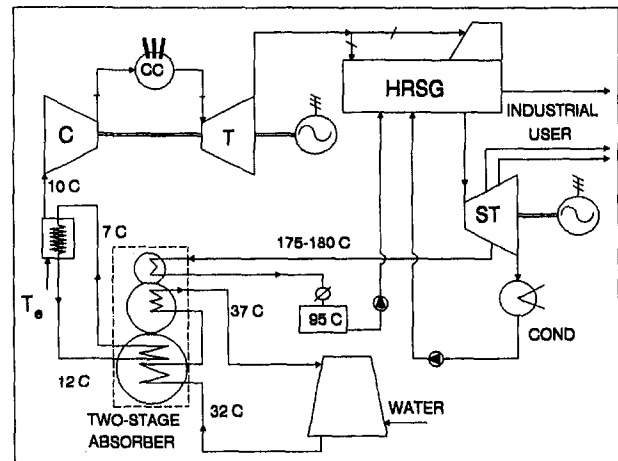

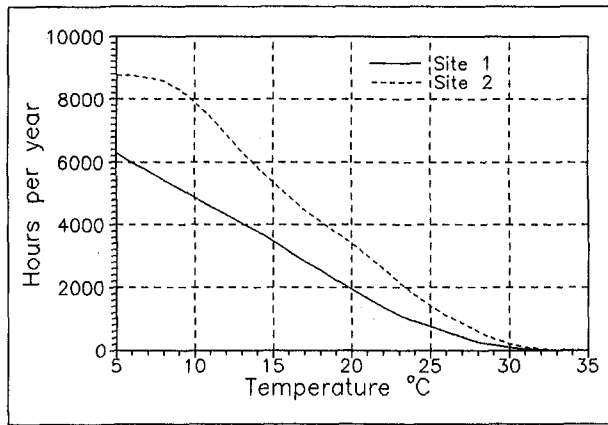**Fig. 2 Plant layout (two-stage absorber)**

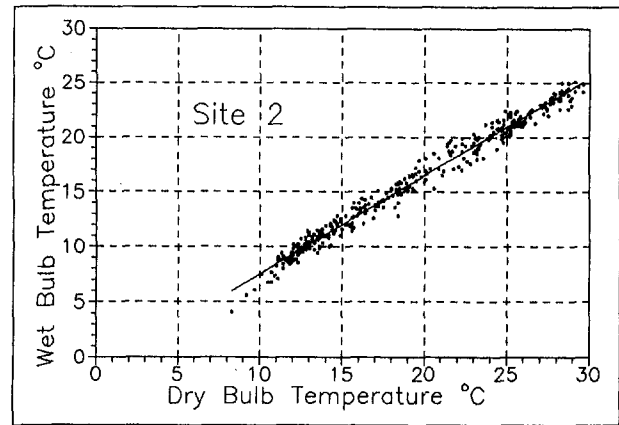Fig. 3 Cumulative annual hours for ambient temperature

Fig. 5 Wet and dry bulb temperature correlation (site 2)

daytime temperature variations, considering the time shift always present between ambient temperature and solar radiation. It was verified that by imposing the maximum temperature one hour later than maximum solar radiation, the measured values available could be fitted more correctly.

In order to evaluate climatic influence on plant performance, two sites were considered, which are representative of two different types of climate. At the first site considered (Site 1, Northern Italy, latitude 45°08′ N) the ambient temperature is higher than 15°C for approximately 3500 hours per year (40 percent of total working hours). Most of these hours are obviously in summer (96 percent of total summer hours) and spring (47 percent of total spring hours), while in fall and winter the air cooling system would only seldom be activated, if it operates for external temperatures higher than 15°C. The second site (Site 2, Southern Italy, latitude 38°13′ N) has a higher average temperature all over the year (ambient temperature > 15°C for 61 percent of total working hours). In these conditions an absorption unit would always be in operation in summer months, while in spring and fall the percentage would also remain considerably high (respectively, 66 and 62 percent). Figure 3 shows the cumulative annual hours in which the ambient temperature is higher than the value on the x axis. In comparison with site 1, we can see that site 2 ambient conditions appear more favorable for the installation of an air cooling system, which would be much more intensively exploited.

Wet bulb temperature evaluation is of the utmost importance for correct design of the evaporative cooling section, and is also a very important parameter for absorption systems. The wetter

the inlet air, the higher the amount of condensation in the cooling coils for the same final temperature. The result is an increase in thermal load on the chiller, without air temperature reduction, and with decrease in cooling section performance. In order to calculate wet bulb temperature, average daily wet and dry bulb temperature values were correlated. The graphs, reported in Figs. 4 and 5 for each site, show a marked linear distribution. Least-square linear relations obtained from the data shown are represented by continuous curves in the figures. These relations allowed correlation of average dry and wet bulb temperatures in our simulation. The method is admittedly approximate, since it supplies a deterministic value of wet bulb temperature for each dry bulb temperature, consequently neglecting statistical variations of wet bulb temperature. This is a compromise between the need for avoiding excessive complication of the model and correlation of the two values in such a way as to reflect the measured data. With the cumulative annual curves for both wet and dry bulb temperatures, it was possible to determine when and for how long the evaporative cooling coils can operate.

Simulation Results

The influence of ambient condition variations on plant performance was calculated on the basis of the analysis given above. Figure 6 shows the power output for three of the solutions considered (Cases A, B, and C) for site 2; the case of site 1 is similar, and there are no significant variations in performance. Evidently both absorption solutions are able to maintain nominal conditions for inlet air temperatures below 25°C, but, of the
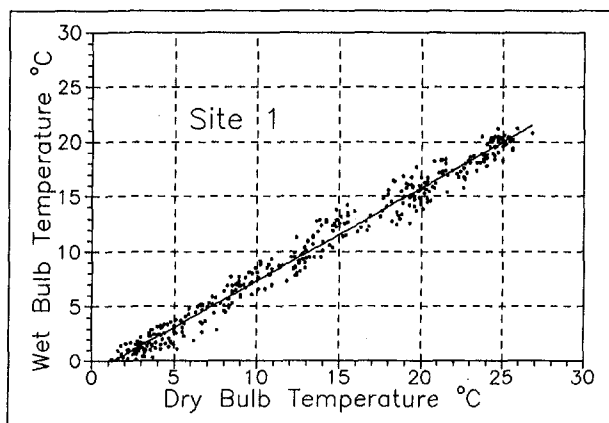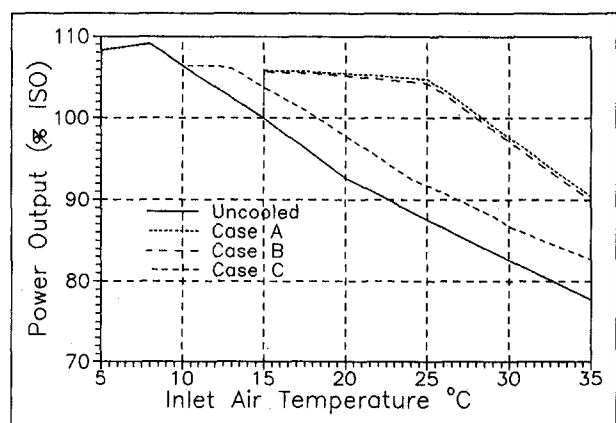

Fig. 4 Wet and dry bulb temperature correlation (site 1)
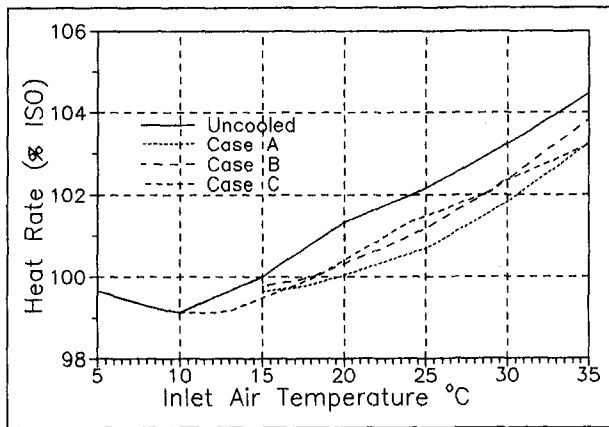

Fig. 6 Plant power output (percentage of ISO rating)

Fig. 7 Plant heat rate (percentage of ISO rating)

Fig. 9 Power output increase (site 2, percentage of uncooled case)

two, the single-stage unit, with higher accessory consumption, has a slightly lower performance. Figure 7 shows that the use of cooling reduces plant heat rate, which has comparable values for the three solutions.

Performance Evaluation.   Simulation was carried out on a yearly basis. Increases in power output are reported in Figs. 8 and 9 for sites 1 and 2, respectively, on a month by month basis, as a percentage of the uncooled case. It can be noted that the two-stage absorber (Case A) gives the maximum power increase in the warmest month (18 percent in July), whereas its single-stage counterpart (Case B) is only slightly less effective. Table 1 shows annual totals calculated from the previous data. While maximum power increase is of the same amount (17–18 percent) for both sites considered, annual total increase for site 2 is much higher than for site 1. In summer months on both sites absorption units work at full load, but ambient conditions on site 2 are more uniform and also give considerable gains in spring and fall. Ebeling et al. (1992) report a 21–25 percent increase in power output on a hot summer day. We also experienced similar high values, but they were limited to a few hours on the hottest days in summer. It should be underlined that results in Figs. 8 and 9 are monthly averages, which are more relevant in the case of a base-load application. Power increase benefits for evaporative cooling are approximately half those of absorption units, but are more evenly distributed over the whole year.

Integrated Solution.   Evaporative cooling proved to be useful for obtaining small temperature variations, while absorption units are more powerful and effective in inlet air cooling, but
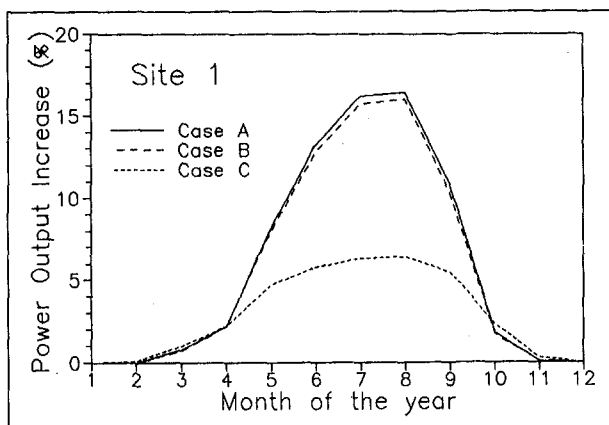
their use is possible only when ambient air temperature is higher than 15°C. Thus the two methods have complementary operating fields, and the integrated solution using both of them was studied. Evaporative cooling works at below 15°C, whereas the absorption chiller is used at higher temperatures and the evaporative unit is turned off. In this way it is also possible to cover the 10–15°C temperature field, which otherwise would remain unchilled, with a small additional investment. This integrated solution was considered in simulation as case D and supplied the data in Table 1. It can be noted that the power increases supplied by the integrated solution are better than those of the other three solutions. However, incremental benefits diminish, i.e., the benefits from the integrated solution are less than the sum of the benefits resulting from the two separate solutions.

Economic Results.   Annual economic benefits of each solution considered were calculated with respect to the uncooled case. The incremental cost of kWh and investment payback were calculated on the basis of sale of electricity at present Italian prices, which favor day over night production. From 6 a.m. to 10 p.m. the price for private utilities is 9.2 ¢/kWh, whereas at night, weekends, and in the vacation month of August the price sinks to 2.5 ¢/kWh. Natural gas cost is 12.8 ¢/Nm³ (8.1 ¢/lb). As for capital cost evaluation, for the evaporative cooling system an investment of $130,000 was estimated, $1,000,000 for the single-stage absorber, and $1,200,000 for the two-stage one. The cost analysis was based on a 15-year period and an interest rate of 10 percent. Variable O&M expenses were estimated at a rate of 0.4 ¢/kWh. The vacation month of August was not considered for the economic balance, since in Italy during this period electricity cost is very low. For the economic analysis an exchange rate of 1550 Italian Lire = $1 was assumed (costs referred to 1994).

Incremental kWh cost is the unit cost of electricity produced in excess of the uncooled plant, and is defined as the increase

Fig. 8 Power output increase (site 1, percentage of uncooled case)

Table 1 Energy simulation results (annual total)

% of uncooled	Site 1		Site 2	
	Δ Power	Δ Fuel	Δ Power	Δ Fuel
Case A	+5.4	+4.9	+9.0	+8.2
Case B	+5.2	+4.9	+8.7	+8.2
Case C	+2.7	+2.3	+3.8	+3.2
Case D	+5.7	+5.2	+9.7	+8.8

Table 2 Annual economic results (site 1)

Site 1	Net Benefit [$/Year]	Incremental kWh Cost [¢/kWh]	Simple Payback [Years]
Case A	358,000	4.1	2.3
Case B	356,000	4.2	2.1
Case C	251,000	3.1	0.5
Case D	377,000	4.1	2.4

Table 4 Economic results (only daytime)

	Site 1		Site 2	
	Net Benefit [$/Year]	Simple Payback [Years]	Net Benefit [$/Year]	Simple Payback [Years]
Case A	400,000	2.1	732,000	1.3
Case B	402,000	1.9	720,000	1.2
Case D	422,000	2.2	780,000	1.4

in total annual cost due to the installation of air cooling section, divided by the surplus in electricity production. The actual year-averaged cost of kWh for the uncooled plant can be estimated at 4.5 ¢/kWh.

Tables 2 and 3 report the net annual benefit, the incremental kWh cost, and simple payback for the four solutions considered for sites 1 and 2. The net benefit reported in the tables is electric savings minus O&M, incremental fuel expenses, and annual capital cost, and is then the annual equivalent of the NPV (net present value) of the investment. Note that incremental kWh costs for the four solutions considered are lower than the value for uncooled plant. Evaporative cooling (case C) is an extremely cost-effective solution, and payback is less than one year, even for a continental climate and cold sites (site 1). Its installation is advisable for all gas turbine plants, if great electricity increases are not required. Both the single- and two-stage systems have a payback of circa 2 years, and their power gain is approximately double that of evaporative cooling. It must be added that payback-oriented analysis can be misleading, since it gives priority to short-term investment. Since we are dealing with paybacks considerably smaller than the lifespan of the components (from 15 to 20 years), the greater yearly saving of the absorption unit leads, in the long run, to higher benefits than those of evaporative cooling. We chose to report our data in terms of simple payback instead of IRR, since use of the former is more widespread, though it is less accurate. The integrated solution (case D), which proved to be the most effective from the power increase standpoint, is also more economical, since it guarantees payback and incremental kWh costs, which are similar to the solution using absorbers, but it has a 6 percent net benefit over the two-stage (case A) and 9 percent over single-stage absorbers (case B).

Incremental cost per installed kW is similar for cases A, B, and D with absorbers, and is approximately $280 per installed kW, while for evaporative cooling (case C) it equals $240 per installed kW. These costs refer to actual annual power increase, calculated by using the curves in Figs. 8 and 9.

The extremely low cost of electricity in Italy during the night and on weekends suggested that we also consider the case in which absorbers are turned off during the night, even in cases

where the temperature is higher than 15°C. Economic results are given for the three cases with absorbers (A, B, and D) in Table 4. All three cases, though not saving all possible electricity, turned out to be more economical than the earlier cases of continuous operation. This happens because the Italian tariff system favors daytime production, and at night the cost of producing electricity is higher than the benefit derived from selling it.

In countries where August can also be considered in the economic balance, the net benefit of cooling, as compared with the Italian situation, increases by 18 percent for site 2 and by 26 percent for site 1, with respect to the cases reported above.

Moreover, savings with inlet air cooling improve, if the gas turbine plant is operated in an electric load following mode, i.e., matching the electricity demand curve, because generally the average electricity purchase price is higher than sale price. In this case net benefits are expected to be even higher than those found here.

Conclusions

The simulation results lead to the following conclusions:

- Evaporative cooling is able to supply valid power increases (2–4 percent on a yearly basis) with rather low investment.
- Absorption cooling can enhance power production by 5–10 percent on a yearly basis, depending on site climate, and up to 18 percent in the warmest months. These benefits are double those supplied by evaporative cooling, and absorption cooling depends much less on humidity conditions. However, investments are higher and plants more complicated. This solution is advisable for base-load production plants.
- The air cooling section with two-stage absorber is more effective than a single-stage one, from the point of view of power increase. Besides, the single-stage unit, which requires about 50 percent more cooling water, has higher running costs.
- The integrated absorber plus evaporative cooling solution assures highest plant performance and yearly net benefit increase.
- In Italy the best solution is to use air cooling plants only during daytime. This is due to the extremely low cost of electricity during nighttime and on weekends.

References

ASHRAE, 1989, *Fundamentals Handbook*, Atlanta, GA.

Table 3 Annual economic results (site 2)

Site 2	Net Benefit [$/Year]	Incremental kWh Cost [¢/kWh]	Simple Payback [Years]
Case A	651,000	3.7	1.5
Case B	631,000	3.8	1.3
Case C	346,000	3.1	0.4
Case D	691,000	3.7	1.5

Casper, R. L., 1993, "Application of the LM6000 for Power Generation and Cogeneration," ASME Paper No. 93-GT-278.

De Lucia, M., Bronconi, R., and Carnevale, E., 1994, "Performance and Economic Enhancement of Cogeneration Gas Turbines Through Compressor Inlet Air Cooling," ASME JOURNAL OF ENGINEERING FOR GAS TURBINES AND POWER, Vol. 116, pp. 360–365.

Ebeling, J., Halil, R., Bantam, D., Bakenhus, B., Schreiber, H., and Wendland, R., 1992, "Peaking Gas Turbine Capacity Enhancement Using Ice Storage for Compressor Inlet Air Cooling," ASME Paper No. 92-GT-265.

Ebeling, J., Balsbaugh, R., Blanchard, S., and Beaty, L., 1994, "Thermal Energy Storage and Inlet Air Cooling for Combined Cycle," ASME Paper No. 94-GT-310.

Hill, J. P., 1992, "Assessing the Economics of Industrial Gas Turbines Cogeneration Applications," ASME Paper No. 92-GT-333.

Kolp, D. A., Flye, W. M., and Guidotti, H. A., 1995, "Advantages of Air Conditioning and Supercharging an LM6000 Gas Turbine Inlet," ASME JOURNAL OF ENGINEERING FOR GAS TURBINES AND POWER, Vol. 117, pp. 513–527.

Biomass Externally Fired Gas Turbine Cogeneration

L. Eidensten

J. Yan

G. Svedberg

Department of Chemical Engineering
and Technology/Energy Processes,
Royal Institute of Technology,
Stockholm, Sweden

This paper is a presentation of a systematic study on externally fired gas turbine cogeneration fueled by biomass. The gas turbine is coupled in series with a biomass combustion furnace in which the gas turbine exhaust is used to support combustion. Three cogeneration systems have been simulated. They are systems without a gas turbine, with a non-top-fired gas turbine, and a top-fired gas turbine. For all systems, three types of combustion equipment have been selected: circulating fluidized bed (CFB) boiler, grate fired steam boiler, and grate fired hot water boiler. The sizes of biomass furnaces have been chosen as 20 MW and 100 MW fuel inputs. The total efficiencies based on electricity plus process heat, electrical efficiencies, and the power-to-heat ratios for various alternatives have been calculated. For each of the cogeneration systems, part-load performance with varying biomass fuel input is presented. Systems with CFB boilers have a higher total efficiency and electrical efficiency than other systems when a top-fired gas turbine is added. However, the systems with grate fired steam boilers allow higher combustion temperature in the furnace than CFB boilers do. Therefore, a top combustor may not be needed when high temperature is already available. Only one low-grade fuel system is then needed and the gas turbine can operate with a very clean working medium.

Introduction

There are two reasons for increasing biomass utilization. One is that fossil fuels are limited resources while biomass represents a renewable energy source, which can make a significant contribution to long-term energy stability. This is especially true in Sweden. Another reason based on environmental considerations is that the utilization of biomass as a substitute for fossil fuel has desirable effects on reducing carbon dioxide emissions contributing to global warming.

Biomass has a reasonable heat of combustion and is usually low in sulfur, nitrogen, and ash. However, biomass is a solid fuel with energy content lower than fossil fuels, both on a per weight basis and especially on a per volume basis.

A major challenge to the use of biomass for energy purpose is to identify conversion technologies for providing power and heat with high efficiency, low cost, and low environmental pollution. Power generation and cogeneration systems involving a gas turbine are among the more promising technologies today. Solid biomass may be used to fuel gas turbines by direct firing, indirect firing, or via gasification. In the gas turbine with biomass gasification, the biomass must first be converted to clean fuel gas, then burned in a gas turbine. This requires development of high-temperature gas cleanup steps to remove particulates, turbine-damaging metals, and NO_x from the gasifier. Direct firing of gas turbines with biomass is constrained by the corrosive and erosive nature of the combustion products. There is not yet a gas turbine capable of withstanding these factors. The externally fired or indirectly fired gas turbine, however, closely resembles the conventional gas turbine. In contrast to the directly fired cycle, the externally fired has high fuel flexibility and can accept fuels of approximately the same quality acceptable in conventional steam turbine plants. Compared with a gas turbine with gasification, the externally fired gas turbine does not need the high-temperature cleanup system and the biomass gasifier. The externally fired gas turbine can accommodate a wide variety of conventional and advanced combustors cur-

rently available commercially or under development, such as fluidized-bed combustion chambers and grate fired furnaces.

Concept of Externally Fired Gas Turbine Cogeneration

Basically, externally fired gas turbines may be incorporated into different types of energy systems in the same way as conventional directly fired gas turbines. The main feature of the externally fired gas turbine is an atmospheric combustor and a high-temperature heat exchanger, which replaces the conventional combustion system in an open gas turbine cycle. Therefore, there is no need for hot gas clean-up in order to protect gas path components of the gas turbine from corrosive and abrasive elements in the fuel. The gas turbine operates on clean air so the gas path is never exposed to the corrosive elements in the fuel. The high-temperature heat exchanger raises the temperature of the air to turbine inlet conditions.

By adding a bottoming system such as a steam turbine cycle or a district heating system, the externally fired gas turbine becomes an externally fired cogeneration system. There are two ways to couple an externally fired gas turbine with a bottoming system to form a cogeneration system, serial coupling and parallel coupling. The serial-coupling and parallel-coupling systems are shown conceptually in Fig. 1. In both systems, biomass is combusted in an atmospheric combustor. Hot combustion gases flow to a high-temperature heat exchanger (HTHx) where air is heated. If the temperature of the air does not reach the desired level, a top combustor may be applied where additional LPG or natural gas is combusted to heat the air to the gas turbine inlet temperature. Heat in the exhaust flue gas from the biomass boiler can be recovered by a bottoming cycle system where steam is generated to drive a steam turbine and/or hot water is produced for district heating purposes.

The serial-coupling system uses exhaust gas from the gas turbine as combustion air for the biomass combustor. In the parallel-coupling system, the exhaust gas, instead, enters a heat recovery system to produce hot water or steam for the bottoming system. A serially coupled externally fired gas turbine for cogeneration in which solid biomass is used as the main fuel is investigated in this research.
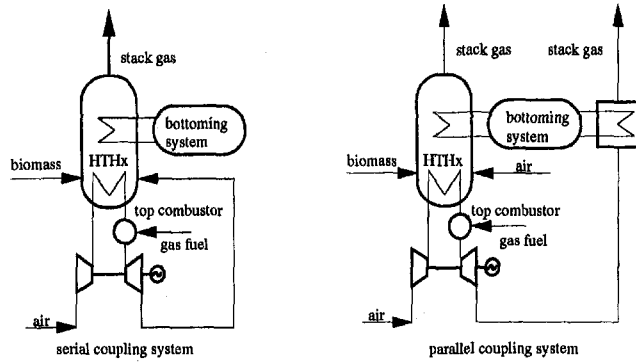
Fig. 1 General concept of externally fired gas turbine cogeneration system

Table 1 Systems studied in this paper

systems	cogeneration systems including:				
	BC	GT	TF	ST	DH
1-C1	CFB	no	no	yes	yes
1-C2	CFB	yes	no	yes	yes
1-C3	CFB	yes	yes	yes	yes
1-C1	GFS	no	no	yes	yes
1-C2	GFS	yes	no	yes	yes
1-C3	GFS	yes	yes	yes	yes
1-C1	GFW	no	no	no	yes
1-C2	GFW	yes	no	no	yes
1-C3	GFW	yes	yes	no	yes

Externally fired gas turbine systems have been studied by several researchers. Coal-burning externally fired gas turbines have been investigated by LaHaye and Zabolotny (1989) and Parson and Bechtel (1991). An externally fired gas turbine with evaporative water addition fueled by biogas from a biomass gasifier has been discussed by De Ruyck and Maniatis (1991). Possibilities to increase power output in cogeneration using an externally fired gas turbine have been analyzed (Sjödin and Svedberg, 1992; Eidensten et al., 1993). Repowering of existing coal-fueled power generation units with an externally fired combined cycle has been discussed by Vandervort et al. (1993). The key technology is the development of ceramic heat exchangers that allow application of air heaters at sufficiently high turbine inlet temperatures for a high efficiency of the combined cycle. A project for demonstration of an externally fired combined cycle has been selected in round 5 of the US Clean Coal program (Junior, 1993). This demonstration plant is the Warren power station of Pennsylvania Electric Company. Another project, Combustion 2000, is also supported by the DOE for developing the high-performance externally fired combine cycle using coal as the fuel (Ruth and Ward, 1993). However, little work has been done on the biomass externally fired gas turbine system. Studies on directly fired gas turbines for cogeneration with biomass gasification have been conducted by Larson (1988, 1992).

Modeling Systems and Assumptions for Simulations

The cogeneration systems in this study (Table 1) involve the following main subsystems: biomass combustion boiler (BC), gas turbine (GT), steam turbine (ST), and district heating (DH) system. In the gas turbine, top firing (TF) and non-top-firing have been considered in the simulations.

One of the simulated systems is illustrated in Fig. 2. This system includes gas turbine, biomass furnace, steam turbine, and district heating system. More detailed discussions about the equipment in the simulations are stated below.

Biomass Boiler. Three types of biomass boiler have been selected for the simulations:

- circulating fluidized bed (CFB) boiler,

- grate fired steam (GFS) boiler, and
- grate fired hot water (GFW) boiler, commercially available for district heating using biomass.

The simulations have been performed on the basis of a constant fuel inputs to the boilers. The fuel inputs to the boilers have been 20 MW and 100 MW for the full load and 10 MW and 50 MW for the part load.

Steam generated in the boiler is at 63 bar/510°C for 20 MW fuel input and 140 bar/540°C for 100 MW. Hot water produced in the grate fired hot water boiler is assumed to be at 17 bar/185°C.

The outlet temperatures of hot air from furnaces have been assumed as 950°C for grate fired boilers, but 800°C for CFB boilers due to bed temperature limitation of the CFB boiler. Considering the development of ceramic heat exchangers, a special case has also been calculated for grate fired steam boiler in which the outlet temperature of hot air from the ceramic heat exchanger in the furnace is 1150°C.

Assumptions made concerning heat losses from boilers and pressure losses are given in Table 2 (Sjödin and Svedberg, 1992).

The stack temperature of the boilers has been assumed to be 135°C.

Gas Turbine. Since the main task of this paper is to present the total performance of the cogeneration system, a simple gas turbine cycle and constant parameters have been assumed. Intercooling, recuperation, and blade cooling of gas turbines have not been considered in this study. The gas turbine is coupled to the biomass boiler in series. The gas turbine exhaust is used as combustion air in the biomass boilers. Thus, the air flow rate through the gas turbine is changed according to the combustion oxygen requirement of the biomass boiler, where the excess air factor is assumed at 1.3 at the full load. This means that the inlet air flow rate of the gas turbine will be varied with the sizes of biomass boiler at full load operation. However, the gas turbine is always arranged to run at full load even with reduced combustion air requirements when the biomass boiler runs at part-load operation.

Nomenclature

BC = biomass combustion boiler
CFB = circulating fluidized bed boiler
DH = district heating
GB = grate fired steam and hot water boilers
GFW = grate fired hot water boiler
GFS = grate fired steam boiler

GT = gas turbine
HTHx = high temperature heat exchanger
LPG = liquefied petroleum gas
ST = steam turbine
TF = top firing
α = power-to-heat ratio

η = efficiency
η_e = electrical efficiency
η_g = generator efficiency
η_{is} = isentropic efficiency
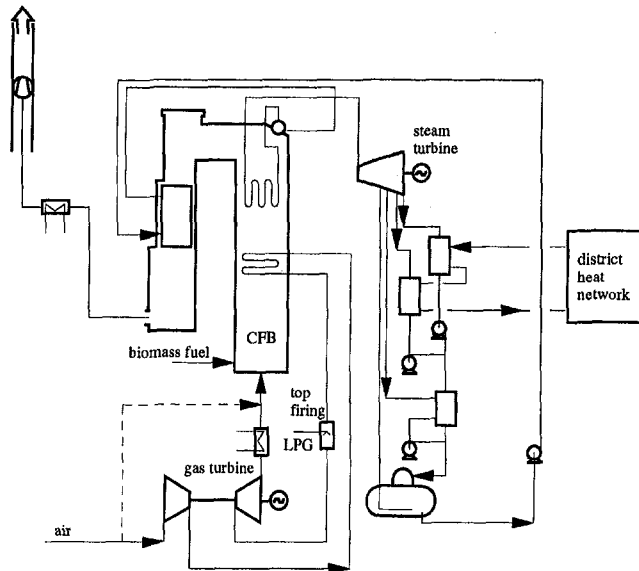η_m = mechanical efficiency

Fig. 2 Simulation configuration (CFB, circulating fluidized bed boiler)

The maximum inlet temperature to the gas turbine is 1200°C when top firing is used. In the case of non-top firing, the inlet temperature has been chosen based on the type of a biomass combustion furnace. Other performance input data are given in Table 2.

Steam Turbine. In the steam cycle, a back-pressure turbine has been used. The steam flows have been extracted from the turbine for feedwater heating or district heating. In the case with a 20 MW boiler, two flows of steam have been extracted from the steam turbine for feedwater heating and for deaerating. District heating water is heated by the steam from the final stage of the steam turbine. In the case with a 100 MW boiler, three flows have been extracted from the steam turbine, one for district heating and two for feedwater heating and deaerating. The steam turbine performance data are given in Table 2.

District Heating System. Based on conditions for typical Scandinavian district heating systems, 60°C has been assumed as return water temperature and 100°C as supply water temperature. The environmental temperature has been assumed at 0°C. The load variances due to the changing seasons have not been considered in this study. It is assumed that all heat produced from the cogeneration system can always be used in the district heating system.

Simulation Results

The main task has been to identify the total performance of biomass cogeneration systems for different biomass combustion furnaces such as CFB boilers, grate fired steam boilers, and grate fired hot water boilers. The fuel inputs of biomass have been 20 and 100 MW for the full-load simulations and 10 and 50 MW for the part-load simulations. The externally fired gas turbine is always arranged to be run at full load even when the boiler is only partially fired.

Three cases of cogeneration systems are classified: without a gas turbine, with a non-top-fired gas turbine, and with a top-fired gas turbine. The total energy efficiency, power-to-heat ratio, and the electrical efficiency represent performance results for the cogeneration systems. The simulations have been carried out using ASPEN PLUS.

Tables 3 and 4 show the simulation results. The tables include outputs of gas turbine (GT), steam turbine (ST), and district heating (DH), and also the performance criteria of total efficiency (η), power-to-heat ratio (α), and the electrical efficiency

(η_e). The total efficiency is the ratio of electric power plus process heat generated to the fuel input. The internal electricity consumption (int. el.) is referred to Sjödin and Svedberg (1992).

The total efficiency, power-to-heat ratio, and electrical efficiency are shown in Fig. 3 for the cases of biomass input 100 MW and 20 MW.

Size of Biomass Boilers. A comparison between the biomass boilers with 100 MW and 20 MW fuel inputs show that the larger size systems have higher total efficiencies, higher power-to-heat ratios, and higher electrical efficiencies. The main reason is that the heat losses from the boilers are assumed to be relatively smaller for larger size cogeneration.

Table 2 Summary of assumptions

Description	Assumptions
Boiler	
heat losses:	
CFB boiler	1% (100 MW)
	1.5% (20 MW)
grate fired boiler	4.5% (100 MW)
	5.5% (100 MW)
pressure losses:	
CFB boiler	0.15 bar
grate fired boilers	0.015 bar
hot air outlet temp:	
CFB boiler	800 °C
grate fired boilers	950 °C
stack temperature	135 °C
excess air factor	1.3
Fuel	
LPG fuel:	
LHV	46.4 MJ/kg
biomass:	
moisture content (w)	50 %
other elements:	
C	0.50 kg/kg (dry)
O	0.44 kg/kg (dry)
H	0.06 kg/kg (dry)
LHV	8.25 MJ/kg
Gas turbine	
turbine η_{is}	0.85
compressor η_{is}	0.85
turbine η_m	0.97
compressor η_m	0.97
generator η_g	0.98
turbine inlet pressure	10 bar
turbine outlet pressure	1.15 bar (CFB)
	1.015 bar (GB)
compressor inlet pressure	1.15 bar (CFB)
	1.015 bar (GB)
Steam turbine	
entry temp	540 °C (100 MW)
	510 °C (20 MW)
entry pressure	140 bar (100 MW)
	63 bar (20 MW)
turbine η_{is}	0.85
turbine η_m	0.97
generator η_g	0.98
back pressure	1.09 bar (20 MW)
	0.58 bar (100 MW)
District heating	
supply temp	100 °C
return temp	60 °C
Environmental	
air temp	0 °C
water temp	0 °C

Table 3 Simulation results (biomass boiler fuel input 20/10 MW)

Full load 20 MW			LPG	output MW			Int.el.	performance (%)		
case	allias	boiler	MW	ST	GT	DH	MWe	total η	α	ηe
1. without	1-C1	CFB	-	4.63	-	12.9	1.3	81	26	17
gas turbine	4-G1	GFS	-	4.39	-	12.3	1.0	78	28	17
	7-H1	GFW	-	-	-	16.8	0.5	82	-	-
2. with non-	2-C2	CFB	-	4.25	1.09	11.9	1.4	79	33	20
top firing	5-G2	GFS	-	3.79	1.75	10.6	1.1	75	41	22
gas turbine	8-H2	GFW	-	-	1.75	14.6	0.6	79	8	6
3. with top	3-C3	CFB	5.77	4.95	3.24	13.8	1.6	79	48	26
firing	6-G3	GFS	3.36	4.13	3.11	11.6	1.3	75	51	25
gas turbine	9-H3	GFW	3.36	-	3.12	15.9	0.8	78	14	10
Part load 10 MW										
1. without	1-C1	CFB	-	2.10	-	6.7	1.0	78	16	11
gas turbine	4-G1	GFS	-	1.98	-	6.4	0.8	76	19	12
	7-H1	GFW	-	-	-	8.4	0.4	80	-	-
2. with non-	2-C2	CFB	-	1.59	1.09	5.1	1.1	67	31	16
top firing	5-G2	GFS	-	1.27	1.75	4.1	0.9	62	51	21
gas turbine	8-H2	GFW	-	-	1.75	5.4	0.5	66	22	12
3. with top	3-C3	CFB	5.77	2.24	3.24	7.1	1.3	72	59	27
firing	6-G3	GFS	3.36	1.58	3.11	5.1	1.1	65	71	27
gas turbine	9-H3	GFW	3.36	-	3.12	6.7	0.7	68	36	18

Types of Boilers

Case 1. Cogeneration Without Gas Turbine. The gas turbine is not included in this system. Power has been generated from the steam turbines, except for the system with a grate fired hot water boiler, which produces only district heating.

The total efficiencies of all three systems with different boilers are 80–84 percent for 100 MW biomass input and 78–82 percent for 20 MW. In the system with 100 MW biomass input, the cogeneration with CFB boilers has the highest efficiency. The cogeneration with grate fired hot water boiler has the highest efficiency for 20 MW biomass input.

Considering the power output, the electrical efficiency is 23 percent for the system with CFB boiler, and 22 percent for that with grate fired steam boiler for 100 MW fuel input. The power-to-heat ratios are about the same for systems with CFB and grate fired steam boilers.

Case 2. Cogeneration With Non-Top-Fired Gas Turbine. A non-top-fired gas turbine is included in this system. Systems with CFB boilers and grate fired hot water boilers have higher efficiencies than the system with grate fired steam boilers. How-ever, the electrical efficiency of the system with the grate fired steam boiler is highest. The system with grate fired hot water boiler has the lowest electrical efficiency because there is no steam turbine in this system.

Case 3. Cogeneration With Top-Fired Gas Turbine. A top-fired gas turbine has been coupled into the cogeneration systems. The total efficiencies of the different systems are almost the same as in Case 1. Systems with CFB boiler and grate fired steam boiler have the electrical efficiencies 32 and 31 percent respectively, for cases with 100 MW biomass input, and 26 and 25 percent, respectively, for cases with 20 MW biomass input. However, the electrical efficiencies for the systems with grate fired hot water boilers are only 11 percent for 100 MW and 10 percent for 20 MW. Systems with CFB boilers and grate fired steam boilers have higher power-to-heat ratios than those with grate fired hot water boilers.

Discussions

The results of these simulations indicate that compared with conventional biomass fired cogeneration systems, the total effi-

Table 4 Simulation results (biomass boiler fuel input 100/50 MW)

| Full load 100 MW			LPG	output MW			Int. el.	performance (%)		
case	allias	boiler	MW	ST	GT	DH	MWe	total η	α	ηe
1. without	1-C1	CFB	-	27.82	-	60.6	4.7	84	38	23
gas turbine	4-G1	GFS	-	26.38	-	57.6	4.0	80	39	22
	7-H1	GFW	-	-	-	84.7	1.8	83	-	-
2. with non-	2-C2	CFB	-	25.56	5.46	55.8	4.9	82	47	26
top firing	5-G2	GFS	-	22.78	8.73	49.9	4.2	77	55	27
gas turbine	8-H2	GFW	-	-	8.73	73.4	2.0	80	9	6.7
	5'-G2	GFS	-	21.40	12.60	46.9	4.2	77	63	30
3. with top	3-C3	CFB	29.03	29.83	16.24	65.0	5.2	82	63	32
firing	6-G3	GFS	16.76	24.85	15.57	54.4	4.5	77	66	31
gas turbine	9-H3	GFW	16.76	-	15.57	80.1	2.3	80	17	11
Part load 50 MW										
1. without	1-C1	CFB	-	12.68	-	31.7	3.5	82	29	18
gas turbine	4-G1	GFS	-	12.01	-	30.1	3.0	78	30	18
	7-H1	GFW	-	-	-	42.4	1.4	82	-	-
2. with non-	2-C2	CFB	-	9.65	5.46	24.2	3.7	71	47	23
top firing	5-G2	GFS	-	7.69	8.73	19.3	3.2	65	68	26
gas turbine	8-H2	GFW	-	-	8.73	27.3	1.6	69	26	14
	5'-G2	GFS	-	6.70	11.78	16.8	3.2	64	91	31
3. with top	3-C3	CFB	29.03	13.54	16.24	33.8	4.0	75	76	33
firing	6-G3	GFS	16.76	9.59	15.57	24.1	3.5	69	90	33
gas turbine	9-H3	GFW	16.76	-	15.57	34.0	1.9	71	40	21
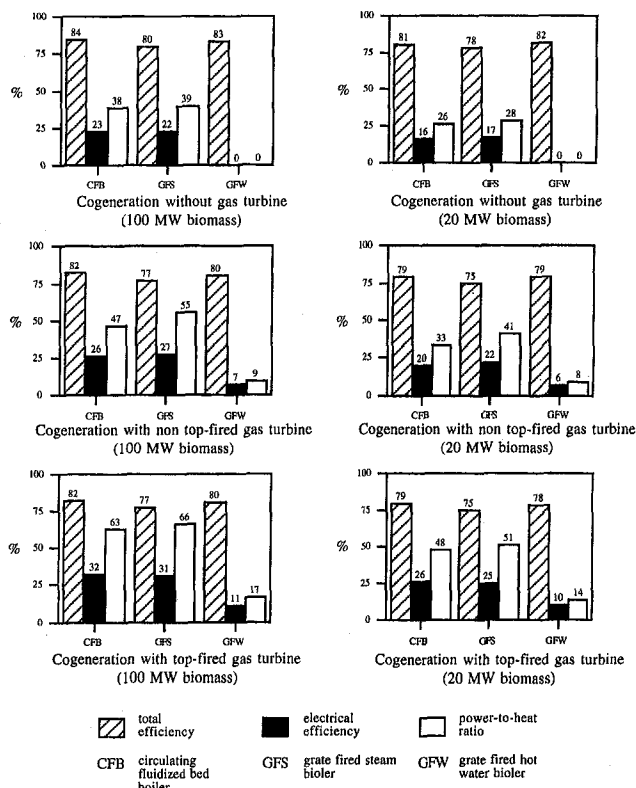
Fig. 3 Graphic presentation of simulation results for biomass combustion boilers at full load with respectively 100 MW (left) and 20 MW (right) input of biomass fuel. Data are also presented in Tables 3 and 4.

ciencies do not vary so much, but the electrical efficiencies increase significantly when an externally fired gas turbine with or without top firing is introduced into the cogeneration systems. For example, in the applications of CFB or grate fired steam boilers, the electrical efficiencies of systems with a non-top-fired gas turbine increase about 25 percent compared with the systems without gas turbines. When top firing is used for the gas turbine, high-quality fuel is needed, which can be considered a complicating factor. This disadvantage is more than compensated by the improved electrical efficiency, especially for the systems with grate fired hot water boilers and the systems with CFB boilers, which means the marginal electrical efficiency for top firing using LPG fuel is quite high.

When the biomass boilers operate at part load (50 percent), the total efficiencies decrease in all cases due to the relatively higher internal electricity consumption and larger stack gas losses. The major factors affecting the electrical efficiencies are the internal electricity consumption and the ratio of LPG to biomass fuel input. The electrical efficiencies increase in Case 3 (with top-fired gas turbine) but decrease in Cases 1 (without gas turbine) and 2 (with non-top-fired gas turbine). The reason for reduced electrical efficiencies is that the internal electricity consumption at part load is proportionally greater than at full load. In Case 2, the decrease is less than in Case 1 because the externally fired gas turbine always operates at full load. The increase of the electrical efficiency in Case 3 is due to higher ratio of LPG to biomass fuel input at part load.

The results show that CFB boilers have higher total efficiency and electrical efficiency than systems with grate fired boilers. However, because of the limitation of the bed temperature of CFB (e.g., 850°C), the hot air from the CFB boiler is unable to reach temperatures over about 800°C. In order to operate a modern commercial gas turbine under the design conditions, a top firing combustor must be used in the systems. If a high-temperature heat exchanger is available, a system with a grate

fired steam boiler can overcome this obstacle. This will solve some practical problems. First, this system does not need the top combustor, which is not commercially available today. Second, the cogeneration system requires only one low-grade biomass fuel system. Third, the gas turbine will operate with a very clean working medium, which result in high availability.

In Tables 3 and 4 under the full load, one can find that the total efficiencies of systems with CFB boilers and grate fired hot water boilers are about the same but higher than those of the systems with grate fired steam boilers. However, the electrical efficiencies of systems with grate fired steam boilers and CFB boilers are about the same but higher than those of systems with grate fired hot water boilers. These observations are explained by the fact that the internal electricity consumption of cogeneration plants, the heat losses in boilers and pressure looses in boilers are strongly dependent on the type of boilers. These factors affect the total efficiencies, electrical efficiencies, and power-to-heat ratios. The systems with CFB boilers have higher internal electricity consumption, higher pressure losses, but lower heat losses than the systems with grate fired boilers. Pressure losses and heat losses are the same for grate fired steam boilers and hot water boilers, but internal electricity consumption is greater in the grate fired steam fired boilers than in the grate fired hot water boilers. The complexities among these factors require a further study to identify the key factors for the performance of the cogeneration systems.

It should be noted that heat produced in the cogeneration systems varies between applications. One assumption that has been made is that the heat can always be used in the district heating system. The heat production is 47−87 MW and 11−17 MW for cogeneration systems with 100 MW and 20 MW biomass input, respectively. The quantity of heat produced from the systems with grate fired hot water boilers is always the greatest. The amount of heat produced from the systems with a CFB or grate fired steam boiler is approximately the same, about 30 percent lower than in the systems with a grate fired hot water boiler.

In Table 4, the simulation results are also given for one special case 5′-G2, in which outlet hot air temperature from the grate fired boiler is 1150°C instead of 950°C as case 5-G2. Both cases have almost the same total efficiency. Case 5′-G2 has higher electrical efficiency and power-to-heat ratio than case 5-G2, which means that the high gas turbine inlet temperature results in the high electrical efficiency and power-to-heat ratio.

The coupling between the gas turbine and the bottoming system has a substantial effect on the performance of the cogeneration system. Further comparison of the serial-coupling and parallel-coupling systems could reveal the important differences. The impact of the parameter changes on the pressure drops and heat losses of the boiler; inlet temperature and pressure ratio of the gas turbine and other parameters should also be investigated.

Conclusions

The externally fired gas turbine is a promising technology for biomass cogeneration because an atmospheric combustor and a high-temperature heat exchanger thereby replace the conventional combustion system in an open gas turbine cycle. Thus, there is no need for hot gas clean-up to protect the gas turbine from corrosive and abrasive elements in the fuel.

When an externally fired gas turbine with or without top firing is introduced into the cogeneration system, the electrical efficiencies increase significantly. Top firing provides great potential for increasing the electrical efficiency and power-to-heat ratios even further. However, a top combustor and additional high-quality fuel are required which increases the complexity of the systems.

The results of this study demonstrate that systems with CFB boilers have a higher total efficiency and electrical efficiency

than systems with grate fired boilers. However, the CFB boiler must be coupled to a top-fired gas turbine in order to get a high electrical efficiency because of the limitation of the bed temperature (e.g., 850°C). A system with a grate fired steam boiler has the potential to overcome this obstacle when a high-temperature heat exchanger is already available. This system will not need a top combustor. These circumstances allow the use of only one low-grade biomass fuel system and the gas turbine will operate with a clean working medium.

Acknowledgments

References

Eidensten, L., Yan, J., and Svedberg, G., 1993, "System Study of Externally Fired Gas Turbines in Different Applications," Final Report to the Swedish National Board for Industry and Technical Development (NUTEK), Sweden [in Swedish].

Junior, I., 1993, "A Bunch of Five for Clean Coal 5," *Modern Power System,* Vol. 13, No. 6 (June).

Larson, E. D., 1988, "Biomass-Fired Steam-Injected Gas Turbine Cogeneration," *ASME Cogen-Turbo,* pp. 57–66.

Larson, E. D., 1992, "Biomass-Gasifier/Gas Turbine Cogeneration in the Pulp and Paper Industry," JOURNAL OF ENGINEERING FOR GAS TURBINES AND POWER Vol. 114, pp. 665–675.

LaHaye, P. G., and Zabolotny, 1989, "Externally-Fired Combined Cycle (EFCC)," presented at the ASME Cogen-Turbo Meeting, Nice, France, Aug. 30–Sept. 2.

Parson, E. L., and Bethtel, T. F., 1991, "Performance Gains Derived From Water Injection in Regenerative, Indirect-Fired Coal-Fueled Gas Turbines," ASME Paper No. 91-GT-288.

Ruth, L., and Ward, J., 1993, "Combustion 2000 Program to Develop Coal Plant Technology," *Power Engineering,* Apr.

De Ruyck, J., and Maniatis, K., 1991, "A Biomass Fueled Cogeneration Plant Based on an Evaporative Gas Turbine Cycle at the University of Brussels," *ASME Cogen-Turbo,* IGTI-Vol. 6, pp. 443–452.

Sjödin, J., and Svedberg, G., 1992, "Possibilities to Increase Power Output in Cogeneration Using an Externally Fired Gas Turbine," Värmeforsk Energiteknik Report 464, Sweden [in Swedish].

Vandervort, C. L., Bary, M. R., Stodard, L. E., and Higgins, S. T., 1993, "Externally-Fired Combined Cycle Repowering of Existing Steam Plants," ASME Paper No. 93-GT-359.

Energy Recovery of Blast-Furnace Gas Coke: The Importance of a Correct Regulation System

D. Laforgia

F. Ruggiero

Istituto di Macchine ed Energetica,
Polytechnic of Bari, Italy

The present work deals with the regulation system of a plant recovering the energy of blast-furnace gas coke residual pressure. Such a plant is equipped with a turbogenerator, which produces electric energy, expanding the gas coke up to the mill pipe network pressure value. Before revamping, the regulation system consisted of an automatic nozzle control of a turbine stator and a throttle valve. Once the system became operative, the regulation system seemed to be inadequate because it caused a significant reduction in energy recovery due to the variation of the gas coke characteristics, compared to the original engineering specifications. A mathematical model for the plant simulation has been developed through the regulation system static and dynamic responses. This simulation, together with a series of experimental tests, identified the causes of the operational problems in the original regulation system. On the basis of the response times of the old regulation system, a valve with reduced intervention inertia has been suggested. The regulation logic was also modified: The valve interventions were directly linked to the pressure variations recorded at the blast furnace top, and no longer to the opening variation of the turbine automatic system. A more rational use of the plant components and its control system, together with an increase of the electric energy production, have been demonstrated.

Introduction

In Steel Mills the blowing in of hot air at the base of the blast furnace is a very delicate step to guarantee an efficient production process. The air, preheated in cowpers, enters the blast-furnace bottom at 0.5 MPa pressure and comes out as gas-coke from the top of the stack at a residual back-pressure of about 0.32 MPa. Gas coke constant pressure means, of course, high production efficiency [1]. In blast furnace No. 5 at the ILVA Steel Mill in Taranto, Italy (where this investigation was carried out), a turbogenerator unit capable of producing a significant amount of electric power recovered from the gas coke expansion has been installed. The turbo unit has been mounted in parallel to the existing Septum valve, thus becoming the back-pressure regulator (Fig. 1). During the design phase, the turbine bypass by means of the Septum valve was considered under emergency conditions only. A quick-opening throttle valve (BV006) had been installed to divert the gas quickly toward the Septum valve in case of unacceptable overpressure due to accidental halt of the turbine. The opening of this valve occurred also in case of abnormal running conditions of the blast furnace, causing an overproduction of gas coke, which could not be cleaned off by the turbine without an increase of the inlet pressure.

In the last years of operation it has been realized that the blast-furnace gas characteristics had changed compared to those of the turbine engineering specifications with an increase in temperature and flow rate. At present conditions, the turbine can be considered slightly undersized. The first effect of this new running condition has been the continuous spill of the gas the turbine could not eliminate. The partial waste of available

energy was further increased by a BV005 valve, which was set up as an on–off valve and not as a regulation valve as needed by the new operating conditions. As a result there was a higher gas-coke spill than necessary.

The present investigation describes the experimental evaluations and the theoretical simulation carried out under different working conditions.

Plant Features

The gas turbogenerator installed is a wet expansion, axial, four-stage Hitachi turbine (Fig. 2) running at 1500 rpm [2, 3]. Its Automatic Nozzle Control (ANC), provided with a regulation field of 31 deg, permits constant pressure upstream of the turbine, at a wide range of flow rate and pressure of the gas produced by the blast furnace.

Table 1 shows the three operational conditions (A = normal; B = minimum; C = maximum) adopted as engineering specifications for the dimensioning of both the turbine and its regulation system. Figure 3 shows the turbine characteristic map as well as the three above-mentioned operating conditions (A, B, and C). The electric power that can be generated according to Eq. (1) ranges from 13,900 kW (B) to 16,610 kW (C) and its design point value sets at 14,820 kW (A):

$$P_e = k_7 n_{\theta i} \eta_m \eta_g \frac{1}{v_{nw}} \frac{P_i}{P_i - P_{vi}} Q_{nd} c_p T_i \left[1 - \left(\frac{P_0}{P_i} \right)^{(k-1)/k} \right] \quad (1)$$

In Eq. (1) coefficient k_7 is an index of the ANC efficiency whose trend is shown in Fig. 4. A hydraulic piston produces the change in angular position of the stage one stator vanes; the percentage of the piston stroke is the abscissa of that figure. The value of 55 percent abscissa implies a vane inclination (conventionally indicated as $\alpha = 0$ deg) to which corresponds $k_7 = 1$. Such an efficiency decreases both at closing ($\alpha_{min} = -13$ deg) and at opening ($\alpha_{max} = +18$ deg) of ANC. α_{min} and
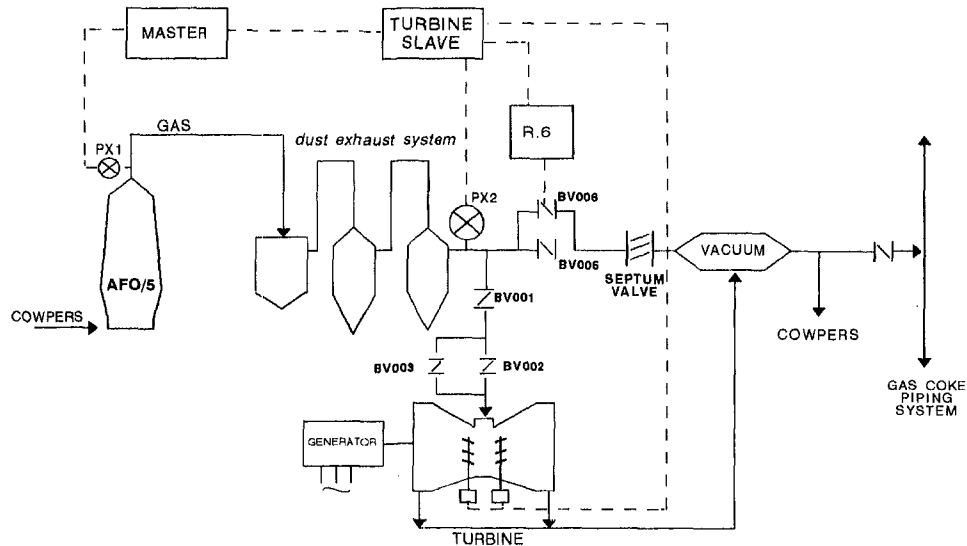
Fig. 1 Schematic of the gas-coke exhaust system including turbine and regulation system
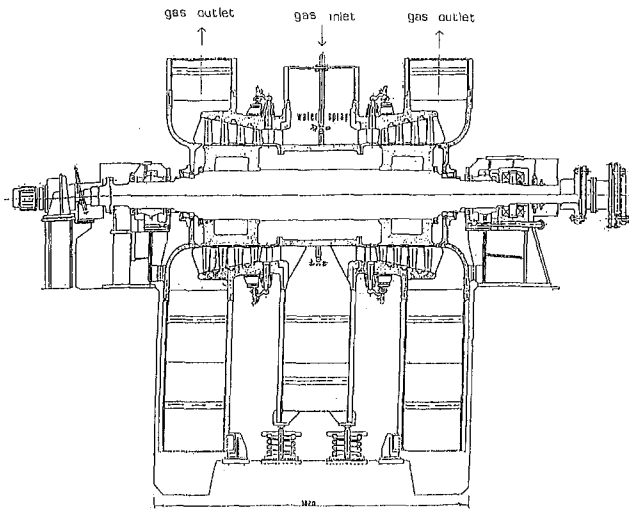
Fig. 2 Schematic drawing of Hitachi turbine

Table 1 Engineering specifications

ENGINEERING SPECIFICATIONS			
Working point	A	B	C
Dry gas flow rate [knm³]	560	540	600
Number of hours per year [h/y]	4.800	2.400	800
Downstream turbine pressure [Mpa]	0,111	0,111	0,111
Turbine gas temperature [°C]	45	45	45
Powder concentration [mg/nm³]	<10	<10	<10
Water concentration [g/nm³]	<15	<15	<15
GAS MEAN CONCENTRATION			
CO (% of volume)	23,5		
CO₂ (% of volume)	20,4		
H₂ (% of volume)	3,1		
N₂ (% of volume)	53,0		

$\alpha_{\max}$ are the angular deviation from the position of maximum efficiency.

Problems in keeping the pressure constant at the blast furnace top arise from the discontinuous operations of cowpers changing and furnace charging. The pressure cannot be held constant even using a battery of correctly time-displaced cowpers, which instantaneously varies the flow of hot air and the pressure at the blast inlet as well. Changing cowpers also produces a secondary effect on the turbine, linked to the pressure variations of the cowper piping supply where the turbine discharges. The induced perturbations propagate to the turbine where the mean pressure oscillates at about 0.01 Mpa. Pressure oscillations can also be

───────── Nomenclature ─────────

c_p = specific heat at constant pressure
D_i = diameter of pipe i
G_i = mass flow of dry AFO gas at ith location
$h/h_{\max}$ = ANC percentage opening
K = isoentropic gas constant = 1.373
k_2 = humidity factor
k_{2p} = humidity factor under average design conditions
k_{2o} = humidity factor under average operating conditions
L_i = pipe i length
P = gas pressure
P_e = electric power

P_i = turbine inlet pressure
P_o = turbine outlet pressure
P_v = vapor pressure
P_{vi} = saturation pressure at temperature T_i
Q = normal gas density = 1.343 kg/nm³
Q_{nd} = dry gas flow in volume
R = characteristic gas constant
T_i = gas temperature at turbine inlet
T_m = gas medium temperature
v_{nw} = normal specific volume of wet gas
X = pressure at AFO throat (process variable)

X_2 = pressure in turbine inlet (process variable)
Y = variable depending on $h/h_{\max}$ variations
δ = pressure variation at turbine inlet
ΔP = friction losses in AFO-turbine pipe
η_g = electric generator efficiency as declared by Hitachi = 0.98
η_m = organic efficiency as declared by Hitachi = 0.973
η_σ = internal thermodynamic efficiency as declared by Hitachi = 0.87
$\eta_{\sigma i}$ = thermodynamic efficiency
ϑ_n = normal gas density = 1.343 kg/nm³
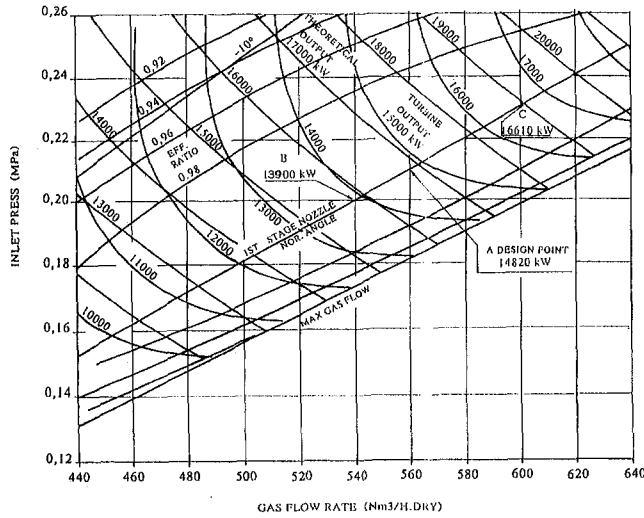λ = numerical coefficient

Fig. 3 Map of the Hitachi turbine

due to obstructions occurring in the stack or to the gas following differential paths when going through the charge. Finally, the variability of the moisture and the ore composition determines a variation of the final ratio of CO and CO_2 in the gas at the top and subsequent changes in the volumetric flow rate of the dry gas produced.

Process Mathematical Model

To evaluate the process dynamic response, a mathematical model of the system connecting the blast furnace to the turbine has been created (Fig. 5).

Indicated by C_i, the capacity of a generic pipe length can be calculated as follows:

$$C_1 = \frac{\pi D^2}{4} L_1 \frac{10^5}{kRT_i} \qquad (2)$$

so that it is possible to calculate the parameter $C_1 = 2400$ [kg/ MPa] for length 1–2 and $C2 = 1300$ [kg/MPa] for length 3–4.

In the dust-exhaust system, the gas is subject to an increase in the mass flow rate because of the washing water, to a loss of pressure due to friction and to a gas cooling up to 58°C. It is, thus, necessary to correct the turbine inlet flow by the introduction of a moisture factor (k_2), which is defined as the ratio of dry gas to wet gas:

$$k_2 = \frac{P - P_v}{P}$$

where the k_2 values can be calculated as follows:

$k_{2p} = 0.9695$ under average design conditions
$k_{2o} = 0.9421$ under average operating conditions

Provided that the pressure can range by 10 percent of its medium value and that the inlet temperature can be considered constant, the sole variable of the process is the pressure (X). As for the friction losses in the pipes and in the dust exhaust system, they can be calculated equal to 0.02 MPa and located in the dust exhaust system only. It follows that in length 2–3 the following relations can be found:

$$G_3 = \frac{G_2}{k_2} \qquad (3)$$

$$X_2 = X - \Delta P \qquad (4)$$

where:

X = pressure at blast furnace (AFO) top
X_2 = pressure at turbine inlet

Assuming that the blast furnace has been fed with non-oxygen-enriched air, the flow rate at the AFO top is simply $G_1 = Q_{nd} \vartheta n$. It can be written as:

$$G_1 - G_2 = C_1 \frac{dX}{dt} \qquad (5)$$

$$G_3 - G_4 = C_2 \frac{dX}{dt} \qquad (6)$$

and thus:

$$\frac{G_1}{k_{2p}} - G_4 = \frac{dX}{dt} \left[C_2 + \frac{C_1}{k_{2p}} \right] \qquad (7)$$

Equation (7) is a first-order differential equation representing the process. To solve such an equation it is necessary to explicit the equation of the mass flow rate of wet gas (G_4) eliminated by the turbine.

Figure 6 shows the characteristic curve of the flow rate versus ANC opening for any value of the pressure entering the turbine. Since the turbine actual operational field corresponds to the stage one stator vanes positioned for values of the actuator piston stroke between 55 and 85 percent of its maximum stroke, it is possible to linearize the curve in the range between 0.55– 0.85 of h/h_{max}:

$$\frac{Q}{Q_{max}} = 0.776 + 0.206 \frac{h}{h_{max}} \qquad (8)$$

Taking into account the maximum volumetric flow rate passing through the turbine, which is a function of the turbine upstream pressure ($Q_{max} = 203500 \cdot X_2$), Eq. (8) can be transformed as follows:

$$Q_4 = 16.10 X_2 \left[3.77 + \frac{h}{h_{max}} \right] \qquad (9)$$

As for the mass flow of wet gas, relating to the engineering specifications, and introducing the values of the coefficients of different parameters related to the real thermodynamic conditions, it is possible to write:

$$G_4 = 16.10 X_2 \left[3.77 + \frac{h}{h_{max}} \right] \qquad (10)$$

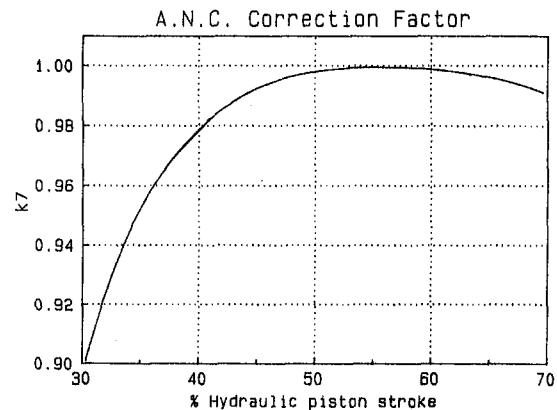Assuming $\lambda = 16.10$ and $Y = 3.77 + h/h_{max}$, Eq. (10) can be simplified to:

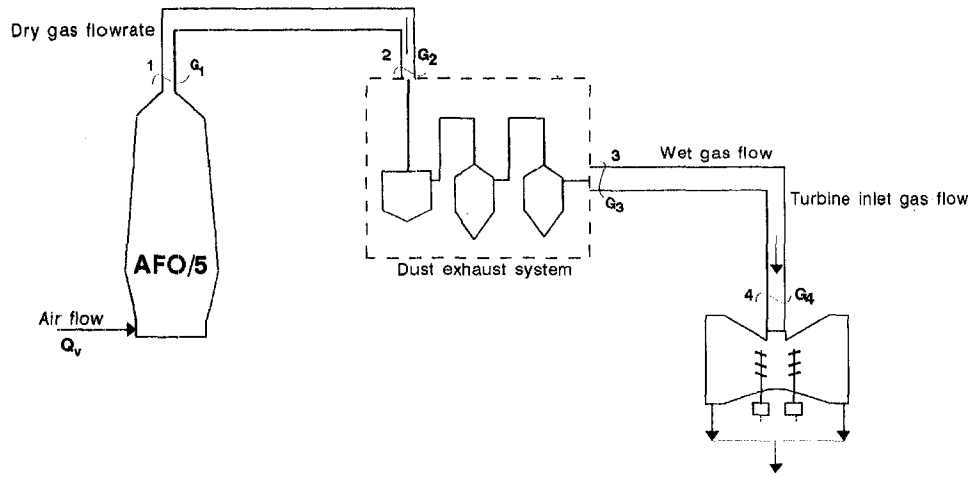Fig. 4 Automatic Nozzle Control correction factor versus hydraulic piston stroke

Fig. 5 Flow diagram of gas-coke system simplified for the matematical model

$$G_4 = \lambda X_2 Y \qquad (11)$$

which allows one to determine the steady characteristic of the process, that is to say, the pressure values (X) at the blast-furnace top by varying the ANC opening at constant flow rate. It can be written:

$$\lambda X_2 Y_0 = \lambda (X_2 - \delta) Y \qquad (12)$$

where

Y_0 = value of Y corresponding to $h/h_{max} = 0.55$
Y = variable according to h/h_{max}
δ = variation of turbine inlet pressure.

Expliciting in k and considering Eq. (4):

$$\delta = X_2 (Y - Y_0) \frac{1}{Y} \qquad (13)$$

$$X = (X_2 - \delta) + \Delta P \qquad (14)$$

After simple operations Eq. (14), which is the process steady response, can be written as follows:

$$X = X_2 \left[1 - \frac{\dfrac{h}{h_{max}} - 0.55}{3.77 + \dfrac{h}{h_{max}}} \right] + \Delta P \qquad (15)$$

Figure 7 shows the trend of Eq. (15). Under normal running conditions (point A of design), the set point of the blast-furnace top pressure is 0.330 MPa, the volumetric flow rate of dry gas is 560 kNm³/h, and the stator vanes are open by 55 percent. If the opening of the ANC increases to 80 percent, the top pressure will reach a new set point of 0.313 MPa.

If in Eq. (7) G_4 is replaced according to Eqs. (10) and (4), it can be written:

$$\frac{G_1}{k_{2p}} - \lambda Y (X - \Delta P) = \frac{dX}{dt} \left[C_2 + \frac{C_1}{k_{2p}} \right] \qquad (16)$$

if

$$a = \lambda Y$$

$$b = \frac{G_1}{k_{2p}} + \lambda Y \Delta P$$

$$A = C_2 + \frac{C_1}{k_{2p}}$$

and considering Y independent of time, Eq. (16) can be rewritten as:

$$b - aX = A \frac{dX}{dt} \qquad (17)$$

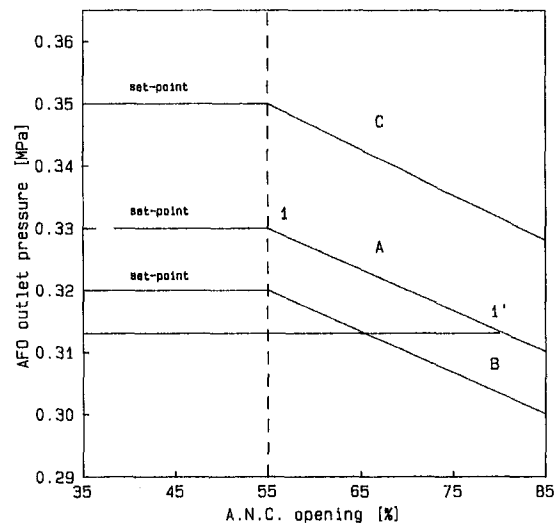This differential equation admits the following solution:

Fig. 6 Gas-coke flow rate versus ANC opening

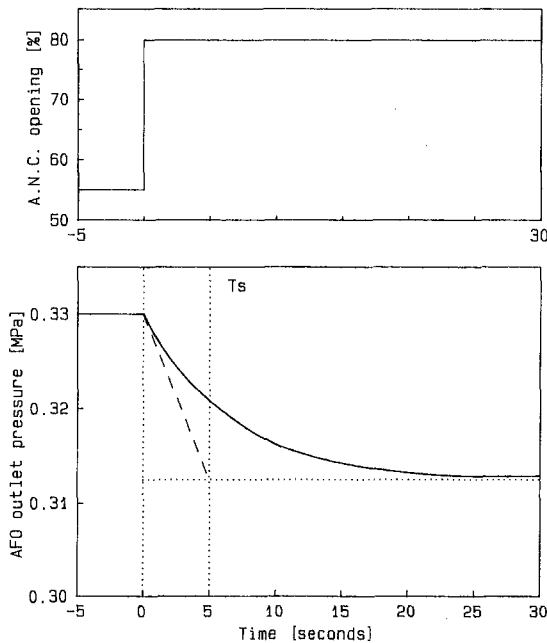Fig. 7 AFO outlet pressure versus ANC opening

Fig. 8 Dynamic response of the process at the original operating conditions

$$X(t) = \frac{b}{a}\left[1 - e^{-(a/A)t}\right] + X_0 e^{-(a/A)t} \qquad (18)$$

which represents the dynamic response of the process.

The value of the constant X_o has been obtained assuming that $t = 0$ means normal running conditions with $X_o = 0.330$ MPa. Calculating the process response for a step change of the regulator, that is to say, from 55 to 80 percent of h/h_{max}, the trend of the process variable X as a function of time is obtained as shown in Fig. 8. From this figure it can be seen that the process time constant is $T_s = 5$ s, which means that the pressure reaches 63 percent of its new equilibrium value in the time T_s, and 98 percent of its final one after about 20 seconds.

Regulation Systems Analysis

The scheme in Figs. 9 and 10 shows the main parts of a regulation system having two pressure detectors-transducers, one of which is located at the blast-furnace top (PX1) and the other one at the dust-exhaust system (PX2). Both are calibrated for a pressure range of 0–0.400 MPa and send a proportional electric signal to the different regulation units. Transducer PX1 sends its signal (relative to the process variable) to the regulator

"MASTER." The possible signal of error between process variable and set point is sent to two parallel "SLAVE" regulators respectively relative to the SEPTUM valve and the turbine by a proportional-integral action. The set point is fixed in the pyrometer room as a function of the conditions desired in the furnace. The two "SLAVE" regulators, after comparing the set point value coming from the "MASTER" with the PX2 transducer signal, give a proportional-integral (eventually modified) signal to control oleodynamic circuits of the both SEPTUM valve and the two rings of the turbine ANC system.

Each hydraulic drive circuit is a regulation loop provided with feed-back, which comprises two regulators with proportional-integral action, a hydraulic servovalve, a hydraulic servomotor, and a feed-back system called "LVDT" that continuously checks the servovalve and servomotor positions (Fig. 10). Therefore, the main regulation system is an in-sequence one where the pressure is controlled at the blast-furnace top and at the turbine inlet, to improve its dynamic response. Actually the old regulation system suffered from two drawbacks:

- by normal operation process of the blast furnace there could be some transients with an overproduction of gas and, thus, with volumetric flow rates, which cannot cross the turbine with a constant pressure;
- there could be some cases of abnormal operation: For example, the safety system automatically closing the turbine when there is an excessive gradient of deviation in the opening of the ANC system.

For this reason a "sub-bypass valve" called the BV006 (Fig. 1) has been installed in parallel to the "main bypass valve" BV005. BV006 is controlled by a regulator in series with the turbine "SLAVE," which is characterized by a fast opening to bypass quickly the overproduction of gas to the SEPTUM.

The valve BV006 is a throttle valve whose diameter is 1200 mm with an operational range of 0.310–0.350 MPa and 50–100°C, with intervention times of:

0.5–2 s at opening
10–20 s at closing

Figure 11 shows the BV006 characteristic curves. For this type of valve the flow coefficient (C_v) is obtained as follows [4]:

$$C_v = 12.36 \frac{G}{\Phi} \frac{(RT_i)^{1/2}}{P_i}$$

where:

P is the pressure upstream of the valve
Φ is the pressure ratio

In the operational pressure range, conditions are always severe so the mass flow rate crossing the valve depends only on
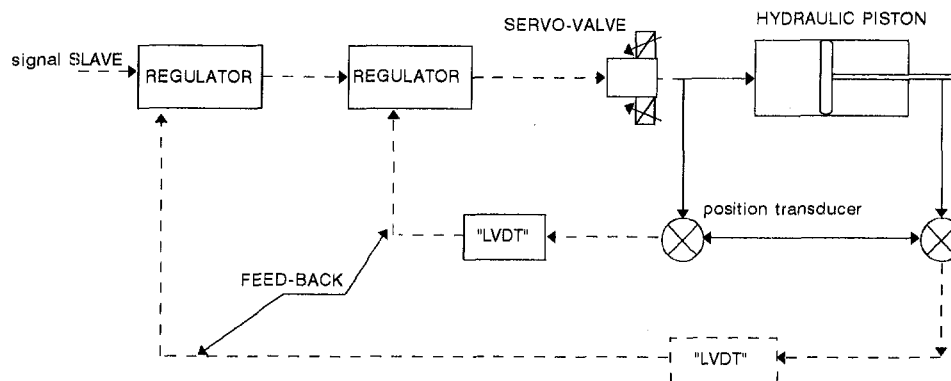

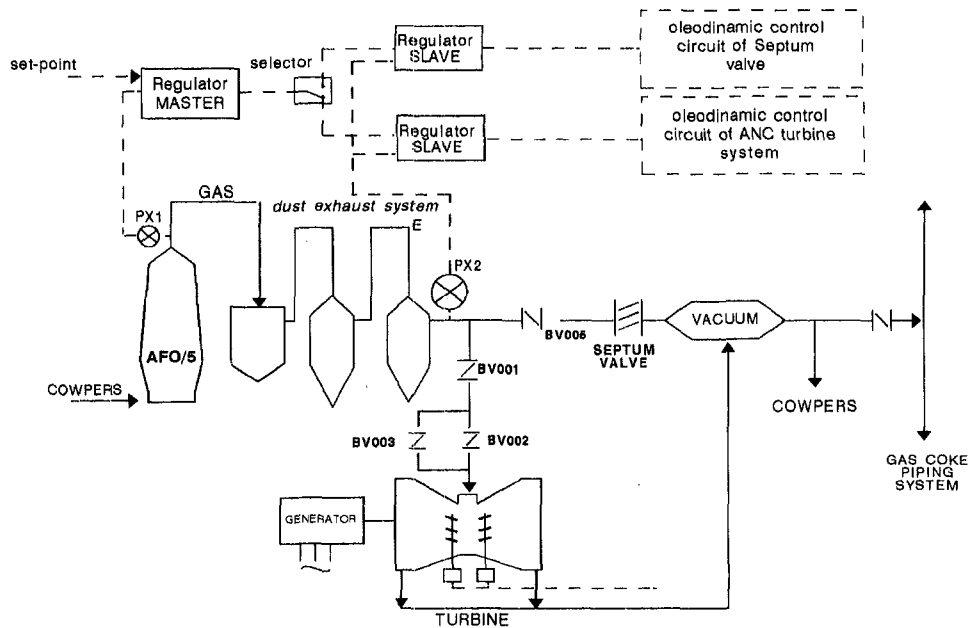**Fig. 9 Schematic of the regulation system**

Fig. 10 General scheme of the hydraulic drive circuit

the thermodynamic conditions upstream of the valve. Replacing the actual valve coefficients as shown in [4], the valve characteristic can be equal to an exponential function having this form:

$$\frac{C_v}{C_{max}} = R^{\beta_1 - 1}$$

R = range experimentally obtained = 48

obtaining, thus, the mass flow rate already mentioned:

$$G = 67.90 P_1 R^{\beta_1 - 1} \qquad (19)$$

where $\beta_1 = \beta / \beta_{max}$ and β is the ratio of gas expansion.

Experimental Results

In order to evaluate the regulation system performance, as well as the theoretical model reliability, several experimental tests have been carried out, monitoring the trends of the following variables:

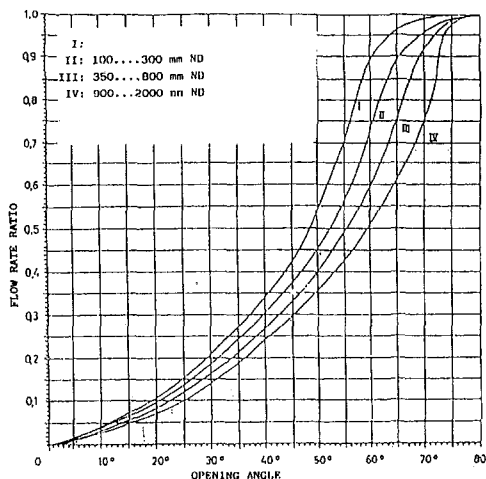- volumetric flow of wet gas in the turbine;
- BV006 valve opening;

Fig. 11 Valve characteristic curves; IV stands for BV006

- electric power produced by the turbogenerator.

These measurements, even though not scientifically exhaustive of the phenomena considered, should be considered a fair representation of the process and the regulation system behavior. The tests have been carried out under the following conditions:

- constant volumetric flow of air at the blast inlet (400 kNm^3/h) and constant pressure at the AFO top of 0.340 MPa (Fig. 12);
- constant volumetric flow of air at the blast inlet (400 kNm^3/h) and variable pressure at the AFO top ranging from 0.320 to 0.340 MPa (Fig. 13);
- variable volumetric flow of air at the blast inlet (360–400 kNm^3/h) and constant pressure at the AFO top of 0.340 MPa (Fig. 14).

It can be immediately realized that the BV006 valve is constantly open by reducing the air blowing at the blast inlet to 360 kNm^3/h and keeping the AFO top pressure to 0.340 MPa, the bypass flow has stopped due to the complete closing of the BV006 valve. Strong flow variations as in Figs. 12–14 are to be related to the cowpers changing. The trends shown are not very good and, since there are only two regulating units (ANC turbine system and BV006 valve), the anomalous functioning of the process depends on them.

At point A of the operating conditions, the turbine should be able to get the following mass flow:

$$G_A = \rho_n Q_{ndA} \frac{1}{k_{1pA}} = 216 \; [\text{kg/s}]$$

Under actual working conditions, the inlet temperature is different, causing a variation of the actual humidity factor and thus an increase in the real mass flow:

$$G_{Aeff} = \rho_n Q_{ndA} \frac{1}{k_{20A}} = 222 \; [\text{kg/s}]$$

As seen passing from the design hypothesis to the operational ones there is an increase of about 3 percent in the actual wet gas flow. To elaborate the new wet gas flow without changing the pressure at the inlet, the turbine has to change the ANC system opening from 55 to 68 percent. Similar considera-
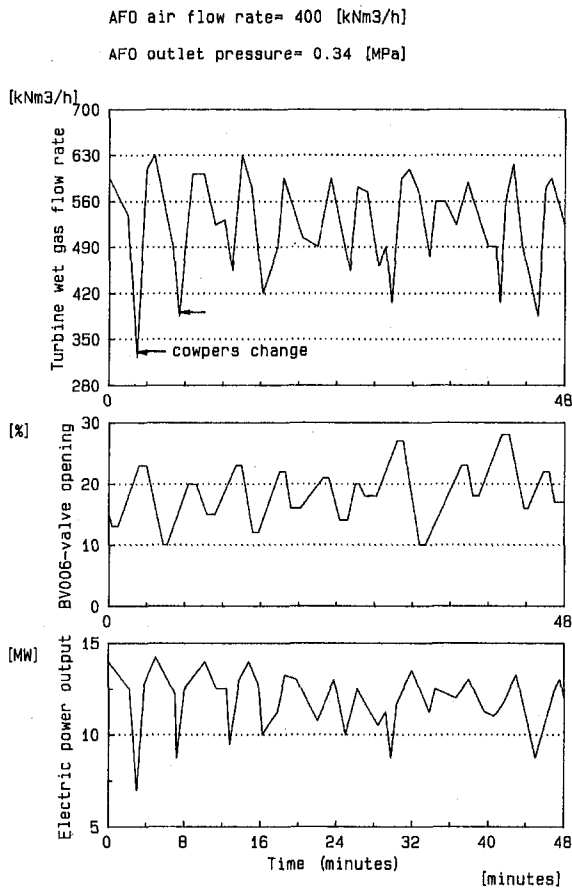
AFO air flow rate= 400 [kNm3/h]

AFO outlet pressure= 0.34 [MPa]

Fig. 12 Experimental investigation of the turbine gas flow rate and BV006 valve behavior (AFO air flow rate = 400 kNm³/h; AFO top pressure = 0.340 MPa)

tions can be made for the points B and C under real conditions (Fig. 16).

The assumption of normal operational conditions (560 [kNm³/h] of dry gas produced) and a required set point of 0.331 MPa, cannot be fulfilled, although the engineering specifications suggested a change in the angular position of the turbine ANC system from 55 to 80 percent. In actual operative conditions the turbine, in fact, cannot maintain, by itself, the expected set point value even though the angular position is increased above 80 percent (Fig. 15). Another interesting remark could concern the mean value of the air flow at the blast inlet. The design has been made taking into account a 53 percent volumetric percentage of nitrogen in the gas coke. A 2 percent variation of the nitrogen volumetric percentage in the gas leads to an estimated 4 percent variation of the dry gas produced.

Finally, since the blast furnace is also fed with enriching O_2 and CH_4, and since they take part in the reduction reactions occurring in the furnace, they contribute to increase the volumetric flows of dry gas produced in a way that was neglected in the design hypotheses.

In conclusion it can be stated that the turbine is not sufficient for the real operational conditions since its operative field of regulation is pretty limited, as shown in Fig. 16. In other words, the turbine is not self-sufficient for all the process regulation needs and there is a call for a larger service of the turbine SLAVE regulator in controlling the BV006 valve opening.

Experimental results, however, have shown an almost complete closing of BV006 valve that cannot be justified by the actual increases in flow. A further investigation had to be carried out to explain this behavior. The BV006 valve is controlled by a series of pulses and pauses; from the ANC system position

each pulse should correspond to a 5 percent variation of the valve maximum opening. To clarify such malfunctioning, an example can be made in which the service times of the turbine "SLAVE" regulator are neglected (proportional-integral action) and step variations are supposed. Assuming that at $t = 0$ the process variable set point is 0.33 MPa and that the furnace is fed with about 377 kNm³/h, that is to say about 560 kNm³/h of dry gas, from Fig. 15 it can be seen that the turbine is able to elaborate the whole flow of gas produced with an opening of 68 percent maintaining the set point value to the AFO top. Then let increase by about 6 percent the air flow at the blast inlet (400 kNm³/h) with subsequent production of dry gas of about 596 kNm³/h. Under these conditions the turbine is no longer able to maintain the set point value imposed even if it gets its maximum opening. At this point both BV006 and the turbine intervene as in Fig. 17, which represents the trend, calculated according to the proposed model of the process dynamic response.

From the analysis of Fig. 17 the following conclusions can be drawn:

- BV006 is masked by the variations of the ANC position and has no control on the pressure, so BV006 can be considered "independent" of the whole regulation system;
- during the pauses of BV006 the pressure is controlled only by the ANC, which is obliged, by means of several "opening-closing" actions, to follow not only the process trend but also the pressure variations caused by BV006;
- BV006 can be completely closed if, as shown by experimental results (Fig. 14), high-pressure values at the AFO top and low air flows at the blast inlet can be kept steady
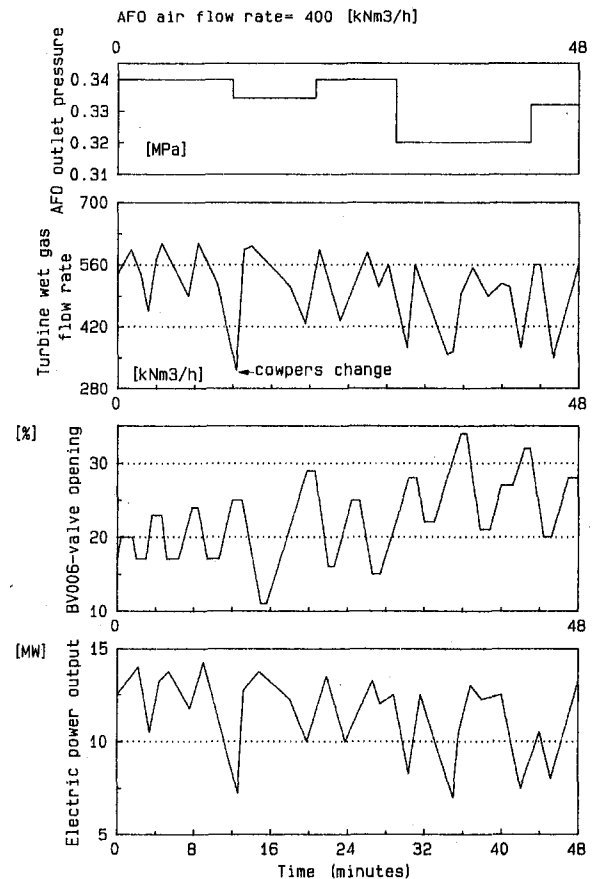

AFO air flow rate= 400 [kNm3/h]

Fig. 13 Experimental investigation of the turbine gas flow rate and BV006 valve behavior (AFO air flow rate = 400 kNm³/h; AFO top pressure ranging from 0.320 to 0.340 MPa)
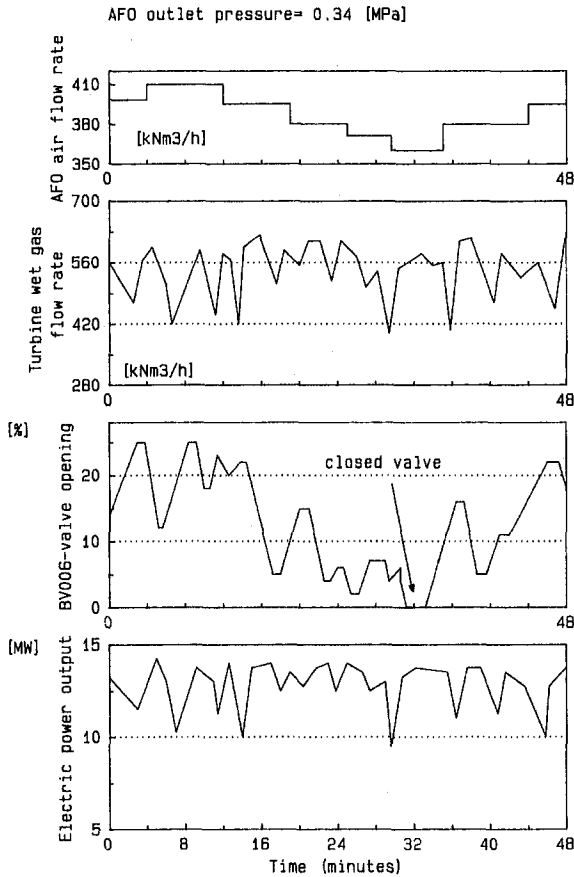
AFO outlet pressure= 0.34 [MPa]

Fig. 14 Experimental investigation of the turbine gas flow rate and BV006 valve behavior (AFO air flow rate ranging from 360 to 400 kNm³/h; AFO top pressure = 0.340 MPa)

for a certain time, that is to create those conditions leading the turbine to run with opening degrees lower than 65 percent.

Moreover, it should be considered that BV006 is a large throttle valve, functioning as an interception valve rather than as a regulation one, and being this, it is unreliable about the opening of 5 percent.
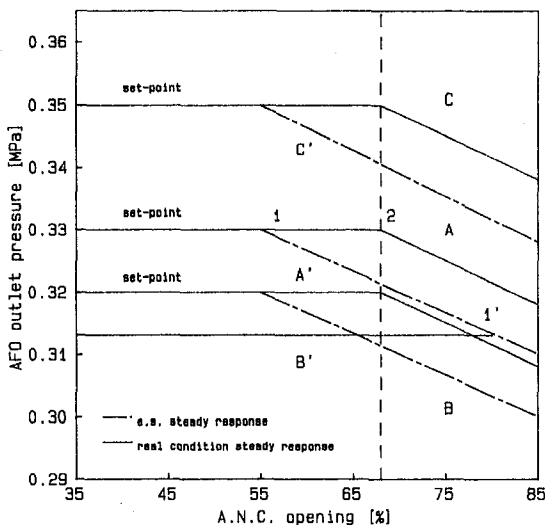
Such regulation caused the following effects:

Fig. 15 Turbine behavior in real gas conditions
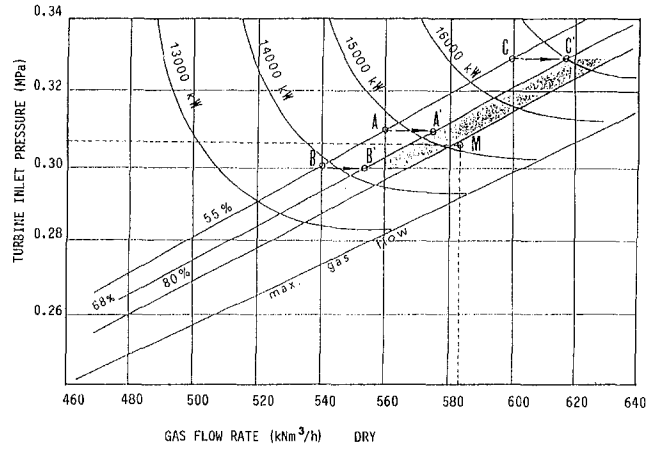

GAS FLOW RATE (kNm³/h)   DRY

Fig. 16   Turbine operating regulation map

- a bad pressure regulation at the blast-furnace top with a high oscillating behavior;
- an excessive stress of the turbine ANC system with subsequent problems of wear and maintenance;
- a loss of electric power produced by the turbine because of the excessive gas flows bypassed by the BV006 valve.

Suggested Solutions

According to the previous analysis, the solution to be suggested should re-examine the single components as well as the

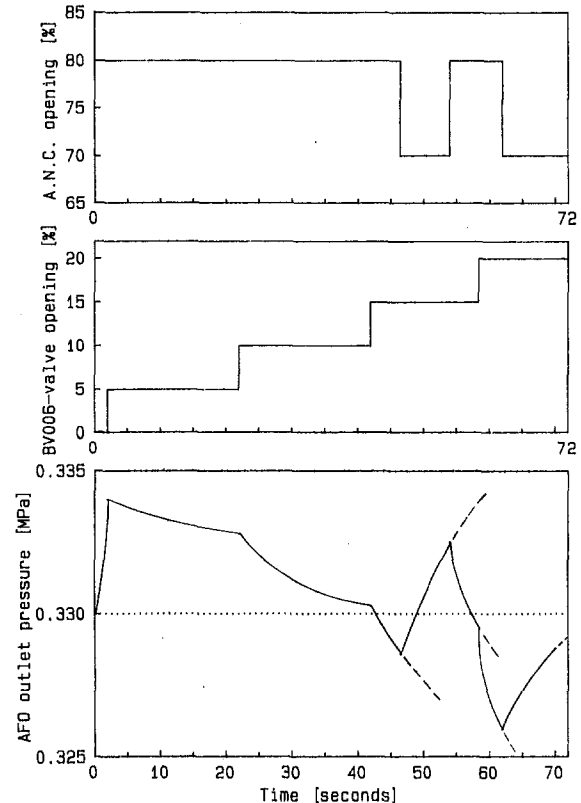AFO air flow rate= 400 [kNm3/h]

Dry gas flow rate= 596 [kNm3/h]

Fig. 17   Predicted behavior of the turbine and BV006 valve regulation (AFO air flow rate = 400 kNm³/h; AFO top pressure = 0.330 MPa)

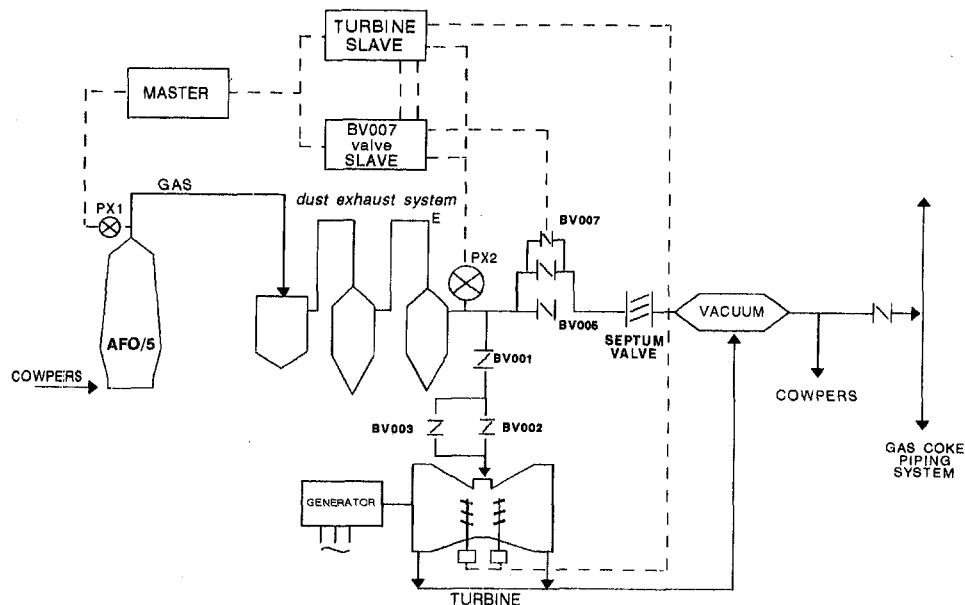**Journal of Engineering for Gas Turbines and Power**

Fig. 18 New regulation system asset with the new BV007 valve

operating logic of the regulation system. The installation of a second throttle valve (BV007), a smaller one, provided with a better regulating function, has been recommended; it has to bypass BV006 valve, which should intervene only under emergency conditions (turbine stop). The BV007 valve has a diameter of 500 mm with a range of 0.310–0.350 MPa and 50–100°C and has the same characteristic as the BV006 valve presented in Fig. 11. But it is not enough to replace BV006 with BV007 in the regulation without changing the operating sequence logic of the system. Even if the BV007 valve has a modulating action instead of a step-by-step one, it must carry out its regulating action according to the pressure variation and not, as it was by BV006, to the turbine ANC system opening. This is why BV007 has to be controlled by a "SLAVE" regulator having the same proportional band and the same information-transmission time as the "SLAVE" regulator of the turbine with which it must work in split range.

So, as shown in Fig. 18, the "MASTER" regulator must send its signal also to BV007 "SLAVE" regulator, which takes it as set point value and compares it with the pressure value coming from the PX transducer. At this point the interventions can follow this path:

1 ANC system in normal regulation
   BV006 and BV007 closed
   BV007 regulator inhibited
2 ANC position higher than 80 percent
   block of the ANC regulator positioned
   access to regulator BV007
3 valve BV007 position lower than 2 percent
   block of the regulator BV007
   re-access to regulator ANC

Such intervention logic should remarkably improve the regulation. In fact, considering the example made for BV006, using the same hypotheses and applying the simulation model created, the dynamic response trend shown in Fig. 19 will be obtained. In this figure it is clear that the new valve with the new regulation logic can bring the value of the process variable in the fixed set point in about 20 s without damaging oscillations.

At this point, it is possible to estimate the energy saving produced by the turbine as a consequence of the installation of the valve will be adopted in the new adjusting system using the valve BV007.

Diagrams of Fig. 12, 13 and 14 show that the medium value of the volumetric flow of wet gas bypassed by the valve BV006 is 40,000 Nm³/h and the pressure medium value upstream the valve is 0.315 MPa. It can be suggested that about 50 percent of this bypassed flow is subtracted to the turbine because of the inefficient regulation performed. So referring to the design conditions, the produced electric power can be evaluated following Eq. (1) that leads to an estimated average increase of 600
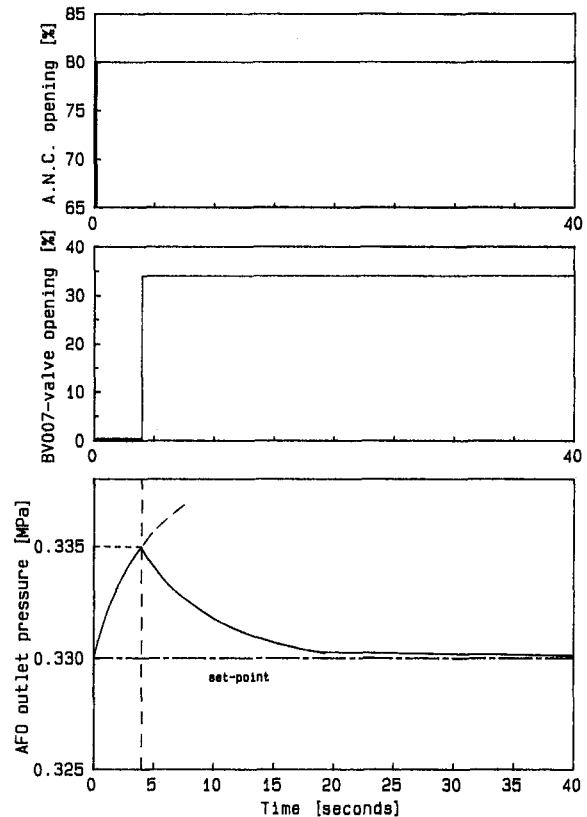

Fig. 19 Dynamic response of the process at the new operating conditions

kW in electric power to be saved. It has also been analyzed the possibility of obtaining a further saving by increasing the ANC system to values higher than 80 percent, as points 1, 2, 3, 4, and 5 of Fig. 20 show a quite good comparison with the design point A (normal running). Table 2 contains the summary of all data relative to the calculations done. The setting of the ANC system opening at values higher than 80 percent is not convenient. In fact, if the turbine inlet pressures are equal and of the order of 0.31 MPa, the ANC system opening varies from 80 to 90 percent, under real operational conditions. There will be a loss of net power at the turbine axis of about 1.5 percent, whereas in design there would have been an increase in power. The great difference between the mean value of electric power the plant can produce (a little lower than 13,000 kW) and the instantaneous power of the turbine as predicted in Table 2, are not surprising. In fact, apart from the estimated capacity of the electric generator (about 97.3 percent, the following factors [3, 5] should also be considered:

- the dust in excess in the gas makes the vane washing system function almost continuously, which limits the turbine power by 0.9 percent;
- the machine power is diminished by about 4.7 percent as seen during the final test.

Conclusions

The development of a mathematical model simulating the whole system and the regulation logic allows one to stress the failures of the engineering specifications. It also allows an accurate analysis of the system behavior during the different working conditions, which, on the other hand, were modified according to the engineering specifications. The original system presented a reduction in the energy recovery of the blast furnace because of an uncorrect regulation system.

The original regulation elements of the plant (a quite large throttle valve and an automatic regulation system of the orientation of the gas turbine stator vanes), were not able to keep steady the pressure set point value at the blast furnace top. In addition, the throttle valve responded to the ANC regulator, remaining always open. During its "pauses" the ANC system followed the pressure variations due to the process trend as well as the disturbances created by the valve itself.

The tests have also shown that the design parameters were below the operational standards with an unavoidable reduction
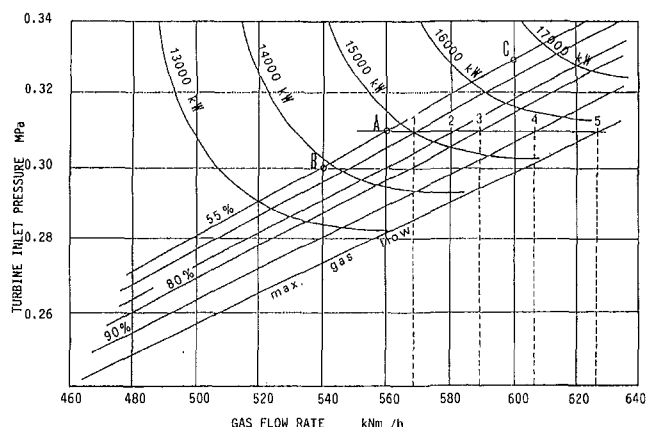
Table 2 Engineering specifications at operating conditions

POINT	% ANC	Engineering Specifications POWER	Engineering Specifications EFFICIENCY	Operating Conditions POWER	Operating Conditions EFFICIENCY
A	55	14820 kW	0.8796	15475 kW	0.8778
1	65	15000 kW	0.8793	15709 kW	0.8774
2	75	15217 kW	0.8742	15812 kW	0.8636
3	80	15400 kW	0.8712	15817 kW	0.8545
4	90	15604 kW	0.8579	15624 kW	0.8259
5	100	15708 kW	0.8352	15018 kW	0.7773

in the turbine regulating field, and that it was necessary that the two regulators intervene without overlapping their effects. Identifying the problem clearly, an accurate analysis of the regulation logic has been carried out, using the predictive model developed, defining a solution that tends to a more rational use of the components and to a higher exploitation of the gas energy level.

The regulation, now, relies on the turbine when the ANC system varies. It relies on the valve when the stator vanes are at their maximum opening, and it is necessary to stabilize the pressure values by bypassing the gas through the Septum.

The energy recovery of about 0.60 MW is quite good but the advantages of this regulation system lead to reduce the running wear of the ANC system and, above all, to stabilize the pressure value at the hopper.

As for the possibility of increasing the recovery by varying the value of maximum opening of ANC the calculation has stressed a power loss not mentioned in the design evaluations. The power loss is caused by a limitation of the turbine capacity due to the excessive dust in the gas and to a difference between the theoretical efficiency values of the plant and the real ones.

A theoretical approach of plant simulation is then indispensable during the design phase and must then be joined with an accurate simulation to verify outstanding running conditions to acquire a better knowledge of the plant possibilities and its regulation system as well.

Acknowledgments

Fig. 20 Turbine operating regulation map with ANC system set at more than 80 percent opening

References

1 Drigo, G., "Recupero di energia del gas di bocca di un altoforno a contropressione mediante turbina," Internal Report, Centro Metallurgico Sperimentale, Rome, 1982.

2 Hitachi TRT Turbine Technical Information, Official Report, Hitachi Zosen Co., Japan, 1981.

3 Hitachi TRT Turbines Procedure for Performance Test, Official Report, Hitachi Zosen Co., Japan, 1981.

4 Regulation Through Throttle Valves, Official Report, Nuovo Pignone S.p.A., Florence, 1974.

5 Caputo, C., "Final Test Report of the Gas Pressure Energy Recovery Implant for AFO-5 Blast furnace at Italsider Mill Plant in Taranto, Italy," Report, Rome, 1984.

6 Jemma, M "Oil Substitution and Energy Saving in Italian Experience," 12th Congress of World Energy Conference, New Delhi, 1983.

7 Manfrida, G., and Stecco, S. S., "Energy-Loss Modeling of Power Plants and Industrial Processes," presented at the 17th IECEC Conference, Los Angeles, 1982.

8 Stecco, S. S., and Manfrida, G., "Second-Law Analysis of Large Steam Power Plants at Nominal and Off-Design Loads," Paper No. 849011, 19th IECEC, San Francisco, 1984.

9 Flow of Fluids Through Valves, Fittings and Pipes, Crane Co., Chicago, IL, 1957.

Slot and Vertical Face Grinding of Aerospace Components

R. B. Mindek, Jr.
Weldon Machine Tool, Inc.,
York, PA 17404

T. D. Howes
Center for Grinding Research and
Development,
University of Connecticut,
Storrs, CT 06269

Workpiece profile accuracy, wheel wear, and thermal damage were investigated for the grinding of slots and vertical faces on MAR-M-247, Inconel 713C, and M-2 tool steel using both alumina and cubic boron nitride (CBN) grinding wheels. It was found when grinding with alumina wheels that the wheel corner and first 2.5 mm of the grinding wheel sidewall account for all the grinding forces in the vertical, horizontal, and transverse directions, and therefore is responsible for all the significant grinding done on the sideface of the workpiece. Since previous work links wheel wear and workpiece thermal damage during grinding to grinding forces, this finding suggests that the area around the wheel corner is the critical region of importance in grinding these types of profiles in terms of wheel wear and the heat input to the workpiece. These, in turn, are linked to workpiece profile accuracy and metallurgical damage. Results also show that striation marks inherent in sidewall grinding can be minimized by controlling the maximum normal infeed rate of the wheel. A method for minimizing the heat input into the workpiece by minimizing grinding force during vertical face grinding is also reported.

Introduction

Creep Feed Grinding Process Description. Creep feed grinding is a heavy stock removal machining process whereby components are manufactured with little or no further finishing required. The traditional role of grinding has been strictly as a finishing process. However, creep feed grinding has made it possible to remove significant amounts of material during the manufacture of components while still maintaining satisfactory dimensional accuracy and surface finish. The development of creep feed grinding has been part of a trend to extend grinding from the traditional role of finishing to one encompassing preliminary stock removal as well.

Initially, one of the main applications of creep feed grinding was in the aerospace industry, where nickel- and cobalt-based superalloys are frequently used. The machining of these materials provided a natural opportunity for the application of creep feed grinding since they were considered very "difficult to machine" by any other process, and because no other economically viable alternative existed. Powell (1979) states that its use has now evolved to the point where it is a competitive, high-efficiency production method for turbine blades, pump rotors, and automobile parts. Vane pump slots, splines in shafts, and retaining grooves in bearings are also produced using this method. It has recently been recognized that various other industries can benefit from creep feed grinding as well, such as the biomedical and computer hardware industries.

Other developments have occurred in parallel with the development of creep feed grinding, without which the process would not have become so successful or have achieved such widespread application. These include: the development of high-porosity alumina wheels, which enhance coolant penetration into the grinding zone; application of continuous dressing of the grinding wheel during grinding; and the development and manufacture of cubic boron nitride (CBN) grinding wheels, second in hardness only to diamond, and having significantly higher thermal conductivity than conventional abrasives.

Creep Feed Grinding Process Limitations. Creep feed grinding can save significant amounts of setup and down time during the production of a workpiece because it combines roughing and finishing into one operation. However, two major limitations affect the implementation of creep feed grinding. The first is wheel wear, which is generally represented in grinding as the ratio of the volume of stock removed over the volume of wheel material worn, or as the G-ratio. The higher the G-ratio, the better the wheel in terms of volume of stock removed before wheel redressing or replacement is necessary. Although wheel wear is important in all grinding processes, it is particularly important in creep feed grinding, since the ability to grind at higher depths of cut facilitates the grinding of profiled geometries, and grinding wheel life is a function of the wear rate of these geometries. The second limitation of the creep feed grinding process is "workpiece burn," which is a limitation in all grinding processes, but is magnified in creep feed grinding because of increased contact length and higher grinding power. The fundamental mechanism of "workpiece burn" or "burn-out" due to film boiling was first put forth by Shafto (1975). This phenomenon is characterized by a rapid rise in the workpiece temperature within the grinding zone. It occurs during the transition from nucleate to film boiling, at approximately 130°C for water-based coolants, as described by Andrew et al. (1985), when a significant drop in the heat transfer coefficient of the coolant is caused by the vapor barrier formed from coalescing nucleate bubbles. Surface damage can occur due to film boiling of the coolant during grinding, as past research by Andrew et al. (1985), Guo and Malkin (1994), Howes et al. (1993), and Powell (1979) has indicated that 'burn-out' is a function of the grinding parameters, wheel composition and coolant parameters used.

The increased power imparted to the workpiece during creep feed grinding is most often characterized using the specific grinding energy, U, defined as:

$$U = \frac{\text{Spindle power}}{\text{Stock removal rate}} = \frac{F_t * V_s}{V_w * a * b} \qquad (1)$$

where F_t = tangential grinding force, V_s = wheel speed, V_w = table speed, a = depth of cut, and b = width of cut. Higher power occurs in creep feed grinding relative to surface grinding because of higher specific energy and higher stock removal as found by Andrew et al. (1985) and confirmed by Guo and
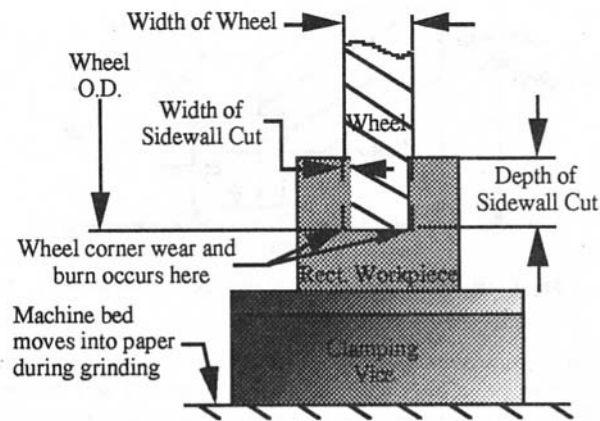
Fig. 1 Schematic of the slot grinding of a simple workpiece profile

Malkin (1994). Longer arc lengths and higher power during creep feed grinding also give rise to much more stringent coolant application requirements relative to surface grinding; increased arc length during creep feed grinding requires that sufficient coolant be available throughout the entire arc of cut in order to prevent permanent metallurgical damage. Thus, correct coolant application and optimization are particularly critical during creep feed grinding, as emphasized by Howes et al. (1993). Lavine and Jen (1991) also show that surface damage of the workpiece is a major limitation of the creep feed grinding process.

Process Limitations During Slot Grinding. A particular case of creep feed grinding is the creep feed grinding of slots, shown in Fig. 1. The grinding of vertical faces, that is of a single side of the slot shown, can be considered with slot grinding since the same mechanisms prevail. The wear and burn limitations present in the creep feed grinding of flat profiles are ever more critical in creep feed slot grinding and are currently problematic to industry. Two factors make these limitations more critical in the creep feed grinding of slots. The first is reduced coolant access to the interface between the grinding wheel and workpiece at the sidewall, which suggests an increased heat flux in this area. This effect is magnified by the critical nature of coolant application in creep grinding in general. The second is the wear mechanism(s), which occur in the critical region around the wheel corner. In slot grinding, the ability to hold tolerances on the corners is a function of the grinding wheel corner wear. Shafto (1975) showed that a clear and independent relationship exists between wheel wear and the maximum normal infeed rate, which occurs at the top of the grinding arc in creep feed grinding. Andrew et al. (1985), Hahn and King (1986), and Malkin (1984) have shown that a link exists between wheel wear and thermal damage to the workpiece. Thus, the ability to understand wheel corner wear is a necessary prerequisite to successful grinding of slots and vertical faces, and ever more critical relative to the difficult-to-grind materials often encountered in the aerospace and power generation industries. For this reason, a program was undertaken at the Center for Grinding Research and Development to understand the wear and thermal limitations during the creep feed grinding of these difficult profiles.

Vertical Face Grinding—Results of Alumina on MAR-M-247 and Inconel 713C

Table 1 shows grinding test results characterized by the amount of wheel usage (i.e., continuous dresser rate reduction) obtained during the grinding of profiled aerospace components during an Industrial Modernization Incentives Program (IMIP) recently conducted at the Grinding Center by Howes et al.

(1993). Operation #1, a spoiler, shroud top grind of MAR-M-247, is a predominantly flat profile, while Operation #2, a seal tip grind, Operation #3, a channel grind, and Operation #4, a straddle grind, represent grinds of predominantly vertical faces of Inconel 713C. The designation "NH-P" in Table 1 represents tests using nonoptimized production coolant nozzles. The other designations used for "Nozzle Type" in Table 1 represent optimized circular nozzles designed by the Grinding Center in order to improve coolant delivery into the grinding zone as described previously by Howes et al. (1993) and Mindek and Webster (1994). Table 1 shows that significant improvements in wheel usage are possible, using coolant optimization, for the grinding of a predominantly flat profile (i.e., for Operation #1). However, when a slot or vertical face is ground, as in Operations #2, #3, and #4, productivity improvements in the form of improved wheel usage are somewhat mixed. For example, significant improvement in wheel usage before burn was achieved when grinding a thin-walled form such as a seal tip, but only a slight improvement for the channel and straddle grind was realized, despite the fact that MAR-M-247, a "difficult-to-grind" material, was ground in Operation #1, relative to Inconel 713C, ground in Operations #2, #3, and #4. While coolant optimization is always desirable for a given application, the lower productivity increase observed when grinding vertical faces suggested that a better understanding of this particular case of creep feed grinding was necessary. And, since wheel wear had been linked to workpiece thermal damage, it was felt that a study should be conducted to understand better the mechanisms causing wheel wear during the grinding of vertical faces in order to

Table 1 Results of aerospace components grinding performed during an IMIP

Trial #	Dresser Feed Rate (% Baseline)	Rt. Noz. Flow (lpm)	Rt. Noz. Pressure (kPa)	Right Nozzle Type	Qualitative Burn Evaluation
Operation 1 - Spoiler, Shroud Top					
1	Baseline	72	827	NH-P	Fair-Poor
2	+32.3	72	827	NH-P	Fair
3	+61.8	72	827	NH-P	Fair-Good
4	+150.0	72	827	NH-P	Good
5	Baseline	72	827	NH-P	Poor
6	Baseline	72	827	NH-P	Poor
7	-26.5	341	248	19.0 mm D	Very Good
8	-26.5	303	200	19.0 mm D	Good
9	-26.5	303	200	19.0 mm D	Good
10	-26.5	303	200	19.0 mm D	Good
11	-26.5	303	200	19.0 mm D	Good
Operation 2 - Seal Tips					
1	Baseline	102	772	NH-P	Good
2	-37.5	102	772	NH-P	Good
3	-50.0	102	772	NH-P	Fair
4	Baseline	303	200	19.0 mm D	Good
5	-25.0	303	200	19.0 mm D	Good
6	-50.0	303	200	19.0 mm D	Fair
7	-62.5	303	200	19.0 mm D	Fair
Operation 3 - Channel					
1	Baseline	303	200	19.0 mm D	Good
2	Baseline	303	200	19.0 mm D	Good
3	Baseline	303	200	19.0 mm D	Good
4	Baseline	303	200	19.0 mm D	Fair-Good
5	-25.0	303	200	19.0 mm D	Fair-Good
6	-25.0	303	200	19.0 mm D	Fair
Operation 4 - Straddle					
1	Baseline	140	662	NH-P	Fair
2	Baseline	140	662	NH-P	Fair-Poor
3	Baseline	140	662	NH-P	Fair-Poor
4	Baseline	140	662	NH-P	Fair-Poor
5	Baseline	318	662	12.7 mm D	Good
6	Baseline	318	662	12.7 mm D	Fair-Good
7	Baseline	318	662	12.7 mm D	Fair-Good

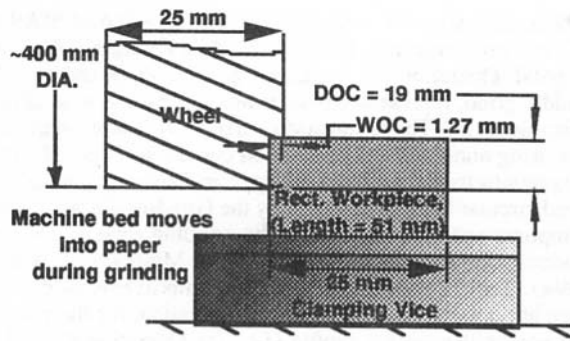Fig. 2 Grinding geometry

Fig. 4 Recessed grinding wheel geometry before grinding

facilitate prevention of workpiece burn and thermal damage during the grinding of these types of profiles.

Sideface Force Investigation

Definition of Grinding Conditions. Unless otherwise stated, all grinding tests reported in the sideface force investigation have used the grinding conditions shown below, using a setup as shown in Fig. 2: DOC/WOC = 19 mm/1.27 mm; CD rate = 2 μm/rev; table speed = 25–508 mm/min; Clnt. = VHP E200, 10 percent in water; wheel speed = 30 m/s; grinding mode = downcut; coolant flow = 231 lpm; wheel type = tyrolit, AO; coolant pres. = 386 kPa (rt.), 69 kPa (lt.); wheel spec. = 89A 60 H9; mat'l = MAR-M-247; nozzle type = 13 mm D, both sides.

Origin and Nature of Sideface Grinding Forces. Tests to investigate the origin and nature of the grinding forces during sideface grinding were conducted on a Blohm Profimat 412 creep feed grinding machine. Two wheel configurations were used. First, grinding tests were conducted with a plain-form wheel geometry having a flat profile on both the outside diameter and the sidewall. Second, identical tests were conducted with the same wheel recessed on the sidewall to determine whether or not grinding forces originate on the sidewall of the wheel. Figure 3 shows the transverse force during 11 grinding runs, each conducted at a table speed of 254 mm/min and a continuous dressing rate of 1 μm/rev, which are typical to industry. The first six runs in this figure shows sideface grinding using a plain-form (i.e., unprofiled) wheel. Note that the peak force during grinding is essentially constant for all six runs, which were done in succession. The last five grinding runs
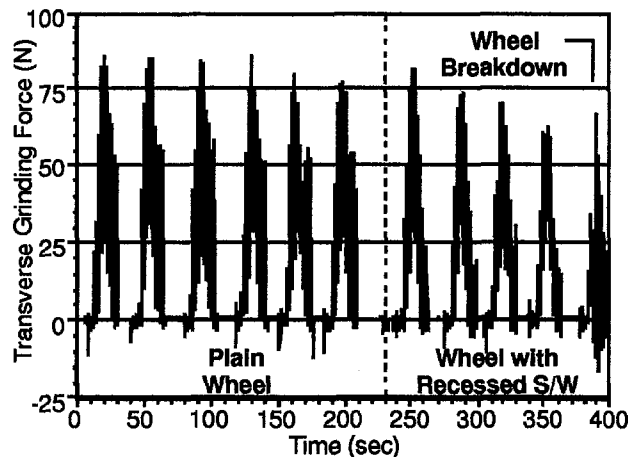

Fig. 3 Transverse grinding force of successive grinding tests with and without wheel recessed on S/W
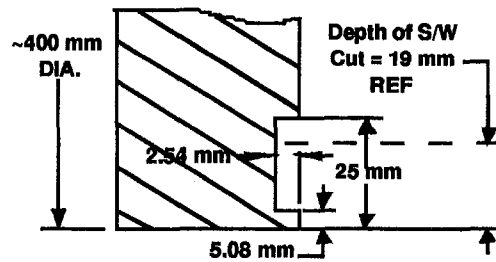
were performed at identical grinding and coolant conditions. However, prior to grinding, the wheel sidewall was recessed radially out to a radius of 5.08 mm less than the wheel radius, as shown in Fig. 4. Since continuous dressing was also used for these last five runs, the height of the sidewall decreased during each run. Despite this fact, the peak forces remained nearly constant for each run conducted with the recessed wheel, with the exception of the last run where the forces dropped because the sidewall of the wheel broke down during the grind. (The break occurred because continuous dressing caused the wheel outside diameter to decrease during each grind and fracture at the wheel corner as the dresser approached the recessed part of the wheel on the last run.) In addition, the peak force measured for the seventh run is shown to be identical to the runs measured for the plain-form wheel, proving that forces originate at the wheel corner and not the side wall.

Striation Pattern Investigation

Discovery of Striation Marks. While grinding sidefaces using the parameters and conditions specified above, we repeatedly observed an arcuate shaped striation pattern on the sideface. Because of their intermittent nature, these markings were first suspected to be caused by vibration of either the workpiece or the wheel during a grinding pass. This possibility was investigated by mounting an accelerometer on the back of a workpiece sideface and repeating several grinds. These tests confirmed that the vibration present did not correlate with the spacing of the striation marks.

Investigation of Wheel Corner Breakdown. After further study and observation of the previously ground workpieces, a noticeable change in fillet radius on the bottom of the workpiece sideface was observed after grinding at a table speed of 127 mm/min. This radius was always larger at the leading edge than the radius of the as-dressed wheel, but became sharper toward the trailing edge, where a corner profile very close to the as-dressed profile was observed. We thought that the fillet radius at the sideface corner was larger at the leading edge than at the trailing edge of the workpiece because, in the downcut mode using continuous dressing, the grinding wheel reaches its point of maximum wear just as the wheel breaks through the back edge of the workpiece, at which point wear rate begins to decrease and continuous dressing predominates and begins to return the corner profile of the wheel to its originally sharpened state. This process occurs because of the nature of the maximum normal infeed rate during the grind, which is defined as the normal infeed at the top of the grinding arc where the relative magnitude and direction of wheel and workpiece velocities create the highest relative infeed velocity. During the grind, the maximum normal infeed rate first increases as the wheel approaches its full depth of cut, remains constant at the full depth of cut, and then decreases as the wheel breaks through the back edge of the workpiece where the depth of cut decreases to zero. Because Shafto's (1975) results have shown that a unique relationship exists between maximum normal infeed rate and wheel wear, it was logical to investigate wheel corner breakdown as a function of maximum normal infeed rate of the
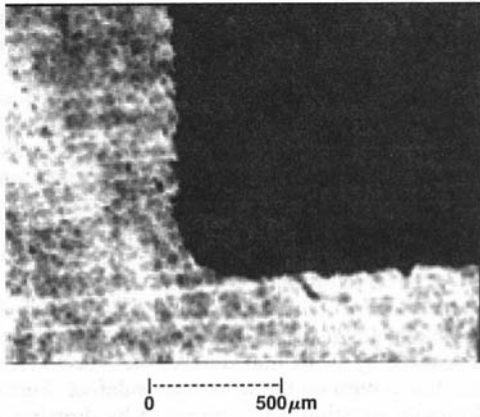
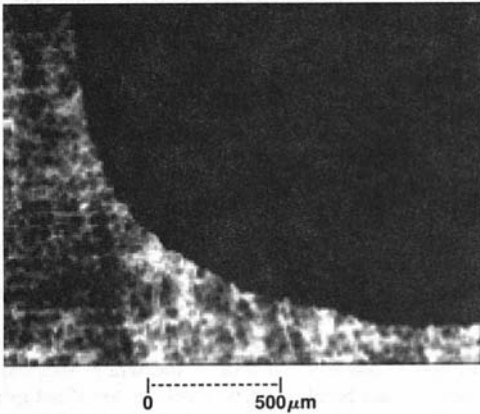Fig. 5(a)   Profile of S/W corner radius, full grind; 19 mm DOC, 1.27 mm WOC, 127 mm/min

Fig. 5(b)   Profile of S/W corner radius when MNIR occurs; 19 mm DOC, 1.27 MM WOC, 127 mm/min

workpiece into the wheel. Thus, the corner fillet radius is large on the leading edge of the workpiece because at the point in the grind when this surface is created, the wheel is just breaking through the back edge of the workpiece at the point of maximum wheel corner wear. However, as the bottom of the grinding wheel traverses along the workpiece, creating the corner profile, continuous dressing gradually overcomes wheel wear after the wheel breaks through the back edge of the workpiece. At this point, the corner fillet radius created gradually becomes sharper as the wheel moves across the workpiece to the trailing edge. We believed that, if the striation marks were the result of corner wheel break-down caused by the maximum normal infeed rate mechanism, some low feed rate should exist at which the wheel break-down would not occur, thus eliminating the striation marks on the sideface. To test this theory, a workpiece was ground successively at table speeds of 127, 102, 76, 51, and 25 mm/min. After examining the workpiece sideface after each grind, striation marks were observed at each table speed except 25 mm/min, where only extremely light streaks were present. Further tests were performed to confirm the explanation for the cause of fillet radius change on the workpiece from the leading edge to the trailing edge. Several workpieces were ground at both 25 and 127 mm/min, stopping in the middle of the grind so that a coupon of the wheel profile could be taken. In these tests, both continuous dressing and dressing of the wheel side-wall were employed. Coupons of the wheel profile were also taken after each full grind. Figure 5(a) shows the profile of the grinding wheel corner after a full grind at 127 mm/min table speed. The corner radius of the wheel measured in this case was 0.13 mm, consistent with fully dressed (as-dressed) wheels,

based on previous tests with a wheel of this specification. Thus, no evidence of wheel corner wear occurring during the grind remains. However, Fig. 5(b) shows the wheel corner profile at 127 mm/min when the grind was stopped at the point of maximum wheel wear. Here, the corner radius was measured to be 0.89 mm, seven times the radius of the as-dressed corner, which proves that significant wear occurs during the grind. When this same grinding pass was continued to the end of the full grind, the radius was again the same as in Fig. 5(a), that is, 0.13 mm. Both calculation and measurement of the change in wheel diameter caused by continuous dressing indicate that the amount of wheel dressed during one grinding pass is of the same order of magnitude as the wheel radius measured during the middle of the grind. Thus, it is likely that continuous dressing has removed the worn corner of the wheel observed during the middle of the grind and returned the wheel corner profile to its originally as-dressed shape by the end of the grind. It was also observed that when a low table speed of 25 mm/min was used, the wheel corner wear rate was low such that the corner profile was maintained throughout the entire grind at the as-dressed radius of 0.13 mm, as shown in Fig. 5(a), and no measurable wheel corner break-down occurred during the grind.

In summary, the evidence shows wheel corner break-down at a table speed of 127 mm/min, where striation marks are observed on the workpiece sideface. In contrast, no evidence of wheel break-down occurs at 25 mm/min, where an improved surface finish is observed on the sideface. This evidence led to the conclusion that wheel break-down, as related to the mechanism of maximum normal infeed rate, was primarily responsible for the striation marks observed throughout the sideface grinding tests.

Vertical Face Grinding Using CBN

Vertical face grinding using a CBN resin bond wheel on M-2 tool steel was conducted to determine whether the same wear mechanisms prevailing with alumina also prevail with CBN. The following grinding conditions were used: DOC/WOC = 6.35 mm/0.127 mm−0.508 mm; HP jet = 1000 psi; coolant = VHP E200, 10 percent in water; table speed = 25−508 mm/min; clnt. flow = 292 lpm; wheel speed: = 45 m/s; clnt. pres. = 655 kPa (rt.), 69 kPa (lt.); grinding mode = downcut; wheel type = CBN resin bond; nozzle type = 13 mm D; wheel spec. = 60/80-R100-B10; mat'l = M-2 tool steel.

Results show that a striation pattern occurs on the workpiece sideface when ground with a CBN resin bond wheel, similar to the pattern observed after grinding with alumina wheels. In addition, a horizontal line is consistently observed across the length of the workpiece, about halfway up the sideface, and appears to coincide with the height at which the corner fillet on the wheel meets the vertical face on the sideface of the workpiece.

The same techniques used with alumina wheels to get rid of marks on the workpiece sideface were employed with the CBN wheel in order to remove similar marks observed on the work-piece sideface, that is, truing the wheel sidewall and grinding at a very slow infeed rate of 25 mm/min. The surface roughness of on-machine measurements of the wheel O.D. and sidewall, respectively, immediately after truing show that the runout on the wheel sidewall after truing, measuring about 25 μm, is larger than the trued O.D. surface, but smaller than the untrued sidewall. Using sidewall truing of the wheel and an infeed rate of 25 mm/min, we were able nearly to eliminate both the striation marks and the horizontal line after one grinding pass. However, on subsequent grinding passes, the marks came back. It is not clear why the marks came back so quickly, and further tests are planned to confirm these results. Thus far, the evidence suggests that the wheel corner radius, initially measured to be about 0.10 mm R immediately after truing, breaks down to a radius approximately equal to the width of cut taken on the
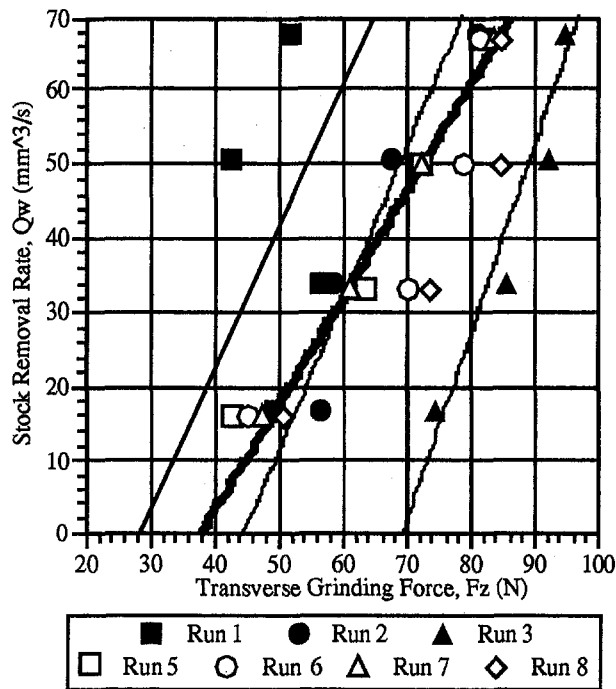
| ■ Run 1 | ● Run 2 | ▲ Run 3 | |
| □ Run 5 | ○ Run 6 | △ Run 7 | ◇ Run 8 |

Fig. 6 Two- and three-nozzle configurations, with and without hp cleaning and redressing of the wheel sidewall

series of tests were conducted with a high-pressure jet (500 psi) directed at the wheel sidewall in order to clean the wheel during grinding as is typically done for CBN wheels on their O.D., with a third cooling nozzle aimed at the wheel sidewall, and with dressing away of the worn abrasive grits between grinding runs. The results of these tests, labeled as Runs 4–7 in Fig. 6, show that the transverse threshold force and WRP remained nearly constant, giving a consistent wheel sharpness on the wheel sidewall, as indicated by the dark black line fitting these data in Fig. 6. In addition, no workpiece burn on the sideface was observed throughout these tests.

In summary, wheel sharpness tests showed that, although wheel sharpness remained constant throughout, increased grinding force, caused by swarf imbedded in the wheel sidewall and worn grits, led to burn on the workpiece sideface. Furthermore, this undesirable situation was eliminated by dressing away of the worn grits, in-process cleaning of the wheel corner and sidewall during grinding, and application of generous cooling in the grinding zone, especially between the wheel sidewall and workpiece sideface.

Conclusions

The following conclusions have been reached from this research:

1 Grinding of flat and vertical profiles on aerospace components suggests that workpiece burn and thermal damage is more likely to occur when grinding vertical profiles. This implies higher wheel usage in production in order to keep the grinding wheel corners and sidewall clean and sharp.

2 Sideface grinding forces are produced by the wheel corner and approximately 2.5 mm of the wheel sidewall.

3 Wheel corner breakdown as it relates to infeed rate, which appears intermittent in nature, is the primary cause of striation marks that are consistently observed on the workpiece sideface after grinding.

4 The presence of significant wheel corner wear occurs during creep feed grinding but may be hidden by the effect of continuous dressing, which tends to restore the corner profile as the wheel breaks through the trailing edge of the workpiece during reduced, maximum normal infeed.

5 The mechanism for CBN wheel corner wear appears to be similar to that for alumina wheels. However, more work is necessary to confirm these preliminary findings.

6 Initial evidence suggests that the grinding wheel corner develops a radius equal to the width of cut taken during the grinding of a vertical face.

7 When using alumina grinding wheels to grind vertical faces, grinding force minimization, leading to reduced incidence of burn on the sideface of the workpiece, is encouraged by removal of worn grits, in-process cleaning of the wheel corner and sidewall, and generous cooling of the grinding zone, especially at the wheel/workpiece sidewall interface.

Acknowledgments

References

Andrew, C., Howes, T. D., and Pearce, T. R. A., 1985, *Creep Feed Grinding,* Industrial Press, Inc., New York.

sideface of the workpiece. This has been confirmed by sidewall grinds using a width of cut of 0.13 mm, where the wheel broke down to a radius of about 0.18 mm in just two passes, and by sidewall grinds using a width of cut of 0.51 mm, where the wheel broke down to a radius of about 0.51 mm after 20 grinding passes. Further tests are planned to substantiate these findings.

Maintaining Wheel Sharpness

The effectiveness of a grinding wheel's ability to grind is often characterized by its sharpness, defined by Hahn and King (1986) as the slope of the stock removal rate versus grinding force plot. This slope is better known as the work removal parameter, WRP, and is usually determined for a particular wheel/workpiece combination. In order to determine the wheel sharpness at the wheel corner and critical surrounding region, wheel sharpness curves were developed for a Tyrolit alumina wheel (spec. 89A 60 H9) on M-2 tool steel for vertical face grinding. After first dressing the wheel O.D. and sidewall, a two-nozzle cooling configuration (i.e., one at each end of the workpiece), and a continuous dressing rate of only 0.125 μm/rev were used to grind the vertical face of a workpiece with the intention of finding the wheel sharpness on the corner and sidewall. It was found that the wheel sidewall became discolored and plugged with workpiece swarf, changing the wheel sharpness characteristic on the sidewall with time. In addition, severe workpiece burn developed on the sideface of the workpiece throughout the tests. This effect can be seen in Runs 1–3 of Fig. 6, which shows a relatively constant work removal parameter, WRP, on the wheel sidewall, but a change in the transverse threshold force for these runs (lighter curve fit lines), which were performed without cleaning or redressing the wheel sidewall between grinding runs. Recalling Eq. (1), we see that increased grinding force increases the specific grinding energy, thereby increasing the grinding power and heat flux into the workpiece. Thus, increasing force is the likely cause for the increase in sideface burn observed throughout the tests. Another

Guo, C., and Malkin, S., 1994, "Analytical and Experimental Investigation of Burnout in Creep-Feed Grinding," *Annals of the CIRP,* Vol. 43/1, pp. 283–286.

Hahn, R. S., and King, R. I., 1986, *Handbook of Modern Grinding Technology,* Chapman & Hall, New York.

Howes, T. D., Webster, J. A., and Mindek, R. B., Jr., 1993, "Optimization of Fluid Application in Creep Feed Grinding," IMIP Final Report, Contract #F33657-91-C-002, Univ. of Connecticut, Center for Grinding Research and Development.

Lavine, A., and Jen, T. C., 1991, "Thermal Aspects of Grinding: Heat Transfer to Workpiece, Wheel, and Fluid," ASME *Journal of Heat Transfer,* Vol. 113, pp. 296–303.

Malkin, S., 1984, "Grinding of Metals: Theory and Application," *J. Applied Metalworking,* Vol. 3, No. 2, pp. 95–109.

Mindek, R. B., Jr., 1993, "Sidewall Force and Wear Investigation Using an Aluminum Oxide Wheel," personal communication to T. D. Howes and J. A. Webster, Center for Grinding Research and Development.

Mindek, R. B., Jr., and Webster, J. A., 1994, "Minimizing Thermal Damage of Aerospace Components Using Coolant Nozzle and Coolant System Optimization," *Proc. 5th International Gas Turbine Institute of the ASME,* Portland, OR.

Powell, J. W., 1979, "Application of Grinding Fluid in Creep Feed Grinding," PhD Thesis, Univ. of Bristol.

Shafto, G. R., 1975, "Creep Feed Grinding," PhD Thesis, Univ. of Bristol.

G. v. Esebeck
ME Department,
Technical University of Berlin,
10623 Berlin, Federal Republic of Germany

M. Kising
Fraunhofer Einrichtung für
Zuverlässigkeit und
Mikrointegration,
13355 Berlin, Federal Republic of Germany

U. Neuhof
ME Department,
Technical University of Berlin,
10623 Berlin, Federal Republic of Germany

Investigation on Ceramic-Metal Joints for Shaft-Hub Connections in Gas Turbines

This paper shows possibilities for joining ceramic rotors to metal shafts. The investigations presented include exemplary joining methods for shaft-hub connections for ceramic rotors in gas turbines, as positive, permanent locking, or a combination of both. Active brazing as well as the combination of brazing or adhesive bonding and positive locking are discussed. Different shaft-hub connections were tested. The results of experimental investigations as static shear, bending, and torsion tests as well as dynamic torsion tests will be presented. In addition to the experimental investigations, finite-element analyses were made. Elastic calculations on simple geometries have shown the influence of different parameters like the thermal coefficients and the geometry at the joint face. Calculations were done to reduce the induced tensile stress in the joint and to increase carrying capacity. The calculations were also transferred to the shaft-hub connections to optimize the geometry of the joint faces.

Introduction

Ceramics are used when the limits of metals with respect to corrosion and resistance to high temperatures as used in engines or turbines are reached. The advantages of ceramics in comparison to metals are their resistance to high temperatures and abrasion, low heat conductivity and low weight. Ceramics based on silicon nitrides and carbides are of special interest for use in gas turbine rotors concerning high temperature and resistance to corrosion. An essential disadvantage of ceramics is their brittleness, which has to be taken into consideration, especially in the design phase. Hybrid ceramic-metal devices are often the only possible solution if monolithic production is difficult. Technical reasons and high costs depend on the volume and complexity of the workpiece or the local loading conditions.

Many characteristic features of technical products are decisively influenced by connections and joining methods. Particularly the integration of ceramic components into a metallic system has to correspond with the design and development and joining method. The increasing demands of technical products lead to higher stress in materials and components.

Automotive engines are one example of this. The latest developments indicate a comeback of gas turbines. Higher technical efficiency could be realized by elevated gas inlet temperatures. Brazed ceramic metal joints have high residual stress states due to different thermal expansion coefficients and this often leads to their failure.

The investigations presented will show how tensile stress states can be reduced by varying the shaping of the joints. In addition the strength behavior can be improved by using positive locking. Only a few geometries are useful to join ceramic rotors to metal shafts in gas turbines or turbochargers. The investigations (experimental tests and theoretical calculations) were closely related to the high specifications (speed, torsion, and temperature) under working conditions.

The development of the design and right choice of joining methods requires deeper knowledge in manufacturing technics and material properties. Up to now there are no active filler metals able to withstand the high thermal loading conditions.

Recent Research

The rapid increase of turbochargers in the last years has two main reasons:

- Substantially greater gas mileage can be realized by using turbochargers in commercial vehicles, mainly where diesel engines are used.
- Turbochargers in passenger cars are used to enlarge the model line of vehicular engines, and as with commercial vehicles, to increase the gas mileage.

Every major car company sell vehicles with turbochargers. Usually the operation temperature is between 850 and 1200°C at the turbo wheel and the maximum speed is between 40,000 and 130,000 min^{-1}. To reduce inertial and bending stress, the turbocharger has to be small (Zinner, 1985). Ceramic rotors consist mostly of hot pressed silicon nitride (HPSN) and hipped reaction bonded silicon nitrides (HIPRBSN) (Huber and Heinrich, 1989).

The decreasing strength and of course the increasing costs of ceramic devices with a big volume force the separation of rotor and shaft of the turbocharger. This led to new problems, namely, the joining of ceramic rotors to metal shafts. Preliminary investigations of the joint face design were based on a tension rod principle. But high speed and high gas inlet temperature forces the search for other design solutions. New principles have to be based on a design with a ceramic shaft and not a centric hole in the ceramic rotor.

In later years most research activities aimed at the joining methods shown in Fig. 1. The applied joining methods can be divided into shrink fitting and active brazing. When shrink fitted metal shafts on ceramic stumps rotate at high speed, high stresses affect the expansion of the metal shaft. Additionally, different thermal coefficients make high oversize of the fit necessary especially under elevated work temperatures. Recently active brazing has been one of the most intensively investigated joining techniques for ceramic joints. During the brazing process, high residual stress states occur in the ceramic metal joint when cooling down. Therefore, interlayers with a low thermal coefficient and a good deformability were applied to minimize the stresses.
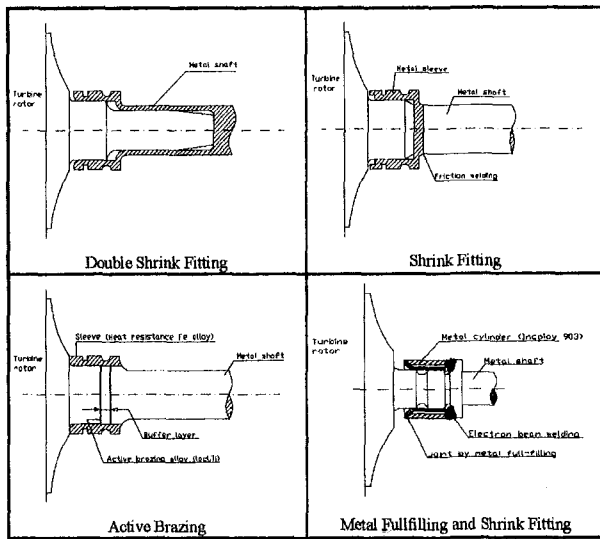
Fig. 1 State-of-the-art joining methods used in Japan (after Katano et al., 1993, and Shimizu et al., 1990)

Fig. 3 Ceramic–metal specimens for shear testing with grooves in the metal joint face

Different Design Variants

The different investigated joining methods are permanent locking and the combination of permanent with positive locking. Yet positive locking has not been tested; only numerical calculations were made.

A speed of 150,000 min^{-1}, a gas inlet temperature of about 1400°C, and a torsion moment of nearly 20 Nm are taken into consideration for the design of shaft–hub connections presented in this paper. At the moment the creep resistance of Ag-based filler metals doesn't allow more than 600°C at the joint area. For the following investigations the geometry of the ceramic rotor (HPSN) was simplified to a disk to reduce the costs.

Permanent Locking. Figure 2 shows different designs of actively brazed joints. These basic investigations were made to show the influence of shaping on the strength behavior.

Ceramic–metal joints should not be stressed in tension or bending but in pressure or shear strength. A symmetric specimen design was chosen in order to keep the equilibrum conditions for the basic investigations. On the one hand the joint faces were grooved for softening, and on the other hand parceled out for minimizing residual stress states (Fig. 3).

Figure 4 shows a possible design of a ceramic rotor joined to the metal shaft by active brazing with an intermediate layer consisting of a tungsten-base alloy. Figure 4 also shows the simplified geometry for the basic investigations to optimize the angle between ceramic and metal.

Positive and Nonpositive Locking. The most promising joining method is positive locking with a three-lobed polygonal profile. By using this profile, the self-centering of the connection
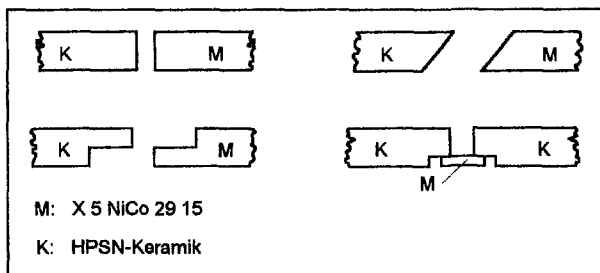
is realized and the profile can be manufactured relatively easily on the ceramic shaft.

Another possibility for joining metal shafts to ceramic hubs is shrink fitting. In this case the heated metal shaft is pushed on the ceramic shaft. Referring to the properties of ceramics, it is always an advantage that the ceramic part is loaded under pressure. Shrink fitting is already used in combination with metal filling, as shown in Fig. 1. Preliminary calculations have shown that fitting without any additional layers causes overly high stresses, so intermediate layers have to be integrated.

Combination of Permanent and Positive Locking. The joining method used for the combination of permanent and positive locking was first invented for adhesive bonding. The adhesives used for these components are epoxy and inorganic adhesives. Epoxy adhesives are characterized by high strength, high elasticity, and good filling ability. However, they can only be used up to maximum temperatures of 300°C. Consequently the use of organic adhesives in turbochargers would lead to ceramic rotors with long shafts and therefore to high volumes. So only inorganic adhesives can be used for joining components in gas turbines.

The main features for this joining method with adhesive preforms are (Esebeck and Beitz, 1993):

- placing shaping surfaces by adhesive preforms at disposal for the purpose of load transmission
- anti-adhesive properties of the modeling connection partner for the purpose of releasing it from the joint
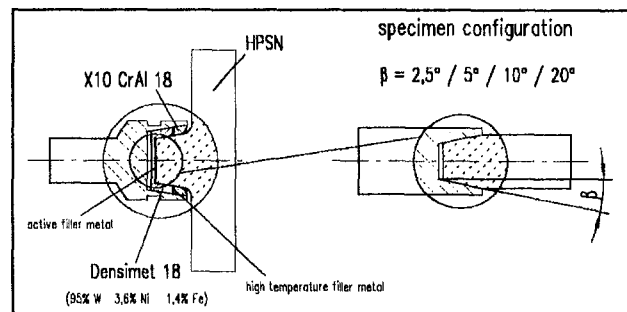

Fig. 2 Different design of ceramic–metal joints (selection)

Fig. 4 Design of a ceramic–metal joint using active brazing for a ceramic rotor
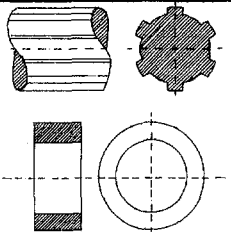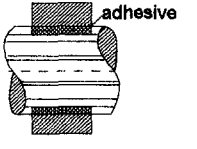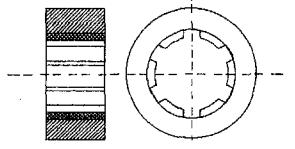
phase	connection partner shaped / smooth	work steps
conditioning		prevent adhesion on the modelling partner and support adhesion on the smooth partner
joining	adhesive	bond joining partners and carry out adhesive hardening process
releasing		seperate connection partners

Fig. 5 Joining method with adhesive preforms

The first attempts to transfer this joining method with adhesive preforms by active brazing instead of adhesive showed that this method had to be modified. Gap widths greater than 0.2 mm are difficult to fulfill with filler metals by active brazing and additionally the bonding of the shaped connection partner to the component has to be prevented, so that the joining method was changed by using shaped tubes, shown in Fig. 6.

The use of inorganic adhesive preforms with a three-lobed polygon profile provide a promising joining method. The preforms are realized on the ceramic shaft, because of its easy
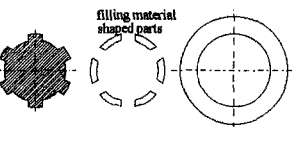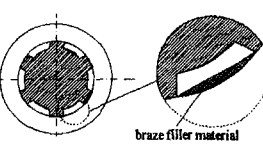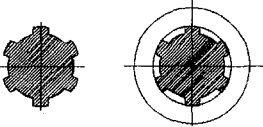
phase	connection partner shaped / smooth	work steps
conditioning	filling material shaped parts	annealing the metal sleeve
joining	braze filler material	positioning of preforms and brazing filler metal and carry out the brazing process
releasing		separate connection partners

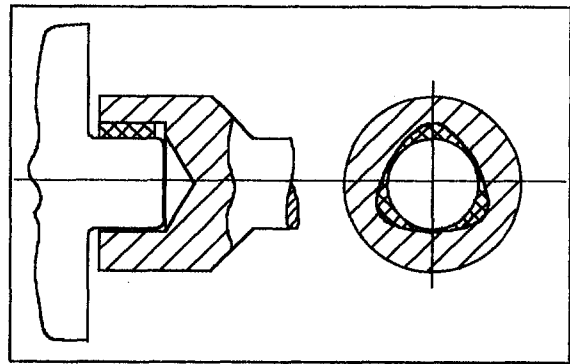Fig. 6 Joining method with braze preforms (Esebeck and Beitz, 1993)

Fig. 7 Realized three-lobed polygonal profile with an inorganic adhesive preform

manufacturing. Figure 7 shows the solution of a three-lobed polygonal profile for gas turbines without an axial fixing.

Experimental Results

Test Equipment. The ceramic–metal specimens as shown in Fig. 3 were tested in a furnace with an adjustable three-zone heater. To guarantee a constant testing temperature of 600°C in the region of the specimen, the upper and lower heaters were set to 800°C and the middle heater to 600°C.

As soon as the three zones reached the desired testing temperature, the specimen was inserted. After 10 minutes the testing temperature reached 600°C, which was measured with a thermoelement in the specimen. The testing force was increased at a rate of 5000 N/min. The number of samples for static tests exceeded seven, excluding sampling inspections. The test equipment also includes torsion test machines, which allow static and dynamic torsion tests of the shaft–hub connections. The machines are equiped with a heating device up to a temperature of 1000°C.

Permanent Locking. Brazed joints with a diagonal joint face show the best strength behavior. The fracture ran orthogonal to the longitudinal axis of the specimen. The bending

1 support
2 support whith ceramic
3 specimen
4 chuck
5 ball and socket joint of HPSN
6 chuck
7 cylindrical screw
8 punch
9 safety ring
10 metallic disc
11 metallic tack
12 upper punch gadget
13 clamb
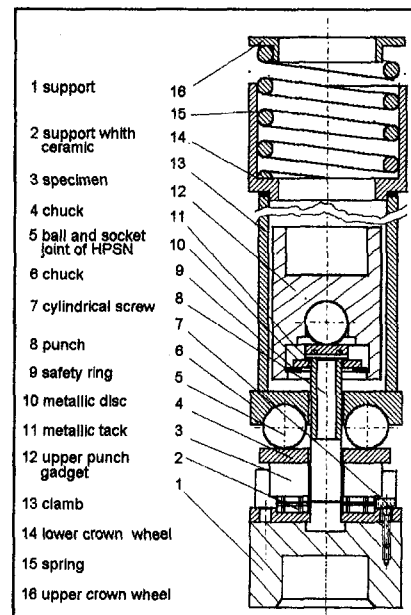14 lower crown wheel
15 spring
16 upper crown wheel

Fig. 8 Equipment for testing ceramic–metal specimens at high temperatures
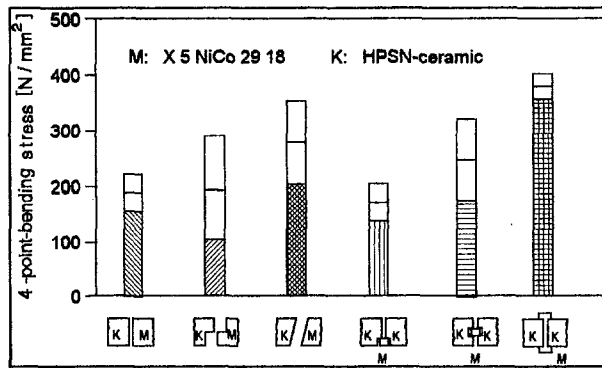
Fig. 9 Maximum bending stress in relation to different joint geometries

Fig. 11 Static torsion tests of different shaft–hub connections with inorganic adhesive preforms (Esebeck and Beitz, 1993)

strength was 30 percent higher in comparison to straight joints. Brazed joints with positive locking, especially with an "I"-profile, gave the highest strength values (Fig. 9, on the right side). The fracture was close to the "I"-profile and had a spherical shape.

The shear strength of brazed joints HPSN-X 5 NiCo 29 18 is similar to that of HPSN-Ck 45 (Fig. 10). Metallic joining faces with two grooves do not improve the shear strength. If the joint face is parceled in small fields there is an improvement of strength, but only for joints of HPSN to steel Ck 45.

Combination of Permanent and Positive Locking. Several previous experimental tests with adhesive and braze preforms have shown the carrying capacity of this joining method. Compared with brazing, the inorganic adhesives show much lower strength, but can be used up to temperatures of 1000 to 1200°C. Figure 11 shows the maximum torsion shear stress of inorganic adhesive preforms with three-lobed polygonal and with spline profile. Due to the high compressive strength of inorganic adhesives, the polygonal profile has higher strength values than the spline profile. The polygonal profile only has an abrupt failure after very high torsional strain, but at lower strain high twisting angles appear (2.5, 5, or 9 deg) on the metal shaft in the ceramic hub.

Figure 12 shows that the shear strength of the shaped braze parts can be increased by varying the geometry of the metal tubes. The absolute torsion shear strength values refers to the hole in the ceramic disk, otherwise the relative torsion shear strength values refers to the effective brazed surface. Using optimized metal tube shapes of Ck 45 cracking always occurred owing to high internal stresses.

Experimental tests of the dynamic torsion shear strength have shown the high carrying capacity of adhesive and braze preforms at high cycling lives (Esebeck, 1994).
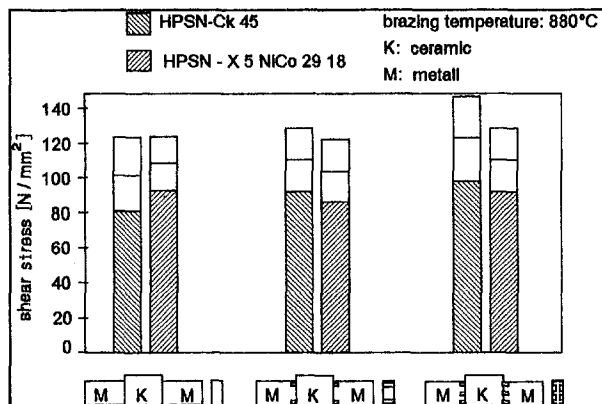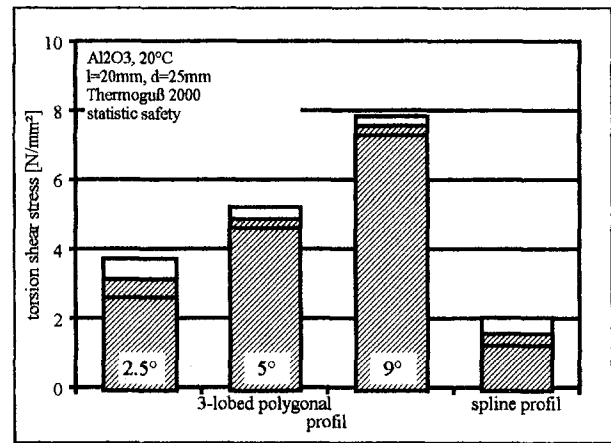
Results of Numerical Investigations

The objective of investigations with FE analysis was to show how the geometry of the connections has to be shaped for reducing residual stress states. Most of the calculations were carried out running linear elastic properties of the material. This led to very high stress values; nevertheless, calculations still can be used for design optimization. The influence of the geometry is very high, especially for brazed connections. Internal stress failure can be prevented by optimizing the geometry.

With the help of elastic calculations, residual stresses were investigated in ceramic–metal joints along the borderline between ceramic and filler metal. Joining faces and specimen designs were varied in respect to decrease the stress maxima at endangered points.

As shown in Fig. 13, the residual stress course at the border of the specimens (the joint face of the metal was grooved/Nut1) shows lower residual stress values at critical points than specimens without grooves (NutO). In comparison with the aligned border (lower curve), finite-element calculations showed double residual stress values at the stepped ceramic to metal border (upper curve).

Figure 14 shows FE calculations for brazed different shaped shaft–hub connections with permanent locking (brazing). Con-

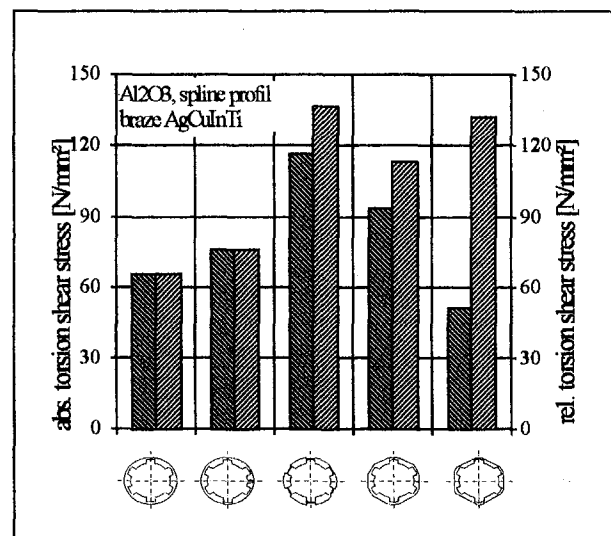Fig. 10 Maximum shear stress for different grooves in the metal part

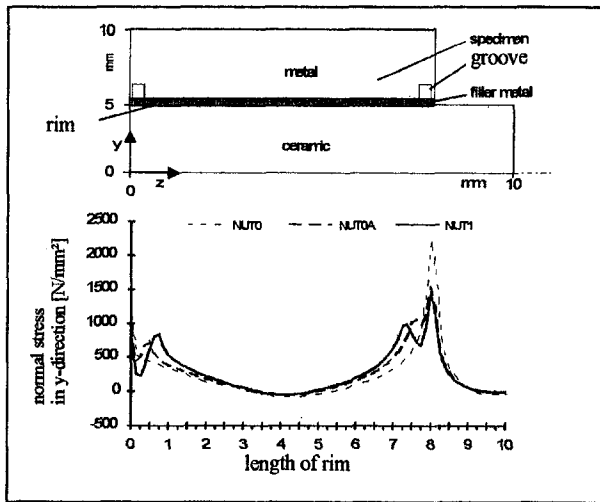Fig. 12 Maximum torsion shear stress of brazed tubes in relation to the geometry

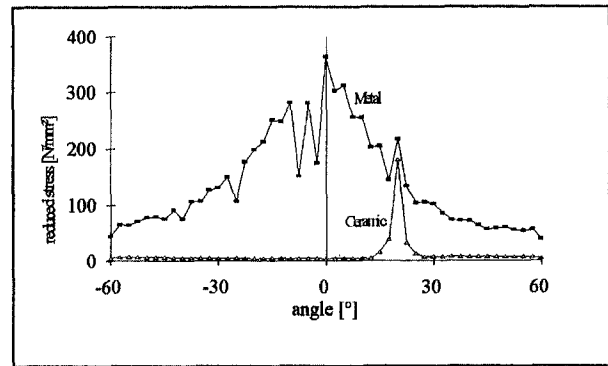Fig. 13 Specimen and normal tensions that goes alongside the border edge from ceramic to filler metal

Fig. 15 Tendency of the reduced stress in a positive locking with a 13 mm three-lobed polygonal profile

0 deg is at the head of the profile. The metal shaft is highly stressed, but uncritical due to high tensile strength values (upper curve). Ceramic is stressed much lower and fulfills the requirements of such applications (lower curve).

figuration No. 4 leads to reduction of the internal stress to about 1861 N/mm², that is, less than 60 percent of the inital state (No. 1).

Preliminary calculations of ceramic–metal joints by positive locking show the low stress state under working conditions, Fig. 15. The figure shows the course of the reduced stress at the contact area of the three-lobed polygonal profile. The angle

Summary

The joining of metal shafts to ceramic hubs were investigated by the use of form elements. Joining technologies as active brazing and adhesive bonding were used. Specimens with different joint faces showed for ceramic–metal connections with positive locking the best four-point bending strength values. The influence of soft joint faces has been investigated on small ceramic–metal specimens as well.

On HPSN-Ck 45-joints with highly different expansion coefficients, the parceling of Ck 45 joint faces led to increased shear strength values. No increase of the strength behavior was established at HPSN-X 5 NiCo 29 18-joints.

Torsion tests of Al_2O_3-cast steel shaft hub connections with inserted anorganic three polygonal form elements pointed to a strength value of 8 N/mm². Active partial brazed shaft hub connections with inserted form elements showed high torsion shear values. The amount of the relative torsion shear value was about 130 N/mm².

The investigations were accompanied by FE calculations. Normal stress values decreased about 30 percent in the specimen, when nutes were inserted on critical points. Active brazed shaft hub connections with different joint geometries showed at critical points residual strength tolerances of about 40 percent. Dynamic tests revealed for shaft hub connections with inserted active brazed form elements a permanent load value of 39 Nm, which is based on a life probability of 90 percent.

No.	sketch	max. tensile stress at the free edge of the ceramic [N/mm²]
1		3119
2		2045
3		2080
4		1861

Fig. 14 FEA calculations of different brazed geometries

Acknowledgments

References

Esebeck, G. v., and Beitz, W., 1993, "Investigations on the Behaviour of Shaft–Hub Connections and Screw Connections of Ceramic and Metal With the Help of Adhesive and Braze Form Components," Third Euro-Ceramics, Faenza Editrice Iberica.

Esebeck, G. v., 1994, "Tragfähigkeit von stoffschlüssig hergestellten Formschluβverbindungen für keramische Bauteile," Dissertation, Technical University Berlin, Schriftenreihe Konstruktionstechnik, Berlin.

Huber, J., and Heinrich, J., 1989, "Keramik im Verbrennungsmotor," *Fortschrittsberichte der Deutschen Keramischen Gesellschaft,* Vol. 4.

Katano, Y., Ando, M., Itoh, T., and Sasaki, M., 1993, "Application of Ceramics to Turbocharger Rotors for Passenger Cars," ASME JOURNAL OF ENGINEERING FOR GAS TURBINES AND POWER, Vol. 115, pp. 9–16.

Kising, M., 1994, "Einfluβ von Werkstückgestaltung und Fertigungsbedingungen auf das temperaturabhängige Festigkeitsverhalten von Keramik-Metall-Lötverbindungen," Dissertation, Technical University Berlin–Düsseldorf, VDI-Verlag.

Shimizu, T., Takama, K., Enokishima, H., Mikame, K., and Tsuji, S., 1990, "Silicon Nitride Turbocharger Rotor for High Performance Automotive Engines," SAE Technical Paper.

Zinner, K. A., 1985, *Aufladung von Verbrennungsmotoren,* 3rd ed., Springer Verlag, Berlin.

W. E. Masincup
Auxiliary Gas Turbines/Depot Branch,
Naval Sea System Command,
Arlington, VA 22307

J. S. Bryan
Advanced Engineering and Research
Associates (AERA),
Arlington, VA 22307

L. M. Ochs
Auxiliary Gas Turbines/Depot Branch,
Naval Sea System Command,
Arlington, VA 22307

Development of an Interactive Electronic Technical Manual

For a number of years, the Navy has been pursuing a means of reducing or eliminating the amount of paper carried on board ship. In particular, technical manuals consume large amounts of storage space. The paper provides a case study of the development of a gas turbine technical manual into an interactive electronic (computerized) format. This paper presents some of the difficulties of the development process, enhancements that have been developed, software selection, graphics complexity, and hardware definition. In addition, a detailed description of a final product will be provided.

1 Introduction

The problem of stowage on Navy ships has long been a significant driver in ship design. For several years, the Navy has been pursuing ways to reduce the volume of paper carried on board each ship, particularly technical manuals. To this end, the Advanced Technical Information System (ATIS) was developed. ATIS displays scanned images of technical manual pages and ship's drawings on a personal computer screen. The images are stored in raster format on an optical disk. ATIS provides a platform to display paper manuals in an electronic format. However, at the time it was developed, the technology was not sufficiently advanced to be able to convert existing manuals into a truly interactive format.

To be termed interactive, an electronic manual must possess "intelligence." It must be able to accept input from the user, interpret it, and use it to facilitate the communication of information to the user. It should lead the user through a logical progression of information contained in diverse areas and, possibly, many types of media; i.e., text, drawings, animations, sound, and/or video.

The technology of today presents previously unimagined opportunities for the efficient development of interactive manuals. The same advancements also provide the basis for effective life cycle management of the product.

As with any new technical product, the standards are continually being defined, making it difficult for published requirements to keep pace with changing definitions. There are many professional quality Interactive Electronic Technical Manuals (IETMs) being produced and delivered in a variety of formats that will meet or exceed defined standards when they are established. There are also IETMs being produced and delivered that will not meet those standards.

Prior to initiating any consideration of an IETM project, it is imperative that two actions be completed; attain a solid functional understanding of what an IETM is and clearly define the goals and expectations for your specific application. You may have to view more than a dozen IETMs before these items are solidly in your grasp, and, with it, a solid foundation for your project. In addition, a process for the development and maintenance of the IETM must be clearly defined.

2 Development of an IETM

2.1 Definition of an IETM. The traditional definitions of what an IETM is share many similar attributes. The shared characteristics of IETM definitions are:

(*a*) The technical manual is in a digitized form on a suitable medium, viewed by means of an automated authoring system.

(*b*) It is designed for electronic screen display to an end user.

(*c*) The format and style of the presented information are optimized for screen presentation to assure maximum comprehension.

(*d*) The elements of technical information are so interrelated that user access to the information they require is facilitated to the greatest extent possible and is achieved by a variety of paths.

(*e*) The computer-controlled IETM Electronic Display Device (EDD) can function interactively (from user request and information input) in providing procedural guidance, navigational directions, and supplemental information.

(*f*) Varying degrees of interactivity, automated information links, graphics sophistication, and functionality are available.

Various classes of IETM have been defined dependent upon their interactive functionality. However, these classifications should not be considered as constraints on a development process. It is more advantageous to begin by defining the functions needed in a specific IETM and tailoring the development process to the need rather than selecting a class that may or may not meet application needs.

2.2 Preplanning. There are numerous considerations when embarking on an IETM project, and little written guidance to follow. Many of the lessons have been learned at great expense, both in schedule slippage and expended labor hours. From that experience, we have prepared a list of items that are highly desirable prerequisites to the initiation of IETM development:

(*a*) The technical content for the system is mature and well documented or this is a new system where all material will be prepared from the onset to IETM requirements.

(*b*) The IETM authoring system is mature and stable. No prerelease versions of development software are used.

(*c*) The IETM developer is familiar with the selected IETM software and end-user target audience.

(*d*) The IETM developer has in-house subject matter experts (SMEs).

(*e*) The IETM product is clearly defined based on customer expectation and concept of use including the operating platform (hardware) requirements.

(*f*) The project team consists of individuals experienced with IETM design, development, and production.

(g) The customer is part of the design team.
(h) The customer has objective written acceptance criteria.
(i) A quality assurance plan and organization are in place.

2.3 Customizing IETM Attributes. The characteristics possible for an IETM application are limitless, but must be defined prior to beginning the development process. Items which must be defined are:

(a) Goal of the application (instruction, information, reference, or a combination).
(b) Level of interactivity (text links, graphics links, level of user response, situational simulations, etc.).
(c) User controls and interface (cuing, "buttons," windows, etc.).
(d) Simulations, if any (animations, video, sound, etc.).
(e) Graphics (line drawings, color, use of three-dimensional models, animations, video, photographs, etc.).
(f) Sound, if any.
(g) Hardware limitations, if any (will existing hardware be used or can new hardware be defined?).

2.4 The Development Process. Scripting the IETM prior to doing any development at the keyboard is essential. A script is an outline of the program flow and the links between various parts of the IETM.

The scripting process should incorporate liberal reviews that include the customer, programmers, graphics and sound developers, animators, scripters and SMEs. This allows timely editing

of material and prevents programing impacts as well as ensuring the customer's vision parallels that of the rest of the development team. Absolutely no programing of a section should occur until the scripting and story boards for that section are approved by the customer.

Story boards illustrate the actual program but in a paper format. All screens, text, user interfaces, program structure, navigation information, and computer file names are defined on story boards. Thus, the story board contains all of the necessary information for graphic and programing personnel to transition the information to electronic format.

During the programing process, incremental reviews should be held based on the development of each program module. These reviews will likely reveal problems that were not apparent in the paper format. The problems found are generally minor in nature and present no serious schedule impact if prior script and story board reviews were thorough.

After all module reviews are complete, the entire program should be installed and tested on a minimum of three hardware systems not used in the development. This will reveal any installation problems that are likely to be experienced, allowing a timely resolution. A representative of the end user group (e.g., ship's force personnel) should participate in the final testing.

Note that during the development of and definition of the hardware and software for an IETM, a process to maintain and update the manual must be concurrently designed. The specifics of how the process will work will depend upon the organiza-
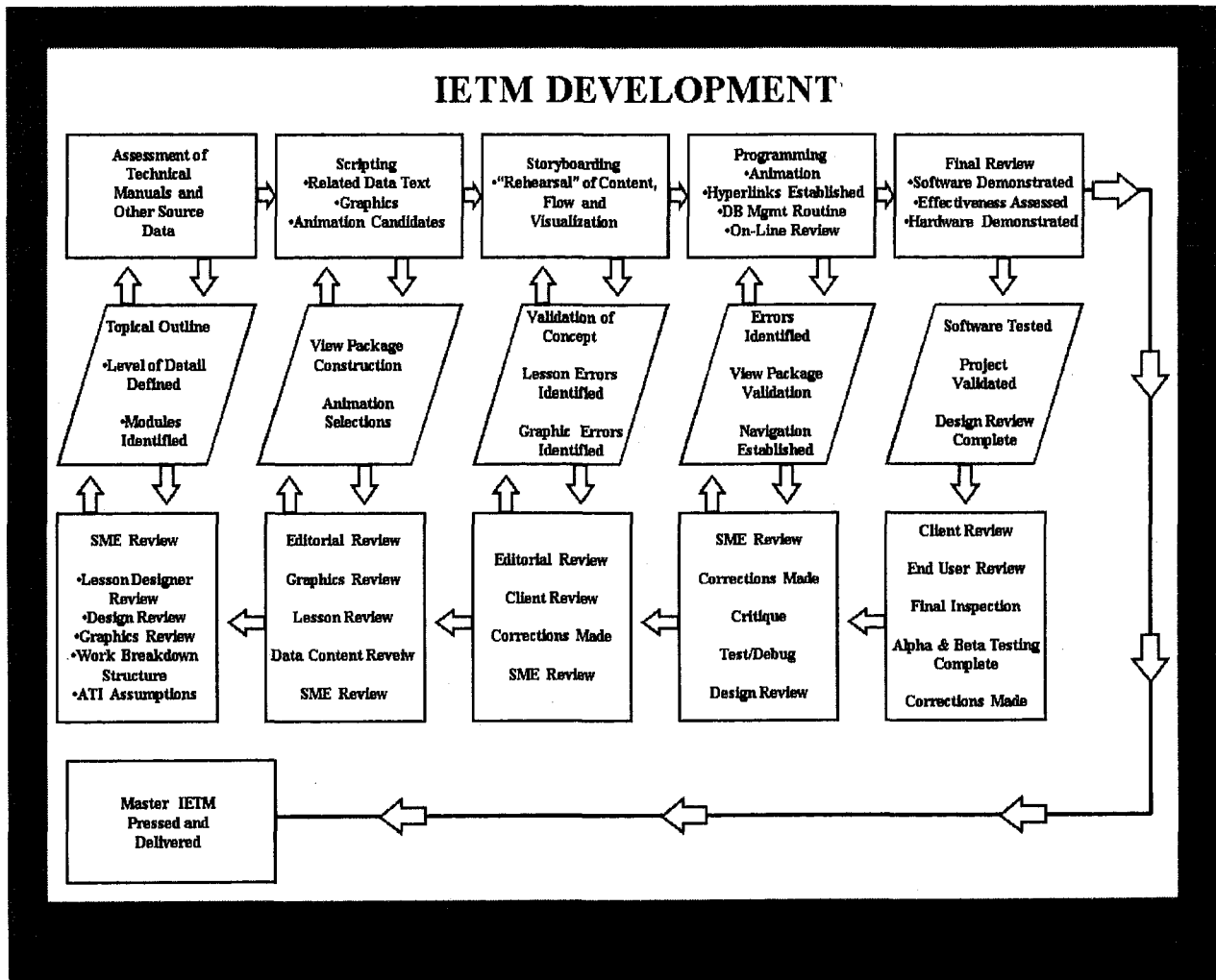

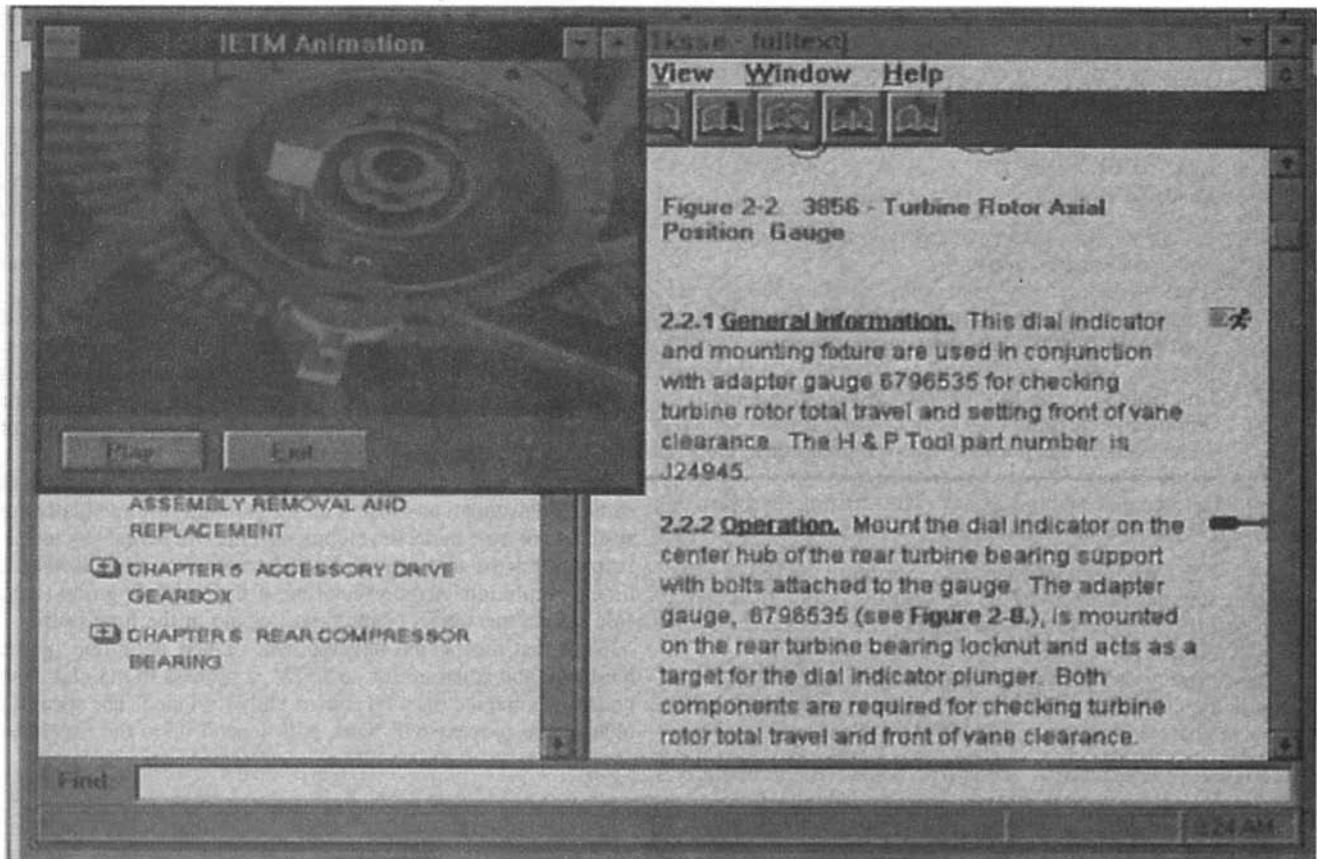Fig. 1 Sample IETM development process

Fig. 2 Typical IETM Screen

tional relationships between users and IETM managers. One approach is shown in Fig. 1. The large amount of interaction between the various elements in the development process are required due to the iterative nature of IETM development.

3 The Final Product

An IETM developed for the Allison 501-K17 Special Support Equipment will be used for the purpose of illustration. The

Fig. 3 Example Quick Reference Guide Screen

manual was originally developed in paper format and later converted to an IETM linked via hyper media and hypertext to a Quick Reference Guide and Specific Maintenance Task Index. The Quick Reference Guide and Maintenance Task Index were developed specifically for use on a computer with text and animations. Thus, some elements of several of the defined classes (MIL-M-87268) of IETMs were integrated into a hybrid IETM that incorporates both linear and hierarchical characteristics into a single IETM.

3.1 Equipment Requirements. The hardware defined for viewing and manipulating this IETM consisted of a minimum 386/33 MHz personal computer with the capability to display 640 × 480 pixels in 256 colors (VGA), running in Microsoft Windows 3.1. It was decided that it would have 4 MB RAM, and a CD-ROM. This configuration was chosen after surveying the end users to identify the available hardware. The decision was made that no significant advantage would be realized in this application with an upgrade to the hardware already available.

3.2 Electronic Manual. The paper manual was converted to an IETM format by taking the original text files and tagging them using Standard Generalized Markup Language (SGML). The tagging process was governed by a Document Type Definition (DTD) standard that defines structure for every SGML document instance in the IETM. The SGML tagged text was imported into a Commercial-Off-The-Shelf (COTS) document display system. Links were established within the manual to provide rapid access to figures and information referenced in other parts of the manual. This step simply converted the paper manual to a user-friendly electronic format, but did not truly make it a fully interactive document.

Scripts and story boards for the Quick Reference Guide and Maintenance Task Index, which established the links between them and the electronic manual, were then prepared. Numerous
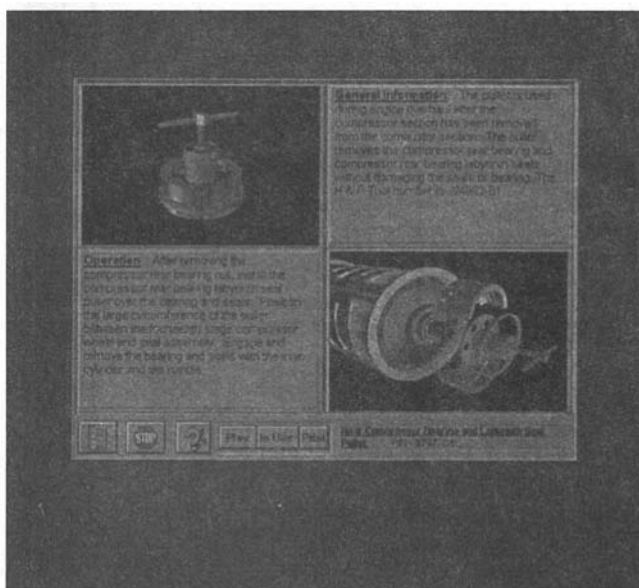
reviews were held to critique the scripts and story boards as each section of the manual was completed. The process continued into the actual program development.

Figure 2 is a typical screen from the IETM. The window in the foreground is an animation from the Quick Reference Guide showing how the tool being described in the manual is used. The Play and Exit buttons start the animation and close the window. The window is accessed from the IETM by double clicking on the icon of the running person at the right side of the IETM screen. The text in the left column of the screen is from the paper manual. The highlighted text indicating ''Figure 2.8'' is a hot link, which allows the user to call the figure up on the screen. The left side of the IETM window contains the table of contents for the manual.

3.3 Quick Reference Guide and Maintenance Task dex. The Quick Reference Guide and Maintenance Task Index are actually two menu systems providing links to the same data. The Quick Reference Guide allows the user to access and view text description of a tool, its uses, and animated views of the tool alone and in use on the engine. These tools can be accessed by part number or nomenclature. Figure 3 is an example of a screen from the Quick Reference Guide.

The Maintenance Task Index arranges the information to accomplish specific maintenance tasks by presenting selected procedures and via hyper links to other relevant information (tool animation, parts lists, etc.).

4 Conclusions

Interactive Electronic Technical Manuals represent a significant improvement in the way technical information can be stored, presented, and used. A cohesive team effort that considers, first and foremost, the needs of the end user, along with the concerns of programmers, graphic and sound developers, SMEs, scripters and animators from initial planning, through delivery and on to the life cycle of the IETM will yield a high-quality and useful product.

Life Cycle Considerations in Propulsion Alternatives for Fast Vessels

D. L. Luck

GE Marine and Industrial Engines,
General Electric Company,
Evendale, OH 45215

Fast vessels are being built and operated for a large range of passenger-carrying applications. Fast cargo-carrying vessels are being considered in a variety of sizes as well. A major decision in design and construction of these vessels is the propulsion system; this decision has major impacts on the operation economics as well as the operational capabilities of the vessels. Factors involved in consideration of propulsion alternatives for fast vessels are examined, with emphasis upon the total life cycle operating implications of these factors. A methodology for considering the factors is suggested, and an example is presented with results of the consideration tradeoffs.

Background

Commercial ships in recent years have relied primarily upon diesel engines to provide propulsion power. The size of the vessel and its operating profile determine the particular configuration of diesel engine, the decision being among low, medium, or high-speed diesels. Low and medium-speed diesels are used for large vessels where the weight and volume of these engines are acceptable. They are able to burn lower quality, cheaper fuel, making them economical to operate.

High-speed vessels, usually defined as those that exceed 30 knots, which have come into use for car and passenger ferry operations, use high-speed diesels or gas turbines as the propulsion systems of choice. The definition of diesel speed ranges is not universal, but for this paper high-speed diesels will be defined as those with output greater than 900 rpm. The choice of whether to use diesels or gas turbines has been determined primarily by the type of the vessel and its power requirement.

Small high-speed vessels that are dynamically supported, i.e., those that are not strictly displacement-type hulls, are usually very weight sensitive. Examples are foil-borne vessels and air cushion vessels. In most cases these vessels make use of gas turbines if the power requirement is at least 3 MW, because gas turbines have a much lower specific weight than diesels.

Large high-speed vessels with power requirements in excess of 30 MW have also found gas turbines to be the best propulsion choice, but for a different reason. For these vessels the lower specific volume of the gas turbine is attractive, because these vessels are volume sensitive. They are carrying low-density cargo, passengers, and vehicles, and the large volume necessary for a medium or low-speed diesel would be unacceptable.

The category of fast vessels that requires power in the 10 to 24 MW range represents a choice that is not so clear. In this size vessel, high-speed diesels are available that can provide the required power with a weight and volume that is not prohibitive. Because the specific fuel consumption of these engines is generally better than available gas turbines, the initial inclination of ship builders and ship operators is toward the diesel. Recent careful examination of all factors have led to consideration and selection of gas turbines for high-speed vessels in this power range. The reasons for these selections and a review of considerations in the choice are examined below.

Gas Turbine Applications

Gas turbines have gained wide acceptance in military ship applications since the early 1970s when newer generation aeroderivative engines were applied by the U.S. Navy and many international navies. Reliability and ease of maintainability have become well established [1]. A variety of configurations has been applied including ships with all gas turbine propulsion, and combinations of gas turbines with diesel engines. Operational considerations such as low noise generation have provided operational advantages for gas turbine propulsion in military ships. The military vessels are generally volume sensitive because of the large manning requirement and the requirement for combat systems.

Commercial vessels have made use of large volume, heavy diesel engines for ships that could accept the physical requirements of these engines. Acceptance of gas turbines for small weight-sensitive ships is exemplified by the Boeing Jet Foils and the Kvaerner Fjellstrand Foilcats. These vessels have power requirements less than 10 MW but are exceptionally weight sensitive because of their dynamic lift. Vessels with dynamic lift are more like airplanes than ships in propulsion selection. It is therefore to be expected that low-specific-weight propulsion systems such as gas turbines will continue to be almost universally chosen for applications of this type.

Large volume-sensitive ships have in recent years also made use of gas turbines for propulsion. Discussion of such applications was provided in [2, 3]. The types of ship in this category include large fast ferries such as the Aquastrada class, the Stena High-Speed Sea Service class, and roll on/roll off vessels such as the U.S. Navy Sealift vessel currently under construction. In addition, several cruise vessels, which are also quite volume sensitive, are being considered for application of gas turbine propulsion.

Medium Power High-Speed Vessels. Commercial vessels with power requirements up to 24 MW range, which are volume sensitive, represent a competitive situation between high-speed diesels and gas turbines. The limits of this power range are somewhat arbitrary. The high end is determined more or less by the maximum available power from four high-speed diesels at about 6.0 MW each. This level of power represents the current requirement of a number of fast ferry designs that have been successfully introduced into the market. Two or four gas turbines can deliver the same power, and therefore represent a lower weight and volume alternative for ship designers and operators. The considerations bearing on this decision are discussed in the following paragraphs, with indications of a quantitative basis for comparison.

Comparison of Propulsion Characteristics

Weight. The lower specific weight of gas turbines compared to high-speed diesels clearly will reduce the total propulsion system weight for a given power requirement. Less obvious is the fact that for a required vessel load capability, the displacement (total weight) of the vessel can be made less, and therefore the power required for a given speed is reduced. This fact must be taken into account in determination of fuel consumption, lube oil consumption, and maintenance. Direct comparison of specific fuel consumption between propulsion alternatives, i.e., the fuel consumption per unit power, can lead to an erroneous conclusion. Because of the lower propulsion weight, greater range may also be achieved by carrying additional fuel if the operating profile demands it.

Total propulsion system weight must be included in any comparison between alternatives. The predominant elements are always the prime movers including all auxiliary supporting systems required. These auxiliary systems include fuel, lube oil, cooling water/air as required, inlet and exhaust ducting and silencers. The weight of foundations to support the systems is also a significant contribution to the total.

A second advantage of the lower specific weight is that power margin is available. For example, the 24 MW of power available from four high-speed diesels may be exceeded by two gas turbines at a lower total weight. The additional power and lower weight provide an excess power margin, which can ensure that speed can be maintained under adverse sea conditions. This capability is particularly important in a scheduled ferry operation where schedule adherence is critical to a successful operation.

Fuel and Lube Oil Consumption. Comparison of total fuel consumption should be made for a given payload delivery capability, because vessels are designed to deliver a particular load at a required speed. The total power requirement is dependent upon vessel total displacement and speed. Fuel consumption is a product of the specific fuel consumption and the power required; specific fuel consumption depends upon power requirement, but is relatively constant near rated power for both gas turbines and diesels. A tradeoff can therefore be approximated by developing a differential relationship between power required and total vessel displacement.

For example, the power requirement can be represented as empirical model data or more simply as a functional relationship such as the following:

$$P = f(\Delta, V) \tag{1}$$

where P is power in MW, Δ is vessel displacement in metric tons, and V is speed in knots. This function relationship may be defined by test data or standard data from a hull series. For displacement hulls a typical relationship is often modeled as

$$P = K\Delta^{\alpha}V^{\beta} \tag{2}$$

The value of the exponent α depends upon the hull form and can range from 0.6 to over 1.0. For determination of power dependence upon displacement at a constant speed, the value of β is not critical. It is usually taken as 3 for displacement hulls, but may be as small as 2 for semiplanning hulls.

To determine the differential dependence of power on small changes in displacement resulting from different propulsion alternatives, the following equation is used:

$$dP/d\Delta = K\alpha\Delta^{(\alpha-1)}V^{\beta} \tag{3}$$

Given the value of power required at one displacement and speed, an estimate of the change in power for a change in displacement can be made. Empirical data from model test can be used for relationship (1) above if it is available. In the example given later, some comparisons are made for assumed functional relationships for power versus displacement.

Lube oil consumption can be compared based upon manufacturer's data for various engines. The rate of consumption will vary slightly with power output but can be estimated as constant rate per unit time operation. Changes in required power for changes in machinery system weight must be taken into account. The important result here is that the rate of lube oil consumption is much greater for diesel engines than for gas turbines.

The economics of operation must include the difference in lube oil price between diesels and gas turbines as well. Considering differences in consumption rate and differences in price, the cost of lube oil usage is generally an order of magnitude higher for diesels than for gas turbines.

Maintenance. Maintenance represents a significant cost of ownership for commercial vessels, particularly those that operate over 3000 hours per year. In assessing estimated maintenance cost, it is important to include not only routine recurring preventive and corrective maintenance, but also the refurbishment and overhaul costs associated with restoring the engines to essentially like new condition. Typically these refurbishment cycles will be accomplished at intervals of 10,000 hours or more, and therefore represent a major maintenance event every 2 or 3 years depending upon the vessel operating profile. Preventive and on-board corrective maintenance can usually be expressed as an average cost per operating hour; the major maintenance events are included by adding their estimated costs after the appropriate number of operating hours. Lower power requirements resulting from lower weight extend engine life and lower maintenance costs.

Rough estimates of maintenance cost can be obtained from specific maintenance cost estimates ($/kW-h) for various prime movers. Although maintenance represents usually 15 or less percent of total operating costs, it is important to include the values because gas turbine average specific maintenance cost is lower than diesel, and it provides an offsetting effect to the normally higher fuel cost for the gas turbines.

Machinery System Volume. The specific volume for gas turbine engines is less than that of diesels, even when allowance is made for gas turbine enclosures usually provided for acoustic and thermal isolation of the engines in the machinery rooms. In large ships with high power requirements that are volume sensitive, the advantage usually drives propulsion plant selection toward the gas turbine, because the large volume of a diesel plant may be unacceptable. In a vessel that carries a very dense cargo, e.g., liquid cargo or ore, the volume of the vessel must provide sufficient displacement to support the cargo. Excess volume is available and a high-specific-volume propulsion prime mover may be acceptable.

In a fast vessel of medium power requirement, the advantage of lower specific volume gas turbines depends upon the vessel configuration. For example, in a catamaran ferry vessel, the engines are located in the side hulls. Additional volume available from a low volume gas turbine may not be of any value for additional cargo, because automobiles or passengers will not be carried in these spaces. However, if the side hulls are slender, multiple diesels may not fit conveniently into the vessel; a related consideration is the transverse spacing required between multiple diesel engines to provide maintenance access. This transverse spacing may result in large input shaft spacing, which complicates the reduction gear design and increases the reduction gear weight.

Vibration and Noise. The noise signatures of gas turbines and diesels are different and must be considered as two elements, structure-borne noise and air-borne noise. The noise promulgated through the vessel structure can be detected by passengers and is ultimately radiated into the water. This element of noise is of particular interest for military ships because of their vulnerability to detection by passive sonar equipment. Structure-borne noise is also important in commercial ships
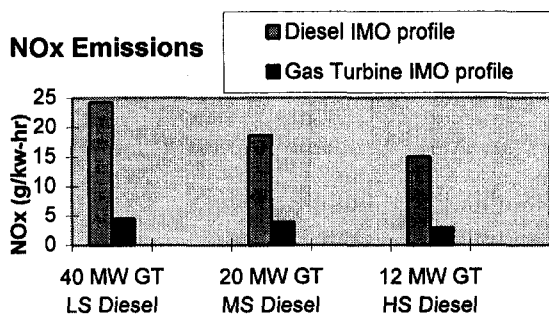
NOx Emissions

Fig. 1 NO$_x$ emissions

Legend: ■ Diesel IMO profile / ■ Gas Turbine IMO profile

(Y-axis: NOx (g/kw-hr); categories: 40 MW GT / LS Diesel, 20 MW GT / MS Diesel, 12 MW GT / HS Diesel)

because of its effect on passengers. Diesel engines tend to produce higher levels of structure-borne noise at the lower end of the audible spectrum than gas turbines. Attenuation of lower frequencies is more difficult than the higher frequencies. Since control of structure-borne noise is accomplished by isolation mounting at the prime mover source, it is more difficult to prevent this noise from propagating throughout the ship. Diesel propulsion vibration is usually detectable throughout the ship; gas turbine structure-borne noise is not.

Air-borne noise is that which is detected from the combustion air inlets and exhausts. Gas turbines produce high-frequency noise, which is most detectable from the air inlets. This requires implementation of inlet silencing measures. Silencing has been done on many military ships that require low noise levels topside due to the presence of personnel as lookouts, or control personnel operating on an open bridge. In commercial vessels, gas turbines have been silenced to extremely low levels because of owner requirements. The gas turbine exhaust is insulated for thermal isolation; this thermal insulation is usually sufficient to provide the required exhaust silencing. Diesel air-borne noise is the reverse of the gas turbine, requiring less silencing in the inlet and more in the exhaust.

Exhaust Emissions. Reduction of air pollution has lead to restrictions on the exhaust emissions of most heat engines applied in various industries, particularly in the United States. The marine industry has been largely exempt until recently from these restrictions. Because of progress in reducing emissions from automobiles, railroads, utility power production, and other sources, in some locations the marine industry has become the largest remaining uncontrolled source of pollution. It is therefore inevitable that controls will be applied to marine vessels as well. This is already beginning to occur in US coastal waters and in Scandinavian waters. The International Maritime Organization is also proposing restrictions which may ultimately be applied on the high seas.

For the fast vessels of medium power requirement being considered here, the coastal restrictions are most relevant. The restrictions usually include emission of both oxides of sulfur (SO$_x$) and oxides of nitrogen (NO$_x$). The production of SO$_x$ is related to the level of sulfur in the fuel and is a particular problem for low and medium-speed diesels that use intermediate viscosity fuel oils that contain large percentages of residual matter from the refining process. For high-speed diesel engines and gas turbines, which operate on distillate fuels without residual contamination, the production of SO$_x$ can be maintained at an acceptable level.

For the production of NO$_x$, the gas turbine has a definite advantage, because the levels are considerably below those of high-speed diesels, and even lower when compared to medium and low speed diesels. Figure 1 gives a relative indication of the production levels of various engines. Diesel NO$_x$ levels can be lowered with various measures including selective catalytic reactors, but these devices add to the weigh, volume, cost, and complexity of the engine, and increase fuel consumption.

Evaluation of the economics of exhaust emissions must include penalties paid for NO$_x$ emitted. Such penalties are being proposed for some locations where air pollution is of particular concern.

Comparison Example The following example is used to illustrate the application of the considerations discussed above in evaluation of propulsion alternative for fast vessel of medium power requirement. Although the assumptions are considered reasonable from current applications, the results are not intended to illustrate any universal conclusion about the relative merits of one propulsion system over the other.

Weight. Survey of weights of high-speed diesels [6] indicates a range of maximum marine power ratings from 5 to 5.8 MW with a range of dry weights from 21 to 39 mtons. Allowing 9 percent additional for auxiliary support systems and fluids, and about 15 percent for foundations, the average specific weight is about 6.7 mtons/MW. For gas turbines the weight must include the complete package including enclosure, supporting systems, and foundations. Allowing for these additions, the specific weight for gas turbines appropriate for the medium powered vessels is about 1.1 mton/MW.

Fuel Consumption. To determine the effect of weight on fuel consumption, consider a nominal 1000 mton displacement vessel requiring 21.6 MW to achieve 38 knots with high-speed diesel propulsion. For a catamaran the value of $\alpha = 1$ can be assumed, and an estimate of KV^β can be calculated from Eq. (2). If the value of $dP/d\Delta$ is calculated from Eq. (3), the result is 21.6 kW/mton. This represents an estimate of the sensitivity of power to weight change around this assumed operating point. A similar calculation could be made from empirical data or model test data.

The incremental change in propulsion weight in going from diesel power to gas turbines at a diesel power requirement of 21.6 MW is estimated from the specific weight averages in the weight paragraph above:

$$d\Delta = (6.7 - 1.1) \text{ mton/MW} \times 21.6 \text{ MW} = 121 \text{ mtons}$$

This result is in quite close agreement with detailed evaluations done recently for specific projects. Using the result from differential power change, the resulting reduction in power due to weight reduction in going from diesel to gas turbines is

$$dP = dP/d\Delta \times d\Delta = 2.6 \text{ MW}$$

The specific fuel consumption for high-speed diesels range from about 195 g/kW-h to about 225 gm/KW-h. The average SFC for gas turbines in this range is about 245 g/kW-h. To evaluate the economic effect, the specific fuel consumptions are estimated as 200 g/kW-h at the low end of the range for diesels, and the average of 245 g/Kw-h for the gas turbine. The cost of distillate fuel is estimated as $160/mton. The results are included in the summary Table 1.

Table 1 Summary of estimated operating costs

	High speed diesel	Gas turbine
Propulsion system weight	145 mtons	24 mtons
Power required for 38 knots	21.6 MW	19.0 MW
Fuel cost/hr	$691/hr	$745/hr
Lube oil cost/hr	$ 21/hr	$ 2/hr
Maintenance cost	$ 97/hr	$ 61/hr
Total cost	$809/hr	$808/hr

Lube Oil Usage. Diesel lube oil usage is estimated to be about 0.65 kg/MW-h at a cost of $1.50/kg; gas turbine lube oil usage is about 0.015 kg/MW-h but at a higher cost of about $6.60/kg. Lube oil consumption cost is estimated for each case using the appropriated value of required power. These operating costs are included in Table 1.

Maintenance. Maintenance costs are difficult to obtain because different manufacturers include different elements in the reported costs. For high-speed diesels, total maintenance average costs range from $0.004/kW-h to about $0.012/kW-h. For gas turbines the maintenance costs are estimated to average about $0.0032/kW-h. The factors involved in gas turbine maintenance costs were discussed in [3]. The appropriate maintenance estimate for each propulsion alternative must reflect the power for that configuration. Lower required power for the lower weight gas turbine improves the major maintenance internals and lowers maintenance costs.

If the average estimated value is used for the gas turbine, and a low estimate of $0.0045/kW-h is assumed for the diesels, the resulting maintenance costs can be included in Table 1.

The figures in Table 1 are not intended to prove the case for one propulsion system or the other with respect to operating costs, but to illustrate the elements to be considered in the comparison, and to illustrate the effect that change in weight has on the result. If the decreased weight effect had not been considered, the fuel consumption cost for the gas turbine-propelled vessel would be approximately $100/h higher and would lead to an erroneous conclusion.

Total life cycle cost must include the initial capital plus installation costs as well as operating costs. No attempt has been made to include these initial costs because they are normally available to a ship operator or builder from manufacturers' offers when a project is being considered. The purpose here is to consider the cost factors for future operations that a potential operator or shipbuilder must estimate, as well as the additional factors that will affect successful application of the vessel in service.

Consideration of Additional Factors. Decision on a propulsion configuration will begin with the economics analysis but will ultimately include consideration of additional factors such as volume, vibration and noise, exhaust emissions, and others. These additional factors may have considerable influence on the decision, especially if the economic comparison shows no clear advantage for one system over another.

Physical fit of propulsion systems depends upon the hull configuration and the requirements of the prime mover and other drive train components. Monohull vessels have fewer constraints than catamarans or swath vessels; mechanical drive is more restrictive than an electric drive transmission. The majority of fast ferry designs in the medium power requirement category have been catamarans. Although electric drive represents possibilities for arrangement flexibility and the possibility of topside placement of prime movers, the initial cost is larger than the more conventional mechanical drive.

Vibration and noise requirements are different, depending upon the length of mission and the external environment in which the vessel will operate. For very short trips, higher levels of internal noise may be acceptable; for longer runs or for vessels that will accommodate passengers overnight, low noise and vibration may be the most important consideration. External noise restrictions will normally be determined by port requirements, or restrictions imposed during the transient of inland waters.

Exhaust emissions will certainly influence economic analyses in the future. Already regulations have been proposed for some coastal areas, which will impose port fees directly related to the levels of emissions from vessels in the restricted areas. These fees have been proposed as dollars per ton of NO_x emitted and could include penalties for other emissions in the future.

- Length   78 meters
- Passengers   450
- Cars   120
- Speed   40 knots
- Propulsion
    - 2 x LM1600 gas turbines
    - Waterjets

Will Enter Service in 1996

Fig. 2   SEAJET® 250

These fees can provide a significant addition to the operating costs indicated in Table 1. In addition, regulation of emissions on the high seas is being considered, and will certainly be imposed at some time in the future.

For fast vessels of the medium power size considered here, a majority of the operation will generally occur within the coastal areas were emission restrictions are currently being imposed. Vessels currently being designed and built will certainly be subject to such restrictions during their operating life. Even if the initial area of operation does not have such restrictions, a potential owner must consider these requirements for potential resale of the vessel to another operator.

Gas turbine technology for marine propulsion offers not only lower emissions levels than diesels with current technology, but is providing even much lower levels currently for land base applications with dry suppression techniques. This technology will be available for future use in shipboard propulsion systems when the regulations become even more restrictive. Diesel technology currently requires add-on systems to clean up the exhausts emission in order to meet the currently proposed required levels.

Vessel Designs. Numerous examples exist of high-speed diesel powered vessels of the type considered here. The INCAT wave piercers, the Ferries Australia Auto Express 94 [4], and the Bazan Mestral are current examples. The gas turbines have been baselined in the NQEA/Danyard SEAJET® 250, the Westamarin 7100 Ocean Flyer, and the Kvaerner Fjellstrand Jumbo Cat. All of these vessels have power requirements in the 20 to 26 MW range, but have arrived at a variety of propulsion alternatives through consideration of the above factors. Figure 2 shows the NQEA/Danyard SEAJET® 250 recently approved for construction. The factors discussed here were influential in the decision to use gas turbine propulsion in this gas turbine powered vessel [5].

Conclusions

Determination of the merits of various propulsion system alternatives for fast vessels depends upon the careful consideration of a number of factors. At high power requirements for volume sensitive vessels and for low power requirements in weight-sensitive vessels, gas turbines enjoy obvious advantages and are usually the propulsion system of choice. For medium power requirements, the choice is not so clear, and requires a careful evaluation of the factors illustrated in this paper. Economics of operation requires a complete analysis of the system effects of propulsion alternatives, particularly the effect of weight reduction on the fuel consumption and on maintenance costs. Exhaust emissions will continue to increase in importance, and will have a direct bearing upon the economics of operation, a well as the acceptability of the vessel in regions having environmental restrictions.

References

1 Reid, R. E., and Hartranft, J. J., "GE LM2500 Marine Gas Turbine Experience Update," ASME Paper No. 91-GT-23.

2 Brady, C. O., and Luck, D. L., "The Increased Use of Gas Turbines as Commercial Marine Engines," ASME JOURNAL OF ENGINEERING FOR GAS TURBINES AND POWER, Vol. 116, 1994, pp. 426–433.

3 Luck, D. L., "Recent Gas Turbine Applications in Large Commercial Vessels," ASME Paper No. 94-GT-120.

4 Anon, "Ferries Australia Unveils New Vehicle Ferry Design . . . ," Fast Ferry International, July–Aug. 1994, p. 11.

5 Jensen, J. V., "A Semi Swath Catamaran Car Ferry—A Joint Danyard/NQA Project," presented at Cruise & Ferry '93, London, May 11–13, 1993.

6 Diesel & Gas Turbine Worldwide Catalog, Vol. 59, 1994 ed.

Compressor Station Recycle System Dynamics During Emergency Shutdown

K. K. Botros

W. M. Jungowski

NOVA Research and Technology
Corporation,
Calgary, Alberta, Canada

D. J. Richards

NOVA Corporation of Alberta,
Calgary, Alberta, Canada

Transient phenomena associated with gas recycling during compressor emergency shutdown (ESD) have been studied both experimentally and numerically. A scaled-down laboratory test rig has been constructed to study the influence of various underlying parameters on ESD operation. Three different configurations representing different design scenarios were tested. The first configuration has a long recycle system with a volume capacitance representing an air-cooled heat exchanger in the recycle loop, and the recycle valve located close to the discharge side. The second one is the same as the first except the recycle valve is placed close to the suction side. In the third configuration, the cooler capacitance was removed from the recycle loop and the piping capacitance on the discharge side was further reduced. Shutdown tests were carried out from different steady-state initial conditions varying the recycle valve opening time, and the synchronization time between the compressor ESD signal and valve opening signal. Numerical simulations based on the solution of the full one-dimensional conservation equations using the method of characteristics were also conducted for the above configurations. Good agreement was obtained between measurements and simulation results. Numerical simulations were used to analyze other cases, which were not investigated experimentally, to further investigate the interaction between equipment and flow parameters. Results indicate that the valve prestroke time is more crucial than the stroke time and that it should be made short to avoid surging the compressor during ESD. Locating the recycle valve as close as possible to the suction or discharge of the compressor helps reduce unit surge during shutdown.

1.0 Introduction

The recycle system is an essential component in the operation of centrifugal compressors used on natural gas transmission systems. It is necessary for startup, shutdown, and surge protection of the compressor unit. As these operations are transient in nature, all dynamic parameters of gas, flow, equipment, and control play an important role and impact on the system performance and safety.

This paper addresses one particular problem related to the emergency shutdown (ESD) of a centrifugal compressor. As gas generator and power turbine technologies are driven mainly by the aircraft industry, current designs exhibit lower rotor inertias than previously used. Due to the low combined inertias of the centrifugal compressor/turbine, the compressor may undergo several deep surge cycles during rapid shaft deceleration [1]. The problem can be further accentuated when coolers are placed within the recycle path as they add extra capacitance on the compressor discharge.

Numerous parameters affect surge, such as the recycle valve characteristics and capacity, its opening delay (i.e., the time between valve open solenoid drop out and the start of stem movement—often called "prestroke" delay) as well as valve travel time (i.e., the time taken for the valve to travel from closed to open position—often called "stroke" time). Additionally, timing of the compressor ESD signal, the fuel gas shutoff signal, fuel gas valve closing time, and fuel gas manifold size contribute to the complexity of the problem.

A need was identified to carry out numerical and experimental investigations into the operation of the recycle system and to examine its transient nature. A scaled-down laboratory test rig has been constructed to study the influence of the various underlying parameters on ESD operation. The fully instrumented test rig comprises all salient components of a compressor/recycle system. Three different configurations were tested to establish correlations between parameters. These are: (*i*) long recycle system, a capacitance representing an air-cooled heat exchanger in the recycle loop and recycle valve close to the discharge side, (*ii*) same as (*i*) except recycle valve placed closer to the suction side, and (*iii*) cooler capacitance removed from the recycle loop and reduced capacitance on the discharge side. This includes long and large diameter pipes, and capacitance volumes such as that of an aerial cooler. Shutdown tests from different steady-state conditions were carried out varying the recycle valve stroke and prestroke times, and the synchronization between compressor ESD signal and valve opening signal.

Numerical simulations based on the solution of the full one-dimensional conservation equations using the method of characteristics were conducted for the above-mentioned configurations and different other cases. Good agreement was obtained between measurements and simulation results. Numerical simulations were then used to analyze other cases that were not investigated experimentally, to investigate further the interaction between equipment and flow parameters.

2.0 Numerical Simulation

The general continuity, momentum, and energy equations for one-dimensional unsteady compressible fluid flow in a pipe were utilized in the numerical investigations. These equations include the effects of friction along the pipe and heat transfer to the surrounding, and can be written as follows:

Copyright © 1996 by ASME
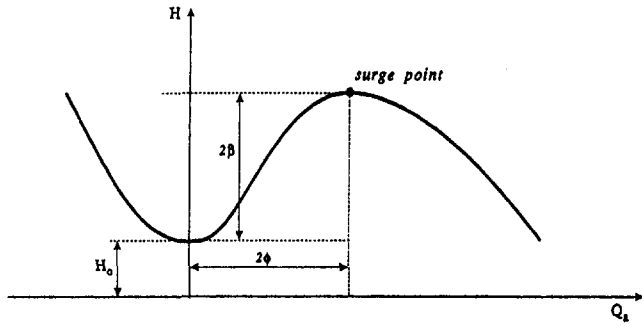
Fig. 1 Steady characteristic cubic model for the compressor to the left of the surge point

Fig. 2 Schematic of a split (dual) shaft compressor/gas turbine system

Continuity

$$\frac{\partial \rho}{\partial t} + \rho \frac{\partial V}{\partial x} + V \frac{\partial \rho}{\partial x} = 0 \qquad (1)$$

Momentum

$$\frac{\partial V}{\partial t} + V \frac{\partial V}{\partial x} + \frac{1}{\rho} \frac{\partial p}{\partial x} + \frac{f_{DW}}{2D} V|V| = 0 \qquad (2)$$

Energy

$$\frac{\partial p}{\partial t} + V \frac{\partial p}{\partial x} - c^2 \left(\frac{\partial \rho}{\partial t} + V \frac{\partial \rho}{\partial x} \right) - E = 0 \qquad (3)$$

where

$$E = \frac{f_{DW}}{2Dc_v} \left(\frac{\partial p}{\partial T} \right)_v V^2 |V| + \frac{4k}{Dc_v \rho} \left(\frac{\partial p}{\partial T} \right)_v (T_a - T)$$

The method of characteristics was used to solve these equations along positive and negative characteristics as well as the path line. The AGA-8 equation of state was used to describe the relationship between pressure, temperature, and density of the gas. The Courant stability criterion was also imposed on the space–time increments to ensure stability of the computation and minimize the numerical diffusion normally caused by implicit schemes. Detailed treatment of solution techniques and the formulation of the pertinent equations for constriction elements,
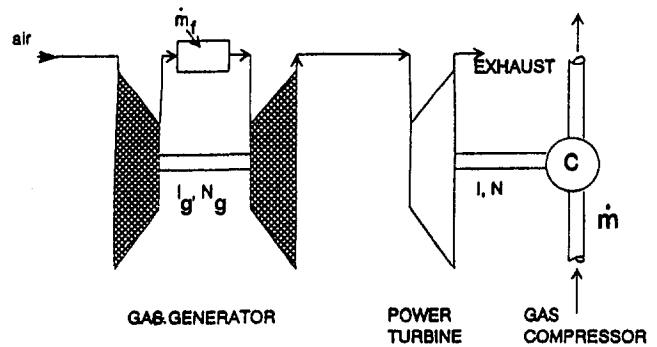
capacitance elements, combining and dividing tee junctions, and end conditions of the whole system can be found in [2].

The compressor system is assumed to respond to any perturbation in a quasi-steady manner. The complete compressor characteristic (to the right and left of the surge point) is therefore needed as a function of the rotational speed. This is furnished by applying the fan laws to the characteristics on the right of the surge point and the cubic representation of the characteristics to the left of the surge point [3] according to the following equation:

$$H_{ss} = H_o + \beta \left[1 + \frac{3}{2} \left(\frac{Q_a}{\phi} - 1 \right) - \frac{1}{2} \left(\frac{Q_a}{\phi} - 1 \right)^3 \right] \qquad (4)$$

(see Fig. 1 for identification of parameters).

The dual (split) shaft gas turbine/compressor arrangement shown in Fig. 2 is considered here, where the gas generator speed (N_g) is different from that of the power turbine/compressor speed (N). The following governing equation can be written to describe the coupling relationship between the compressor, driver, and power turbine:

$$\dot{m}_f \cdot \text{LHV} \cdot \eta_{th}(N, W)$$

$$= I_g \cdot N_g \cdot \frac{dN_g}{dt} + I \cdot N \cdot \frac{dN}{dt} + \frac{\dot{m} \cdot H_{ad}(\dot{m}, N)}{\eta_m \cdot \eta_{ad}(\dot{m}, N)} \qquad (5)$$

This equation describes implicitly the relationship between η_{th}, N_g, H_{ad}, η_{ad}, and N. Here, H_{ad} and η_{ad} are known from the

--- Nomenclature ---

A = inside cross-sectional area of the pipe
c = speed of sound in the gas
C_g = valve sizing coefficient
c_v = specific heat at constant volume
D = pipe inside diameter
f_{DW} = Darcy Weisbach friction factor
H = adiabatic head across the compressor
H_{SS} = steady state adiabatic head across the compressor
H_o = adiabatic head at zero flow
I = combined inertia of the compressor/power turbine rotor
I_g = inertia of the gas generator rotor
k = heat transfer coefficient between the gas and surrounding based on pipe inside diameter
L = pipe length

LHV = lower heating value of the fuel gas
$\dot{m}$ = gas mass flow rate through the compressor
$\dot{m}_c$ = gas mass flow rate through the check valve
$\dot{m}_f$ = fuel gas mass flow rate
N = angular rotational speed of the compressor/power turbine
N_o = angular rotational speed of the compressor/power turbine at initial steady-state condition before shutdown
N_g = angular rotational speed of the gas generator
p = gas pressure
Q_a = actual inlet flow rate to the compressor
Q_s = actual inlet flow at surge point
t = time

T = gas temperature
x = space coordinate along a pipe
V = gas velocity
V_c = cooler volume
T_a = ambient temperature
W = output power of the power turbine
W_o = output power of the power turbine at initial steady-state condition before shutdown
β = parameter defined in Fig. 1
η_{th} = thermal efficiency of the gas turbine
η_m = mechanical efficiency of the coupling between compressor and power turbine
η_a = adiabatic efficiency of the compression process
ρ = gas density
ϕ = parameter defined in Fig. 1
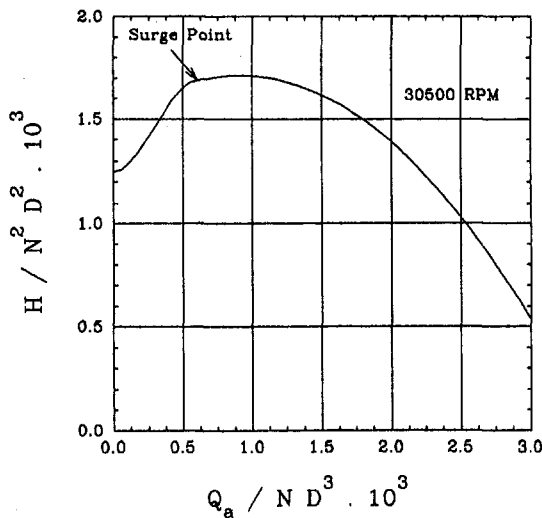τ = time scale constant

Fig. 3 Full compressor characteristics

compressor characteristics and the application of the fan laws, while η_{th} and N_g are related to the power turbine performance. Odom [4] proposed a simple correlation between the turbine output power and thermal efficiency and these were used in the numerical simulation. Control of the compressor operation is effected by specifying the fuel gas mass flow rate ($\dot{m}_f$) to the gas turbine, and solving Eq. (5) with those describing the gas dynamics in the associated piping system. In the case of shutdown, fuel gas flow ($\dot{m}_f$) decreases in a manner determined from the fuel gas shutoff signal, fuel gas manifold arrangement, and fuel gas valve closing time. A time-dependent function can be imposed on ($\dot{m}_f$) describing these factors and introduced into Eq. (5). The laboratory model utilized an electric driver so the left-hand side of Eq. (5) is set to zero exactly at the shutoff signal. This concept will become more apparent later in the paper.

3.0 Laboratory Setup

A laboratory model was designed to scale down the piping geometry of a specific compressor station on NOVA's transmission system. This station was considered unique as it features large capacitance in the recycle system brought about by an air-cooled heat exchanger placed in the recycle path. Also, the unit compressor/power turbine combined inertia is relatively low, resulting in surging the unit after shutdown from high head steady operating point. The laboratory model consists of a SUN-FLO-B500f model single-stage centrifugal compressor driven by a variable speed electric motor, and the flow medium is air. The performance characteristic of this compressor, at speed = 30,500 rpm is shown in Fig. 3. Other compressor parameters are:

- compressor maximum power = 7.6 kW
- blade tip maximum Mach number = 0.6
- impeller outer diameter = 0.127 m
- impeller mean inlet diam = 0.038 m
- compressor/motor inertia = 5.531 kg.cm^2
- maximum speed = 31,000 rpm

The recycle valve chosen for the lab model is an NPS 1-$\frac{1}{2}$ Fisher EZ valve with a quick opening trim. The valve characteristic is shown in Fig. 4. As the first 30 percent of its full travel is nearly linear and is adequate for the test loop, the stroke of the valve was restricted to 30 percent by an artificial stop. Both valve prestroke delay and stroke time can be varied from 55 ms to 1000 ms by adjusting valve control components.

The following similarity numbers are applied to the compressor shutdown operation:

$$N_1 = \frac{L}{cN_0}\frac{dN}{dt}\;;\quad N_2 = \frac{V_c}{AcN_0}\frac{dN}{dt}\;;$$

$$\text{and}\quad N_3 = \frac{IN_0^2}{W_0}\cdot\frac{dN}{N_0 dt} \tag{6}$$

A time scale factor (τ) can then be defined as:

$$\tau = \frac{IN_0^2}{W_0} \tag{7}$$

The first similarity number (N_1) is used to scale down the pipe length, the second (N_2) to scale down the cooler or other capacitance volume, and the third (N_3) to scale down the shaft inertia. The recycle valve prestroke and stroke times are scaled down using the time scale constant (τ). Flow Mach number is very small in the present study (maximum 0.07). Although a large mismatch between field and laboratory respective Reynolds number exists, the effects of viscous damping in the phenomenon during shutdown is negligible.

The dimensions of the three configurations (A, B, and C) are depicted in Fig. 5. The main piping run is NPS 3 and the recycle line is NPS 1$\frac{1}{2}$ pipe. A variable capacitance cylinder/piston arrangement is included in the main piping on the compressor discharge. This capacitance is to represents the cooler capacitance in the actual compressor station and can be varied between 6 to 30 liters simulating full size coolers volume capacitance of 2.5 to 12.7 m^3.

Two 60 m sections of pipe (NPS 3) terminated by two partially throttled valves simulate the suction and discharge system of the compressor. This length of pipe was sufficient to delay reflections from the boundaries that may interfere with the compressor/recycle interaction. A split-type check valve is located immediately downstream of the recycle line tie-in on the compressor discharge. The timing and sequence of recycle valve opening with respect to compressor shutdown signal is controlled by an electronic control/delay circuit.

Configuration A is a scaled-down model of NOVA compressor station featuring a long recycle line, a capacitance simulating a cooler in the recycle loop, and the recycle valve located close to the discharge of the compressor (Fig. 5(a)).

Configuration B is the same as Configuration A except that the recycle valve has been relocated closer to the suction of the compressor (Fig. 5(b)).
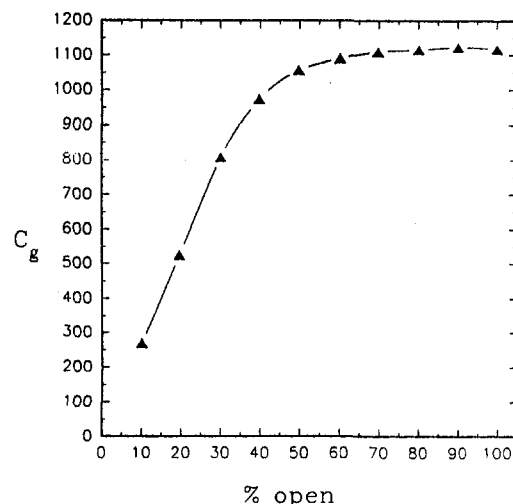
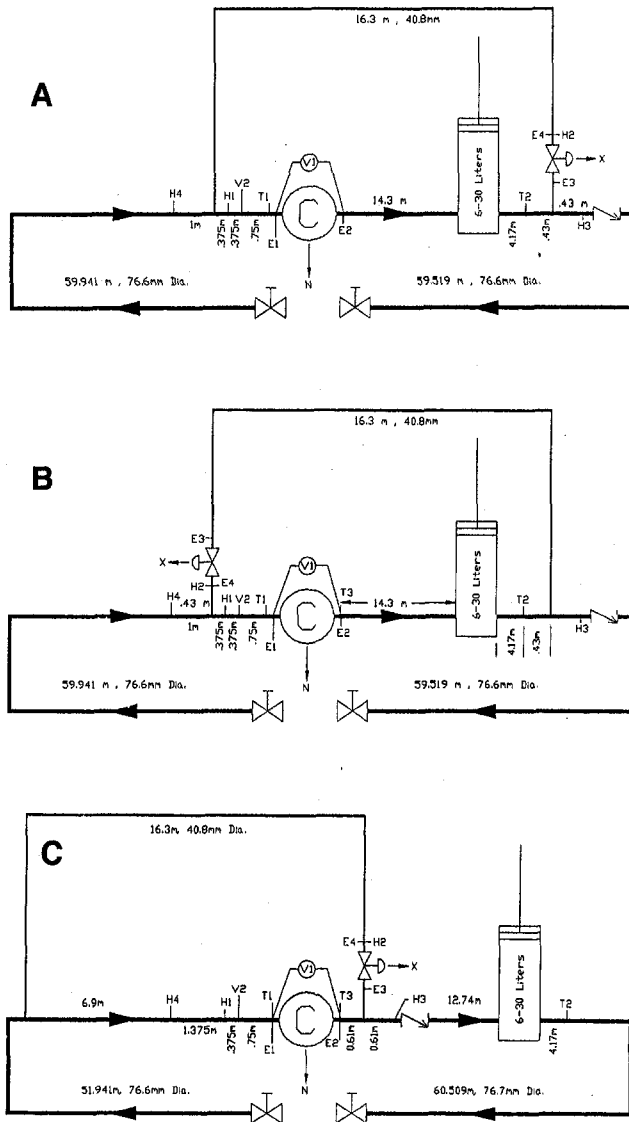

Fig. 4 Recycle valve characteristic

A

B

C

Fig. 5 Laboratory test rig configurations

Configuration C has the same length of the recycle line as Configuration A but the capacitance between compressor discharge and recycle valve was minimized by relocating the tie-in point closer to the compressor discharge. The cooler capacitance is, thus, located outside the recycle loop (Fig. 5(c)).

The test rig is instrumented as shown in Fig. 5 for instantaneous measurements of pressures and velocities. Four Endevco pressure transducers are identified by the letter (E). Additionally, the differential pressure across the compressor was also measured by a Validyne pressure transducer (V1) for verification of the difference between E1 and E2 measurements. Velocities were measured by four hot film (HF) anemometers (identified with letter H in Fig. 5). The probes are located at the centerline of the pipe at the respective location.

The mean velocity and the flow rate at these locations can be estimated based on the ratio between the mean and centerline velocities at the prevailing Reynolds number (Re), assuming fully developed velocity profile across the diameter of the pipe. In the range of Re of the experiment, this ratio was approximately 0.81. This ratio provided good agreement between measurements and simulation results that were obtained in the steady range of operation. However, it should be recognized that this may not be the case in transient and unsteady flow since

fully developed velocity profile is not attainable in transient conditions.

In order to verify the hot film measurements and to determine flow direction, a calibrated standard pitot tube (V2) was located 0.375 m downstream of hot film probe H1 as shown in Fig. 5. The pitot tube reports a positive reading when the flow is positive. The magnitude of the flow velocity is taken from the hot film as it has better time response to flow variation than the pitot tube. However, the pitot tube helps to establish the flow direction. Temperature measurements were taken at three locations by miniature copper-constantan thermocouples, and are used to correct for velocity measurements by the hot films.

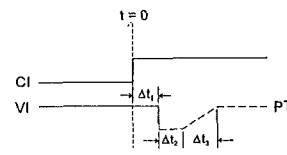## 4.0 Results of Measurements

Various tests were conducted on the three configurations mentioned above for varying timing between compressor shutdown signal and recycle valve opening signal (Table 1). These tests are characterized by three time increments: Δt_1—between the compressor stations signal (CI) and valve opening command signal (VI), Δt_2—denoting valve prestroke time, and Δt_3—valve stroke time determined by a position transmitter (PT) on the valve. When (CI) signal is leading $\Delta t_1 > 0$, otherwise $\Delta t_1 < 0$. In all cases, the compressor was shut down from an initial steady state operating point at 30,500 rpm. The following are a brief description and discussion of results of selected cases conducted on the three test configurations.

4.1 Configuration A Case 21 is a basic case where the steady-state point was well to the right of the surge point ($Q_a/Q_s = 1.8$), as shown in Fig 6(a). Following a shutdown without opening the recycle valve, the compressor slowed down to zero speed without experiencing reversed flow. This is primarily due to the fact that the system characteristic impedance always intersects the compressor performance characteristic at the right of the surge point, a phenomenon that will be further explained in Section 7.3. The H-Q_a profile shown is considered to be the desirable shutdown profile for an ESD.

Case 54 is a shutdown case from initial steady-state condition close to the surge point ($Q_a/Q_s = 1.15$). The recycle valve

Table 1 Experimental cases for the three test configurations

|	Case	Δt_1 (ms)	Δt_2 (ms)	Δt_3 (ms)	Comments
Configuration A	21	-	-	-	high flow - recycle valve closed - no surge
	54	-	-	-	low flow - recycle valve closed - surge occurred
	55	0	40	70	no surge
	56	-140	40	70	no surge
	58	200	40	70	surge occurred
	59	0	70	700	no surge
	60	0	70	1000	no surge
	61	-	-	-	recycle valve open - no surge
	61R	0	70	500	no surge
	62	0	70	400	no surge
	67	-70	70	400	no surge
	68	-270	70	400	no surge
	69	-470	70	400	no surge
	71	100	40	70	surge occurred
Configuration B	74	0	70	70	no surge
	75	-	-	-	recycle valve closed - surge occurred
	77	-100	70	70	no surge
	80	100	70	70	surge occurred
	81	200	70	70	surge occurred
	82	0	420	1000	surge occurred
	86	-400	470	1000	no surge
	87	-	-	-	high flow - recycle valve closed - no surge
Config. C	89	-	-	-	recycle valve closed - surge occurred
	90	0	80	80	no surge
	91	50	80	80	no surge
	95	-500	580	1000	no surge
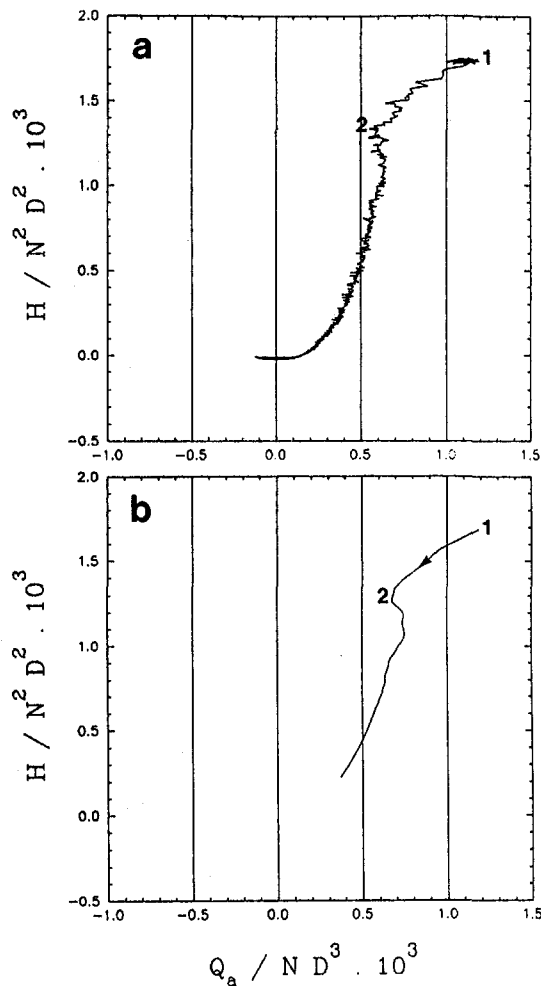
Fig. 6 Measurement and simulation results of case 21: (a) measurements; (b) simulation

remained closed as well in this case. The results of the compressor performance during shutdown are shown in Fig. 7(a), indicating several surge (reverse flow) cycles as the compressor is winding down. The corresponding speed deceleration curve shows waviness in the profile as a result of the varying torque as the compressor flow fluctuates from positive flow (high torque) to negative flow (low torque), and vise versa. Full explanation of this is given in [5].

Figure 7(d) also shows the centerline velocity at the compressor suction (HF1), manifesting some fluctuations in varying amplitude. The lower amplitudes correspond to reversed flows, while higher amplitudes correspond to the compressor recovering to positive flow. This is confirmed from the pitot tube measurements (DPV2) shown in Fig. 7(h). Other hot-film measurement results are also shown in Fig. 7(e, f, g) for reference. The pressure fluctuations in E1, E2, E3, and E4 (Fig. 7(i, j)) follow the same trend of the flow fluctuations. This experiment shows clearly that the compressor undergoes several surge cycles if the recycle valve does not open and the initial steady-state operating condition of the compressor was close to the surge point before shutdown. Discussions on the simulated results will follow in the next section.

Case 55 is the first normal scenario of a shutdown operation. This case gives a coincidental signal to shutdown the compressor and open the recycle valve. A prestroke delay of approximately 40 ms of the recycle valve followed by 70 ms stroke time were observed. The results of this case are shown in Fig. 8. The H-Q_a plot (Fig. 8(a)) shows the typical desired trend

of a shutdown case when the recycle valve opens to keep the compressor out of surge. Starting from the steady-state flow point, the compressor would follow the system characteristic slope to the left to a point where the recycle valve starts to open permitting higher flow to go through the compressor resulting in a "swan-neck" shaped profile. The compressor then winds down to zero flow, zero head, and zero speed in a typical manner as case 21 above.

The compressor speed deceleration (Fig. 8(b)) is faster in this case compared to case 54 due to the fact that the flow through the compressor remained positive, resulting in higher fluid torque applied to decelerate the compressor. The results show that the compressor did not undergo any reversed flow condition and good agreement was demonstrated between the hot film (HF1—Fig. 8(c)) and the pitot tube (DPV2—Fig. 8(g)) velocity measurements. Pressure measurements (Fig. 8(h, i)) are consistent with expected profiles showing disturbances caused by opening the recycle valve.

In case 58 the recycle valve signal was delayed 200 ms. This is equivalent to increasing the prestroke time to 240 ms while retaining the stroke time. The test objective is to determine the effect of increasing the prestroke. The results are shown in Fig. 9. It is clearly shown that the compressor has undergone one surge cycle before positive flow was established as a result of opening the recycle valve 240 ms later.

The prestroke delay was then shortened in case 71 to 140 ms. The results are shown in Fig. 10. Comparing the H-Q_a plots of Cases 55, 58, and 71 (Figs. 8(a), 9, and 10) shows that the prestroke time is important in insuring compressor stability during shutdown. Increasing prestroke runs the risk of surging the compressor during shutdown from a steady state point close to the surge point.

In cases 59, 60, 61R, and 62 the prestroke delay of the recycle valve was maintained the same at approximately 70 ms while the valve stroke time was varied. This was effected by means of changing the control settings on the recycle valve assembly. The valve stroke time ranged between 400 and 1000 ms in these four cases, which is considerably longer than the previous cases where this stroke was approximately 70 ms. Figure 11(a) shows the results of the longest stroke (case 60) indicating that the compressor did not undergo any surge cycles during shutdown process. The trend of shutdown profile was similar to Case 55 when the stroke was set to 70 ms only. This 1000 ms stroke time corresponds to approximately 2000 ms (i.e., 2 seconds) in the field considering the dynamic similarity discussed earlier. It appears as a result of these tests that the more decisive factor in preventing the compressor from surging during shutdown operation is the prestroke delay and not the stroking time. This is an important finding and should direct the attention of both engineers and valve manufacturers to optimize or minimize the valve prestroke time than the stroke time.

Other Configuration A cases shown in Table 1 did not result in surging the compressor as could have been predicted from the findings given above.

4.2 Configuration B. The results of case 75 are similar to that of Configuration A, case 54, except different noise was observed resulting from different rattling waves in the closed-end legs of the recycle line.

Case 74 shows a prestroke delay of 70 ms and a stroke of 70 ms with the shutdown signal synchronized with valve open signal. The H-Q_a profile following shutdown is shown in Fig. 12(a) manifesting a "sickle" shape. Comparison between this case and case 55 (Fig. 8(a)) shows that there is a slight improvement of case 74 manifested by the decrease in the magnitude of the flow drop following the shutdown, which can be seen clearly from the hot film measurements (HF1 of Fig. 12(b) compared to HF1 of Fig 8(c)). The conclusion is that relocating the recycle valve closer to the compressor suction has resulted in an improvement of the shutdown operation, thus minimizing
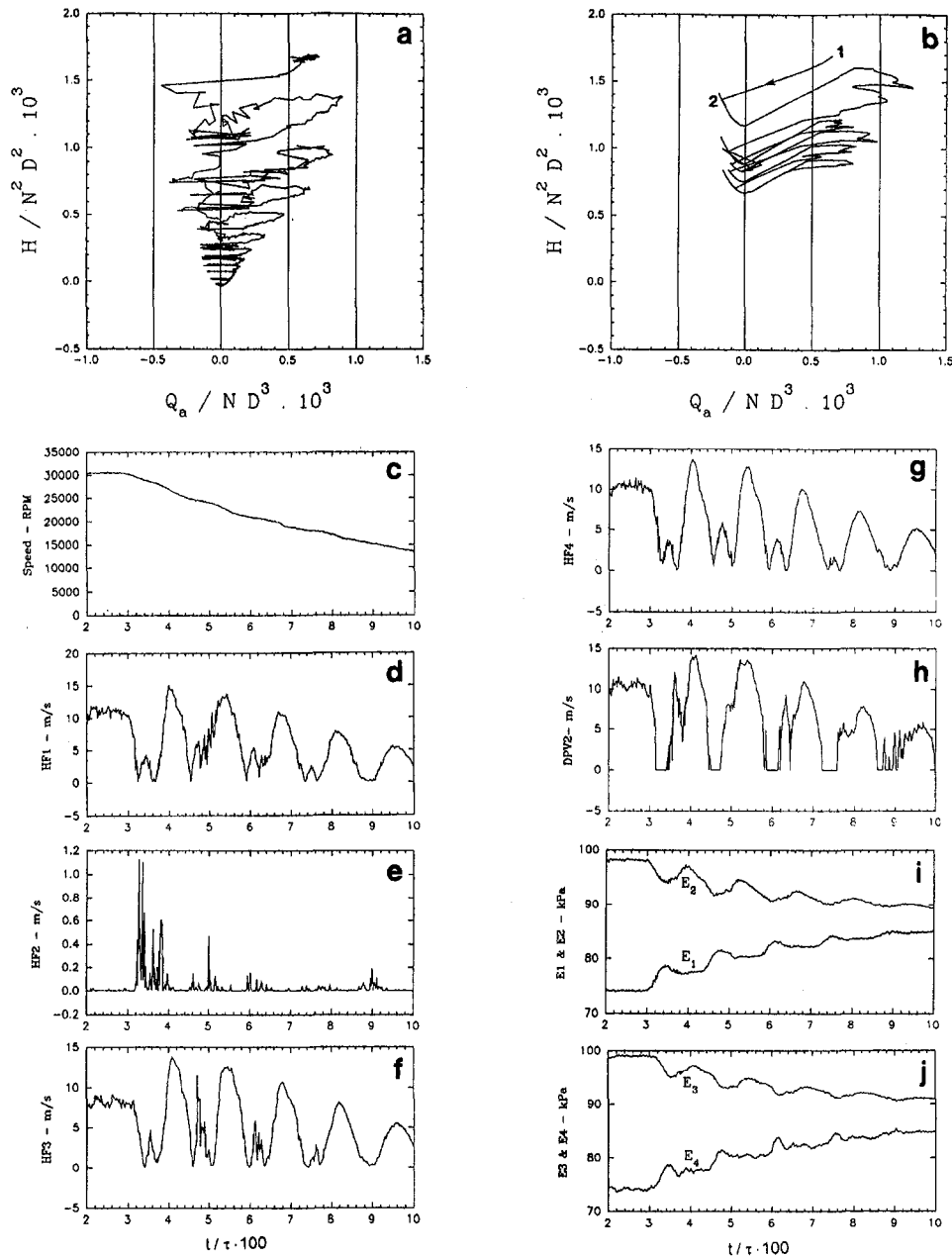
Fig. 7 Measurement and simulation results of case 54: (a, c–j) measurements; (b) simulation

the risk of the compressor surge. This is expected since the effect of opening the recycle valve is that compression wave will arrive earlier to the compressor inlet than in the case of a longer line of Configuration A. The fact that this case has a longer prestroke delay than case 55 also supports this conclusion.

Case 77 is a surge-free shutdown case as expected since the recycle valve opening signal was advanced 100 ms ahead of the compressor shutdown signal.

In case 80, the signal to the recycle valve was delayed 100 ms while the valve prestroke and stroke times remained the same. The resulting H-Q_a plot shown in Fig. 13 indicates compressor surge. Similar trend is obtained for cases 81 and 82.

Increasing the stroke time to 1000 ms while maintaining the prestroke at 70 ms (case 86) resulted in surge-free shutdown operation as is shown in Fig. 14. Case 87 is a repeat of case 21 (Configuration A) with similar results obtained.

4.3 Configuration C. This configuration is different from the previous two in that both the tie-in points of the recycle line on suction and discharge were relocated while the total recycle line length was maintained. The recycle valve was located close to the compressor discharge as shown in Fig. 5(c). Four tests were conducted on this test rig configuration. A brief description and evaluation of these tests is given below.

The baseline test of a compressor shutdown without opening the recycle valve (case 89) was conducted and results are comparable to Cases 54 and 75 before since the recycle valve did not participate in the shutdown.

A typical compressor shutdown test was then conducted (case 90) in which coincidental signals were sent to the compressor and the recycle valve. The resulting prestroke in this case was approximately 80 ms and the valve stroke was also 80 ms. The shutdown process is shown on the H-Q_a plot of Fig. 15(a) manifesting again the typical "sickle" shape of a shutdown
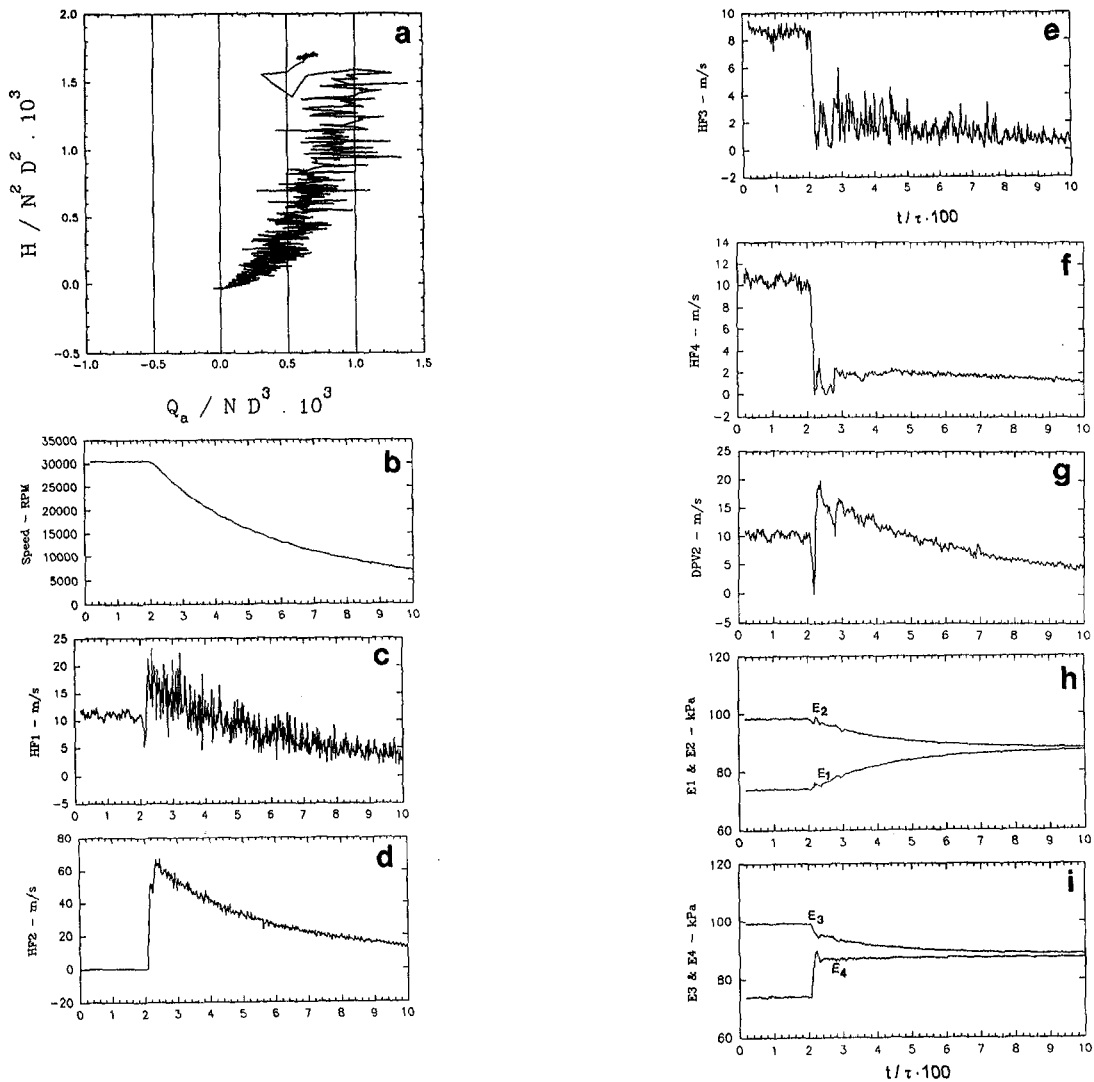
Fig. 8 Measurement and simulation results of case 55: (a–i) measurements; (j–q) simulation

with no surge cycles. One notes here that the amount of flow drop immediately following compressor shutdown is also small compared to the similar case of Configuration A (Case 55) and the same as Configuration B (case 74). Compare the HF1 measurements of these cases (Figs. 8(c), 12(b), 15(b)). Comparing cases 74 and 90 indicates that locating the recycle valve close to either the compressor suction or discharge will have the same effect in minimizing the flow reduction following a shutdown. This is due to the fact that an effective positive flow is quickly established through the compressor as it takes a shorter time for the pressure waves to arrive at the compressor to effect this increase in flow. Although the effect is the same, the nature of the pressure and flow disturbances are different in the two cases. In the case when the recycle valve is close to the compressor suction, the pressure wave and associated positive flow arrive at the compressor inlet first and helps in moving the operating point to the right. In the case when the recycle valve is located close to the discharge side, a rarefaction wave, propagating upstream as a result of opening the recycle valve, arrives at the compressor discharge first. This rarefaction wave is associated with negative flow relative to direction of propagation, which is positive with respect to the compressor, hence producing the same effect of moving the operating point on the H-Q_a plot to the right.

Increasing the prestroke by 50 ms as shown in Table 1 (case 91), only increases the risk of surge but no reverse flow was

observed. Keeping the prestroke time the same, at 80 ms, and increasing the stroke to 1000 ms (case 95) also did not affect the results.

5.0 Comparison Between Experimental and Numerical Results

A few cases were selected to perform numerical simulation of the respective shutdown scenarios. These cases are:

Configuration A—Cases 21, 54, 55, 60

Configuration C—Case 90

In all cases, steady-state operation conditions were first established numerically by adjusting the amount of suction and discharge valve throttling equally to obtain the required flow through the compressor matching the measured condition. The speed of the compressor was maintained constant at 30,500 rpm during this steady-state operation. Transient shutdown procedure is then initiated by means of changing two boundary conditions. First, the compressor operating condition is changed from a constant speed to a shutdown where the left-hand side of Eq. (5) is set to zero when the shutdown signal is initiated, leaving the fluid torque and shaft inertia to interact according to Eq. (5). Second, the recycle valve is opened according to the required prestroke and stroke periods in each case.
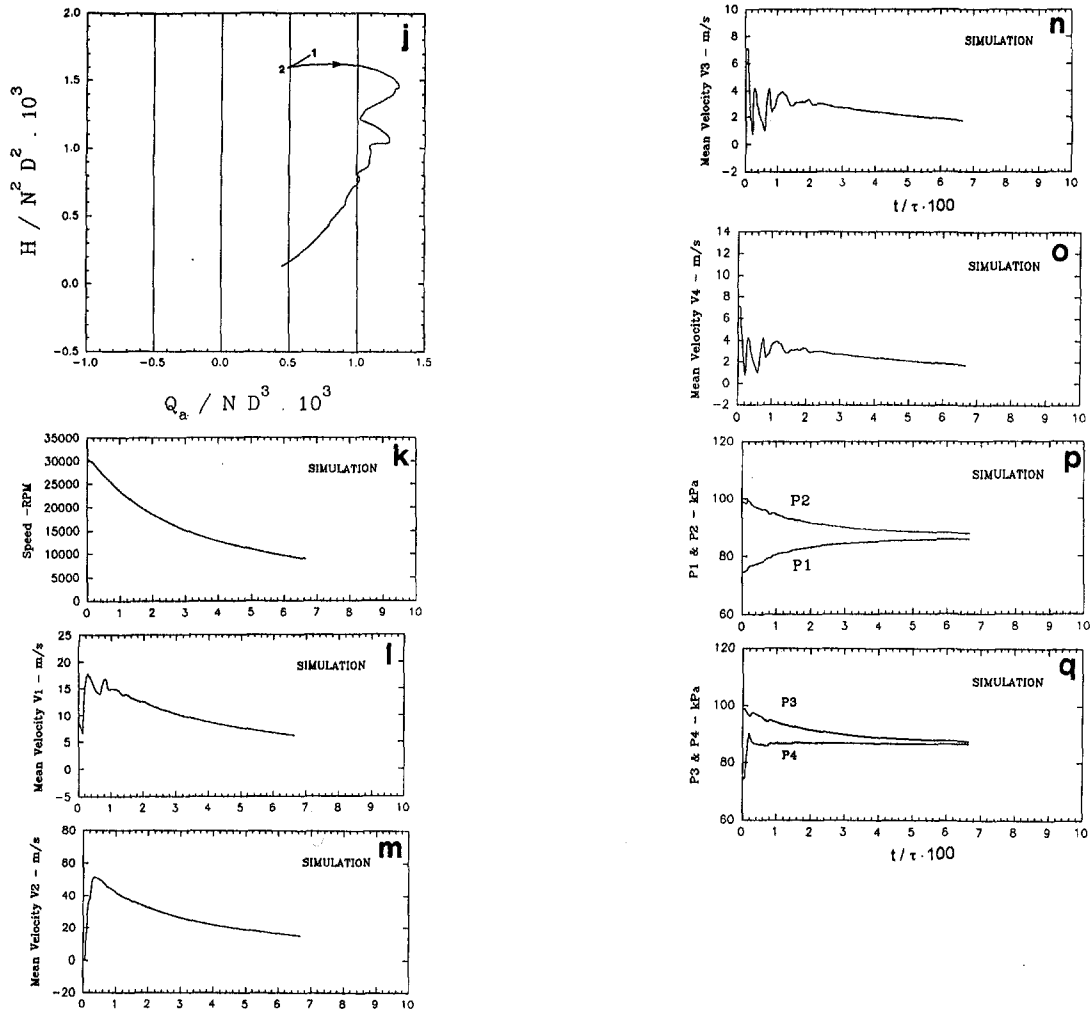
Fig. 8 (Continued)

The result of the numerical simulation for case 21 is shown in Fig. 6(*b*). Good agreement between measurement and simulation is demonstrated in this case. An obvious kink on the *H*-Q_a plot is shown around point 2. At this location, the first reflection of the pressure wave arrives at the compressor and changes the slope of the characteristic. Prior to this point, how-

Fig. 9   Measurement results of case 58

Fig. 10   Measurement results of case 71

Fig. 11 Measurement and simulation results of case 60: (a) measurements; (b) simulation

ever, the slope is more or less constant and matches the combined characteristic impedance of the NPS 3 pipe on the suction and discharge. Figure 7(b) shows simulation results of case 54, where the compressor is shown to be undergoing several surge cycles during shutdown. Although there is no exact match, the overall trends of the measurement and simulation are similar.
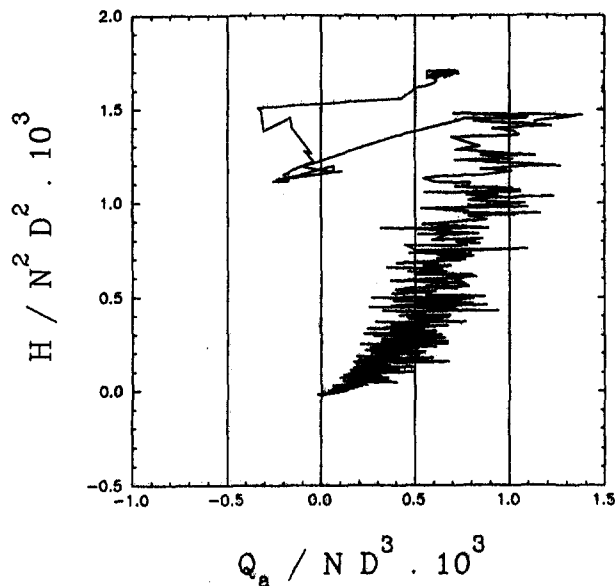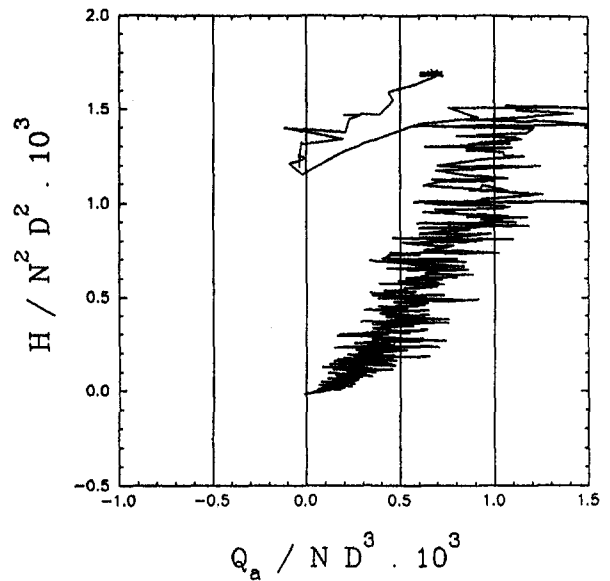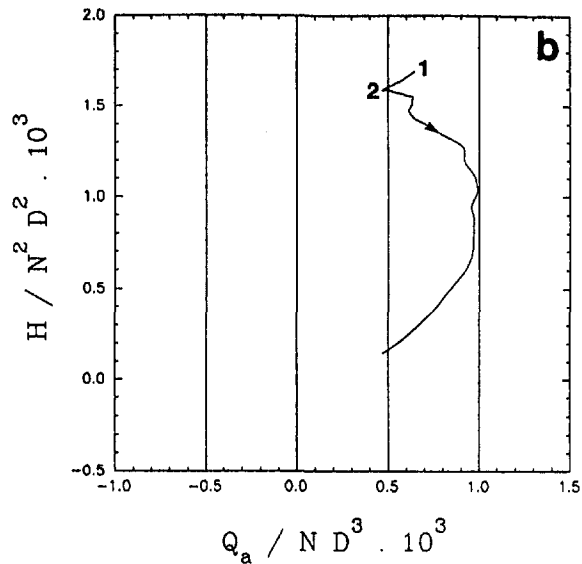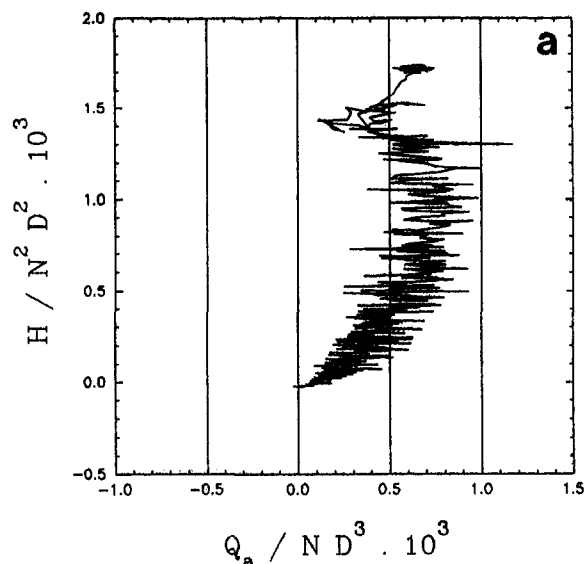
All flow parameters of case 55 are given in Fig. 8(j–q). In this case, the recycle valve opens and prevents the compressor from surging. The typical "sickle" shape previously described as a normal shutdown scenario is duplicated numerically and is in good agreement with the measurements. The slope of the plot between points 1 and 2 again corresponds to the combined characteristic impedance of the main pipe. The sudden increase in the flow past point 2 is obviously due to the recycle valve starting to open. A discrepancy is observed for the flow past point 2, where the simulation results seem to indicate higher flow than that measured. This can be explained as the test rig uses hot films to measure the centerline flow velocity. The mean flow velocity is then estimated based on an assumed fully developed turbulent velocity profile. For the range of Reynolds number of 4×10^4, the power law exponent assumes the value 6.6, resulting in a ratio between the mean velocity and centerline velocity equal to 0.81 [6]. Comparison between HF1 measurements and mean velocity simulation results shown in Figs. 8(c) and 8(l) clearly confirms this ratio in the steady-state range prior to shutdown (HF1 = 10.8 m/s, V1 = 8.6 m/s). Following shutdown, the flow undergoes a transient unsteady condition and the assumption of fully developed velocity profile becomes
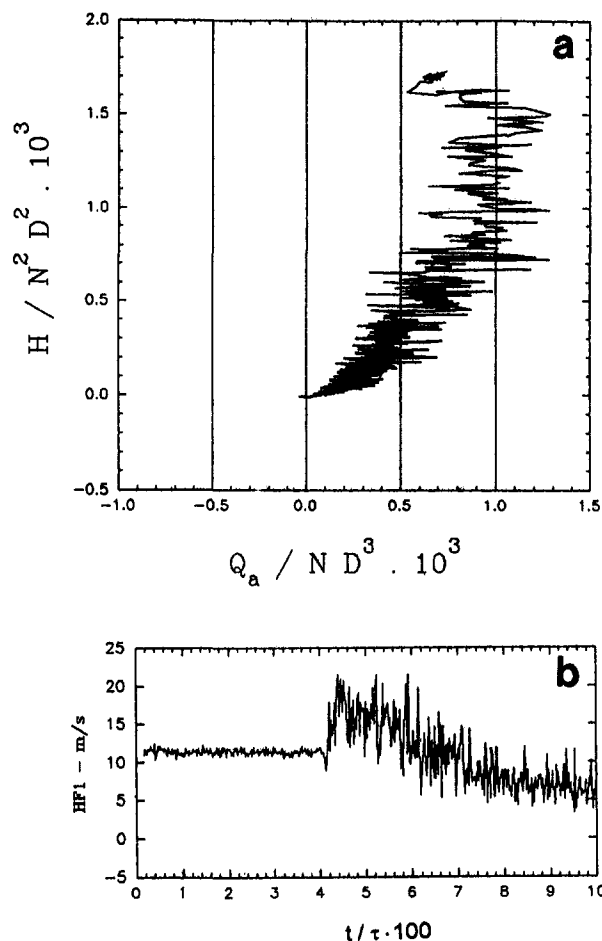

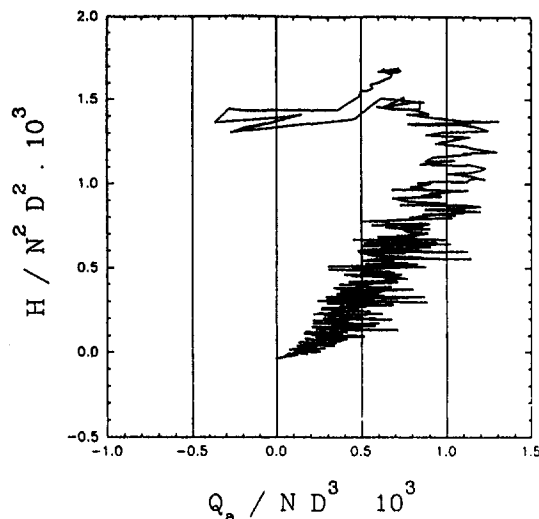Fig. 12 Measurement results of case 74: (a) P-Qa plot; (b) hot-film measurement

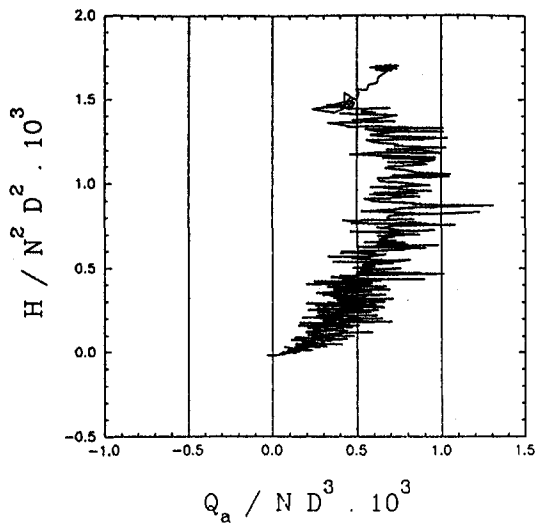Fig. 13 Measurement results of case 80

Fig. 14 Measurement results of case 86

normalized time of 2 in the experimental results. Comparison between the measured centerline velocity and simulated mean velocity in the recycle line (Figs. 8(d) and 8(m)) shows the same trend; however, the magnitude is distorted due to the reason discussed above. Again, good agreement between the flow through the check valve and the main run flow upstream of the recycle tie-in point on the suction side is demonstrated in these figures. Pressure profiles at the compressor suction and discharge show excellent agreement including small pressure oscillations due to valve opening (Figs. 8(h, i, p, q)). The same applies to the pressure traces across the recycle valve.

The results of simulation for case 60 are shown in Fig. 11(b). The sickle shape of the H-Q_a plot during shutdown is similar for both measurement and simulation. The apparent shift of the actual inlet flow is again due to discrepancy between the mean and centerline velocity during transient conditions.

One case from Configuration C was selected for comparison. This is case 90, which also shows good agreement (see Fig. 15).

6.0 Parametric Study of Various Configurations

The previous section demonstrated a satisfactory agreement of the simulation method. The method was then used to conduct a parametric study on various recycle system configurations in an attempt to elaborate on measurement results systematically.

Six different recycle system configurations were considered and are shown schematically in Fig. 16. The first three configurations correspond exactly to the tested configurations A, B, and C, and are also labeled with the same letters. Configuration D is a reverse of Case C where the recycle valve is located close to the compressor suction instead of the discharge. Configuration E represents a very short recycle line, where the

invalid, i.e., the assumed ratio between the mean velocity and centerline velocity does not hold. During the transient period, the ratio between the mean velocity from simulation and centerline velocity from measurements is not constant or matching the steady-state value, and for the most part is greater than 0.81. This explains the apparent discrepancy of the H-Q_a plots of Figs. 8(a) and 8(j), and other cases presented here.

Figures 8(b) and 8(k) also show the good agreement between compressor speed deceleration curves. Note that a normalized time of 0 in the simulation results corresponds to a

Fig. 15 Measurement and simulation results of case 90: (a, b) measurements; (c, d) simulation
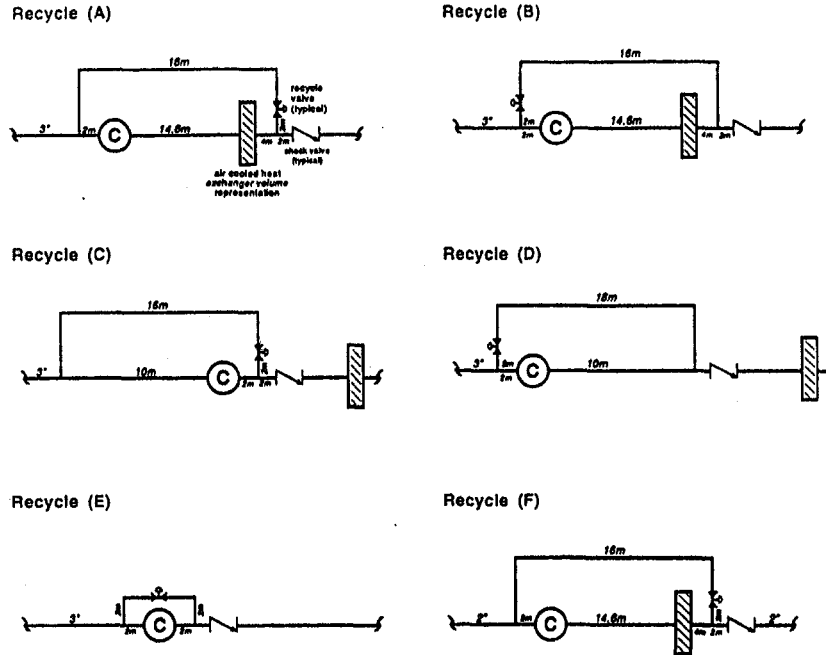
Fig. 16 Six different recycle system configurations considered in the numerical parametric study

recycle valve is located close to the compressor on both sides due to the short recycle line. Configuration F is the same as A, except the mainline size was made smaller (NPS 2 instead of NPS 3) in order to show the effect of the mainline characteristic (specific) impedance on shutdown.

The process adopted in the following analysis is based on conducting two simulations per configuration. The first simulation is performed assuming that the recycle valve does not open, and determines the time taken from the shutdown signal to the last positive flow through the compressor before the first surge occurs. The second simulation is actually a trial and error process in which the recycle valve is opened ahead of the surge point at different times to prevent surge. The shortest time required between the valve starting to lift off its seat (beginning of the stroke) and the previously established time to surge from the first simulation determines how critical the recycle system is to valve prestroke. Clearly, the shorter the time the less stringent the demand will be on the recycle valve prestroke time.

Figures 17(a, b) show the result of Configuration A following a shutdown while the recycle valve is closed. Here the compressor experienced the first reversed flow occurrence at 85 ms from the shutdown signal. The slope of the H-Q_a plot from the steady-state point (1) to the last positive flow point (2) follows the slope determined from combined characteristic impedance corresponding to the NPS 3 mainline. Notice also in Fig. 17(b) that the check valve ($\dot{m}_c$ is the mass flow rate through the check valve) closes after the compressor goes into surge and is closed due to the reversed flow through the compressor and not due to a reflected wave from far downstream boundary. Hence, the length of the discharge pipe is deemed to be adequate and does not affect the phenomenon examined here. The results of the second simulation are shown in Figs. 17(c, d), where it was found by trial and error that the recycle valve has to start to open at 42 ms to prevent the compressor from undergoing reversed flow. Therefore, we say that the valve has to start to

open 43 ms before the critical point when the flow through the compressor is reversed.

In Configuration B, the surge point occurs at 101 ms after the shutdown signal. To prevent this from happening, the recycle valve has to start to open at 88 ms. This means that a time difference of 13 ms is required between the two events, which represents some improvements over Configuration A.

Configuration C represents less capacitance in the recycle loop and the recycle valve is located close to the compressor discharge. The results of simulation for this configuration indicate that the time difference is (106 − 100 = 6 ms). Configuration D results gave a time difference of (111 − 105 = 6 ms). Results for configuration E are similar, giving a time difference of (119 − 113 = 6 ms). The following is a summary of the five configurations:

Configuration	A	B	C	D	E
Time difference (ms)	43	13	6	6	6

Examining the location of the recycle valve with respect to the compressor in these configurations and correlating this with the resulting time difference clearly shows that when the recycle valve is located close to the compressor (on either the suction or the discharge), minimum advance time is required to open the recycle valve ahead of the expected surge point to prevent the compressor from undergoing surge, during shutdown operation. This conclusion substantiates the observation drawn from the experimental results of Section 4.0 above.

Simulation results of Configuration F shown in Fig. 18 indicate that there is no need to open the recycle valve since the slope of the main line characteristic impedance is high enough to prevent the compressor from going into surge. Notice that the slope 1–2 of Fig. 18(a) is twice that of any of Fig. 17(a). This is primarily due to area ratio between 2″ and 3″ mainlines and the resulting characteristic impedance of the pipe.
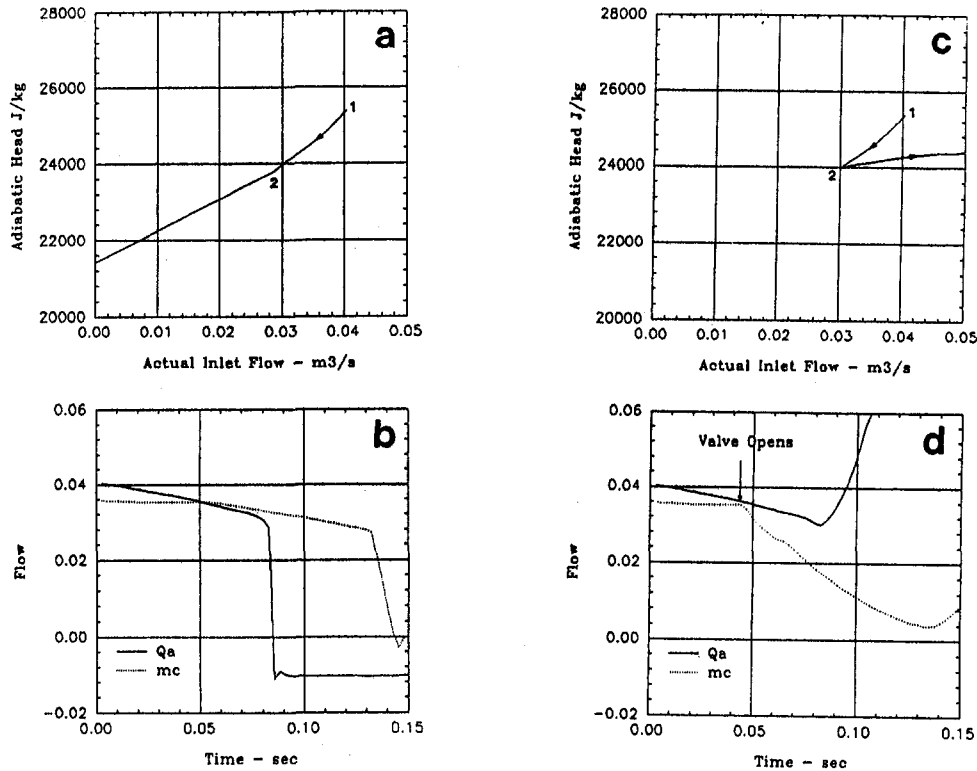
Fig. 17 Numerical results of configuration A of Fig 16: (a, b) recycle valve closed; (c, d) recycle valve opened

7.0 Conclusions

The following conclusions are drawn from the present investigation:

1 The recycle valve prestroke delay is more important than the stroke time. It should be made as short as possible to prevent the compressor from undergoing surge following shutdown. This is an important conclusion, which should attract the attention of valve manufacturers and design engineers. Although the stroke time is not important, it is postulated that the initial phase of the valve lifting off its seat contributes to the fate of the compressor following a shutdown. A minimum C_g coefficient should be established in this initial phase, following which any stroke time (within reason) to the full opening of the valve would be acceptable.

2 It was clearly demonstrated that the recycle valve should be located as close as possible to the compressor with no preference to either the suction or the discharge side of the compressor. If this is implemented, the capacitance of the other side of the recycle system does not affect the results nor will it increase the risk of surging the unit following a shutdown. However, it may be preferable to choose the discharge side rather than the suction side, as from experience, locating the recycle valve close to the compressor suction could affect the inlet flow measurements and could also generate flow turbulence, which may start a sequence of instabilities leading to a compressor surge.

3 The three important decisive parameters in determining whether the compressor would undergo surge cycles (reversed flow) following shutdown are illustrated in the sketch of Fig 19. These are:

(i) The characteristic impedance of the combined suction and discharge main pipe to the compressor determines the slope of the system characteristic line of the pressure/flow disturbance (line 1–2 and line 3–4 in the figure). The smaller the diameter of this pipe, the steeper the characteristics and the better chance that a positive solu-
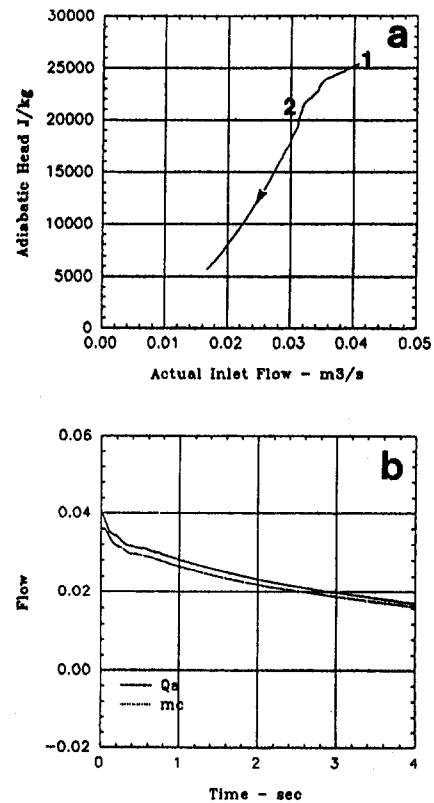

Fig. 18 Numerical results of configuration F of Fig. 16 (recycle valve closed)
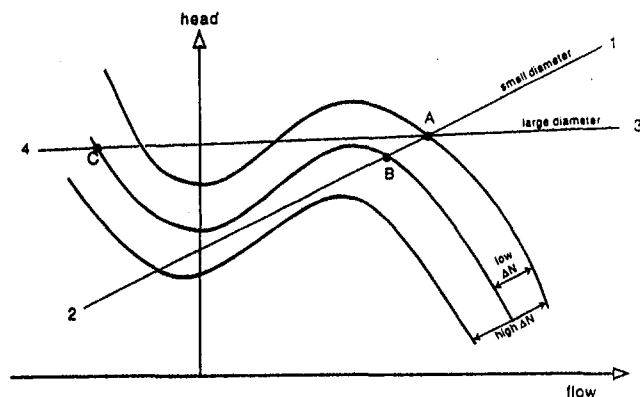
Fig. 19 Relation between compressor and mainline characteristics

tion exists, as defined from the intersection of this line with the compressor characteristics at the next speed line (at time $t - \Delta t$). It is shown that line 1–2 will result in stable operation during shutdown, while that of 3–4 (corresponding to larger diameter) would result in a surge situation. From the impedance aspect, it is better to make main run size as small as possible in order to increase the characteristic impedance and hence steepen the characteristic line. However, one limitation is imposed and that is the level of acceptable pressure losses permitted on the suction and discharge yard piping (commonly restricted to 35 kPa each).

(ii) The shape of the compressor characteristics (wheel map). It is not clear whether a flat characteristic would be better than a steeper one or not.

(iii) The drop in the compressor speed (ΔN) in the time interval (Δt) is function of the shaft inertia. For higher shaft inertia, the magnitude of (ΔN) is small and hence a solution exists in the positive region of the compressor (point B). This means that the operating point of the compressor will be moving along the characteristic line (1–2) slowly as the compressor decelerates. For lower shaft inertia, the magnitude of (ΔN) is large and a solu-

tion does not exist on the positive side; then a jump (surge) to the negative side of the characteristic would occur.

4 Following an emergency shutdown of a centrifugal compressor, the compressor can undergo surge cycles (reversed flow) during deceleration to zero speed. The risk of surge occurring increases with low compressor/power turbine shaft inertia and with shutdown cases from an initial steady state operating point close to the surge control line (i.e., low flow). Driven mainly by the aircraft industry, the current trend of the gas turbine technology is to lower inertia rotors. This poses some problems and engineering challenges when these aeroderivative machines are used in natural gas transmission systems. More involved shutdown control protocols and time sequencing of signal are necessary to synchronize the recycle valve opening with the shutdown signal to prevent surge during shutdown.

Acknowledgments

References

1 Botros, K. K., Richards, D. J., Brown, R. J. and Stachniak, D. M., "Effects of Low Power Turbine/Compressor Rotor Inertia During Shutdown," presented at the 1993 Symposium on the Industrial Application of Gas Turbines, Canadian Gas Association, Banff, Alberta, Oct. 13–15, 1993.

2 Botros, K. K., and Petela, G., "Transient Simulation of Compression Systems," presented at the 1994 ASME Fluids Engineering Division, Summer Meeting—Advances in Computational Methods in Fluid Dynamics, Lake Tahoe, NV, June 19–23, 1994.

3 Moore, F. K., and Greitzer, E. M., "A Theory of Post-stall Transients in Axial Compression Systems: Part I—Development of Equations," ASME JOURNAL OF ENGINEERING FOR GAS TURBINES AND POWER, Vol. 108, 1986, pp. 68–76.

4 Odom, F. M., "Tutorial on Modelling of Gas Turbine Driven Centrifugal Compressors," presented at the PSIG Annual Meeting, Oct. 18–19, 1990.

5 Botros, K. K., "Transient Phenomena in Compressor Stations During Surge," ASME JOURNAL OF ENGINEERING FOR GAS TURBINES AND POWER, Vol. 116, 1994, pp. 133–142.

6 Schlichting, H., Boundary-Layer Theory, 7th ed., McGraw-Hill, New York, 1955, pp. 599–600.

Optimization of Regenerated Gas Turbines

D. S. Beck

Engineering Consultant,
Wellesley, MA 02181

An algorithm for the optimization of regenerated gas turbines is given. For sets of inputs that are typical for automotive applications, the optimum cycle pressure ratio and a set of optimized regenerator parameters that maximize thermal efficiency are given. A second algorithm, an algorithm for sizing regenerators based on outputs of the optimization algorithm, is given. With this sizing algorithm, unique regenerator designs can be determined for many applications based on the presented optimization data. Results of example sizings are given. The data indicate that one core (instead of two cores) should be used to maximize thermal efficiency. The data also indicate that thermal efficiencies of over 50 percent should be achievable for automotive applications if ceramic turbines are used.

1 Introduction

Theory shows that regenerated Brayton cycles can achieve significantly higher thermal efficiencies than diesel cycles. The thermal efficiencies of regenerated Brayton cycles are strongly dependent on the overall performance of the regenerators. In automotive regenerated gas turbines (which operate under regenerated Brayton cycles) ceramic-core rotary regenerators are used to transfer heat from the exhaust-gas flow to preheat the compressed-air flow (for a description of rotary regenerators see Kays and London [1]).

The overall regenerator performance includes heat transfer performance, seal-leakage performance, and pressure-drop performance. These performances conflict (see Harper and Rohsenow [3] for explanation), so they must be balanced properly for the cycle to achieve a maximum thermal efficiency. The performances of regenerated gas turbines have suffered because the systems have not been properly optimized.

To aid in optimization, Harper and Rohsenow [3] show effects of independent variations of effectiveness, seal leakage, core and header pressure drops, core thickness, core rotation rate, and core gas-flow mass velocity on thermal efficiency and power output. Their results demonstrate approximate effects of variations of these parameters on the performance of any regenerated gas turbine; however, the trends given by Harper and Rohsenow [3] are precise only for a particular base-case regenerator. Thus, the trends they give are of limited use to the designer.

Currently, regenerator designers must rely on their own experience supplemented by data on trends (such as those given by Harper and Rohsenow [3]); more precise design methods have not been available. In most currently practiced methods, effectiveness is set; core and header pressure drops are estimated; cycle pressure ratio is chosen to maximize thermal efficiency [1]; and the regenerator is designed in part by making arbitrary design choices (such as for gas velocity on one side, for convective-conductance ratio, etc. {see Wilson [4]}).

An optimization algorithm is given in the next section. With this algorithm, the thermal efficiency of the regenerated gas turbine is maximized through optimization of cycle pressure ratio and of a set of regenerator-design-parameter values. Re-

sults of calculations for sets of input parameters that are of interest are given in Section 3. A second algorithm, a regenerator sizing algorithm, is given in Section 4. With this sizing algorithm, unique regenerator designs that produce the maximum thermal efficiency for the inputs to the optimization algorithm are achieved. Results of example sizing calculations are given in Section 4.

The optimization method described in this paper is general. Beck and Wilson [14] describe a method for optimizing regenerators for particular engines. Their method is included in the commercial software RGT-OPT.[2]

2 Method

Optimization of a regenerated gas turbine requires an accurate model of the system's performance. Governing equations that accurately model regenerated gas turbines are given first.

2.1 Compressor and Turbine. The required pressure ratio across the compressor is

$$r_C = r \left[\frac{2 + (\Delta P_0/P_0)_C}{2 - (\Delta P_0/P_0)_C} \right] \qquad (1)$$

where $(\Delta P_0/P_0)_C$ is the normalized pressure drop due to an air filter upstream of the compressor or to a pollution-control device downstream of the exhaust side (C_X side) of the regenerator. The pressure ratio across the turbine is

$$r_E = r \left[\frac{2 - (\Delta P_0/P_0)_N}{2 + (\Delta P_0/P_0)_N} \right]$$

$$\times \left[\frac{2 - (\Delta P_0/P_0)_H}{2 + (\Delta P_0/P_0)_H} \right] \left[\frac{2 - (\Delta P_0/P_0)_X}{2 + (\Delta P_0/P_0)_X} \right] \qquad (2)$$

For given pressure ratios and polytropic total-to-total efficiencies, the outlet total temperatures of the compressor and turbine, respectively, are

$$T_{0Co} = T_{0Ci} r_C^{R/(\overline{c_{pC}} \eta_{p00C})} \qquad (3)$$

and

$$T_{0Eo} = T_{0Ei} r_E^{-R\eta_{p00E}/\overline{c_{pE}}} \qquad (4)$$

[2] RGT-OPT is a trademark of Douglas S. Beck and is available from him.

The average specific heat capacities are calculated as follows:

$$\overline{c_{pC}} = c_p \left(\frac{T_{0Ci} + T_{0Co}}{2} \right) \tag{5}$$

$$\overline{c_{pE}} = c_p \left(f, \frac{T_{0Ei} + T_{0Eo}}{2} \right) \tag{6}$$

The correlations of Chappell and Cockshutt [5] were used to calculate the specific heat capacities.

2.2 Combustor. A finite normalized pressure drop across the combustor, $(\Delta P_0/P_0)_H$, is required for proper combustion. The required fuel addition to achieve a given Turbine Entry Temperature (TET) for a given combustor inlet temperature was calculated using the correlations of Chappell and Cockshutt [5].

2.3 Regenerator. Equations that describe regenerator heat transfer, leakage, and pressure-drop performances are given in this subsection. These performances must be balanced to maximize the thermal efficiency of a regenerated gas turbine.

2.3.1 Heat Transfer Performance. A regenerator's heat transfer performance is quantified by its effectiveness. For optimization of a regenerated gas turbine, correlations that permit rapid calculation of effectiveness are required.

Effectiveness has been calculated for different ranges of system-parameter values. Analytical results are available for infinitely fast core rotation ($C_{ROT} \rightarrow \infty$): for $C_{ROT} \leq \infty$, finite-difference integration schemes have been used.

Coppage and London [6] give an analytical result that is valid for

1   $0 \leq NTU \leq \infty$;

2   $C_{ROT} = \infty$;
3   $0 \leq C_{RAT} \leq 1$;
4   $0 \leq (hA)' \leq \infty$; and
5   $\lambda = 0$.

The following result is identical to the effectiveness of a counterflow recuperator with zero axial conduction:

$$\epsilon_{CF} = \begin{cases} \dfrac{1 - \exp(-NTU[1 - C_{RAT}])}{1 - C_{RAT}\exp(-NTU[1 - C_{RAT}])} & \text{if } C_{RAT} < 1 \\[3mm] \dfrac{NTU}{1 + NTU} & \text{if } C_{RAT} = 1 \end{cases} \tag{7}$$

Lambertson [7] considered finite core-rotation rates. He gives calculated effectiveness data for the following ranges of system-parameter values:

1   $1 \leq NTU \leq 10$;
2   $1 \leq C_{ROT} \leq \infty$;
3   $0.1 \leq C_{RAT} \leq 1$;
4   $0.25 \leq (hA)' \leq 1$; and
5   $\lambda = 0$.

He also gives the following rotation effect[3]:

$$\Delta_{ROT} = \frac{-1}{9C_{ROT}^{1.87}} \tag{8}$$

With this rotation effect, effectiveness can be calculated to

---

[3] Lambertson [7] defines his rotation effect with an opposite sign. In this report, "effects" are defined to be negative for effectiveness reductions.

——— Nomenclature ———

As = core-material area available for conduction, m^2

$As' = As_N/As_X$

$BS/A = [\dot{m}_{Xlc}\sqrt{RT_d n}]/[P_c\alpha\gamma\delta(R_o - R_i)\sqrt{2}]$ (seal-leakage parameter)

c = specific heat capacity, J/kg − K

C = heat-capacity rate, W/K

$C_f = 2\tau_0/(\rho_{fluid}U^2)$ (fluid-friction coefficient)

$C_N' = C_N/C_{in}$

$C_{RAT} = C_N/C_X$

$C_{ROT} = C_R/C_N$

D_H = 4 times the passage area divided by the wetted perimeter (hydraulic diameter), m

D_o = outer diameter of the regenerator-core annulus, m

$f = \dot{m}_{fuel}/\dot{m}_{air}$ (fuel-to-air ratio)

$Fo = SC\lambda/[2(1 - SC)C_{ROT}]$ (Fourier number)

h = convective heat transfer coefficient, W/m^2 − K

(hA) = convective conductance, W/K

$(hA)' = (hA)_N/(hA)_X$

k = thermal conductivity, W/m − K

$l = As_S/[2(R_o - R_i)n]$, m

L = length of a core passage (or core thickness), m

$\dot{m}$ = mass-flow rate, kg/s

n = number of labyrinth-seal throttlings

N_{cores} = number of heat-exchanger cores

$NTU = (hA)_N/\{C_N[1 + (hA)']\}$ (Number of Transfer Units)

$Nu = hk_{fluid}/D_H$ (Nusselt number)

$p = \dfrac{\text{core voids volume}}{\text{total core volume}}$ (porosity)

P = pressure, Pa

$\dot{Q}_{in}$ = rate of heat addition to the heater or combustor, W

r = pressure ratio (with no subscript, $\equiv P_{0Co}/P_{atm}$)

R = gas constant for air = 286.96 J/kg − K

R_i = inner radius of the regenerator-core annulus, m

R_o = outer radius of the regenerator-core annulus, m

$Re = UD_H/\nu$ (Reynolds number)

$SC = As_S/(As_S + As_N + As_X)$ (Seal Coverage)

T = temperature, K

$TET = T_{0Ei}$ (Turbine Entry Temperature), K

u = velocity, m/s

U = average fluid velocity, m/s

$W' = \dot{W}_{out}/(C_{in}T_{atm})$ (specific power)

$\dot{W}_{out}$ = engine power output, W

y = vertical coordinate in oblique-flow headers (see Fig. 1), m

Y_i = inlet-header height (see Fig. 1), m

Y_o = outlet-header height (see Fig. 1), m

α = direct-seal-leakage flow coefficient

$\beta = k_R(ReC_f)/D_H^2$ (flow-friction parameter), W/m^3 − K

γ = carry-over factor for labyrinth seals

δ = seal clearance, m

$\Delta_o = (Nu \, k_R D_o^4)/(D_H \dot{W}_{out})^2$, m/W − K

$\Delta_{ROT} = (\epsilon_{ROT} - \epsilon_{CF})/\epsilon_{CF}$

$\Delta_{AC} = (\epsilon_{AC} - \epsilon_{CF})/\epsilon_{CF}$

$\Delta_{scl} = [Nuk_R]^{1/8}/[\sqrt{l}\alpha\gamma\delta D_H^{1/4}]$, W$^{1/8}$/m$^{15/8}$ − K$^{1/8}$

$\Delta_S = [\epsilon_{ROT,AC,S} - \epsilon_{ROT,AC}]/[\epsilon_{ROT,AC} - \epsilon_{ROT,AC,S}(SC \rightarrow 1)]$

$(\Delta P_0/P_0) = 2(P_{0i} - P_{0o})/(P_{0i} + P_{0o})$

$\epsilon = (T_{0No} - T_{0Ni})/(T_{0Xi} - T_{0Ni})$ (effectiveness)

$\hat{\epsilon}$ = effectiveness estimate (calculated from a correlation)

$\zeta = y/Y_o$

η = efficiency

$\eta_{TH} = \dot{W}_{out}/\dot{Q}_{in}$ (thermal efficiency)

within 1 percent for the following ranges of system-parameter values:

1 $1 \leq \text{NTU} \leq 9$;
2 $1.25 \leq C_{\text{ROT}} \leq 5$;
3 $0.9 \leq C_{\text{RAT}} \leq 1$;
4 $0.25 \leq (hA)' \leq 1$; and
5 $\lambda = 0$.

Kays and London [1] modify the exponent in the rotation effect from 1.87 to 1.93, and they recommend the use of the resulting rotation effect for $\epsilon \leq 90$ percent. The author recommends the following rotation effect, which comes from correlation of effectiveness data calculated using Lambertson's method [7]. This effect permits accurate effectiveness calculation for all practical ranges of system-parameter values.

$$\Delta_{\text{ROT}} = - \left[(0.0018636 \text{ NTU}^2 + 0.39482 \text{ NTU} + 9.5909) \right.$$
$$\left. \times (C_{\text{ROT}}^{-0.0025\text{NTU}+1.65}) \right]^{-1} \quad (9)$$

Banhke and Howard [8] considered the effect of axial conduction in the core. They give calculated effectiveness data for

1 $1 \leq \text{NTU} \leq 100$;
2 $1 \leq C_{\text{ROT}} \leq \infty$;
3 $0.9 \leq C_{\text{RAT}} \leq 1$;
4 $0.25 \leq (hA)' \leq 1$;
5 $0 \leq \lambda \leq 0.32$;
6 $0.25 \leq As' \leq 1$; and
7 $SC = 0$.

Shah [2] gives the following expression for correlation of Bahnke and Howard's [8] data:

$$\epsilon_{\text{ROT},AC} = \epsilon_{CF} \left(1 - \frac{1}{9C_{\text{ROT}}^{1.93}} \right) \left(1 - \left[\frac{1}{2 - C_{\text{RAT}}} \right] \right.$$
$$\left. \times \left[\frac{1}{1 + \text{NTU} - \kappa \text{ NTU}^3/a^2} - \frac{1}{1 + \text{NTU}} \right] \right) \quad (10)$$

where

$$a \equiv 2\sqrt{\text{NTU}^2 + \frac{\text{NTU}}{\lambda}} \quad (11)$$

and

$$\kappa \equiv 4 - \left[\frac{8}{a} \right] \left[1 - \frac{1 - e^{-a}}{\sinh a} \right] \quad (12)$$

Shah [2] reports that this correlation agrees with Bahnke and Howard's [8] data to within 1 percent for

1 $1 \leq \text{NTU} \leq 20$;
2 $2 \leq C_{\text{ROT}} \leq \infty$;
3 $0.9 \leq C_{\text{RAT}} \leq 1$;
4 $0.25 \leq (hA)' \leq 1$; and
5 $0 \leq \lambda \leq 0.08$.

From Shah's [2] correlation, the following axial-conduction effect can be inferred:

$$\Delta_{AC} = - \left[\frac{1}{2 - C_{\text{RAT}}} \right]$$
$$\times \left[\frac{1}{1 + \text{NTU} - \kappa \text{ NTU}^3/a^2} - \frac{1}{1 + \text{NTU}} \right] \quad (13)$$

Beck [9] considered the effect of seal width on regenerator effectiveness. He gives Matlab[4] code for calculating effectiveness data under the assumptions of axial conduction and finite seal width. His method was used to verify the accuracy of the following seal-width effect.

$$\Delta_S = \exp\{ (-1.16C_{\text{ROT}}$$
$$- 13.88) Fo^{(0.1245\lambda - 0.01798 C_{\text{ROT}} + 0.9653)} \} - 1 \quad (14)$$

Using the expression for the effectiveness of a counterflow recuperator (Eq. (7)) and for the rotation, axial-conduction, and seal-width effects given above (Eqs. (9), (13), and (14)), effectiveness can be calculated accurately by the following equation:

$$\epsilon_{\text{ROT},AC,S} = (1 + \Delta_{\text{ROT}})(1 + \Delta_{AC})(1 + \Delta_S)\epsilon_{CF}$$
$$- [\Delta_S][\epsilon_{\text{ROT},AC,S}(SC \to 1)] \quad (15)$$

where

$$\epsilon_{\text{ROT},AC,S}(SC \to 1) = 0.50505 + 0.257/(C_{\text{ROT}} - 0.5) \quad (16)$$

In Table 1 are shown effectiveness data calculated using Beck's [9] method and effectiveness estimates calculated using the recommended correlation (Eq. (15)) and Shah's [2] correlation (Eq. (10)). Note that $\hat{\epsilon} \equiv \epsilon_{\text{ROT},AC,S}$ (from Eq. (15)), and $\hat{\epsilon}_{\text{Shah}} \equiv \epsilon_{\text{ROT},AC}$ (from Eq. (10)) in Table 1. Comparison of the effectiveness data with the effectiveness estimates from the correlations shows that the recommended correlation can be more accurate than Shah's [2].

---

[4] ©Copyright The MathWorks, Inc. 1984–1992. Matlab is commercial software with linear-algebra functions.

────────── **Nomenclature (cont.)** ──────────

Θ = angle subtended by the relevant annulus area, deg
$\lambda = k_R As_N(1 + 1/As')/(LC_N)$ (conduction parameter)
μ = viscosity, kg/m − s
$\nu = \mu/\rho$ (kinematic viscosity), m^2/s
ρ = density, kg/m^3
τ_0 = passage-wall shear stress, Pa
τ_{ROT} = period for one rotation of the regenerator core, s

Subscripts

0 = total or stagnation
AC = considering axial condution in the regenerator core

atm = atmospheric
c = carry-over
C = of compressor
CF = of a counterflow recuperator
d = direct
E = of expander or turbine
H = of heater or combustor
i = at the inlet
in = into a heat engine
l = leakage
m = in regenerator-core passages
N = on the heat-exchanger side of minimum heat-capacity rate
o = at the outlet

p = evaluated at constant pressure; polytropic
r = of a flow resistance
R = of the regenerator core
ROT = considering regenerator-core rotation
S = considering seal width
Shah = reference to R. K. Shah's [2] effectiveness correlation
st = static
tot = total
X = on the heat-exchanger side of maximum heat-capacity rate

Table 1 Comparison of effectiveness correlations

NTU	250	100	50	20
C_{ROT}	5	7	3	5
C_{RAT}	0.99	0.99	0.97	0.98
$(hA)'$	0.8	1.3	1.0	0.7
λ	0.001	0.01	0.01	0.001
As'	0.9	1.2	0.9	0.6
SC	0.08	0.1	0.1	0.06
ϵ	0.9976	0.9814	0.9745	0.9559
$\hat{\epsilon}$	0.9970	0.9804	0.9745	0.9559
$(\epsilon - \hat{\epsilon})/\epsilon$ (%)	0.06	0.10	0	0
$\hat{\epsilon}_{Shah}$	0.9932	0.9822	0.9694	0.9553
$(\epsilon - \hat{\epsilon}_{Shah})/\epsilon$ (%)	0.44	-0.08	0.52	0.06

2.3.2 Leakage Performance. Harper [10] gives a comprehensive analysis of coupled direct and carryover seal leakages. The principal result of his analysis is the following implicit expression for the total seal leakage (direct and carry-over combined):

$$\frac{1}{1 + \dot{m}_{Xlc}/\dot{m}_{Xltot}} - \frac{1}{1 + (\dot{m}_{Xlc}/\dot{m}_{Xltot})(1/r)}$$
$$- \ln\left[\frac{1 - (\dot{m}_{Xlc}/\dot{m}_{Xltot})(1/r)}{1 - \dot{m}_{Xlc}/\dot{m}_{Xltot}}\right] = \left(\frac{BS}{A}\right)^2 \quad (17)$$

Total seal leakage decreases as carry-over leakage, $\dot{m}_{Xlc}$, decreases. Total seal leakage also decreases as the dimensionless seal-leakage parameter, BS/A, increases. An expression for the carry-over leakage is

$$\dot{m}_{Xlc} = C_{ROT}\left[\frac{p}{1 - p}\right]\left[\frac{1}{(\rho c)_R}\right] C_N \rho_c \quad (18)$$

In the optimization algorithm, the core-material specific heat capacity per unit volume, $(\rho c)_R$, is an input. The parameters C_N and ρ_c are calculated from inputs to the algorithm. The parameters C_{ROT} and p are optimized in the algorithm.

An expression for the seal-leakage parameter is

$$\frac{BS}{A} = \left\{\left(\frac{\dot{m}_{Xlc}}{P_c C_N^{1/4}}\right)\left(\frac{\pi^{3/4}}{2}\right)\sqrt{RT_d}k_N^{1/8}\Delta_{scl}\right\}$$

$$\times \left\{p\left(\frac{As'}{1 + As'}\right)^5 \frac{(1 - SC)^6}{\lambda[1 + (hA)'][1 - p]^7 NTU}\right\}^{1/8}$$

$$\times \left\{\frac{[1 - (R_i/R_o)^2]^{3/4}}{[1 - R_i/R_o]^{3/2}}\right\} \quad (19)$$

In the optimization algorithm, the seal leakage is assumed to leak from the compressor outlet to the outlet of the C_X side of the regenerator. Harper and Rohsenow [3] show that regenerator performance is modeled accurately under this assumption for high-effectiveness regenerators.

The seal-clearance parameter Δ_{scl} is an input to the optimization algorithm. The pressure of the carry-over leakage, P_c; the temperature of the direct leakage, T_d; and the thermal conductivity of the air on the compressed-air side (C_N side), k_N, are calculated from inputs to the algorithm. The remaining parameters in Eq. (19) are optimized in the algorithm.

2.3.3 Pressure-Drop Performance. In a regenerator, a serious effectiveness reduction can be incurred through a nonuniform flow distribution in the core (see Wilson [11]). A uniform

flow distribution can be produced with pressure drops in the inlet and outlet headers. London et al. [12] give analyses of flows in two-dimensional oblique-flow headers that effect uniform flow distributions in the core. Their results were used in the optimization algorithm although three-dimensional headers typically are used in practice: The functional dependencies of the relevant parameters on pressure-drop performance should be similar for three-dimensional and two-dimensional oblique-flow headers, and the magnitudes of their pressure drops could be made close through proper design. A schematic of a rotary-regenerator-core cross section with inlet and outlet headers is shown in Fig. 1. Nomenclature is defined in the figure.

The principal results of the analyses of London et al. [12] for counterflow headers are that the velocity profile at the exit of the outlet header is

$$\frac{u_o}{U_o} = \frac{\pi}{2}\sin\left(\frac{\pi}{2}\zeta\right); \quad (20)$$

that the inlet and outlet headers are box-shaped; and that the shape of the inlet header is given by

$$\frac{Y_i}{Y_o} = \sqrt{\left(\frac{4}{\pi^2}\right)\frac{\rho_{sto}}{\rho_{sti}}} \quad (21)$$

They give criteria for validity of their analyses:

$$\frac{\Delta P_{st,m+r}}{\frac{1}{2}\rho_{sti}U_i^2} > \frac{1}{2} \quad (22)$$

and

$$\frac{Y_i}{L} < \frac{1}{3} \quad (23)$$

These results and criteria were used to calculate the core and header pressure drops required for uniform flow distribution.

There is a conflict between designing a heat exchanger for good heat transfer performance and good pressure-drop performance for cases in which the two flows are at substantially different pressures, because on the high-pressure side the core pressure drop may be too low to produce uniform flow distribution. Wilson [13] has proposed the use of a distributing partial screen to produce good flow distribution in low-pressure-drop cases.

The static-pressure drop across the core is

$$P_{sti} - P_{sto} = \Delta P_{st,m+r} \quad (24)$$

where $\Delta P_{st,m+r}$ is the sum of the static-pressure drops across the core and across a partial fluid-flow screen that would be
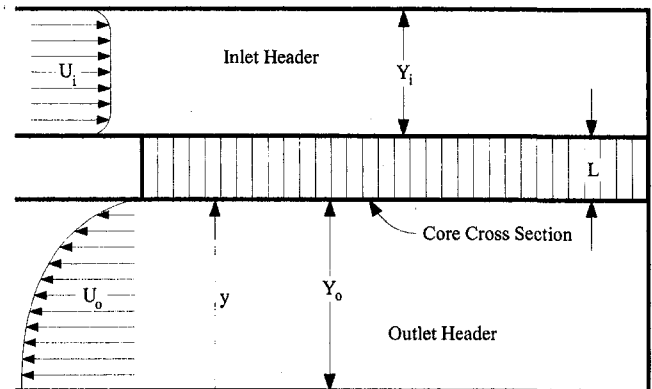
Fig. 1 Schematic of a rotary-regenerator-core cross section with inlet and outlet headers

Journal of Engineering for Gas Turbines and Power

used to satisfy the criterion given by Eq. (22). The static pressure drop across the core can be calculated by

$$\Delta P_{stm} = \frac{2\beta}{\lambda} \left(\frac{\nu}{c_p}\right)_m \left(\frac{C}{C_N}\right)\left(\frac{As_N}{As}\right)\left(\frac{1 + As'}{As'}\right)\left(\frac{1 - p}{p}\right) \quad (25)$$

The normalized squared-mean velocity at the exit of the outlet header can be calculated from Eq. (20):

$$\frac{\overline{u_o^2}}{U_o^2} = \frac{\pi^2}{4} \int_0^1 \left(\sin \frac{\pi}{2} \zeta\right)^2 d\zeta \quad (26)$$

or

$$\frac{\overline{u_o^2}}{U_o^2} = \frac{\pi^2}{8} \quad (27)$$

Conservation of mass and Eq. (21) are used to obtain

$$\left(\frac{U_o}{U_i}\right)^2 = \frac{4}{\pi^2}\left(\frac{\rho_{sti}}{\rho_{sto}}\right) \quad (28)$$

Equations (27) and (28) are used to calculate the squared-mean velocity at the exit of the outlet header:

$$\overline{u_o^2} = \left(\frac{U_i^2}{2}\right)\left(\frac{\rho_{sti}}{\rho_{sto}}\right) \quad (29)$$

The pressure drops across the headers, the core, and the partial screen result in a total-pressure drop from the entrance of the inlet header to the exit of the outlet header. Two inputs to an algorithm that determines the header pressure drop are β and U_i. These parameters are also inputs to the optimization algorithm. Calculations in the header-pressure-drop algorithm follow:

1 $T_{sti} = T_{0i} - U_i^2/(2\overline{c_{pi}})$ where $\overline{c_{pi}} \equiv c_p[(T_{sti} + T_{0i})/2]$;
2 $P_{sti} = P_{0i}(T_{sti}/T_{0i})^{\overline{c_{pi}}/R}$;
3 $\rho_{sti} = P_{sti}/(RT_{sti})$;
4 $\overline{T_0} \equiv (T_{0i} \pm T_{0o})/2$;
5 $\mu_m = \mu_{air}(\overline{T_0})$;
6 $c_{pm} = c_{p_{air}}(\overline{T_0})$;
7 guess P_{0o};
8 $\overline{P_0} \equiv (P_{0i} + P_{0o})/2$;
9 $\rho_m = \overline{P_0}/(R\overline{T_0})$;
10 calculate ΔP_{stm} from Eq. (25);
11 $\Delta P_{st,m+r} = \max [(0.3)\rho_{sti}U_i^2, \Delta P_{stm}]$;
12 guess $\overline{u_o^2}$;
13 $T_{sto} = T_{0o} - \overline{u_o^2}/(2\overline{c_{po}})$ where $\overline{c_{po}} \equiv c_p[(T_{sto} + T_{0o})/2]$;
14 $P_{sto} = P_{0o}(T_{sto}/T_{0o})^{\overline{c_{po}}/R}$;
15 $\rho_{sto} = P_{sto}/(RT_{sto})$;
16 $\overline{u_o^2} = (U_i^2/2)(\rho_{sti}/\rho_{sto})$;
17 go to step 12 until convergence;
18 $P_{sto} = P_{sti} - \Delta P_{sti,m+r}$;
19 $P_{0o} = P_{sto}(T_{0o}/T_{sto})^{\overline{c_{po}}/R}$; and
20 go to step 7 until convergence.

2.4 Optimization.
The equations given in the subsections above were incorporated in a Matlab function. In this function, cycle thermal efficiency was calculated as a function of a set of input-parameter values and of a set of parameters that were varied to achieve maximum thermal efficiency. The Matlab function, CONSTR, was used for the optimization.

2.4.1 Inputs and Optimized Parameters.
In the given equations, eight parameters appear that theoretically could be varied to maximize thermal efficiency: r, C_{ROT}, λ, As', SC, p, R_i/R_o, and NTU; however, the last four of these should be fixed for practical reasons.

Regenerator effectiveness increases with regenerator size or NTU. The only deterrent to increasing NTU is the weak dependence of BS/A on NTU ($BS/A \propto \text{NTU}^{-1/8}$). This is not a strong enough deterrent to prevent an optimal NTU that would be associated with a regenerator that would be too large for automotive applications. For automotive applications, a bound must be put on the core-diameter parameter, Δ_o. Then, NTU can be calculated from this core diameter:

$$\text{NTU} = \left\{ \Delta_o k_N T_{atm}^2 \left(\frac{C_{in}}{C_N}\right)^2 (W')^2 \pi^2 \left[1 - \left(\frac{R_i}{R_o}\right)^2\right]^2 \right\}$$

$$\times \{As'(1 - SC)^2(1 - p)p\}$$

$$\times \{16(1 + As')[1 + (hA)']\lambda\}^{-1} \quad (30)$$

If the core diameter was permitted to increase without bound, then the optimal R_i/R_o that would maximize thermal efficiency would be $R_i/R_o = 1$; the only place R_i/R_o appears in the equations in the previous subsections is in the BS/A equation, and $BS/A \to \infty$ as $R_i/R_o \to 1$. With a bounded D_o, however, there is a strong incentive for $R_i/R_o \to 0$ to increase the core annulus area and NTU (see Eq. (30)). For mechanical considerations, a finite R_i/R_o must be used, so a finite R_i/R_o was input to the optimization algorithm.

For a fixed regenerator-core annulus area, direct seal leakage decreases with increasing seal width (or SC). For fixed flow areas, however, increased SC must be associated with a larger annulus area and a larger $R_o - R_i$ for a fixed R_i/R_o. Seal-leakage penalties due to increases in $R_o - R_i$ are greater than the gains of the associated increases in SC. Thus, the net effect of increasing seal width is to increase, not decrease, seal leakage. From Eq. (19), $BS/A \propto (1 - SC)^{3/4}$. Also, Eq. (30) shows that NTU increases with decreasing SC. Theoretically, $SC = 0$ should be used. For mechanical considerations, a finite SC must be used, so a finite SC was input to the optimization algorithm.

The core porosity, p, appears in the equations for NTU (Eq. (30)), ΔP_{stm} (Eq. (25)), $\dot{m}_{Xlc}$, (Eq. (18)), and BS/A (Eq. (19)). Regenerator size (or NTU) is maximized with a porosity of $p = 0.5$; core pressure drop (ΔP_{stm}) decreases with increasing p; carry-over leakage ($\dot{m}_{Xlc}$) decreases with decreasing p; and BS/A increases with increasing p. It was found that the optimization algorithm invariably converged on porosities that were larger than currently can be manufactured. Therefore, currently achievable porosities were input to the optimization algorithm.

The four parameters that were varied to maximize thermal efficiency are

1 r,
2 C_{ROT},
3 λ, and
4 As'.

Inputs to the optimization algorithm are

1 η_{p00C},
2 η_{p00E},
3 TET,
4 $(\Delta P_0/P_0)_H$,
5 T_{atm},
6 P_{atm},
7 Δ_{sci},
8 $(\rho c)_R$,
9 β,
10 $U_{Co}(U_i$ in Eq. (29)),
11 $U_{Eo}(U_i$ in Eq. (29)),
12 R_i/R_o,
13 Δ_o,
14 SC, and
15 $(\Delta P_0/P_0)_C$.

3 Results

Optimizations were performed to determine sets of optimal parameter values for various inputs. For all runs, $T_{atm} = 288K$; $P_{atm} = 1E5Pa$; $\Delta_{scl} = 4E4W^{1/8}/m^{15/8} - K^{1/8}$; $(\rho c)_R = 2.6E6$ $J/m^3 - K$; $U_{Co} = U_{Eo} = 50$ m/s; $R_i/R_o = 0.2$; $SC = 0.04$; and $p = 0.8$ were used. The seal-clearance parameter, Δ_{scl}, was set so that a cycle pressure ratio of $r = 4.5$ produced a total seal leakage of $\dot{m}_{Xcl} = 5$ percent. Depending on values for Nu, k_R, l, and D_H, Harper's [10] theory typically is invalid for $\Delta_{scl} < 1E6$; however, his theory was used for even these values of Δ_{scl}. His theory was used based on the assumptions that the functional dependence of seal leakage on system-parameter values is preserved for $\Delta_{scl} < 1E6$ and that seal-leakage magnitudes can be correlated through proper choice of $\alpha\gamma$. The value for $(\rho c)_R$ was chosen for a ceramic core. The values for U_{oC} and U_{oE} were considered to be typical of gas turbines.

Other inputs for each run are given in Table 2. Some current designs of regenerated gas turbines employ two cores to reduce thermal gradients in the engine. Two optimizations were performed for two-core designs. The compressor and turbine efficiencies should be achievable for automotive applications. The turbine entry temperatures were chosen for a metallic turbine (1250 K) and ceramic turbines (1450 K and 1683 K). The values for the pressure drops and β and Δ_o that are listed in Table 2 are typical for automotive applications. Results for different values of β and Δ_o can be used to determine optimal regenerator-core passage geometries.

Results of the optimizations are given in Table 3. From these results, the following trends can be inferred. As should be expected (see Wilson [4]), thermal efficiency increases with TET and the compressor and turbine efficiencies. Thermal efficiency decreases with increases in the sum of the total-pressure drops

Table 3 Optimization results

run	optimized parameters					optimization outputs				
	η_{TH} (%)	r	C_{ROT}	λ	As'	C'_N	NTU	T_N (K)	T_X (K)	W'
1	43.0	2.22	3.57	5.21E-4	0.693	1.03	159	734	741	0.310
2	49.6	2.28	2.62	7.31E-4	1.09	1.05	238	821	831	0.434
3	54.6	2.21	3.01	8.00E-4	0.740	1.07	353	926	939	0.544
4	45.8	2.17	3.00	5.07E-4	0.788	1.03	185	731	739	0.327
5	51.9	2.09	2.63	6.70E-4	0.944	1.05	240	822	832	0.417
6	56.6	2.05	3.15	8.51E-4	0.824	1.07	309	928	940	0.523
7	41.5	2.50	4.40	2.75E-4	0.830	1.03	76.0	729	740	0.345
8	48.5	2.55	2.87	3.38E-4	0.706	1.05	122	815	827	0.479
9	54.0	2.50	2.97	4.49E-4	0.699	1.07	160	918	933	0.618
10	43.9	2.43	2.64	2.49E-4	0.727	1.03	90.3	726	738	0.362
11	50.7	2.38	2.87	3.13E-4	0.697	1.05	130	815	827	0.476
12	55.9	2.35	2.85	4.22E-4	0.690	1.07	165	918	933	0.611
13	36.6	3.30	3.04	1.36E-4	0.822	1.03	21.6	714	744	0.411
14	44.7	3.37	3.19	1.59E-4	0.746	1.05	38.1	801	825	0.576
15	51.2	3.30	3.31	1.88E-4	0.791	1.07	57.9	901	925	0.755
16	38.7	3.21	2.51	1.36E-4	0.705	1.03	23.5	711	741	0.432
17	46.5	3.22	2.67	1.56E-4	0.723	1.05	40.4	798	823	0.592
18	53.1	3.08	7.02	1.97E-4	0.703	1.06	53.6	901	923	0.749
19	49.1	2.31	3.08	6.64E-4	1.09	1.03	201	724	731	0.389
20	54.7	2.29	2.89	8.93E-4	1.19	1.05	266	811	821	0.508
21	58.9	2.35	3.00	1.17E-3	1.46	1.07	355	911	925	0.666
22	51.6	2.12	3.04	5.71E-4	1.07	1.03	218	725	732	0.377
23	56.7	2.13	3.00	7.79E-4	1.05	1.05	285	813	822	0.491
24	60.6	2.22	3.07	1.09E-3	1.23	1.07	377	912	926	0.655
25	47.9	2.60	3.00	3.24E-4	0.859	1.03	101	718	728	0.433
26	53.9	2.59	3.01	4.11E-4	0.912	1.05	146	804	816	0.569
27	58.6	2.55	3.00	5.82E-4	1.14	1.07	172	905	921	0.723
28	50.2	2.39	3.04	2.79E-4	0.781	1.03	111	719	728	0.424
29	55.8	2.36	3.09	3.67E-4	0.687	1.05	145	806	817	0.546
30	60.2	2.39	3.00	5.31E-4	1.07	1.07	180	907	922	0.705
31	44.0	3.30	3.00	1.33E-4	0.741	1.02	32.5	706	727	0.501
32	50.9	3.27	3.00	1.59E-4	0.728	1.04	50.2	791	811	0.665
33	56.4	3.28	3.05	1.91E-4	0.784	1.06	73.9	889	910	0.861
34	46.0	3.17	3.00	1.33E-4	0.881	1.03	34.6	704	725	0.515
35	52.5	3.16	3.03	1.58E-4	0.738	1.04	52.3	789	809	0.678
36	57.8	3.27	3.24	1.99E-4	0.710	1.06	75.7	885	905	0.895
37	41.4	2.22	5.60	4.64E-4	0.693	0.500	130	734	742	0.288
38	41.7	2.09	3.00	9.28E-4	0.718	0.497	286	736	743	0.266

Table 2 Inputs to the optimization algorithm

run	N_{cores}	η_{p00C}	η_{p00E}	TET (K)	$\left(\frac{\Delta P_0}{P_0}\right)_H$	β $\left(\frac{W}{m^3-K}\right)$	Δ_o $\left(\frac{m}{W-K}\right)$	$\left(\frac{\Delta P_0}{P_0}\right)_C$
1	1	0.80	0.85	1250	0.06	12E6	0.01	0.06
2	1	0.80	0.85	1450	0.06	12E6	0.01	0.06
3	1	0.80	0.85	1683	0.06	12E6	0.01	0.06
4	1	0.80	0.85	1250	0.04	12E6	0.01	0.04
5	1	0.80	0.85	1450	0.04	12E6	0.01	0.04
6	1	0.80	0.85	1683	0.04	12E6	0.01	0.04
7	1	0.80	0.85	1250	0.06	12E6	2E-3	0.06
8	1	0.80	0.85	1450	0.06	12E6	2E-3	0.06
9	1	0.80	0.85	1683	0.06	12E6	2E-3	0.06
10	1	0.80	0.85	1250	0.04	12E6	2E-3	0.04
11	1	0.80	0.85	1450	0.04	12E6	2E-3	0.04
12	1	0.80	0.85	1683	0.04	12E6	2E-3	0.04
13	1	0.80	0.85	1250	0.06	12E6	2E-4	0.06
14	1	0.80	0.85	1450	0.06	12E6	2E-4	0.06
15	1	0.80	0.85	1683	0.06	12E6	2E-4	0.06
16	1	0.80	0.85	1250	0.04	12E6	2E-4	0.04
17	1	0.80	0.85	1450	0.04	12E6	2E-4	0.04
18	1	0.80	0.85	1683	0.04	12E6	2E-4	0.04
19	1	0.85	0.90	1250	0.06	12E6	0.01	0.06
20	1	0.85	0.90	1450	0.06	12E6	0.01	0.06
21	1	0.85	0.90	1683	0.06	12E6	0.01	0.06
22	1	0.85	0.90	1250	0.04	12E6	0.01	0.04
23	1	0.85	0.90	1450	0.04	12E6	0.01	0.04
24	1	0.85	0.90	1683	0.04	12E6	0.01	0.04
25	1	0.85	0.90	1250	0.06	12E6	2E-3	0.06
26	1	0.85	0.90	1450	0.06	12E6	2E-3	0.06
27	1	0.85	0.90	1683	0.06	12E6	2E-3	0.06
28	1	0.85	0.90	1250	0.04	12E6	2E-3	0.04
29	1	0.85	0.90	1450	0.04	12E6	2E-3	0.04
30	1	0.85	0.90	1683	0.04	12E6	2E-3	0.04
31	1	0.85	0.90	1250	0.06	12E6	2E-4	0.06
32	1	0.85	0.90	1450	0.06	12E6	2E-4	0.06
33	1	0.85	0.90	1683	0.06	12E6	2E-4	0.06
34	1	0.85	0.90	1250	0.04	12E6	2E-4	0.04
35	1	0.85	0.90	1450	0.04	12E6	2E-4	0.04
36	1	0.85	0.90	1683	0.04	12E6	2E-4	0.04
37	2	0.80	0.85	1250	0.06	12E6	2E-3	0.06
38	2	0.80	0.85	1250	0.06	12E6	0.01	0.06

and with increases in the core fluid friction (or β). Also, thermal efficiency increases with the regenerator diameter (or Δ_o), because effectiveness increases with regenerator size.

Low ($\approx 2 - 3$) cycle pressure ratios are optimal for all cases. Small regenerators (of low effectiveness) have the highest optimal pressure ratios, because the pressure ratio for maximum thermal efficiency increases as effectiveness decreases (see Wilson [4]). Typically, $C_{ROT} \approx 3$. The optimal value for the conduction parameter, λ, principally is determined by balancing pressure drop with NTU: Thick cores of low λ have high pressure drop but also have high heat transfer area and NTU.

For most of the cases considered, the mass-flow rate through the C_N side (compressed-air side) of the regenerator is sufficiently low to necessitate a partial fluid-flow screen for all but very low As' values. Therefore, the pressure drop across the C_N side approximately is constant (to satisfy the criterion given by Eq. (22)) for most of the calculations. For a fixed core outer diameter, NTU is maximized with equal convective conductances on either side of the regenerator ($(hA)' = 1$). Therefore, heat transfer performance is greatest for $(hA)' = 1$ and $As' \approx 1$.[5] The pressure drop across the C_X side decreases with the flow area and As'. The optimal As' values were determined by balancing improved heat transfer performance with improved pressure-drop performance.

Compare the results of optimizations for one-core and two-core designs for identical values for the other inputs (compare run 7 with run 37 and run 1 with run 38). The optimal thermal efficiencies for the two-core designs are lower than the optimal thermal efficiencies for the one-core designs. The principal cause of the performance difference between the two designs

---

[5] The convective-conductance ratio, $(hA)'$, has a different value from the solid-area ratio, As', due to the differences in the fluid conductivities on each side of the regenerator.

is a seal leakage that is nearly twice as high for the two-core design, which is due to a total seal length that is nearly double that of the one-core design. However, in more global optimizations, small reductions in thermal efficiencies from using two cores instead of one may be offset by improved geometric flexibility.

4 Regenerator Sizing

The outputs of the optimization algorithm are the maximum thermal efficiency, the optimized parameters (r, C_{ROT}, λ, and As'), and five additional parameters (C_N', NTU, $\overline{T}_N$, $\overline{T}_X$, and W'). From these parameters, the inputs to the optimization algorithm, and some case-specific parameters ($\dot{W}_{\text{out}}$, D_H, and Nu), a unique regenerator design is determined. The relevant calculations are:

1 $C_{\text{in}} = \dot{W}_{\text{out}}/(W'T_{\text{atm}})$;
2 $C_N = C_{\text{in}}C_N'$;
3 $k_N = k_{\text{air}}(\overline{T}_N)$;
4 $k_X = k_{\text{air}}(\overline{T}_X)$;
5 $k_R = k_R[(\overline{T}_N + \overline{T}_X)/2]$;
6 $(hA)' = As'(k_N/k_X)$;
7 $As_N = \{(D_H C_N)/\sqrt{\text{Nu}\, k_N k_R}\}$
   $\{[(1 - p)/p]\text{NTU}[1 + (hA']\lambda As'/[1 + As']\}^{1/2}$;
8 $L = [k_R As_N/(C_N\lambda)][(1 + As')/As']$;
9 $\Theta_N = 2\pi(1 - SC)As'/(1 + As')$;
10 $\Theta_X = \Theta_N/As'$;
11 $As_S = [SC/(1 - SC)][(1 + As')/As']As_N$;
12 $c_R = c_R[(\overline{T}_N + \overline{T}_X)/2]$; and
13 $\tau_{\text{ROT}} = \{As_N L(\rho c)_R/C_N\}\{[1 + As']/[(1 - SC) \times As'C_{\text{ROT}}]\}$.

The sizing algorithm was applied to data from some of the optimizations that are given in Section 3. Outputs from the optimizations are given in Table 3. Sample sizing calculations were performed for some case-specific parameters that are of interest for automotive applications. In all of the calculations, a hydraulic diameter of $D_H = 0.5$ mm was used. This approximately is the smallest hydraulic diameter that is achievable with current manufacturing techniques. A Nusselt number of Nu = 4.1 was used. This is the theoretical value for a 2×1 rectangular passage geometry.[6] The work outputs for each run are listed in Table 4. Also, results of the sizing calculations are listed in Table 4.

5 Conclusions

An algorithm for optimizing designs of regenerated gas turbines is given. With this algorithm, a set of design parameters are optimized to maximize the thermal efficiency of the regenerated gas turbine. Also, a regenerator-sizing algorithm is given. With this algorithm, unique regenerator designs are determined for any particular application from results of the optimizations. Data are given for input parameters that are of interest for automotive applications. Optimization data are given for one-

---

[6] Outdated regenerator-core manufacturing techniques produced cores with highly nonuniform irregular passage geometries. Experimentally determined heat transfer and fluid-friction parameters associated with these cores have differed significantly from theoretical values calculated for regular geometries. Therefore, experimentally determined values have been used in design. Advances in core manufacturing techniques soon should lead to close agreement between experimentation and theory.

Table 4   Power outputs and results of regenerator-sizing calculations

run	$\dot{W}_{out}$ (kW)	L (m)	θ_N (deg.)	θ_X (deg.)	As_S (m^2)	τ_{ROT} (s)
1	10	0.266	141	204	3.33E-3	140
2	10	0.259	180	165	3.32E-3	254
3	10	0.292	147	199	3.33E-3	308
10	10	0.290	145	200	1.49E-3	107
11	10	0.298	142	204	1.49E-3	131
12	10	0.278	141	204	1.49E-3	155
34	75	0.245	162	184	3.54E-3	36.0
35	75	0.268	147	199	3.52E-3	50.6
36	75	0.277	143	202	3.54E-3	63.6

core and two-core designs of regenerated gas turbines. Higher thermal efficiencies are achieved with one-core designs. The optimization data indicate that thermal efficiencies over 50 percent should be achievable for automotive applications if ceramic turbines are used.

References

1 Kays, W. M., and London, A. L., Compact Heat Exchangers, 3rd ed., McGraw-Hill, New York, 1984.
2 Shah, R. K., "A Correlation for Longitudinal Heat Conduction Effects in Periodic-Flow Heat Exchangers," ASME JOURNAL OF ENGINEERING FOR POWER, Vol. 97, 1975, pp. 453–454.
3 Harper, D. B., and Rohsenow, W. M., "Effect of Rotary Regenerator Performance on Gas-Turbine-Plant Performance," Transactions of the ASME, Vol. 75, July 1953.
4 Wilson, D. G., Design of High-Efficiency Turbomachinery and Gas Turbines, The M. I. T. Press, Cambridge, MA, 1984.
5 Chappell, M. S., and Cockshutt, E. P., "Gas Turbine Cycle Calculations: Thermodynamic Data Tables for Air and Combustion Products for Three Systems of Units," NRC, Aeronautical Report LR-579, National Research Council of Canada, Aug. 1974.
6 Coppage, J. E., and London, A. L., "The Periodic-Flow Regenerator—A Summary of Design Theory," Transactions of the ASME, Vol. 75, 1953, pp. 779–787.
7 Lambertson, T. J., "Performance Factors of a Periodic-Flow Heat Exchanger," Transactions of the ASME, Vol. 80, 1958, pp. 586–592.
8 Bahnke, G. D., and Howard, C. P., "The Effect of Longitudinal Heat Conduction on Periodic-Flow Heat Exchanger Performance," ASME JOURNAL OF ENGINEERING FOR POWER, Vol. 86, 1964, pp. 105–119.
9 Beck, D. S., "The Effect of Seal Width on Regenerator Effectiveness," ASME JOURNAL OF ENGINEERING FOR GAS TURBINES AND POWER, Vol. 116, 1994, pp. 574–582.
10 Harper, D. B., "Seal Leakage in the Rotary Regenerator and Its Effect on Rotary-Regenerator Design for Gas Turbines," Transactions of the ASME, Vol. 79, Feb. 1957.
11 Wilson, D. G., "A Method of Design for Heat-Exchanger Inlet Headers," ASME Paper No. 66-WA/HT-41.
12 London, A. L., Klopfer, G., and Wolf, S., "Oblique Flow Headers for Heat Exchangers," ASME JOURNAL OF ENGINEERING FOR POWER, Vol. 90, 1968.
13 Wilson, D. G., private communication, 1991.
14 Beck, D. S., and Wilson, D. G., Gas-Turbine Regenerators, Chapman and Hall, New York, 1996.

Regenerator Effectiveness During Transient Operation[1]

D. S. Beck

Engineering Consultant,
Wellesley, MA 02181

Current designs of regenerative gas turbines include high-effectiveness rotary regenerators. The regenerators make the gas turbines highly efficient during steady-state operation. During engine transients, however, engine efficiency can be low because high-effectiveness regenerators tend to have large cores with large thermal masses, and it can take a long time (minutes for example) for these regenerators to reach their steady-state effectivenesses. The following criterion determines the response time of regenerators:

$$\tau_{ss} \sim \frac{(mc)_R}{C_X},$$

where τ_{ss} (s) is the time period of transient operation; $(mc)_R$ (J/K) is the heat capacity of the core; and C_X (W/K) is the heat-capacity rate of the exhaust. This criterion has been verified through analysis and experimentation. The criterion enables the designer to estimate the fraction of an operating cycle during which the regenerator will have reduced effectiveness.

Introduction

Regenerative gas turbines are attractive alternatives to diesel engines and spark-ignition engines for automobiles. Theory indicates that during steady-state operation regenerative gas turbines should achieve higher thermal efficiencies. Further, regenerative gas turbines are potentially lower in cost, require less maintenance, require less space, and pollute less.

To be competitive with diesel and spark-ignition engines, regenerative gas turbines must not only be highly efficient during steady-state operation, but, in addition, transients in response to changes in power levels must be short, because engine efficiency is reduced during these transients. The effectiveness response of the regenerator determines the transient response of a regenerative gas turbine (the other components respond much more quickly). This paper quantifies the effectiveness responses of regenerators during transient operation, so the designer can determine engine efficiency for a complete operating cycle.

Periodic-flow regenerators are used in automotive gas turbines to transfer heat from the exhaust to preheat the compressed air (see Beck and Wilson [1] for details of periodic-flow regenerators). Rotary regenerators with high effectivenesses ($\epsilon > 95$ percent) are required for high steady-state thermal efficiencies. High-effectiveness regenerators have large heat transfer areas (per unit of gas flow). Cores typically cannot be made highly porous ($p > 80$ percent) due to manufacturing considerations, so large heat transfer areas are accompanied by massive cores. These massive cores have large thermal inertias and slow temperature responses. Regenerators that include these cores have slow effectiveness responses. Gas turbines with slowly responding regenerators operate at low thermal efficiency during the long response times, because additional fuel is required to compensate for low regenerator effectiveness. For example, regenerator effectiveness is zero immediately after engine start-up. Thus, a low-pressure-ratio regenerative gas turbine could

have a low thermal efficiency (below 20 percent) immediately after engine start-up.

London et al. [2] report transient responses of regenerators to step changes of inlet flow temperature. This paper assumes the inlet flow temperatures are constant and determines the transient outlet flow temperatures as the cores respond from an initially uniform temperature distribution. The results of London et al. [2] are relevant when considering set point changes. This paper's results are relevant when considering the length of time from engine start-up that is required for the engine to reach steady-state thermal efficiency. The methods described in this paper have been included in the commercial software RGT-OPT™[2] [3], which optimizes regenerative gas turbines and calculates transient characteristics of regenerators including effectiveness responses and transient core temperature distributions.

This paper gives theory, then results, of experiments with regenerator cores. For both the theory and the experiments, we first consider the response of a regenerator core to a single flow exposure. These responses provide insight into the transient behavior of regenerator cores. Also, responses to single flow exposures were used to experimentally determine the heat capacities of core specimens. After the responses to single flow exposures, we consider effectiveness responses.

Theory

The following gives the theory for the transient response of regenerator cores. First we consider the physical phenomena and make some simplifications for the analysis. Then we consider single flow exposures, which are used to quantify the heat transfer performance of regenerator cores. Then we consider effectiveness responses.

Physical Phenomena. Figure 1 shows a schematic of a passage tube of a regenerator core. The passage tube initially has a uniform temperature distribution, T_{R0}. Then, fluid enters the passage with a different temperature, T_i, and heats or cools the passage-tube walls through forced convection. The fluid flow's velocity profile develops after a hydraulic development length, x_{Hcrit}. The fluid flow's dimensionless temperature profile,

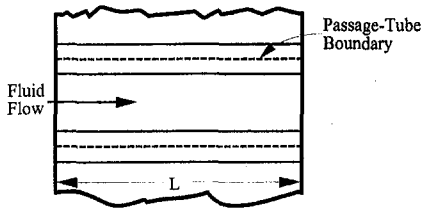[2] RGT-OPT is a trademark of the author, and is available from him.

Fig. 1 Schematic of an isolated regenerator passage tube (the ratio D_H/L is much larger than what is typical for gas turbines)

$$\Theta \equiv \frac{T_0 - T_1}{T_0 - T_m} \qquad (1)$$

(where T_0 is the temperature at the fluid–solid interface; T_1 is the temperature in the fluid domain; and T_m is the mixed-mean temperature in the fluid domain), develops after a thermal development length, x_{THcrit}. Heat conducts in all three directions in the passage tube. In addition to conduction associated with convection, heat conducts axially in the fluid. Heat also radiates along the length of the passage.

Between exposures to the two fluid flows, passage tubes rotate under seals. While a passage tube is under a seal, a small amount of fluid flows into (or out of) the passage due to direct seal leakage. When the passage tube is under seals, heat conducts in all three directions. During seal coverage there is free convection. Also, heat radiates along the length of the passage during seal coverage.

Simplifying Assumptions We simplify the analysis of regenerators with the following assumptions:

1 Negligible conduction through passage-tube boundaries;
2 Laminar flows;
3 Negligible axial conduction in the fluid;
4 Hydraulically and thermally fully developed flows;
5 Constant properties of each fluid and of the core material;
6 Negligible radiation between surfaces of the regenerator core;

7 Negligible heat transfer from passage-tube walls at the ends of passages;
8 Negligible free convection under seals;
9 Negligible flows into and out of passages under seals;
10 Heat capacity of the core material much greater than the heat capacities of either of the fluids in the passages; and
11 Negligible effects of low core porosity on heat transfer.

The first assumption is valid in a regenerator if the passages are sufficiently small and the flows are sufficiently uniform over the flow areas. The second assumption is valid for low Reynolds numbers: $Re_{D_H} < 2300$ (see Potter and Foss [4]). For gas turbine applications, typically $50 < Re_{D_H} < 200$. The third assumption is valid for large Péclét numbers: $Pe_{D_H} > 10$ (see Shah and London [5]). For air flows, the Prandtl number is Pr ≈ 0.7. Therefore, for air-breathing regenerative gas turbines, the Péclét number typically lies in the range $35 < Pe_{D_H} < 140$.

The fourth assumption is accurate if the development lengths are a sufficiently small portion of the total passage length. Kays and Crawford [6] give the following equation for the hydraulic development length, x_{Hcrit}:

$$\frac{x_{Hcrit}}{D_H} = \frac{Re_{D_H}}{20}, \qquad (2)$$

where D_H is the hydraulic diameter. A typical hydraulic diameter for a passage in a gas turbine regenerator is $D_H = 0.5$ mm. A typical Reynolds number is $Re_{D_H} = 50$. A typical core thickness is in the range $L = 50$–150 mm. Therefore,

$$\frac{x_{Hcrit}}{L} \approx 1\text{–}3 \text{ percent.} \qquad (3)$$

Kays and Crawford [6] give the following criterion for the thermal development length:

$$\frac{x_{THcrit}}{D_H} \approx (0.05)\, Pe_{D_H}. \qquad (4)$$

Therefore,

$$0.6 \text{ percent} \leq \frac{x_{THcrit}}{L} \leq 2 \text{ percent.} \qquad (5)$$

--- **Nomenclature** ---

As = solid area of the core, m^2
As' = solid area ratio $\equiv As_N/As_X$
C = heat-capacity rate, W/K
C_{RAT} = heat-capacity-rate ratio $\equiv C_N/C_X$
C_{ROT} = dimensionless core-rotation rate $\equiv C_R/C_N$
D_H = hydraulic diameter, m
h = convective heat transfer coefficient, W/m^2-K
(hA) = convective conductance, W/K
$(hA)'$ = convective-conductance ratio
k = thermal conductivity, W/m-K
L = core thickness or flow length, m
$(mc)_R$ = heat capacity of a regenerator core, J/K
N_p = porosity number = $(k/k_R)(1 - p)/p$ for parallel-plate regenerators
N_{pass} = number of passages
NTU = Number of Transfer Units $\equiv (hA)_N/(C_N[1 + (hA)'])$
Nu = Nusselt number
Nu_H = Nusselt number with a boundary condition of a constant wall heat flux $\equiv hk_f/D_H$

p = core porosity, the ratio of voids volume of the core to the total volume
Pe = Péclét number = $Re_{D_H}Pr$
Pr = Prandtl number
Re_{D_H} = Reynolds number
SC = Seal Coverage, the fraction of the core face area covered by seals
t = time, s
T = temperature, K
T_1 = temperature at a solid–fluid interface, K
T_m = mixed-mean temperature, K
T_i = fluid inlet temperature, K
T_o = fluid outlet temperature, K
T_{R0} = initial core temperature, K
t^* = dimensionless time $\equiv Ct/(mc)_R$
$\dot{V}$ = volumetric flow rate, m^3/s
x = coordinate in the direction of fluid flow, m
x_{Hcrit} = hydraulic development length, m
x_{THcrit} = thermal development length, m

ϵ = regenerator effectiveness, the ratio of heat transferred to the maximum heat that could be transferred by a perfect heat exchanger of infinite size
ζ = dimensionless length $\equiv x/L$
Θ = dimensionless temperature
λ = dimensionless core-conduction parameter $\equiv k_R(As_N + As_X)/(LC_N)$
$(\rho c)_R$ = specific heat capacity per unit volume of the core material, J/m^3-K
τ_{ss} = time period to steady-state effectiveness, s
τ^*_{Xss} = dimensionless time period to steady-state effectiveness

Subscripts

f = of the fluid
N = on the compressed-air side
R = of the regenerator core
S = of a seal
ss = steady-state
X = on the exhaust side

In a typical gas turbine regenerator, the development lengths are sufficiently small to assume hydraulically and thermally fully developed flows.

Kays and London [7] discuss the effects of temperature-dependent fluid properties. The fifth assumption is accurate if the properties are calculated at average temperatures. The sixth assumption typically is valid for gas turbine applications because the views from the hot passage portions to the cool passage portions typically are poor.

The seventh assumption is valid for gas turbine applications because the heat transfer areas occupied by passage-tube ends are typically small portions of the total heat transfer areas, especially for high-porosity cores. The eighth assumption is valid for the typically small passage diameters associated with gas turbine applications. The ninth assumption is valid for low direct seal leakage. The tenth assumption is valid for gas flows through ceramic or metallic cores.

The eleventh (and final) assumption is valid if the porosity number, N_p, is sufficiently low, or the core porosity is sufficiently high. Highly porous cores lead to negligible reductions in heat transfer (see Beck and Wilson [1]). In addition, highly porous cores are optimal for achieving a high gas turbine efficiency if the pressure drops and leakages of the regenerator are considered (see Beck and Wilson [1]). Thus, highly porous cores typically are used for regenerative gas turbines.

Single Flow Exposures. This section derives the theory for regenerator cores subjected to single flow exposures. With a single flow exposure, a regenerator core initially has a uniform temperature distribution, and is then instantaneously exposed to a flow with a different temperature. In addition to the simplifying assumptions given above, we assume no conduction in the core material. We assume this because the response times of gas turbine regenerators are nearly independent of axial core conduction.

Under the given assumptions, one of the two governing equations for a single flow exposure is

$$\frac{\partial T}{\partial t^*} + \frac{C}{(hA)} \frac{\partial}{\partial \zeta} \left(\frac{\partial T}{\partial t^*} \right) + \frac{\partial T}{\partial \zeta} = 0, \qquad (6)$$

where T is the fluid temperature; $t^* \equiv Ct/(mc)_R$, a dimensionless time; C is the flow heat-capacity rate; (hA) is the convective conductance; $\zeta \equiv x/L$ is a dimensionless coordinate in the flow direction; and L is the core thickness. Equation (6) applies for the fluid temperature. The second governing equation applies for the core material, but it is similar to Eq. (6) (the only difference is the core temperature, T_R, replaces the fluid temperature, T). The boundary conditions associated with these equations are:

1. $T(\zeta; t^* = 0)$, the initial temperature distribution in the fluid ($= T_{R0}$, the initial core temperature);
2. $T_{R0} = T_R(\zeta; t^* = 0)$, the initial temperature distribution in the core material; and
3. $T_i = T(\zeta = 0; t^*)$, the inlet temperature of the flow.

We do not attempt an analytical solution to Eq. (6), except for the limiting case as the ratio of the flow heat-capacity rate to the convective conductance approaches infinity: $C/(hA) \to \infty$ (which could be effected with a thin core). For this case, the core material acts as a lumped body, and the outlet-temperature response is

$$T_o = T_i + \frac{(hA)}{C} \exp \left\{ \frac{-(hA)t^*}{C} \right\} (T_{R0} - T_i), \qquad (7)$$

which is a first-order response with a dimensionless time constant of $C/(hA)$.
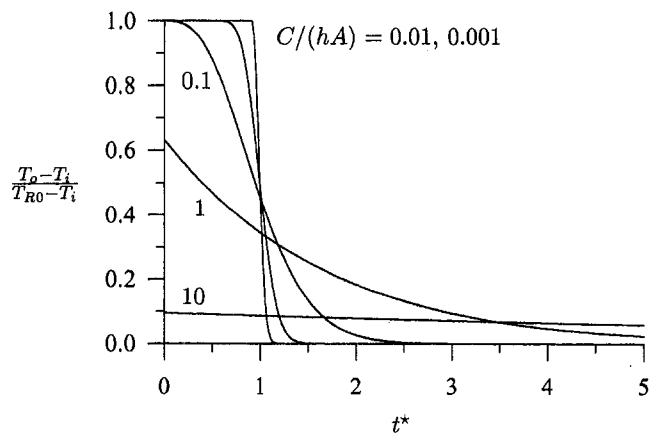
Fig. 2 Responses of the outlet temperature of the fluid flow to single flow exposures of a regenerator-core passage

For general $C/(hA)$ values, we can solve Eq. (6) numerically. Figure 2 shows plots of the resulting solutions.

For high values of the ratio $C/(hA)$, the plots in Fig. 2 approach first-order responses given by Eq. (7): for a fixed value of the flow heat-capacity rate (C), the convective conductance is small, so heat is removed slowly from (or added slowly to) the passage-tube walls. For low values of the ratio $C/(hA)$, the plots approach a step function:

$$\frac{T_o - T_i}{T_{R0} - T_i} = \begin{cases} 1 & \text{if } t^* < 1 \\ 0 & \text{if } t^* > 1 \end{cases}. \qquad (8)$$

For low values of the ratio $C/(hA)$, heat is removed from (or added to) the passage-tube walls at the maximum rate (which is limited by the difference between the initial core temperature and the flow temperature, $T_{R0} - T_i$), until the core achieves the fluid flow's inlet temperature.

The designer can use the temperature responses to single flow exposures to determine the heat transfer performance of regenerator cores. The designer is usually faced with one of two situations: (1) The heat capacity of a core specimen $[(mc)_R]$ is known, but the convective conductance $[(hA)]$ is unknown; or (2) the convective conductance is known from theory or otherwise, but the heat capacity of the core is unknown. In either of these situations, the designer should first determine the heat-capacity rate of the flow to which the core is exposed. Then, either the heat capacity of the core or the convective conductance should be determined. The unknown quantity (either the heat capacity or the convective conductance) should then be determined by matching the experimental results with the theory. Below we show how to test ceramic regenerator cores using this procedure.

Effectiveness Responses. Now we give the theory for the transient response of regenerator effectiveness. We consider cold start-ups in which the core initially has a uniform temperature distribution and is then rotated between cold and hot flows in its manner of normal operation. We are interested in determining how long it will take for the effectiveness of the regenerator to reach its steady-state value. First we list the governing equations. Then we give results (for more detail, see Beck and Wilson [1]).

The governing equations for effectiveness responses were derived from the eleven assumptions listed above. While a passage tube is exposed to the compressed-air flow,

$$C_{RAT} \frac{\partial T_N}{\partial \zeta} + \frac{(1 - SC)As'}{(1 + As')} \frac{\partial T_N}{\partial t_X^*}$$
$$+ \frac{(1 - SC)As'}{(1 + As')\text{NTU}[1 + (hA)']} \frac{\partial}{\partial \zeta} \left(\frac{\partial T_N}{\partial t_X^*} \right)$$

$$- \frac{\lambda As' C_{\text{RAT}}}{(1 + As')} \frac{\partial^2 T_N}{\partial \zeta^2}$$

$$- \frac{\lambda As' C_{\text{RAT}}}{(1 + As') \text{NTU}[1 + (hA)']} \frac{\partial^3 T_N}{\partial \zeta^3} = 0. \quad (9)$$

Also,

$$C_{\text{RAT}} \frac{\partial T_R}{\partial \zeta} + \frac{(1 - SC)As'}{(1 + As')} \frac{\partial T_R}{\partial t_X^*}$$

$$+ \frac{(1 - SC)As'}{(1 + As') \text{NTU}[1 + (hA)']} \frac{\partial}{\partial \zeta} \left(\frac{\partial T_R}{\partial t_X^*} \right)$$

$$- \frac{\lambda As' C_{\text{RAT}}}{(1 + As')} \frac{\partial^2 T_R}{\partial \zeta^2} = 0. \quad (10)$$

While a passage tube is under a seal,

$$\frac{\partial^2 T_R}{\partial \zeta^2} = \frac{(1 - SC)}{C_{\text{RAT}} \lambda} \frac{\partial T_R}{\partial t_X^*}. \quad (11)$$

When a passage tube is exposed to the exhaust flow,

$$- \frac{\partial T_X}{\partial \zeta} + \frac{(1 - SC)}{(1 + As')} \frac{\partial T_X}{\partial t_X^*}$$

$$- \frac{(1 - SC)(hA)'}{(1 + As') \text{NTU}[1 + (hA)'] C_{\text{RAT}}} \frac{\partial}{\partial \zeta} \left(\frac{\partial T_X}{\partial t_X^*} \right)$$

$$- \frac{C_{\text{RAT}} \lambda}{(1 + As')} \frac{\partial^2 T_X}{\partial \zeta^2}$$

$$+ \frac{\lambda (hA)'}{(1 + As') \text{NTU}[1 + (hA)']} \frac{\partial^3 T_X}{\partial \zeta^3} = 0. \quad (12)$$

Also,

$$- \frac{\partial T_R}{\partial \zeta} + \frac{(1 - SC)}{(1 + As')} \frac{\partial T_R}{\partial t_X^*}$$

$$- \frac{(1 - SC)(hA)'}{(1 + As') \text{NTU}[1 + (hA)'] C_{\text{RAT}}} \frac{\partial}{\partial \zeta} \left(\frac{\partial T_R}{\partial t_X^*} \right)$$

$$- \frac{C_{\text{RAT}} \lambda}{(1 + As')} \frac{\partial^2 T_R}{\partial \zeta^2} = 0. \quad (13)$$

Some boundary conditions associated with these equations are:

1   $\partial T_R / \partial \zeta |_{\zeta=0,1} = 0$;
2   $\partial T_{N,X} / \partial \zeta |_{\zeta=0,1} = 0$;
3   $T_R(t_X^* = 0; \zeta) = T_{R0}$;
4   $T_N(t_X^*; \zeta = 0) = T_{Ni}$; and
5   $T_X(t_X^*; \zeta = 1) = T_{Xi}$.

The first boundary conditions result from the assumption of no heat transfer from passage tube ends. The second boundary conditions result from the assumption of no axial conduction in the fluid. In addition to the numbered boundary conditions given above,

1   The initial core temperature profile when a passage enters the compressed-air side is equal to the final temperature profile when the passage exits from under the preceding seal;

2   The final core temperature profile when a passage exits from the compressed-air side is equal to the initial temperature profile when the passage enters under the proceding seal;
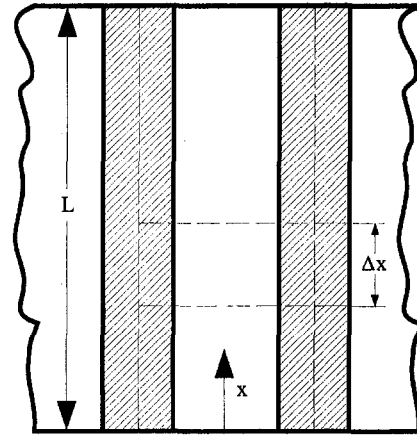

Fig. 3   Isolated regenerator passage tube

3   The initial core temperature profile when a passage enters the exhaust side is equal to the final temperature profile when the passage exits from under the preceding seal; and

4   The final core temperature profile when a passage exits from the exhaust side is equal to the initial temperature profile when the passage enters under the proceding seal.

A passage tube is exposed to the compressed air for

$$\tau_{X_N}^* = \frac{As'(1 - SC)}{(1 + As') C_{\text{ROT}} C_{\text{RAT}}}. \quad (14)$$

A passage is under one of the two seals for

$$\frac{\tau_{X_S}^*}{2} = \frac{SC}{2 C_{\text{ROT}} C_{\text{RAT}}}. \quad (15)$$

A passage is exposed to the exhaust for

$$\tau_{X_X}^* = \frac{(1 - SC)}{(1 + As') C_{\text{ROT}} C_{\text{RAT}}}. \quad (16)$$

The author solved these equations numerically (subject to the boundary conditions). This paper addresses effectiveness-response times (not effectiveness magnitudes). Therefore, we give results in terms of normalized effectivenesses, ϵ / ϵ_{ss}. For steady-state effectiveness results, see Beck [8], Beck and Wilson [1], or commercial software such as RGT-OPT™ [3].

When we make time dimensionless, normalized effectiveness responses are independent of the dimensionless core-rotation rate (C_{ROT}), except for low values of the product of the heat-capacity-rate ratio and the dimensionless core-rotation rate (e.g., $C_{\text{RAT}} C_{\text{ROT}} < 1$) for which the core rotates few times before steady-state effectiveness is reached. Normalized effectiveness responses are nearly independent of the dimensionless core size (NTU) and the heat-capacity-rate ratio. Also, normalized effectiveness responses are independent of the convective-conductance ratio, $(hA)'$, and of axial conduction (which depends on the parameters λ, SC, and As'). Figure 4 shows plots of normalized effectiveness responses for various values of NTU, and Fig. 5 shows plots of responses for various values of C_{RAT}.[3]

From the plots of normalized effectiveness responses, we infer the following criterion for the dimensionless time period to steady-state effectiveness:

$$\tau_{X_{ss}}^* \equiv \frac{C_X \tau_{ss}}{(mc)_R} \sim 1, \quad (17)$$

where C_X is the greater of the two heat-capacity rates (typically

---

[3] The steps in the plots result from simplification in the numerical-integration algorithm.
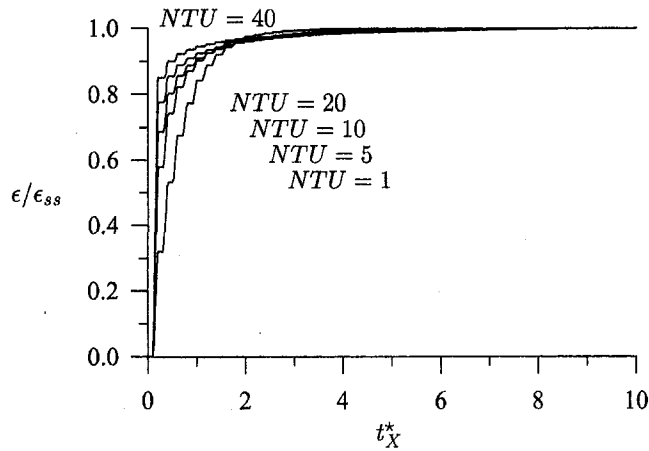

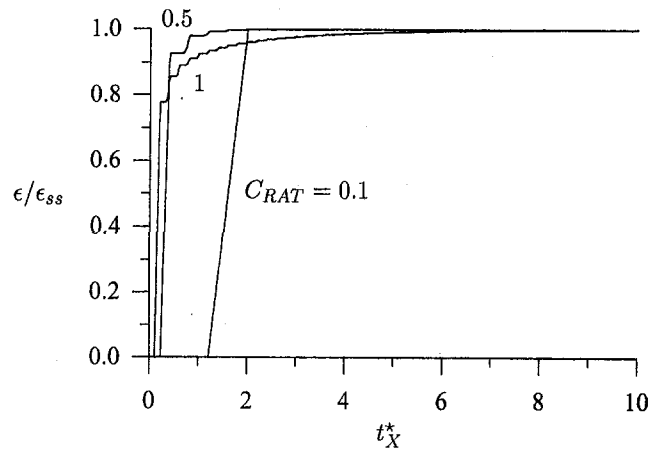**Fig. 4 Normalized effectiveness responses for $C_{RAT} = (hA)' = 1$; NTU = 1, 5, 10, 20, and 40.**

Fig. 5 Normalized effectiveness responses for $(hA)' = 1$; NTU = 20; C_{RAT} = 0.1, 0.5, and 1

the heat-capacity rate of the exhaust in regenerative gas turbines); τ_{ss} is the (dimensional) time period to steady-state effectiveness; and $(mc)_R$ is the heat capacity of the core. In terms of dimensional time, this criterion can be expressed as

$$\tau_{ss} \sim \left\{ \frac{NTU[1 + (hA)'][1 + As']C_{RAT}}{4As'(1 - SC)k_N} \right\}$$

$$\times \left\{ \frac{(\rho c)_R D_H^2}{Nu_H} \left(\frac{1 - p}{p} \right) \right\}, \quad (18)$$

where

NTU = Number of Transfer Units, a dimensionless core size;

$(hA)'$ = convective-conductance ratio, the ratio of the convective conductance on the compressed-air side (C_N side) to that on the exhaust side (C_X side);

As' = solid-area ratio, the ratio of the solid area on the compressed-air side to that on the exhaust side;

C_{RAT} = heat-capacity-rate ratio, the ratio of the heat-capacity rate on the compressed-air side to that on the exhaust side;

SC = Seal Coverage, the fraction of the core face area covered by seals;

k_N = thermal conductivity of the compressed air, W/m-K;

$(\rho c)_R$ = specific heat capacity per unit volume of the core material, J/m³-K;

D_H = hydraulic diameter of the core passages, m;

Nu_H = Nusselt number associated with the passage geometry; and

p = core porosity, voids volume divided by total volume.

The regenerator designer determines values for the parameters NTU, $(hA)'$, As', C_{RAT}, and SC in the first term of Eq. (18) in different ways, depending on the design procedure used. In the method of Kays and London [7] and in the method for direct regenerator design (see Beck and Wilson [1]), NTU is calculated from a specified effectiveness, $(hA)'$ or As' is specified (one results from specification of the other), and C_{RAT} is calculated. In optimal design, NTU, $(hA)'$, As', C_{RAT} and SC are determined through optimization of the regenerative gas turbine for steady-state operation (see Beck and Wilson [1] and Beck [9]). The principal contributor to the first term in Eq. (18) is NTU: High-effectiveness regenerators with high values of NTU produce long response times. The parameters in the second term of Eq. (18) are characteristics of the core material and of the

core-passage geometries. For a fast effectiveness response, a highly porous core with small passages and a low specific heat capacity per unit volume should be used. The Nusselt number, which is a function of passage geometry, should also be large. For many practical cases (especially for ceramic cores), passage size and geometry and core porosity are determined principally by manufacturing considerations; however, Eq. (18) should be considered when choosing a regenerator core for a particular application.

Example Calculation. For an example of the use of Eq. (18), consider Wilson's [10] regenerator design. The relevant design data are:

NTU = 22;
$(hA)'$ = 1;
As' = 1.05;
C_{RAT} = 0.990;
SC = 0.2;
k_N = 0.0569 W/m-K;
$(\rho c)_R$ = 2.60 MJ/m³-K;
D_H = 0.511 mm;
Nu_H = 2.65; and
p = 0.708.

From Eq. (18), the response time is on the order of 49 seconds: $\tau_{ss} \sim 49$. From Fig. 4 we conclude that the effectiveness of Wilson's [10] regenerator would reach 90 percent of its steady-state value in about one minute ($t^* = 60/49$) and practically
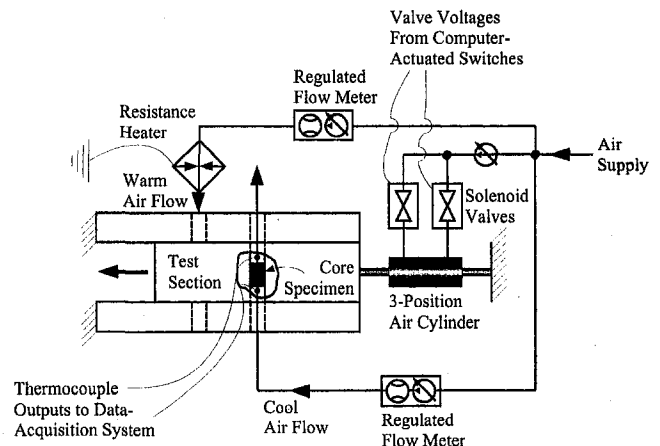

Fig. 6 Schematic of an experimental apparatus for tests of the heat transfer performance of regenerator core specimens

Table 1 Descriptions of components in the experimental apparatus

Letter	Component Description
A	MetraByte SM-OAC5, 120 VAC output module
B	MetraByte SRA-01, solid-state I/O board
C	Dwyer 100 SCFH flow meter
D	Humphrey H180-4E1, two-position five-port solenoid valves
E	Watts R384-02 C, miniature regulator
F	Allenair APD $1\frac{1}{2} \times 3 \times 3$, pneumatic-linear-actuator cylinder
G	Corning cordierite cylindrical regenerator-core specimen
H	Dwyer 50 SCFH flow meter
I	MetraByte PWR-51A, 5-V 1-AMP power supply
J	MetraByte MB-01, direct-connection module mounting rack
K	MetraByte MB37-T, T-type thermocouple module
L	Omega 0.003-inch T-type thermocouple wire
M	MetraByte C-8MB1, DAS-8 to MB-01 rack cable
N	Electrical-resistance heater
O	MetraByte DAS-8, eight-channel A/D interface
P	NPC 486 VLB/66 computer
Q	MetraByte PIO-12, 24-line parallel I/O board
R	MetraByte C1800, 37-conductor 18-inch cable
S	Test section

Table 2 Core-specimen data

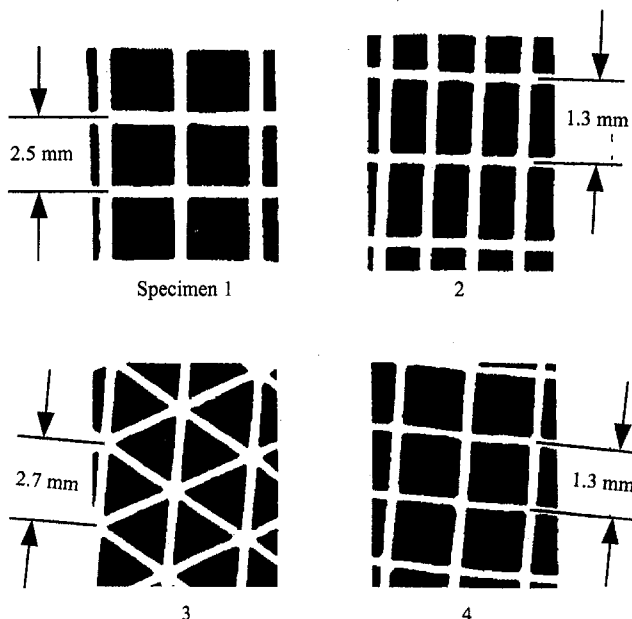| Specimen Number	L (mm)	N_{pass}	(hA) (W/K)	$(mc)_R$ (J/K)
1	67	68	1.91	14.1
2	67	405	14.6	19.9
3	66	145	4.49	17.1
4	60	209	5.25	8.93

100 percent of its steady-state value in under eight minutes (t^* = 8 × 60/49).

Experimental Results

This section describes experiments that verified the theory for transient operation detailed in the previous sections. First we describe the experimental apparatus that was used. This apparatus is not only useful for testing the transient response of regenerator cores, but it is also generally useful for measuring the heat transfer performance of regenerator cores.

After we describe the apparatus, we compare experimental results for single flow exposures and for effectiveness responses with the theory given above. Finally, we conclude that regenerator cores respond in a dimensionless time period, $\tau^*_{Xss} \sim 1$.

Experimental Apparatus. Figure 6 shows a schematic of the experimental apparatus that was used to test regenerator core specimens. Table 1 lists the components for the reader that would like to build a similar apparatus for testing regenerator cores. With the apparatus, single flow exposures as well as

simulations of regenerator operation can be performed. For a single flow exposure, the central block of the test section (component S in Table 1) is first moved to its left position and the specimen (G) is heated to a uniform temperature. Then the central block is quickly moved to its right position (the position shown in the schematic) and the core is cooled. For a simulation of a regenerator's operation, the core is alternately exposed to the cool and warm flows. Between exposures, the central block is moved to a central position in which both ends of the specimen are sealed. This simulates travel under seals in an actual regenerator.

Consider the cool-air flow. Air flows from the air supply, through a regulated flow meter (H), then through the core specimen. Thermocouples (L) at each end of the specimen are used to record the air temperature at the inlet and at the outlet of the specimen. The flow path is similar for the warm-air flow except the flow passes through an electrical-resistance heater (N) between a flow meter (C) and the specimen.

Consider the linear-actuator system. Commands are sent at specified intervals from software to move the central block of the test section. The commands travel via the input/output (I/O) board (Q) to the output modules (A). These output modules open and close circuits that include two-position solenoid valves (D). The valves direct the regulated (E) compressed-air flow to four ports on the linear-actuator cylinder (F). Thus, the linear actuator can be moved to any of three positions.

Consider the data acquisition system for measuring the flow temperatures. The thermocouple modules (K) process the thermocouple voltages. The resulting voltages travel to the analog-to-digital (A/D) interface (O), and the software records them.

Figure 7 shows end-view enhanced[4] pictures of the core specimens that were tested. The convective conductances were calculated from the conductivity of air ($k_f \approx 0.029$ W/m-K) and from data for the thicknesses of the specimens (L) and for the number of passages that each specimen contained. Table 2 lists these data. For square passages (Specimens 1 and 4),

$$(hA) = 4k_f L N_{pass} \, Nu; \tag{19}$$

for 2 × 1 rectangle passages (Specimen 2),

$$(hA) = 4.5k_f L N_{pass} \, Nu; \tag{20}$$

and for equilateral-triangle passages (Specimen 3),

$$(hA) = 5.20k_f L N_{pass} \, Nu. \tag{21}$$

Table 2 lists the resulting core-specimen data.

Next we show how the heat capacities of the core specimens (which are listed in Table 2) were measured with single flow exposures.

Single Flow Exposures. Single flow exposures were used to determine the heat capacities of all of the core specimens. For all runs, the specimens were exposed to a warm flow of $\dot{V}_{warm} = 7.87E - 4$ m^3/s, then a cool flow of $\dot{V}_{cool} = 3.93E -$

Specimen 1

2

2.5 mm

1.3 mm

3

4

2.7 mm

1.3 mm

Fig. 7 End-view enhanced pictures of magnified core specimens

[4] The pictures were enhanced to delineate between passages and passage tubes.
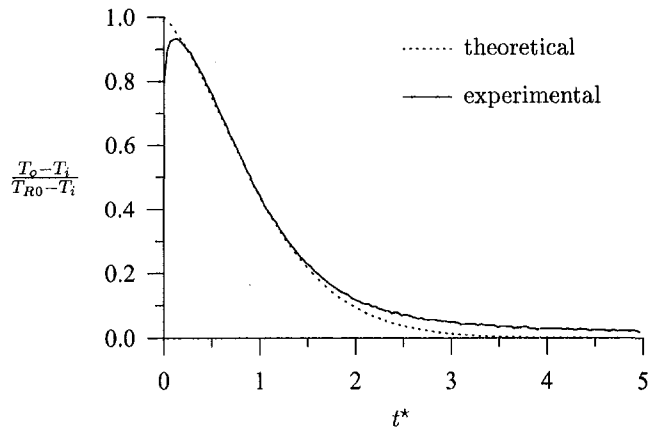
Fig. 8   Response of core specimen 1 to a single flow exposure

Fig. 9   All effectiveness-response data from runs 1–12

4 m³/s. Figure 8 shows a typical response and the associated theoretical response. The experimental responses are slower for high values of dimensionless time $[t^* \equiv Ct/(mc)_R]$ due to conduction from the specimen peripheries. Also, the convective heat transfer coefficient (h) has a lower value for a constant-wall-temperature boundary condition than for a boundary condition of a constant wall heat flux. For small time, the temperature distribution in the core material is uniformly equal to the initial temperature distribution, T_{R0}. For large time, the temperature profile in the core material is uniformly the flow inlet temperature, T_i. Therefore, the experimental responses are slower than the theoretical responses for small and large times due to the reduced convective heat-transfer coefficient. Otherwise, agreement between experimentation and theory is good. Table 2 lists the resulting heat capacities of the core specimens.

Effectiveness Responses. Table 3 gives details of twelve experimental effectiveness-response runs. Figure 9 plots all of the data from the twelve runs. The experimental data verify the criterion, $\tau_{Xss}^* \sim 1$.

Conclusions

We draw the following conclusions concerning the transient response of regenerators. A regenerator core responds in a dimensionless time period $\tau_{Xss}^* \equiv C_X \tau_{ss}/(mc)_R \sim 1$, or a dimensional time period
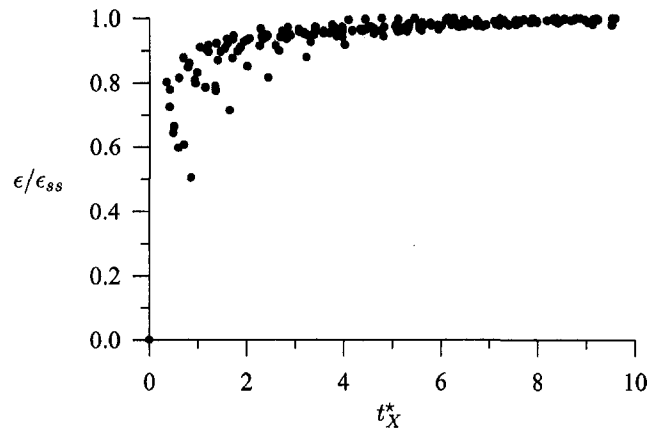
Table 3   Details of experimental effectiveness-response runs

Run Number	Specimen Number	V_N (m³/s)	V_X (m³/s)	τ_N (s)	$\tau_S/2$ (s)	τ_X (s)
1	1	3.93E-4	7.87E-4	5	1	5
2	1	3.93E-4	7.87E-4	10	1	5
3	1	3.93E-4	7.87E-4	15	1	5
4	2	3.93E-4	7.87E-4	5	1	5
5	2	3.93E-4	7.87E-4	10	1	5
6	2	3.93E-4	7.87E-4	15	1	5
7	3	3.93E-4	7.87E-4	5	1	5
8	3	3.93E-4	7.87E-4	10	1	5
9	3	3.93E-4	7.87E-4	15	1	5
10	4	3.93E-4	7.87E-4	5	1	5
11	4	3.93E-4	7.87E-4	10	1	5
12	4	3.93E-4	7.87E-4	15	1	5

$$\tau_{ss} \sim \left\{ \frac{\mathrm{NTU}[1 + (hA)'][1 + As']C_{\mathrm{RAT}}}{4As'(1 - SC)k_N} \right\}$$

$$\times \left\{ \frac{(\rho c)_R D_H^2}{\mathrm{Nu}_H} \left(\frac{1 - p}{p} \right) \right\} \quad (22)$$

This response time is a function of parameters that are fixed for a given regenerator design (see the discussion below Eq. (18) for details). It is independent of core-rotation rate, which is the only practically available control input. Therefore, the response time is a function of only the flows, the core size, and other physical parameters, and it cannot be reduced with a control system.

References

1 Beck, D. S., and Wilson, D. G., Gas-Turbine Regenerators, Chapman and Hall, New York, 1996.
2 London, A. L., Sampsell, D. F., and McGowan, J. G., "The Transient Response of Gas Turbine Plant Heat Exchangers—Additional Solutions for Regenerators of the Periodic-Flow and Direct-Transfer Types," ASME JOURNAL OF ENGINEERING FOR POWER, Vol. 86, 1964.
3 User's manual for RGT-OPT, available from Douglas Stephen Beck, 1996.
4 Potter, M. C., and Foss, J. F., Fluid Mechanics, Great Lakes Press, Inc., Okemos, MI, 1982.
5 Shah, R. K., and London, A. L., "Laminar Flow Forced Convection in Ducts," Advances in Heat Transfer, Academic, New York, 1980.
6 Kays, W. M., and Crawford, M. E., Convective Heat and Mass Transfer, McGraw-Hill, New York, 1980.
7 Kays, W. M., and London, A. L., Compact Heat Exchangers, 3rd ed., McGraw-Hill, New York, 1984.
8 Beck, D. S., "The Effect of Seal Width on Regenerator Effectiveness," ASME JOURNAL OF ENGINEERING FOR GAS TURBINES AND POWER, Vol. 116, 1994, pp. 574–582.
9 Beck, D. S., "Optimization of Regenerated Gas Turbines," ASME JOURNAL OF ENGINEERING FOR GAS TURBINES AND POWER, Vol. 118, this issue, pp. 654–660.
10 Wilson, D. G., Design of High-Efficiency Turbomachinery and Gas Turbines, The MIT Press, Cambridge, MA, 1984.

Diesel NO$_x$ Catalytic Converter Development: A Review

M. J. Heimrich

Southwest Research Institute,
San Antonio, TX 78228

This paper summarizes the findings of several technical articles on diesel NO$_x$ catalytic converter technology. Simplified theoretical reactions for NO$_x$ removal are discussed. Currently, development of catalytic NO$_x$ control technology for diesel engines is focused on systems that incorporate fuel hydrocarbons as the chemical reducing agent. Copper- and zeolite-based catalysts have been the predominant systems studied to date, but now catalysts containing precious metals are being investigated. Observed NO$_x$ reduction efficiencies typically ranged from 10 to 30 percent on actual engine exhaust systems when exhaust hydrocarbon enrichment strategies were used. Effects of carbon monoxide, sulfur dioxide, and water on NO$_x$ reduction efficiencies are reviewed. Recommendations for future research include attempts to broaden the temperature range of efficient NO$_x$ reduction, improving hydrocarbon selectivity toward the NO$_x$ reduction reaction, and the development of a supplementary reductant delivery system suitable for transient diesel engine operation.

Introduction

Emissions of oxides of nitrogen (NO$_x$) are produced by internal combustion engines, and are known to contribute to the formation of smog and ground-level ozone by reaction with hydrocarbons in the presence of sunlight. Motor vehicles produce a significant percentage of the atmospheric NO$_x$ emissions. In particular, heavy-duty diesel vehicles are currently estimated to produce 33 percent of the total on-road vehicle NO$_x$ emissions [1]. To improve air quality in urban areas, the California Air Resources Board (CARB) and the United States Environmental Protection Agency (US EPA) continue to establish increasingly stringent emission standards for new passenger cars and heavy-duty vehicles. This paper highlights some of the most recent publications on lean NO$_x$ catalyst systems, particularly those describing NO$_x$ control systems tested using diesel engine exhaust.
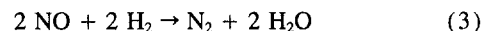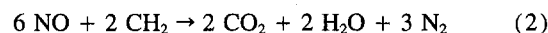
The purpose of this review is to allow emission control engineers with limited experience in lean NO$_x$ catalyst technology an opportunity to become acquainted with the issues facing the catalyst researcher and the diesel engine designer. In the "Technical Background" section of this paper, simplified chemical equations are used to convey catalytic NO$_x$ removal mechanisms for stoichiometric and lean-burn engine exhaust streams. The "Literature Survey" section provides an overview of studies that have applied experimental lean NO$_x$ catalytic converter technology to diesel engines. Finally, the author provides recommendations for future work based on industry needs.

Technical Background

Catalytic removal of NO$_x$ in engine exhaust can be accomplished by nonselective reduction, selective reduction, and decomposition. An example of nonselective reduction is the three-way catalytic converter used in current-technology gasoline-powered automobiles. Three-way catalytic converters simultaneously control emissions of hydrocarbons (HC), carbon monoxide (CO), and NO$_x$. Engine-out NO$_x$ emissions can be reduced by up to 90 percent in stoichiometric exhaust, because there is essentially no excess oxygen (O$_2$) following combustion. In this environment, NO$_x$ emissions are chemically reduced using exhaust CO, HC, hydrogen (H$_2$) and other combustion

products as shown in Eqs (1)–(3)[2]. In these equations, "CH$_2$" is used to represent exhaust hydrocarbons. This process is termed "nonselective" catalytic reduction because hydrocarbons, CO, or H$_2$ can all be NO$_x$ reducing agents.

NO$_x$ Reduction in Stoichiometric Exhaust (Nonselective Catalytic Reduction)

$$2\,NO + 2\,CO \rightarrow 2\,CO_2 + N_2 \tag{1}$$

$$6\,NO + 2\,CH_2 \rightarrow 2\,CO_2 + 2\,H_2O + 3\,N_2 \tag{2}$$

$$2\,NO + 2\,H_2 \rightarrow N_2 + 2\,H_2O \tag{3}$$

Traditional three-way catalytic converters, however, do not control NO$_x$ emissions in oxygen-rich exhaust at normal exhaust system temperatures. Historically, catalytic reduction of NO$_x$ emissions in lean exhaust has been accomplished using ammonia (NH$_3$) or some other reducing agent injected into the exhaust, often into the catalyst bed [3, 4]. This process of using a specific reducing agent is referred to as "selective" catalytic reduction (SCR) and is commonly used to control NO$_x$ emissions from stationary sources. With SCR, reducing agents, such as ammonia, preferentially react with NO$_x$ in lean exhaust. Ideally, NO$_x$ emissions are chemically reduced to form nitrogen and water, as represented in Eq. (4) [5]:

Selective Catalytic Reduction With NH$_3$

$$4\,NO + 4\,NH_3 + O_2 \rightarrow 4\,N_2 + 6\,H_2O \tag{4}$$
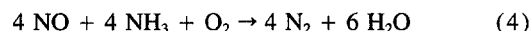
Ammonia injection, however, does not appear to be practical for controlling NO$_x$ emissions from mobile sources, because ammonia is not commonly accepted as a safe and practical onboard vehicle fuel. Furthermore, unless carefully metered, the ammonia itself can be emitted during transient operation as an undesirable pollutant. This emission of reductant is referred to as "ammonia slip" in stationary source parlance.

Reduction of NO$_x$ emissions also can be accomplished using hydrocarbons as the reducing agent [5–7]. This process is also termed "selective" catalytic reduction, because the hydrocarbons or their intermediate products produced through partial decomposition on the catalyst preferentially react with the NO$_x$ rather than the oxygen. In the case of diesel engines, exhaust hydrocarbons are not available in sufficient quantities for complete NO$_x$ reduction. A possible source of additional hydrocarbon reductants is the fuel. There is now a growing body of literature describing concepts and techniques for delivering hydrocarbon fuel as a reductant to a lean NO$_x$ catalyst (some of

these concepts will be discussed later in this paper). The chemical reduction of NO_x, using a hydrocarbon reductant, is given in Eq. (5) [8]:

Selective Catalytic Reduction With Hydrocarbon

$$2 NO + CH_2 + \tfrac{1}{2} O_2 \rightarrow N_2 + CO_2 + H_2O \qquad (5)$$
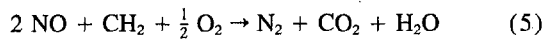
In this equation, "CH_2" is used to represent exhaust gas hydrocarbons. Exhaust gas and engine fuel hydrocarbon constituencies are known to be very different; therefore, these chemical relationships may not adequately represent the real situation.

Chemical "decomposition" is another mechanism that can potentially control NO_x emissions. The chemical decomposition of NO (nitric oxide), the principal constituent of NO_x in engine exhaust, to nonpolluting compounds is given in Eq. (6):

NO_x Decomposition

$$2 NO \rightarrow N_2 + O_2 \qquad (6)$$

Decomposition of NO_x is thermodynamically favorable at temperatures below 900°C, but the activation energy required for this reaction in engine exhaust is too high without the use of a catalyst. Several catalysts promote this reaction at temperatures below 600°C, but none of these have sufficient activity or durability to be practical [5, 6]. Catalytic removal of NO_x by decomposition is inherently simpler than by chemical reduction, because no reducing agent is required. The decomposition of NO_x suggests an emission control strategy that is independent of exhaust gas composition or reductant injection systems.

The focus of this paper is to review catalyst technologies that reduce NO_x in diesel exhaust using added hydrocarbon as the reducing agent (selective catalytic reduction with hydrocarbon). Other reducing agents, such as ammonia or urea, are not discussed further. Two catalyst technologies that have been discussed in the literature are the copper ion exchanged ZSM-5 zeolite and the platinum impregnated zeolites. Other technologies identified in the literature include copper impregnated alumina. These technologies are reviewed in the following discussion.

Literature Survey—Experiments With Diesel Engine Exhaust

In a study by Heimrich et al. [9], lean NO_x catalyst cores were prepared in the laboratory and evaluated in diesel engine exhaust. Experimental diesel NO_x catalysts were prepared by coating zeolite powders onto a ceramic catalyst support. Sodium cations (Na^+) in the zeolite were exchanged with copper cations (Cu^{2+}) to increase catalytic activity. The copper ion exchange procedure was developed by Iwamoto [6]. Three copper zeolite catalysts were investigated, with the primary difference in the formulations being the type of zeolite. A copper-mordenite zeolite catalyst demonstrated NO_x reduction efficiencies of 95 percent while previously adsorbed exhaust gas hydrocarbons were available on the zeolite. When the previously adsorbed diesel exhaust gas hydrocarbons were consumed, NO_x reduction quickly decreased, as shown in Fig. 1. A copper ZSM-5 zeolite catalyst demonstrated longer periods of NO_x reduction, albeit at a lower conversion efficiency of approximately 50 percent. A copper Y-type zeolite catalyst sustained a modest level of NO_x conversion activity for the periods tested. All experiments were conducted with an NO_x inlet concentration of 200 to 300 ppm. This reference shows that exhaust hydrocarbons are an effective NO_x reductant (when they are used efficiently, and are available in sufficient quantities).

A supplemental hydrocarbon (ethylene) was added to the exhaust stream in an attempt to improve NO_x conversion efficiency. Ethylene addition improved NO_x conversion efficiency from 10 to 50 percent on one formulation tested [9, 10]. Remarkably, the catalyst-out hydrocarbon concentration did not
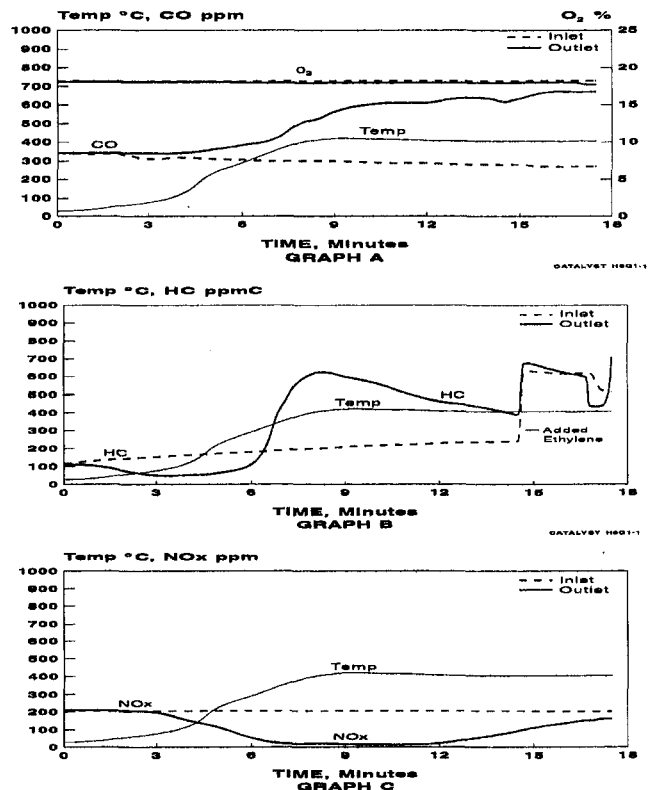

Fig. 1 Emissions response for a Cu-mordenite catalyst on a bench reactor using diesel engine exhaust

exceed the engine-out hydrocarbon concentration for an extended range of ethylene addition. That is, hydrocarbon addition to the exhaust gas did not result in increased hydrocarbon emissions with the catalyst tested. This finding is extremely important if fuel addition is considered as a supplemental NO_x reductant.

Space velocity experiments showed decreasing NO_x conversion efficiency at space velocities greater than 30,000 per hour (h^{-1}) [10]. These results suggest a proportionally larger catalyst volume than typically used for gasoline engines.

Initial catalyst characterization efforts identified a method to determine excess copper deposition on the surface of ion-exchanged zeolite catalysts. Scanning electron microscopy (SEM) using a backscattered electron imaging (BEI) detector and x-ray EDS (energy-dispersive spectroscopy) were used to study copper impregnation [10].

Engler et al. [11] conducted a thorough investigation of lean NO_x catalyst performance under diesel exhaust gas conditions. Catalysts consisted of activated zeolites impregnated with the Groups IB and VIII elements of the periodic table. In this reference, the influences of exhaust hydrocarbon concentration, hydrocarbon species, carbon monoxide, sulfur dioxide, and water on catalytic NO_x reduction were reported. Thermal stability and catalyst poisoning were also studied. Some of these test results are discussed in the following paragraphs.

Calculated equilibrium constants show that several NO_x decomposition and NO_x reduction reactions are thermodynamically possible [11]. Diesel engines, however, do not always provide enough gaseous hydrocarbons for the reduction of NO_x. By assuming a stoichiometric reaction of NO_x with available hydrocarbons, it would appear that for a diesel engine, it would be necessary to increase the concentration of exhaust hydrocarbons to obtain maximum NO_x conversion. This increase can be accomplished with a diesel engine fuel injector system modified to produce higher engine-out HC emissions [11, 12]. An alternate approach is the injection of diesel fuel, upstream of the NO_x

Table 1 Catalytic NO$_x$ reduction efficiency

Zeolite Catalyst Element	Fresh Catalyst		Aged Catalyst	
	Temp, °C	Conversion Efficiency, %	Temp, °C	Conversion Efficiency, %
Cu	375	85[a]	425	55
Pt	225	55[b]	225	50
Rh	225	40[b]	–	0
Ir	350	25	400	20
Ag	375	35[a]	400	10
Au	375	30[a]	400	10
Pd	225	20	275	10

[a]Negative CO-conversion rate (CO was produced)
[b]Simultaneously controlled NO$_x$, HC, CO
Adapted from Engler [11]

converter [11, 13]. Reaction mechanisms for NO$_x$ reduction proposed by Inui et al. [14] and Iwamoto et al. [15] are summarized again by Engler [11].

Experimental catalysts were prepared by coating cordierite honeycombs, followed by impregnation with salts of the active metals. Reported catalyst formulations were prepared with copper (Cu), palladium (Pd), platinum (Pt), rhodium (Rh), gold (Au), silver (Ag), and iridium (Ir). Catalysts were aged both in an oven and on an engine.

Catalyst bench test performance results clearly show that the metals used for impregnation have a significant influence on the NO$_x$ reduction efficiency. Peak catalyst performance (adapted from data reported in [11]) is summarized in Table 1. Notice that after laboratory oven aging, only the platinum sample showed stable NO$_x$ reduction. The platinum-impregnated zeolite catalyst was shown to simultaneously control emissions of HC, CO, and NO$_x$ [11].

The influence of exhaust gas space velocity on the platinum-impregnated catalyst [11] is compared with that of previous NO$_x$ catalysts in an unsupported (powder) form [16, 17]. These early catalyst investigations concluded that NO$_x$ reduction decreased dramatically with increasing space velocities. Engler estimates his catalysts, in the monolithic form, were evaluated at a space velocity 15 times greater than the unsupported catalysts in previous studies. Data suggest that a good compromise between high reduction efficiencies and high space velocity can be obtained at space velocities between 40,000 h^{-1} and 60,000 h^{-1}.

Exhaust gas HC concentration and constituency were shown to influence NO$_x$ reduction efficiency. Increased HC concentrations tended to increase the NO$_x$ reduction efficiency while shifting the maximum NO$_x$ conversion point to slightly higher temperatures. Reduction of NO$_x$ was shown to be more efficient with olefinic hydrocarbons than paraffinic hydrocarbons [5–7, 10, 11].

Carbon monoxide was shown not to be effective as an NO$_x$ reductant in lean exhaust. An experiment was performed to determine the influence of exhaust CO content on NO$_x$ reduction. Results from a synthetic gas reactor show that while the CO concentration increased from 0 to 700 ppm, NO$_x$ (with an exhaust HC concentration of 30 ppm) decreased only slightly. Carbon monoxide had a negligible effect on NO$_x$ reduction [11].

Further studies show that in the absence of oxygen, almost no NO$_x$ reduction was achieved with a platinum-containing zeolite catalyst. This suggests that the oxidation of hydrocarbons has an important influence on NO$_x$ reduction [11]. Water was shown to decrease NO$_x$ reduction, but unaged catalysts in a test reactor still exhibited NO$_x$ reduction of 55 percent in exhaust containing 10 volume-percent water (actual diesel exhaust typically contains 5 to 10 volume-percent water). Sulfur dioxide does not directly hinder the reaction, however, synthetic gas tests reveal that the overall catalyst activity decreased due to the adsorption of the poisoning elements sulfur and phosphorus [11].

A lean NO$_x$ catalyst evaluation was performed using two diesel vehicles and the European ECE vehicle test cycle [11]. During these tests, a constant level of 800 ppm of gaseous hydrocarbons ($C_4H_8/C_4H_{10} = 2/1$) was added to the engine exhaust. The platinum-zeolite catalyst was evaluated following 50 hours of engine bench aging. Significant NO$_x$ reduction was observed for only one of the vehicles.

Vehicle "A" demonstrated an NO$_x$ conversion of approximately 23 percent with an unaged catalyst and approximately 19 percent conversion after 50 hours of diesel catalyst aging. In addition to the observed NO$_x$ reduction, particulate and CO emissions were also reduced by 50 percent. The hydrocarbon emission for this ECE test increased by a factor of two because of the addition of fuel in the exhaust system [11]. This increased hydrocarbon emission, or "slip," can be easily corrected with the proper catalyst formulation, as demonstrated by other catalysts tested.

In a paper by Herzog et al. [12], a summary of NO$_x$ reduction strategies for heavy-duty direct-injection engines was presented. Herzog presented data showing catalytic NO$_x$ control increasing from approximately 17 percent to 30 percent with the use of a modified fuel delivery system. The modified fuel system increased fuel-specific organic soluble particulate emissions and decreased carbonaceous (insoluble) fuel-specific particulate emissions. Although engine fuel injection modifications increased engine-out organic soluble particulate emissions, the catalyst reduced catalyst-out soluble particulate to the same level prior to injection modifications. It was not clear what effect the modifications had on engine performance or fuel economy. Temperature at maximum NO$_x$ reduction efficiency shifted from 250°C to approximately 350°C with the modified fuel injection system. Data presented suggest that hydrocarbons and soluble particulates can be used to reduce NO$_x$ emissions, thereby controlling multiple undesirable emissions simultaneously. Modifying the diesel engine fuel system to increase gaseous HC or organic particulate emissions is a possible approach for improved catalytic NO$_x$ reduction.

In February of 1992, Herzog concluded that in spite of very promising initial results, there is a large amount of development work remaining to be done prior to commercialization. Herzog's recommended goals included:

- Expanding the temperature window of high NO$_x$ conversion rates
- Achieving NO$_x$ conversion rates of 50 to 60 percent
- Improving catalyst activity in the presence of sulfur dioxide
- Avoiding the formation of sulfates at higher exhaust temperatures
- Assuring high conversion rates over the lifetime of the engine.

Another method for introducing hydrocarbons to the NO$_x$ catalyst is to use an exhaust auxiliary fuel spray system. Such an approach was taken by Sumiya et al., and was described in a paper on catalytic reduction of NO$_x$ in diesel engine exhaust [13]. Diesel fuel spray experiments were conducted on a laboratory fixed-bed flow reactor and on an actual diesel engine. Copper-containing catalysts were prepared by impregnating gamma-alumina (γ-Al$_2$O$_3$) with aqueous solutions of copper salts. In this paper, laboratory studies of the fundamental interaction between NO$_x$, oxygen, and hydrocarbons over a copper-containing catalyst was reported. The mechanism of NO$_x$ reduction by the addition of diesel fuel ahead of the catalyst is discussed in [13].

Maximum NO$_x$ reduction efficiencies using copper-based catalysts and an experimental fuel spray system on a bench flow

Table 2 Fuel injection experiments on a bench reactor

Reductant	No Water		Water–10%	
	Maximum NO$_x$ Reduction, %	Temp, °C	Maximum NO$_x$ Reduction, %	Temp, °C
Propene	30	400	10	450
Diesel Fuel	–	–	30	450
Diesel Fuel	–	–	50[a]	450
[a]Higher fuel-to-NO$_x$ ratio				

reacter are given in Table 2. In the absence of water vapor in the exhaust, a 30 percent NO$_x$ reduction was realized at 400°C with propene (C$_3$H$_6$) as the reductant. Reduction of NO$_x$ dropped to 10 percent when water was added to the exhaust stream. Note that the point of maximum NO$_x$ reduction shifted toward higher temperatures with the addition of water. Using diesel fuel as the reductant, NO$_x$ reduction efficiency increased from 10 percent to 30 percent in exhaust gas containing 10 percent water vapor. Reduction of NO$_x$ improved to 50 percent with higher fuel-to-NO$_x$ ratios.

Sumiya studied the NO$_x$ reduction reactivity of individual hydrocarbons and diesel fuel. He ranks the NO$_x$ reduction reactivities of alkanes, alkenes, alkynes, and diesel fuel at 450°C as follows:

NO$_x$ Reduction Reactivity
In the absence of water vapor:

alkynes > diesel fuel > alkenes > alkanes

In the presence of water vapor:

diesel fuel > alkynes > alkenes > alkanes

Note that diesel fuel was the best NO$_x$ reductant in the presence of water vapor. Sumiya suggests that heavy saturated hydrocarbons in diesel fuel are converted to more active hydrocarbons through carbon–carbon bond breaking over the catalyst [13]. These active hydrocarbons react with NO$_x$ with higher selectivity at lower temperature, even in the presence of water vapor [13]. Sumiya states that these results suggest that a further-developed fuel addition technique should result in greater NO$_x$ reduction at lower fuel-to-NO$_x$ ratios at lower temperatures. Sumiya further states improvements in fuel spray technology may possibly result in an effective aftertreatment technology for diesel engines [12].

Sumiya also studied the removal of NO$_x$ from the exhaust of an actual diesel engine utilizing an exhaust fuel injection scheme. His engine-exhaust catalyst was prepared by coating a ceramic foam substrate with copper-containing γ-Al$_2$O$_3$ [13]. The foam substrate acted as a low-efficiency particulate trap, as well as an NO$_x$ reduction catalyst. Sumiya's engine was run at a constant speed and load. As seen with the catalyst reactor experiments, NO$_x$ reduction efficiency increased with the fuel-to-NO$_x$ ratio. An NO$_x$ reduction of 30 percent at 450°C was achieved with fuel spray in the exhaust system. Sumiya states in his paper that the fuel spray system was subsequently improved to achieve greater NO$_x$ reduction in engine testing at temperatures of approximately 400°C. Improvements were a result of more effective diesel fuel vaporization. This paper concludes with a proposed system for controlling NO$_x$ and particulates. Advanced NO$_x$ control is suggested by using a microprocessor-controlled diesel fuel spray system that introduces fuel only under high-NO$_x$ conditions.

Catalytic reduction of NO$_x$ in diesel engine exhaust was studied on a bench reactor by Konno et al. and published in 1991 [18]. Catalyst formulations prepared in this study were copper-

ion exchanged ZSM-5 zeolites (Cu-ZSM-5). Without the use of supplemental hydrocarbons, Cu-ZSM-5 catalysts reduced NO$_x$ by 25 percent at 400°C. When exhaust hydrocarbons were increased, NO$_x$ reduction efficiency increased to 80 percent. Water in the exhaust gas decreased the NO$_x$ reduction efficiency. Oxygen and sulfur appeared to have only a small effect on catalytic NO$_x$ reduction activity. Maximum NO$_x$ reduction was observed at 400°C and did not decrease with space velocities up to 20,000 h^{-1}. These tests were performed using actual diesel engine exhaust with the particulate and water removed.

Performance Summary

A summary of the lean NO$_x$ catalyst literature reviewed for this paper is given in Table 3. Catalytic reduction of NO$_x$ (by hydrocarbon) has been observed as high as 50 percent on a continuous basis, and as high as 95 percent on a temporary basis (using previously adsorbed hydrocarbon reductants on the catalyst). Supplemental hydrocarbon reductants were required to chemically reduce NO$_x$. Fuel spray systems were used to deliver hydrocarbon reductants to the catalyst. Detailed information was not available on the fuel spray systems employed.

Many different metals and zeolite structures have been investigated for NO$_x$ reduction in lean exhaust. Initially, the Cu-ZSM-5 zeolite received most of the attention (in the literature) because of its superior performance compared to other early lean NO$_x$ catalyst formulations. Another promising catalyst formulation uses cobalt (Co) as the active metal, but this catalyst needs a higher temperature to operate than the copper-based catalysts. Recently, attention has been focused on developing silica aluminum phosphate-based zeolites that have improved pore structures and better hydrothermal durability [8, 19]. Test results on these catalysts, unfortunately, are not yet available.

Recommendations for Future Work

Areas of future research for the development of the diesel NO$_x$ catalyst and emission control system include:

- Widening the temperature range where maximum catalytic NO$_x$ reduction occurs. A lean NO$_x$ catalyst with a wider catalytically active temperature range is necessary for controlling NO$_x$ emissions during transient exhaust temperature operation.
- Improving catalyst hydrocarbon selectivity for the NO$_x$ reduction reaction. Current-technology demonstration catalysts are observed to make inefficient use of added hydrocarbon reductants [20].
- Improving catalytic NO$_x$ removal efficiency over transient engine operation. A catalyst with 70 percent NO$_x$ removal efficiency would reduce 5.0 gram/brake horsepower-hour (g/bhp-hr) engine-out emissions to 1.5 g/bhp-h. Total particulate emissions can be further reduced with a diesel NO$_x$ catalyst (organics [21] are oxidized in many of the platinum-containing lean NO$_x$ catalysts).
- Obtaining higher NO$_x$ reduction efficiency at higher exhaust gas space velocities. Moderate NO$_x$ reduction efficiencies have been achieved at space velocities in the range of 20,000 h^{-1} to 40,000 h^{-1}. For heavy-duty diesel truck engines, space velocities near 100,000 h^{-1} are desired so that catalytic converters will not be excessively large.
- Minimizing the catalytic production of undesirable organic and sulfate emissions. Proper selection of a catalyst wash-coat, for example, has been shown to lower the production of sulfates [21].
- The development of a hydrocarbon enrichment system to provide the required NO$_x$ reductants. The quantity of NO$_x$ reductants in the exhaust stream could be increased using engine-out hydrocarbon emissions or injecting fuel directly into the exhaust system [20].

Table 3 Summary of diesel NOx catalyst literature: experimental results using actual exhaust

Author	Ref.	NOx Reduction, %	Catalyst	Space Velocity, h⁻¹	Engine	Reductant	Delivery	Comments
Heimrich (Southwest Research Institute)	9	95	Cu-Mordenite	20,000	Diesel	Adsorbed Exhaust HC	None	Exhaust HCs can be used as Reductants
	9	50	Cu-ZSM-5	20,000	Diesel	Adsorbed Exhaust HC	None	No increased total HC emission
	9	50	Cu-Zeolite	Up to 30,000	Diesel	Ethylene plus Exhaust HC	Bottle	Particulate removed
Engler (Degussa)	11	10-85 (unaged) 10-55 (aged)	Zeolites impregnated with Group IB and VIII elements	40,000 (estimated from unsupported catalysts)	Synthetic Gas	C_3H_6/C_3H_8	None	HC/NOx = 2400 ppmC/ 270 ppm
	11	23/19 (aged/unaged)	Pt-Zeolite	Transient Space Velocity	Diesel (IDI)	800 ppm C_4H_8/C_4H_{10} (2/1) plus exhaust HC	Bottle	Vehicle test, 50-hour catalyst aging
Herzog (AVL-LIST)	12	17-30	Zeolite	–	Diesel	Fuel	Engine Fuel System	Modified Fuel System Fuel economy not given
Sumiya (Riken)	13	30/10 (0% water/ 10% water)	Cu-Al₂O₃	15,000	Synthetic Gas	C_3H_6	Bottle	Bench test, HC/NOx = 5100 ppmC/ 800 ppm
	13	30/50 (fuel/increased fuel)	Cu-Al₂O₃	15,000	Synthetic Gas	Diesel Fuel		Bench test, 10% water, maximum Fuel/NOx mass ratio = 5
	13	30	Cu-Al₂O₃	–	Diesel	Diesel Fuel	Spray System	Fuel/NOx mass ratio = 5
Konno (Hokkaido University)	18	25/50 (without/with ethylene)	Cu-ZSM-5	20,000	Diesel	Ethylene	Bottle	Water and particulate removed
	18	80	Cu-ZSM-5	20,000	Diesel	Light oil	Drip	

- The development of an efficient fuel spray schedule to minimize the potential fuel economy penalty. The net fuel economy penalty could be further lessened by calibrating the diesel engine for more efficient operation with further advanced fuel injection timing, and controlling the resulting increase in NOx emissions catalytically. This calibration also would result in reduced engine-out particulate emissions [13].

The ultimate goal for lean NOx catalyst research is the development of a decomposition catalyst that does not require additional hydrocarbon for NOx removal. The decomposition catalyst, however, has not yet shown practical feasibility in actual engine exhaust.

Acknowledgments

References

1 "Request for Proposals" (RFP) entitled "Demonstration of a Non-additive Lean NOx Catalytic Converter for Heavy-Duty Diesel Vehicles," State of California Air Resources Board, RFP No. 92–7, Sept. 14, 1992.

2 Heimrich, M. J., "Air Injection to an Electrically-Heated Catalyst for Reducing Cold-Start Benzene Emissions From Gasoline Vehicles," SAE Paper No. 902115, 1990.

3 Kivosky, J. R., Koradia, P. B., and Lim, C. T., "Evaluation of a New Zeolite Catalyst for NOx Reduction With NH₃," American Chemical Society, Ind. Eng. Cem, Prod. Res. Dev., Vol. 19, 1980, pp. 218–225.

4 Urban, C. M., Dietzmann, H. E., and Fanick, E. R., "Emission Control Technology for Stationary Natural Gas Engines," ASME JOURNAL OF ENGINEERING FOR GAS TURBINES AND POWER, Vol. 111, 1989, pp. 369–374.

5 Held, W., Konig, A., Richter, T., and Puppe, L., "Catalytic NOx Reduction in Net Oxidizing Exhaust Gas," SAE Paper No. 900496, 1990.

6 Iwamoto, M., Yahiro, H., Tanda, K., Mizuno, N., Mine, T., and Kagawa, S., "Removal of Nitrogen Monoxide Through a Novel Catalytic Process. 1.

Decomposition of Excessively Copper Ion Exchanged ZSM-5 Zeolites," The Journal of Physical Chemistry, Vol. 95, No. 9, American Chemical Society, 1991.

7 Truex, T. J., "NOx Reduction Under Lean-Burn Conditions," Johnson Matthey Technology Centre.

8 Iwamoto, M., and Mizuno, N., "NOx Emission Control in Oxygen-Rich Exhaust Through Selective Catalytic Reduction by Hydrocarbon," submitted to the Journal of Automobile Engineering, Part D of the Proceedings of the Institution of Mechanical Engineers, 1992.

9 Heimrich, M. J., Jones, K. B., and Bykowski, B. B., "Preparation and Evaluation of Lean NOx Catalysts," ASME Paper No. 93-ICE-30, 1993.

10 Heimrich, M. J., and Deviney, M. L., "Lean NOx Catalyst Evaluation and Characterization," SAE Paper No. 930736, 1993.

11 Engler, B. H., Leyrer, J., Lox, E. S., and Ostgathe, K., "Catalytic Reduction of NOx With Hydrocarbons Under Lean Diesel Exhaust Gas Conditions," SAE Paper No. 930735, 1993.

12 Herzog, P. L., Burgler, L., Winklhofer, E., Zelenka, P., and Cartellieri, W., "NOx Reduction Strategies for DI Diesel Engines," SAE Paper No. 920470, 1992.

13 Sumiya, S., Muramatsu, G., Matsumura, N., Yoshida, K., and Schenck, R., "Catalytic Reduction of NOx in Diesel Exhaust," SAE Paper No. 920853, 1992.

14 Inui, T., Kojo, S., Shibata, M., Yoshida, T., and Iwamoto, M., "NO Decomposition on Cu-Incorporated A-Zeolites Under the Reaction Condition of Excess Oxygen With a Small Amount of Hydrocarbons," Zeolite Chemistry and Catalysis, 1991, p. 355.

15 Sata, S., Hirabayashi, H., Yihiro, H., Mizuno, N., and Iwamoto, M., "Iron Ion-Exchanged Zeolite: The Most Active Catalyst at 473 K for Selective Reduction of Nitrogen Monoxide by Ethane in Oxidizing Atmosphere," Catal. Letters, Vol. 12, No. 193, 1992.

16 Hama, H., Kintaichi, Y., Sasaki, M., Ito, T., and Yoshinari, T., "High Efficiency of Alumina and H-Zeolite Catalysts for Selective Reduction of Nitrogen Monoxide by Methanol in the Presence of Oxygen and Water Vapor," Appl. Catal. A: General, Vol. 88, Nos. L1–L7, 1992.

17 Sato, S., Yu-u, Y., Yahiro, H., Mizuno, N., and Iwamoto, M., "Cu-ZSM-5 Zeolite as Highly Active Catalyst for Removal of Nitrogen Monoxide From Emissions of Diesel Engines," Appl. Catal., Vol. 70, Nos. L1–L5, 1991.

18 Konno, M., Chikahisa, T., Murayama, T., and Iwamoto, M., "Catalytic Reduction of NOx in Actual Diesel Engine Exhaust," SAE Paper No. 920091, 1992.

19 Monroe, D. R., DiMaggio, C. L., Beck D. D., and Matekunas, F. A., "Evaluation of a Cu/Zeolite Catalyst to Remove NOx From Lean Exhaust," SAE Paper No. 930737, 1993.

20 Heimrich, M. J., "Demonstration of a Non-additive Lean NOx Catalytic Converter for Heavy-Duty Diesel Vehicles," Task 2 Interim Report to the State of California Air Resources Board, Contract No. 92-310, SwRI Project 08-5744, June 1, 1994.

21 Khair, M. K., and Bykowski, B. B., "Design and Development of Catalytic Converters for Diesels," SAE Paper No. 921677, 1992.

An Automated Diagnostic Expert System for Diesel Engines

R. K. Autar

Department of Mechanical Engineering,
University of Adelaide,
Adelaide, South Australia

Fault diagnosis of diesel engines can be a tedious time-consuming process, resulting in extended downtime, thus reducing productivity and increasing operational cost. This problem can be accentuated when experienced expert maintenance personnel are in short supply and also when the rate of development of new-generation engines using leading edge technology does not permit maintenance personnel to keep up with this change. An automated diagnostic system based on artificial intelligence criteria using mechanical signature analyses (MSA) of signals acquired from engine mounted sensors can overcome this problem by providing expert and consistent diagnostic advice. This paper describes the development and implementation of an automated diagnostic expert system for diesel engines. The system uses vibration signals together with oil pressure and temperature, crankcase pressures, exhaust gas temperature and pressure, exhaust emissions, manifold noise levels, inlet manifold pressure, fuel delivery pressure, and instantaneous engine speed to monitor and diagnose engine faults. State-of-the-art techniques used for signal processing to generate data required for effective diagnosis from raw signals acquired form the engine mounted sensors are described. Complexities of signal processing for diesel engines are discussed and solutions of a practical nature suggested. Signal analysis techniques relating to fault condition evaluation are also described.

1 Introduction

The need to improve diagnostic equipment for engine fault identification, whether installed on-board or workshop-based, is widely recognized. Ideally, diagnostic systems should provide explicit fault-source information that can locate the root cause for the malfunction, but a major impediment to developing this facility has been the difficulty of discriminating between possible faults using limited signal information. A system that can provide explicit fault-source information needs to rely on mechanical signature analyses (MSA) of the engine's operating variables, that is, temperatures, pressures, speed, and exhaust emissions together with other signals that appear as a result of the operating variables, such as engine surface vibrations, crankshaft speed fluctuations, oil pressure transients, and manifold noise levels.

This paper specifically addresses the concepts for, and the requirements of, a workshop-based diagnostic system. However, the same system can be used to implement a permanently installed, continuously monitoring on-board diagnostic system by incorporating an on-board data logging facility, which periodically downloads acquired data into a central computer. The diagnostic system described is an extension of the manual version of CAMODE (Computer Aided Maintenance of Diesel Engines) that has been developed at the University of Adelaide, South Australia [1]. CAMODE is a knowledge-based system (expert system) and the manual version requires manual input of symptoms exhibited by, and results of specific tests on, faulty engines to diagnose faults in the engine. Fault diagnoses are made using the hypotheses and tests criteria with extensive use of production rules resident in the knowledge base of the system. The manual version relies on the end-user to provide input information to the system, which is usually in the form of observable symptoms, results of particular tests, and readings from engine instrumentation. As a result, the types of fault that can be diagnosed by the manual system are those that are very basic in nature and those that are usually present in isolation. More complex faults, or concurrently existing faults, are difficult to diagnose, in the former case due to the inability to detect any observable symptoms, and in the latter case due to masking and cross effects caused by the multitude of symptoms that are usually present. The need for a sensor-based system thus arises. With the implementation of such a system within an expert system environment, an intelligent, automated diagnostic system is realized. This system will not only perform at a level that is comparable to a human expert, but will invariably expedite diagnosis of faults when used by less experienced maintenance personnel. The benefits that such a system can be expected to provide are highlighted by Autar et al. [1].

A range of proprietary diagnostic equipment is available already for workshop use, but typically these provide information that requires further interpretation before remedial action can be defined. This is unsatisfactory because it depends on the uncertain expertise of the diagnostician, and is subject to variability between different diagnosticians. The interpretation of signal information using a computer in an expert system environment, which would also present specific fault information to the operator, would be a significant advantage as expert advice and decision making criteria are preserved and the effects of variability between individuals is eliminated. The major problems to overcome are those of providing relevant information to the computer and of developing reliable interpretation software in expert system form.

The following sections discusses the hardware and software that comprises the system. The various sources of information available on the engine that can be used in fault diagnosis, and the corresponding sensors used for signal acquisition in the automated diagnostic system, are discussed. Limitations in the interpretation of signals in their raw form, and methods of enhancing signal information for more effective diagnosis, are also discussed. Strategies that can be used for diagnosing engine faults with limited information are highlighted.

2 System Architecture and Functionality

CAMODE software is configured in a layered fashion and can therefore be used either to perform diagnosis on a specific
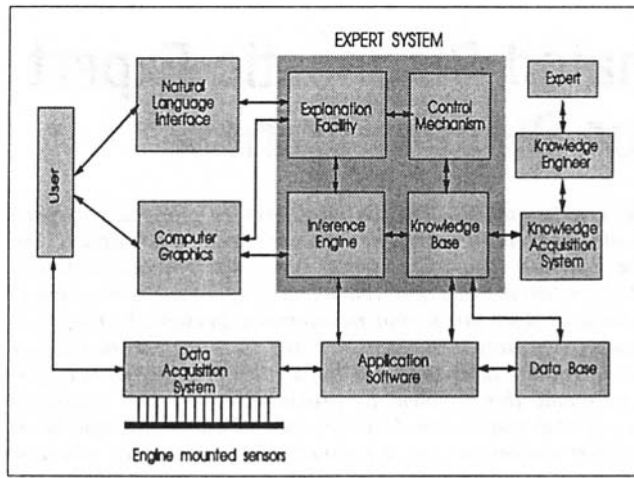
Fig. 1 System architecture of CAMODE

engine subsystem, such as the cooling system, or to perform a complete performance-based diagnosis to detect faults and gather data for condition monitoring of the whole engine. The software provides diagnosis at two levels: manual diagnosis, which resulted from the first phase of the development program, and automated diagnosis. Both of these systems use an expert system environment to simulate a human expert's diagnostic logic by encapsulating the expert's knowledge in the form of rules, which are stored in the knowledge base of the system. The knowledge base is designed so that it can be easily modified or new knowledge easily added.

The system's primary function is to diagnose engine faults; however, other functions, such as advising on appropriate service and repair procedures, parts, and tools requirements to carry out these service and repair procedures, testing and adjusting procedures, and on specifications data, are also included in the system and may be accessed during a consultation. The system also provides diagnostic schedules for faults addressed by the system; these are also available in hard-copy form so that diagnoses may be carried out on machines that break down in the field, and where access to the automated or manual system may not be possible.

Educational and training facilities in the form of a symptoms evaluator, which may be used to assess the troubleshooting capabilities of less experienced personnel, and a systems operation guide, which describes functional details and operating characteristics of engine components, are also incorporated in the system. The system is implemented and delivered to operate on the IBM personal computer and compatibles. Extensive on-line help and explanation facilities are available on the system to maximize ease of use. Extensive graphic and text data for knowledge transfer, primarily while advising on repair procedures, are utilized.

The nucleus of the automated diagnostic system is the manual version of CAMODE which is programmed with EGERIA™, a higher level programming language specifically designed for writing a range of expert system applications. CAMODE comprises the following eight modules:

1 Troubleshooter
2 Maintenance and repair adviser
3 Parts and tools requirements
4 Specifications data
5 Test procedures
6 Troubleshooting scheduler
7 Symptom evaluator
8 Systems operation

Each of these modules is capable of being accessed and used as a stand-alone module; however, modules 2, 3, 4, and 5 are

also accessible during a troubleshooting session. The option of accessing each of the modules for use as a stand-alone system was a prerequisite, since maintenance personnel may wish to get only a specific piece of information while working on an engine.

The automated diagnostic system uses additional features, which are linked to the manual version of CAMODE to form a complete system (Fig. 1). These additional components, principally the data acquisition system and the signal processing and signal analysis software (application software) linked with the knowledge base, form the heart of the system. The data acquisition system comprises engine-mounted sensors and a software driven analogue-to-digital (A/D) converter. The signals acquired by the acquisition system are processed by software that also acts as a data reduction system, by getting rid of unnecessary information and only post-processing useful data. The information thus gathered is stored in a data base system for use by the expert system in the diagnosis of faults. All the necessary information relating to fault detection and classification is stored as rules in the knowledge base of the system. The system utilizes engine surface vibration, lubricating oil pressure and temperature, engine coolant temperature and pressure, exhaust temperature and pressure, inlet manifold pressure and noise levels, fuel delivery pressure, crankcase pressure, exhaust gas composition, and instantaneous engine speed, obtained from the following types of sensor:

1 Accelerometers
2 Pressure transducers
3 Thermocouples
4 Exhaust gas analysers
5 Microphones
6 Engine speed encoder
7 Engine cycle reference encoder (optical or magnetic tachometer)

Sensor locations, typical signal types, and the faults identifiable from an analysis of the various signals, are discussed under the respective sections below. A schematic of operational details of the system is shown in Fig. 2. Data acquired from the different engine-mounted sensors during the diagnosis or a service period are processed and stored in databases. These data or signatures are compared to those that were acquired when the engine was commissioned and changes are evaluated by the expert system. The changes in the different signatures reflect the condition of the different engine components and are compared
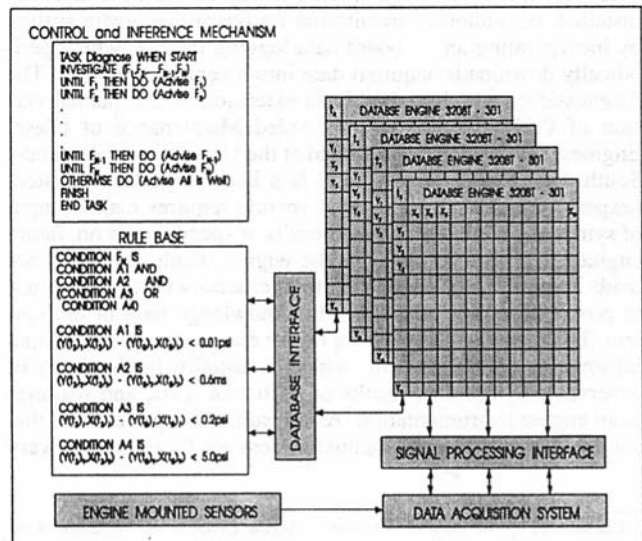

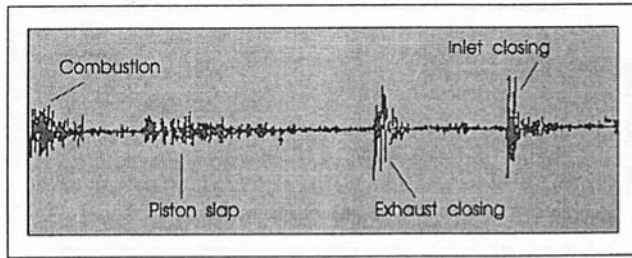Fig. 2 Schematic of operational details of CAMODE

Fig. 3 Vibration signature at the cylinder head of a single cylinder engine

Fig. 4 Vibration signal of a CAT3208T engine

against the rules that are encapsulated into the knowledge base of the system. Any abnormalities are reported and the actions to be taken are recommended.

3 Vibration Signature Analysis

Accelerometers used to measure engine surface vibration provide information on the condition of the various moving parts in the engine together with other transient events that comprise the operation of a diesel engine, that is, valve operation, piston slap, fuel injection and combustion, diesel knock, bearing knocks, and gear meshing. The vibration signature acquired from a malfunctioning engine is compared with the template signature acquired when the engine was commissioned and known to be in "good" condition and differences between the two lead to identification and diagnosis of faults.

The application of vibration analysis for fault detection and diagnosis in rotating machinery is fairly well established due to the simple nature of the signals generated. Fault detection and diagnosis in rotating machinery usually requires signal analysis at the rotating speed frequencies or their harmonics, and analysis of faults is therefore very straightforward. However, with reciprocating machinery such as diesel engines, the events involved in their operation generate trains of vibration; each cylinder superimposes its own excitations with a delay depending on the firing sequence. The vibrations of an engine are in fact similar to a succession of transients. These transient signals are variable from cycle to cycle and much random noise is present. Time synchronous averaging (TSA) of the signals over a number of engine cycles result in a statistically stable signal and randomly occurring noise averages to zero. TSA utilizes an engine cycle encoder to synchronize signal acquisition to a specific point in the engine cycle. A one per cycle event marker from the camshaft gear wheel is used as a cycle reference encoder, which is also used as a trigger for signal acquisition.

Although the events occurring in one cylinder's cycle are widely separated in time (this is illustrated in Fig. 3), events can overlap with other events from the cycle of a different cylinder, or events can have only marginal separation, making specific event analysis difficult. This phenomena is common in small and compact multi-cylinder engines where it is not unusual for the combustion event of one cylinder to corrupt signals due to another source like a piston slap or a valve closing event of some other cylinder. A typical case is shown for the Caterpillar 3208T marine engine where the valve event acquired from the cylinder head of the engine (Fig. 4) is seen to be in close proximity of a combustion event. Although timing of these events can be ascertained by application of windows in the frequency and time domains, evaluating the condition of the valve seats, which requires frequency analysis of the signal, may be difficult because of leakage of some of the combustion event's energy into the windowed valve event. In such cases other filtering techniques such as adaptive noise cancellation (ANC) [2] can be applied. An example of the results achieved using ANC on the CAT3208T engine is illustrated in Fig. 5. Figure 5(a) shows the frequency analysis of the corresponding
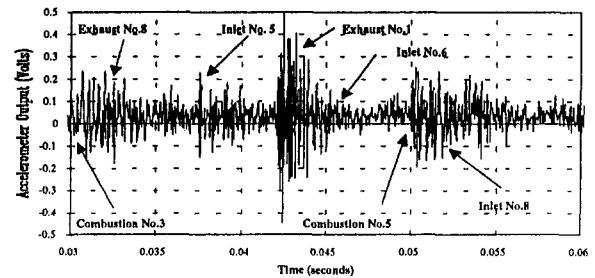
time synchronous averaged time domain signal of an inlet valve closing event. Figure 5(c) shows the frequency domain signature of a valve closing event measured with the valve actuated pneumatically in the absence of any combustion signal. The large amount of energy centred at 13 kHz in the spectrum of Fig. 5(c) can be seen clearly. In contrast, Fig. 5(a) shows a spectrum dominated by combustion event energy between 9 and 12 kHz with little apparent energy at 13 kHz. Figure 5(b) shows the same signal as in Fig. 5(a) except that active noise cancellation has been used to remove the combustion event signature, leaving just the valve event with its dominant spectral energy centered at 13 kHz.

Vibration signature analysis can provide by far the most information about the condition of internal parts of machinery. However, because of possible ambiguities that can arise with vibration signature analysis, other signals such as temperatures, pressures, engine speeds, etc., are used as complementary signals to strengthen the diagnosis. Nonetheless, it should be mentioned that as more powerful signal processing algorithms are developed, the quality of vibration signatures will improve and thus improvements in its application to machinery diagnostics will be reflected. Typical faults that can be diagnosed in a diesel engine using vibration signature analysis are:

1. Cylinder compression and combustion faults
2. Fuel knocks
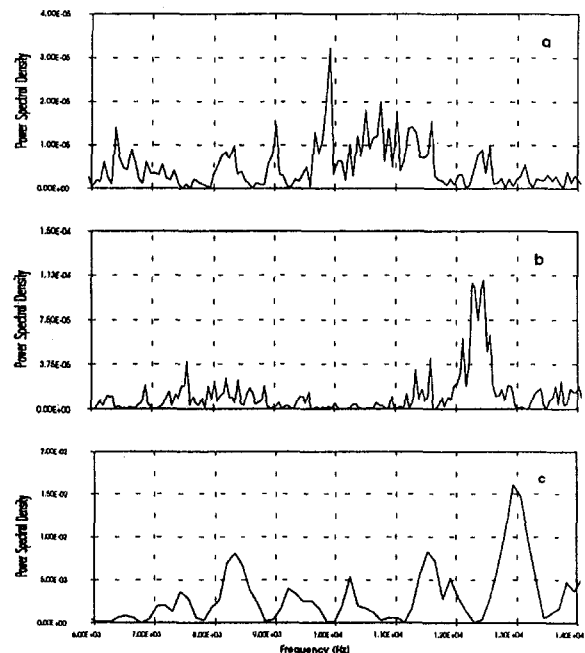3. Valve seating problems
4. Valve tappet clearances

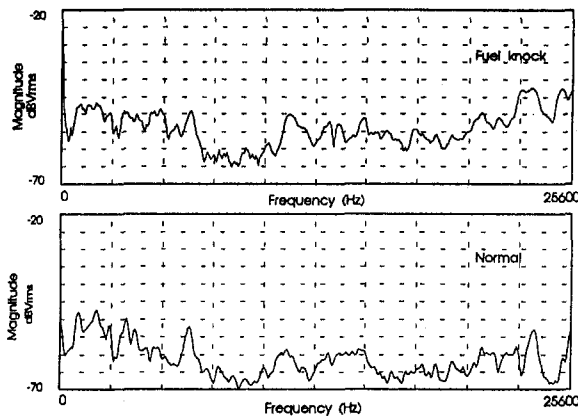

Fig. 5 ANC results for an inlet valve of a CAT3208T engine

Fig. 6 Vibration signature showing the effect of fuel knock

5 Piston slap
6 Valve mechanism faults

Examples of some of these are given in Figs. 6 and 7 where excessive tappet clearances and fuel knock due to inferior fuel are quite evident when the signatures of the faulty engine are compared to those of a normal engine.

4 Lubricating Oil Pressure and Temperature Analysis

Adequate lubrication is critically important for the safe and satisfactory performance of a reciprocating engine. The lubricating oil pump must be able to provide filtered oil to the various parts through the oil galleries and also force the oil through the oil cooler before it is returned to the oil sump. To provide sufficient flow for satisfactory performance, the oil pump must be able to provide sufficient delivery pressure on the supply side. The steady-state delivery pressure is sufficient to diagnose oil pump failures and the differential pressure across the oil filters can be used to diagnose filter problems. Lubricating oil temperatures can be used to diagnose oil cooler problems.

Due to the continuously varying system impedance of the lubrication system in an engine, transient signals are present on top of the steady-state signal produced by the constant pressure
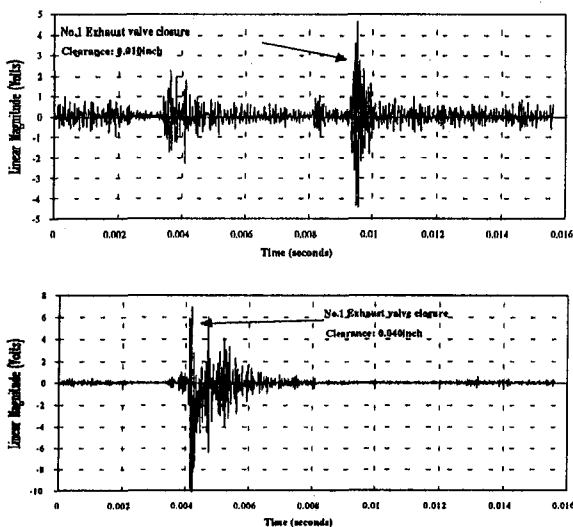

Fig. 7 Vibration signature showing the effect of excessive valve clearance
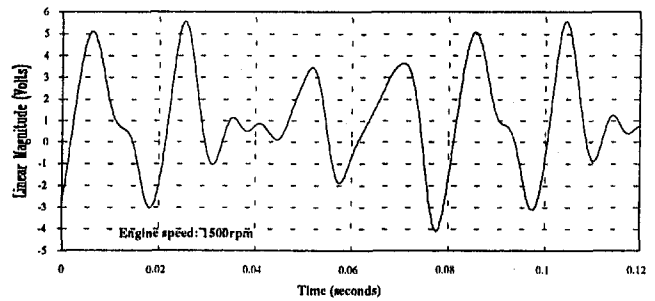

Fig. 8 Oil pressure transient signal

delivered by the oil pump [3]. These transient signals (Fig. 8) are generated at specific times during the engine cycle and each transient is associated with a specific component, e.g., a specific big-end/journal bearing combination. The transient pressure fluctuations result from the matching and mismatching of lubrication supply holes in the journal/bearing combination and are transmitted through the oil supply network. Low transient signals reveal excessive wear in the journal/bearing combination and when signals are referenced to the engine cycle using the engine cycle reference encoder, the specific faulty journal/bearing can be diagnosed.

5 Engine Coolant Temperature and Pressure Analysis

Engine cooling system problems can result in severe engine performance degradation. They can result from very minor problems such as loose fan belts, defective thermostats, lack of coolant, or from major problems such as blown cylinder head gaskets, cracked cylinder heads, and cracked engine blocks. Usually overheating is the major problem, but overcooling can also cause performance degradation. Measurements of the steady-state temperatures and pressures of the coolant while the engine is running at some specific speed are used to diagnose faults in the cooling system. Although overheating due to the minor problems listed above will cause some pressure rise within the system, excessive pressure increases can be an indication of a major problem such as a blown cylinder head gasket, a cracked cylinder head, etc., resulting in combustion gases getting into the cooling system. Overheating due to other problems such as incorrect fuel injection timing, excessive exhaust back pressure, etc., is diagnosed by observing the signals from accelerometers, which would show variations in injection timing, or from exhaust pressure sensors, which would show increased backpressure in the exhaust system.

6 Exhaust Temperature and Pressure Analysis

Abnormal exhaust temperatures can indicate malfunctions in the fuel system of a diesel engine. Problems such as "overfueling" or "under-fueling" of cylinders cause temperature variations of the exhaust gases of the particular cylinder. Other problems such as inferior fuel quality, incorrect fuel injection timing, and exhaust restrictions results in overall temperature variations of the exhaust gases. Specific cylinder problems can be diagnosed if a fast response temperature sensing probe is used that is able to measure the temperature of the gas discharged from each of the cylinders as it flows through the exhaust manifold. Identification of cylinders can be achieved by referencing the acquisition of the signal to the engine cycle using the engine cycle reference encoder. There are significant problems in measuring exhaust gas temperatures of specific cylinders. It is not only a hardware problem, that is, requiring a very fast response temperature probe (1–2 ms), but also one of being able to sustain such delicate probes in the very harsh environment that exist in the exhaust manifold of a diesel en-
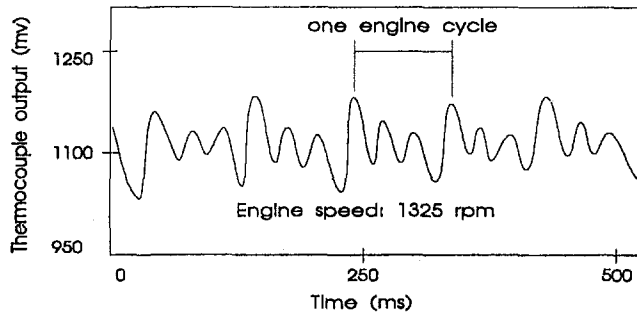
Fig. 9 Exhaust gas temperature transients from one bank of cylinders

Fig. 11 Blowby pressure transients

gine. Figure 9 shows the temperature transients from the left bank of cylinders for a Caterpillar 3208T engine. Note that the response of the thermocouple was not quick enough to separate two of the pulses.

Exhaust gases discharged from the cylinder flow through the exhaust manifold past the turbocharger turbine, through the mufflers and out through the exhaust pipes. Optimum engine performance is dependent on correct exhaust backpressure. Excessive backpressure, which can be caused by either exhaust blockage/restriction or turbocharger fouling, is diagnosed by measuring the backpressure. Cylinder specific problems can also be diagnosed by use of exhaust pressure transients that can be picked up by a fast response pressure transducer. Uneven combustion between cylinders can be easily distinguished using these transients; however, the root cause of this problem cannot be pinpointed using these signals alone. Exhaust pressure transient signals can be a useful indicator to narrow down the search for the root cause of the problem, and use of other appropriate signals can then be made to locate the source of the problem. Figure 10 shows the exhaust pressure transient signals acquired from a Caterpillar 3208T engine that had a misfire on cylinder number 7.

7 Inlet Manifold Pressure Analysis

Inlet manifold pressures are usually a good indication of an engine's "breathing" efficiency and can be used to diagnose faults that may be present in the air inlet systems. Typically, a turbocharged engine operates at positive pressures at the inlet manifold, and associated problems such leaks in the inlet manifolds, dirty air filters, and defective turbochargers will be revealed by monitoring inlet manifold pressures. Positive identification of each of these faults is made possible through use of complementary signals from other sensors.

8 Crankcase Pressure Analysis

High crankcase pressures can indicate the existence of excessive blowby past the piston and therefore can be an indication of the condition of the piston, rings, and cylinder liner. A rapid
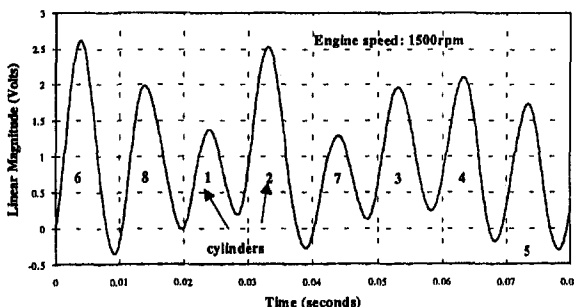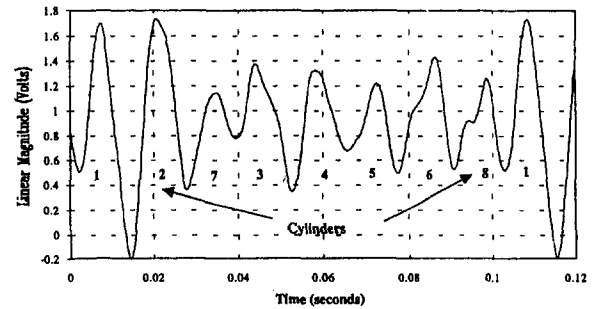
response transducer when synchronized to the engine cycle indicates the specific cylinder causing excessive crankcase pressure and thus expedites the diagnosis. Overlapping of signals from different cylinders would somewhat distort the signals as shown for the CAT3208T engine in Fig. 11. Other problems, such as crankcase breather defects, causing pressure build-up in the crankcase results in a rise in the mean crankcase pressure, which is easily measured and diagnosed.

9 Fuel Delivery Pressure Analysis

The primary fuel system of a diesel engine supplies fuel to the fuel injection pump and the fuel feed pump therefore has to supply fuel at the specified delivery pressure at various engine speeds. Malfunctioning of the fuel feed pump may result in fuel starvation and subsequently power loss, misfiring, or rough running. Monitoring the primary fuel system pressure quickly reveals the fault.

10 Exhaust Gas Analysis

Exhaust gas analysis not only reveals problems in the fuel system, mechanical components of the engine, and problems of fuel quality, but is nowadays necessary for the monitoring of the level of pollutants such as NO_x, HC, and CO. Diesel engine exhaust gases comprise CO, CO_2, HC, NO_x, and O_2. The levels of each of the constituents can indicate the level of combustion efficiency, quality of fuel, mechanical efficiency of the engine, compression ratio, volumetric efficiency, and fuel system performance. Complementary signals from other sensors can assist in locating the source of the problem. Smoke levels in the exhaust gases can also be used to diagnose fuel quality and other mechanical faults. Figure 12 shows the effect of fuel injection timing error on the levels of the various exhaust gas constituents.

11 Instantaneous Engine Speed Analysis

This diagnostic technique [4] is based on measuring the instantaneous angular speed of the flywheel on the engine, re-
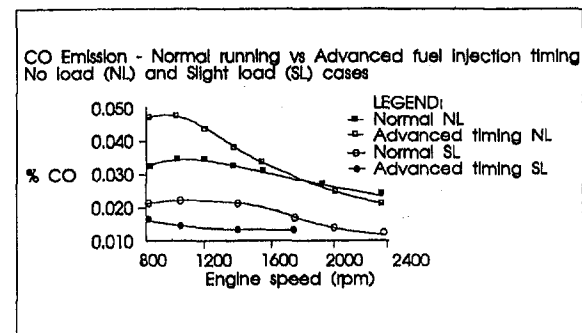

Fig. 10 Exhaust pressure transients

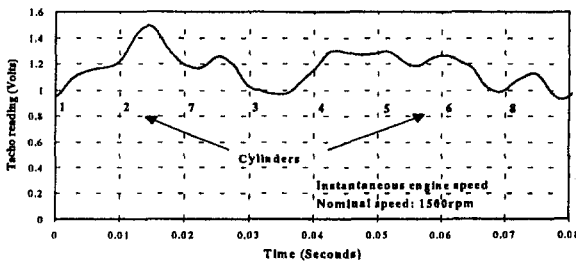Fig. 12 Exhaust emission levels for incorrect injection timing

Fig. 13 Flywheel speed acceleration for a faulted engine

cording more that 200 speed measurements per engine cycle. During the operation of an engine, deterioration of performance can occur due to either loss of compression or incorrect fueling of individual cylinders. The most frequent causes for the former are incorrect valve settings or burnt valves; however, piston rings, cylinder liners, cylinder head gaskets, etc., can also be the cause. Faulty fueling is often caused by malfunctioning injectors or malfunction of the engine control system. Analysis of instantaneous engine speed can quickly reveal the problematic cylinder and also the type of fault, that is, compression or fueling fault.

Experimentally recorded speed waveforms not only show less acceleration for faulted cylinders, but also a lesser slope for trailing healthy cylinders. In Fig. 13, for instance, cylinder No. 7 is faulted, while the following cylinder No. 3 has no fault. The engine speed decreases during the firing period of cylinder No. 7, it is approximately constant during the firing of cylinder No. 3, and recovers fully at the next firing cylinder, No. 4. Trailing healthy cylinders generally exhibit less slope than the unfaulted reference. The cylinder fault criterion can thus be stated as follows: A cylinder is identified as potentially faulty if the slope of its acceleration speed waveform is less than the reference acceleration slope of the healthy engine. A healthy cylinder firing after a faulty one shows less slope than the reference, and is identified as faulty only if the trailing cylinder's slope is equal to or less than the slope of the faulty cylinder.

12 Inlet Manifold Noise Levels

Valve leakage remains one of the most commons faults for engine malfunctions and only slight imperfections of the valve seats lead to significant performance degradation of the engine. If left undetected, major damages to the engine can result. The conventional method of testing for valve leakage is not only laborious but time consuming. An alternate in-situ means of detecting valve leakage is by measuring the noise levels in the inlet manifolds. Leakages at the valve seat generate high-velocity flows and this causes the ambient sound pressure level in the far field of the leakage but still within the manifold to increase (Fig. 12). Source location may then be carried out using signal correlation of two microphones located some distance apart from each other.

13 Diagnostic Strategies

Diagnosis is a step-by-step process that attempts to ascertain the internal characteristics of a physical system. What makes diagnosis difficult is the large amount of knowledge and experience it requires. First, it requires knowledge of equipment and how it operates normally. Second, it requires the gathering of information about failed equipment and their fault symptoms. Third, it requires knowledge of the type of equipment information it is necessary to gather that is relevant to the fault. Fourth, it requires an ability to use the knowledge about the equipment and the information gathered to explain how the fault could have occurred. Fifth, it requires the ability to form a hypothesis

and perform some tasks to provide further information that either confirms or refutes the hypothesis. The process of gathering information and formulating and testing hypotheses may need to be done several times if the hypotheses formulated turn out negative. Only at the end of this process, when a positive diagnosis is reached, can the diagnostician repair the fault or replace the malfunctioning part.

The goal of any diagnostic expert system is to characterize the internal status of a system using physical evidence and behavioral symptoms together with intuitive reasoning. This objective is typically implemented by:

   (*a*) classification involving the selection of one of several faults, or

   (*b*) localization requiring a form of constraint propagation narrowing the diagnosis to a single primitive component. These objectives are fulfilled through the development of a diagnostic expert system whose performance is determined by several factors.

Of primary importance in determining the performance of a diagnostic expert system is understanding actually what knowledge is to be used and how that knowledge should be formalized, represented, and integrated. Many cases of equipment diagnosis have been successfully demonstrated through the development of first-generation systems, which use only the shallow or heuristic knowledge of human expert in the form of production rules [5]. The first generation of expert systems for hardware diagnosis was based primarily on the largely empirically derived knowledge of the human expert. The manual diagnostic system in CAMODE is primarily based on this type of knowledge. The automated system of CAMODE uses deep reasoning, relying on explicit fault-symptom relationships that are characterized by the signals generated by the engine components. Heuristic reasoning is used together with qualitative physics governing the operation of the engine components to establish the operational state of the engine.

The system generally uses all of the associated source signals to diagnose a particular fault. This ensures a positive identification of the root cause for the malfunction. However, where all the associated signals cannot be accessed, the system relies upon "diagnosis by a process of elimination" for fault diagnosis. Typically, this may be the case for diagnosing partial power loss due to a slight leak at one of the valves. Very slight defects causing a valve to leak might not be sufficient to alter the vibration signal from that valve to change appreciably; therefore, the vibration signal would not be a good indicator. The faulty valve can still be diagnosed by a process of elimination where all the other associated signals, that is, compression event, blowby past the piston rings, and fuel injection are found to be within the acceptable range. Then from this information
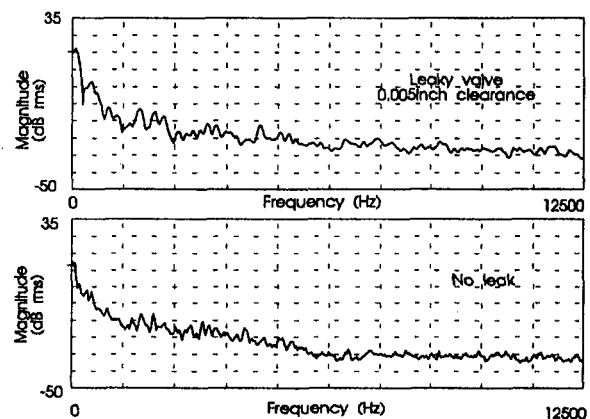

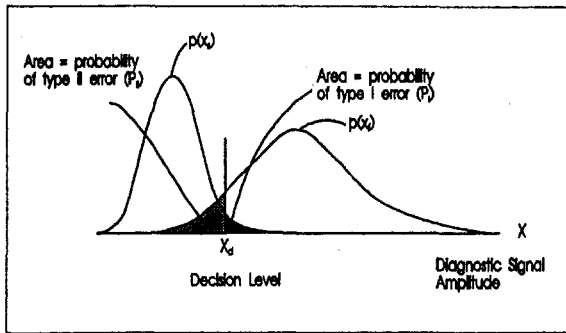Fig. 14 Inlet manifold noise level for a leaky valve

Fig. 15 Type I and Type II errors

it can be concluded that the malfunction is due to a valve leakage since no other component can be linked to this problem. Another example of this method of diagnosis is for worn valve mechanisms. Normally, to diagnose this problem, disassembly and measurement of the mechanisms would be required. Application of this process would conclude this diagnosis by eliminating all the other candidates for the cause of the malfunction.

14 Decision Analysis and Classification Systems

Diagnosis of faults also involves decision analysis and classification [6] of faults. Decision analysis and classification systems is a major component of a diagnostic system and is in-built into the knowledge base of CAMODE. Machinery operating variables are usually not sufficiently well defined when the machine is operating near the "normal-failure" margin, and therefore there is always a likelihood of classifying a normal machine as having failed. The assignment of the engine to one category or the other, that is, normal or failure mode, is weighted not only by the likelihood of its being in that category based on past statistics, but also by the cost of possible errors termed Type I or Type II. A Type I error occurs if a system is classified as having failed when it has not. In this case, an unnecessary cost is incurred for prematurely repairing the engine. Type II error occurs when a system is classified as normal when it has in fact failed. In this case, the possibility of unwarranted expenses can be faced if the system breaks down and causes other damages to the engine systems.

Fault decision system in CAMODE are multidimensional; that is, measurements on several associated signals on the malfunctioning component are available to determine its state. To illustrate decision analysis, however, a one-dimensional case is considered in which only a single metric x, a "diagnostic signal," determines the fault condition. This signal can be viewed to be the amplitude of a piston slap impact event. An engine without a fault will produce a distribution of metric $p(x/s)$, shown in Fig. 15. When the engine is in a faulty condition, the metric changes, and the probability distribution for the metric is $p(x/f)$. The basic problem now is to select a decision level x_d so that when the metric exceeds this value, a faulty condition

is announced, but when it is less than x_d, a safe condition is announced. It is unfortunate however that no matter what the decision level is set at, wrong decisions will be made. The area of $p(x/s)$ in the region $x > x_d$ defines the probability of a Type I error P_I. The area of $p(x/f)$ in the region $x < x_d$ defines the probability of a Type II error P_{II}. The cost of errors is most important and decisions in CAMODE are based upon the cost of any consequential expenses due to breakdown failure resulting in downtime and labor and materials costs. It would have to be appreciated, however, that the selecting and setting of the decision levels may not be absolute across a range of engines even in the same organization, but will vary from machine to machine depending on its operational environment and conditions. The decision levels would differ for different organizations as a result of different economic and other policies. The selection of the decision levels is generally a long and tedious process, which requires enormous amounts of data that also have to be analyzed to extract statistical qualities that are usually required for such exercises.

15 Conclusions

An automated diagnostic system for diesel engines using engine-mounted sensors, which pinpoints the explicit fault using the expert system criterion, is suggested and is being successfully synthesized. The system is based on the manual diagnostic system, CAMODE, which has been developed at the University of Adelaide, and aims to minimize the use of intrusive sensors, and attempts to keep implementation costs to a level that would make the system a viable option for all levels of industry. The system is implemented on an IBM personal computer and is configured to operate in a multilevel fashion so that it can be used either to diagnose malfunctioning engine subsystems, or to diagnose the complete engine, or to gather information from the engine for condition monitoring purposes.

The automated diagnostic system is being developed around the Caterpillar 3208T marine engine, and with slight modification is adaptable to other engines. The system makes extensive use of computer graphics to communicate with the end-user, thus maximizing ease of use.

References

1 Autar, R. K., Hansen, C. H., Pickles, J. M., "Computer Aided Maintenance of Diesel Engine by Use of an Expert System," presented at MECH '91 International Mechanical Engineering Congress and Exhibition—Conference 6: Maintenance Engineering, Emerging Technologies and a New Professionalism, Sydney, July 8–12, 1991; the Institution of Engineers, Australia Preprints of papers, pp. 14–20 (National Conference Publication No. 91/12).

2 Widrow, B., Glover, R., McCool, J., Kaunitz, J., Williams, C., Hearn, R., Zeidler, J., Dong, E., Goodlin, R., "Adaptive Noise Cancelling: Principles and Applications," Proceedings of the IEEE, Vol. 63, No. 12, Dec. 1975.

3 Seth, B. B., "Oil Pressure Signatures for Engine Lubrication System Monitoring," Engine Testing, SP-582, International Off-Highway & Powerplant Congress & Exposition, Milwaukee, WI, Sept. 10–13, 1984, SAE Publications.

4 Mauer, G. F., and Watts, R. J., "A Method for Cylinder Specific Engine Fault Diagnostics," Proceedings of the 1st International Machinery Monitoring & Diagnostics Conference, Las Vegas, NV, Sept. 11–14, 1989.

5 Gilmore, J. F., and Gingher, K., "A Survey of Diagnostic Expert System," presented at SPIE Applications of Artificial Intelligence V, Orlando, FL, 1987.

6 Lyon, R. H., Machinery Noise and Diagnostics, Butterworths, 1987.

R. E. Olsen

H. K. Newhall

Oronite Technology Group,
Chevron Chemical Company,
Richmond, CA 99999

G. A. Eberhard

Oronite European Technical Center,
Rotterdam, The Netherlands

Automotive Diesel Fuel Emissions Durability Trends

Regional mandates for reduced exhaust emissions, sustainable over the useful lives of vehicles or equipment, are influencing diesel fuel compositions and engine designs. Laboratory and real-world examples are provided to illustrate that both fuel composition and engine design can impact injector deposit formation and injector spray-hole corrosion rates, with associated potentials for deterioration of emissions compliance. Potential impacts of poor lubricity fuels are also discussed. A field test in California of a deposit control additive in trucks with Cummins L10 engines is detailed, including measurements of transient cycle emissions performance using conventional and reformulated fuels.

Introduction

This paper is organized into three major sections, beginning with general discussion of regional trends for emissions regulations and fuel lubricity. Then, becoming more specific, fuel injector deposits, spray hole corrosion, and engine test methods are examined. The final, and arguably most important section, provides a comprehensive summary of a fourteen truck field test designed to quantify the effects of clean and deposited fuel injectors on emissions and performance.

Throughout the paper, performance examples are provided for a commercially available multifunctional additive. Except where noted, the formulations all contained a constant level of the deposit control dispersant component.

Regional Trends

Differences of crude supply, refining infrastructure, regulatory requirements, and government tax and price control policies have created significant differences in automotive diesel fuel compositions within and among regions. Inconsistencies in diesel fuel composition may stress the engine makers' ability to optimize performance, as evidenced by the Engine Manufacturers Association's (EMA) recent proposals to ASTM regarding "premium" diesel specifications [1]. The EMA proposals are reproduced in the appendix as Table 5, and include recommended requirements for a range of fuel properties, including lubricity and injector detergency. The historical paradigm of the fuel tolerant diesel engine seems to be changing, as attempts to comply with strict emissions requirements continue to reveal performance sensitivities to fuel composition.

There are many criteria for performance and properties of automotive diesel fuel, some of which are listed in Table 1. This paper will focus on three areas considered to have direct implications regarding emissions durability—lubricity, injector deposits, and spray-hole corrosion. In addition, emissions data are presented that show statistically firm benefits for reformulated high cetane fuel.

Fuel interactions with crankcase lubrication are well documented. We refer to the work of McGeehan [2] and others, who have shown that fuel sulfur levels, end points, and aromatics levels can have substantial and complex effects on base depletion, soot loading, and ring-zone deposits.

Emissions Regulations. The effects of fuel system deposits on emissions and performance often arise unexpectedly. This was exemplified by the US gasoline fuel injector fouling crisis

of 1985 [3], when deposits in new design electronic injectors suddenly appeared during consumer service. To account for degradation of emissions performance as engines age, US emissions standards [4] apply deterioration factors that create, in effect, even more stringent requirements for performance when new. To the extent that deterioration factors required by these regulations capture real-world deterioration mechanisms, the estimates should have validity.

Fuel system deposit formation processes are complex and usually best estimated from experiment rather than theory. For example, the gasoline-injected vehicles of 1985 all passed their requisite 80,000 km on-road emission durability tests, yet the failure mode of deposit formation during engine-off hot-soak was not discovered until they were in consumer hands. For diesels, we anticipate similar uncertainties about factors influencing emissions deterioration, particularly over the extended 8-year or 464,000-km compliance period.

Vehicle inspection and maintenance programs have been another approach toward control of emissions deterioration. In California, for example, regulations are presently in place for heavy-duty vehicles that mandate periodic smoke tests, and authorize random road-side inspections [5]. In addition, consumers may identify suspected high emitters, who then may be required to demonstrate compliance. For these rules, smoke levels are determined using the snap-idle procedure, where opacity is recorded during rapid accelerations from idle to maximum governed rpm with the transmission disengaged [6, 7]. This method is simple, but its validity has been challenged [8]. That is a controversial topic, but regardless of outcome, we see this experience as a harbinger of requirements for improved emissions durability on a global scale.

Lubricity. Within the organizations of ASTM, SAE, ISO, and CEC, cooperative efforts are under way to develop better knowledge of fuel lubricity characteristics and fuel system equipment lubricity requirements. Specific cases of injector or pump failures, particularly in Sweden and Canada, have been conclusively linked to insufficient fuel lubricity, yet the market specific incidence rates have proven difficult to quantify. There is much disagreement about the magnitude of the problem, possibly corresponding to true differences of magnitude among specific applications, regions, or duty cycles. Nevertheless, we expect that premature wear of certain fuel-lubricated components may contribute to deterioration of exhaust emissions, and as a result the issue of fuel lubricity will face growing scrutiny as regional emission regulations mandate fuel refining changes.

While no consensus has been reached on lubricity test methods or performance requirements, many feel that the standard BOCLE test (ASTM D 5001, Ball On Cylinder Lubricity Evaluator) has proven inadequate to represent lubricity modes in

Table 1 Diesel fuel performance criteria

Aromatics	Odor
Cetane	Stability/Oxidation
Cold Flow	Sulfur
Crankcase Oil Interactions	Viscosity
Energy Content	Volatility
Foaming	Water Tolerance
Injector Deposits	
Injector Spray Hole Corrosion	
Lubricity	

Table 2 Scuffing BOCLE performance recommendations

Organization	Recommended Minimum Load, g
Stanadyne	3500 g
EMA	3300 g
CA Governor's Task Force	3000 g
Chevron Products Company	
Production Target	2600 g
API	2200 g

Fig. 1 Cummins L10 unit injector design

diesel fuel systems. The US Army modified Scuffing BOCLE procedure, as developed by Lacey [9], is rapidly gaining acceptance in the U.S., and may become the basis for new lubricity performance requirements, as shown in Table 2 [10, 11].

The Scuffing BOCLE test method has been shown by Nikanjam [12] to be sensitive to both fuel viscosity and to the presence of surface active polar materials. These polar materials can be naturally occurring elements of the crude, or additives such as the low molecular weight carboxylic acid "lubricity component" shown in Table 3. Refinery hydrogen processing, used to reduce fuel sulfur and aromatics, also can remove some of the polar materials that help provide boundary-layer lubricity. The performance of a finished fuel in the Scuffing BOCLE test appears to show a complex dependence on the source of crude oil, extent of hydrogenation, viscosity, and additives.

Fuel Injector Deposits

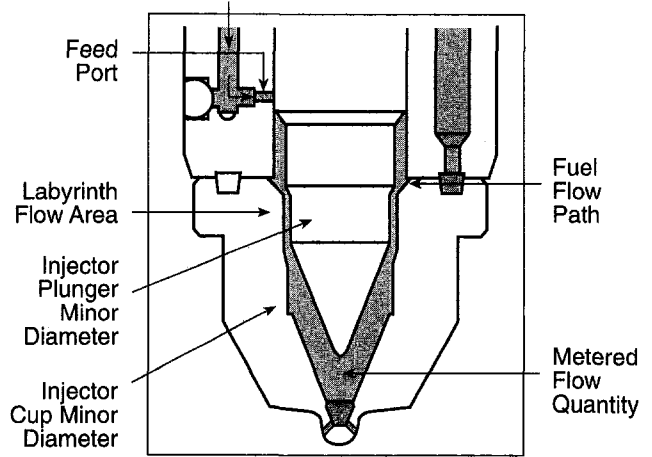**Cummins L10 Injector Depositing Test.**   During 1991, in a fashion reminiscent of BMW of North America's

vehicle testing campaign for gasoline intake valve deposit control [13], Cummins Engine Company offered to the petroleum industry an engine test method and "superior" performance standard for diesel fuel injector deposit control [14]. This standard was developed in response to consumer complaints of power loss caused by fuel injector deposits. The "Cummins L10 Injector Depositing Test" features PT type unit injectors of open-cup design (Fig. 1) and is the only standardized direct injection deposit test available anywhere. A complete list of the Cummins "superior" fuel criteria is provided in the appendix as Table 6.

Developed by Gallant and others over a period of several years, the 125-h laboratory engine procedure is designed to reproduce a real-world deposit problem [15]. Deposit buildup, principally on the plunger surfaces near the labyrinth flow area, reduces the flow of fuel to fill the cup, and, thereby, restricts power output. Deposits in the feed port have similar effects, as does leakage caused by wear of the plunger and bore surfaces. All of these effects will vary on an individual cylinder basis.

Availability of the L10 Injector Depositing Test helped accelerate development of improved deposit control additive systems for diesel fuel. It has proven to be a severe test, requiring substantially stronger dispersant additives and/or higher dosages than were commonly used at that time.

Interestingly, the L10 test is sensitive to base fuel composition, and contrary to the expectations of many, the new low-sulfur fuels we've tested show similar, if not greater, deposit

Table 3   US Army modified scuffing BOCLE response

Minimum Load (Single Determinations)

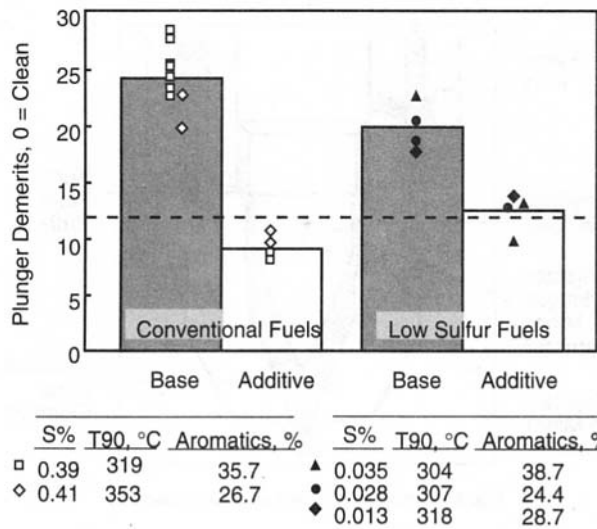|	Retail Sample, 1Q94 U.S. Mid-Continent	Winterized Blend With 20% Low Sulfur Jet	
		Jet	Blend
Sulfur, ppm 240		150	
Nitrogen, ppm 60		30	
Vis. at 40°C, cSt 2.0			1.85
	Minimum Load (Single Determinations)		
Base	2300 g	2100 g	
Multi-Functional Additive	2500 g	2600 g	
Multi-Functional Additive Plus 35 mg/kg Lubricity Component	3500 g	2900 g	

Fig. 2 Comparison of conventional and low-sulfur fuels (L10 test, tandem engines)

Deposit Area

Fig. 4 Throttling pintle nozzle

severity than their conventional predecessors. The pooled standard deviation for the 18 repeat observations included in Fig. 2 was 1.87 demerits.

Competitive business pressures to qualify the lowest cost additive systems have revealed some weaknesses of the L10 Injector Depositing Test procedure and protocol. Presently, the test is offered by three contract laboratories. One uses direct-coupled tandem engines to follow the 15 seconds closed-throttle, 15 seconds loaded operating cycle in alternating sequence. The other two use single engines connected with dynamometers. "As shown in Fig. 3, the tandem engine installation appears, in this limited dataset, to be about twice as severe in terms of additive dosage requirement. Much of this variability between labs has been shown to relate to differences in the visual deposit rating process. Recently, the ASTM L10 Surveillance Panel has completed several deposit rating workshops that have enabled substantive improvements of lab to lab reproducibility versus what we encountered in Fig. 3. Following the Surveillance Panel round robin, Cummins Engine Company announced that any of the three labs can be used to qualify fuels for Superior Performance [16].

Test Protocols. The inherent variability of engine testing needs to be considered when tests such as the L10 are used for qualification of fuels and fuel additives. For example, in the case of crankcase lubricants, the Chemical Manufacturers Association (CMA)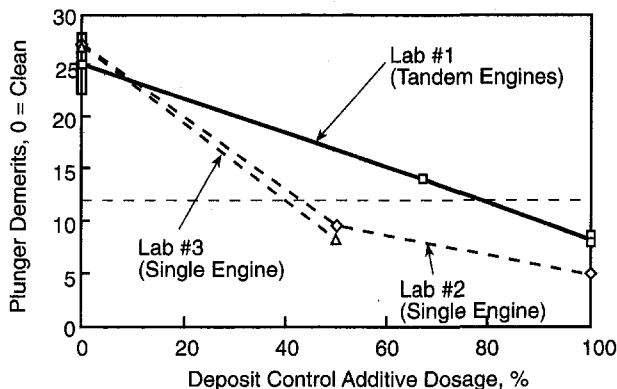 helped lead industry efforts to establ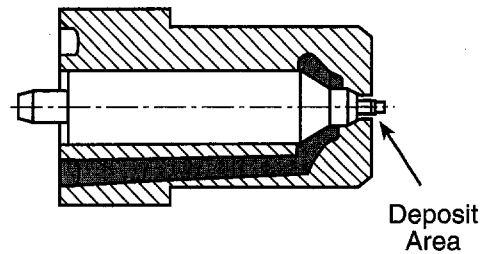ish formal mechanisms to ensure that engine test data are meaningful indicators of lubricant performance, and not "bounce-through" passes or otherwise statistically unrepresentative or procedurally invalid results [17]. The CMA protocol for lubes requires registration of all engine test attempts. This is coupled with API rules for acceptability of "read-across" of similar formulations across various oil grades.

For fuels testing, no similar "code of practice" or equivalent standards for performance qualifications have been established. To help fill this void, Cummins Engine Company suggested specific criteria for the L10 Injector Depositing Test [13]. For each candidate fuel, they specified a maximum of three qualification attempts. A single passing result was sufficient if obtained on the first attempt, or if attempted twice then the average of results must qualify. For three attempts, two of the runs must qualify.

In commercial practice, however, the L10 Injector Depositing Test is often used to qualify additive packages rather than finished fuels. Without limitation to a specific batch of test fuel, the criterion for a maximum of three qualification attempts is difficult to apply, and valid comparisons of individual test results becomes difficult or impossible. In these cases, alternative constraints are needed. In our view, requirements for replicate results, with defined expiration dates, would encourage development of more meaningful performance data. Regardless how the protocol is handled, the importance of fuel composition to deposition tendency and additive effectiveness should not be underestimated.

Indirect Injection Engines. In Europe, the automotive, petroleum, and chemical industries are working together toward development of standardized fuel system deposit control tests, and one result is the Peugeot XUD9 light-duty injector fouling test [18]. Efforts to standardize this 6-h procedure are under way now, including round-robin comparisons among independent laboratories. The Peugeot XUD9 test is intended to evaluate deposit forming tendencies in throttling pintle nozzles (Fig. 4) designed for indirect injection engines typical of European design practice.

With throttling pintle nozzles, carbonaceous deposits invariably form on the pintle tip and interior spray-hole surfaces, restricting the initial orifice size and injection rate. The quantity of deposit can be measured using the ISO 4010 airflow procedure [19], where a sonic pressure differential is maintained so that the air flow rate is directly proportional to orifice cross-sectional area. Typical ISO 4010 flow curves for the Peugeot XUD9 are shown on expanded log/log scales in Fig. 5. Flow values at 0.1-mm pintle lift are normally used to characterize the initial injection rate, or pilot flow. In the case shown, pilot flow was reduced to less than 10 percent of the new nozzle level. Manufacturers recognize that deposits are inevitable and calibrate the new, clean nozzle flow higher than desired to compensate for an anticipated level of deposit buildup. Optimization of pilot flow is difficult, as deposits vary with fuel and duty cycle, and the desired level is a function of fuel ignition qualities [20]. When pilot flow is restricted, cold engine combustion noise and smoke emissions can suffer [21].
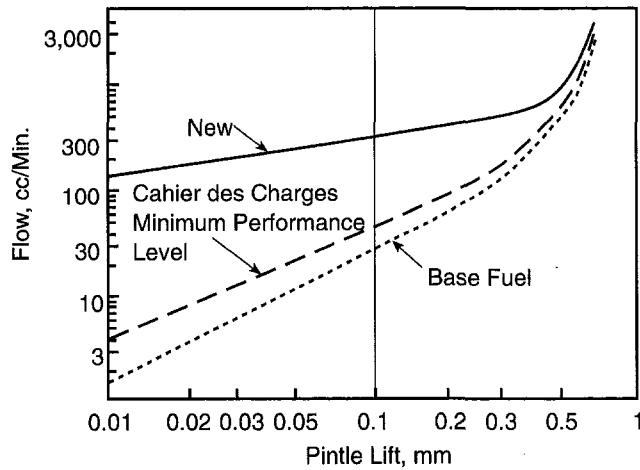

Fig. 3 Comparison of L10 injector depositing test labs

Fig. 5 Peugeot XUD9 throttling pintle nozzle deposit restriction

Fig. 7 Comparison of DI multihole and IDI nozzle flow characteristics

To encourage improvements in diesel fuel quality, Peugeot and Renault developed the "Cahier des Charges" requirements. This list, reproduced in the appendix as Table 7, spans a range of criteria including cetane, distillation, and sulfur. The requirement for diesel fuel detergency is to maintain Peugeot XUD9 pilot flow at not less than 15 percent of the new nozzle level at 0.1 mm lift. While this represents a 50 percent improvement over the severe base fuel result shown in Fig. 5, it still leaves an 85 percent restricted nozzle and plenty of room for even better deposit control performance. Based on our product surveys, dispersant additive dosages typically required for Cahier des Charges qualification are about half that needed for "Superior" performance in the Cummins L10 Injector Depositing Test (tandem-engine version).

Direct Injection Engines. Worldwide, the most common nozzle type for direct injection engines is the multihole pintle design illustrated in Fig. 6. The spray holes are carefully sized and oriented to optimize spray pattern and fuel/air mixing. The primary functional result of deposits is to alter spray pattern and localized combustion stoichiometry.

Flow curves for direct injection multihole nozzles are unlike those previously described for indirect injection engines, as the principal roles of the pintle are to prevent fuel leakage once injection is complete and seal the cup from combustion gases. For multihole nozzles, the ISO 4010 air flow test provides a measure of total orifice area, but unfortunately cannot characterize individual spray holes or the spray pattern (Fig. 7).

An extreme case of multihole injector fouling was observed in India by Pundir et al. [22], who reported worst cylinder flow restrictions as large as 22 percent. For a four-hole nozzle, that would be equivalent to virtually complete plugging of one spray hole, and the magnitude of functional disruptions, while not measured in that experiment, must have been large. Relatively little information linking multihole deposits with functional upsets presently resides in the public domain, but industry activity in this area appears to be accelerating [23] (Fig. 8).
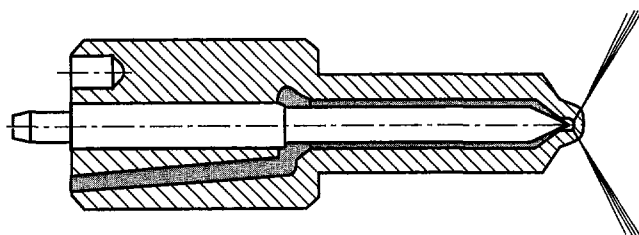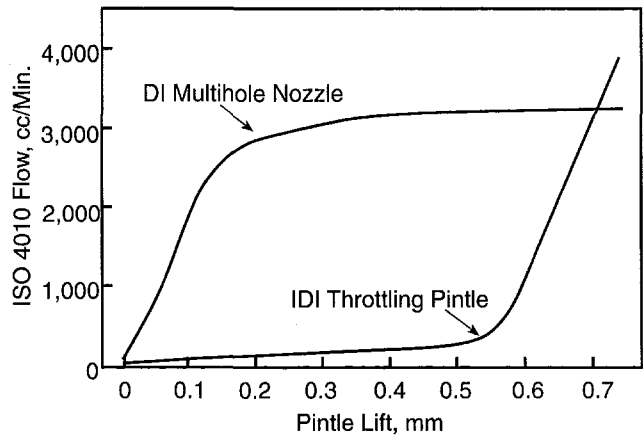

Fig. 8 Multihole nozzles sampled from bus fleet in India, results for most restricted injector (from [21])

Fuel Injector Spray-Hole Corrosion

As an element of their "superior" fuel performance criteria, Cummins also included recommendations for spray-hole corrosion performance. Their basis is a 200-h laboratory engine test method using the Cummins N14 engine with Celect unit injectors, nominal 0.4 percent sulfur fuel, and low-temperature idle operating conditions [24]. Two independent laboratories in the U.S. now offer this engine test. For superior qualification, the maximum injector flow increase is 0.3 percent.

The primary mechanism of spray-hole corrosion is believed to relate to condensation of sulfuric acid during cold operation and is further believed to be metallurgy specific. N14 lab engine results for a multifunctional additive are shown in Fig. 9, along with data from a 20,000-km field test using a popular multihole injector design.

Emissions Durability Field Test

Commercial Fleet. Beginning in late 1992 and continuing through August 1993, a new deposit control additive was field tested in California using 14 trucks equipped with Cummins L10 engines (300 HP version, 1989 and 1990 calibrations). The injectors were of the same step plunger design as used in the L10 Injector Depositing Test.

Seven trucks consumed nonadditized fuel purchased according to the fleet's traditional bid practice, and seven ran the same base fuel blended with additive. Test length ranged from

Fig. 6 Direct-injection multihole nozzle

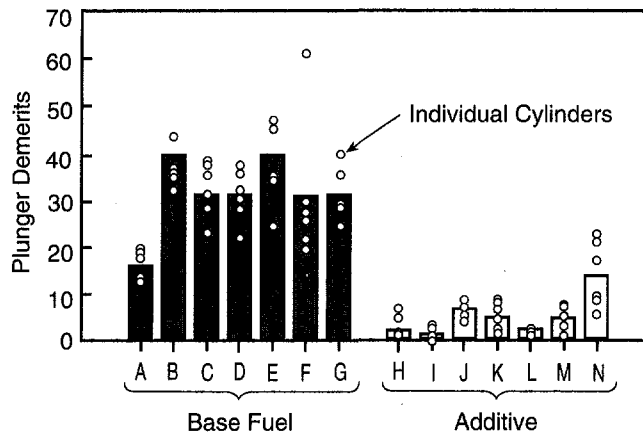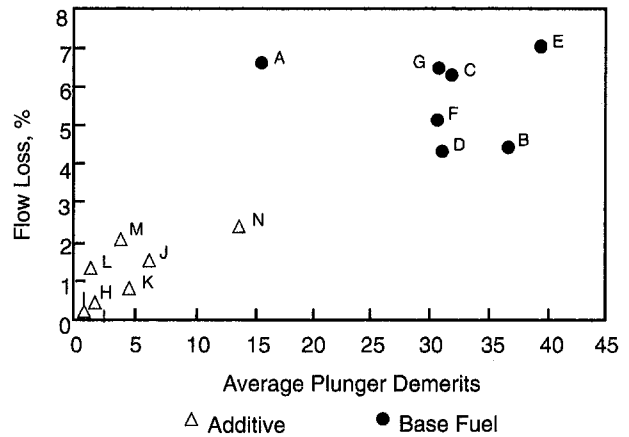Fig. 10   L10 field test plunger demerits ratings

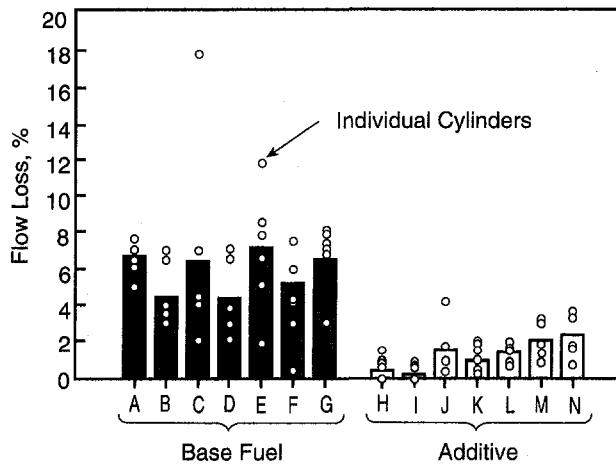

Fig. 12   Rating and flow correlation

Fig. 11   L10 field test injector flow losses

48,693 km to 135,350 km, with an average of 95,459 km. The primary objective was to assess the real-world performance of a multifunctional additive formulation, which satisfied all lab test requirements for Cummins Superior Fuel Performance. At conclusion, the field test injectors were installed in a carefully controlled laboratory dynamometer stand for emissions tests.

Injector Deposits. Final injector plunger demerit ratings for each of the 14 trucks are summarized in Fig. 10 and hydraulic flow test data in Fig. 11. Considerable variation was observed among individual cylinders.
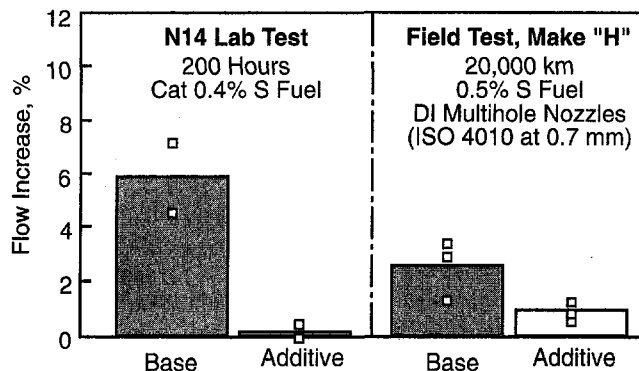

Fig. 9   Spray-hole corrosion

The field test plunger demerit ratings, determined at an independent laboratory, are in good general agreement with results of the 125-h L10 lab engine test. The field test injector flow data show much greater differentiation between additive and base than normally seen in the lab engine, which suffers from unrealistically high levels of plunger to barrel wear caused by the severe operating cycle. One injector, on base fuel, showed evidence of feed-port plugging, with greater than 17 percent flow loss.

When averaged over all cylinders, the plunger demerit ratings show an encouraging correlation versus flow loss ($R2 = 0.72$). However, when individual cylinder data were analyzed, this correlation disappeared amidst the noise ($R2 = 0.40$), and a substantially larger sample size would be needed to resolve any statistical relationship. This may be explained by relatively large effects of randomly distributed plunger and barrel wear (Fig. 12).

Emissions Experiment.   To evaluate the functional benefits of injector deposit control, we installed the field test injectors in a laboratory engine. This enabled more precise control of test conditions than would be possible with vehicles, and more importantly, separated injector durability effects from general power train and chassis wear and tear. Injectors were always maintained in their original set groupings and cylinder assignments. One set of injectors (Truck H, additive) was inadvertently damaged during inspection, leaving 13 injector sets available for emissions testing, 7 sets base fuel, and 6 sets additive.

The design of the emissions experiment can be viewed as consisting of three distinct phases. The original test design, Phase 1, showed higher than expected variance among injector sets. As a result, our sample size of 13 injector sets was too small to resolve the benefits of injector cleanliness with statistical confidence. To reduce the variance associated with mechanical differences among injectors, we decided to compare each set with itself by repeating the tests after manual removal of plunger deposits. This cleanup work became Phases 2 and 3 of the experiment as outlined below:

Phase 1—Compare base versus additive injector sets (13 total), using two fuels to maximize applicability of results. Measurements included:

- Rated torque.
- Transient cycle emissions (PM, NO_x, HC, and CO).
- Emissions under steady 90 km/h road-load conditions to enable comparisons not confounded by torque level differences among sets.
- Three-mode exhaust smoke according to Federal procedure.

Phase 2—Isolate the effect of plunger deposits from other differences among the injector sets by comparing emissions

Table 4 Emissions test fuels

	Conventional Fuel	Reformulated Fuel
Cetane Number	41	58
Gravity, API	31.3	38.0
Sulfur, ppm	4200	220
Nitrogen, ppm	186	68*
Aromatics (HPLC), %	38.5	15.3
T90, °C	330	315
Vis at 40°C	3.27	2.40
Heat of Combustion, BTU/gal., gross	140,700	139,000

*Before Addition of 3000 mg/kg Alkyl Nitrate Cetane Improver

before and after manual cleaning of plungers. This phase included only four injector sets, all from base fuel trucks. The same emissions measurements as in the first phase were performed, except only one fuel was used.

Phase 3—Continuation of Phase 2 to include manual cleanup of the remaining nine injector sets. Different from Phase 2 by facility changes at the contract engine laboratory, which interrupted the expanded experiment, and an unscheduled engine rebuild necessitated by valve guide seal failures. Initial results of Phase 3 showed a statistically significant severity shift which distorted comparisons with phases 1 and 2. When this was discovered, we stopped the test.

The federal transient cycle is defined according to percentages of an engine's rated torque and speed [4]. In this experiment, rated torque was expected to vary among injector sets according to their plunger deposit levels, so a distinct transient cycle was defined for each of the 13 injector sets using the conventional fuel.

Test Fuels. To maximize applicability of the emissions work, we selected one "conventional" fuel and another high cetane "reformulated" fuel as shown in Table 4. The reformulated fuel is substantially similar to a CARB-certified alternative fuel [25].

Statistical Analysis. PHASE 1—The results were analyzed to compare the two fuel groups (conventional and reformulated), and to compare the two injector set groups (base fuel and additive). Of the 13 injector sets included in this experiment, seven received base fuel and six received additive. The differences observed between injector set groups with conventional fuel were not different from those with reformulated fuel, so the average was used. Results are summarized in the appendix, Table 8.

PHASE 2—Percent changes in each emission variable from before cleaning to after cleaning were analyzed to determine the effect of cleaning plungers using the paired t-test. For each of the four injector sets, there were two determinations before cleaning, and these were averaged for comparison with the single values determined after cleaning. Results are summarized in the appendix, Table 9.

Phase 1 Results. As expected, the additive injector sets gave, on average, 1.6 percent more torque and power than the base fuel sets, and these differences were statistically significant at the 0.05 level. It is important to note that these injectors were of the improved step-plunger design. Even greater power loss would be expected with the original design injectors.

Comparing the conventional and reformulated fuels, averaged over all 13 injector sets, the reformulated fuel gave 1.0 percent less power than the conventional fuel, and again this difference was statistically significant. This power difference agrees well with the 1.2 percent difference in volumetric energy density.

For emissions data, when comparing the base fuel and additive injector populations, the results from Phase 1 of the experiment were significant only for HC. Variability among individual injector sets was high and obscured many differences. Following normal fleet practice, the field test used remanufactured RECON injectors, and this choice may have contributed to the high variability. Directionally, however, particulates and CO were lower for the additive injectors, and NO_x was higher.

High variability among injector sets within the base and additive populations can be readily seen in Fig. 13, where transient cycle composite particulate emissions are plotted for both test fuels. The 24 percent difference in average composite particulates between conventional and reformulated fuels was statistically significant at the 0.001 level.

To compensate for engine variability, manufacturers establish emissions certification targets, which are considerably lower than the regulated levels. This is apparent in our results, which show composite particulates for conventional fuel averaging 26 percent less than the 1988 Federal standard of 0.6 g/hp-h. Even the worst of the injector sets was in compliance at 0.51 g/hp-h.

As regulations tighten, however, we expect increased pressure on engine and engine component manufacturers to reduce variability. Figure 14 compares the magnitude of benefit we observed for reformulated fuel versus the magnitude of variability among injector sets. Variability associated with the experimental process, including base engine, sampling, instrument drift, and injector set changeouts, was estimated based on 11 repeat tests of five different injector sets. The process variability was about half as large as the variability observed among field test injectors.
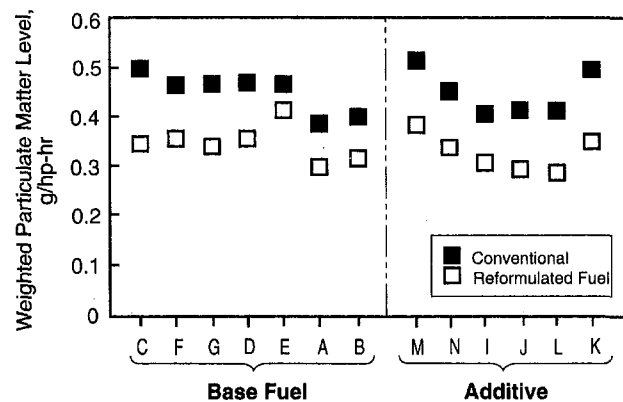
1988 Standard Is 0.6 g/bhp-hr

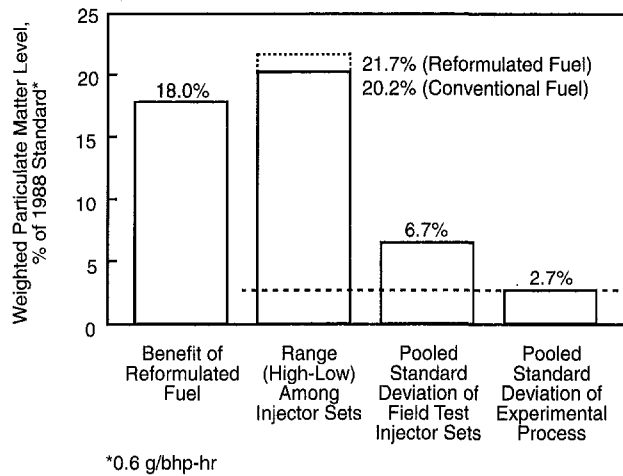**Fig. 13 Transient particulates, Phase 1**

Fig. 14   Variability among injector sets

*0.6 g/bhp-hr

Fig. 15   Differences between reformulated and conventional fuels, transient cycle, 13 injector sets

Fig. 16   Benefits of cleaned plungers, transient cycle, four injector sets

These estimates of variability highlight the difficulties associated with emissions durability testing. For an experiment such as our phase 1 design to succeed (i.e., provide significance for between-group differences in composite particulates at the 0.05 level), we now estimate that a fleet of 26 trucks would have been needed, 13 per fuel. This estimate is derived from studentized range analysis of beta error at the 0.2 level, using the standard deviation observed in phase 1 (0.040) and the magnitude of effect observed in phase 2 (0.046). For the more conventional type of durability experiment that compares the performance of vehicle fleets, there are more sources of variation than in our experiment, so an even larger fleet size would be needed.

Several of the key differences between conventional and reformulated fuels are plotted on a percentage basis in Fig. 15. In this star diagram, the center point (origin) represents a 10 percent detriment, and all points outside of the dashed zero circle represent advantages for the reformulated fuel. HC, NO$_x$, and particulate all showed benefits that were statistically significant, as summarized in the appendix. Both Smokes A and B were poorer statistically, but it must be noted that the particular engine tested was found to be out of compliance with the 1988 standards for smoke by factor of about 25 percent. More complete data are summarized in the appendix.

Phase 2 Results. During Phase 2, we evaluated cleanup of four base fuel injector sets. The cleanup was performed manually, by delicately soaking the removed plungers in a solvent bath. The injector bodies were not disturbed, as we desired to determine if the deposited area used to rank fuel/additive effectiveness in the 125-h Injector Depositing Test would link with emissions performance. Deposits in the spray holes and/ or feed port areas were not disturbed.

As shown in Fig. 16, the data developed during Phase 2 are encouraging, in that substantial differences were observed between deposited and cleaned injectors. Transient particulates were reduced by 10 percent, on average, which compares favorably with the 24 percent difference observed between conventional and reformulated fuels. Smoke A and C were reduced, on average, after plunger cleaning by 11 percent and 6 percent, respectively. NO$_x$ emissions, on the other hand, increased by 5 percent, on average, although presumably this just represents a return to their original new engine level. From the mechanistic standpoint, the data appear consistent with an injection timing shift caused by deposits. Changes in individual cylinder fueling rates may also be important, but measurements of combustion pressures and ignition delays would be needed to understand the root causes of deposit upset with PT injectors.
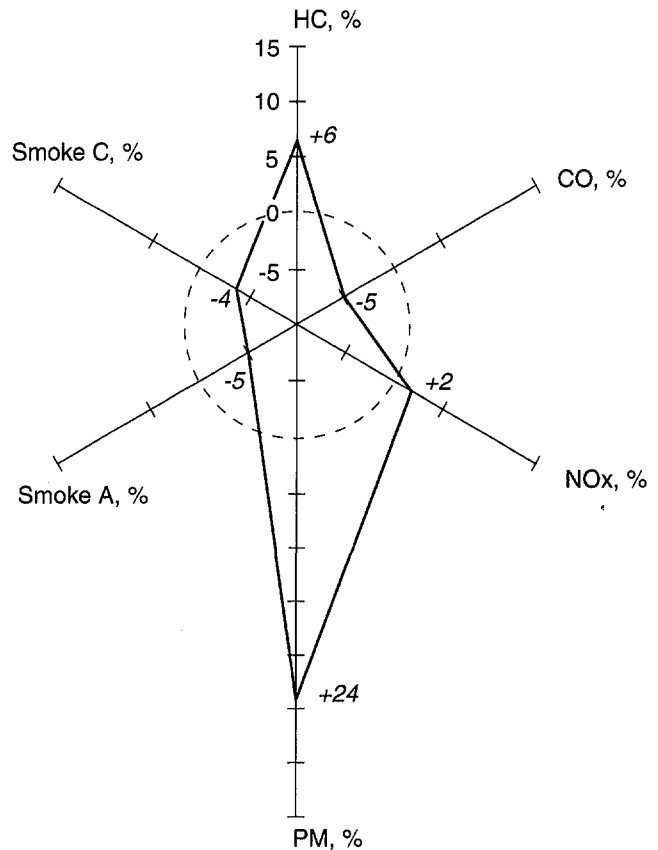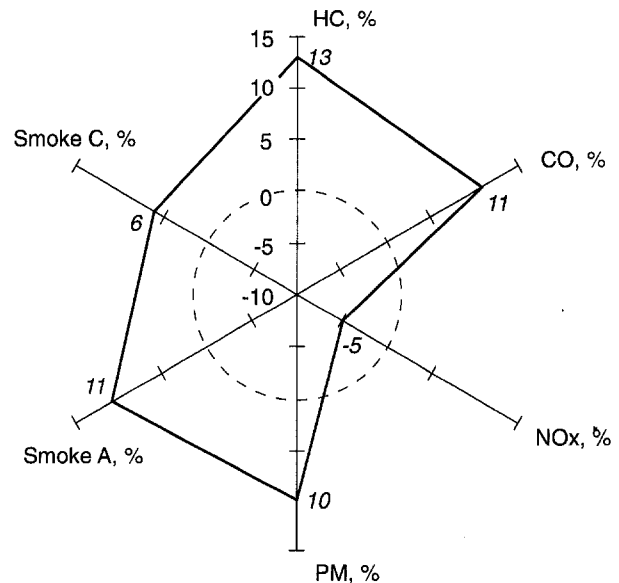
When a paired t-test was applied to the phase 2 data, all of the emission parameters shown in Fig. 16 were significantly different from zero at the 0.10 level. However, the Phase 2 experiment by itself lacks verification that the performance changes were caused by deposit removal, and not simply by the processes of injector disassembly and plunger removal. Therefore, firm conclusions cannot be supported until additional data are developed.

Closure

Growing worldwide emphasis on diesel emissions durability is forecast, with possible new requirements for fuel lubricity, fuel detergency, fuel corrosion protection, and in-use vehicle inspection and maintenance programs. In Thailand and Colombia, regulations are already in place which require diesel fuel deposit control additives, and more nations are expected to follow suit.

Acknowledgments

We would like to recognize contributions from the worldwide Oronite Fuel Additives Team, including Jaime Lopez, Byron Anshus, Ned Johns, Jeff Toman, Ruben Carrillo, Henk Sengers, Gary Parsons, Dave Roche, Eric Burk, and the entire Richmond engine laboratory staff. In addition, consultations with members of Chevron Products Company were greatly appreciated, including in particular Manuch Nikanjam and Bob Farina.

We also wish to acknowledge support from our customers and partners in these field test programs.

References

1   Engine Manufacturers Association proposal for a separate standard for premium diesel fuel, meeting of ASTM Committee D2, Subcommittee E, June 20, 1994.

2   McGeehan, J. A., et al., "Selecting Diesel Crankcase Oils to Use With Low-Sulfur Fuel," SAE Paper No. 932845, 1993.

3   Taniguchi, B. Y., et al., "Injector Deposits—The Tip of Intake System Deposit Problems," SAE Paper No. 861534, 1986.

4   Code of Federal Regulations, Vol. 40, Part 86, 1999.

5   Section 2182 of Title 13, California Code of Regulations, 1999.

6   SAE Procedure J1667 (Draft Version 6.0), 1999.

7   California Assembly Bill No. 584, 1999.

8   CARB Public Hearing 12/10/92.

9   Lacey, P. I., "The US Army Scuffing Load Test," Belvoir Fuels and Lubricants Research Facility, Southwest Research Institute, San Antonio, TX, June 1993.

10   Report of the Diesel Fuel Task Force Prepared for the Governor of California, Feb. 18, 1994 (DCN 93-674-062-01/RCN 674-062-04-00).

11   Chevron Products Company Technical Bulletin FTB-3-1 Dated 4-15-94.

12   Nikanjam, M., and Henderson, P. I., "Lubricity of Low Sulfur Diesel Fuels," SAE Paper No. 932740, 1993.

13   Bitting, W., et al., "Intake Valve Deposits—Fuel Detergency Requirements Revisited," SAE Paper No. 872117, 1987.

14   Cummins Engine Company, Materials Specification No. 60032, 1999.

15   Gallant, T. R., et al., "Cummins L10 Injector Depositing Test to Evaluate Diesel Fuel Quality," SAE Paper No. 912331, 1991.

16   Cusano, C. M., Cummins Engine Co., letter to ASTM Surveillance Panel Members, May 8, 1995.

17   Chemical Manufacturers Association Petroleum Product Approval Code of Practice, Sept. 1992 plus updates, Washington, DC.

18   Draft Procedure for Diesel Engine Injector Nozzle Coking Test, CEC PF-26, Feb. 1992.

19   ISO 4010-1977 (E), International Standard, "Road Vehicles—Calibrating Nozzle, delay pintle type," 1999.

20   Fortnagel, M., et al., "Requirements of Diesel Fuel Quality, Effects of Poor Quality Fuels," API 47th mid-year meeting, 1982.

21   Olsen, R. E., Ingham, M. C., and Parsons, G. M., "A Fuel Additive Concentrate for Removal of Injector Deposits in Light-Duty Diesels," SAE Paper No. 841349, 1984.

22   Pundir, B. P., et al., "Indian Diesel Fuel Quality and Performance," Hydrocarbon Technology, 15 Aug. 1992.

23   Caprotti, R., et al., "Diesel Additive Technology Effects on Injector Hole Erosion/Corrosion, Injector Fouling and Particulate Traps," SAE Paper No. 932739, 1993.

24   Cummins N14 200-Hour Injector Spray Hole Corrosion Test, Engineering Test Services Technical Report ETS-92-063, Charleston, SC, 1999.

25   Nikanjam, M., et al., "Development of the First CARB-Certified California Alternative Diesel Fuel," SAE Paper No. 930728, 1993.

APPENDIX

Table 5   EMA proposed standard for premium diesel fuels

Property	Test Method	No. 1PD	No. 2PD
Flash Point, °C, Min.	D 93	38	52
Water and Sediment, % Max.	D 1796	0.05	0.05
Distillation % Vol. Recovery	D 86		
90%, °C		260 Max.	329 Max.
End Point, °C		288 Max.	357 Max.
Kinematic Vis. 40°C	D 445	1.3-4.1	1.9-4.1
Ash, % Max.	D 482	0.01	0.01
Sulfur, % Max.	D 2622	0.05	0.05
Copper Corrosion, Max. 3h	D 130	No. 3	No. 3
Cetane No., Min.	D 613	50	50
Cetane Index, Min.	D 4737	45	45
Rams Carbon, 10% Residue	D 524	0.15	0.15
API Gravity	D 287	40-44	34-38
Lubricity, Grams, Min.	D 5001 (Modified)	3300	3300
Accel. Stab. mg/L, Max.	D 2274	15	15
Detergency	Cummins Injector Depositing Text	CRC Rating <10 Flow Loss <5%	
Cold Filter Plugging Pt., °C	IP 309	-40	-24

Table 6   Cummins superior fuel criteria

Fuel Property	Test Method	Requirement
Injector Cleanliness	Cummins L-10 Injector Depositing Test	Plunger Rating: ≤10 + 1 Std Injector Flow Loss: ≤5%
Injector Spray Hole Corrosion Control	Cummins Celect Injector Spray Hole Corrosion Test	Flow Increase: ≤0.3%*
Elastomer Comparability	3 Weeks at 71°C +/- 3°C, Elastomers Each in Separate Containers	Meet Physical Property Pass/Fail Criteria*
Fuel Filter Media Compatibility	3 Weeks in Cat 1K + Water, 5 Days/71°C and 2 Days/Ambient (Twice Required Additive Dosage)	Maximum 0.2" Hg Increase in Pressure Drop Relative to New Filter*
Fuel Pump Wear and Corrosion	ASTM D 130 Copper Corrosion, 3 Hours at 100°C	No Increase in Rating, Relative to Base*
	ASTM D 5001 BOCLE	Wear Scar Diameter Not to Exceed Base Result*

*Caterpillar 1K Base Fuel is Required

Physical Properties	Limits	Future Evolution
Density at 15°C NF T 60 101	0.820-0.850 Concession on Maximum Value if Cetane Index >50 and if Cetane Number >51: Maximum Density 0.855	0.820-0.850
Viscosity at 40°C NF T 60 100	2.0-4.5 cSt	-
Distillation % Evaporation at 250°C % Evaporation at 350°C % Evaporation at 370°C NF M 07 002	<60% >85% >95%	-
Sulfur - NF T 60 142	<0.15% Weight	Objective <0.05% at 10/01/95
Composition Aromatics Naphthenics Mass Spectrometry ASTM D 2425-83	<30% <40%	Di + Tri Aromatics Content ≤9.0% (HPLC Method, CEN/TC19/WG18 Method)
Oxidation Stability ASTM D 2274	<1.5 mg/100 mL	-
Rust Preventing Characteristics ASTM D 665-83 Procedure A (Distilled Water)	<5% ("Light" or "Moderate" Rusting)	-
Cetane Number NF M 07 035	>50	-
Cetane Index ASTM D 4737/90	>49	-
Detergency	Detergent Presence Confirmed by Demonstration of Efficiency on Reduction of Injector Deposits, CEC PF 26 Test Procedure With 85% Maximum Flow Reduction at 0.1 mm Needle Lift	-
Foaming	Presence of Additive to be Confirmed by Demonstration of Efficiency. Distributor May Use In-House Method	BNP Method to be Defined
Cold Weather Characteristics CP = Cloud Point NF T 60 105 CFPP = NF M 07 042 PP = Pour Point NF T 60 105	Summer: as EN 590 Specification Winter: From 11/01 to 12/14, and From 3/01 to 3/31: CP ≤-5°C, CFPP - 15°C, PP -18°C From 12/15 to 2/28; CP ≤-8°C, CFPP -20°C, PP -21°C	CEN Method to be Defined
Biological Characteristics	M 07 070 Method "Light" Contamination	-
Total Acid Number NF T 60 112	Max. 0.08 mg KOH/g	-
Lubricity	-	Method to be Defined by CEC PF 26

Table 8   Emissions data—phase 1

	1988 U.S. Standards	Avverage of Base and Additive Groups		% Difference	Confidence Level	Avg. of Conventional + Reformulated Fuels		% Difference	Confidence Level
		Reform. Fuel (13 Sets)	Convent. Fuel (13 Sets)			Additive (6 Sets)	Base (7 Sets)		
HC Emissions, g/bhp-Hr									
Transient	1.3	0.500	0.533	-6.2	++	0.535	0.500	7.0	++
Rated		0.158	0.146	8.2	+++	0.145	0.158	-8.2	+++
90 kph Road Load		0.162	0.158	2.5	0	0.163	0.157	3.8	0
NOx Emissions, g/bhp-Hr									
Transient	10.7	4.81	4.91	-2.1	++	4.91	4.81	2.1	0
Rated		5.71	5.77	-1.0	0	5.85	5.65	3.6	0
90 kph Road Load		5.09	5.19	-1.9	+++	5.16	5.13	0.6	0
CO Emissions, g/bhp-Hr									
Transient	15.5	3.214	3.059	5.1	++	3.070	3.190	-3.8	0
Rated		0.706	0.695	1.6	0	0.681	0.717	-5.0	0
90 kph Road Load		0.630	0.677	-6.9	++	0.630	0.674	-6.5	0
PM Emissions, g/bhp-Hr									
Transient	0.6	0.334	0.442	-24.4	++++	0.380	0.390	-2.6	0
Rated		0.113	0.148	-23.6	++++	0.125	0.136	-8.1	0
90 kph Road Load		0.087	0.152	-42.8	++++	0.116	0.122	-4.9	0
Smoke Tests, % Opacity									
A - Acceleration	20	35.1	33.5	4.8	++	34.6	34.1	1.5	0
B - Lug Down	15	2.4	2.5	-4.2	0	2.5	2.5	0.0	0
C - Peak	50	64.3	61.9	3.9	++++	63.3	63.0	0.5	0
BSFC, Lb/bhp-Hr									
Rated		0.335	0.340	-1.5	+++	0.338	0.337	0.3	0
90 kph Road Load		0.332	0.337	-1.5	++++	0.334	0.336	-0.6	0
Transient		0.374	0.380	-1.6	++++	0.376	0.377	-0.3	0
Power, hp									
Rated		296	299	-1.0	++	301	296	1.7	++
Torque, Ft-Lbf									
Rated		742	749	-0.9	++	752	740	1.6	++
Cycle Work, hp-Hr		21.97	21.99	-0.1	0	22.00	21.95	0.2	0

Key to Confidence Levels:

0	>0.10
+	0.10
++	0.05
+++	0.01
++++	0.001

NOTES:

- Rated rpm = 2100
- 90 km/hr road load = 178 bhp at 1700 rpm
- Transient Emission Levels Weighted According to CFR Description, Sections 86.1330 and 86.1342
- Smoke Tests Conducted According to CRF Description, Section 86.884

Table 9 Emissions data—phase 2

	1988 U.S. Standards	Before Cleaning (4 Sets) Avg. of 2 Determinations	After Cleaning (4 Sets) Single Determination	% Difference	Confidence Level
HC Emissions, g/bhp-Hr					
Transient	1.3	0.503	0.438	-13.0	+
Rated		0.138	0.134	-3.3	0
90 kph Road Load		0.143	0.132	-7.4	0
NOx Emissions, g/bhp-Hr					
Transient	10.7	4.93	5.17	4.8	+++
Rated		5.84	6.20	6.3	+++
90 kph Road Load		5.27	5.46	3.7	+
CO Emissions, g/bhp-Hr					
Transient	15.5	3.401	3.015	-11.3	+
Rated		0.790	0.763	-3.5	0
90 kph Road Load		0.850	0.535	-37.1	++
PM Emissions, g/bhp-Hr					
Transient	0.6	0.453	0.407	-10.2	+
Rated		0.160	0.168	4.8	++
90 kph Road Load		0.159	0.130	-18.4	++
Smoke Tests, % Opacity					
A - Acceleration	20	34.3	30.7	-10.6	++++
B - Lug Down	15	2.7	2.5	-7.3	0
C - Peak	50	62.5	58.5	-6.3	+
BSFC, Lb/bhp-Hr					
Rated		0.340	0.339	-0.5	0
90 kph Road Load		0.339	0.335	-1.2	0
Transient		0.381	0.380	-0.4	0
Power, hp					
Rated		301	303	0.8	0
Torque, Ft-Lbf					
Rated		752	757	0.7	0

Key to Confidence Levels:

0	>0.10
+	0.10
++	0.05
+++	0.01
++++	0.001

NOTES:

- Rated rpm = 2100
- 90 km/hr road load = 178 bhp at 1700 rpm
- Transient Emission Levels Weighted According to CFR Description, Sections 86.1330 and 86.1342
- Smoke Tests Conducted According to CRF Description, Section 86.884